Advancing Water Distribution System Resilience: Data-Driven Failure Prediction and Large-Scale Pipeline Mechanics

by

Shih-Hung Chiu

A dissertation submitted in partial satisfaction of the

requirements for the degree of

Doctor of Philosophy

in

Engineering - Civil and Environmental Engineering

and the Designated Emphasis

in

Computational and Data Science and Engineering

in the

Graduate Division

of the

University of California, Berkeley

Committee in charge:

Professor Kenichi Soga, Chair
Professor Bin Yu
Professor Maria Laura Delle Monache

Summer 2026

Advancing Water Distribution System Resilience: Data-Driven Failure Prediction and Large-Scale Pipeline Mechanics

Copyright 2026
by
Shih-Hung Chiu

Abstract

Advancing Water Distribution System Resilience: Data-Driven Failure Prediction and Large-Scale Pipeline Mechanics

by

Shih-Hung Chiu

Doctor of Philosophy in Engineering - Civil and Environmental Engineering

and the Designated Emphasis in

Computational and Data Science and Engineering

University of California, Berkeley

Professor Kenichi Soga, Chair

Urban water distribution networks are essential to public health, economic activity, and community resilience, yet utilities must simultaneously manage aging buried assets and deploy new pipelines capable of surviving extreme environmental hazards. These challenges arise at different stages of the infrastructure life cycle and therefore require complementary approaches. Existing pipelines generally lack direct condition-monitoring systems and must be assessed using incomplete historical records, whereas newly installed systems can be evaluated through controlled experiments that reveal their structural behavior and failure mechanisms.

For existing infrastructure, conventional asset-management approaches commonly rely on pipe age and previous failures, which provide only a partial representation of deterioration. This study combined left-truncated and right-censored survival analysis with ensemble machine-learning models to identify degradation drivers and support near-term rehabilitation prioritization. Previous failure history emerged as the strongest predictor of subsequent failure, while operating pressure, pipe diameter, material, and geotechnical exposure also influenced deterioration. Material-specific analyses further showed that these relationships varied across pipe types. Tree-based machine learning models, evaluated over a defined capital-planning horizon using decision-oriented ranking metrics, outperformed the utility's existing heuristic and identified a subset of first-time failures by incorporating physical, operational, environmental, and spatial information. Spatial evaluation showed that some unpredicted failures occurred near highly ranked pipes, suggesting that pipe-level risk rankings could also support coordinated corridor- or neighborhood-scale rehabilitation planning.

For newly installed infrastructure, isolated component tests and full-scale system experiments were used to determine how hazard-resilient segmented pipelines accommodate extreme ground deformation. Tension, compression, four-point bending, and biaxial tests on ductile iron and iPVC joints showed that performance was governed primarily by localized restraint mechanics rather than nominal pipe strength alone. Locking-segment orientation, groove geometry, gasket-tooth configuration, restraint stiffness, and fitting design substantially altered joint stiffness, deformation compatibility, leakage behavior, and failure location. Small-diameter ductile iron specimens generally failed through localized bell or spigot fracture, whereas large-diameter systems were more frequently controlled by displacement or ejection of segmented locking components. The iPVC tests revealed a related trade-off between flexibility and hydraulic resilience: flexible restraints accommodated greater rotation but could permit earlier leakage, while rigid restraints maintained sealing longer but promoted abrupt pipe-wall fracture. Distributed fiber optic sensing resolved localized wedging, asymmetric restraint engagement, cross-sectional distortion, and strain redistribution that were not evident from discrete measurements alone. In the full-scale split-basin experiment, most of the imposed fault displacement was accommodated through joint movement, with deformation progressing through sequential joint activation. The system response was governed by the combined effects of longitudinal friction along the pipe barrels, localized passive resistance at enlarged bells, and restraint engagement after available joint travel was exhausted. Finite-element analyses further showed that reproducing the staged response required explicit representation of friction–displacement coupling, bell anchoring, and evolving joint kinematics.

Overall, this work establishes a life-cycle framework for improving the resilience of urban water infrastructure. For aging networks, statistically rigorous and operationally aligned models transform incomplete historical records into actionable rehabilitation priorities. For newly installed systems, continuous strain measurements and full-scale testing reveal the localized mechanics that control structural and hydraulic performance under extreme deformation. Together, these findings support a transition from reactive management based primarily on age and observed failures toward more proactive asset prioritization, joint design, and system-level resilience assessment.

To my family and friends,

For your unwavering patience, love, and support—thank you. This milestone is as much yours as it is mine.

Contents

Contents ii

List of Figures vi

List of Tables xv

1 Introduction 1
- 1.1 Research Background . . . 1
- 1.2 Research Hypothesis . . . 3
- 1.3 Research Objectives . . . 5
- 1.4 Structure of the Dissertation . . . 5

2 Network-Scale Pipe Degradation Factor Analysis 8
- 2.1 Introduction . . . 8
- 2.2 Literature Review . . . 9
- 2.3 Methodology . . . 13
  - 2.3.1 Nonparametric Estimation: Kaplan-Meier Analysis . . . 13
  - 2.3.2 Semiparametric Modeling: Cox-Proportional Hazard Model . . . 14
- 2.4 Data . . . 16
  - 2.4.1 Pipe-Intrinsic Data . . . 17
  - 2.4.2 Operational and Historical Data . . . 17
  - 2.4.3 Environmental Data . . . 18
- 2.5 Result . . . 22
  - 2.5.1 Analysis of Pipeline Longevity Patterns . . . 22
  - 2.5.2 Effects of Pipeline Degradation Factors . . . 25
  - 2.5.3 Material-Specific Effects on Pipeline Degradation . . . 27
  - 2.5.4 Sensitivity Analysis on Continuous Variables . . . 33
- 2.6 Conclusions . . . 35

3 Data-Driven Vulnerability Assessment for Aging Water Networks 37
- 3.1 Introduction . . . 37
- 3.2 Literature Review . . . 39

3.2.1 Risk-Based Rehabilitation and Asset Prioritization . . . 39
3.2.2 Physical and Statistical Pipe-Failure Models . . . 39
3.2.3 Machine Learning for Pipe-Failure Prediction . . . 40
3.2.4 Data Quality and Class Imbalance . . . 41
3.2.5 Model Transferability and Decision-Oriented Evaluation . . . 42
3.2.6 Research Gap and Contributions . . . 43
3.3 Data . . . 43
3.4 Methodology . . . 46
3.4.1 Model Training and Temporal Cross-Validation . . . 46
3.4.2 Performance Evaluation Metrics . . . 47
3.5 Results . . . 49
3.6 Discussions . . . 52
3.6.1 ML and In-House Model Predictions Evaluation . . . 52
3.6.2 Cross-Model Validation of High-Risk Asset Profiles . . . 53
3.6.3 Spatial and Temporal Analysis of False Negatives . . . 56
3.7 Conclusions . . . 60
3.8 Future Works . . . 62

4 Component-Level Experimental Framework **63**
4.1 Motivation and Failure Modes of Jointed Pipeline Components . . . 63
4.2 Prior Component-Level Testing and Research Gap . . . 66
4.3 Testing Protocols and Sensor Integration . . . 70
4.4 Definitions and Calculation Approach . . . 72
4.4.1 Joint Openings . . . 72
4.4.2 Moments . . . 72
4.4.3 Rotations . . . 73
4.5 Organization of the Component-Level Mechanics Chapters . . . 74

5 Component-Level Mechanics of ERDIP Joints **75**
5.1 Introduction of Earthquake-Resistant Ductile Iron Pipe (ERDIP) . . . 75
5.2 Tension Performance . . . 78
5.2.1 Experimental Setup and Instrumentation . . . 78
5.2.2 Failure Mode . . . 81
5.2.3 Axial Strain . . . 84
5.2.4 Hoop Strain . . . 87
5.2.5 Conclusion of ERDIP Tension Test . . . 89
5.3 Four-Point Bending Performance . . . 90
5.3.1 Four-Point Bending Test Experimental Setup and Instrumentation . . . 90
5.3.2 8-inch ERDIP Bending Performance . . . 96
5.3.3 36-inch ERDIP Bending Performance . . . 109
5.3.4 48-inch ERDIP Bending Performance . . . 120
5.3.5 Conclusion of ERDIP Bending Test . . . 131

5.4 Biaxial Tension Performance . . . 133
5.4.1 Experimental Setup and Instrumentation . . . 133
5.4.2 Failure Mode . . . 138
5.4.3 Axial Strain . . . 142
5.4.4 Hoop Strain . . . 147
5.4.5 Conclusion of ERDIP Biaxial Tension Test . . . 155
5.5 Summary and Discussions of ERDIP Experiments . . . 155
5.5.1 Performance of 8-inch ERDIP Configurations . . . 155
5.5.2 Bending Performance of Large-Diameter ERDIP . . . 157
5.5.3 Scaling Effects on Seismic Resilience . . . 157

6 Component-Level Mechanics of Alternative Ductile-Iron Joint Systems 159
6.1 High Deflection and High Pressure Restraint (HDSS) Pipe . . . 159
6.1.1 Introduction of HDSS . . . 159
6.1.2 Experimental Setup and Instrumentation . . . 161
6.1.3 Four-Point Bending Performance . . . 163
6.1.4 Conclusion of HDSS Experiment . . . 170
6.2 Hazard Resistant Ductile Iron Pipe (HRDIP) . . . 173
6.2.1 Introduction of HRDIP . . . 173
6.2.2 Experimental Setup and Instrumentation . . . 174
6.2.3 Four-Point Bending Performance . . . 179
6.2.4 Conclusion of HRDIP Experiment . . . 187

7 Component-Level Mechanics of Joints for iPVC Pipes 189
7.1 Introduction of iPVC Pipe . . . 189
7.2 Tension Performance . . . 191
7.2.1 Experimental Setup and Instrumentation . . . 191
7.2.2 Failure Mode . . . 195
7.2.3 Hoop Strain . . . 202
7.2.4 Conclusion of iPVC Tension Test . . . 204
7.3 Compression Performance . . . 206
7.3.1 Experimental Setup and Instrumentation . . . 206
7.3.2 Failure Mode . . . 209
7.3.3 Axial Strain . . . 210
7.3.4 Hoop Strain . . . 214
7.3.5 Conclusion of iPVC Compression Test . . . 216
7.4 Four-Point Bending Performance . . . 217
7.4.1 Experimental Setup and Instrumentation . . . 217
7.4.2 Failure Mode . . . 222
7.4.3 Axial Strain . . . 225
7.4.4 Hoop Strain . . . 231
7.4.5 Conclusion of iPVC Four-Point Bending Test . . . 235

7.5 Summary and Discussion of iPVC Experiments . . . 237

8 Comparative Mechanics and Seismic Design Implications 240
8.1 Overview of the Component-Level Experimental Program . . . 240
8.2 Influence of Restraint Geometry on Load Transfer Mechanisms . . . 242
8.3 Structural Capacity versus Hydraulic Resilience . . . 243
8.4 Effect of Scale and Material Stiffness on Failure . . . 244
8.5 Localization of Damage and Joint Ductility . . . 244
8.6 Implications for Seismic Pipeline Design . . . 245

9 System-Level Performance of Hazard Resilient Pipes under Large Ground Deformation 247
9.1 Introduction . . . 247
9.2 Literature Review . . . 248
9.2.1 Pipeline Response to Permanent Ground Deformation . . . 248
9.2.2 Soil–Pipeline Interaction in Segmented Systems . . . 249
9.2.3 Full-Scale Split-Basin Testing . . . 249
9.2.4 Distributed Fiber Optic Sensing for Buried Infrastructure . . . 252
9.2.5 Research Gap and Contributions . . . 252
9.3 Experimental Design . . . 253
9.3.1 Split Basin Experimental Setup . . . 253
9.3.2 Instrumentation Layout and Data Acquisition Plan . . . 254
9.3.3 Soil Property . . . 256
9.4 Definitions and Analytical Calculation Approaches . . . 257
9.4.1 Joint Kinematics and Rotations . . . 257
9.4.2 Bending Moment Approximation . . . 258
9.4.3 Segmental Lateral Displacement . . . 258
9.5 Numerical Model . . . 259
9.6 Results . . . 260
9.6.1 Ultimate Limit State and Fracture Mechanics . . . 260
9.6.2 Progressive Joint Kinematics and Sequential Mobilization . . . 262
9.6.3 Evolution of Internal Flexure and Global Deflection . . . 264
9.6.4 Axial Load Transfer and Frictional Soil Coupling . . . 271
9.6.5 Evaluation of Peak Demands and Numerical Fidelity . . . 275
9.7 Conclusion . . . 276

10 Conclusions and Future Works 280
10.1 Conclusions . . . 280
10.2 Recommendations for Future Works . . . 284

Bibliography 287

List of Figures

2.1 Water distribution network in the east bay of San Francisco Bay Area 16
2.2 Overview of pipe characteristics 19
2.3 Overview of environmental data 21
2.4 Kaplar-Meier curve for subsets of the pipe data 23
2.5 Hazard ratios from the pooled (network-wide) Cox proportional hazards model for predictors associated with pipeline failure risk. 29
2.6 Cox proportional hazard ratio on estimating variables contributing to pipeline degradation regarding different pipe materials 32
2.7 Sensitivity analysis of Hazard Ratios for continuous variables across different pipe materials. Shaded areas represent the 95% confidence intervals. 34

3.1 Cumulative gain curves comparing the predictive performance of Random Forest, XGBoost, and the in-house model (as of 2020) for a 3-year predictive horizon. The main plot illustrates global network performance, while the inset isolates the operationally constrained top 10% prioritization bandwidth. Shaded regions indicate ±1 standard deviation across the seven temporal evaluation periods. . . 49
3.2 Continuous evaluation of model performance via global Receiver Operating Characteristic (ROC) curves. Markers indicate network prioritization thresholds. . . 51
3.3 Feature importance of the models. 53
3.4 Comparative evaluation of machine learning architectures against the utility's in-house baseline model, tracking (a) the ability to predict first-time failures and (b) the prioritization agreement rate within constrained operational thresholds. . 54
3.5 Stratified catch rates at the top 3% operational intervention threshold across various physical, environmental, and historical asset categories. Results reflect a 3-year predictive horizon. 55
3.6 Distribution of caught versus missed failures (false negatives) for the Random Forest model at the top 3% operational threshold. Density and absolute failure counts are stratified across key asset attributes. 57
3.7 Historical annual failure counts across the 34-year observation window, separated by primary pipe materials. Note the accelerating trend in Asbestos Cement failures in recent years. 58

3.8 Cumulative spatial distribution of missed failures compared to a random baseline. The plot demonstrates that the vast majority of false negatives occur within a tight geographical radius of the Top-3% predicted high-risk pipes. 60

4.1 Representative plan view of a buried water-main alignment showing pipe segments, changes in alignment, tie-ins, roadway crossings, and adjacent utilities [42]. 64
4.2 Representative barrel-controlled failure modes of continuous pipelines subjected to permanent ground deformation [123] 65
4.3 Conceptual kinematic response of a segmented buried pipeline subjected to longitudinal permanent ground deformation. Relative soil movement mobilizes distributed soil–pipe resistance and produces axial tension and compression demands along the pipeline [5] 65
4.4 Representative field-observed failure modes of jointed pipeline systems subjected to earthquake-induced ground deformation: (a) tensile joint opening, (b) joint distortion and loss of hydraulic integrity, (c) compression-induced pipe-barrel tearing, and (d) localized joint shear failure [89] 67

5.1 Schematic drawing of TR-XTREME ERDIP joint [127] 76
5.2 Recommended three installation positions of ERDIP [127] 76
5.3 Spigot end locking mechanism of ERDIP tension experiment. (a) factory-manufactured weld bead. (b) Field-installed snap ring. 77
5.4 Elevation view drawing of the ERDIP tension experimental setup. 78
5.5 ERDIP tension experiment setup. 79
5.6 Wire pots installation plan of ERDIP tension experiment. 80
5.7 Fiber optic sensor installation plan of ERDIP tension experiment. 80
5.8 ERDIP tension experiment instrumentation setup. 80
5.9 ERDIP tension test result of average joint opening and water pressure 82
5.10 Failure of joint with factory-manufactured weld bead 83
5.11 Failure of joint with field-installed snap ring 83
5.12 Sketch of failure mode of the specimen with field-grooved snap ring 84
5.13 Strain distribution in the axial direction before failures (i.e., 170-kips tensile force for specimen with factory-manufactured weld bead; 180-kips tensile force for specimen with field-installed snap ring) 85
5.14 Bell deformation mechanism [32] 86
5.15 Strain distribution in the circumferential direction before failures (i.e., 170-kips tensile force for specimen with factory-manufactured weld bead; 180-kips tensile force for specimen with field-installed snap ring) 88
5.16 Sketch of squatting mechanism 89
5.17 Overview of the experimental setup of 8-inch ERDIP four-point bending test . . 91

5.18 Locking segments orientation for ERDIP 8-inch four-point bending test. 12 o'clock indicates single slot located at the crown; 9 o'clock refers to single slot positioned at the sprinline. . . . 92
5.19 Overview of the experimental setup of ERDIP four-point bending test for large-diameter pipes (48-inch ERDIP setup as an example) . . . 93
5.20 Wired pots and strain gauges plan for 8-inch ERDIP bending test . . . 94
5.21 DSS plan for 8-inch ERDIP bending test . . . 95
5.22 Wired pots plan for large-scale ERDIP bending test (use 48-inch test as example) 96
5.23 DSS plan for large-scale ERDIP bending test (use 48-inch test as example) . . . 97
5.24 Moment, rotation (joint deflection angle), and water pressure of 8-inch ERDIP four-point bending test . . . 98
5.25 Sketch of the internal joint of 8-inch ERDIP four-point bending test . . . 99
5.26 Mises stress distribution of the specimens at 11-degree deflection of 8-inch ERDIP four-point bending test. (a) Specimen-12, (b) Specimen-9 . . . 100
5.27 Failure of Specimen-12 of 8-inch ERDIP four-point bending test. (a) Bell, (b) Spigot . . . 100
5.28 Failure of Specimen-9 of 8-inch ERDIP four-point bending test. (a) Bell, (b) Spigot 101
5.29 Sketch of the failure mechanism of 8-inch ERDIP four-point bending test . . . 101
5.30 Axial strain vs. rotation (defelction angle) of Specimen-12 of 8-inch ERDIP four-point bending test . . . 102
5.31 Axial strain vs. rotation (defelction angle) of Specimen-9 of 8-inch ERDIP four-point bending test . . . 103
5.32 Axial strain distribution before failures (i.e., 12.5-degree rotation) of 8-inch ERDIP four-point bending tests . . . 104
5.33 Strain distribution in the circumferential direction of Specimen-12 under 12.5-degree rotation (defelction) condition of 8-inch ERDIP four-point bending test. (a) sensor on the bell end (b) sensor on the middle of the bell (c) sensor on 3.5-inch away from the bell face (d) sensor on the spigot about 18-inch away from the bell face . . . 106
5.34 Sketch of the mechanism of the bell and the corresponding locations of circumferential sensors. . . . 107
5.35 Strain distribution in the circumferential direction of Specimen-9 under 12.5-degree rotation (defelction) condition of 8-inch ERDIP four-point bending test. (a) sensor on the bell end (b) sensor on the middle of the bell (c) sensor on 3.5-inch away from the bell face (d) sensor on the spigot about 18-inch away from the bell face . . . 108
5.36 ERDIP 36-inch four-point bending test data (a) Force, time, and water pressure (b) Moment, rotation, and water pressure . . . 110
5.37 Aftermath of ERDIP 36-inch four-point bending test specimen. (a) No obvious crack was found. (b)(c) Locking segments (blue) locations after the experiment . 112
5.38 Cross-sectional sketch of locking segments in 36-inch ERDIP bell . . . 112
5.39 Sketch of the 36-inch ERDIP bell bending deforming mechanism . . . 113

5.40 Axial strain vs joint rotation of 36-inch ERDIP four-point bending test 114
5.41 Axial strain development of bell pipe (northside pipe) when fail (i.e., 10.25-degree HWP rotation) 116
5.42 Axial strain development of spigot (northside pipe) when fail (i.e., 10.25-degree HWP rotation) 117
5.43 Strain distribution in the circumferential direction when fail (i.e., 10.25-degree HWP rotation). (a) Sensor on the spigot (b) Sensor on the top of the inserts (c) Sensor on the centerline of the specimen (d) Sensor on the bell pipe 118
5.44 Waterfall plot of strain development of sensors on the bell 119
5.45 Data of 48-inch ERDIP four-point bending test (a) Rotation, time, and water pressure (b) Moment, rotation, and water pressure 121
5.46 Aftermath of the 48-inch ERDIP bending specimen. (a) No obvious crack was found. (b) Locking segments (blue) locations after the experiment 123
5.47 Cross-sectional sketch of locking segments in bell 123
5.48 Sketch of the bell deforming mechanism. Blue arrows indicate spigot–bell relative motion during bending; red arrows indicate axial tension induced by internal water pressure 124
5.49 Axial strain versus joint rotation based on the VWP measurement approach. The results are presented for four sequential test stages: (i) self-weight deflection, (ii) water pressurization to 75 psi, (iii) actuator loading, and (iv) water pressurization to 250 psi 125
5.50 Axial strain development of the pipe when close to failure (i.e., 6-degree VWP rotation). Note that the white spaces are the sensor gaps because of the joint or loading saddle. (a) Top (b) West (c) Bottom-west (d) Bottom-east (e) East. (a through c). 126
5.50 Axial strain development of the pipe when close to failure (i.e., 6-degree VWP rotation). (a) Top (b) West (c) Bottom-west (d) Bottom-east (e) East. Note that the white spaces are the sensor gaps because of the joint or loading saddle. (Continued: d and e) 127
5.51 Strain distribution in the circumferential direction when close to failure fail (i.e., 6-degree VWP rotation). (a) Sensor on the spigot (b) Sensor on the top of the inserts (c) Sensor on the center of the bell (d) Sensor on the edge of bell and pipe 129
5.52 Waterfall plot of strain development of sensors on the bell of 48-inch ERDIP four-point bending test 130
5.53 Sketch of the experimental setup of 8-inch ERDIP bi-axial tension test 134
5.54 Experimental setup of 8-inch ERDIP bi-axial tension test 134
5.55 Instrumentation plan of strain gauges and wired pots of the biaxial tension test 137
5.56 Instrumentation plan of DSS of the biaxial tension test. Note that blue lines indicates longitudinal Nanzee 5mm fiber optic cables and red line is the Nanzee 0.9mm fiber optic cable installed in circumferential direction 138
5.57 Failure of bell of bi-axial tension test 139

5.58 Moment and rotation results of bi-axial tension test. Note that blue line indicates Specimen-9 while black line is from Specimen-12 . . . 140
5.59 Sketch of the bell after Push Down stage of bi-axial tension test . . . 141
5.60 Axial force and average joint opening of bi-axial tension test. Note that blue line indicates Specimen-9 while black line is from Specimen-12 . . . 141
5.61 Stress distribution of the cross-section of the bell under the Pull stage of bi-axial tension test . . . 142
5.62 Axial strain vs. rotation of Specimen-9 of bi-axial tension test . . . 143
5.63 Axial strain vs. rotation of Specimen-12 of bi-axial tension test . . . 144
5.64 Strain development of bell pipe in the longitudinal direction under 8.36-degree rotation. (a) Top side of Specimen-9, (b) West side of Specimen-9, (c) Top side of Specimen-12, (d) West side of Specimen-12 . . . 145
5.65 Strain development of spigot in the longitudinal direction under 8.36-degree rotation. (a) Top side of Specimen-9, (b) West side of Specimen-9, (c) Top side of Specimen-12, (d) West side of Specimen-12 . . . 146
5.66 Strain development of bell pipe in longitudinal direction under 140 kips axial force loading condition. (a) Top side of Specimen-9, (b) West side of Specimen-9, (c) Top side of Specimen-12, (d) West side of Specimen-12 . . . 147
5.67 Strain development of spigot in longitudinal direction under 140 kips axial force loading condition. (a) Top side of Specimen-9, (b) West side of Specimen-9, (c) Top side of Specimen-12, (d) West side of Specimen-12 . . . 148
5.68 Hoop strain vs. rotation of Specimen-9 of bi-axial tension test . . . 149
5.69 Hoop strain vs. rotation of Specimen-12 of bi-axial tension test . . . 150
5.70 Strain distribution in the circumferential direction of Specimen-9 under 8.3-degree rotation condition. (a) sensor on the bell pipe (b) sensor at the mid location of the bell (c) sensor on top of the locking segments on the bell (d) sensor on the spigot . . . 151
5.71 Strain distribution in circumferential direction under Specimen-12 under 8.3-degree rotation condition. (a) sensor on the bell pipe (b) sensor at the mid location of the bell (c) sensor on top of the locking segments on the bell (d) sensor on the spigot . . . 152
5.72 Joint deformed mechanism in Push Down stage of bi-axial tension test . . . 152
5.73 Strain distribution in the circumferential direction of Specimen-9 under 140 kips loading condition. (a) sensor on the bell pipe (b) sensor at the mid location of the bell (c) sensor on top of the locking segments on the bell (d) sensor on the spigot . . . 153
5.74 Strain distribution in the circumferential direction of Specimen-12 under 140 kips loading condition. (a) sensor on the bell pipe (b) sensor at the mid location of the bell (c) sensor on top of the locking segments on the bell (d) sensor on the spigot . . . 154

6.1 Photo of HDSS bell pipe and spigot . . . 160

6.2 Schematic of the joint of HDSS pipe [126] . . . 160
6.3 Elevation view drawing of the HDSS four-point bending experimental setup . . . 161
6.4 Front view (north side on the left) of the HDSS four-point bending test setup. Note that the actuator was used for the first test while the hydraulic cylinders were used for the second test. . . . 162
6.5 HDSS four-point bending test position transducers setup . . . 163
6.6 HDSS four-point bending test DSS instrumentation plan . . . 164
6.7 Experimental results of HDSS four-point bending experiment. (a) Force and vertical displacement. (b) Moment and rotation. . . . 165
6.8 Joint failure of HDSS four-point bending test (a) West side (b) East side. . . . 166
6.9 Axial strain vs joint rotation of HDSS four-point bending test. Note that the lighter colors indicate the results from test 1 and the more vibrant colors indicate the results from test 2. . . . 167
6.10 Axial strain development of bell pipe (northside pipe) of HDSS four-point bending test under 4.0-degree deflection condition (before failure). . . . 168
6.11 Axial strain development of spigot (southside pipe) of HDSS four-point bending test under 4.0-degree deflection condition (before failure). . . . 169
6.12 Strain distribution in the circumferential direction under 4.0-degree deflection condition of HDSS four-point bending test. (a) sensor on the spigot (b) sensor on the top of the inserts (c) sensor on the centerline of the specimen (d) sensor on the bell pipe. . . . 171
6.13 Sketch of the bell deforming mechanism of HDSS four-point bending test. . . . 172
6.14 Sketch of the locking segment moving mechanism of HDSS pipe. As the spigot squatt, the locking segments tend to separate and move upward. . . . 172
6.15 Schematic of the bell of Kubota NS-type ductile iron pipe. . . . 175
6.16 HRDIP bell setup . . . 176
6.17 HRDIP four-point bending experimental setup design . . . 176
6.18 HRDIP setup overview . . . 177
6.19 HRDIP four-point bending experiment strain gauge, wire pots, and position transducer instrumentation plan . . . 178
6.20 HRDIP four-point bending experiment DFOS instrumentation plan . . . 178
6.21 Moment, rotation, and water pressure of HRDIP four-point bending experiment 179
6.22 Large deformation and failure of HRDIP . . . 180
6.23 Falure of the gland and bolt of HRDIP . . . 181
6.24 Spigot failure of HRDIP test . . . 181
6.25 Axial strain and joint rotation of HRDIP four-point bending experiment . . . 182
6.26 Axial strain development of bell pipe under 19-degree rotation condition of HRDIP four-point bending test. (a) East side, (b) Top side, (c) West side, (d) Bottom side 183
6.27 Axial strain development of spigot under 19-degree rotation condition of HRDIP four-point bending test. (a) East side, (b) Top side, (c) West side, (d) Bottom side 185
6.28 Hoop strain and joint rotation of HRDIP four-point bending experiment . . . 186

6.29 Strain distribution in the circumferential direction under 19-degree rotation condition of HRDIP four-point bending test. (a) sensor on the bell end (b) sensor on the center of the bell (c) sensor on the centerline of the specimen (d) sensor on the spigot . . . 188

7.1 Experimental test setups for the jointed pipes equipped with different fittings and restraints . . . 190
7.2 Gaskets for the plastic fittings . . . 191
7.3 Schematic drawing of the iPVC tension test experimental setup . . . 192
7.4 Complete assembled iPVC tension test setup . . . 192
7.5 Position transducers for displacement monitoring of the joint of the iPVC tension test . . . 194
7.6 Instrumentation plan of fiber optic sensors of the iPVC tension test specimens . 194
7.7 Axial force, average joint opening, and water pressure results of the specimens. Note that iPVC8-T1 indicates Specimen-R while iPVC8-T2 is Specimen-T . . . 195
7.8 Failure of Specimen-R and -T of iPVC tension test . . . 197
7.9 Axial strain vs load of iPVC tension test. (Left) South pipe. (Right) North Pipe 198
7.10 Sketch of pipe-fitting deformation mechanism . . . 199
7.11 Axial strain development along pipes of Specimen-R under 32,000-LBS axial loading condition. (a) Top, (b) West side, (c) Bottom, (d) East side . . . 200
7.12 Axial strain development along pipes of Specimen-T under 11,500-LBS axial loading condition. (a) Top, (b) West side, (c) Bottom, (d) East side . . . 201
7.13 Strain distribution in the circumferential direction of Specimen-R under 32,000-LBS loading condition . . . 203
7.14 Sketch of the fitting deformation under axial force . . . 204
7.15 Strain distribution in the circumferential direction of Specimen-T under 11,500-LBS loading condition . . . 205
7.16 Drawing of the iPVC compression test experimental setup . . . 207
7.17 Completely assembled iPVC compression test setup . . . 208
7.18 Position transducers for displacement monitoring of the joint of the iPVC compression test . . . 208
7.19 Instrumentation plan of fiber optic sensors of the iPVC compression test specimens 209
7.20 Force versus average joint closing for the sleeve with Reiberlok gasket of iPVC compression test . . . 210
7.21 Failure of the iPVC compression test specimen . . . 211
7.22 Axial strain vs load of iPVC compression test. (Left) East pipe. (Right) West Pipe 212
7.23 Axial strain development of the iPVC compression specimen under 70,000-LBS axial loading condition. (a) Top, (b) South, (c) Bottom, (d) North . . . 213
7.24 Strain distribution in the circumferential direction of the Specimen under 32,000-LBS loading condition . . . 215
7.25 Sketch of fitting deformed mechanism . . . 216
7.26 Schematic drawing of the iPVC four-point bending experimental setup . . . 217

7.27 Experimental setup of iPVC four-point bending test (Specimen-EBAA as example) 218
7.28 Position transducers for displacement monitoring of Specimen-EBAA 219
7.29 Position transducers for displacement monitoring of Specimen-RCT 220
7.30 Position transducers for displacement monitoring of specimen-RL 220
7.31 DSS plan for Specimen-EBAA 221
7.32 DSS plan for Specimen-RCT 221
7.33 DSS plan for specimen-RL 221
7.34 Moment, rotation, and water pressure of the tests 223
7.35 Large deformation of Specimen-EBAA. Note that no structural failure was found 224
7.36 Large deformation and failure of Specimen-RCT 225
7.37 Large deformation of Specimen-RL and failure mode 226
7.38 Axial strain and joint rotation of Specimen-EBAA. West pipe on the left and East pipe on the right 227
7.39 Axial strain and joint rotation of Specimen-RCT. West pipe on the left and East pipe on the right 228
7.40 Axial strain and joint rotation of Specimen-RL. West pipe on the left and East pipe on the right 229
7.41 Axial strain development under 18-degree rotation condition across all specimens 230
7.42 Strain distribution in the circumferential direction of Specimen-EBAA under 18-degree rotation condition. (a) Sensor F3 (b) Sensor F4 (c) Sensor F5 (d) Sensor F6 232
7.43 Sketch of EBAA 1900 restraint deformation mechanism 233
7.44 Strain distribution in the circumferential direction of Specimen-RCT under 18-degree rotation condition. (a) Sensor F3 (b) Sensor F4 (c) Sensor F5 (d) Sensor F6 234
7.45 Sketch of stress concentration at the boundary of pipe and RCT restraint of Specimen-RCT 235
7.46 Strain distribution in the circumferential direction of Specimen-RL under 18-degree rotation condition. (a) Sensor F3 (b) Sensor F4 (c) Sensor F5 (d) Sensor F8 236
7.47 Sketch of fitting deformed mechanism of Specimen-RL 237

9.1 Plan view of the split-basin experimental setup configured for a 50-degree strike-slip fault simulation. The apparatus utilizes three hydraulic actuators to drive the moving box relative to the fixed box. The testing array comprises five ERDIP segments, with the central two joints initially set to a fully inserted state and the outer two joints positioned at mid-extension. Local component labels for all pipe segments and joint assemblies is indicated. 254

9.2 Experiment and instrumentation setups. (a) Plan view of the split-basin testing apparatus configured with a 5-foot (1.5-meter) total soil profile. The ERDIP system is positioned on a 1-foot (0.3-meter) compacted soil bedding and overlain by 3 feet (1.0 meter) of soil backfill. (b) Installation of position transducer and DSS at joints (Joint 4 for example). 255
9.3 Instrumentation plan for the split-basin fault rupture test. The wire potentiometers (WPs, marked in orange) are deployed to monitor localized joint rotations. Each monitoring array comprises four sensors mounted at 90-degree intervals around the spigot circumference with their target anchors secured directly to the adjacent bell face. Longitudinal fibers (marked in blue) are oriented along the crown (0°), springlines (90°, 270°), and oblique axes (135°, 215°) to capture primary flexural and axial strain gradients. 256
9.4 Schematic representation of the buried jointed pipeline system. 260
9.5 Aftermath of pipe specimens where joint structural failure happened at Joint 4. (a) Crack started at the wall thickness transition region, single slot and locking segment boundary. (b) Crack initiated from bell face and propagated throughout the bell casing. 262
9.6 Joint rotation and fault displacement. (a) In-plane joint rotation and fault displacement. (b) Out-of-plane joint rotation and fault displacement. 265
9.7 Moment distribution on the specimen at multiple fault displacement conditions. Simulation 1 utilizes a conventional framework that omits friction-displacement coupling at the soil-pipe interface and localized joint anchoring, whereas Simulation 2 explicitly incorporates these complex interaction mechanics. 266
9.8 Progressive schematic of pipeline kinematics and moment-induced deformations under fault rupture. (Continued on next page.) 268
9.8 Progressive schematic of pipeline kinematics and moment-induced deformations under fault rupture. Note: Deformations are exaggerated for illustrative purposes. 269
9.9 Lateral displacement along pipe. 270
9.10 Axial force distribution at multiple fault displacement condition. 273
9.11 Evolution of axial force along the middle pipe section (Pipe M) under progressive fault displacements. The shaded regions indicate the analytical domains-corresponding to 10–40% and 60–90% of the pipe length-where linear regression (dashed lines) was applied to the force profiles. The slopes of these regressions (dF/dx) represent the interfacial soil friction per unit length. 274
9.12 Comparison of peak kinematic and structural responses between the large-scale experiment and FEM predictions across progressive fault displacements. 277

List of Tables

2.1 Hazard ratios (HR) with 95% confidence intervals (CI) and p-values from the pooled Cox proportional hazards model (all materials combined). 28
2.2 Hazard ratios (HR) with 95% confidence intervals (CI) from material-specific Cox proportional hazards models. 33

3.1 Pipeline inventory and historical failures (1990–2024) 44
3.2 Predictive model features and attribute descriptions 45
3.3 Predictive model catch rate summary (3-year horizon) 50

4.1 Representative component-level studies of hazard-resilient pipeline joints 69
4.2 Summary of the experimental testing matrix 71
4.3 Characteristics of selected NanZee strain sensor cables 71

5.1 Summary of 8-inch ERDIP tension test results. WB indicates specimen with factory-manufactured weld bead and HDSS indicates the specimen with field-installed HDSS snap ring. 81
5.2 Summary of 8-inch ERDIP four-point bending test specimens and configurations 91
5.3 Summary of maximum moment and rotation for 8-inch ERDIP bending specimens 97
5.4 Summary of failure metrics for 36-inch ERDIP bending specimen 111
5.5 Summary of failure metrics for 48-inch ERDIP bending specimen 122
5.6 Summary of experimental rotational capacities and failure mechanisms across ERDIP diameters 132
5.7 Summary of test schedule and specimen configurations for combined loading tests 135
5.8 Summary of testing phases, loading conditions, and structural boundary conditions 136
5.9 Summary of ultimate limit states for 8-inch ERDIP combined loading tests . . . 142
5.10 Summary of experimental results across various testing configurations of 8-inch ERDIP tests 156

6.1 Summary of four-point bending test terminations 162
6.2 Summary of HDSS four-point bending test results 165

7.1 Summary of iPVC tension test specimens 193
7.2 Summary of iPVC tension test results 196
7.3 Summary of iPVC four-point bending test log 219

7.4 Summary of four-Point bending test results 224

8.1 Summary of the component-level experimental programs and principal findings. 241

9.1 Representative Cornell full-scale split-basin pipeline tests. 251
9.2 Calibrated soil and structural parameters used in the numerical simulations . . . 261
9.3 Maximum joint rotations and sign conventions. In-plane: + bends toward the north side, − toward the south. Out-of-plane: + bends upward, − downward. . 264
9.4 Friction estimates at each fault displacement 272

Acknowledgments

First and foremost, I would like to express my deepest gratitude to my advisor, Professor Kenichi Soga, for your unwavering mentorship, encouragement, and support throughout my doctoral studies. I am deeply thankful for your patience, kindness, and belief in me. Thank you for being an incredible advisor and for the many opportunities you gave me to broaden my perspective and grow as an independent researcher.

I am also sincerely grateful to the members of my qualifying examination and dissertation committees—Professors Bin Yu, Maria Laura Delle Monache, and Dimitrios Zekkos—for your time, thoughtful feedback, and valuable guidance. Your insightful questions and constructive comments helped strengthen both my research and this dissertation.

I would also like to extend my sincere thanks to my colleague Maksymilian Jasiak for your generous support, from brainstorming research ideas to conducting experiments and solving complex on-site challenges. I am deeply appreciative of Tianyu Han, Dr. Chien-Chih Wang, and Dr. Yaobin Yang for your invaluable contributions to numerous fiber optic projects. Your insightful discussions and troubleshooting skills truly made the impossible possible. Special thanks to Dr. Qinglai Zhang for our outstanding collaboration spanning experimental investigations and finite element modeling. My research would not have been nearly as complete without your support. I am also grateful to Professor Wonjun Cha and Professor Dayu Apoji for our regular meetings and the valuable guidance you consistently provided. Finally, I would like to acknowledge our dedicated laboratory technicians, Shakhzod Takhirov, Irik Larson, Philip Wong, and John Kochan. My experimental work simply could not have been completed without your expertise and support.

This research would not have been possible without the invaluable support of Clifford Chan, Carlton Chan, David Katzev, Dustin La Vallee, Karen Lee, Pongsiri (Eng) Prachyaratanawooti, and Tara Sweet of the East Bay Municipal Utility District, as well as Khadija Durbas of the Los Angeles Department of Water and Power. I am sincerely grateful for the practical engineering insights and expertise you shared throughout our discussions. Your collaboration ensured that this research remained grounded in real-world challenges and relevant to engineering practice.

I would like to express my deepest gratitude to my family, whose unwavering love and support have been a constant source of strength throughout my doctoral journey. To my parents, thank you for your unconditional love and for encouraging me to pursue a Ph.D. Your steadfast belief in me has sustained me through every challenge and milestone along the way. To my brother, thank you for being a reliable anchor for our family during my time at Berkeley.

Lastly, I want to thank all the friends I have made throughout my Ph.D. journey. The hours we spent together after work were essential in re-energizing me and giving me the motivation to persevere. Thank you all for making this chapter of my life so memorable.

Chapter 1

Introduction

1.1 Research Background

Water distribution networks (WDNs) are among the most critical components of urban infrastructure, providing safe and reliable drinking water while supporting public health, fire protection, and economic development. However, many developed countries are facing the severe challenge of aging underground water infrastructure. Large portions of existing pipeline networks were installed more than a century ago and are now operating well beyond their designed service life. Consequently, water utilities experience hundreds of thousands of water main failures annually, resulting in significant water loss, costly emergency repairs, service interruptions, and social and economic consequences [54, 74, 63, 6]. These challenges are further intensified by the immense capital costs of infrastructure renewal. Although pipeline replacement and rehabilitation frequently consume the vast majority of a water utility's Capital Improvement Program (CIP) budget, the sheer expense of underground construction typically restricts utilities to replacing 1% (100-year replacement cycle) or less of their pipeline inventory each year [63, 6]. As a result, effective and proactive asset management has become one of the foremost priorities for water utilities.

Addressing this infrastructure challenge requires a dual approach because the engineering needs of legacy infrastructure differ fundamentally from those of the modern systems being designed to replace it. For existing buried pipelines, the primary challenge is predictive asset management. Since these assets were installed long before structural monitoring technologies became available, utilities must infer their condition from historical records rather than direct observation. In practice, rehabilitation decisions are commonly guided by heuristic risk-scoring systems based primarily on pipe age and historical failure records [140, 52, 110]. Although these approaches are straightforward to implement, they often create a reactive management cycle by repeatedly prioritizing assets that have already failed while overlooking vulnerable pipes that have yet to experience their first failure.

Extensive post-failure investigations and laboratory studies have shown that pipeline deterioration is governed by a complex interaction among material properties, environmental

conditions, and operational loading [101, 64, 11, 130, 78, 50]. While these forensic studies provide valuable mechanistic insight into localized failure processes, they are inherently limited in their ability to explain deterioration across an entire water distribution network. In contrast, historical utility databases contain decades of accumulated information describing how diverse combinations of soil conditions, traffic loading, pipe characteristics, and operational stresses influence the deterioration of thousands of individual assets. Extracting these relationships from large-scale historical datasets provides an opportunity to bridge the gap between physical deterioration mechanisms and network-scale asset management. Such data-driven approaches enable utilities to move beyond static heuristic models toward proactive rehabilitation strategies based on quantified pipeline deterioration behavior.

Building upon this understanding of degradation mechanisms, the next challenge is to predict which individual pipeline segments are most likely to fail within a practical planning horizon. Recent advances in machine learning have improved the ability to model complex nonlinear relationships in infrastructure datasets; however, a disconnect often remains between academic model development and utility practice. Predictive models are frequently evaluated using global statistical metrics that measure overall classification performance across an entire dataset. Because pipeline failures represent only a small fraction of the total asset population, a model can achieve excellent global accuracy while failing to identify the relatively few pipes that are actually at imminent risk of failure. Although statistically acceptable, such models provide limited value for infrastructure management.

In practice, water utilities operate under constrained CIP budgets that typically support rehabilitation planning over three- to five-year investment cycles. Within each planning period, only a small percentage of the highest-risk pipeline inventory can realistically be replaced. Consequently, predictive models should be formulated around practical utility planning horizons and evaluated according to their ability to accurately prioritize the limited number of assets that are most likely to fail within available rehabilitation budgets. Aligning predictive analytics with operational decision-making transforms machine learning from a purely statistical exercise into a practical decision-support tool capable of preventing costly pipeline failures and improving long-term asset management.

Conversely, for newly installed pipelines and future network expansions, the engineering challenge shifts from predicting age-related degradation to ensuring structural resilience against extreme geohazards. Earthquake-induced permanent ground deformation (PGD) has repeatedly caused catastrophic pipeline failures during major seismic events, severing critical lifelines when they are needed most [84, 83, 122, 53, 132]. To mitigate this vulnerability, modern pipeline design has moved away from continuous, rigid barrels toward highly engineered, hazard-resilient segmented systems capable of accommodating massive soil displacements through complex joint kinematics [4, 91, 93, 104]. However, a critical research gap remains in quantifying the actual mechanical performance and progressive deformation of these joints under severe loading. Traditional discrete instrumentation (e.g., localized strain gauges) is inherently insufficient for this task; it often misses localized strain peaks and fails to capture the continuous deformation profiles required to validate true joint mechanisms. By integrating advances in experimental sensing technologies, particularly Dis-

tributed Fiber Optic Sensing (DFOS), into pipe component experiments, researchers can capture continuous high-resolution strain patterns to definitively understand the kinematic evolution and structural limits of these segmented joints [47, 111, 114, 21].

While component-level testing successfully establishes the ultimate capacity of isolated connections, engineers must also understand the integrated mechanical behavior of these systems under soil-structure interactions. In the field, surrounding soil confinement fundamentally alters load transfer across the pipeline assembly. Therefore, transitioning to system-scale physical testing, specifically large-scale split-basin fault rupture experiment, is necessary to bridge this gap. In these laboratory settings, continuous strain measurements obtained through DFOS enable the precise observation of macroscopic soil-pipe anchoring and distinct, highly localized failure mechanisms. Furthermore, by synthesizing the high-resolution strain profiles obtained from both the isolated component tests and these full-scale system experiments, researchers can rigorously calibrate advanced numerical models. This empirical calibration is critical for evaluating how specific modeling assumptions impact predictive accuracy, ultimately establishing a validated finite element framework capable of supporting extensive future parametric studies. Looking forward, this continuous sensing technology extends beyond experimental validation; DFOS can be directly embedded into newly installed pipelines at critical fault crossings to continuously monitor their dynamic strain responses in the field, paving the way for truly smart, self-reporting water infrastructure [3].

Recognizing these complementary challenges, this dissertation integrates data-driven infrastructure analytics with experimental structural mechanics to provide a comprehensive life-cycle perspective on pipeline resilience. The research begins by developing statistical and machine learning frameworks to predict and understand deterioration drivers for existing, unmonitored networks using historical utility data. This macro-scale assessment then informs a transition to experimental structural mechanics, which evaluates the performance of newly installed, hazard-resilient systems through a two-tiered physical approach: first, by benchmarking isolated component-level joint kinematics, and subsequently, by evaluating the integrated system-level survivability of the pipeline assembly under simulated permanent ground deformation. Collectively, this research bridges the gap between the reactive management of our aging past and the proactive, data-informed design of our resilient future.

1.2 Research Hypothesis

This dissertation is founded on the premise that improving the reliability and resilience of water distribution infrastructure requires different but complementary engineering approaches for existing and newly installed pipeline systems. Existing buried pipelines must be managed using historical asset information because direct structural monitoring is generally unavailable, whereas newly installed pipelines provide opportunities to improve structural resilience through enhanced design, experimental validation, and integrated sensing technologies. Guided by this life-cycle perspective, the following research hypotheses are

proposed:

- **Pipeline deterioration is driven by multifactorial stress interactions, not just asset age**

  While conventional heuristic methods rely heavily on age and historical breaks, true degradation is dictated by the complex interplay of material properties, environmental conditions, and operational stressors. Quantifying these interactions using statistically rigorous data-driven approaches provides a more reliable basis for deterioration assessment than conventional heuristic asset management methods.

- **Actionable pipeline failure prediction requires alignment with utility operational practice**

  Global statistical accuracy metrics is often insufficient for infrastructure datasets where failures represent an extreme minority, as a model can achieve high accuracy by primarily predicting stable performance. By aligning machine learning models with realistic planning horizons and rehabilitation budget constraints enables more effective identification and prioritization of vulnerable pipeline assets.

- **Continuous spatial monitoring is essential to resolve highly localized joint kinematics**

  Because conventional discrete point sensors inherently obscure highly localized strain peaks, continuous spatial observation is necessary to accurately resolve the complex deformation mechanics and ultimate performance limits of emerging segmented pipeline architectures.

- **System-level pipeline resilience relies on integrated multi-joint mechanics and soil-pipe interaction**

  While component-level testing establishes baseline mechanical capacities, it cannot account for surrounding soil confinement or the progressive joint kinematics of a full assembly. Consequently, system-scale physical validation, in addition to component testing, is required to capture how loads actively propagate across the pipeline network, revealing true macroscopic failure modes and providing the empirical data necessary to accurately calibrate predictive numerical models.

- **Unifying network-scale analytics with asset-scale mechanics enables resilient life-cycle management**

  Improving urban water security requires bridging the gap between aging legacy systems and future installations. Integrating data-driven prioritization frameworks for existing, unmonitored networks with experimentally validated mechanical designs and embeddable continuous sensing strategies for new pipelines provides a comprehensive, proactive blueprint for sustainable infrastructure management.

1.3 Research Objectives

To test these hypotheses, the objective of this dissertation is to develop integrated methodologies that improve both the operational management of existing networks and the structural design of new pipelines. To accomplish this, the research pursues the following specific objectives:

- **Quantify complex pipeline deterioration drivers**

  Formulate a semi-parametric survival analysis framework utilizing a spatially integrated, 150-year infrastructure dataset to isolate the relative physical, operational, and environmental stressors driving pipeline degradation.

- **Develop an operationally aligned predictive data-driven framework**

  Design and evaluate ensemble data-driven models tailored to the practical financial realities of utility management, optimizing predictive performance for short-term capital improvement planning horizons (e.g., 3-year cycles) and highly constrained rehabilitation budgets (e.g., 100-year replacement rate).

- **Characterize the joint component structural limits of hazard-resilient pipes**

  Systematically benchmark the ultimate performance limit states, complex joint kinematics, and localized structural vulnerabilities of emerging segmented pipeline architectures through rigorous physical testing equipped with high-resolution DFOS.

- **Evaluate the integrated, system-level response of multi-segment pipelines under large ground deformation**

  Execute large-scale split-basin fault rupture experiments on a multi-joint pipeline assembly. By integrating DFOS with finite element methods (FEM), this work dissects the system-level response of buried pipelines into the underlying soil–pipe interaction mechanisms and identifies the fundamental processes governing localized joint failure.

1.4 Structure of the Dissertation

This dissertation is organized into ten chapters, conceptually divided into two primary themes: the data-driven assessment of existing pipeline networks (Chapters 2 and 3) and the physical mechanical evaluation of newly installed hazard-resilient systems (Chapters 4 through 9):

- **Chapter 1: Introduction**

  Presents the research background, identifies the knowledge gaps concerning existing unmonitored networks and new resilient pipeline design, states the research hypotheses and objectives, and outlines the organization of the dissertation.

- **Chapter 2: Network-Scale Pipe Degradation Factor Analysis**

  Develops a survival-analysis framework to investigate long-term pipeline deterioration using a 150-year dataset from an urban water utility. Kaplan–Meier estimators and Cox proportional hazards (Cox-PH) models are employed to quantify the effects of physical, environmental, and operational factors on pipeline failure.

- **Chapter 3: Data-Driven Vulnerability Assessment for Aging Water Networks**

  Presents a data-driven framework for predicting short-term pipeline failures using Random Forest and XGBoost models. The framework is designed around practical capital improvement planning horizons and evaluated using ranking-based metrics that reflect realistic rehabilitation budget constraints.

- **Chapter 4: Component-Level Experimental Framework**

  Establishes the motivation, definitions, and analytical calculation approaches for evaluating jointed pipeline components, alongside the integration of distributed fiber optic sensing (DFOS) into the experimental testing protocols.

- **Chapter 5: Component-Level Mechanics of ERDIP Joints**

  Experimentally evaluates the structural behavior of US Pipe TR-XTREME Earthquake Resistant Ductile Iron Pipe (ERDIP). Tests are analyzed across multiple pipe diameters to characterize failure modes, strain development, and load transfer.

- **Chapter 6: Component-Level Mechanics of Alternative Ductile-Iron Joint Systems**

  Expands the component-level investigation to evaluate the mechanics and high-deflection performance of alternative geometries, specifically focusing on HDSS and Kubota HRDIP ductile iron joint systems under four-point bending.

- **Chapter 7: Component-Level Mechanics of Joints for iPVC Pipes**

  Investigates the tension, compression, and bending performance of iPVC systems, characterizing polymer-specific failure modes and providing a comparative counterpart to the ductile iron investigations.

- **Chapter 8: Comparative Mechanics and Seismic Design Implications**

  Synthesizes the component-level findings to evaluate the influence of restraint geometry, scale, and material stiffness on load transfer and structural capacity, detailing broader implications for seismic pipeline design.

- **Chapter 9: System-Level Performance of Hazard Resilient Pipes under Large Ground Deformation**

Investigates the system-level behavior of segmented pipelines subjected to simulated fault rupture through large-scale split-basin testing. DFOS and FEM simulations are integrated to evaluate soil–pipeline interaction, progressive joint kinematics, and sequential mobilization.

- **Chapter 10: Conclusions and Future Works**

  Summarizes the principal findings of the dissertation, discusses the limitations of the present study, and provides recommendations for future research.

Chapter 2

Network-Scale Pipe Degradation Factor Analysis

2.1 Introduction

Aging water infrastructure presents a growing financial, operational, and public-health challenge for developed cities, many of which continue to operate pipes installed more than a century ago. In the United States, an estimated 240,000 to 300,000 water main breaks occur annually, resulting in the loss of more than 2 trillion gallons of treated water and approximately $2.6 billion in repair and replacement costs [54, 74]. Beyond these direct costs, pipe failures disrupt service, damage surrounding infrastructure, increase water losses, and create potential contamination pathways. Understanding the mechanisms that govern pipeline deterioration is therefore essential for maintaining system reliability and prioritizing limited infrastructure investments.

Pipeline failure is not governed by chronological age alone. Vulnerability reflects the combined influence of material, geometry, operating conditions, installation history, soil environment, geospatial hazards, and external loading. Consequently, pipes of similar age and material may exhibit substantially different service lives. This heterogeneity limits the effectiveness of age-based replacement strategies and makes it difficult to identify assets that are deteriorating before their first recorded failure. Despite this complexity, many utilities rely on simplified scoring systems in which risk is calculated from a weighted combination of a few attributes, often dominated by previous failure history and pipe age. Although these models are easy to implement, their weights are frequently based on expert judgment or institutional experience rather than statistically estimated relationships. As a result, they may identify assets with known problems but provide limited insight into previously unfailed pipes exposed to unfavorable physical, operational, or environmental conditions.

This study addresses these limitations using a large, spatially resolved dataset from an urban water utility in the San Francisco Bay Area. The dataset combines nearly 150 years of pipe installation history, beginning in the 1870s, with documented water-main failures

from 1990 through 2022. Physical, operational, and environmental attributes are linked at the individual pipe-segment level, enabling deterioration patterns to be examined across materials, installation periods, operating conditions, and environmental exposures.

Historical utility records present important statistical challenges because the observation period is much shorter than the service history of many assets. Older pipes may have been installed decades before systematic failure records began, leaving their early failure histories unobserved. These assets are subject to left truncation, or delayed entry, because they are included only after surviving to the observation window. Pipes that remain operational at the end of the study are right censored because their eventual failure times are unknown. Ignoring these features can introduce survivorship bias and distort estimates of infrastructure vulnerability [68, 109].

To address these challenges, the study applies two complementary survival-analysis methods. Kaplan–Meier (KM) curves provide non-parametric comparisons of survival behavior across pipe characteristics such as material, diameter, pressure, and environmental exposure [57]. Cox proportional hazards (Cox-PH) models then estimate the relative effects of multiple degradation factors while incorporating delayed entry and right censoring [38]. This multivariable framework makes it possible to determine whether observed relationships remain important after accounting for correlated pipe characteristics.

The objective is to identify and quantify the physical, operational, and environmental factors associated with long-term deterioration. Particular attention is given to distinguishing network-wide degradation drivers from material-specific effects. By replacing heuristic weights with statistically derived estimates of relative failure hazard, the study provides an empirical foundation for future failure prediction, risk-based replacement planning, and long-term infrastructure management.

2.2 Literature Review

Pipeline deterioration is influenced by interacting physical, operational, environmental, and historical factors. Characteristics such as pipe material, age, length, diameter, and operating pressure are commonly used as indicators of failure susceptibility because they are generally available in utility asset databases and can be linked to individual pipe segments [140, 52, 110]. Although chronological age is frequently used as a proxy for condition, it represents exposure duration rather than a direct measurement of remaining structural capacity. Reviews of statistical and physically based deterioration models have shown that pipes of similar age can exhibit different performance because of differences in material properties, manufacturing and installation quality, operational loading, maintenance history, and environmental exposure [64, 110].

Pipe material strongly influences both the dominant deterioration mechanism and the response to applied loads. Metallic pipes may experience internal and external corrosion, graphitization, localized pitting, cracking, and joint deterioration. Investigations of cast iron pipe failures have shown that structural performance depends on the combined effects of

corrosion, manufacturing characteristics, defects, and loading conditions [72]. Mechanistic and reliability-based models have consequently examined how corrosion growth reduces the residual strength and estimated service life of cast iron water mains [103, 77]. Asbestos cement pipes are affected by a distinct combination of chemical and mechanical deterioration processes. Hu and Hubble identified age, diameter, climate, clay soils, construction and maintenance practices as factors associated with asbestos cement pipe deterioration, together with possible chemical attack from conveyed water and soil pore water [49]. Laboratory and material-characterization studies have also documented calcium leaching, mineralogical changes, and progressive weakening of the cementitious matrix in aged asbestos cement pipes [142]. Together, these findings show that the mechanisms and relative importance of deterioration factors can differ substantially among pipe materials.

Geometric characteristics also influence pipeline performance. Pipe diameter is associated with wall thickness, stiffness, material type, hydraulic function, and historical manufacturing standards, making its independent effect difficult to isolate. Studies of cast iron pipes have linked corrosion-induced section loss and structural resistance to pipe geometry and wall thickness [103, 72]. Pipe length is likewise relevant because longer segments provide greater exposure to localized defects and adverse environmental conditions. Andreou et al. incorporated age, length, diameter, pressure, and previous failure history into an individual-pipe survival framework and showed that the factors associated with failure varied according to the pipe's deterioration stage and prior break history [1]. Their work demonstrated the value of modeling pipe characteristics jointly rather than interpreting geometric variables as isolated indicators of failure.

Operational pressure represents another widely studied factor. Internal pressure generates circumferential and longitudinal stresses and may contribute to failure when pipe strength has been reduced by corrosion, cracking, joint deterioration, or other damage. Empirical studies have reported associations between pressure conditions and water-main break occurrence, while also showing that pressure-related effects may vary spatially and among pipe materials [73, 52, 70]. These findings indicate that pressure should be evaluated together with pipe material and structural condition rather than treated as an isolated predictor.

Previous failure history has also been incorporated into many deterioration and asset-management models. Earlier proportional-hazards studies included prior breaks as predictors of subsequent failure behavior [1]. Statistical and neurofuzzy approaches have similarly used failure history alongside attributes such as material, age, and diameter when evaluating pipe condition and maintenance priorities [37]. Although prior failures can provide valuable information about asset vulnerability, models that depend strongly on recorded break history may provide less information about pipes that have not yet experienced a documented failure.

Environmental conditions can further differentiate the performance of pipes with otherwise similar physical characteristics. Soil properties affect both the mechanical support of buried pipes and the electrochemical environment surrounding metallic infrastructure. Soil moisture, resistivity, pH, aeration, dissolved ions, and microbial activity have been identified as factors influencing corrosion potential, while soil texture affects drainage, moisture retention, oxygen transport, and electrolyte conductivity [130, 78]. Variations in soil stiffness,

compaction, and moisture may also contribute to settlement, shrink–swell deformation, and loss of bedding support. Pipe–soil interaction studies have demonstrated that these processes can generate bending stresses, joint movement, and localized structural demands [101, 64].

Geospatial hazards impose additional demands on buried pipelines. Fault rupture, liquefaction, seismic shaking, slope movement, and permanent ground deformation can subject pipelines to axial strain, bending, rotation, and joint displacement [50]. Observed earthquake damage has also been used to develop pipeline fragility relationships based on ground-motion intensity, permanent ground deformation, and pipeline characteristics [10]. This body of work primarily addresses pipeline response to seismic and ground-deformation hazards and is distinct from studies of gradual settlement or long-term soil-related deterioration.

Roadway context has also been considered in infrastructure-management research. Pipes located within transportation corridors may be influenced by pavement construction, trench backfill, excavation activity, traffic conditions, and maintenance practices. However, roadway classification may also be correlated with pipe size, installation period, construction standards, and rehabilitation priorities, making its independent relationship with pipe failure difficult to determine. Research on co-located road and water infrastructure has emphasized the benefits of coordinating maintenance and rehabilitation decisions to account for shared costs and system interdependencies [80].

A wide range of engineering and statistical approaches has been developed to model water-main deterioration. Traditional methods include deterministic decision rules, empirical scoring systems, regression-based failure models, and parametric lifetime distributions [61, 64, 11, 115, 62]. Deterministic systems are relatively easy to implement but often rely on predefined thresholds or expert-selected weights. Regression-based models relate observed break counts or failure rates to physical, operational, and environmental attributes. These methods are useful for identifying network-level trends, although some formulations require aggregation by time period, geographic area, or pipe cohort, which can reduce information about individual failure times and observation durations.

Parametric lifetime models assume that failure times follow a specified probability distribution. When the assumed distribution adequately represents the failure process, these models can be used to estimate survival probabilities, deterioration rates, and expected service life [68]. Their results, however, depend on the selected distribution and its corresponding hazard structure. A single parametric distribution may not adequately describe a heterogeneous network containing different materials, installation periods, and deterioration mechanisms [64, 109]. Physical–probabilistic approaches provide additional mechanistic detail by combining structural analysis, corrosion progression, and reliability calculations [69, 77]. These approaches may require detailed information on pipe geometry, defect characteristics, material properties, and condition that is difficult to obtain consistently across an entire utility network.

Historical utility records introduce further statistical complications. Many water systems contain pipes installed decades, and sometimes more than a century, before systematic digital failure records became available [2, 139]. Older pipes may therefore enter the available dataset only after surviving for a substantial portion of their service lives, while failures

occurring before the observation period are unknown or absent. This condition is known as left truncation, or delayed entry. Pipes that remain operational at the end of the observation period are right censored because their eventual failure times are unknown [68]. Failure to account for these temporal characteristics may bias deterioration estimates. Left-truncated populations are conditioned on assets having survived long enough to enter the observation period, while pipes that failed and were removed earlier may not appear in the available records. Treating such assets as though they had been continuously observed from installation can assign exposure time to periods during which failures were not systematically recorded. Excluding right-censored assets also removes information about the duration for which those pipes remained operational. Previous studies and reviews have identified incomplete histories, delayed entry, and survival selection as important issues in statistical water-pipe deterioration analysis [109, 139, 2].

Survival analysis provides a statistical framework for analyzing time-to-failure data in the presence of censoring and delayed entry. The Kaplan–Meier estimator provides a non-parametric estimate of the survival function and incorporates information from right-censored observations without requiring a predetermined lifetime distribution [57]. KM curves are useful for comparing survival patterns among pipe groups, although they do not independently estimate the effects of multiple correlated predictors. The Cox-PH model extends survival analysis by estimating the relative association between multiple covariates and failure hazard while leaving the baseline hazard unspecified [38]. Left-truncated assets can be included by allowing each pipe to enter the risk set only after it becomes observable, while right-censored assets contribute information until their final observation [68]. This structure is appropriate for infrastructure datasets containing assets with different installation dates and observation periods, provided assumptions such as proportional hazards and appropriate risk-set specification are evaluated.

Existing research has generally followed two separate directions. Network-scale statistical models have been used to identify broad relationships across large asset inventories, but pooled analyses may mask differences in deterioration behavior among pipe materials and may rely on incomplete historical records without fully addressing delayed entry and censoring [109, 139, 2]. In contrast, material-focused studies provide detailed insight into specific mechanisms, such as corrosion-induced strength loss in cast iron or chemical degradation of asbestos cement, but their findings are often based on a single material, deterioration process, or loading condition and may not be directly transferable to a heterogeneous utility network [103, 72, 49, 142]. Consequently, limited attention has been given to evaluating a common set of physical, operational, and environmental factors at both the network and material levels while simultaneously accounting for left truncation, right censoring, and correlations among predictors.

This study addresses these limitations by combining a pooled network-wide Cox-PH model with separate models for the major pipe-material groups. This framework explicitly incorporates delayed entry and right-censored observations, integrates spatially resolved geohazard, soil, roadway, pressure, and asset characteristics, and evaluates whether the associations between these factors and failure hazard vary among materials. The approach

therefore distinguishes broadly shared degradation drivers from material-dependent relationships that may be concealed in an aggregate model. By providing directly comparable and interpretable hazard ratios, the study establishes a more transparent empirical basis for understanding heterogeneous pipeline deterioration and developing locally calibrated, risk-informed asset-management strategies.

2.3 Methodology

Survival analysis is a statistical framework specifically designed to model time-to-event data, where the outcome of interest is the time until an event occurs. In infrastructure applications, this event typically corresponds to asset failure, making survival analysis well suited for characterizing pipe deterioration processes. A key advantage of survival analysis is its ability to properly account for right-censored observations, representing assets that remain in service at the end of the observation period. By modeling failure as a stochastic process, survival analysis provides a flexible and rigorous approach for examining how deterioration evolves over time under varying conditions.

Survival analysis methods can be broadly classified into non-parametric, semi-parametric, and parametric approaches, each serving a distinct purpose. Non-parametric methods, such as the KM estimator, make no assumptions about the underlying failure-time distribution and are primarily used for exploratory analysis and visualization of survival behavior across groups. Semi-parametric models, most notably the Cox-PH model, allow the effects of covariates to be quantified without specifying the baseline hazard function, making them particularly suitable for assessing the influence of individual attributes on failure risk. Parametric models, in contrast, assume a specific functional form, such as weibull analysis [131], for the survival distribution and are often used for extrapolating survival probabilities beyond the observed data.

2.3.1 Nonparametric Estimation: Kaplan-Meier Analysis

The KM estimator, also known as the product limit estimator, is a non-parametric statistic used to estimate the survival function $S(t)$ from lifetime data. In the context of urban infrastructure management, it represents the cumulative probability that a pipe segment will remain failure-free beyond a specific age t. Unlike parametric models, the KM method does not assume a specific underlying distribution for failure times, allowing the survival patterns to emerge directly from the observed data. This flexibility makes it an essential tool for identifying the "wear-out" phase of the water distribution network.

The KM estimator is especially valuable for water distribution systems management because it naturally accommodates right-censored observations, including pipes that remain in service at the end of the observation window as well as pipes retired without a recorded failure. The survival function is estimated as the product of conditional survival probabilities over observed failure times:

$$S(t) = \prod_{t_i \leq t} \left(1 - \frac{d_i}{n_i}\right) \tag{2.1}$$

where d_i denotes the number of failures occurring at time t_i, and n_i represents the number of pipe segments "at risk" (functioning and not yet censored) just prior to that time. The resulting survival curve is characterized by a series of declining horizontal steps, where each vertical drop signifies a recorded failure and the horizontal distance reflects the time between consecutive failures.

2.3.2 Semiparametric Modeling: Cox-Proportional Hazard Model

Building on the non-parametric insights provided by the KM analysis, this study employs the Cox-PH model to quantify the effects of pipe characteristics, operational conditions, and environmental factors on failure risk. The Cox-PH model is a semi-parametric regression framework that relates the instantaneous hazard of failure to a set of covariates without requiring specification of the baseline hazard function. This separation allows the underlying aging process to be modeled flexibly while isolating the marginal contributions of individual degradation drivers. The Cox-PH model expresses the hazard function as

$$h(t, X) = h_0(t) \exp\left(\sum_{j=1}^{k} \beta_j X_j\right), \tag{2.2}$$

where $h(t, X)$ denotes the instantaneous failure risk at age t given a vector of covariates $X = (X_1, \ldots, X_k)$. The baseline hazard $h_0(t)$ represents the age-dependent failure rate common to all pipe segments, while the exponential term scales this baseline according to the presence and magnitude of covariate effects. A key assumption of the Cox-PH framework is that the ratio of hazards between any two pipe segments remains constant over time (proportional hazards). For two covariate vectors X and X^*, the hazard ratio is given by

$$\frac{h(t, X)}{h(t, X^*)} = \frac{h_0(t) \exp\left(\sum_{j=1}^{k} \beta_j X_j\right)}{h_0(t) \exp\left(\sum_{j=1}^{k} \beta_j X_j^*\right)} = \exp\left(\sum_{j=1}^{k} \beta_j (X_j - X_j^*)\right). \tag{2.3}$$

This formulation demonstrates that covariate effects act multiplicatively on the baseline hazard. Under this assumption, the relative influence of stressors—such as traffic loading or groundwater—remains approximately constant throughout the asset lifecycle.

To estimate the coefficients β, the model relies on the construction of a *risk set* at each failure time. Because systematic failure records often begin long after installation, data is left-truncated; a pipe is only observed if it survives to an entry age t_i^{entry}. The Cox-PH model accommodates this by defining the risk set $\mathcal{R}(t)$ as the collection of all pipes effectively "at risk" of failure at time t:

$$\mathcal{R}(t) = \left\{ i : t_i^{\text{entry}} \leq t \leq t_i^{\text{exit}} \right\}, \tag{2.4}$$

where t_i^{exit} denotes the observed failure or censoring time.

This definition links the risk set to the hazard function through the *partial likelihood*. At any observed failure time t_i, the probability that the failure occurred in that specific pipe, rather than any other pipe in the risk set, is the ratio of its hazard to the sum of hazards of all pipes in $\mathcal{R}(t_i)$:

$$L_i(\beta) = \frac{h(t_i, X_i)}{\sum_{j \in \mathcal{R}(t_i)} h(t_i, X_j)} = \frac{\exp(X_i \beta)}{\sum_{j \in \mathcal{R}(t_i)} \exp(X_j \beta)}. \tag{2.5}$$

By maximizing this likelihood, the model accounts for the delayed entry of older assets (via $\mathcal{R}$) while quantifying how covariates (X) increase the probability of failure relative to the peer group.

The estimated coefficients β_j provide a direct measure of each covariate's contribution to failure risk. Their exponentiated form, $\exp(\beta_j)$, yields the hazard ratio (HR) associated with a one-unit increase in X_j:

$$\text{HR}_j = \exp(\beta_j) \quad \Rightarrow \quad \begin{cases} \text{HR}_j = 1, & \text{no effect on failure risk,} \\ \text{HR}_j < 1, & \text{reduced hazard (protective effect),} \\ \text{HR}_j > 1, & \text{increased hazard (risk factor).} \end{cases} \tag{2.6}$$

Under this framework, hazard ratios are interpreted as relative changes in failure risk associated with a given covariate, holding all other factors constant. A hazard ratio equal to unity ($HR = 1$) indicates that the covariate has no measurable effect on failure risk relative to the reference condition. Values less than unity ($HR < 1$) indicate a protective effect, whereby the associated pipe segments experience a reduced instantaneous failure risk at any given age, while values greater than unity ($HR > 1$) indicate an increased risk, implying that exposure to the corresponding condition accelerates the deterioration process and elevates failure likelihood throughout the service life. The magnitude of deviation from unity reflects the strength of the effect, with values farther from one corresponding to stronger influences on degradation behavior.

For continuous covariates, the HR represents the multiplicative change in instantaneous failure risk associated with a one-unit increase in the variable, whereas for categorical covariates it represents the risk relative to a designated reference group. Because HRs are time-invariant under the proportional hazards assumption, their interpretation reflects persistent differences in deterioration rates rather than transient effects at specific ages. Consequently, HRs provide a basis for comparing degradation mechanisms across pipe populations and for prioritizing assets subject to elevated long-term risk. It is important to note that HRs quantify relative rather than absolute failure probabilities and should therefore be interpreted in conjunction with baseline survival curves to fully characterize lifecycle performance. Accordingly, the primary objective of this study is to estimate the relative effects of pipeline

degradation factors on failure risk, while the baseline hazard, representing the common age-related deterioration process, is treated as a nuisance component and is not the focus of inference.

2.4 Data

This study integrates pipe inventory, operational, and environmental datasets to support a comprehensive assessment of water distribution pipe deterioration. Pipe inventory and historical failure records were obtained from a water utility serving the East Bay of the San Francisco Bay Area. The service area is visualized in Figure 2.1. These data include pipe material, diameter, installation year, and recorded main breaks, as well as operational water pressure. Environmental datasets were compiled from multiple authoritative sources and include soil type, geological hazard zones, roadway functional classification, and groundwater levels. All datasets were spatially linked to the pipe network, enabling the assignment of location-specific environmental attributes to individual pipe segments for subsequent failure analysis.

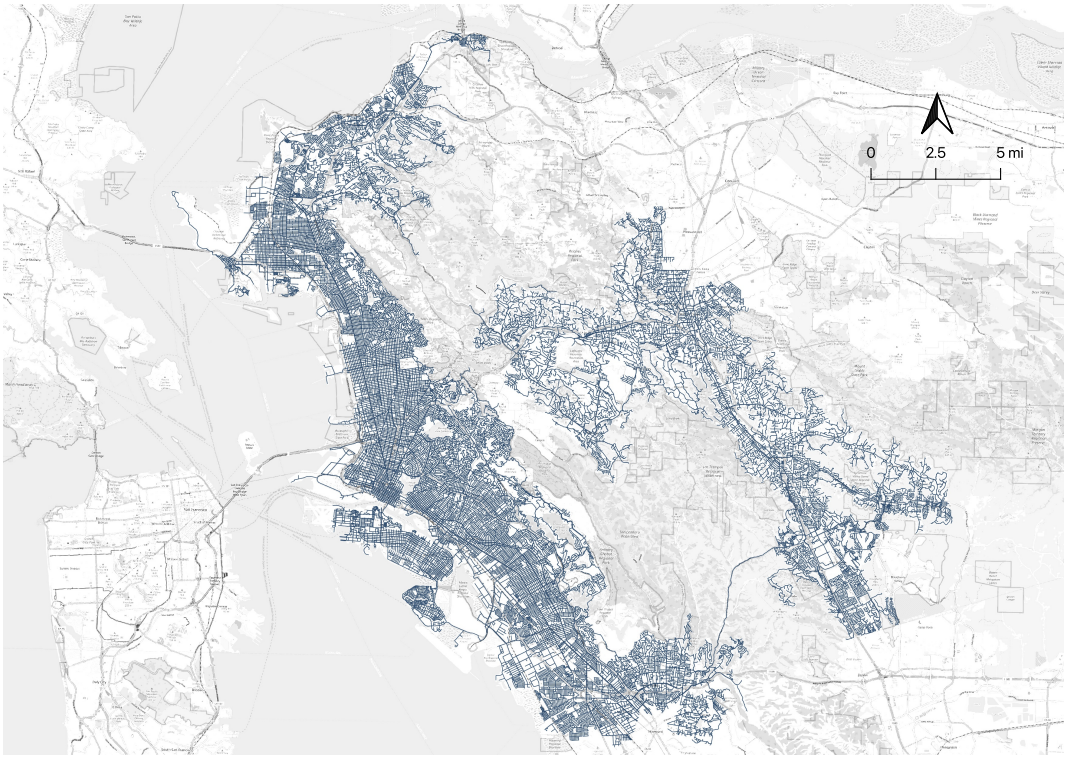


Fig. 2.1. Water distribution network in the east bay of San Francisco Bay Area

2.4.1 Pipe-Intrinsic Data

The pipe inventory covers a 332-square-mile service area, serves approximately 1.4 million customers, and includes about 4,200 miles of water distribution pipelines with diverse materials and diameters. The dataset provides approximately 150 years of pipe installation history, with comprehensive records of physical characteristics—such as material, diameter, length, and installation year—dating back to 1876. In addition, the dataset includes 32 years of historical failure information, with main break records available from 1990 through 2022. As a result, the inventory contains pipes currently in service that are up to approximately 150 years old. The smallest analytical unit in the dataset is the Record Management ID (RMID), which serves as the primary key for analysis. The dataset comprises 80,825 RMIDs, most of which are approximately 250 feet in length. Within a RMID, all the pipes were constructed under the same project.

Figure 2.2 summarizes key characteristics of the pipe inventory. Figure 2.2a shows that cast iron (31.5%), asbestos cement (30.8%), steel (25.4%), and non-metallic (12.3%) pipes account for the majority of the network by total mileage. Other materials, such as ductile iron, together comprise less than 1% of the total pipe length and are therefore excluded from this study.

Pipe installation year distributions reveal strong material-dependent deployment patterns. Cast iron pipes were predominantly installed in earlier decades, with installation peaks in the mid-20th century. Asbestos cement pipes peaked in the late 20th century, while steel pipes became increasingly common beginning in the 1960s and continue to be installed. Non-metallic pipes—primarily polyvinyl chloride (PVC) and high-density polyethylene (HDPE)—appear more frequently after 2000. This temporal stratification indicates that material effects are intrinsically confounded with pipe age and historical construction practices.

Figure 2.2b presents pipe diameter distributions by material. This study focuses on distribution pipes with diameters less than 16 inches (400 mm). Smaller diameters, particularly 6-inch (150 mm) and 8-inch (200 mm) pipes, account for the majority of total pipe length, especially among cast iron and asbestos cement pipes. Larger diameters are comparatively rare and are predominantly associated with steel pipes.

2.4.2 Operational and Historical Data

Operational water pressure measurements from 90,156 piezometers were spatially linked to pipeline segments using buffered geographic information system (GIS) intersections. A 10-ft (3-m) buffer was applied to both pipe centerlines and pressure points to account for mapping uncertainty, and pressure points intersecting each RMID were assigned accordingly. When multiple pressure observations were available, the maximum pressure was used for failure modeling. Figure 2.2c shows the spatial distribution of operational pressure, with a mean of 75 psi and a maximum of 180 psi.

Historical main break records indicate that failure occurrence across the pipe inventory is highly uneven. As shown in Figure 2.2d, most pipes have experienced no recorded failures, while a small subset exhibits multiple failures, resulting in a heavy-tailed failure count distribution. Note that since the non-metallic pipes are fairly new, no pipes had experienced more than 2 failures.

2.4.3 Environmental Data

To enhance the quality and spatial resolution of environmental influence to pipeline degradation, such as soil properties, ground movement, groundwater conditions, and external loads, multiple geo-spatial datasets were incorporated into the dataset.

Groundwater Level

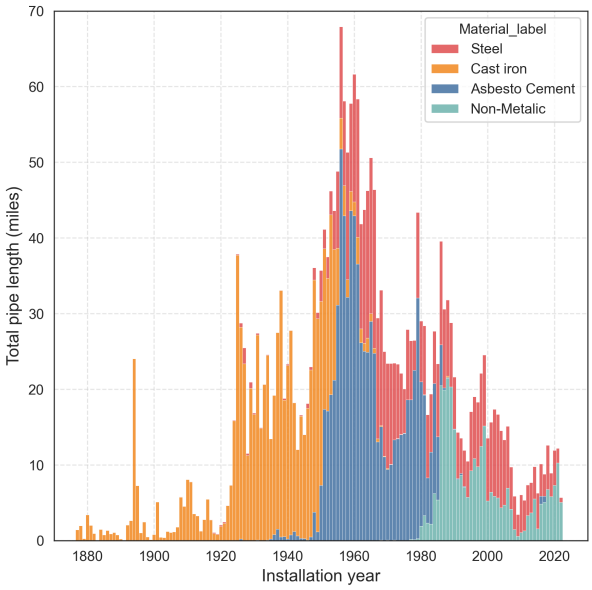
Groundwater depth is included as a spatially continuous environmental variable to represent hydrogeological conditions influencing corrosion processes, buoyancy forces, and soil stability. Groundwater level observations were obtained from two authoritative databases: the California Department of Water Resources [18] and the California State Water Resources Control Board GeoTracker database [19]. These measurements are collected at discrete monitoring locations across the study area and do not directly coincide with pipeline locations. To approximate the spatially continuous groundwater table and assign groundwater depth to each pipe segment, a kriging interpolation model [39] was applied. As shown in Figure 2.3a, the resulting groundwater depth distribution is strongly right-skewed, with most pipe segments located above relatively shallow groundwater levels and a smaller subset exposed to deeper water tables.

Fault Zone

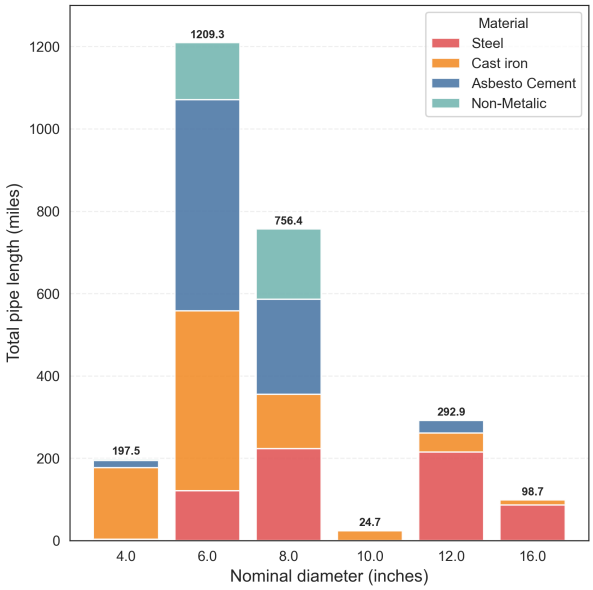
Geological faulting can introduce ground displacement, seismic loading, and stress concentrations that adversely affect buried pipelines. Fault zone data used in this study are obtained from the Quaternary Fault and Fold Database maintained by the United States Geological Survey [125]. Each RMID is evaluated to determine whether its associated pipe geometry intersects or crosses a mapped fault zone. The result is presenting in Figure 2.3b. Pipes intersecting fault zones represent a relatively small fraction of the total network length; however, these crossings occur across all pipe materials and installation eras. This indicates that exposure to fault-related hazards is not confined to a single asset class and supports the inclusion of fault proximity as an independent geological risk factor in the failure model.

Landslide Zones

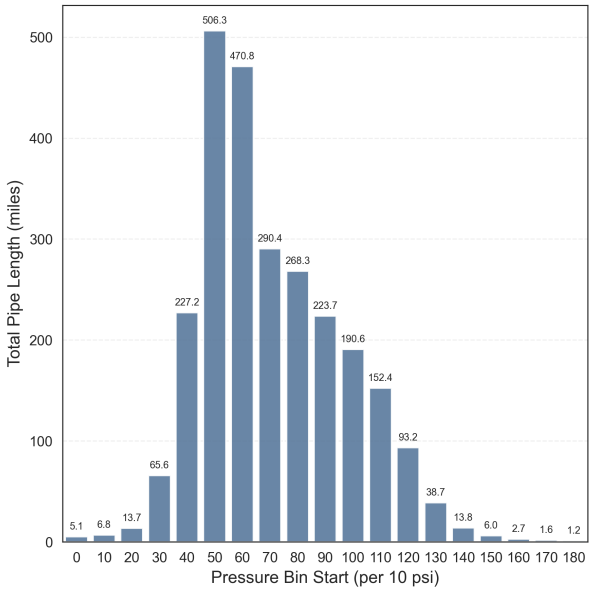
Landslide activity poses additional risks to pipeline integrity through soil displacement, loss of ground support, and increased mechanical stress. Landslide data are sourced from the USGS [125] and include both existing and potential landslide regions represented as



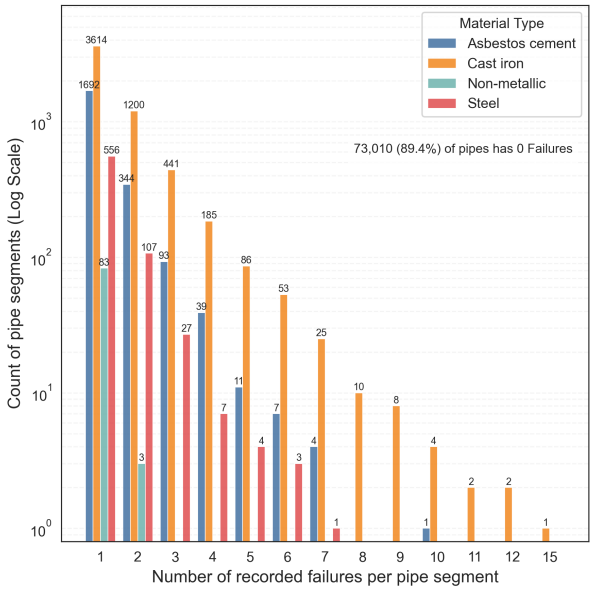
(a) Distribution of pipe installation year regarding material types



(b) Distribution of pipe diameter respect to pipe materials



(c) Water pressure distribution of pipe segments



(d) Number of previous failures of pipe material

Fig. 2.2. Overview of pipe characteristics

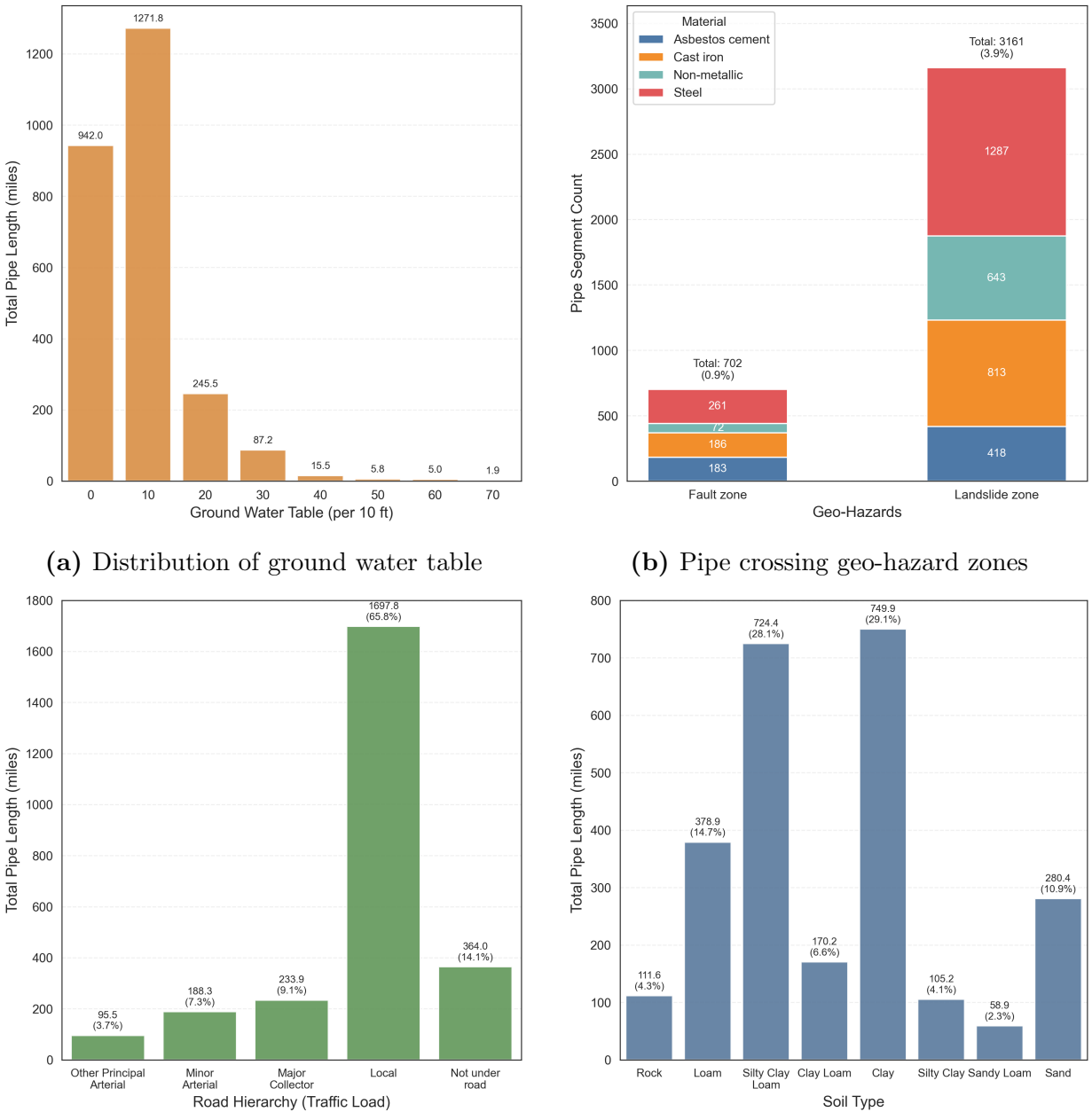
polygon features in GIS. Pipes are evaluated to determine whether they intersect or lie within the mapped landslide region. This approach identifies pipelines located within or in close proximity to slope instability zones, which represent localized but potentially severe sources of failure risk associated with ground movement.

Traffic Load

Traffic-induced loading can contribute to pipe deterioration through vibration and dynamic surface loads transmitted to the subsurface. In this study, traffic loading is approximated using roadway functional classification, which serves as a proxy for traffic volume and operational intensity. Roadway data were obtained from the California Road System – Functional Classification database provided by Caltrans [17]. The functional classification system categorizes roadways based on intended use and level of service. Based on this classification, pipes were categorized into six roadway exposure classes: other principal arterial roads, minor arterial roads, major collector roads, minor collector roads, local roads, and not under road. These classes represent a descending hierarchy of traffic loading intensity, with principal and minor arterials associated with the highest traffic volumes and loads, followed by collector roads, local roads, and pipe segments not located beneath roadway corridors. The resulting distribution indicates that most pipe segments are located beneath local roads or outside roadway corridors, while relatively few pipes are associated with arterial roadways. This imbalance suggests that the majority of assets experience low to moderate traffic-induced loading.

Soil Type

Soil type is one of the key environmental factor influencing pipe corrosion potential, ground support conditions, and long-term structural performance. Soil data used in this study are obtained from the United States Department of Agriculture [124] and are represented as polygon features in the GIS environment. To associate soil types with pipeline segments, a spatial intersection approach is employed. After the merging process, the USDA dataset initially identifies 263 distinct soil types. To streamline analysis and focus on corrosion-relevant characteristics, these soil types are reclassified into 8 generalized categories (rock, loam, clay, clay loam, silty clay, silty clay loam, sand, sandy loam) following established pedological classification frameworks. The USDA Soil Taxonomy recognizes soil textural classes based on sand, silt, and clay percentages, and this 8-category scheme aligns with grain-size classification principles while capturing corrosion-relevant distinctions critical to pipe degradation assessment. These distinctions include drainage characteristics (well-drained versus poorly drained soils), volumetric stability (clay soils with high shrink-swell potential), oxygen availability (silty clays with reduced aeration versus sandy soils with high permeability), and redox conditions affecting electrochemical corrosion rates. From Figure 2.3d, the resulting soil composition of the network is dominated by clay, silty clay loam, and loam soils, while rock and sandy loam soils are comparatively rare.



(a) Distribution of ground water table

(b) Pipe crossing geo-hazard zones

(c) Traffic loads represented by road hierarchy

(d) Soil type

Fig. 2.3. Overview of environmental data

2.5 Result

2.5.1 Analysis of Pipeline Longevity Patterns

The KM survival curves (Figure 2.4) illustrate how failure risk evolves over time across key asset, environmental, and operational attributes. Clear separation is observed for geospatial hazard exposure, with pipes intersecting fault zones or located within landslide-prone areas exhibiting markedly faster declines in survival probability compared with non-exposed pipes. The divergence between curves becomes more pronounced at intermediate to later service ages, suggesting that cumulative ground deformation and long-term geohazard processes increasingly influence failure risk as assets age.

Material-dependent survival patterns are clearly evident across the network, with distinct deterioration trajectories and data characteristics for each pipe type. Steel pipes demonstrate a gradual, steady decline over time but maintain the highest long-term survival probability at advanced ages. In contrast, cast iron pipes present a uniquely shaped survival curve, exhibiting a near-perfect survival in their early years before experiencing a steep, continuous decline. Because cast iron pipes represent the oldest installed cohort in the network, this initial plateau does not reflect exceptional early-life durability, but rather a classic case of left-truncated data. Since rigorous failure records only span recent decades, the early-life failures of these vintage pipes went unrecorded. Consequently, the model only captures the surviving, more robust assets, creating a survivorship bias that inflates their apparent early-age reliability. Meanwhile, asbestos cement pipes demonstrate a markedly sharper decline as they age, dropping steeply and indicating a higher vulnerability compared to the metallic cohorts. Finally, although non-metallic pipes display a sharp initial decline in survival, the abbreviated curve and wide confidence intervals suggest limited failure records for this specific material. Given these distinct, material-specific deterioration trajectories and historical data artifacts, subsequent pipeline degradation factor estimating modeling is conducted separately by pipe material.

Operational and design characteristics further differentiate survival behavior. Smaller-diameter pipes, particularly 4-inch (100 mm) and 6-inch (150 mm) pipes, exhibit more rapid declines in survival probability than larger-diameter pipes (8–16 inches). One potential reason can be attributed to structural considerations, as smaller pipes typically have thinner wall thicknesses, reducing their capacity to withstand cumulative soil movements and chemical corrosion [1, 103, 77]. Operational water pressure also shows a strong association with survival outcomes. Pipes operating under high pressure (>90 psi) experience substantially steeper survival declines compared with pipes operating under normal pressure (<90 psi), indicating the cumulative effect of sustained internal loading on failure risk.

Roadway exposure and traffic loading exhibit graded survival patterns. Pipes located beneath local roads show lower survival probabilities over time compared with those beneath major arterials or outside roadway corridors. This pattern likely reflects differences in construction standards, loading histories, and maintenance practices [69, 80]. However, the observed effect is also confounded by pipe diameter distribution: 63.8% of pipes located

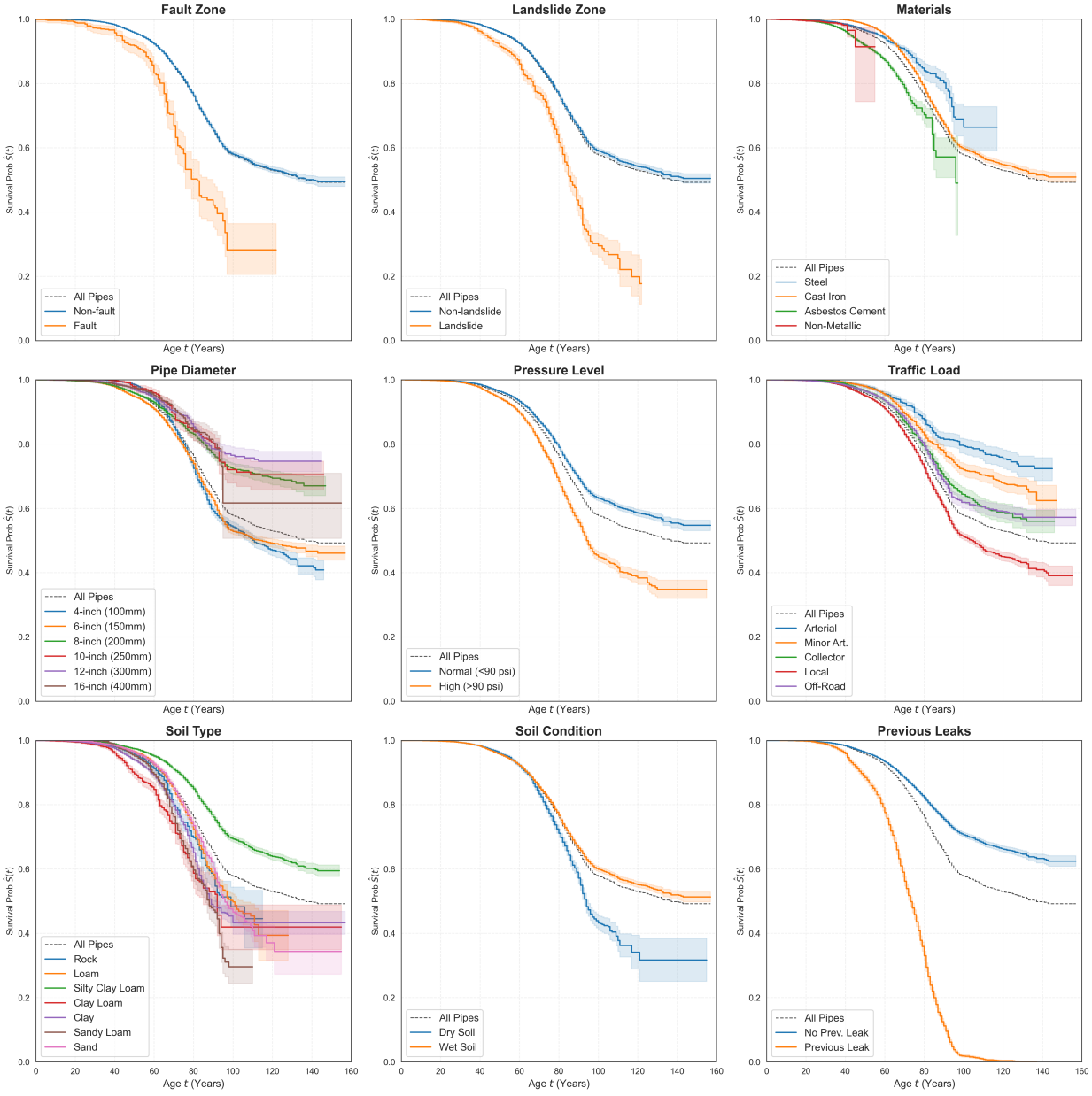


Fig. 2.4. Kaplar-Meier curve for subsets of the pipe data

beneath local roads are 4-inch and 6-inch pipes, compared with 27.0% for other principal arterials, 37.2% for minor arterials, and 36.7% for major collectors. Because smaller-diameter pipes have been shown to degrade earlier, pipes beneath local roads may appear more failure-prone due to the combined influence of traffic exposure and smaller pipe sizes.

Soil-related effects on pipeline degradation are highly heterogeneous and are primarily governed by mineralogy, fines content, and degree of saturation. Previous research demonstrates that soil texture directly correlates with electrochemical corrosion potential by controlling moisture retention, oxygen diffusion, and electrolyte conductivity [130]. Furthermore, studies specifically examining water mains have documented how soil grain size and texture dictate pipe corrosion rates through capillary water transport and oxygen ingress mechanisms [103]. These dynamics manifest in distinct survival patterns depending on the surrounding soil matrix. Pipes located in silty clay and silty clay loam soils generally exhibit relatively higher survival probabilities. This improved longevity is attributed to the stable moisture, high buffering capacity, and anaerobic conditions of these soils, which facilitate the formation of protective oxide layers [20]. In contrast, pipes buried in clay-rich and sandy loam soils experience more rapid survival declines, reflecting detrimental differences in soil stiffness, drainage, and susceptibility to volumetric change. These specific soils often experience unstable saturation, creating cyclic oxygen-rich and oxygen-limited conditions that aggressively accelerate localized pitting.

To examine the complex, non-linear influence of soil moisture on pipe degradation, soils in the study area are classified into dry and wet categories based on capillary rise, groundwater depth, and an assumed pipe cover depth of 3 feet (1 m). The degree of moisture fundamentally alters oxygen transport kinetics, corrosion area evolution, and acidification rates. Specifically, intermediate saturation (S = 20–40%) proves to be the most damaging state by maximizing the active corrosion area, whereas full saturation physically suppresses oxygen diffusion and enables the formation of a protective sulfide layer. This theoretical behavior aligns with the network's KM curves, which indicate that pipes in classified "dry" soil conditions actually degrade more rapidly than those in consistently "wet" environments. This accelerated deterioration is likely driven by increased exposure to seasonal wet–dry cycles [130, 45], which continually disrupt passivating scales and exacerbate localized corrosion and material fatigue. Notably, the discrepancy in survival probability between pipes in dry and wet soils only manifests after approximately 60 years of service. This delayed divergence reveals that soil moisture dynamics exert a cumulative, long-term influence on structural integrity rather than acting as an early-life failure driver, ultimately dictating the lifespan of the corrosion-prone metallic materials and environmentally sensitive asbestos cement pipes. These interactions are examined further in the subsequent material-specific section.

The most pronounced survival separation is observed for pipes with a history of previous failures. Assets that have experienced prior leaks exhibit rapid declines in survival probability, particularly beyond mid-life, indicating strong temporal dependence in pipe failures and reinforcing failure history as one of the most influential predictors of future risk [1, 37].

2.5.2 Effects of Pipeline Degradation Factors

To quantify the relative influence of pipeline degradation drivers across the entire network, a pooled (network-wide) Cox-PH model considering left-truncated time was fitted to all pipe segments, combining all material types. The estimated HRs, along with 95% confidence intervals (CI), are summarized in Figure 2.5 and Table 2.1. HRs represent the multiplicative change in instantaneous failure risk associated with each predictor, holding all other variables constant.

Among all variables, previous failure history emerges as the most influential predictor of future failure risk. Pipes with at least one prior failure exhibit a HR of 6.03 (95% CI: 5.78-6.29), indicating more than a six times increase in instantaneous failure risk compared with pipes without prior failures. This pronounced effect likely reflects unresolved structural weaknesses, localized corrosion, installation defects, or adverse geological conditions that persist after an initial failure, resulting in strong temporal dependence and elevated susceptibility to subsequent breaks [1, 37].

Several environmental and operational factors are also associated with increased degradation risk. Pipes located within fault zones and landslide zones show HR of 1.42 (1.23–1.63) and 1.29 (1.19–1.39), respectively, indicating that the pipes located within a geo-hazard zone is approximately 30-40% more likely to fail than those installed at not geo-hazard prone areas. These elevated risks can be due to the cumulative impacts of ground deformation, differential settlement, and repeated soil movement, which can progressively compromise pipe integrity over time [10, 70]. Similarly, operational water pressure exhibits a statistically significant effect, with a HR of 1.05 per 10 psi increase (1.04–1.06). This indicates that, for every 10 psi increase in sustained operating pressure, the instantaneous failure risk increases by approximately 5%. Sustained high internal pressure could accelerates fatigue, crack propagation, and joint deterioration, amplifying the effects of other degradation mechanisms [73].

Structural characteristics also play a critical role in degradation behavior. Relative to the 10-inch (250 mm) reference group, 4-inch (100 mm) and 6-inch (150 mm) pipes exhibit HR of 1.33 (95% CI: 1.14–1.55) and 1.25 (95% CI: 1.08–1.46), respectively. These estimates indicate that, holding all other factors constant, 4-inch pipes experience approximately a 33% higher instantaneous failure risk, and 6-inch pipes a 25% higher risk, compared with 10-inch pipes. This elevated vulnerability, as discussed in the previous section, could be because smaller-diameter pipes generally have thinner wall thicknesses and lower structural redundancy, which reduces their capacity to withstand internal pressure fluctuations, external loading from surrounding soil and traffic, and progressive material loss due to corrosion. As a result, smaller pipes are potentially more susceptible to cumulative degradation processes that accelerate failure over time. In contrast, no statistically significant differences are observed for larger-diameter pipes. Pipes with diameters of 8 inches (200 mm), 12 inches (300 mm), and 16 inches (400 mm) exhibit HR of 0.97 (95% CI: 0.83–1.14), 0.94 (95% CI: 0.79–1.11), and 0.90 (95% CI: 0.73–1.12), respectively, indicating failure risks comparable to that of the 10-inch reference group.

Several predictors exhibit moderate but meaningful effects on pipeline degradation. Pipes

located beneath local roads and major collector roads show HRs of 1.26 (95% CI: 1.07–1.36) and 1.18 (95% CI: 1.04–1.34), respectively, compared with pipes beneath principal arterials. Furthermore, pipes located outside roadway corridors exhibit an elevated risk (HR = 1.20, 95% CI: 1.07–1.36). The finding that pipes beneath local and collector roads exhibit higher failure risks than those under principal arterials, despite the latter carrying significantly higher traffic volumes, can be attributed to underlying differences in engineering standards and maintenance priorities. Principal arterials are typically constructed with thicker pavement layers and superior trench backfill quality; this higher shear modulus distributes vehicle loads much more effectively, reducing the localized stress transmitted to buried assets [58]. In contrast, local roads are frequently built to minimum pavement thickness thresholds and are more susceptible to deferred maintenance. This lack of maintenance accelerates surface degradation and increases road roughness. Studies have demonstrated that vehicular loading is a complex stochastic process, and uneven pavements cause continuous excitation of a vehicle's suspension; the resulting dynamic vibrations and transient fluctuations in the wheel–road contact force are significantly more damaging to buried pipelines than the static weight of the vehicles alone [121]. Additionally, major utilities often practice "opportunistic maintenance" on arterial routes, strategically coordinating water main replacements with planned road resurfacing projects to optimize system reliability and minimize disruption [80]. Conversely, pipes located in minor streets or entirely outside roadway corridors remain in less-controlled burial environments with limited oversight. This inherently poorer bedding support limits the pipe's ability to resist external loads and soil movement, which may contribute to the elevated failure vulnerabilities observed in these zones.

The influence of soil composition on pipeline longevity is highly heterogeneous, critically impacting the late-stage degradation of susceptible materials like cast iron and asbestos cement. Clay loam soils elevate failure risk (HR = 1.31, 1.11–1.54) due to their high plasticity; seasonal shrink–swell cycles strip away uniform bedding support and induce destructive longitudinal bending stresses, while shrinkage cracks facilitate rapid oxygen diffusion [49]. Similarly, coarse-grained sandy loams (HR = 1.14, 0.99–1.32) sustain highly aerobic, cyclic wet–dry conditions that act as a potent catalyst for localized electrochemical pitting [55, 113]. Conversely, fine-grained soils like silty clay loam (HR = 0.76, 0.67–0.88) and silty clay (HR = 0.73, 0.61–0.87) demonstrate a protective influence. Their low permeability and microscopic pore structure restrict capillary water transport and oxygen ingress [103], fostering a stable, anaerobic environment that encourages the formation of passivating oxide layers [20]. Furthermore, an independent evaluation of wet soil conditions reveals no statistically significant impact on failure risk (HR = 0.97, 0.88–1.06). This reinforces the physical kinetic mechanisms of underground deterioration: continuous full saturation physically obstructs oxygen diffusion and stifles corrosion [130]. It is the intermediate saturation and repeated wet–dry cycling, rather than sustained moisture, that continually fractures passivating scales and aggressively drives pipe failure.

The finding shows that pipe age, when expressed per 10-year increment, yields an HR of 0.89 (95% CI: 0.88–0.90). Rather than indicating that pipes physically gain strength over time, this HR below unity is primarily a manifestation of the survivorship effect and unob-

served heterogeneity linked to the left-truncated nature of the utility's historical records [2]. Because systematic failure logging only initiated in 1990 for a distribution network featuring installations dating back to the 1870s, the dataset is subject to a 120-year observation gap. While the Cox-PH model mathematically adjusts for this delayed entry into the risk set, it cannot account for the physical filtering of the population during the unrecorded period. The most vulnerable or poorly installed components from earlier eras likely failed and were replaced prior to 1990, leaving only the more robust segments to "survive" into the modern observation window. The nuances of this survivorship bias, including how it disproportionately affects legacy materials will be discussed in further detail in a later section through sensitivity analysis.

Overall, the pooled Cox-PH results indicate that pipeline degradation is driven by a combination of historical failure behavior, geohazard exposure, operational loading, and structural characteristics, with pipe material also exhibiting a statistically significant association with failure risk. Relative to asbestos cement pipes, cast iron shows a decreased hazard (HR = 0.76, 95% CI: 0.72-0.81), while steel and non-metallic pipes exhibit substantially lower hazards (HR = 0.46, 95% CI: 0.42-0.50; and HR = 0.27, 95% CI: 0.21-0.34, respectively), corresponding to approximately a 54% and 73% reduction in instantaneous failure risk. While these differences partially stem from contrasts in intrinsic material properties, jointing systems, and corrosion resistance, they also reflect confounding with installation periods, pipe diameters, and historical construction standards. Because these pooled effects serve as aggregate indicators rather than pure measures of intrinsic material performance, material-specific Cox-PH models are examined in the following section to isolate and evaluate the dominant, material-dependent degradation mechanisms driving failure within each individual pipe material class.

2.5.3 Material-Specific Effects on Pipeline Degradation

To further investigate the dominant drivers of failure within each material class, separate Cox-PH models considering left-truncated time were estimated for each major pipe material class: asbestos cement, cast iron, steel, and non-metallic pipes. The resulting HRs and 95% confidence intervals are reported in Table 2.2 and visualized in Figure 2.6.

Asbestos Cement Pipes

Hu and Hubble (2007) [49] investigated asbestos cement pipe deterioration by correlating historical failure data with corresponding environmental, physical, and operational settings. Their analysis established that asbestos cement pipe failures are primarily driven by pipe age, diameter, climate fluctuations, and the presence of expansive clay soils, alongside chemical attacks from soil pore water. The analysis of our dataset aligns with these findings, demonstrating that asbestos cement pipes are sensitivity to historical, structural, operational, and environmental stressors.

Table 2.1. Hazard ratios (HR) with 95% confidence intervals (CI) and p-values from the pooled Cox proportional hazards model (all materials combined).

Variable type	Predictor	HR (95% CI)	p-value
Continuous	Age (per 10 years)	0.89 (0.88–0.90)	<0.001
	Operational pressure (per 10 psi)	1.05 (1.04–1.06)	<0.001
Binary	Within landslide zone	1.29 (1.19–1.39)	<0.001
	Within fault zone	1.42 (1.23–1.63)	<0.001
	Wet soil condition	0.97 (0.88–1.06)	0.480
	Has previous failure	6.03 (5.78–6.29)	<0.001
Categorical	*Material type*		
	Asbestos cement	*Reference*	—
	Cast iron	0.76 (0.72–0.81)	<0.001
	Non-metallic	0.27 (0.21–0.34)	<0.001
	Steel	0.46 (0.42–0.50)	<0.001
	Soil type		
	Rock	*Reference*	—
	Sandy loam	1.14 (0.99–1.32)	0.071
	Sand	0.85 (0.76–0.95)	0.003
	Loam	0.95 (0.83–1.09)	0.454
	Silty clay loam	0.76 (0.67–0.88)	<0.001
	Clay loam	1.31 (1.11–1.54)	0.001
	Clay	1.11 (0.97–1.27)	0.143
	Silty clay	0.73 (0.61–0.87)	<0.001
	Road hierarchy		
	Other principal arterial	*Reference*	—
	Minor arterial road	1.06 (0.93–1.21)	0.355
	Major collector road	1.18 (1.04–1.34)	0.009
	Local road	1.26 (1.13–1.41)	<0.001
	Not under road	1.20 (1.07–1.36)	0.002
	Pipe diameter		
	10-inch (250 mm)	*Reference*	—
	4-inch (100 mm)	1.33 (1.14–1.55)	<0.001
	6-inch (150 mm)	1.25 (1.08–1.46)	0.004
	8-inch (200 mm)	0.97 (0.83–1.14)	0.729
	12-inch (300 mm)	0.94 (0.79–1.11)	0.455
	16-inch (400 mm)	0.90 (0.73–1.12)	0.361

Note: Categories labeled as *Reference* represent hazard baselines against which hazard ratios for other categories within the same variable are estimated. Values are updated based on the consolidated dataset across all material types.

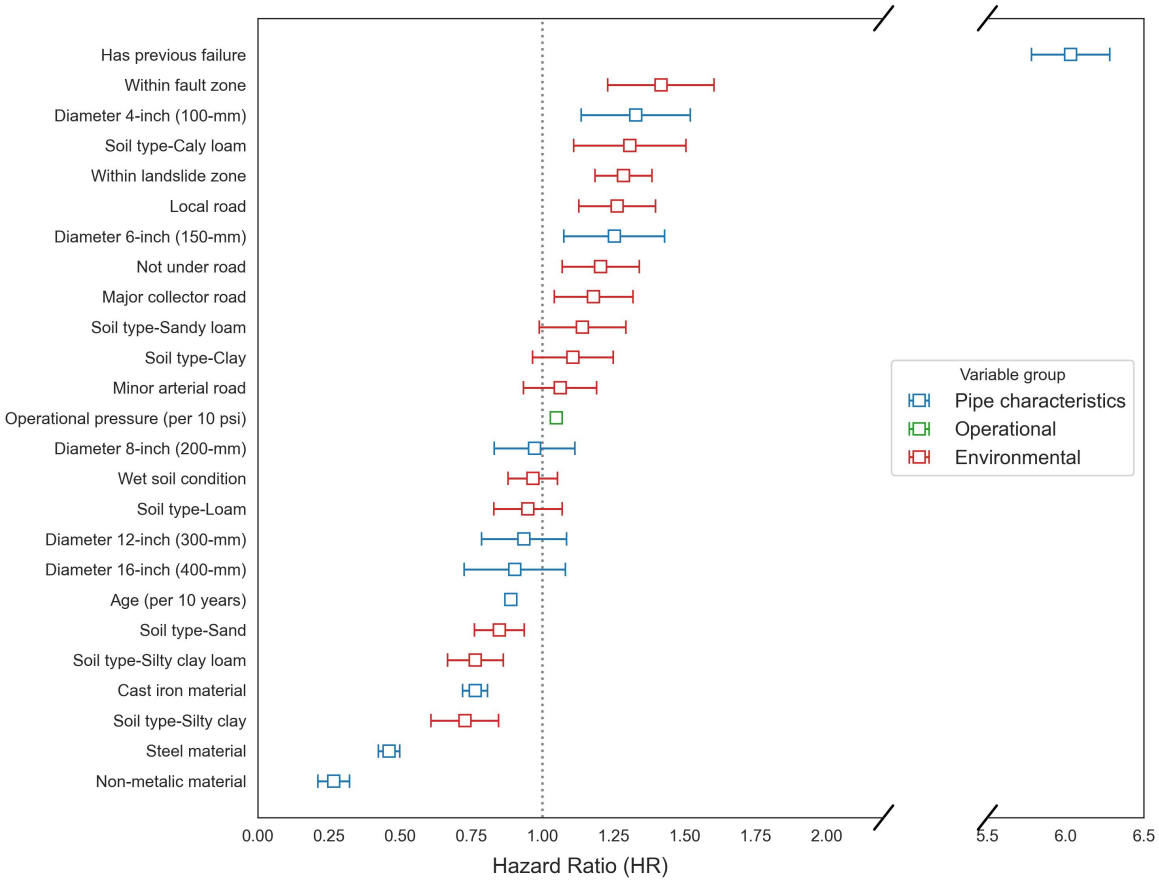


Fig. 2.5. Hazard ratios from the pooled (network-wide) Cox proportional hazards model for predictors associated with pipeline failure risk.

The data demonstrates that a pipe's failure history is the strongest predictor of its future deterioration. Much like the pooled model, an asbestos cement pipe segment that has previously failed is nearly nine times more likely to fail again (HR = 8.84, 95% CI: 8.08–9.66), highlighting a distinct clustering effect driven by localized vulnerabilities. In contrast, the hazard ratio associated with pipe age appears artificially protective (HR = 0.81 per 10 years, 95% CI: 0.79–0.83). Rather than indicating an increase in physical strength, this reflects the strong survivorship effect discussed earlier.

Structurally and operationally, smaller diameter asbestos cement pipes offer significantly reduced resistance to external loads. Compared to the baseline 250 mm (10-inch) diameter pipes, 100 mm (4-inch) and 150 mm (6-inch) pipes face an elevated risk of failure (HR = 1.35, 95% CI: 1.15–1.59; HR = 1.11, 95% CI: 1.02–1.22), owing to their thinner pipe walls. Operational pressure acts as an additional active degradation driver (HR = 1.07 per 10

psi, 95% CI: 1.06–1.08), accelerating structural fatigue as higher internal hydraulic loading constantly stresses the brittle cementitious matrix, a phenomenon similarly observed by Lopez et al. (2024) [70].

Environmentally, geo-hazards and localized soil conditions critically influence asbestos cement pipe degradation through coupled physical and chemical processes. Because asbestos cement is an inherently brittle material, it is highly vulnerable to the massive axial and bending strains imposed by permanent ground deformations. Consequently, asbestos cement pipes located within landslide zones (HR = 1.49, 95% CI: 1.25–1.78) and fault zones (HR = 1.39, 95% CI: 1.05–1.83) exhibit higher failure likelihoods. At a localized level, clay-loam (HR = 1.46) and clay soils (HR = 1.06) severely elevate degradation risk. As noted by Hu and Hubble (2007) [49], expansive clays undergo extreme volumetric shrink–swell changes with fluctuating moisture, removing uniform bedding support and inducing destructive longitudinal bending stresses on the rigid pipe barrel. Concurrently, these specific soils retain moisture and concentrate aggressive pore-water solutes, which promotes the continuous decalcification and chemical leaching of the alkaline cement matrix [142]. This coupled chemo-mechanical attack creates a porous, mechanically unstable degraded layer that ultimately destroys the pipe's structural integrity. By contrast, soils with lower permeability mitigate this risk by preventing aggressive solute transport.

Cast Iron Pipes

The main degradation indicator of cast iron pipes is the failure history (HR = 4.53, 4.33-4.74), indicating that the pipe with previous failures is four times more likely to fail comparing to the others, similar to the observation in Christodoulou and Deligianni (2010) [37]. In addition to the leak history, cast iron pipes demonstrate sensitivity to operational loading, geospatial hazards, and soil environment. Increasing pipe diameter is associated with reduced failure risk, which aligns with historical manufacturing standards where smaller-diameter cast iron pipes were cast with thinner walls, offering less mechanical resistance to environmental stresses [72]. Operational pressure remains a slight degradation driver (HR = 1.04 per 10 psi, 1.03–1.04). As with asbestos cement pipes, pipe age also exhibits a survivorship effect (HR = 0.90 per 10 years, 0.89–0.91), reflecting the persistence of higher-performing assets within the observation window rather than a causal reduction in deterioration.

Geospatial hazard exposure plays an important role in cast iron pipe performance. Pipes located within landslide zones (HR = 1.13, 1.03–1.24) and fault zones (HR = 1.31, 1.10–1.55) exhibit elevated failure risk. Cast iron pipes exhibit disproportionate sensitivity to soil type compared with other pipe materials. Sandy loam soils (HR = 1.23, 1.10-1.37) maintain aerobic conditions enabling oxygen-driven corrosion and Sandy loam is ranked by independent studies as the most aggressive soil due to cyclic wet-dry saturation patterns [55, 113]. In contrast, silty clay loam soils restrict oxygen transport to the metal surface through low permeability and fine pore structure; this oxygen-limited environment promotes anaerobic conditions and reduces cast iron corrosion to HR = 0.79 (CI: 0.74-0.85). Mineral composition and texture fundamentally control cast iron corrosion mechanisms, distinguishing their

vulnerability from chemically resistant asbestos cement and non-metallic materials. In addition, wet soil conditions are associated with lower failure risk relative to dry conditions (HR = 0.88, 95% CI: 0.82–0.94), indicating that cast iron pipes tend to perform better under consistently wet environments than under dry one; it is the repeated wet–dry cycles, rather than sustained moisture alone, that aggressively contribute to degradation processes such as coating deterioration, localized stress concentration, and corrosion initiation.

Roadway exposure further influences cast iron pipe degradation. Pipes located beneath local roads show elevated failure risk (HR = 1.13, 1.06–1.20), which may reflect increased traffic-induced loading and vibration. This effect is likely compounded by historical construction practices. Many cast iron pipes currently in service were installed under older design standards that permitted thinner wall thicknesses, particularly for smaller-diameter pipes [72]. Because a large share of these small-diameter cast iron pipes are located beneath local roads, the combined effects of reduced structural capacity and sustained surface loading may contribute to their elevated vulnerability.

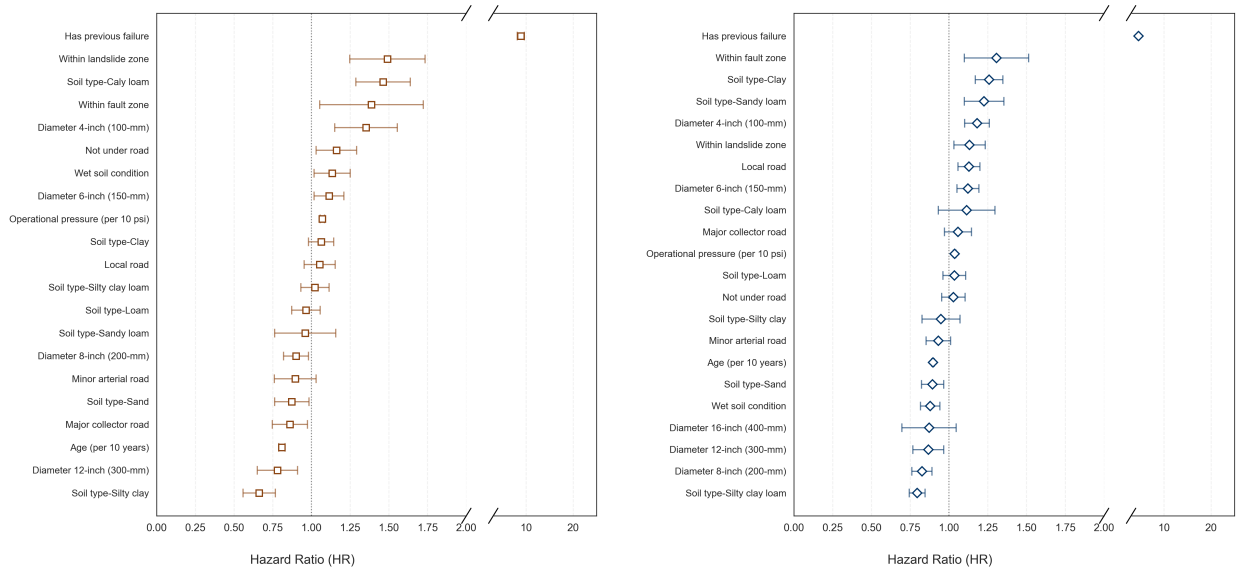
Steel Pipes

Steel pipes exhibit comparatively weaker sensitivity to many environmental factors, but remain influenced by historical failure records, geospatial stressors and certain soil conditions. Steel pipe with previous failure is in average 19 times more likely to fail (HR = 19.13, 16.01-22.86) than the others. Exposure to landslide zones (HR = 1.54, 95% CI: 1.27–1.86) and fault zones (HR = 1.73, 95% CI: 1.18–2.56) substantially increases failure risk, consistent with steel pipes' susceptibility to bending, axial stress, and joint distress induced by ground movement. The influence of soil conditions on steel pipes, while generally moderate, reveals critical patterns related to moisture and aeration. Pipes in sandy loam soils face an elevated failure risk (HR=1.28,1.01–1.62). This is likely due to the high permeability and aeration of sandy textures, which can facilitate oxygen transport to the pipe surface—a key driver of aerobic corrosion [20]. Furthermore, the fluctuating moisture levels in well-drained loams can disrupt protective oxide films or coatings, accelerating localized pitting. Interestingly, pipe diameter and age do not show statistically significant effects for steel. This stability reflects the more recent installation of steel assets and a more uniform structural performance compared to older, brittle materials.

Non-Metallic Pipes

Non-metallic pipes exhibit limited statistically significant associations across most predictors. Pipe diameter, age, and operational pressure [70] do not show strong effects, and geospatial hazard exposure is also insignificant. This pattern likely reflects both the relatively recent installation of non-metallic pipes and their material properties, which are generally designed to tolerate larger deformations without brittle failure. Compared with more rigid materials, non-metallic pipes such as PVC and HDPE possess greater flexibility and strain capacity, allowing them to better accommodate ground movement, differential settlement, and external

loading. In addition, non-metallic pipes are inherently resistant to electrochemical corrosion, eliminating one of the dominant long-term degradation mechanisms affecting metallic pipes.



(a) Asbestos cement pipe

(b) Cast iron pipe

(c) Steel pipe

(d) Non-metallic pipe

Fig. 2.6. Cox proportional hazard ratio on estimating variables contributing to pipeline degradation regarding different pipe materials

Table 2.2. Hazard ratios (HR) with 95% confidence intervals (CI) from material-specific Cox proportional hazards models.

	Asbestos cement		Cast iron		Steel		Non-metallic	
Predictor	**HR (95% CI)**	**p-value**	**HR (95% CI)**	**p-value**	**HR (95% CI)**	**p-value**	**HR (95% CI)**	**p-value**
Continuous								
Age (per 10 years)	0.81 (0.79–0.83)	<.001	0.90 (0.89–0.91)	<.001	0.99 (0.96–1.01)	0.379	1.03 (0.95–1.11)	0.499
Operational pressure (per 10 psi)	1.07 (1.06–1.08)	<.001	1.04 (1.03–1.04)	<.001	1.03 (1.02–1.05)	<.001	1.02 (0.99–1.06)	0.243
Binary								
Within landslide zone	1.49 (1.25–1.78)	<.001	1.13 (1.03–1.24)	0.009	1.48 (1.25–1.75)	<.001	1.05 (0.76–1.46)	0.751
Within fault zone	1.39 (1.05–1.83)	0.020	1.31 (1.10–1.55)	0.002	1.47 (1.04–2.08)	0.029	—	—
Wet soil condition	1.13 (1.02–1.26)	0.025	0.88 (0.82–0.94)	<.001	0.96 (0.85–1.09)	0.514	0.98 (0.74–1.30)	0.903
Has previous failure	8.84 (8.08–9.66)	0.000	4.53 (4.33–4.74)	0.000	19.13 (16.01–22.86)	<.001	—	—
Categorical (Diameter)								
Diameter 10-in (250 mm)	*Reference*	—	*Reference*	—	*Reference*	—	*Reference*	—
Diameter 12-in (300 mm)	0.78 (0.65–0.94)	0.008	0.87 (0.77–0.98)	0.021	0.99 (0.89–1.09)	0.788	—	—
Diameter 16-in (400 mm)	—	—	0.87 (0.70–1.09)	0.226	0.89 (0.78–1.03)	0.119	—	—
Diameter 4-in (100 mm)	1.35 (1.15–1.59)	<.001	1.18 (1.10–1.27)	<.001	1.22 (0.90–1.64)	0.197	—	—
Diameter 6-in (150 mm)	1.11 (1.02–1.22)	0.021	1.12 (1.05–1.20)	<.001	1.03 (0.93–1.15)	0.519	1.02 (0.86–1.21)	0.800
Diameter 8-in (200 mm)	0.90 (0.82–0.99)	0.028	0.83 (0.76–0.89)	<.001	1.02 (0.92–1.12)	0.723	0.99 (0.83–1.17)	0.873
Categorical (Soil Type)								
Rock	*Reference*	—	*Reference*	—	*Reference*	—	*Reference*	—
Sandy loam	0.96 (0.76–1.21)	0.720	1.23 (1.10–1.37)	<.001	1.28 (1.01–1.62)	0.038	0.92 (0.70–1.21)	0.551
Sand	0.87 (0.76–1.00)	0.049	0.89 (0.82–0.97)	0.008	1.10 (0.96–1.26)	0.185	—	—
Loam	0.96 (0.87–1.07)	0.471	1.03 (0.96–1.11)	0.371	0.96 (0.85–1.08)	0.505	0.99 (0.77–1.27)	0.933
Silty clay loam	1.02 (0.93–1.12)	0.648	0.79 (0.74–0.85)	<.001	0.99 (0.89–1.10)	0.834	0.99 (0.80–1.24)	0.961
Clay loam	1.46 (1.29–1.66)	<.001	1.11 (0.93–1.33)	0.238	0.98 (0.83–1.17)	0.839	0.92 (0.74–1.15)	0.478
Clay	1.06 (0.98–1.15)	0.142	1.26 (1.17–1.35)	<.001	0.97 (0.88–1.07)	0.563	1.10 (0.91–1.32)	0.317
Silty clay	0.66 (0.56–0.79)	<.001	0.95 (0.83–1.09)	0.451	0.85 (0.65–1.11)	0.226	1.07 (0.70–1.63)	0.757
Categorical (Road Hierarchy)								
Other principal arterial	*Reference*	—	*Reference*	—	*Reference*	—	*Reference*	—
Minor arterial road	0.90 (0.76–1.05)	0.185	0.93 (0.85–1.02)	0.110	0.91 (0.78–1.05)	0.190	—	—
Major collector road	0.86 (0.75–0.99)	0.038	1.06 (0.97–1.15)	0.198	1.04 (0.91–1.19)	0.552	—	—
Local road	1.05 (0.95–1.16)	0.315	1.13 (1.06–1.20)	<.001	1.07 (0.97–1.17)	0.170	1.03 (0.82–1.29)	0.801
Not under road	1.16 (1.03–1.31)	0.014	1.03 (0.95–1.11)	0.484	0.94 (0.84–1.05)	0.282	1.02 (0.77–1.34)	0.903

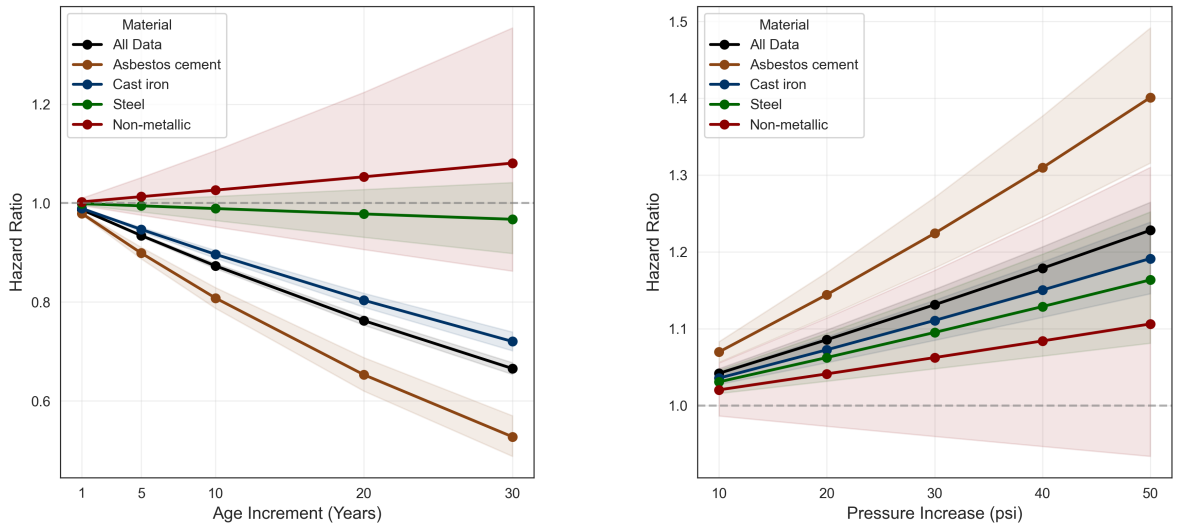
Note: Reference levels represent hazard baselines against which HRs are estimated. Some categories has not enough data for meaningful estimation and are marked as '–'.

2.5.4 Sensitivity Analysis on Continuous Variables

To further evaluate the impact of temporal and operational stressors, a sensitivity analysis was conducted across varying increments of pipe age (Figure 2.7a) and internal pressure (Figure 2.7b). The age sensitivity analysis reveals a widening divergence in material performance over longer increments. For asbestos cement and cast iron, the CI tighten significantly as the age increment increases, confirming a statistically robust survivorship effect. The asbestos cement and cast iron pipes show sharp declines in risk with relatively narrow intervals, suggesting that surviving assets are more reliable than the general population. In contrast, the steel and non-metallic categories display much broader shaded areas, particularly at the 20- and 30-year increments. Notably, for both steel and non-metallic pipes, the value of 1.0 remains consistently within the 95% CI across nearly all age increments. This lack of statistical divergence from the baseline suggests that age is not a significant driver of degradation for these materials within the observed window.

Regarding operational pressure, the sensitivity analysis indicates that asbestos cement

pipes are the most significantly affected by increases in internal loading. The hazard ratio for asbestos cement pipes climbs sharply and stays consistently above the other material types, with a narrow 95% CI that remains entirely above the 1.0 baseline. This indicates a statistically robust and predictable relationship where higher pressure directly accelerates failure for asbestos cement assets. Steel and cast iron pipes follow a similar pattern to one another, both exhibiting a gradual increase in failure risk as pressure increments rise. While their trajectories are less aggressive than that of asbestos cement, the steady upward trend in their hazard ratios suggests a meaningful, albeit slightly more moderate, sensitivity to operational pressure. In contrast, non-metallic pipes show no significant effect across the entire pressure horizon. The CI for these materials is notably wider, likely due to a smaller dataset, and consistently overlaps the 1.0 baseline. This indicates that for non-metallic assets, internal pressure is not a statistically significant driver of degradation within the observed ranges, reflecting their superior strain tolerance and flexibility compared to rigid metallic and cementitious alternatives.



(a) Age sensitivity analysis by material

(b) Water pressure sensitivity analysis by material

Fig. 2.7. Sensitivity analysis of Hazard Ratios for continuous variables across different pipe materials. Shaded areas represent the 95% confidence intervals.

2.6 Conclusions

This study evaluated water distribution pipe deterioration using survival analysis applied to a large, spatially integrated utility dataset. The analysis combined nearly 150 years of installation history, more than three decades of recorded failures, and pipe-level physical, operational, and environmental attributes. By accounting for left-truncated and right-censored observations, the framework addressed important limitations of historical infrastructure records and produced statistically derived estimates of the factors associated with pipeline failure hazard.

Kaplan–Meier survival curves revealed substantial heterogeneity in pipeline longevity across pipe materials, diameters, operating-pressure levels, geospatial-hazard exposure, soil conditions, roadway contexts, and previous failure histories. These findings reinforce previous research showing that chronological age alone is insufficient to represent pipe condition and that deterioration is influenced by structural, operational, environmental, and historical factors [64, 110]. The distinct survival patterns among materials also supported the use of material-specific models rather than assuming that all degradation factors affect the network uniformly.

The pooled Cox proportional hazards model identified previous failure history as the strongest network-wide predictor. Pipes with at least one recorded failure exhibited more than six times the instantaneous failure hazard of pipes without a previous failure, consistent with earlier studies identifying break history as an important predictor of subsequent failure [1, 37]. Geospatial exposure was also important: pipes within fault and landslide zones experienced approximately 42% and 29% higher failure hazards, respectively. Each 10 psi increase in operating pressure was associated with an approximately 5% increase in hazard, while 4-inch and 6-inch pipes exhibited higher hazards than the 10-inch reference group. Soil and roadway variables showed more moderate and heterogeneous associations. Clay loam was associated with elevated hazard, whereas silty clay and silty clay loam were associated with lower hazards relative to the reference soil category. These results are consistent with prior research showing that soil texture, moisture, aeration, electrochemical properties, and mechanical support can influence buried-pipe deterioration [101, 130, 78]. However, the estimated soil effects are specific to the conditions represented in this utility and should not be interpreted as universal rankings of soil aggressiveness. Roadway context was also associated with failure hazard, but roadway class may capture differences in pipe size, installation period, trench construction, maintenance history, and other unobserved conditions. It should therefore not be interpreted as a direct measure of traffic-induced loading.

A primary contribution of this study is the direct comparison of pooled and material-specific Cox-PH models. Previous research has often emphasized either network-wide prediction or individual deterioration mechanisms within a particular material. The present analysis connects these perspectives by evaluating a common set of factors across the full network and then estimating their effects separately for asbestos cement, cast iron, steel, and non-metallic pipes. The results show that pooled hazard ratios can conceal meaningful differences in both the magnitude and statistical significance of individual predictors.

Asbestos cement pipes showed strong associations with previous failure, operating pressure, smaller diameter, geospatial exposure, and selected soil conditions. These results are broadly consistent with studies linking asbestos cement deterioration to pipe geometry, clay soils, environmental exposure, and weakening of the cementitious matrix [49, 142]. Cast iron pipes were influenced by previous failure, diameter, pressure, geospatial exposure, and soil type, supporting earlier work on the combined effects of corrosion, pipe geometry, manufacturing characteristics, and external loading [72, 103]. Steel pipes were most strongly associated with previous failure, geospatial hazards, operating pressure, and selected soil conditions, while age and diameter were not statistically significant within the observed period. Few predictors were significant for non-metallic pipes; however, this likely reflects their more recent installation, shorter observation histories, fewer recorded failures, and wider confidence intervals rather than an absence of deterioration processes.

The sensitivity analysis clarified the interpretation of age and pressure across materials. Hazard ratios below one for increasing age increments in asbestos cement and cast iron pipes should not be interpreted as evidence that these assets strengthen over time. Instead, they are consistent with survival selection in a network where many legacy pipes were installed long before systematic failure records began. Although delayed-entry models correctly define when surviving pipes enter the observed risk sets, they cannot recover assets that failed and were removed before the beginning of the available record. Pressure effects also varied by material: asbestos cement exhibited the strongest and most consistent increase in hazard, cast iron and steel showed more moderate increases, and no statistically significant pressure association was observed for non-metallic pipes within the available data.

Overall, this study advances pipeline deterioration analysis by integrating long-term infrastructure records with spatially resolved physical, operational, and environmental data in a survival framework that accounts for delayed entry and right censoring. The findings demonstrate that network-wide estimates can mask substantial differences in the magnitude and significance of failure predictors across pipe materials. The resulting hazard ratios provide interpretable, statistically derived measures of relative failure risk and offer an empirical basis for improving utility risk-assessment practices that currently rely on fixed, experience-based weights.

Future research should extend the framework using recurrent-event models to represent multiple failures on the same pipe, time-varying covariates to capture changing pressure and environmental conditions, and spatial models to account for geographic dependence and unobserved local factors. Additional information on repairs, burial depth, wall thickness, coatings, soil chemistry, and pipe condition would strengthen the physical interpretation of the estimated relationships. Flexible parametric survival models could also be evaluated for forecasting beyond the observed period, provided their distributional assumptions are carefully validated.

Chapter 3

Data-Driven Vulnerability Assessment for Aging Water Networks

3.1 Introduction

Urban water distribution networks (WDNs) are deteriorating at a rate that exceeds the capital rehabilitation budgets available to most municipalities. Across the United States and Canada, approximately 20% of buried water pipelines are currently operating beyond their intended design life, contributing to an estimated $452 billion deferred maintenance backlog. In the United States alone, water main failures result in the loss of roughly 2 trillion gallons of treated water each year. As a result, many utilities remain in a reactive mode of asset management, addressing failures only after catastrophic pipe ruptures occur [63, 6]. The consequences of these failures extend well beyond water loss, frequently disrupting co-located infrastructure, damaging roadways, interrupting transportation systems, and imposing substantial socio-economic costs on communities [7, 80].

Although proactive rehabilitation strategies offer a potential alternative, they are often guided by heuristic scoring systems based on utility judgment, which typically rely on a combination of pipe age and previous failure records. While existing literature consistently demonstrates that previous failure history is a strong predictor of future breaks [67, 106], relying predominantly on these records creates a fundamentally reactive prioritization cycle. In practice, in-house utility models tend to continually cater to pipes that have already failed rather than evaluating the true structural integrity of the broader network. Consequently, these traditional approaches frequently overlook critical "first-time failure" assets—pipes that are highly vulnerable to degradation but have not yet recorded a physical break. This limitation is particularly troublesome given that capital constraints typically restrict utilities to replacing 1% or less of their network inventory annually. Under such constraints, waiting for an initial failure to trigger prioritization results in the inefficient allocation of limited resources and a failure to prevent catastrophic first-time ruptures.

Predictive modeling provides a means of extending rehabilitation decisions beyond simple

age- and failure-history rules. Statistical and machine-learning models can integrate physical pipe characteristics with operational, environmental, spatial, and historical information to estimate the likelihood of future failure. Machine-learning methods are particularly useful for representing nonlinear relationships and complex associations among variables that may be difficult to specify in advance. However, predictive accuracy alone does not guarantee operational value. For a model to support asset management, its prediction horizon and evaluation criteria must correspond to the actual decisions faced by utilities. This distinction is important because utilities typically cannot intervene on every asset assigned an elevated failure probability. Instead, they must select a relatively small subset of pipes for inspection, rehabilitation, or replacement within a defined budget and planning period. Global performance measures calculated across an entire network may therefore provide an incomplete assessment of practical usefulness. A model may achieve strong overall discrimination while failing to capture many observed failures among the highest-ranked assets that a utility could realistically address. Decision-oriented evaluation should consequently examine model performance within the limited portion of the network that can be included in a capital program.

This study develops a machine-learning framework for near-term water-main failure prediction using a 34-year historical dataset from a utility in the San Francisco East Bay region of California. Random Forest (RF) and eXtreme Gradient Boosting (XGBoost) models are developed using pipe-level physical, operational, environmental, and historical attributes. The prediction outcome is defined over a three-year planning horizon so that model outputs correspond to a specified capital-planning period rather than an undefined future risk.

Model performance is evaluated both globally and within the highest-ranked portions of the network. In particular, Recall@k is calculated for the top 1–5% of pipe segments, representing a range of constrained rehabilitation budgets. This evaluation determines how many observed failures are captured when intervention is limited to the assets assigned the highest predicted risks. The analysis also examines whether the models improve the identification of first-time failures relative to approaches dominated by age or previous failure history. The study focuses not only on statistical predictive performance, but also on whether model outputs can support practical, budget-constrained rehabilitation planning.

Accordingly, this chapter addresses three principal questions: (1) how accurately can ensemble machine-learning models identify water-main failures within a defined three-year planning horizon; (2) how effectively do the models capture failures when rehabilitation is limited to the highest-ranked 1–5% of network assets; and (3) can the models improve the identification of first-time failures that may be overlooked by prioritization approaches dominated by previous break history? By aligning the prediction horizon, evaluation metrics, and asset-ranking process with utility planning constraints, the study seeks to develop a framework that is not only statistically robust but also directly relevant to budget-constrained rehabilitation decision-making.

3.2 Literature Review

3.2.1 Risk-Based Rehabilitation and Asset Prioritization

Water-main asset management requires utilities to balance the probability of failure, the consequences of failure, and the cost of intervention. Risk-based rehabilitation frameworks commonly combine estimates of failure likelihood with measures of service disruption, repair cost, hydraulic importance, or impacts on customers and surrounding infrastructure. Raspati et al. developed a risk-based approach in which the probability and consequences of pipe breaks were combined to support rehabilitation prioritization [106]. Similar work on co-located road and water infrastructure has shown that coordinated maintenance planning can reduce shared costs and account for dependencies between infrastructure systems [80]. In practice, many prioritization approaches rely on a limited number of readily available asset variables. Pipe age and previous failure history are particularly common because they are recorded by most utilities and are easily incorporated into scoring systems. Previous failures often provide useful information about persistent vulnerability, but dependence on failure records can reinforce reactive decision-making by favoring assets that have already broken. Pipes without a failure history may receive low priority even when their physical, operational, or environmental characteristics indicate elevated vulnerability.

Kumar et al. demonstrated the practical limitations of simple heuristics in a machine-learning application developed for Syracuse, New York [67]. Their gradient-boosted model predicted water-main breaks over a three-year period and outperformed heuristics based on pipe age and previous failures when evaluated using precision among the highest-ranked 1% of assets. The study established an important precedent for aligning predictions with a defined near-term planning horizon and evaluating performance within a realistically constrained intervention set. However, predictions were generated at the city-block level rather than for individual pipe segments, requiring pipe characteristics within each block to be aggregated and potentially obscuring asset-level variation. In addition, the primary evaluation focused on precision at a single budget threshold. These limitations leave opportunities to evaluate failure capture across multiple feasible rehabilitation levels, preserve pipe-segment-level information, and assess model performance specifically for assets without previous recorded failures.

3.2.2 Physical and Statistical Pipe-Failure Models

Early water-main deterioration studies relied primarily on engineering models, deterministic rules, regression methods, and probability distributions. Reviews by Kleiner and Rajani, Nishiyama and Filion, and Scheidegger et al. document the development of models based on failure counts, break rates, survival times, and physical deterioration processes [63, 82, 108]. These approaches established that pipeline failure is influenced by multiple characteristics, including material, age, diameter, length, installation period, operating conditions, soil properties, and failure history.

Regression-based methods have included linear, Poisson, negative-binomial, and proportional-hazards formulations. Yamijala et al., for example, evaluated statistical models for individual-pipe break data and emphasized the influence of model structure and available explanatory variables [140]. Such models provide interpretable coefficients and can reveal broad deterioration trends, but they often require assumptions about the functional form of predictor effects, event independence, or the distribution of failure counts and times.

Parametric lifetime models, including Weibull-based approaches, represent deterioration by assuming a specified probability distribution for failure time. These models can estimate survival probabilities and expected service life when their assumptions are appropriate. Their performance may deteriorate, however, when a heterogeneous network contains materials, installation cohorts, and environmental conditions with substantially different hazard patterns [108].

Physical and physical–probabilistic models provide a more mechanistic representation of deterioration. These approaches may combine structural analysis, corrosion progression, loading, and reliability calculations to estimate changes in pipe capacity over time. Li et al., for example, integrated finite-element analysis and probabilistic reliability assessment to evaluate the time-dependent performance of deteriorating cast iron pipes [69]. Such models can provide detailed insight into failure mechanisms, but they require information such as wall thickness, defect geometry, material strength, burial conditions, and corrosion state that is rarely available consistently across an entire utility network.

Operational conditions have also been incorporated into statistical and physical models. Martinez et al. evaluated the relationship between pressure and pipe breaks, demonstrating the importance of hydraulic conditions in failure analysis [73]. Nevertheless, pressure effects may vary with material, diameter, structural condition, and location, making them difficult to represent through a single deterministic rule.

3.2.3 Machine Learning for Pipe-Failure Prediction

The increasing availability of digital asset records, geographic information systems, and computational resources has encouraged the use of machine learning for water-main failure prediction. Reviews of artificial-intelligence applications and deterioration predictors describe a growing range of methods, including decision trees, support vector machines, artificial neural networks, ensemble methods, and hybrid models [41, 110]. These approaches are attractive because they can represent nonlinear relationships and high-order associations without requiring a predetermined parametric failure function.

Comparative studies indicate that no single method performs best for every utility or dataset. Giraldo-González and Rodríguez compared statistical and machine-learning methods for pipe-failure modeling and showed that performance depended on the modeling approach, data structure, and prediction objective [46]. Thus, machine learning should not be assumed to outperform statistical methods universally; rather, its potential advantage lies in its flexibility when sufficient, representative data are available.

Tree-based ensemble models have received particular attention. Random Forest constructs multiple decision trees using bootstrap samples and randomized predictor subsets, reducing the variance and instability associated with a single tree [14]. XGBoost sequentially builds trees to correct earlier errors and includes regularization and computational procedures designed for efficient learning from structured data [22]. Both methods can capture nonlinear relationships and interactions among pipe, environmental, and operational characteristics. Winkler et al. developed a pipe-failure classification framework using decision trees and ensemble methods, showing that boosted trees combined with random undersampling could identify nonlinear failure patterns in imbalanced utility data [136]. Snider and McBean later applied XGBoost to predict time to failure for individual ductile iron pipe segments and reported better performance than the Random Forest and neural-network models evaluated in their case study [112]. However, their analysis focused on a single material and excluded pipes without observed failures. In subsequent work, they compared gradient-boosted trees with a Weibull proportional-hazards model and showed that excluding right-censored assets can bias machine-learning predictions toward shorter failure times [113]. Collectively, these studies demonstrate the value of ensemble tree methods while highlighting limitations related to censoring, material coverage, class imbalance, and planning-horizon selection.

Barton et al. developed a gradient-boosted tree model for a large UK network and extended predicted failure probability through a weighted risk analysis incorporating selected consequences of failure [8]. Their study highlighted the need to move from probability prediction toward decision support and noted that utilities may be primarily interested in the small proportion of pipes with the highest risks. However, the consequence weights relied partly on expert judgment, and the model grouped assets spatially rather than predicting every individual pipe independently.

Other recent research has expanded pipe-failure prediction by incorporating a broader range of environmental and spatial information. Fan et al. evaluated machine-learning models using physical, operational, and environmental pipe attributes, demonstrating the value of combining multiple sources of utility data [44]. Hu et al. extended this direction through a graph-neural-network framework that represented spatial relationships between roads and pipelines [48]. These studies highlight the potential benefits of incorporating infrastructure interdependencies and spatial context into failure prediction. However, more complex models may require detailed relational data, greater computational resources, and additional effort to interpret and implement. This tradeoff supports the continued evaluation of tree-based ensemble models, which can capture nonlinear relationships among diverse pipe-level predictors while remaining comparatively practical for utility-scale risk ranking.

3.2.4 Data Quality and Class Imbalance

Machine-learning applications to WDNs face persistent challenges related to data completeness and class imbalance. Pipe failures typically represent only a small fraction of the total network population, producing highly imbalanced classification datasets. Under these conditions, a model can achieve high overall accuracy by predicting that most pipes will not fail

while identifying only a small proportion of the failures relevant to rehabilitation planning. Beig Zali et al. developed a semisupervised clustering approach for pipe-failure prediction under imbalanced conditions [9], while Motiee and Sattari proposed an interpretable framework that addressed both imbalance and recurrent failure records [76]. These studies show that rare-event structure must be considered during model development, sampling, validation, and performance interpretation.

Historical utility records also frequently contain missing or incomplete attributes. Kabir et al. applied Bayesian model updating to address uncertainty in water-main failure prediction [56], while Xu and Sinha combined survival analysis with machine-learning-based imputation to address missing information in pipe-break records [138]. These approaches demonstrate that predictive performance depends not only on algorithm selection but also on the quality and completeness of the underlying asset data.

Incomplete failure histories create an additional challenge. Many pipes were installed decades before systematic failure recording began, meaning that earlier failures, repairs, or replacements may be absent from the available data. This left-truncated structure can introduce survival-selection effects and distort relationships between pipe age, failure history, and future risk [2]. Although the present chapter focuses on near-term classification rather than survival estimation, incomplete records can still affect predictor construction and model interpretation, particularly for variables based on age and previous failures.

3.2.5 Model Transferability and Decision-Oriented Evaluation

A major limitation of data-driven pipe-failure models is their uncertain transferability across utilities. Networks differ in material composition, installation practices, climate, soil conditions, pressure regimes, maintenance policies, and data-recording standards. Daulat et al. evaluated the generalizability of pipe-failure models and identified substantial challenges when transferring trained models between utilities [40]. Consequently, strong performance within one case study should not be interpreted as evidence that the same model or predictor relationships will remain valid elsewhere. Utility-specific calibration and external validation are therefore important when predictive models are used to support infrastructure decisions.

Even within the utility for which a model is developed, conventional performance metrics may not fully represent operational usefulness. Accuracy, area under the receiver-operating-characteristic curve, precision, recall, and F1 score summarize performance across the full dataset, but utilities generally cannot intervene on every asset assigned elevated risk. Rehabilitation programs are constrained by available budgets, construction capacity, coordination requirements, and acceptable levels of service disruption. The more relevant question is therefore whether observed failures are concentrated among the relatively small number of assets that a utility can realistically inspect, rehabilitate, or replace. Previous studies have taken important steps toward this type of decision-oriented evaluation. Kumar et al. assessed precision among the highest-ranked 1% of assets over a three-year prediction period [67]. Barton et al. similarly emphasized high-risk subsets and combined predicted failure probability with selected consequences to support strategic planning [8]. These studies

demonstrate the value of evaluating models within realistic intervention sets rather than relying exclusively on full-network averages.

3.2.6 Research Gap and Contributions

Nevertheless, important gaps remain. Many studies evaluate only one ranking threshold, making it difficult to assess how performance changes under different rehabilitation budgets. In addition, precision-focused evaluation indicates how many selected assets fail but does not directly quantify the proportion of all future failures captured within the intervention set. Recall@k provides this complementary perspective by measuring the share of observed failures contained within the top-ranked fraction of the network. Evaluating Recall@k across several values of k therefore allows model usefulness to be examined under multiple capital-deployment scenarios. It also provides a practical basis for determining whether predictive models can improve the identification of first-time failures that would be overlooked by prioritization strategies dominated by previous break history.

This study addresses these gaps by comparing RF and XGBoost models for predicting water-main failures within a user defined planning horizon (3-year for example). Performance is evaluated across the highest-ranked 1–5% of pipe assets using Recall@k, allowing the results to be interpreted under different capital-deployment scenarios. The analysis also evaluates model performance for assets without previous failures to determine whether machine learning can identify vulnerabilities that would be overlooked by failure-history-based prioritization. Accordingly, the chapter investigates three principal questions: whether ensemble models can reliably identify near-term pipe failures; how their practical value changes as the feasible intervention fraction varies; and whether they improve the detection of first-time failures relative to conventional age- and history-based approaches.

3.3 Data

To develop and validate the predictive models, this study utilizes a comprehensive pipeline inventory and historical failure dataset provided by the collaborated water utility. The distribution system serves water at the East Bay of San Francisco Bay Area, with majority of the pipes made of cast iron, asbestos cement, steel, and non-metallic, which are the focuses of this study. The pipeline within the network was built as early as 1880s; however, failure records were not systematically recorded until 1990. The failure records used in this study span from 1990 - 2024. Over the 34-year observation period, the utility recorded a total of 18,921 pipe failures. Across the entire system, this translates to an overall network degradation rate of 14.87 breaks per 100 miles per year.

The structural performance varies across different pipe materials, as detailed in Table 3.1. Cast Iron (Material C) constitutes roughly 31% of the network's physical length (1,158.3 miles) but exhibits a high vulnerability to degradation, suffering 33.58 breaks per 100 miles per year. Consequently, Cast Iron assets are responsible for a staggering 69.9% of all histor-

ical network failures. Asbestos Cement (Material A) similarly demonstrates a high failure rate, accounting for 22.1% of total network breaks. In sharp contrast, Non-metallic pipes (Material N) prove to be more resilient or simply because they are younger, experiencing only 0.79 breaks per 100 miles per year and representing less than 1% of total system failures. This highly disproportionate distribution of failures across material cohorts highlights the complex nature of pipeline degradation.

Table 3.1. Pipeline inventory and historical failures (1990–2024)

Material	**Pipes** (n)	**Length (mi)**	**Failures**	**Rate**[a]	**Total (%)**[b]
Overall Network					
All Types	110,947	3,743.0	18,921	14.87	100.0
By Material Cohort					
C (Cast Iron)	34,176	1,158.3	13,226	33.58	69.9
A (Asbestos Cement)	29,657	1,108.7	4,183	11.10	22.1
S (Steel)	34,264	1,019.6	1,389	4.01	7.3
N (Non-metallic)	12,850	456.4	123	0.79	0.7

[a] Failure rate expressed as breaks / 100 miles / year.

[b] Proportion of total network failures attributed to this material.

To accurately model the complex deterioration mechanisms of the water distribution network, a robust set of 19 predictor variables was engineered for each pipe segment by integrating utility-provided asset records with authoritative environmental databases. Physical attributes, operational pressure, and historical maintenance logs were sourced directly from the collaborating utility's inventory. To capture external degradation drivers, these internal records were spatially joined with public geotechnical and environmental datasets. Specifically, groundwater levels were interpolated from the California Department of Water Resources [18] and the GeoTracker database [19]; geological hazards, including fault and landslide zones, were identified via the USGS Quaternary Fault and Fold Database [125]; traffic loading was approximated using Caltrans roadway classifications [17]; soil properties were derived from the USDA SSURGO database [124]; and time-averaged shear-wave velocity (Vs30) predictions were generated using AlphaEarth [16]. As detailed in Table 3.2, these features are systematically categorized into four domains: physical attributes, operational characteristics, environmental and geospatial factors, and historical performance.

Table 3.2. Predictive model features and attribute descriptions

Attribute (Type)	**Range / Categories**	**Description & Preprocessing**
Physical Attributes		
Pipe Age (*Cont.*)	3 – 159 yr	Prediction Year (T) − Installation Year.
Diameter (*Cont.*)	4.0 – 16.0 in	Nominal pipe diameter.
Length (*Cont.*)	0.0 – 336.5 ft	Transformed using $\log(1 + \text{length})$.
Material (*Cat.*)	Asbestos Cement (A), Cast Iron (C), Non-metallic (N), Steel (S)	One-hot encoded.
Operational Characteristics		
Oper. Pressure (*Cont.*)	0.3 – 319.7 psi	Set to -1 if unknown.
Pressure Zone (*Cat.*)	39thAve, Acorn, ... (41 total)	One-hot encoded.
Service District (*Cat.*)	Central, East, North, South	One-hot encoded.
Environmental & Geospatial Factors		
Soil Type (*Cat.*)	Rock, Water, Loam, Silty Clay Loam, Clay Loam, Clay, Silty Clay, Sand Loam, Sand	Based on Unified Soil Classification System.
Road Hierarchy (*Cat.*)	Major Arterial, Secondary Arterial, Collector, Local	Indicates traffic loading.
Landslide Zone (*Bin.*)	0 / 1	1 = Within landslide hazard area.
Fault Zone (*Bin.*)	0 / 1	1 = Within fault zone.
Groundwater (*Cont.*)	-5.8 – 168.8 ft	Depth to groundwater .
Wet Flag (*Bin.*)	0 / 1	1 = Historically wet soil conditions.
Vs30 (*Cont.*)	151.0 – 676.1 m/s	Predicted shear-wave velocity (AlphaEarth).
Green Zone (*Bin.*)	0 / 1	1 = Soil contaminated zone.
Historical Performance (Calculated up to Anchor Year T)		
Prior Fails (All) (*Count*)	0 – 18	Total failures on this segment before T.
Prior Fails (5-yr) (*Count*)	0 – 8	Failures on this segment in interval $[T-5, T)$.
Ext. Fails (All) (*Count*)	0 – 47	Total failures on the parent extension before T.
Ext. Fails (5-yr) (*Count*)	0 – 14	Failures on parent extension in interval $[T-5, T)$.

3.4 Methodology

3.4.1 Model Training and Temporal Cross-Validation

To evaluate the predictive models under realistic utility operational constraints, the historical failure dataset was strictly partitioned chronologically. Random data splitting in infrastructure deterioration modeling frequently introduces data leakage, where future failure data inadvertently informs past predictions. To prevent this and to accurately simulate a utility's forward-looking planning process, we implemented a temporal walk-forward backtesting scheme across seven sequential evaluation years ($T \in \{2015, \ldots, 2021\}$). For each evaluation year T, the problem is formulated as a binary classification task: for each pipe segment, the model predicts whether it will experience at least one failure within the subsequent planning horizon of Δt years. While multiple planning horizons were formulated, this study focuses on a 3-year horizon ($\Delta t = 3$) as the primary case study to directly align with standard medium-term utility capital improvement cycles.

Rather than utilizing a single, static dataset, the network's state was captured through a series of temporal snapshots. For a given snapshot, an anchor year, t, was established. The model's features, such as age, cumulative failure history, and environmental conditions, were calculated strictly using data available up to year t. The target variable was then defined as a binary indicator of whether a pipeline experienced a failure within the subsequent predictive horizon, $(t, t + \Delta t]$.

To train the models for a specific evaluation year T, the anchor year t is iteratively shifted forward from 1990 up to $T - \Delta t$. The snapshots from these rolling windows are stacked row-by-row to form a comprehensive training "mega-matrix." Capping the training snapshots at $T - \Delta t$ prevents label-window overlap between the training phase and the out-of-time testing phase. This temporal stacking technique augments the training data while allowing the model to learn time-dependent degradation patterns. For the utility dataset, this mega-matrix reaches approximately 2.3 to 2.7 million rows per evaluation year. Two ensemble tree models (RF and XGBoost) were trained in parallel for every unique combination of predictive horizon (Δt) and evaluation year (T). Both models ultimately output a continuous failure probability score for each pipe segment, which is then utilized to rank all pipes network-wide from highest to lowest risk.

Mathematically, let the water distribution network consist of a set of N pipelines, denoted as $P = \{p_1, p_2, \ldots, p_N\}$. To formulate the predictive model, the temporal state of each pipeline is defined relative to an anchor year, t. For a given pipeline p_i at anchor year t, we define a feature vector $\mathbf{x}_{i,t} \in \mathbb{R}^d$ representing d covariates. The objective is to predict the likelihood of failure within a specific forward-looking planning horizon, denoted as Δt. The target variable, $y_{i,t,\Delta t}$, is defined as a binary indicator:

$$y_{i,t,\Delta t} = \begin{cases} 1, & \text{if pipeline } p_i \text{ experiences a failure in the interval } (t, t + \Delta t] \\ 0, & \text{otherwise} \end{cases}$$

To construct the training mega-matrix, $D_{train,T}$, for a specific evaluation year T, the anchor year t is iteratively advanced from the initial observation year ($t_{start} = 1990$). To guarantee zero data leakage, the maximum anchor year for training is restricted to $T - \Delta t$:

$$D_{train,T} = \bigcup_{t=t_{start}}^{T-\Delta t} \left\{ \left(\mathbf{x}_{i,t}, y_{i,t,\Delta t} \right) \right\}_{i=1}^{N}$$

By formulating the training data in this manner, the ML algorithms learn a generalized mapping function $f : \mathbf{x} \rightarrow [0, 1]$. This function predicts the probability of failure $\hat{p}$ given the state of the network at any time t:

$$\hat{p}(y_{i,t,\Delta t} = 1 \mid \mathbf{x}_{i,t}) = f(\mathbf{x}_{i,t}; \theta)$$

where θ represents the optimized parameters of the respective ensemble model.

Performance is assessed exclusively using an out-of-time testing dataset, $D_{test,T}$, composed of a single network snapshot taken at the evaluation year T. The model relies strictly on features calculated up to year T to predict failures in the unseen future interval $(T, T+\Delta t]$:

$$D_{test,T} = \left\{ \left(\mathbf{x}_{i,T}, y_{i,T,\Delta t} \right) \right\}_{i=1}^{N}$$

For the 3-year horizon case study ($\Delta t = 3$), this mathematical separation is repeated across the seven evaluation years, generating seven distinct, non-overlapping testing periods: 2015–2017, 2016–2018, 2017–2019, 2018–2020, 2019–2021, 2020–2022, and 2021–2023. This walk-forward validation proves the models' capacities to inform true forward-looking Capital Improvement Programs across shifting temporal conditions.

3.4.2 Performance Evaluation Metrics

To effectively evaluate the models' predictive capabilities, their theoretical outputs must first be mapped to operational reality. In the context of binary failure prediction, this evaluation relies fundamentally on the confusion matrix, categorizing predictions into four discrete outcomes:

- True Positive (TP): A pipeline is predicted to fail and subsequently experiences a failure.
- False Positive (FP): A pipeline is predicted to fail but does not (a false alarm resulting in unnecessary inspection).
- True Negative (TN): A pipeline is predicted to survive and does not experience a failure.
- False Negative (FN): A pipeline is predicted to survive but unexpectedly fails (an unmitigated rupture).

From these operational outcomes, standard diagnostic metrics are derived. Recall (or True Positive Rate) measures the proportion of actual failing pipes that the model successfully identifies, defined as $TP/(TP + FN)$. Additionally, the False Positive Rate (FPR) measures the proportion of healthy infrastructure incorrectly flagged for failure, defined as $FP/(FP + TN)$.

While these foundational classification metrics, and their continuous counterparts like the Area Under the Receiver Operating Characteristic Curve (ROC-AUC), are standard in data science, they are frequently misleading for evaluating infrastructure predictive models due to severe class imbalance. For the utility dataset, the cumulative failure rate across the entire 34-year history is only about 11%, which translates to a positive failure class of approximately 0.5% of the entire number of pipes within any given predictive window. In such an imbalanced environment, a model could achieve 99.5% global accuracy simply by predicting that no pipes will ever fail. Similarly, the global ROC-AUC metric is distorted because it heavily rewards models for correctly classifying the massive majority of low-risk pipes (True Negatives) that the utility would never inspect regardless of the risk score.

Furthermore, utility managers are strictly constrained by capital rehabilitation budgets, typically limiting them to intervening on only 1% to 5% of their network inventory during any given planning cycle. Because global metrics like ROC-AUC fail to reflect these operational realities and the extreme scarcity of failures, this study instead evaluates model efficacy using Cumulative Gain, quantified specifically as Recall at $k\%$ (also referred to as capture rate). This metric directly assesses a model's ability to concentrate the true positive failures within the highly constrained, highest-ranked subset of the network.

To calculate this, the ensemble models output a continuous predicted failure probability, $\hat{p}$, for each pipeline in the out-of-time test set. All N pipelines are then ranked in descending order based on this probability score. For a specific operational intervention threshold $k\%$ (e.g., $k \in \{1, 3, 5, 10\}$), the utility targets a highly constrained subset of size N_k:

$$N_k = \left\lfloor \frac{k}{100} \times N \right\rfloor$$

The Cumulative Gain at threshold k is then calculated as the ratio of actual failures captured within this targeted subset to the total number of actual failures in the entire network during that evaluation window:

$$\text{Recall@}k\% = \frac{\sum_{j=1}^{N_k} y_{(j)}}{\sum_{i=1}^{N} y_i}$$

where $y_{(j)}$ represents the true binary failure label of the j-th highest-ranked pipeline, and the denominator represents the total sum of true failures across the network. By calculating this metric across the top 1%, 3%, 5%, and 10% of the ranked inventory, a direct, actionable translation of algorithmic performance into utility capital planning capacity is provided.

3.5 Results

The predictive efficacy of the models was evaluated against the utility's existing baseline using cumulative gain curves, which directly illustrate the models' ability to prioritize high-risk assets. Figure 3.1 presents the percentage of failures caught (y-axis) relative to the percentage of pipes inspected (x-axis) over the 3-year planning horizon. To provide a robust performance estimate across shifting temporal conditions, the curves for the RF and XGBoost models represent the mean performance across all seven out-of-time evaluation periods. The shaded regions surrounding these curves denote ±1 standard deviation from the mean, demonstrating the high stability and low variance of the ensemble methods. For comparative analysis, the in-house LoF model result is plotted as a static benchmark, utilizing the utility's calculated scores as of the 2020 operational year.

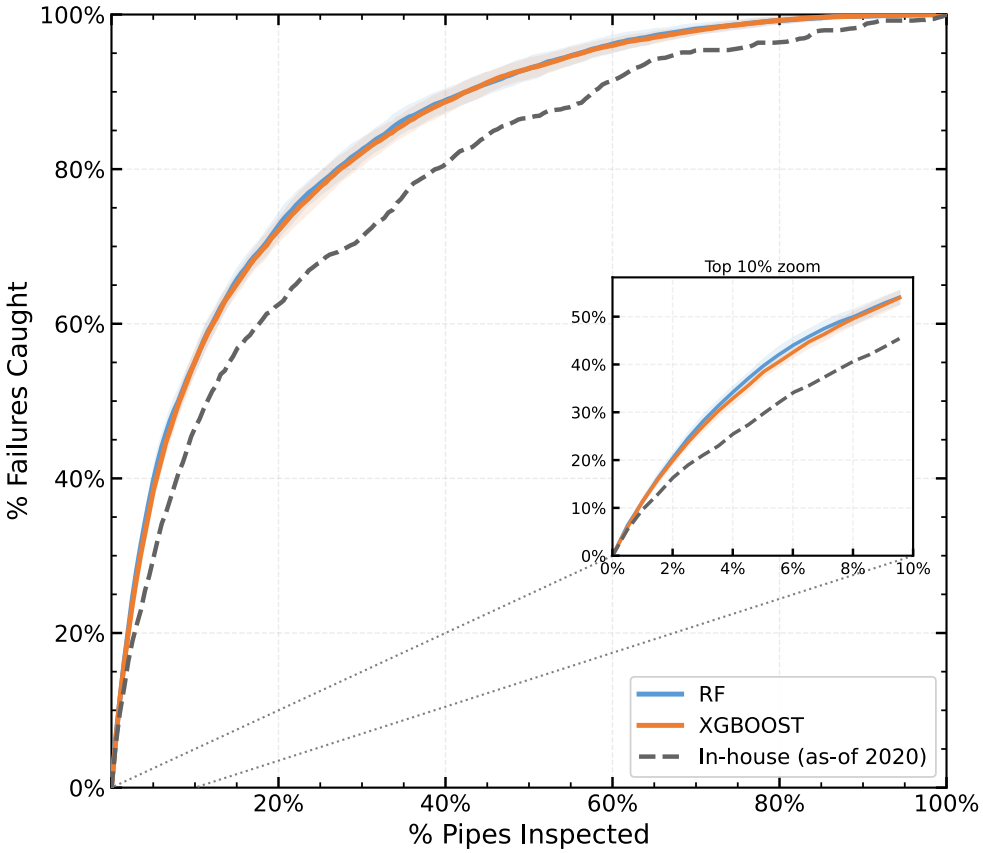


Fig. 3.1. Cumulative gain curves comparing the predictive performance of Random Forest, XGBoost, and the in-house model (as of 2020) for a 3-year predictive horizon. The main plot illustrates global network performance, while the inset isolates the operationally constrained top 10% prioritization bandwidth. Shaded regions indicate ±1 standard deviation across the seven temporal evaluation periods.

As depicted in the overall curve, both ML models outperform the utility in-house prioritization model across the entire network domain. However, because municipal capital improvement programs typically restrict annual rehabilitation to 1% or less of the total inventory, global capture rates are less operationally relevant than concentrated performance. The inset plot in Figure 3.1 specifically provides a top 10% zoom, visually emphasizing the models' behavior within this highly constrained, realistic operational bandwidth.

Table 3.3. Predictive model catch rate summary (3-year horizon)

Model	Top 1%	Top 3%	Top 5%	Top 10%
RF	11.3% ± 0.5%	28.0% ± 1.3%	39.6% ± 1.4%	55.1% ± 1.4%
XGBoost	11.4% ± 0.6%	27.0% ± 1.0%	38.3% ± 1.1%	55.1% ± 1.4%
In-house (as-of 2020)	9.6%	21.0%	29.6%	46.5%

Note: Machine learning models report the mean ± standard deviation across evaluation years.

To quantify these improvements within actionable capital planning limits, Table 3.3 details the specific capture rates at the operationally critical thresholds: the top 1%, 3%, 5%, and 10% of prioritized assets. At the restrictive 1% intervention threshold, XGBoost successfully identifies 11.4% (± 0.6%) of future failures, while RF model captures 11.3% (± 0.5%), compared to the 9.6% capture rate of the 2020 in-house model. As the prioritization bandwidth expands to the 3% and 5% thresholds, representative of multi-year capital planning cycles, the performance divergence between the data-driven models and the traditional heuristic approach becomes more pronounced. At the 5% threshold, RF model captures 39.6% (± 1.4%) of all system failures, and XGBoost captures 38.3% (± 1.1%). In contrast, the in-house baseline model captures only 29.6% of failures at this same volume. Furthermore, the narrow standard deviations reported for both ML models show that the model performance is reliable across all evaluation snapshots.

To validate the foundational ranking capabilities of the algorithms, Figure 3.3 presents the global Receiver Operating Characteristic (ROC) curves for both models. Across the full probability distribution, the algorithms perform well above a random baseline, achieving an AUC-ROC of 0.853 for the Random Forest model and 0.851 for the XGBoost model (Figure 3.2). The markers placed along these continuous curves explicitly denote the operationally relevant top 1%, 3%, 5%, and 10% network prioritization thresholds. While these global ROC-AUC scores are mathematically robust, they must be contextualized by the network's severe class imbalance. Because the ROC metric equally weights the massive majority of low-risk, healthy pipes (True Negatives) that the utility would never actually inspect, the global area under the curve is inherently inflated. Ultimately, while the ROC curve remains the standard academic benchmark for verifying overall model competence, it does not reflect capital constraints. From an asset management perspective, the top k% cumulative gain could serve as a more intuitive and practical measure for utility owners, directly translating

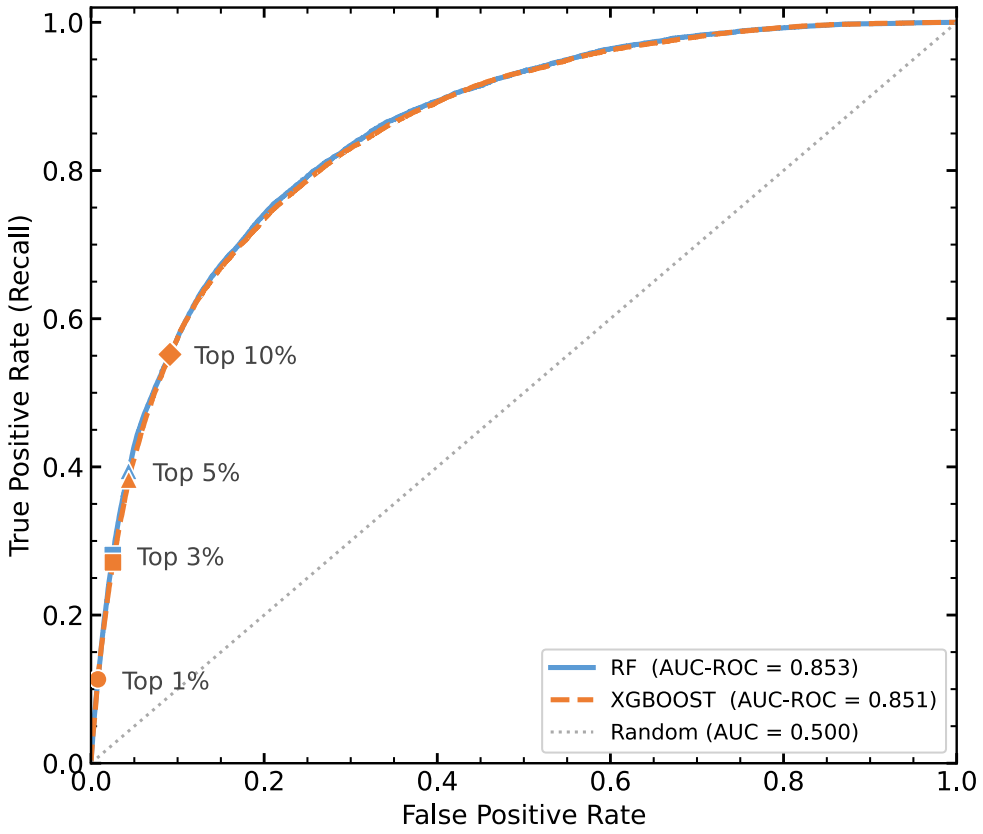


Fig. 3.2. Continuous evaluation of model performance via global Receiver Operating Characteristic (ROC) curves. Markers indicate network prioritization thresholds.

algorithmic performance into actionable rehabilitation cycles.

While predictive accuracy is the primary objective of the ML framework, understanding the driving factors behind the models' risk prioritization is essential for utility managers to trust and validate the algorithmic outputs. Because both RF and XGBoost are ensemble tree-based architectures, feature importance can be extracted inherently from the model training process without requiring external perturbation techniques.

For the RF model, feature importance is calculated using the Mean Decrease in Impurity (often Gini importance). This metric quantifies the total reduction of the criterion (e.g., Gini impurity [15]) brought by a specific feature across all splits in all trees in the forest, normalized so that the sum of all feature importances equals 1.0. For the XGBoost model, importance is typically evaluated using the Gain metric [22], which measures the relative contribution of the corresponding feature to the model calculated by taking each feature's contribution for each tree in the model. To ensure the reported importances represent stable degradation markers rather than artifacts of a specific temporal snapshot, the scores were averaged across all seven walk-forward evaluation years, with the standard deviations plotted

as error bars.

Figures 3.3a and 3.3b illustrate the mean feature importance rankings for the 3-year predictive horizon. The most striking observation across both architectures is the dominance of a pipeline's cumulative past failures, denoted as *PreFail - Pipe (all)*. In the XGBoost model, this single feature accounts for over 50% of the predictive weight, while in the RF model, it accounts for nearly 45%. This reliance aligns with the physical mechanics of infrastructure deterioration: pipe failure is generally an accelerating process. A pipeline that has ruptured in the past possesses a fundamental, systemic weakness that is rarely fully mitigated by a localized clamp or sleeve repair. Similarly, *PreFail - Proj. (all)*, which tracks the historical failures of the broader installation cohort or project, ranks highly in both models, confirming that adjacent pipes from the same vintage and contractor share similar risk profiles.

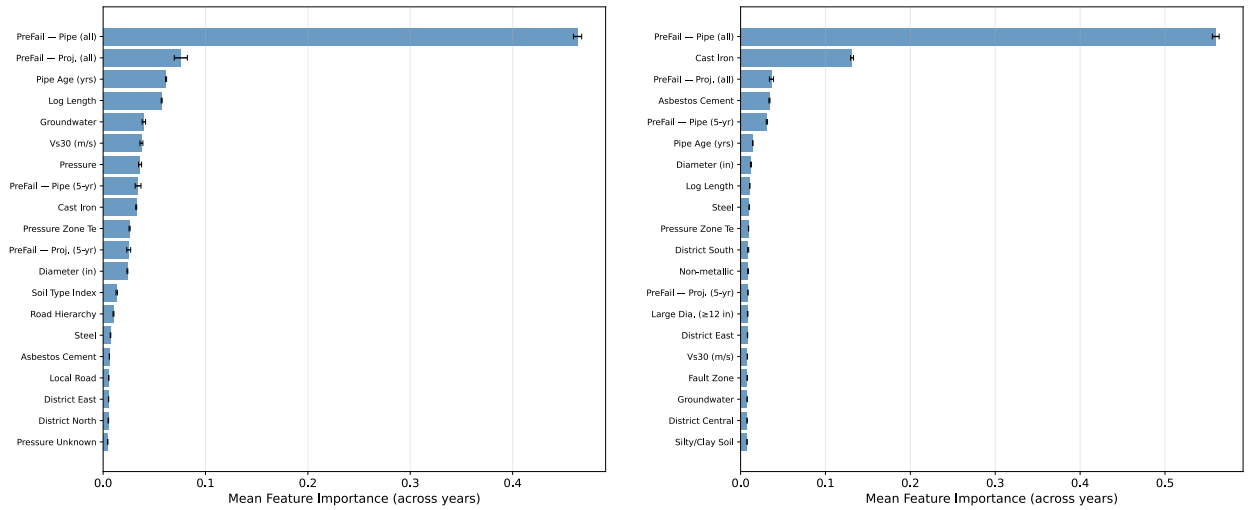
Beyond the dominant influence of historical break records, the two algorithms exhibit distinct, yet physically sensible, divergence in how they prioritize secondary features. The XGBoost architecture heavily prioritizes material categories, ranking *Cast Iron* as its second most important feature and heavily weighting *Asbestos Cement*. This directly reflects the baseline inventory statistics, where cast iron accounts for more than 60% of all network failures despite making up a smaller fraction of the total length.

Conversely, the RF model places a higher emphasis on continuous deterioration variables and spatial/environmental conditions. *Pipe Age (yrs)* and *Log Length* emerge as the third and fourth most critical features. Furthermore, the RF model demonstrates a higher sensitivity to the geotechnical and environmental realities of the pipeline network. Variables such as *Groundwater* and *Vs30 (m/s)* (the time-averaged shear-wave velocity in the top 30 meters of soil) appear prominently in the top ten features. *Vs30* serves as a proxy for soil stiffness and seismic site classification. Ultimately, these feature importance distributions show that both models are not simply finding stochastic correlations, but are mapping the well-documented physical realities of infrastructure degradations.

3.6 Discussions

3.6.1 ML and In-House Model Predictions Evaluation

To fully contextualize the operational value of the ensemble framework, it is necessary to compare its prioritization behavior directly against the collaborating utility's existing heuristic model. The critical divergence between the methodologies lies in the identification of first-time failures. Figure 3.4a evaluates the models' capacities to capture failures on pipe segments that possess zero historical break records. The in-house baseline model demonstrates a fundamental blind spot for these assets, capturing nearly 0% of first-time failures within the top 1% and 3% operational thresholds. This indicates that the heuristic approach is strictly reactive, requiring a pipeline to experience at least one unmitigated rupture before it accrues enough risk penalty to trigger rehabilitation. Conversely, the ML models



(a) Random forest model **(b)** XGBoost model

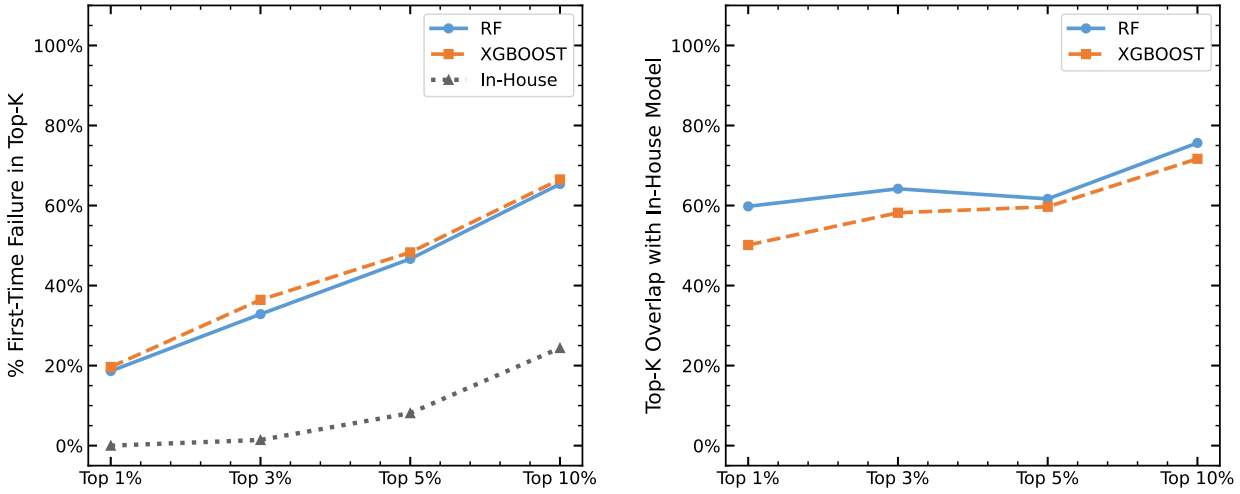
Fig. 3.3. Feature importance of the models.

demonstrate a potentially more proactive predictive capacity. Within the top 1% threshold, both RF and XGBoost models successfully identify approximately 20% of first-time failures, climbing to nearly 40% within the top 5% threshold. This could help utility to shift from a reactive historical tracking approach to a proactive environmental degradation model represents a reduction in unmitigated risk for the utility.

Despite this proactive advantage, the ML algorithms still align with the utility on the most obvious degradation cases. Figure 3.4b illustrates the percentage of Top-K ranked assets where the ML models and the in-house baseline model overlap. Within the most constrained operational bandwidth (the top 1% to 5%), the XGBoost and Random Forest models exhibit an approximate 50% to 65% agreement rate with the in-house prioritization. This substantial overlap could be because, as demonstrated in the feature importance analysis, both the data-driven models and the utility's internal logic heavily penalize pipelines with extensive historical break records. Consequently, both approaches successfully identify the most severely degraded, repeatedly failing assets in the network, demonstrating that the ensemble framework augments, rather than contradicts, existing operational logic.

3.6.2 Cross-Model Validation of High-Risk Asset Profiles

To assess whether the ML models systematically underperform for particular infrastructure cohorts, predictive performance was disaggregated across a range of physical, operational, and environmental categories. Figure 3.5 presents the models' catch rates within the top 3% prioritization threshold, which is representative of a typical multi-year capital planning horizon.



(a) First-Time Failure Capture Rate **(b)** Top-K Overlap

Fig. 3.4. Comparative evaluation of machine learning architectures against the utility's in-house baseline model, tracking (a) the ability to predict first-time failures and (b) the prioritization agreement rate within constrained operational thresholds.

For these stratified analyses, the catch rate is defined as the proportion of actual failures within a given cohort that were successfully identified by the model within its top $k\%$ ranked assets (top 3% in this case). Specifically, the cohort-specific catch rate is calculated as:

$$\text{Catch Rate}_c = \frac{\text{Failures in cohort } c \text{ captured within Top-}k\% \text{ predictions}}{\text{Total observed failures in cohort } c}$$

where c denotes a specific infrastructure cohort (e.g., material type, diameter class, or prior-failure category). For example, if a cohort experienced 100 failures during the study period and the model successfully prioritized 40 of those failures within its top 3% ranked assets, the corresponding catch rate would be 40%. A notable observation across all nine subplots is the similarity between the RF and XGBoost results. The two models exhibit comparable patterns across nearly all cohorts, suggesting that both ensemble approaches are leveraging similar information contained within the data.

The disaggregated results demonstrate that historical failure information plays a primary role in model prioritization. In both the *By Prior Failure Count* and *By Prior-Failure Status* subplots, catch rates generally increase with the number of previous failures. Assets with a documented history of repeated breaks are captured at substantially higher rates than those with no prior failures, with catch rates approaching 95% for segments that have experienced more than five historical breaks. While this pattern does not imply that prior failures alone determine model predictions, it suggests that failure history is a strong indicator of elevated future risk within the dataset.

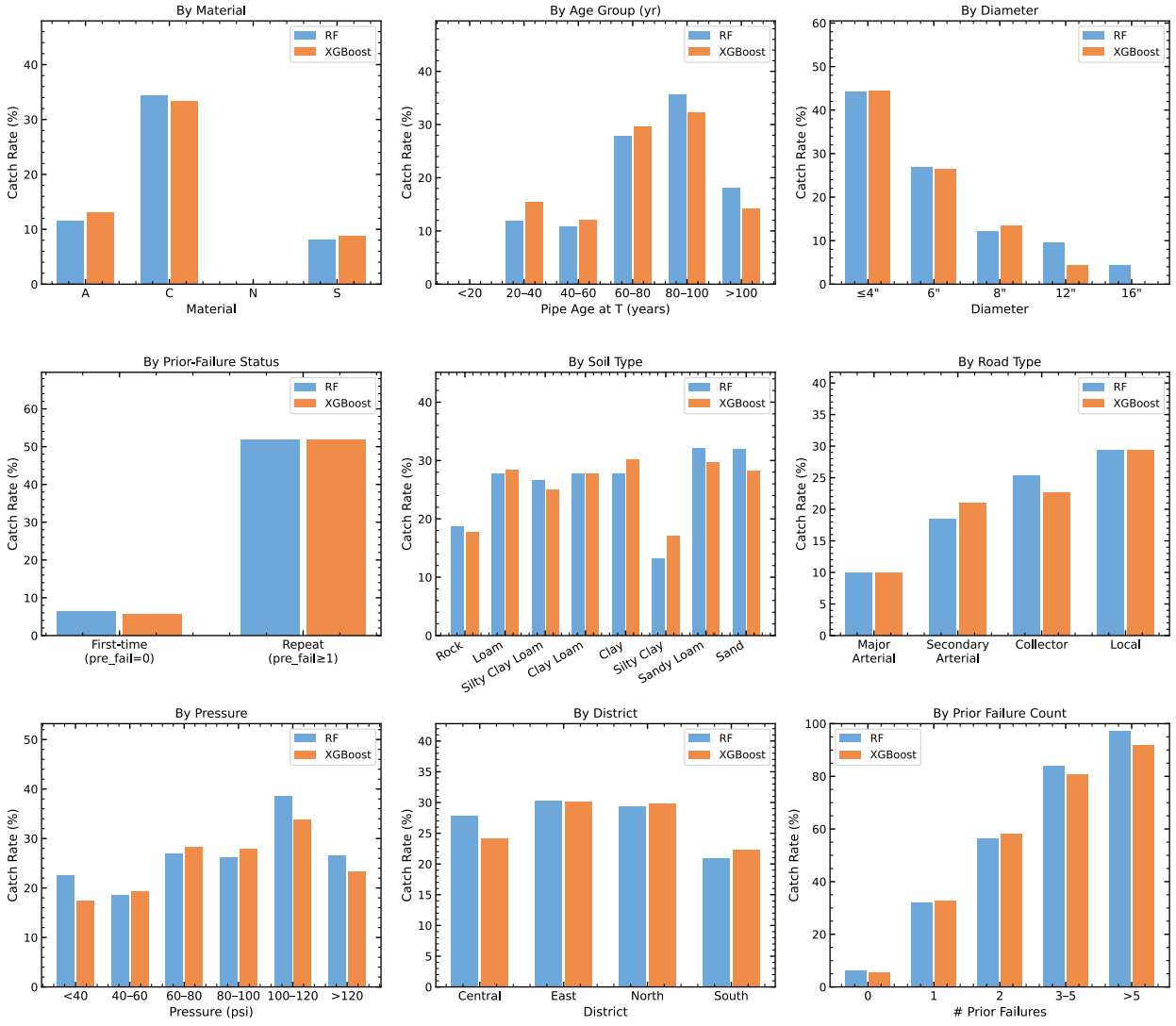


Fig. 3.5. Stratified catch rates at the top 3% operational intervention threshold across various physical, environmental, and historical asset categories. Results reflect a 3-year predictive horizon.

Performance variations across physical pipe characteristics also align with several factors. In the *By Material* cohort, Cast Iron (C) pipes exhibit the highest catch rates, being selected at significantly higher frequencies than Asbestos Cement (A) and Steel (S) segments. Notably, neither model captures any Non-metallic (N) pipes within this highly constrained threshold. Because these materials are relatively recent additions to the network, they have accrued very few, if any, historical breaks, meaning they lack the established degradation markers and advanced age necessary to trigger the models' risk penalties. Similarly, the *By Age Group* analysis shows relatively strong predictive capture for pipes in the 80–100 year age range. The *By Diameter* subplot reveals that smaller distribution mains ($\leq$ 4 inches) are captured at notably higher rates than larger pipes, while the largest mains ($\geq$ 16 inches) exhibit significantly lower capture rates. These patterns suggest that the models are particularly effective at identifying risk among asset classes that are often associated with higher vulnerability, although the observed relationships should be interpreted as correlations rather than direct causal effects.

The operational and environmental characteristics show a similar tendency. The *By Pressure* analysis indicates that catch rates are generally higher for pipes operating in the 100–120 psi range, suggesting that the models may be sensitive to operational conditions that coincide with elevated failure occurrence in the historical record. Furthermore, the *By Road Type* analysis demonstrates higher catch rates for pipes beneath local roads compared to major arterials, likely reflecting utility practices where arterial mains receive stricter installation standards or proactive replacement, making their rare failures more stochastic and difficult to predict.

Taken together, the stratified analyses demonstrate that both models converge on a high-risk asset profile driven by intersecting vulnerabilities. The algorithms predominantly target segments exhibiting combinations of these factors: older cast iron material, small diameters, higher operating pressures, location beneath local roads, or a documented history of prior distress. Recognizing this algorithmic profile allows utility managers to better contextualize the predictive outputs and deploy complementary assessment strategies for asset cohorts that fall outside these targeted demographics.

3.6.3 Spatial and Temporal Analysis of False Negatives

While understanding the framework's predictive successes is important, examining its failures can provide valuable insight into the limitations of data-driven degradation modeling. In particular, analysis of false negatives, assets that failed during the study period but were not prioritized within the model's top-ranked predictions, helps identify failure mechanisms and infrastructure characteristics that are less effectively captured by the available predictor variables. Because the preceding stratified analysis demonstrated agreement between the RF and XGBoost models, with both exhibiting highly similar prioritization behavior across infrastructure cohorts, the following evaluation focuses exclusively on the RF model as a representative ensemble framework. Figure 3.6 presents the distribution of captured and

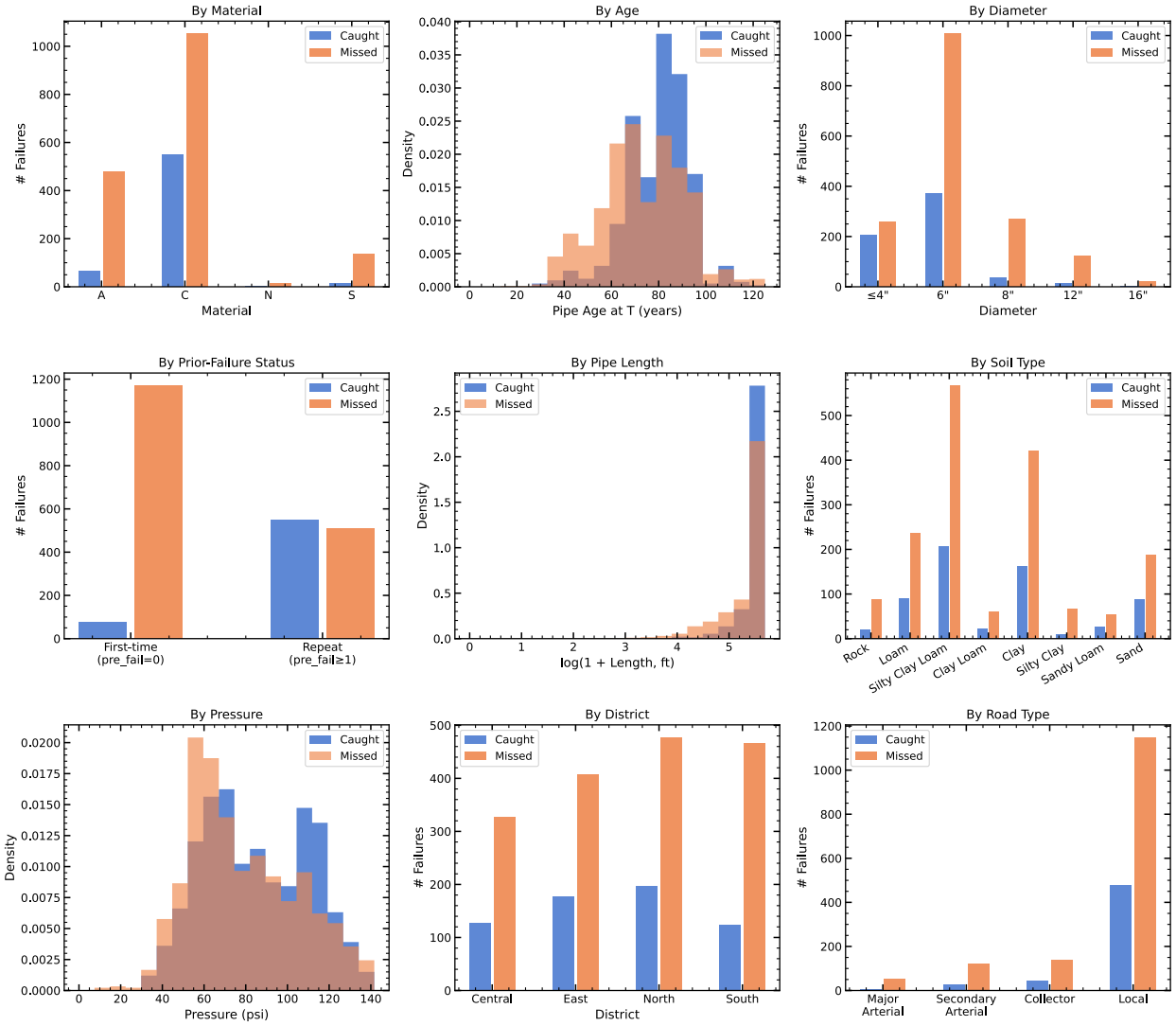


Fig. 3.6. Distribution of caught versus missed failures (false negatives) for the Random Forest model at the top 3% operational threshold. Density and absolute failure counts are stratified across key asset attributes.

missed failures within the top 3% prioritization threshold with 3-year evaluation horizon, same as the results reported above.

The most prominent driver of false negatives is the absence of historical distress markers. As shown in the *By Prior-Failure Status* subplot, the majority of missed targets are first-time failures. Because the ensemble framework inherently assigns high predictive weight to previous break records (as established in the feature importance analysis), pipeline segments experiencing their very first rupture frequently lack the statistical penalty required

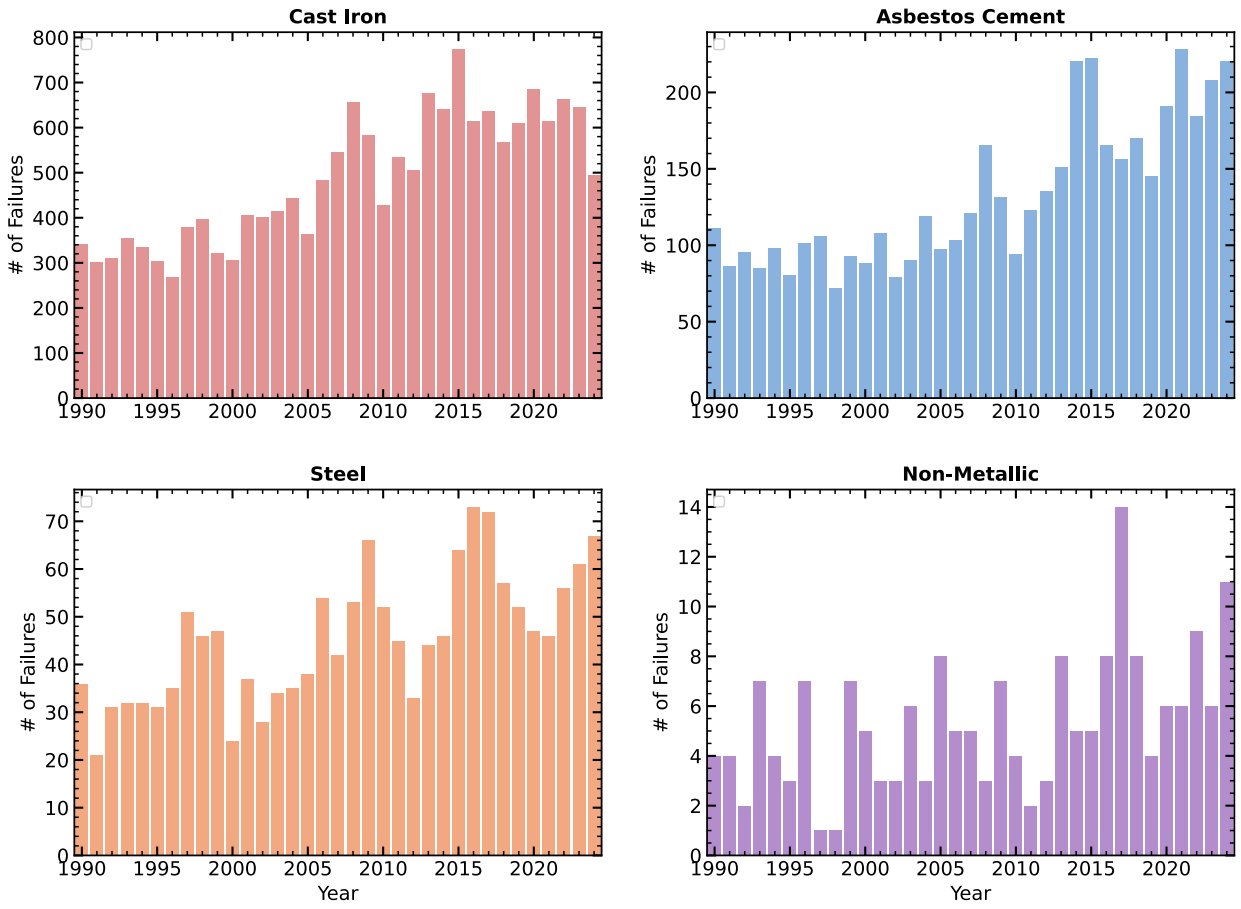


Fig. 3.7. Historical annual failure counts across the 34-year observation window, separated by primary pipe materials. Note the accelerating trend in Asbestos Cement failures in recent years.

to be elevated into the highly constrained top 3% prioritization bracket. Beyond historical tracking, the false-negative distributions reveal a critical, material-specific deterioration trend occurring within the network. In the *By Material* subplot of Figure 3.6, Asbestos Cement (A) pipes exhibit a severe disproportion in predictive capture, with missed failures outnumbering caught failures. To understand this predictive gap, Figure 3.7 plots the raw historical failure counts by material over the 34-year observation window. While Cast Iron failures have remained persistently high but relatively stable over time for the recent years, Asbestos Cement pipes demonstrate an accelerating upward trend, escalating from roughly 100 failures per year in the 1990s to consistently exceeding 200 failures per year in the most recent decade.

This systemic surge indicates that the Asbestos Cement cohort, mostly installed in the mid-to-late 20th century, is currently entering an accelerated, end-of-life failure phase. Be-

cause ML algorithms rely on historical training data to map future outcomes, they can lag when a material cohort transitions non-linearly into a new state of advanced fatigue, particularly if those aging asbestos cement pipes are breaking for the very first time. Consequently, the missed failures are highly concentrated in the demographic profile typical of these asbestos cement distribution mains: segments around 60 to 80 years of age (Figure 3.6, *By Age*) and smaller 6-inch diameters (*By Diameter*).

Recognizing this limitation is critical for both utility asset management and future algorithmic development. Operationally, it suggests that while the ML framework is highly tuned for optimizing the rehabilitation of degraded Cast Iron, the utility may need to deploy a supplementary, cohort-based replacement strategy specifically targeted at aging asbestos cement pipes. Methodologically, the inability to capture this accelerating failure trend shows a limitation of static historical training sets. It indicates that future model iterations could consider to incorporate dynamic temporal features or non-stationary failure models to capture material cohorts transitioning into accelerated, end-of-life fatigue phases.

While the preceding analysis highlights how emerging temporal trends drive a portion of the model's false negatives, it is also important to analyze the spatial distribution of these unpredicted failures. Figure 3.8 evaluates the geographic correlation between the model's predictions and its blind spots by plotting the cumulative fraction of failed pipes against their physical distance to the nearest Top-3% prioritized pipes. To establish a baseline for spatial randomness, the proximity of random non-failing pipes to the prioritized assets is also plotted as a dashed line.

The resulting cumulative distribution function reveals a spatial clustering effect. The solid curve representing missed failures ascends far more rapidly than the random non-failing baseline. Specifically, over 50% of all missed failures occur within just 0.1 miles (approximately 500 feet) of a top-ranked high-risk pipe. In the context of the collaborating utility's dataset, this radial distance equates to about two standard pipe segment units (where an average segment is approximately 250 feet). Expanding the radius to 0.25 miles captures over 80% of the model's false negatives.

This divergence from spatial randomness shows that infrastructure degradation could be localized. Even when the ML framework fails to assign a high enough probability score to trigger intervention on a specific, individual pipe segment, it successfully identifies the broader geographical zone of elevated risk. This clustering is physically intuitive, as adjacent pipelines often share similar compounding degradation drivers: identical corrosive soil profiles, equivalent seismic and differential settlement stresses, shared hydraulic pressure zones, and similar contractor installation practices.

From a methodological perspective, this strong spatial correlation highlights a critical pathway for future algorithmic development. Explicitly integrating spatial clustering mechanics or neighborhood-level risk diffusion into future predictive frameworks could improve their ability to anticipate localized failures and boost overall capture rates. Operationally, this spatial proximity aligns the framework's outputs with existing utility capital planning strategies. Because utilities typically execute continuous, block-by-block rehabilitation rather than segment repairs, the algorithm's top-ranked predictions can serve as

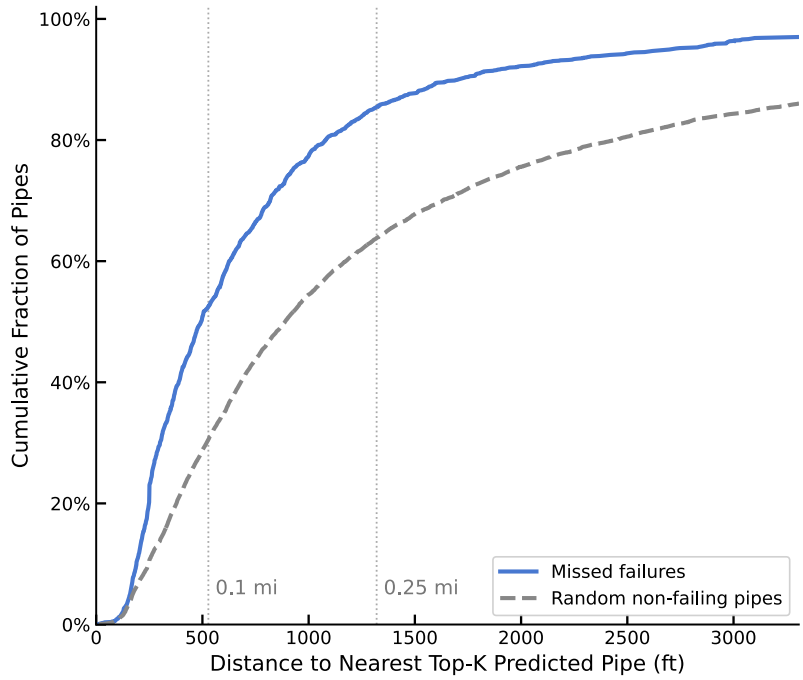


Fig. 3.8. Cumulative spatial distribution of missed failures compared to a random baseline. The plot demonstrates that the vast majority of false negatives occur within a tight geographical radius of the Top-3% predicted high-risk pipes.

optimal geographic anchors for these projects. By centering neighborhood-scale replacements around these highest-priority targets, utilities inherently capture the surrounding unpredicted breaks, which could neutralizing the impact of the model's false negatives.

3.7 Conclusions

This study developed and evaluated an ensemble machine-learning framework for predicting near-term failures in a buried water distribution network, with particular emphasis on operational relevance for utility asset management. Random Forest and XGBoost models were trained using pipe-level physical, operational, environmental, and historical attributes, and predictions were generated for a defined capital-planning horizon (e.g., three years). Under an illustrative 100-year replacement cycle, a three-year capital program would address approximately 3% of the network, allowing the resulting rankings to be interpreted in relation to a realistic intervention capacity.

By evaluating performance at the individual pipe-segment level across multiple intervention thresholds, this study advances previous decision-oriented frameworks [67, 8]. Rather than relying on spatially aggregated block-level predictions or purely global classification

metrics, the use of Recall@k provides a realistic measure of how failure capture changes as rehabilitation capacity expands. Furthermore, by successfully applying these ensemble models to a highly heterogeneous, multi-material network, this work addresses persistent challenges related to class imbalance and data censoring noted in earlier time-to-failure studies [136, 112, 113]. Ultimately, these comparisons demonstrate that prediction accuracy alone is insufficient; the unit of analysis, intervention threshold, and existing decision processes fundamentally dictate the practical value of a model.

The application of this framework yielded several critical operational insights for proactive utility management:

- **Improved Failure Capture at Scale:** The ensemble models captured approximately 30% of observed future failures within the highest-ranked 3% of pipe segments. When the intervention threshold expanded to the top 10% of the network, the models captured approximately 55% of future failures, outperforming the utility's existing in-house model (46.5%). While improvements were modest at the most restrictive 1% threshold, where both models prioritized pipes with extensive failure histories, the machine-learning models successfully identified additional vulnerable assets as capacity expanded.

- **Identification of First-Time Failures:** While previous break history heavily influenced both the machine-learning and utility models, the ensemble models successfully identified future failures among pipes with no previous recorded breaks. This demonstrates that physical, operational, environmental, and spatial attributes contain critical vulnerability information, allowing utilities to supplement reactive prioritization.

- **High-Risk Asset Profiles and Material Blind Spots:** Model interpretation identified a recurring high-risk profile consisting primarily of older, small-diameter cast iron mains operating under elevated pressure. Conversely, predictive performance was weaker for some asbestos cement cohorts exhibiting rapidly increasing failure rates. This suggests that static historical attributes struggle to represent nonstationary deterioration in materials transitioning into accelerated failure phases.

- **Spatial Anchoring for Rehabilitation:** Many unpredicted failures were located near highly ranked pipe segments. This suggests that individual pipe-level predictions can serve as geographic anchors for corridor- or neighborhood-scale investigations. Combining these rankings with spatial screening can capture nearby vulnerabilities, reduce repeated excavations, and improve coordination with co-located infrastructure projects.

The results reinforce that the predictive capability of any data-driven framework is constrained by the quality and completeness of its underlying records. Many of the predictors available in this study represent indirect indicators of deterioration, such as asset characteristics, environmental exposure, operating conditions, and previous failures, rather than

direct measurements of current pipe condition. Missing installation details, incomplete early failure histories, changes in maintenance practices, and limited information on repairs may further restrict model performance and interpretation. The estimated results are therefore specific to the utility, observation period, and data structure examined, and they should not be treated as universally transferable risk relationships. Future models may benefit from time-varying features that represent changes in cohort condition, recent failure intensity, operating pressure, climate, and environmental exposure.

3.8 Future Works

Future work should extend the framework while retaining the individual pipe segment as the primary prediction unit. Rather than aggregating pipes into city blocks before model development, spatial and construction-era information could be introduced through neighborhood-level features, hierarchical effects, or relationships among nearby pipes. Pipe segments installed in the same area and period may share construction practices, bedding conditions, materials, design standards, or environmental exposures that are not fully represented by the available asset attributes. Modeling these shared conditions could help determine whether failures cluster within common installation cohorts and whether neighboring pipes provide useful information about an individual segment's risk. Pipe-level predictions could then be grouped after estimation to define coordinated corridor- or neighborhood-scale rehabilitation projects. This approach would preserve asset-level variation while supporting the project-level planning required for efficient construction and capital programming.

The framework could also be extended from probability-of-failure prediction toward a comprehensive consequence-of-failure (CoF) assessment. The current models estimate which pipes are most likely to fail within a defined planning horizon, but failure likelihood alone does not indicate the severity of the resulting impacts. Future research could combine predicted failure probabilities with CoF indicators such as pipe diameter, customer population affected, critical-facility service, hydraulic importance, repair cost, traffic disruption, property damage, environmental impacts, and the availability of network redundancy. Integrating these components would produce a risk measure based on both the likelihood and consequences of failure, allowing a lower-probability but high-consequence transmission main to be compared with a higher-probability but lower-consequence distribution pipe. Where possible, CoF components could be quantified using hydraulic simulations, service-area analysis, repair and disruption records, traffic data, and economic estimates. Scenario-based or multi-criteria approaches could then be used to examine how rehabilitation priorities change under different utility objectives, including service reliability, public safety, financial cost, and equity. Ultimately, combining spatially structured probability-of-failure estimates with locally calibrated CoF measures would advance the framework from pipe-failure prediction toward project-level, risk-based capital planning.

Chapter 4

Component-Level Experimental Framework

4.1 Motivation and Failure Modes of Jointed Pipeline Components

Earthquake-induced permanent ground deformation (PGD) can impose severe axial, transverse, and rotational demands on buried water pipelines, potentially disrupting water supply and fire-fighting capacity when these services are most critical [84]. Pipeline damage associated with surface fault rupture, liquefaction-induced lateral spreading, settlement, and landsliding has been documented following numerous earthquakes, including the San Fernando, Northridge, Kocaeli, Canterbury, and Chi-Chi events [83, 122, 23, 53, 145, 85, 132]. The resulting pipeline response depends on the magnitude, orientation, and spatial extent of ground movement; the resistance provided by the surrounding soil; and the material, geometry, and connection details of the pipeline.

A buried water main is not composed solely of uniform pipe barrels. As illustrated by the representative plan view in Figure 4.1, a typical installation may include straight pipe segments, bends, fittings, restrained connections, material transitions, service or branch connections, and tie-ins to the existing network. The pipeline may also cross roadways and pass near drainage, sewer, electrical, and other buried infrastructure. These geometric and structural discontinuities influence how axial force and bending moment are transmitted along the alignment. Bends, fittings, and restrained joints may locally alter stiffness and redirect the load path, while utility crossings and construction constraints may affect burial depth, alignment, and soil support. Consequently, the response of the overall pipeline depends on both the mechanical behavior of its individual components and the interaction among those components.

Continuous pipelines accommodate imposed ground displacement primarily through axial strain, bending, ovalization, and localized deformation of the pipe barrel. Early analytical models represented this response using tensioned-cable formulations [79], with later mod-

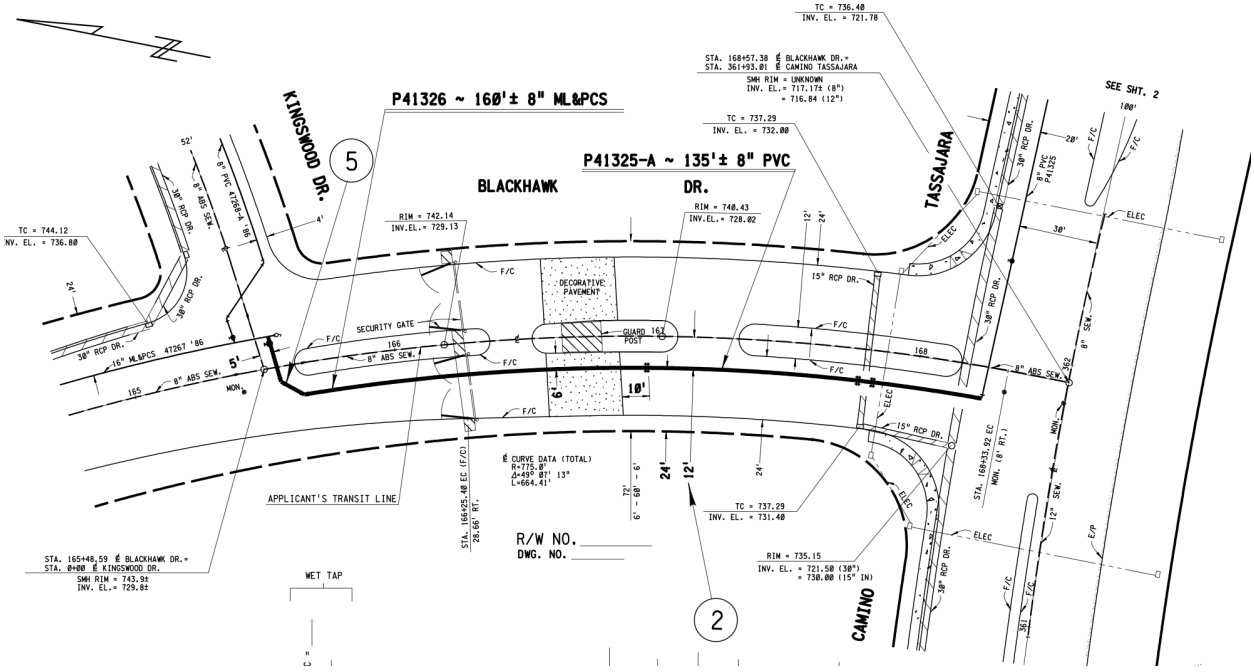


Fig. 4.1. Representative plan view of a buried water-main alignment showing pipe segments, changes in alignment, tie-ins, roadway crossings, and adjacent utilities [42].

els incorporating lateral soil resistance [60] and pipe bending stiffness [129]. Under tensile loading, excessive axial strain can cause yielding or rupture, whereas transverse and compressive demands can produce bending failure, local wrinkling, buckling, and loss of flow area. Representative examples of these barrel-controlled failure modes are shown in Figure 4.2. Field observations from the Kocaeli earthquake, for example, documented severe localized wrinkling and reduction of the internal diameter of a large welded-steel water-transmission pipeline subjected to fault-induced compression [122].

Whereas the damage modes in Figure 4.2 develop primarily through deformation of a continuous pipe barrel, segmented pipelines introduce additional response mechanisms because adjacent barrels are connected through discrete joints. Hazard-resilient systems are designed to accommodate a portion of the imposed ground movement through controlled axial slip and joint rotation, thereby limiting damaging strain in the adjoining pipe barrels. Their performance depends not only on the strength of the pipe material but also on the interaction among the bell or fitting, spigot, gasket, locking or restraint mechanism, and neighboring pipe segments.

The transfer of longitudinal ground movement into a segmented pipeline is illustrated conceptually in Figure 4.3. Relative movement of the surrounding soil mobilizes distributed soil–pipe resistance and produces opposing regions of axial tension and compression. The resulting demand must be accommodated through a combination of pipe-barrel deforma-



(a) Tensile rupture **(b)** Bending failure **(c)** Localized buckling

Fig. 4.2. Representative barrel-controlled failure modes of continuous pipelines subjected to permanent ground deformation [123]

tion, joint opening or closure, and restraint engagement. Restrained joints may initially permit relatively low-resistance axial movement before a projection, locking ring, tooth, or restraint segment engages and begins transferring substantial force across the connection [91, 93]. When several joints are installed in series, the imposed deformation may be distributed progressively among neighboring connections rather than concentrated entirely at one location.

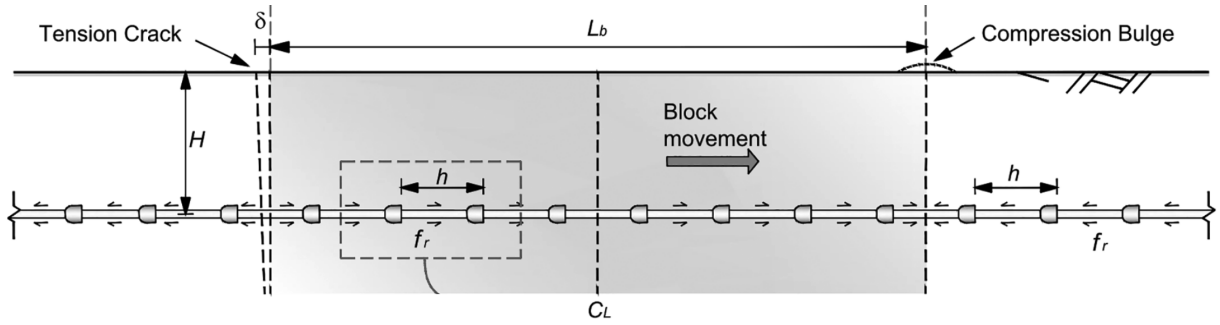


Fig. 4.3. Conceptual kinematic response of a segmented buried pipeline subjected to longitudinal permanent ground deformation. Relative soil movement mobilizes distributed soil–pipe resistance and produces axial tension and compression demands along the pipeline [5]

The ability of the pipeline to accommodate the demands illustrated in Figure 4.3 depends on the relative capacities of its individual components. As ground deformation concentrates

stress at the connections, the pipe barrel, bell or fitting, spigot, gasket, and restraint mechanism perform distinct structural or hydraulic functions and may therefore develop different limit states [135, 93, 144]. The pipe barrel transfers axial force and bending moment between connections and may experience tensile yielding, rupture, local buckling, ovalization, or tearing. The bell or fitting houses the gasket and restraint system but may develop localized cracking where restraint forces are introduced. The spigot transfers load into the restraint and may pull out, fracture, or develop concentrated damage near a weld bead, projection, locking segment, or toothed contact [95, 116, 87]. The gasket maintains hydraulic integrity but may leak when excessive opening, rotation, telescoping, ovalization, or uneven contact reduces gasket compression [94]. Locking rings, restraint segments, teeth, and external collars are intended to prevent complete separation, but concentrated or asymmetric engagement may damage the restraint, bell, spigot, or adjoining pipe barrel.

Representative field-observed examples of these competing limit states are shown in Figure 4.4 [89]. Tensile ground movement produced excessive joint opening in Figure 4.4a, while distortion and separation of rubber-ring joints resulted in loss of hydraulic integrity in Figure 4.4b. Under compressive movement, telescoping of the joint transferred deformation into the adjacent steel pipe barrel, resulting in tearing, as shown in Figure 4.4c. Transverse movement may instead concentrate shear demand at the connection, as illustrated in Figure 4.4d. These observations demonstrate that hydraulic loss of service and structural failure do not necessarily occur simultaneously, and that damage may shift between the joint and pipe barrel depending on the imposed loading mode.

The component-level loading configurations adopted in this dissertation were selected to isolate the principal demands and failure modes illustrated in Figures 4.2 and 4.4. Direct-tension tests quantify available axial slip, restraint engagement, pullout resistance, and the potential for excessive joint opening or tensile failure. Compression tests evaluate joint closure, telescoping, component contact, bottoming, local buckling, and the transfer of compressive demand into the pipe barrel. Four-point bending tests characterize moment–rotation behavior, angular flexibility, gasket performance, and localized joint or barrel damage under transverse deformation. Biaxial tests combine axial displacement and bending to determine whether interaction between these demands changes the capacity or failure sequence observed under independent uniaxial loading. Together, these experiments connect the field-observed limit states to controlled measurements of joint kinematics, hydraulic integrity, load transfer, and structural failure.

4.2 Prior Component-Level Testing and Research Gap

Component-level experiments have been widely used to quantify the deformation capacity and failure mechanisms of pipeline connections. Conventional rigid or partially flexible joints may experience leakage, pullout, local cracking, or limited rotational capacity when



(a) Tension-induced opening of an asbestos-cement pipe joint



(b) Distortion and separation of rubber-ring joints with loss of hydraulic integrity



(c) Compression-induced tearing of the pipe barrel adjacent to a telescoped joint



(d) Localized shear damage at an asbestos-cement pipe joint

Fig. 4.4. Representative field-observed failure modes of jointed pipeline systems subjected to earthquake-induced ground deformation: (a) tensile joint opening, (b) joint distortion and loss of hydraulic integrity, (c) compression-induced pipe-barrel tearing, and (d) localized joint shear failure [89]

subjected to large axial and transverse demands [59, 107, 135]. Restrained axial-slip joints were developed to provide greater deformation capacity by allowing controlled movement before a mechanical restraint engages. Although this mechanism reduces the likelihood of complete separation, restraint engagement produces a marked increase in joint stiffness and transfers greater force into the bell, spigot, restraint, and adjoining pipe barrels.

A substantial body of component-level research on hazard-resilient pipeline joints was conducted through the Cornell Geotechnical Lifelines Large-Scale Testing facility. These studies examined restrained ductile iron and thermoplastic systems under direct tension, compression, cyclic loading, and four-point bending.

For the U.S. Pipe TR-XTREME system, direct-tension and four-point bending tests quantified axial slip, restraint engagement, tensile capacity, and moment–rotation behavior across multiple pipe diameters [116, 95, 96]. These studies further showed that the position and engagement of individual locking segments can influence joint stiffness, leakage, and localized structural damage. The prior TR-XTREME program therefore provides an important experimental foundation for the ERDIP studies presented in the following chapter.

Parallel studies of Kubota ERDIP established the extension, contraction, rotation, and locking mechanisms that produce a chain-like pipeline response [91]. Direct-tension tests documented the progression from relatively free joint opening to locking-ring engagement and ultimate tensile response under internal pressure [93]. Four-point bending tests subsequently established moment–rotation relationships and evaluated leakage and structural behavior across several ERDIP diameters [94]. Collectively, these studies demonstrated that restrained ductile iron joints can accommodate substantial axial displacement and rotation, while also showing that ultimate behavior depends on localized contact and force transfer among the restraint components.

Component testing has also been extended to thermoplastic pipeline systems. Tests of restrained Bionax PVCO joints characterized axial and rotational response and demonstrated the importance of localized deformation near external restraints [118, 119]. Subsequent comparative programs involving PVC, PVCO, and iPVC established common procedures for evaluating axial displacement, cyclic response, bending, leakage, and connection failure. Ihnotic et al. compared several pressurized thermoplastic pipe and coupling configurations using tension, compression, cyclic, and bending tests [51]. Ramos et al. evaluated reinforced C900 PVC joints under direct tension and axial cyclic loading, documenting their displacement capacity and failure mechanisms [105]. Berty et al. subsequently applied tension, compression, cyclic, and four-point bending tests to develop a seismic performance-classification framework for reinforced iPVC connections [13, 12].

Additional testing of toothed-gasket fittings demonstrated that available deformation capacity depends on insertion depth, fitting geometry, restraint configuration, and the manner in which axial load is transferred into the pipe wall [87]. Ramos et al. further examined biaxial loading and showed that simultaneous transverse curvature and axial displacement produce interacting demands that may alter pullout response and failure sequence [104]. These findings indicate that tension, compression, and bending capacities cannot always be treated as independent when a connection is subjected to multidirectional ground deforma-

tion.

Table 4.1. Representative component-level studies of hazard-resilient pipeline joints

Study or program	System	Loading	Principal contribution
Cornell Bionax program [118, 119]	Restrained PVCO	Tension, compression, and four-point bending	Characterized pipe material properties and joint force–displacement and moment–rotation behavior. Tensile failure localized near the external restraint, while the joint retained substantial rotational flexibility.
Cornell TR-XTREME program [116, 95, 96]	Restrained ductile iron	Tension, compression, and four-point bending	Quantified axial capacity and moment–rotation response for 6- and 12-in. joints and demonstrated that locking-segment orientation influences bending response, leakage, and ultimate joint behavior.
Cornell Kubota ERDIP program [93, 94]	Restrained ductile iron	Direct tension and four-point bending	Characterized axial-slip and locking-ring engagement and developed moment–rotation and leakage relationships for 6-, 12-, and 16-in. joints.
Ihnotic et al. [51]	PVC, PVCO, and iPVC	Tension, compression, cyclic, and four-point bending	Compared the axial and transverse response of several pressurized thermoplastic pipes and coupling configurations using a common component-testing framework.
Ramos et al. [105]	Reinforced C900 PVC joints	Tension and axial cyclic loading	Measured displacement capacity, connection strength, and failure mechanisms of reinforced gasketed bell-and-spigot joints.
Berty et al. [13, 12]	iPVC with reinforced connections	Tension, compression, cyclic, and four-point bending	Evaluated five connection systems through twenty full-scale tests and applied the results within a seismic performance-classification framework.
O'Rourke et al. [87]	iPVC fitting with toothed gasket	Direct tension and compression	Quantified load–displacement, leakage, and failure behavior and showed how fitting and insertion geometry govern available tensile and compressive deformation.
Ramos et al. [104]	Jointed thermoplastic pipelines	Combined axial and transverse loading	Demonstrated that simultaneous bending and axial displacement produce interacting demands that are not represented by independent uniaxial tests.

Table 4.1 summarizes the experimental studies most relevant to the component-level framework adopted in this dissertation. Collectively, these studies establish the importance of axial-slip capacity, rotational flexibility, restraint engagement, hydraulic integrity, and localized component response. However, most prior investigations focused on a limited range of products, pipe diameters, or loading combinations and relied primarily on discrete instrumentation. Consequently, the spatial development of strain and the initiation of localized damage near bells, spigots, fittings, and restraint components often remained incompletely resolved.

The component-level program presented in the following chapters extends this literature in three principal ways:

- It applies a common experimental and analytical framework to ductile iron and thermoplastic systems spanning distribution- and transmission-scale diameters and subjected to axial tension, compression, four-point bending, and biaxial loading.
- It uses distributed fiber optic sensing to resolve continuous strain development, restraint engagement, load transfer, and damage localization in regions that cannot be characterized adequately using discrete point sensors alone.
- It evaluates structural and hydraulic response using consistent definitions of joint opening, rotation, moment, leakage, serviceability, and ultimate failure, thereby providing a common basis for interpreting the individual test programs.

The purpose of this framework is therefore not limited to establishing an ultimate load or displacement for each connection. Rather, it is intended to determine how deformation is accommodated, how force and moment are transferred following restraint engagement, where damage initiates, and whether hydraulic loss of service precedes or follows structural failure.

4.3 Testing Protocols and Sensor Integration

To evaluate the mechanical limits of various pipeline materials at the component level, a comprehensive series of tests—including tension, four-point bending, biaxial tension, and compression—were performed across a range of materials, diameters, and joint designs. Table 4.2 outlines the specific testing matrix, detailing the number of specimens and manufacturers for each pipe configuration. In past studies, traditional strain gauges have typically served as the primary strain-measuring sensors. However, these gauges provide only discrete, localized measurements, which presents a significant limitation when evaluating complex structural behaviors. Because they cannot capture data between sensor locations, these point-sensors inherently create blind spots where peak strains, localized yielding, or crack initiations may go undetected. To overcome these limitations and capture a continuous, high-resolution strain profile across the pipeline specimens, DFOS, specifically Distributed Strain Sensing (DSS), was integrated into all experimental setups.

Unlike conventional electrical sensors, the fiber-optic-based DSS approach utilizes the physical properties of light and the glass core of the fiber optic cable itself as the sensing element. As light travels through the optical fiber, inherent microscopic anomalies in the glass cause a fraction of the light to backscatter via Rayleigh scattering. When the fiber is subjected to mechanical strain, the optical path length changes, resulting in a measurable shift in the backscattered light's spectral signature [114]. By analyzing these shifts, an interrogator can continuously map localized strain changes across hundreds or thousands of points along a single optical cable. In addition to offering unprecedented spatial resolution, DSS provides distinct advantages for structural testing, including immunity to electromag-

Table 4.2. Summary of the experimental testing matrix

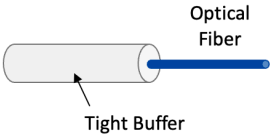
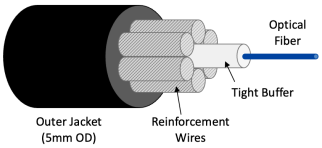
Test Method	8" ERDIP *(U.S. Pipe)*	36" ERDIP *(U.S. Pipe)*	48" ERDIP *(U.S. Pipe)*	48" HDSS *(U.S. Pipe)*	24" HRDIP *(Kubota)*	8" iPVC *(PPI Pipe)*
Tension Test	✓(2)					✓(2)
Bending Test	✓(2)	✓(1)	✓(1)	✓(1)	✓(1)	✓(4)
Bi-axial Tension Test	✓(2)					
Compression Test						✓(1)

Note: Numbers in parentheses indicate the quantity of specimens tested.
Abbreviations: ERDIP = Earthquake Resistant Ductile Iron Pipe; HDSS = High Deflection and High Pressure Restraint; HRDIP = Hazard Resistant Ductile Iron Pipe; iPVC = Innovative Polyvinyl Chloride.

netic interference, lightweight profiles that do not alter the structural stiffness of the test specimen, and superior resistance to environmental degradation.

The DSS system utilized in these pipe component experiments consisted of a high-resolution optical interrogator and specifically selected fiber optic cables. Strain profiles were recorded using a LUNA ODiSI 6104, an Optical Frequency Domain Reflectometry (OFDR) based interrogator capable of delivering thousands of strain measurements per meter of fiber. Operating in its advanced interrogation mode, the ODiSI achieves a sensor gauge pitch (i.e., distance between measurement points) as dense as 0.65 mm over cable lengths up to 100 meters. Data can be acquired at a measurement rate of up to 250 Hz with an accuracy of less than ±1 microstrain, providing the high-fidelity data required to capture highly localized deformation events near pipe joints and material yielding zones.

Table 4.3. Characteristics of selected NanZee strain sensor cables

Manufacturer	Cable type	Side view
NanZee Sensing Technology Co.	0.9-mm-diameter tight-buffer cable	
NanZee Sensing Technology Co.	5-mm-diameter tight-buffer with steel reinforcement cable	

To balance the need for measurement sensitivity with physical survivability during rigorous testing, two distinct types of fiber optic strain cables manufactured by NanZee Sensing

Technology Co. were deployed, as detailed in Table 4.3. The first type is a 0.9-mm-diameter tight-buffer cable. Although its minimal protective coating renders it inherently fragile, this thin profile offers exceptional strain transfer sensitivity and permits a smaller minimum bending radius. Because it can tightly conform to the geometry of the pipe barrel without optical signal loss, the 0.9-mm cable was specifically selected to measure circumferential (hoop) strains. The second type is a 5-mm-diameter armored cable, which incorporates a protective sheath and internal steel wire reinforcement. While less flexible than the tight-buffer variant, its robust construction provides critical protection for the delicate optical core against crushing and localized pinching. Because this heavily armored profile is the standard choice for actual field deployments, the 5-mm cable was utilized for all longitudinal (axial) strain measurements to ensure sensor survivability and closely replicate field application practice.

4.4 Definitions and Calculation Approach

4.4.1 Joint Openings

To measure the joint opening of the specimens, four wire potentiometers (wire pots) are installed around the circumference of the pipe at 90-degree intervals. To capture the relative displacement, the wire pots are fixed to one side of the pipe, while their corresponding targets are anchored to the other side, ensuring that the measurement cables span directly across the joint. The average joint opening is then calculated as the mean of these four localized readings.

4.4.2 Moments

To evaluate the structural demands on the pipe, the system is first idealized as a simply supported beam. The total internal bending moment comprises two primary components: the moment induced by self-weight and the moment generated by the externally applied load. The self-weight, which includes the combined mass of the pipe and water contains in the pipe, is assumed to be uniformly distributed along the span. The maximum bending moment induced by this self-weight is calculated as:

$$M_{\text{distrib}} = \frac{wl^2}{8} \tag{4.1}$$

where w is the uniform load due to the self-weight, and l is the total span length between the supports.

In addition to the self-weight, the discrete moment induced at the designated loading points is determined using standard static equilibrium. For a discrete load applied to the system, the corresponding moment is given by:

$$M_{\text{central}} = \frac{PL}{2} \tag{4.2}$$

where P is the applied load and L is the distance from the support to the point of load application.

4.4.3 Rotations

Having established the statics of the bending moment, the kinematic response of the pipeline, specifically the localized rotation (or joint deflection) at the mechanical joints, is also quantified. To capture this behavior, two distinct geometric approaches are considered based on the available instrumentation.

The first method derives rotation primarily from vertical displacement measurements obtained via position transducers located underneath the specimens. Assuming the adjacent pipe segments behave as rigid bodies, the rotations on either side of the joint are computed using the relative vertical displacements between specified measurement points. These individual rotations are expressed as:

$$\theta_1 = \tan^{-1}\left(\frac{\Delta v_1}{d_1}\right) \tag{4.3}$$

$$\theta_2 = \tan^{-1}\left(\frac{\Delta v_2}{d_2}\right) \tag{4.4}$$

where Δv_1 and Δv_2 represent the relative vertical displacements between pairs of sensors, and d_1 and d_2 are the corresponding horizontal distances separating those sensors. The total cumulative rotation accommodated by the joint using the vertical wire potentiometer (VWP) approach is therefore the sum of the adjacent rotations:

$$\theta_{\text{VWP}} = \theta_1 + \theta_2 \tag{4.5}$$

Alternatively, the second approach leverages horizontal displacement measurements captured by position transducers installed circumferentially around the pipe joint. This method assumes that the vertical separation between the upper and lower sensors remains constant throughout the loading process and that out-of-plane displacements are negligible. Assuming symmetric rotation about the joint's axis, the total rotation computed via the horizontal wire potentiometer (HWP) approach can be directly expressed as:

$$\theta_{\text{HWP}} = 2\tan^{-1}\left(\frac{\Delta h}{2d_h}\right) \tag{4.6}$$

where Δh is the relative horizontal displacement recorded between the two measurement points, and d_h is the baseline vertical distance between them.

4.5 Organization of the Component-Level Mechanics Chapters

The component-level experimental program is presented in the following three chapters, organized according to pipeline material, joint configuration, and loading condition. Together, these chapters examine how different restraint mechanisms accommodate axial displacement and rotation, transfer force and moment between connected components, maintain hydraulic integrity, and ultimately develop structural damage under large deformation.

Chapter 5 presents the most extensive component-level test program and focuses on US Pipe TR-XTREME Earthquake Resistant Ductile Iron Pipe (ERDIP). Tension, four-point bending, and biaxial tension–bending tests were conducted on 8-in.-diameter ERDIP joints representative of water-distribution applications. Four-point bending tests were also performed on 36-in.- and 48-in.-diameter ERDIP assemblies representative of large-diameter transmission pipelines. This combination of tests provides a basis for examining the effects of loading condition and pipe diameter on joint opening, rotation, restraint engagement, hydraulic performance, and structural response.

Chapter 6 examines two alternative restrained ductile iron joint systems under four-point bending: a 48-in.-diameter US Pipe High Deflection and High Pressure Restraint system and a 24-in.-diameter Kubota NS-type Hazard Resistant Ductile Iron Pipe system. These experiments extend the component-level investigation to joint configurations with different restraint geometries and deformation mechanisms.

Chapter 7 investigates restrained iPVC pipeline joints under axial tension, axial compression, and four-point bending. Three connection systems are considered: plastic fittings incorporating toothed rubber gaskets, EBAA 1900 restraints, and RCT restraints. The experiments characterize how the fitting geometry, gasket, and mechanical restraint interact under different loading conditions and provide a polymer-pipeline counterpart to the ductile iron systems examined in the preceding chapters.

Chapter 8 synthesizes the findings from these individual test programs to evaluate comparative mechanics and seismic design implications. Building upon the preceding component-level data, this chapter examines the influence of restraint geometry on load transfer mechanisms and analyzes the critical balance between structural capacity and hydraulic resilience. It further explores how scale and material stiffness dictate joint failure, as well as the relationship between damage localization and joint ductility.

Although Chapters 5 through 7 evaluate distinct pipeline systems, the results are interpreted using the common definitions, calculation procedures, and performance measures established in this chapter. This organization enables the individual test programs to be presented independently while maintaining a consistent analytical baseline for the comprehensive comparisons and design implications discussed in Chapter 8.

Chapter 5

Component-Level Mechanics of ERDIP Joints

5.1 Introduction of Earthquake-Resistant Ductile Iron Pipe (ERDIP)

The earthquake-resistant ductile iron pipe (ERDIP) system was developed to accommodate large ground displacements while maintaining hydraulic integrity. Commercially available in nominal diameters ranging from 6 to 48 inches, the ERDIP system is specifically designed to maintain full water service following severe seismic events. A series of experimental programs was conducted to characterize the performance of the ERDIP system under multiple loading conditions. The testing matrix included nominal 8-inch distribution pipes subjected to pure direct tension, four-point bending, and combined biaxial tension, as well as large-scale four-point bending tests on 36-inch and 48-inch diameter transmission pipeline specimens.

Based on the specifications of the manufacturer [127], the nominal 8-inch ERDIP joint provides a capability of accommodating a total of 2.9 inches (73.7 mm) of axial travel alongside a 5.0-degree multi-axial rotation capacity. In larger transmission line applications, these operational tolerances expand; the nominal 36-inch joint is engineered to operate with a deflection capacity of 7.0 degrees and an axial movement capacity of 4.6 inches (116.8 mm), while the 48-inch joint provides 5.5 degrees of deflection alongside an identical 4.6 inches (116.8 mm) of axial extension. The main operational components of the joint are shown in the schematic drawing in Figure 5.1.

To ensure a secure and watertight joint during assembly, a specialized elastomeric rubber gasket is first placed inside the bell cavity to prevent leakage. The tapered spigot end is then inserted into the enlarged bell, passing through the gasket to establish a continuous hydraulic seal throughout the full range of displacement. Following spigot insertion, discrete ductile iron locking segments are inserted through a single slot opening on the top of the bell face and guided into an internal circumferential cavity within the bell. These locking segments create a positive mechanical lock between the bell's interior bearing surface and a factory-welded

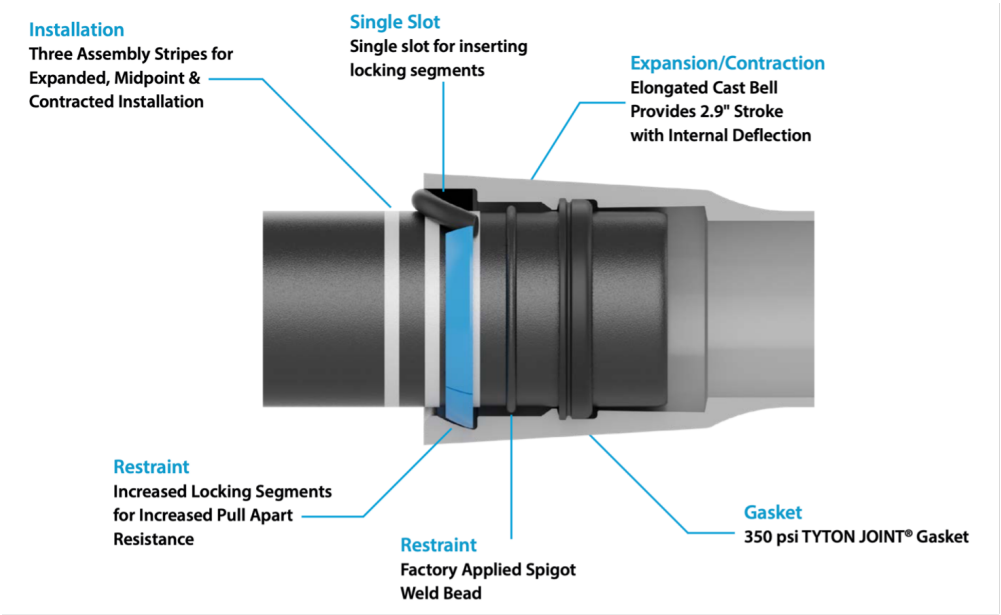


Fig. 5.1. Schematic drawing of TR-XTREME ERDIP joint [127]

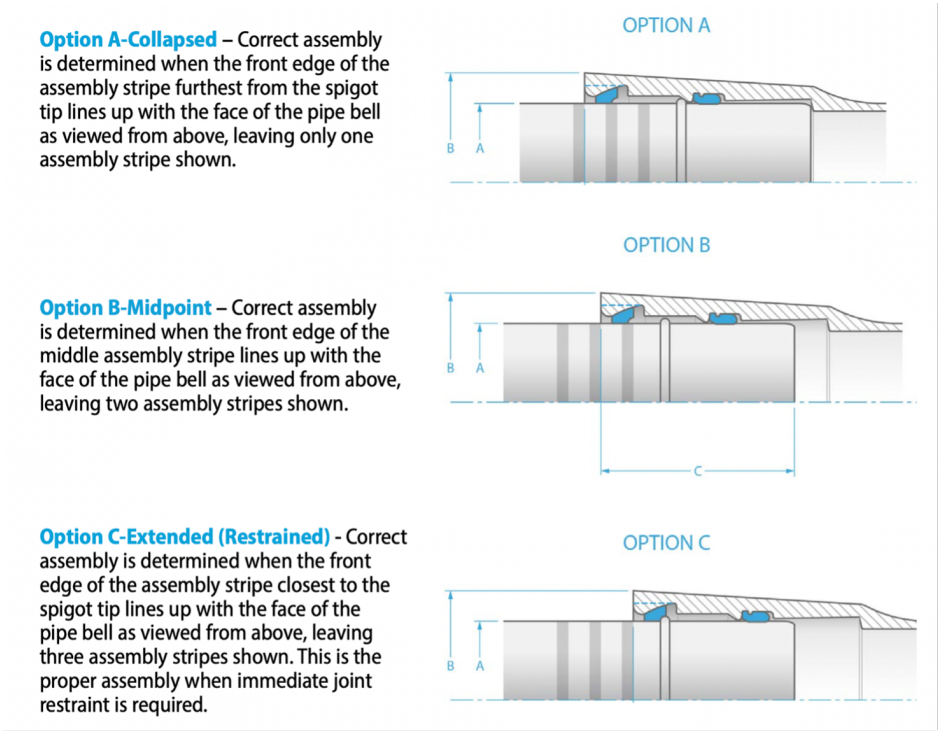


Fig. 5.2. Recommended three installation positions of ERDIP [127]

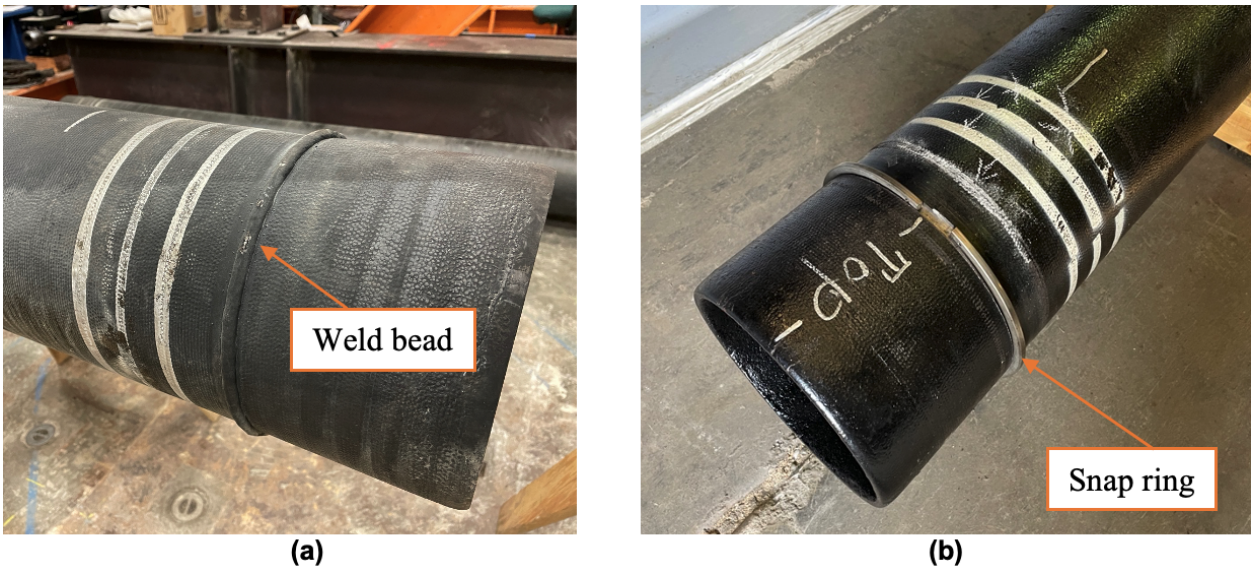


Fig. 5.3. Spigot end locking mechanism of ERDIP tension experiment. (a) factory-manufactured weld bead. (b) Field-installed snap ring.

circumferential bead (as shown in Figure 5.3a), functioning as a retainer weldment located on the spigot end. However, on-site pipe cutting can remove the factory-installed weld bead. To address this, U.S. Pipe offers the HDSS QuikLok system, which allows installers to cut, groove, and install a snap ring onto the spigot, preserving the strength and deflection capacity of the original joint while providing field flexibility, as illustrated in Figure 5.3b. Finally, a tailored rubber retainer is installed through the bell's slot opening at the crown of the pipe, positioned between the locking segments to apply an inward radial spring load that keeps them securely in place as the joint is extended to engage the restraint mechanism.

To accommodate varying expected ground deformation regimes in the field, three distinct white indicator stripes are painted on the spigot to clearly define the installation position along the insertion path. As shown in Figure 5.2, the manufacturer recommends three primary baseline installation configurations: the collapsed position (maximizing available tensile pullout capacity), the midpoint position (providing a balanced capacity for both axial extension and compression), and the extended location (maximizing the capacity to absorb localized ground shortening). For the experimental scope of the following studies, depending on the testing objectives, different initial installation locations (collapsed, mid-point, or extended) and spigot-end locking features (weld bead or snap ring) were selected.

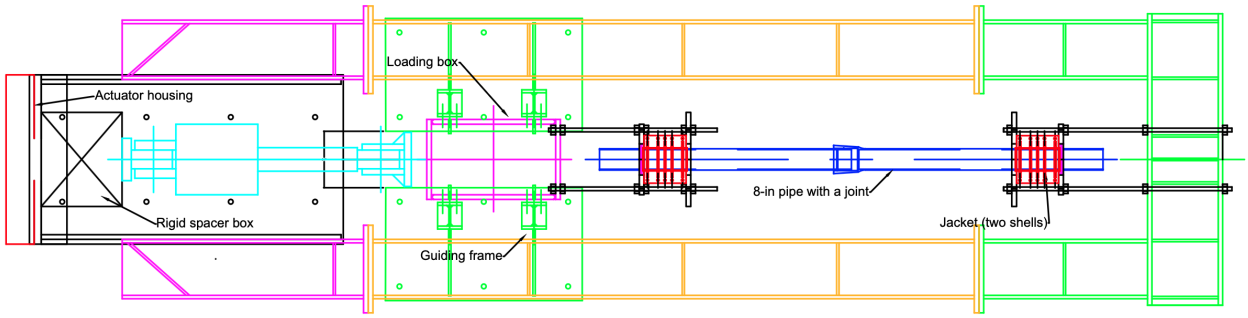


Fig. 5.4. Elevation view drawing of the ERDIP tension experimental setup.

5.2 Tension Performance

While factory-welded joints provide highly controlled restraint under idealized conditions, real-world pipeline alignments frequently require construction crews to cut pipes on-site to accommodate precise tie-ins or bypass unforeseen underground utilities. Because cutting the pipe permanently removes the factory-applied weld bead, field-installed restraint mechanisms become an absolute practical necessity to restore the pipeline's seismic resilience. To understand how this field modification impacts internal load transfer and ultimate capacity, this study specifically evaluates the structural performance and failure mechanics of the field-adaptable HDSS QuikLok system compared against the baseline factory-installed weld bead. Two nominal 8-inch pipe specimens were prepared for monotonic direct tension testing: Specimen-WB, representing the idealized condition equipped with the factory-manufactured weld bead, and Specimen-HDSS, representing the field-modified condition equipped with the field-installed snap ring.

5.2.1 Experimental Setup and Instrumentation

The design of the experimental setup is shown in Figure 5.4. A self-reacting frame was designed to accommodate both the loading and reaction sections. The system employed a hydraulic actuator with a capacity of 940 kips in compression with a total stroke of 12 inches for Specimen-WB test (Test 1) and a compression capacity of 314 kips and a total stroke of 12 inches actuator for Specimen-HDSS test (Test 2). To restrain the pipeline, two specially designed jackets were utilized. The hydraulic actuator applied force to the spigot through a loading fixture, which bore against the weld bead at the pipe's end. A similar mechanism was used to secure the bell pipe to the reaction beam. An overview of the experimental setup is shown in Figure 5.5.

Specimen-WB was tested at midpoint position, with the spigot inserted halfway through the bell. In contrast, Specimen-HDSS was tested in a fully extended position, where the locking segments were initially in contact with the spigot's snap ring. Although the starting

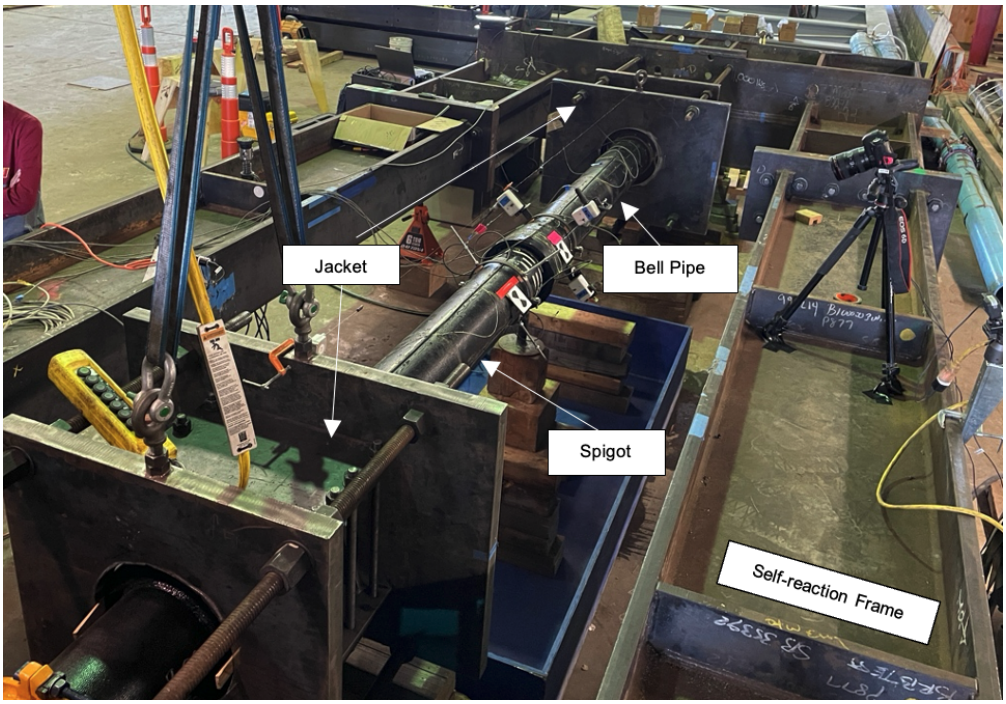


Fig. 5.5. ERDIP tension experiment setup.

positions differed, the spigot's travel within the bell prior to full engagement required minimal force. Consequently, this initial positioning did not affect the ultimate joint performance, specifically the maximum axial force required to break the pipe. During the experiment, the specimens were pressurized using the in-house water supply, reaching 50 psi for Specimen-WB and 70 psi for Specimen-HDSS. A hydraulic actuator then applied an axial tensile load to the spigot until significant structural failure occurred, culminating in severe water leakage.

The locations of the instruments are shown in Figure 5.6 and Figure 5.7. Detailed lists of the instrumentation can be found in Chiu et al. (2023) and (2025) [32, 29]. Four position transducers (or wired pots herein) were placed on the bell pipe at 45 degrees apart from the quarter points around the circumference and were fixed to the spigot to measure the joint opening for both tests. The sensor arrays were configured to capture both longitudinal and circumferential deformations across the pipe specimens and the critical bell section. For longitudinal strain measurements, cables (F10–F17) were attached continuously along both pipes, spaced at 90-degree intervals around the circumference. To capture circumferential strains (F1–F9), three sensor rings were installed along the barrel of both pipes with approximately 16-inch spacing. Furthermore, to specifically monitor the localized deformation mechanics of the joint, three additional circumferential sensors were instrumented directly on the bell: one at the bell end, one at the midpoint of the bell section, and one positioned directly over the internal locking segments (approximately 3.5 inches from the bell face). The instrumental serup is pictured in Figure 5.8.

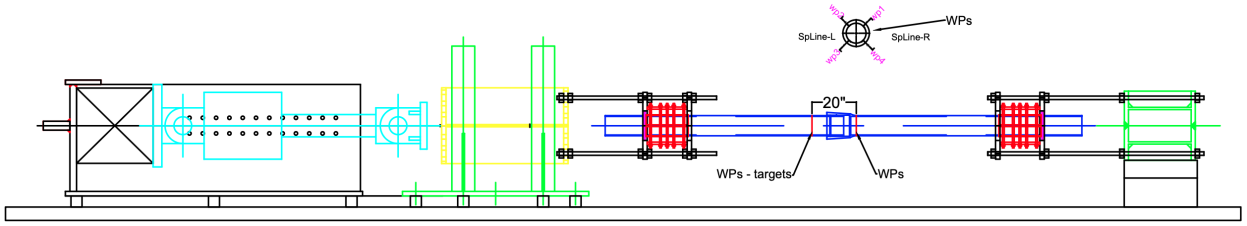


Fig. 5.6. Wire pots installation plan of ERDIP tension experiment.

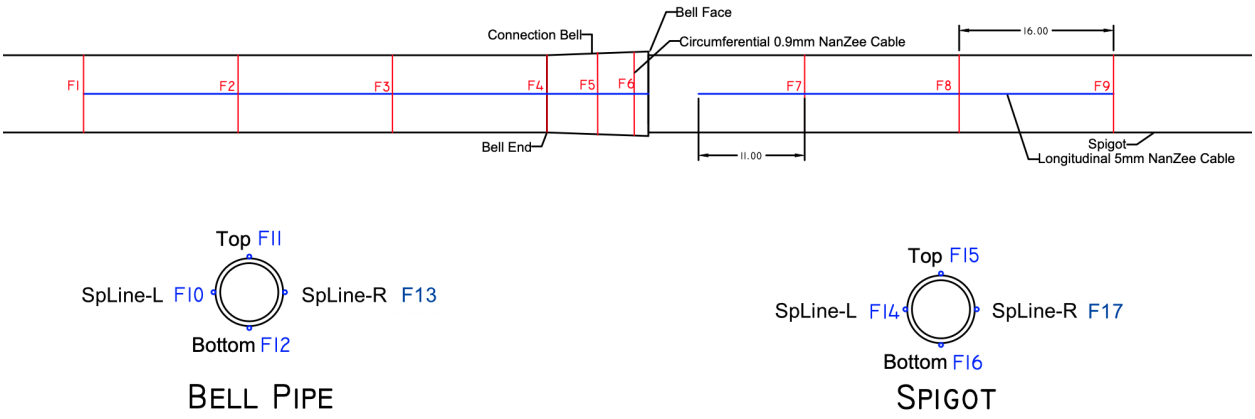


Fig. 5.7. Fiber optic sensor installation plan of ERDIP tension experiment.

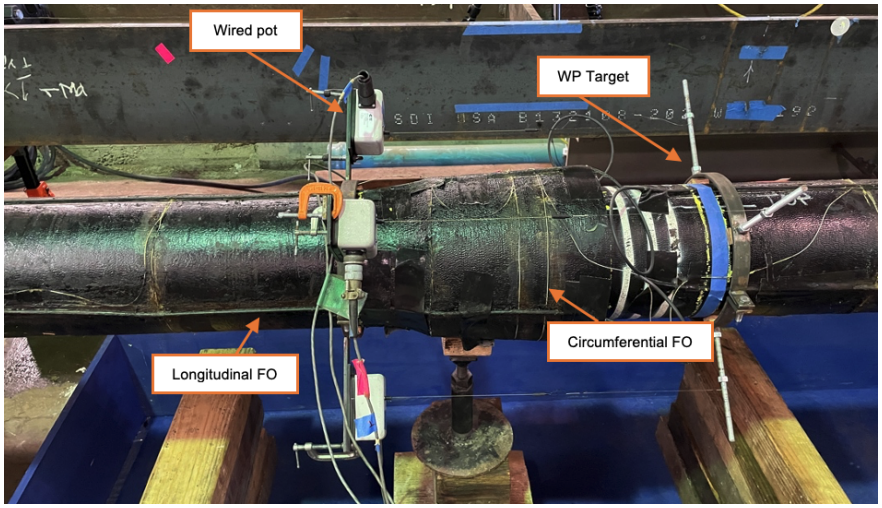


Fig. 5.8. ERDIP tension experiment instrumentation setup.

5.2.2 Failure Mode

During the direct tension tests, a monotonic force was applied along the longitudinal axis of the spigot. To accurately measure the resulting joint opening, four wire potentiometers were positioned 90 degrees apart around the circumference of the bell pipe. As established in the previous section, the two specimens were tested under different initial installation conditions to evaluate distinct locking mechanisms: a factory-manufactured weld bead (Specimen-WB) and an HDSS QuikLok snap ring (Specimen-HDSS). Specimen 1 was installed at the midpoint position, allowing for initial free sliding before engagement. Conversely, Specimen 2 was installed in the collapsed position, meaning the test commenced with the locking segments already in direct contact with the restraint ring, resulting in zero initial free sliding.

The average joint opening, calculated from the four wire potentiometer readings, is plotted against the applied axial force in Figure 5.9. For Specimen 1 (Specimen-WB), the locking segments engaged the weld bead after approximately 1.8 inches of free sliding. While the theoretical sliding distance from the midpoint should be 1.5 inches, this slight discrepancy is likely attributable to initial setup tolerances. Following engagement, Specimen 1 reached a peak axial force of 174 kips at a total joint opening of 2.46 inches. In contrast, Specimen 2 (Specimen-HDSS) engaged immediately and reached a slightly higher ultimate axial resistance of 190.3 kips at an average joint opening of 0.5 inches.

Table 5.1 summarizes the ultimate performance and hydraulic integrity limits of both tests. While the ultimate axial capacities of the factory-manufactured weld bead and the HDSS snap ring were comparable, their structural failure locations and leakage behaviors varied significantly. For Specimen-WB, structural failure of the bell occurred at the 174-kip peak load; however, the joint successfully maintained its watertight seal at this stage. Total loss of water pressure did not occur until an additional 2.9 inches of axial movement was applied. Conversely, Specimen-HDSS suffered an immediate drop in water pressure exactly at the point of maximum axial force. This variation in post-peak hydraulic resilience is driven by distinct localized failure mechanisms, which are detailed in the subsequent section.

Table 5.1. Summary of 8-inch ERDIP tension test results. WB indicates specimen with factory-manufactured weld bead and HDSS indicates the specimen with field-installed HDSS snap ring.

Parameter	**Specimen-WB**	**Specimen-HDSS**
Locking Mechanism	Weld bead	HDSS QuikLok
Max. Load (kips)	174	190
Water Leakage Joint Opening (in.)	2.9	0.5
Failed Section	Bell	Spigot
Test Date	7/15/22	7/11/24

Structural failure of Specimen-WB occurred at the bell, adjacent to the locking segments,

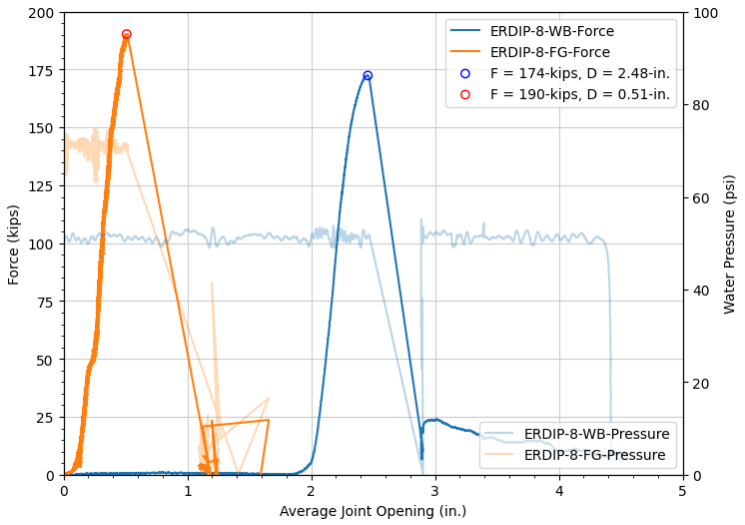


Fig. 5.9. ERDIP tension test result of average joint opening and water pressure

under an applied axial force of 174 kips and an average joint opening of approximately 2.5 inches. As the locking segments were heavily loaded during pullout, a severe fracture initiated in the upper-west quadrant and propagated through the bottom of the bell, as shown in Figure 5.10. Remarkably, this structural damage did not immediately compromise the joint's hydraulic seal. The specimen sustained internal water pressure without severe leakage until the average joint opening reached 4.4 inches. This delayed leakage demonstrates the system's robust capacity to remain functional and continue supplying water even after sustaining severe structural damage to the bell casing. It should be noted that the sudden pressure drop visible in Figure 5.9 was an instrumentation artifact—a temporary misreading by the water pressure gauge induced by the violent vibration of the bell fracturing—rather than a true loss of hydraulic containment.

In contrast, the Specimen-HDSS test concluded at a higher peak force of 190.3 kips, characterized by a catastrophic tensile failure of the spigot and an immediate, simultaneous loss of hydraulic integrity. As illustrated in Figure 5.11a, the failure localized specifically at the spigot groove. The reduced wall thickness at this machined cross-section, combined with the concentrated bearing pressure exerted by the snap ring against the locking segments, induced severe localized stress concentrations. This culminated in a complete circumferential tensile fracture around the groove, shearing the spigot and leaving the fractured terminal end trapped within the bell. Upon rupture of the groove, the snap ring dislodged (Figure 5.11b), and the main spigot barrel was entirely pulled out of the joint assembly (Figure 5.12). Because this mechanical separation entirely bypassed the internal gasket seal, the joint was immediately rendered incapable of retaining water pressure.

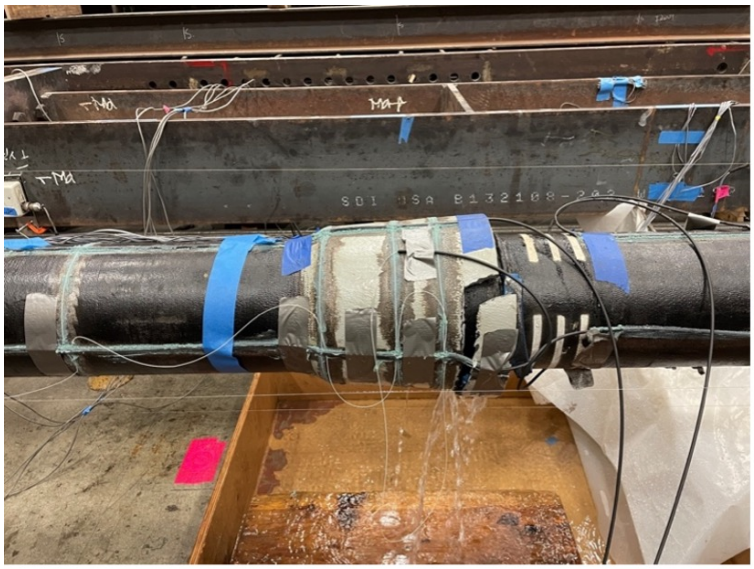


Fig. 5.10. Failure of joint with factory-manufactured weld bead



(a) Tension failure at the circumference of the groove

(b) Failed off snap ring

Fig. 5.11. Failure of joint with field-installed snap ring

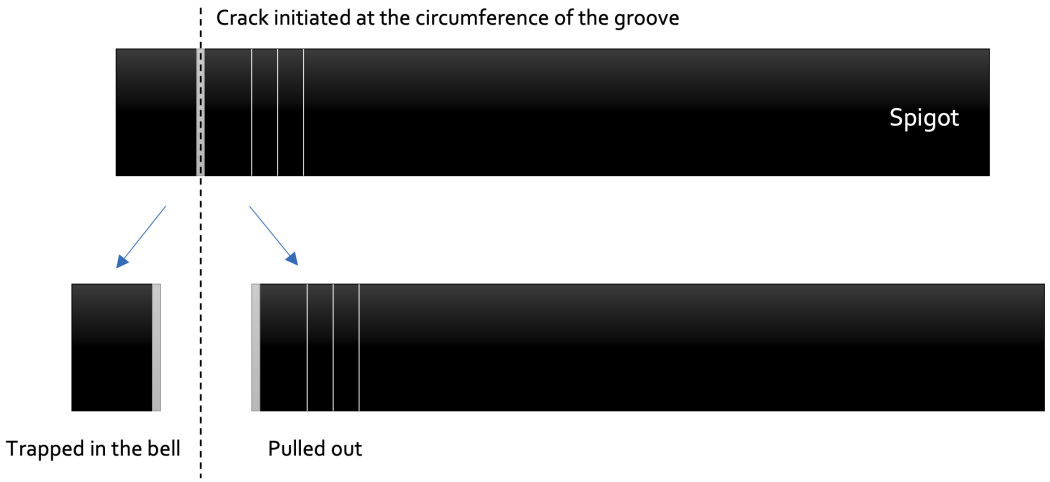


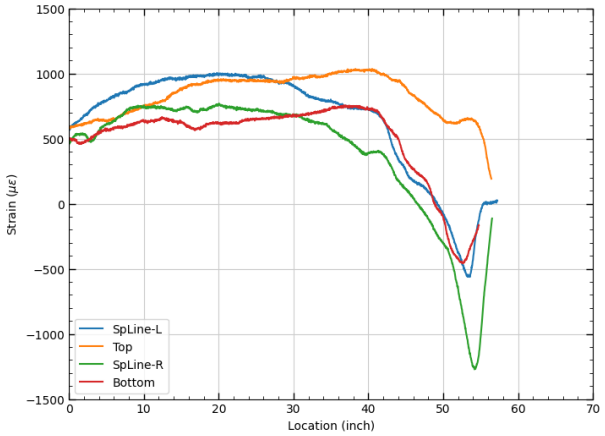
Fig. 5.12. Sketch of failure mode of the specimen with field-grooved snap ring

5.2.3 Axial Strain

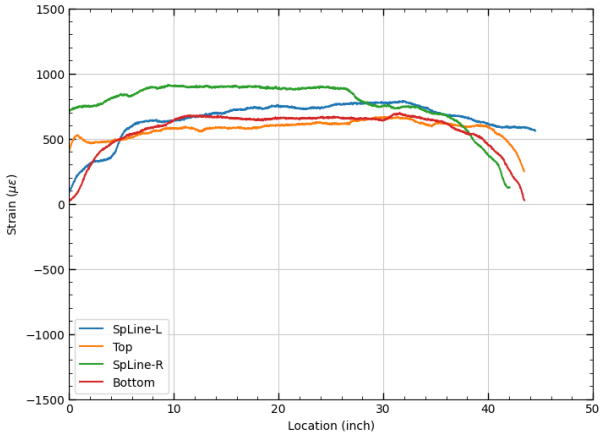
Figure 5.13 presents the longitudinal distributed strain profiles extracted from both tension tests right before the failure occurs (170-kips loading condition for Specimen-WB and 180-kips axial load for Specimen-FG). For the bell pipes (Figures 5.13a and 5.13c), the spatial strain distributions are plotted from the pipe end (left) toward the bell face (right). Conversely, for the spigot barrel (Figures 5.13b and 5.13d), the profiles are oriented from the inserted tip (left) extending outward to the main spigot body (right). While the applied direct tension predominantly induced tensile strains across both specimens, a highly localized zone of severe compressive strain (at locations around 50-55 inches) was recorded on the outer surface of the bell, immediately adjacent to the internal locking segments. This compressive anomaly is driven by a localized bending moment: as the locked spigot is pulled outward, the locking segments exert a severe wedging action against the inner bell cavity, forcing the bell to dilate radially and inducing high surface compression just behind the bearing face.

The mechanics of this load transfer are stage-dependent. Prior to the engagement of the spigot's weld bead against the internal locking segments, the joint extends freely with zero force transfer and no structural deformation. However, upon direct mechanical contact, the axial pullout force is immediately transferred into the locking segments. Because of the angled geometry of the internal cavity, this axial force resolves into a powerful radial wedging action that actively expands the bell. This localized kinematic mechanism aligns with the finite element Von Mises stress contours presented in Figure 5.14 [32], which clearly identify severe stress concentrations localized around the bell, predicting the ultimate structural yielding and fracture locations observed during physical testing.

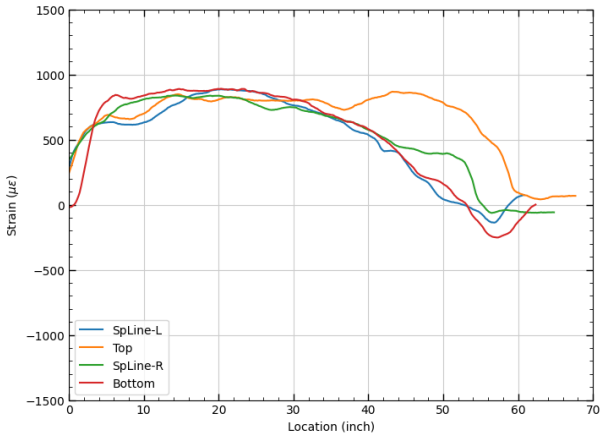
Notably, this localized bending and radial expansion behavior was significantly less pro-



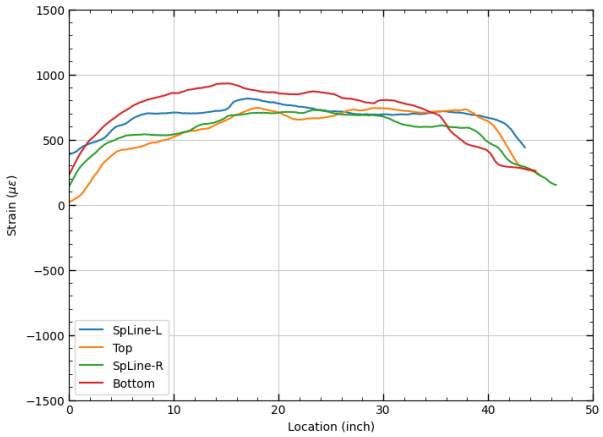
(a) Axial strain on bell pipe of Specimen with factory-manufactured weld bead



(b) Axial strain on spigot of Specimen with factory-manufactured weld bead



(c) Axial strain on bell pipe of Specimen with field-installed snap ring



(d) Axial strain on spigot of Specimen with field-installed snap ring

Fig. 5.13. Strain distribution in the axial direction before failures (i.e., 170-kips tensile force for specimen with factory-manufactured weld bead; 180-kips tensile force for specimen with field-installed snap ring)

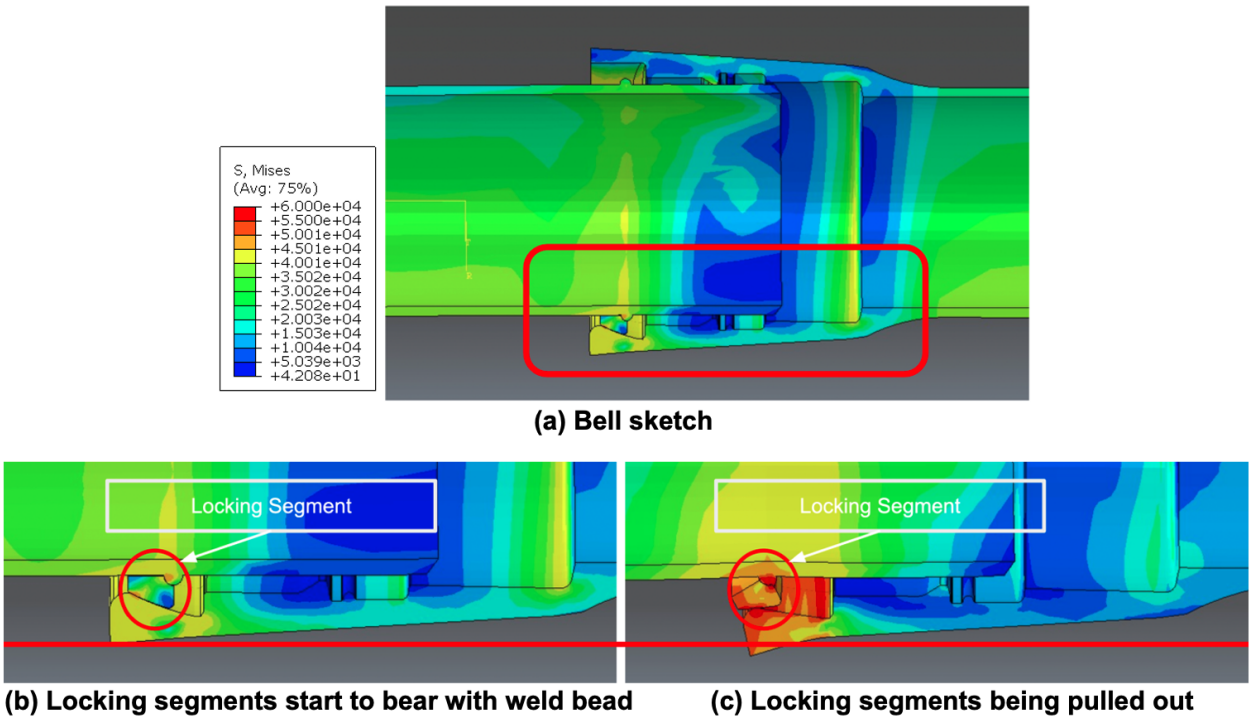


Fig. 5.14. Bell deformation mechanism [32]

nounced along the top crown of the bell. This spatial variance is attributed to two specific joint assembly features. First, no rigid locking segments are positioned at the exact top crown; instead, this space is occupied by the rubber retainer insert used during installation. The lower elastic stiffness and high compressibility of this rubber insert severely limit its ability to transfer outward radial forces, effectively relieving the local bending demand on the bell casing at this location. Second, specifically for Specimen-FG, the snap ring features a gap at the top crown for installation purpose, which fundamentally prevents direct axial-to-radial force transfer across that specific circumferential sector.

In contrast to the complex flexural deformations observed on the bell, Figures 5.13b and 5.13d demonstrate a highly uniform mechanical response across the spigot. Consistent with the monotonic axial boundary conditions, pure tensile strains were recorded throughout the inserted spigot sections. The measured strain magnitudes remained consistent across all four circumferential monitoring locations (top, bottom, and both springlines) for both tests. This axisymmetric strain distribution confirms that the discrete locking segments provide a highly effective, evenly distributed concentric force transfer from the spigot barrel into the surrounding bell assembly.

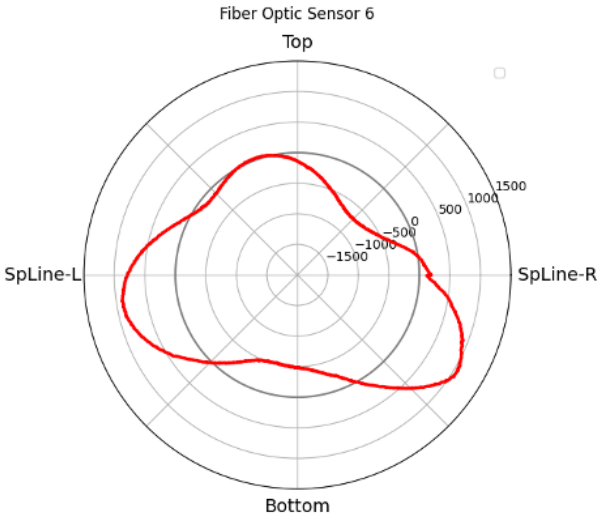
5.2.4 Hoop Strain

To evaluate the multiaxial deformation behavior of the joints, circumferential (hoop) strains were analyzed immediately prior to structural failure, extracted at 170 kips of axial force for Specimen-WB and 180 kips for Specimen-FG, as presented in the polar plots of Figure 5.15. Theoretically, hoop strain measurements along the unconfined pipe barrel should exhibit a standard Poisson's effect, where large longitudinal tensile forces induce relatively uniform compressive strains in the circumferential direction due to the diametric contraction of the pipe wall, as observed by Chiu et al. (2023) [32] and Chiu et al. (2025) [27].

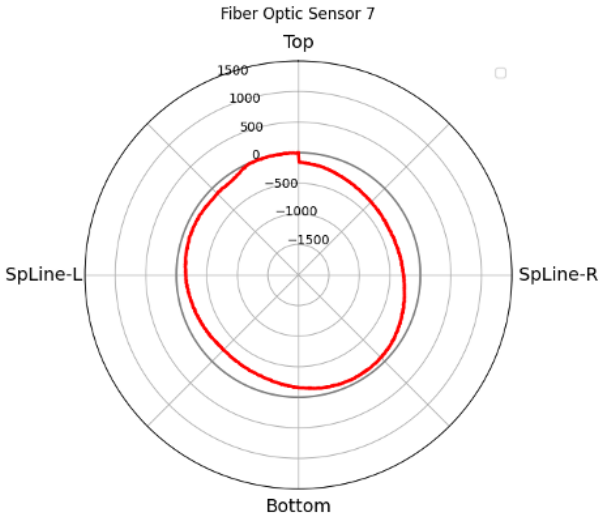
In contrast, the hoop strain behavior measured at the bell, captured by Sensor 6 positioned directly above the locking segments (Figure 5.15a), reveals a highly localized and complex deformation mechanism. Contact between the factory-welded bead and the internal locking segments generates an outward radial force that causes the bell to deform into an elliptical or "squatting" shape. This deformation mode produces vertical compression near the top and bottom crowns and lateral expansion at the springlines. Notably, the peak compressive strain does not occur perfectly at the top crown; instead, it is offset by approximately 45 degrees. This absolute maximum compressive strain, observed as the pronounced inward peak in the upper-right quadrant of Figure 5.15a, corresponds directly to the initiation point of the primary structural fracture that subsequently propagated through the bottom region of the bell. This location aligns with the physical boundary between the rigid ductile iron locking segments and the compressible top sealing rubber. The contrast in material stiffness at this interface alters the load transfer path, ultimately inducing a critical stress concentration. Examining the corresponding strain pattern on the spigot (Figure 5.15b), the profile exhibits a relatively uniform, circular compressive shape consistent with concentric diametric shrinkage. However, the spigot shrinks slightly more at the springlines and less along the vertical axis. This subtle asymmetry occurs because the top of the joint is sealed by the highly compressible rubber rather than a rigid locking segment, resulting in reduced vertical force transfer and slightly less diametric contraction in that direction, as illustrated in Figure 5.16a.

The deformation mechanics of Specimen-FG differ fundamentally from the rigid weld-bead configuration, driven by the unique kinematics of the snap ring assembly. Unlike the rigidly welded bead in Specimen-WB, the snap ring in Specimen-FG is not permanently bonded to the spigot and contains a physical installation gap at the top crown. Under extreme tensile loading, the combined vertical compression and lateral expansion of the bell permit the unconstrained spigot to shift potentially upward within the joint cavity, as illustrated in Figure 5.16b. This upward kinematic movement locally widens the snap ring gap near the top crown, thereby relieving bearing pressure at both the top and bottom crowns. Simultaneously, the upward shift enhances physical contact and force transfer along the lateral springlines, producing larger tensile strains in these regions while reducing compressive strain transfer along the vertical axis, as shown in the bell profile (Figure 5.15c). Consequently, the spigot response of Specimen-FG (Figure 5.15d) lacks the relatively uniform contraction seen in Specimen-WB. While compressive shrinkage remains evident along the

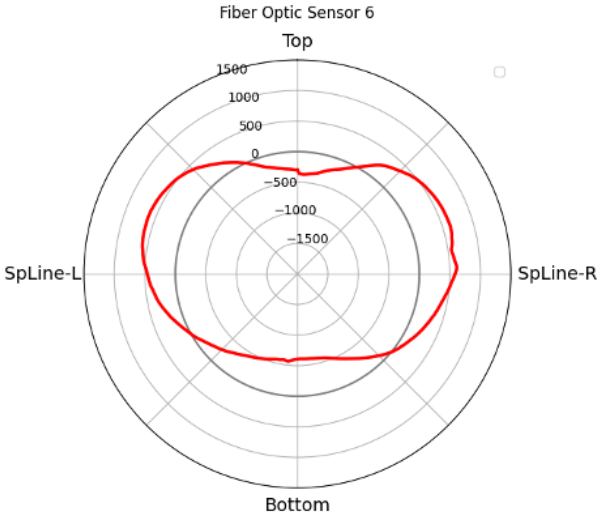
lateral springlines, the strains near the top and bottom crowns approach zero.



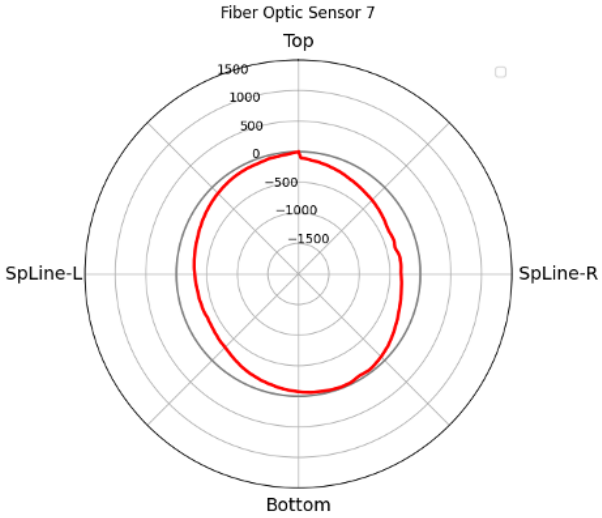
(a) Hoop strain on bell of Specimen with factory-manufactured weld bead



(b) Hoop strain on spigot of Specimen with factory-manufactured weld bead



(c) Hoop strain on bell of Specimen with field-installed snap ring

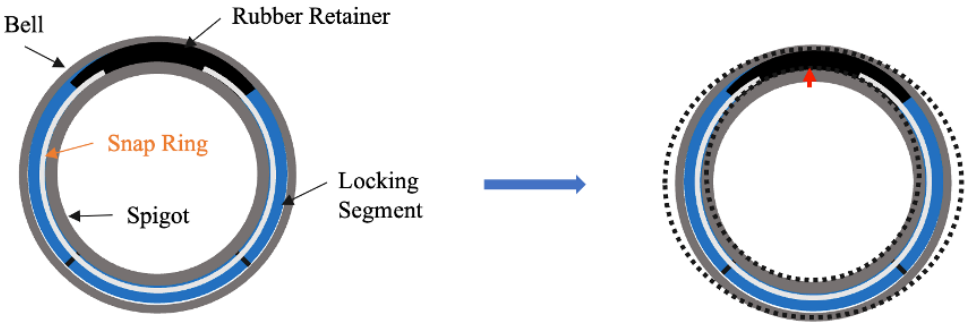


(d) Hoop strain on spigot of Specimen with field-installed snap ring

Fig. 5.15. Strain distribution in the circumferential direction before failures (i.e., 170-kips tensile force for specimen with factory-manufactured weld bead; 180-kips tensile force for specimen with field-installed snap ring)



(a) Specimen with factory-manufactured weld bead



(b) Specimen with field-installed snap ring

Fig. 5.16. Sketch of squatting mechanism

5.2.5 Conclusion of ERDIP Tension Test

This section documented the experimental evaluation of two nominal 8-inch ERDIP joint configurations—a factory-manufactured weld bead (Specimen-WB) and a field-installed snap ring (Specimen-FG)—subjected to monotonic direct tension. While both joint configurations successfully accommodated massive axial deformations and reached comparable ultimate tensile capacities prior to structural failure, their ultimate limit states and post-failure kinematic behaviors diverged.

The primary distinction between the two test specimens lies in their structural failure locations and the resulting impact on systemic hydraulic resilience. Specimen-WB exhibited a highly robust, ductile failure progression. The joint casing ultimately fractured at the bell due to extreme localized bearing forces; however, the internal elastomeric gasket successfully bridged the structural damage, maintaining hydraulic integrity and water service for nearly three additional inches of forced axial pullout. In contrast, Specimen-FG suffered a sudden, catastrophic circumferential tensile fracture located at the machined spigot groove. Because this failure mode physically severed the main pipe barrel and entirely bypassed the internal sealing mechanism, the joint lost water pressure immediately upon rupture, offering no post-

peak hydraulic reserve.

Analysis of the distributed fiber-optic strain data revealed the underlying mechanical mechanics driving these divergent failure modes. Longitudinally, both specimens exhibited similar foundational behaviors: as the locked spigot was pulled outward, the internal locking segments exerted a severe wedging action against the bell cavity, inducing significant radial expansion and yielding highly localized compressive strains on the outer bell surface. However, circumferential (hoop) strain analysis exposed fundamental differences in the cross-sectional load transfer paths. In Specimen-WB, the rigidly fixed weld bead transferred outward radial forces consistently, causing an asymmetric "squatting" distortion that concentrated critical bearing stress at the stiffness boundary near the top insertion slot, directly precipitating the bell fracture. Conversely, the unbonded snap ring in Specimen-FG permitted upward vertical kinematic shifting of the spigot. While this shifting relieved vertical bearing pressure on the bell, it fundamentally altered the internal force distribution, eliminating uniform concentric restraint and ultimately driving stress concentrations into the reduced wall thickness of the spigot groove. Ultimately, these tests demonstrate that while macroscopic axial capacities may appear similar, subtle geometric variances in joint restraint mechanisms dictate the internal load transfer paths that govern both structural failure modes and post-earthquake hydraulic reliability.

5.3 Four-Point Bending Performance

To evaluate the flexural performance and rotational kinematics of the restrained joints, a series of full-scale four-point bending tests were conducted. The first phase of this testing program utilized two nominal 8-inch ERDIP specimens assembled with differing locking segment orientations: one with the insertion slot positioned at 12 o'clock (the crown) and the other at 9 o'clock (the springline). The primary objectives of these tests were to characterize the continuous moment-rotation response of the restrained joint and to identify the critical deflection thresholds that initiate localized structural damage or compromise the system's hydraulic integrity. Two additional four-point bending tests were executed on 36-inch and 48-inch diameter ERDIP specimens to evaluate the flexural limit states and corresponding failure mechanisms of large-scale transmission pipelines.

5.3.1 Four-Point Bending Test Experimental Setup and Instrumentation

The experimental configuration for the small-diameter four-point bending tests is illustrated in Figure 5.19. A central hydraulic actuator was positioned over the joint centerline, defined as 3.25 inches offset from the bell face. Load was transferred from the actuator through a rigid steel spreader beam to two loading saddles, positioned symmetrically at 33.5 inches from the centerline on both the spigot and bell pipe. The entire assembly was simply supported on

heavy-duty rollers located 100.5 inches from the centerline, creating a total simply supported clear span of 201 inches.

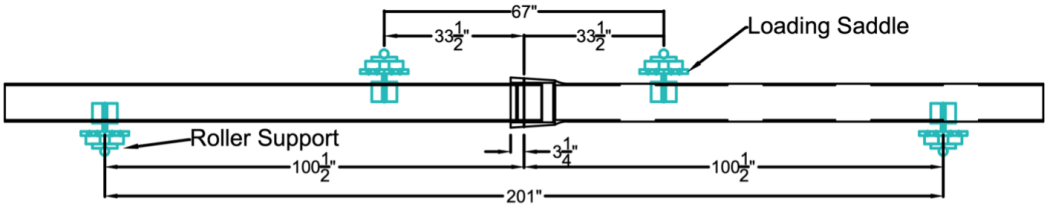


Fig. 5.17. Overview of the experimental setup of 8-inch ERDIP four-point bending test

Both specimens were initially assembled in the fully extended position (indicated by three visible white installation stripes on the spigot). In this configuration, the internal locking segments were fully engaged against the spigot weld bead prior to loading, ensuring that any induced flexural curvature would immediately mobilize the joint's restraint mechanism.

The testing protocol was executed in three distinct stages: internal pressurization, self-weight deflection, and monotonic actuator loading. First, the joint assembly was internally pressurized to house pressure of 50 psi. Second, temporary shoring was removed, allowing the unconstrained pipeline to deflect under its own self-weight. Finally, the actuator applied a monotonically increasing downward force, driving the joint through progressive deflection angles until severe structural damage and loss of hydraulic containment (water leakage) occurred.

Table 5.2. Summary of 8-inch ERDIP four-point bending test specimens and configurations

Test No.	Specimen	Test Date	Locking Segments Orientation
1	Specimen-12	11/30/2022	12 o'clock
2	Specimen-9	12/15/2022	9 o'clock

While the macroscopic loading geometry remained identical for both tests, the orientation of the internal locking segments was varied to evaluate its effect on flexural capacity and failure mechanics. In the first test (Specimen-12), the bell insertion slot was oriented at the 12 o'clock (top crown) position, distributing the three rigid ductile iron locking segments to the 3, 6, and 9 o'clock positions. In the second test (Specimen-9), the insertion slot was rotated to the 9 o'clock (springline) position, shifting the rigid locking segments to the 12, 3, and 6 o'clock positions, as illustrated in Figure 5.18. A complete summary of the testing matrix is provided in Table 5.2.

For the large-scale four-point bending tests, to accommodate the massive load demands of the 36-inch and 48-inch ERDIPs, a highly specialized self-reacting structural test frame

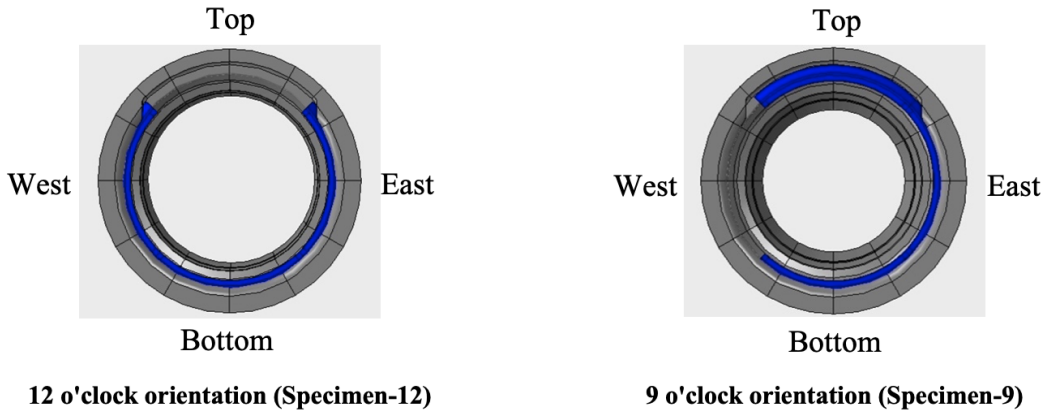


Fig. 5.18. Locking segments orientation for ERDIP 8-inch four-point bending test. 12 o'clock indicates single slot located at the crown; 9 o'clock refers to single slot positioned at the sprinline.

was designed, eliminating the need for external floor anchorage. As illustrated in Figures 2-1 and 2-2, the system consisted of two heavy-duty structural frames connected longitudinally by wide-flange I-beams at both the top and bottom, all securely anchored to four 2-inch-thick steel base plates. Monotonic vertical loads were applied using a high-capacity hydraulic actuator (460 kips capacity, 36-inch stroke) mounted at the mid-span of the upper frame. The actuator force was distributed through a central spreader beam that transferred the load to two 6-inch-diameter rollers spaced 12 feet apart. Custom-fabricated steel saddles were installed at all loading and reaction points to ensure uniform pressure distribution and prevent localized stress concentrations on the curved pipe surfaces.

While the macroscopic structural frame remained constant, the specific boundary conditions were tailored to each specimen. For the 36-inch diameter ERDIP test, the simply supported reaction span was set to 32 feet. The joint was initially assembled in the fully retracted position, with the bell's insertion slot oriented at the top crown. In contrast, the 48-inch diameter ERDIP test utilized a slightly shorter reaction span of 30 feet. For this larger specimen, the actuator's centerline was perfectly aligned with the joint's kinematic centerline, explicitly defined as 9 inches offset from the bell face, and the joint was assembled in the fully extended position prior to loading.

The experimental loading protocols varied slightly between the two specimens to evaluate different operational load combinations. The 36-inch test, conducted on March 11, 2025, was executed in three primary stages. First, the pipe was filled with water and pressurized to approximately 75 psi. With the bell securely fixed, this internal pressure induced a longitudinal thrust force that drove the unconstrained spigot axially from its fully retracted state to its fully extended state, actively engaging the restraint mechanism. Second, temporary shoring was removed, allowing the pipeline to deflect downward under its own self-weight and induce initial flexural rotations. Finally, while maintaining an internal pressure of approximately 75

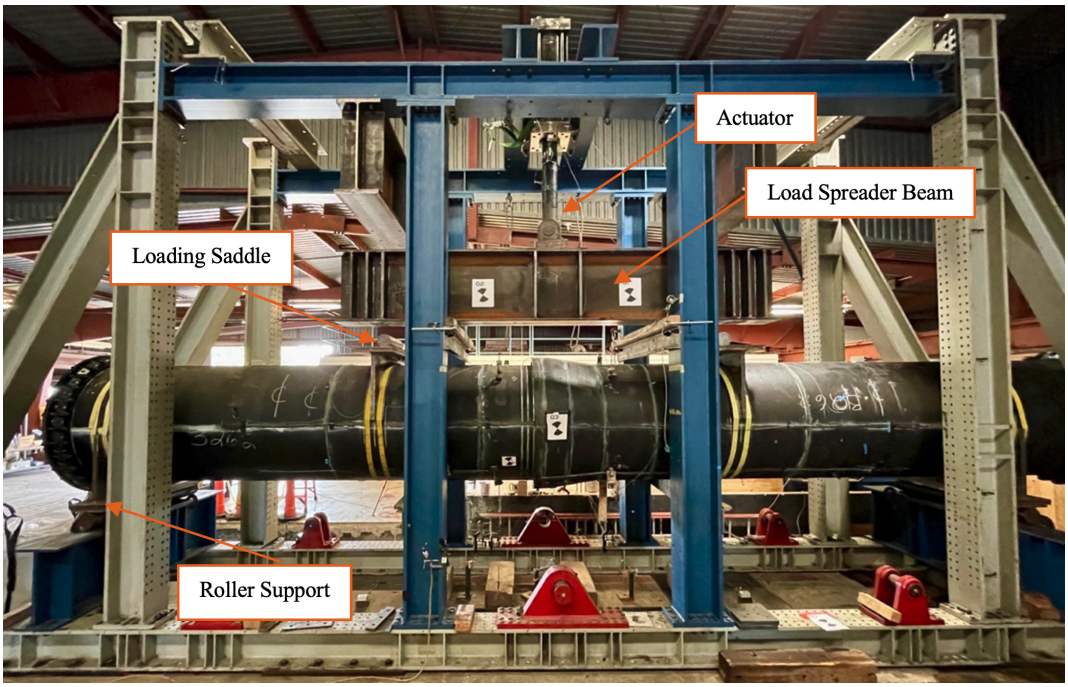


Fig. 5.19. Overview of the experimental setup of ERDIP four-point bending test for large-diameter pipes (48-inch ERDIP setup as an example)

psi, the hydraulic actuator applied a monotonic downward displacement to drive the joint to a greater rotation.

The 48-inch test, conducted on July 30, 2025, followed a more rigorous four-stage procedure designed to evaluate extreme internal pressure combinations under severe geometric distortion. First, beginning from the fully extended joint position, temporary supports were removed to allow the pipe to deflect under self-weight. Second, the specimen was pressurized to a baseline house pressure of 75 psi. Third, the hydraulic actuator applied monotonic downward loading until the joint exceeded its target rotation of 5.5 degrees. Fourth, while mechanically holding this extreme flexural deformation, the internal water pressure was dramatically increased to a target of 250 psi. Because the test setup purposefully lacked horizontal axial restraints at the pipe ends, the extreme pressure acting on the end caps generated massive longitudinal tensile forces. This critical final stage subjected the highly rotated joint to severe biaxial loading—simultaneous extreme bending and direct tension—simulating the absolute worst-case kinematic demands of a major seismic event.

To comprehensively monitor both global joint kinematics and micro-scale material deformations, a consistent instrumentation philosophy was deployed across all four-point bending tests. This strategy relied heavily on wire potentiometers to track macroscopic displacements and distributed strain sensors (DSS) to capture continuous strain profiles, with the specific sensor networks scaled to accommodate both the 8-inch distribution pipes and the

large-diameter transmission pipelines.

For the nominal 8-inch specimens, the instrumentation matrix was further augmented with discrete strain gauges. To record localized material yielding, these discrete gauges were installed at four cross-sectional planes: two on the bell pipe and two on the spigot. Each plane featured four sensing stations, with each station consisting of a bi-axial strain gauge rosette to independently measure longitudinal and circumferential strains, totaling 32 individual gauges. To prevent physical interference with the continuous DSS lines, these discrete gauge stations were intentionally offset by approximately 20 degrees from the standard cross-sectional quarter points (top, bottom, and springlines).

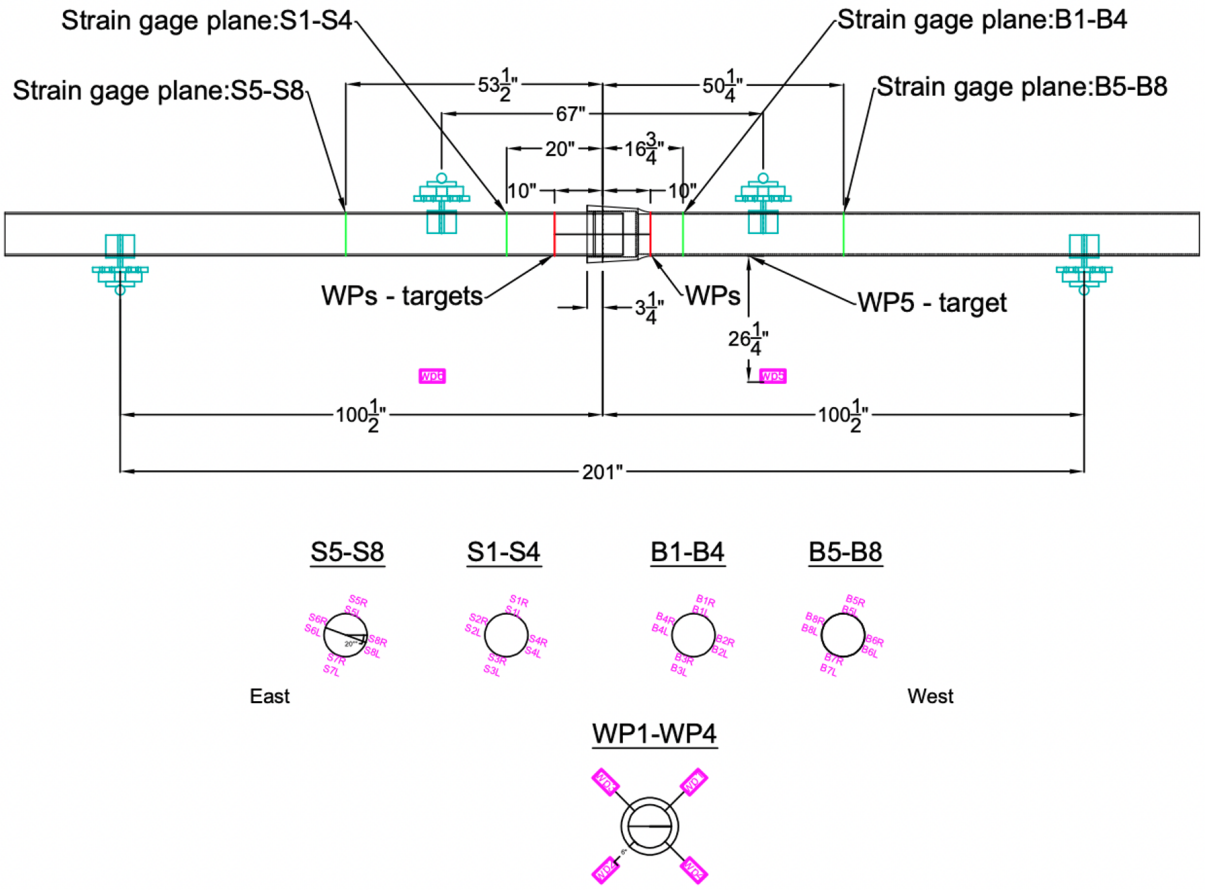


Fig. 5.20. Wired pots and strain gauges plan for 8-inch ERDIP bending test

Global joint kinematics and macroscopic pipe displacements for the 8-inch tests were tracked using a network of eight wire potentiometers. To measure the relative joint opening (axial pullout), four potentiometers were mounted to the bell and anchored to the spigot, positioned evenly at 45-degree offsets from the main quarter points. To track absolute spatial displacement, the remaining two potentiometers were affixed directly to the main barrels of

both the bell and spigot. These were positioned on the bottom crown to monitor vertical deflections. The instrumentation plan is shown in Figure 5.20.

To measure longitudinal bending strains, continuous fiber optic lines (F12–F19) were bonded along the full length of both pipes, spaced at 90-degree intervals around the circumference. To capture complex cross-sectional distortion and localized radial expansion, circumferential DSS (F1–F11) were also installed. Four circumferential rings were spaced at approximately 18-inch intervals along the unconfined lengths of both the bell and spigot barrels. To specifically target the intricate deformation mechanics within the joint itself, three additional circumferential sensors were concentrated directly on the bell: one at the bell face, one at the mid-section of the bell cavity, and one positioned exactly over the internal locking segments. The DSS plan is shown in Figure 5.21. More detailed instrumentation logs are presented in Chiu et al. (2023) [35].

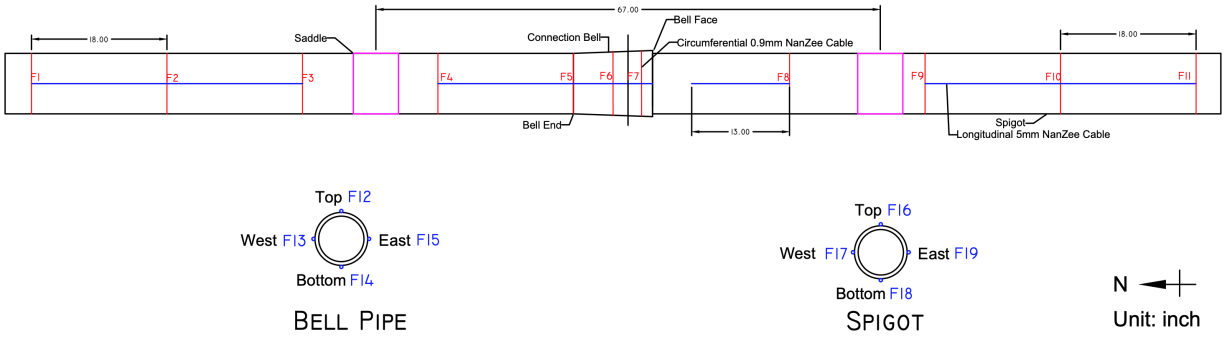


Fig. 5.21. DSS plan for 8-inch ERDIP bending test

For the large-diameter transmission pipeline specimens (36-inch and 48-inch), the overarching instrumentation strategy mirrored the small-diameter tests, utilizing discrete transducers for macroscopic kinematics and DSS for micro-scale continuous strain profiles. However, the specific sensor topologies were scaled and adapted to accommodate the massive geometry and physical support constraints of the heavy-duty experimental frame.

Macroscopic applied forces and centerline deflections were continuously monitored using a high-capacity load cell and a position transducer integrated directly into the hydraulic actuator. To capture the deflected shape of the massive pipe barrels, a network of supplementary position transducers was deployed along the longitudinal axis of both specimens, as shown in Figure 5.22.

The longitudinal DSS arrays (labeled S8 through S17) were strategically bonded to the exterior pipe surfaces to capture global bending mechanics. Because the massive custom steel support saddles physically obstructed the absolute bottom crown of the pipe (the 180° position), a standard symmetric sensor layout was not feasible. Instead, the longitudinal sensors were deployed at five accessible angular intervals: the top crown (0°), the east and west springlines (90° and 270°), and two localized lower quadrants offset by 45° from the

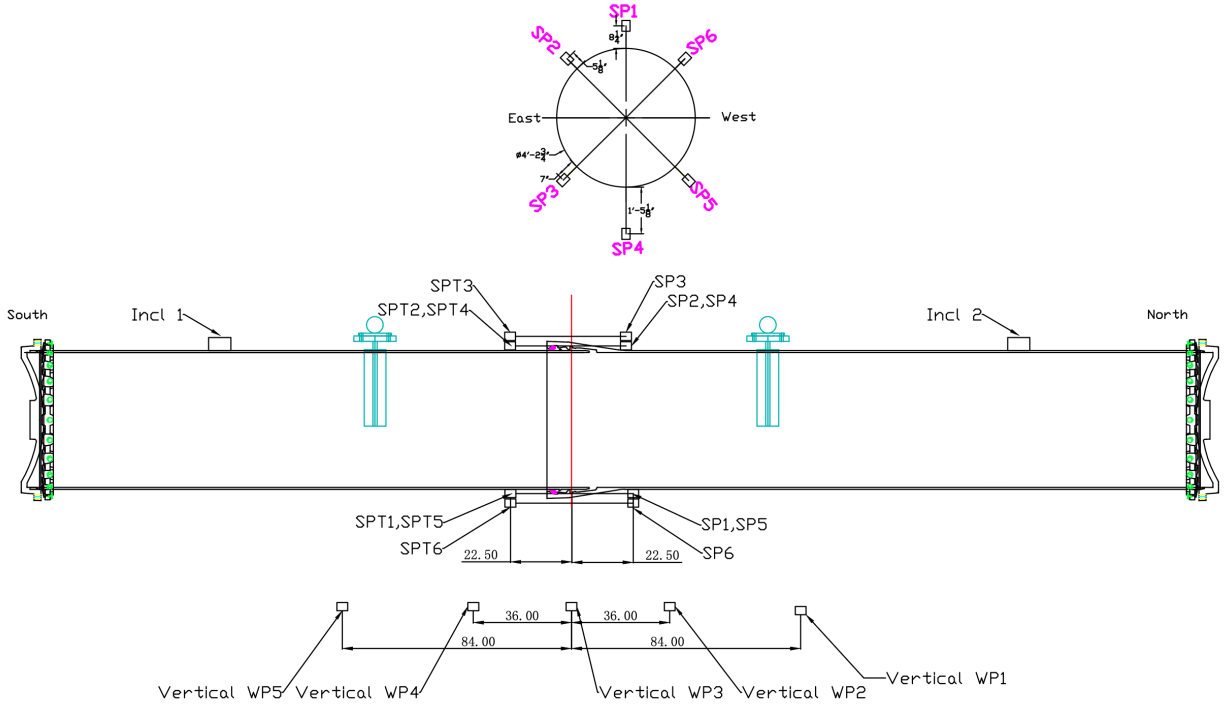


Fig. 5.22. Wired pots plan for large-scale ERDIP bending test (use 48-inch test as example)

bottom center (135° and 215°). This modified layout successfully captured the extreme tensile demands on the lower half of the pipe without experiencing physical crushing at the supports.

To monitor complex cross-sectional distortion and localized radial expansion, seven continuous circumferential DSS (labeled S1 through S7) were installed on each specimen. Consistent with the targeted mechanics observed in the 8-inch tests, four rings were distributed along the unconfined main pipe barrels to capture baseline diametric contraction. The remaining three rings were concentrated directly on the bell to monitor the internal restraint engagement: one positioned at the distal bell face, one at the geometric center of the bell cavity, and one positioned explicitly over the internal locking segments. The instrumentation plan is illustrated in Figure 5.23.

5.3.2 8-inch ERDIP Bending Performance

Joint Moment and Deflection

As established in the experimental protocol, the joint assemblies were first internally pressurized to 50 psi. Temporary shoring beneath the loading saddles was then removed, allowing the simply supported pipelines to deflect downward under their own self-weight. Once static

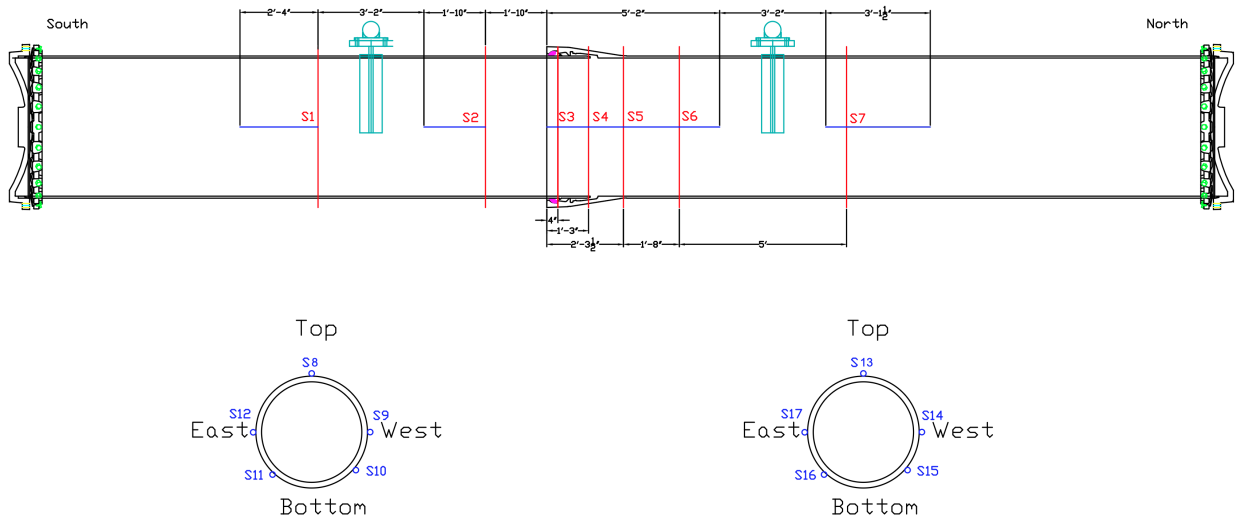


Fig. 5.23. DSS plan for large-scale ERDIP bending test (use 48-inch test as example)

equilibrium was achieved, a monotonic vertical load was applied to the central spreader beam and transferred symmetrically through the twin saddles. The resulting continuous moment-rotation (deflection) relationships were calculated using the VWP approach (Equation 4.5) and are presented in Figure 5.24. Due to physical interference between the heavy test frame and the vertical wire potentiometers, data during the initial self-weight deflection stage could not be captured. Consequently, Figure 5.24 plots only the forced-actuation phase. Both specimens maintained hydraulic integrity up to extreme flexural deformations, with catastrophic water leakage initiating near 13.0° of rotation. However, their ultimate capacities differed: Specimen-12 reached a maximum recorded rotation of 13.2° with a corresponding ultimate moment of 763.6 kip-in, whereas Specimen-9 reached a similar rotation of 13.1° but sustained a significantly higher ultimate moment of 1153.2 kip-in, as listed in Table 5.3.

Table 5.3. Summary of maximum moment and rotation for 8-inch ERDIP bending specimens

Specimen	**Locking Segments Orientation**	**Max. Moment (kip-in)**	**Max. Rotation (degree)**
Specimen-12	12 o'clock	763.6	13.2
Specimen-9	9 o'clock	1153.2	13.1

The pronounced variance in flexural stiffness and ultimate moment capacity is directly attributable to the circumferential orientation of the internal locking segments. Beyond

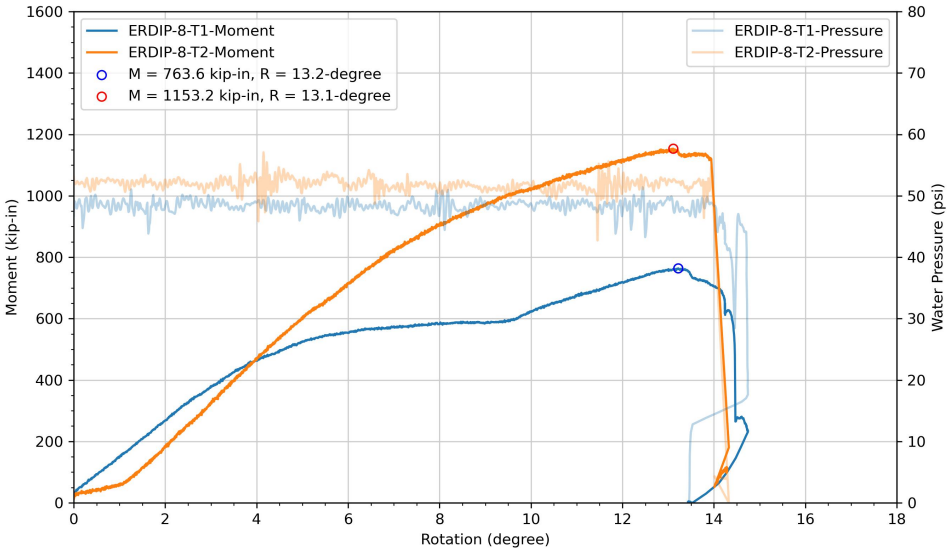


Fig. 5.24. Moment, rotation (joint deflection angle), and water pressure of 8-inch ERDIP four-point bending test

an initial rotation of 4.0°, Specimen-12 consistently exhibited a lower rotational stiffness, requiring substantially less applied moment to achieve equivalent deflections compared to Specimen-9. In Specimen-12, the insertion slot is located at the 12 o'clock position (the extreme compressive fiber in positive bending). Because this slot is sealed only by a compressible rubber retainer rather than a rigid ductile iron locking segment, the top crown of Specimen-12 offers minimal internal compressive bearing resistance, resulting in a softer global moment-rotation response. In contrast, Specimen-9 features a solid metallic locking segment at the 12 o'clock position, providing massive compressive bearing resistance and yielding a significantly stiffer, higher-capacity joint.

Conversely, during the very early stages of loading (rotations less than 4.0°), Specimen-12 paradoxically demonstrated a stiffer response than Specimen-9. It is hypothesized that this initial discrepancy stems from subtle geometric imperfections during the seating of the joint prior to testing. Under idealized conditions, the spigot naturally rests flush against the internal lower bearing surface of the bell cavity, as illustrated in Figure 5.25. However, it is suspected that the spigot of Specimen-9 was initially seated slightly off-center, resting precariously on the edge of this internal bedding. As initial flexure was applied, the spigot may have slipped radially downward into its fully seated position. This unresisted internal rigid-body motion would translate macroscopically as "free" rotation, causing Specimen-9 to register an artificially low moment resistance during the first few degrees of deflection until full internal bearing contact was finally established.

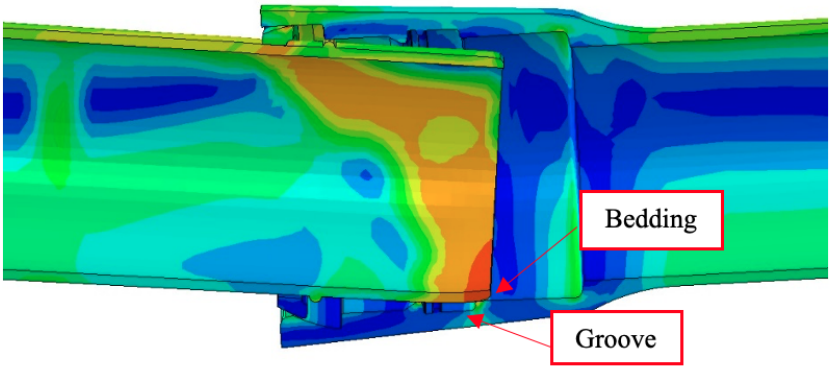


Fig. 5.25. Sketch of the internal joint of 8-inch ERDIP four-point bending test

Failure Mode

The experimental protocol dictated that monotonic loading continue until critical structural failure or the loss of hydraulic containment, evidenced by a sudden drop in internal water pressure. For both tests, ultimate failure was governed by localized structural yielding at the extreme tensile fiber (the bottom crown) of the spigot. While Specimen-12 and Specimen-9 sustained severe water leakage at different ultimate moments (763.6 kip-in and 1153.2 kip-in, respectively), both specimens achieved a nearly identical ultimate rotational capacity of approximately 13.0 degrees during the forced-actuation phase. This observation indicates that while the circumferential orientation of the internal locking segments heavily dictates the joint's flexural stiffness and moment capacity, it has a negligible influence on the ultimate kinematic deflection limits of the ERDIP assembly.

Figure 5.26 [35] presents the von Mises stress contours extracted from the finite element (FE) simulations for both specimens at an applied rotation of 11.0 degrees. The numerical analysis corroborated the physical observations: extreme von Mises stress localized precisely at the bottom crown of the spigot, rapidly exceeding the nominal 42,000 psi yield stress of ductile iron (indicated by the high-intensity contour regions). This concentration of plastic strain directly correlates with the structural deformation and eventual hydraulic failure observed experimentally. Furthermore, the FE models confirmed that while the bottom spigot underwent severe plastic yielding, the upper compressive section of the joint assembly remained largely within the elastic regime for both configurations. Ultimately, the interaction between the rigid bell cavity and the plastically yielding spigot dictates the joint's limit state, reinforcing the conclusion that ultimate flexural capacity is fundamentally governed by the overarching pipe geometry rather than the specific placement of the restraint segments.

Figure 5.27 illustrates the physical failure pattern of Specimen-12. Consistent with the preliminary FE analysis predictions, the bell remained structurally intact, with yielding and ultimate failure isolated to the spigot barrel. As shown in Figure 5.27a, the spigot exhibited

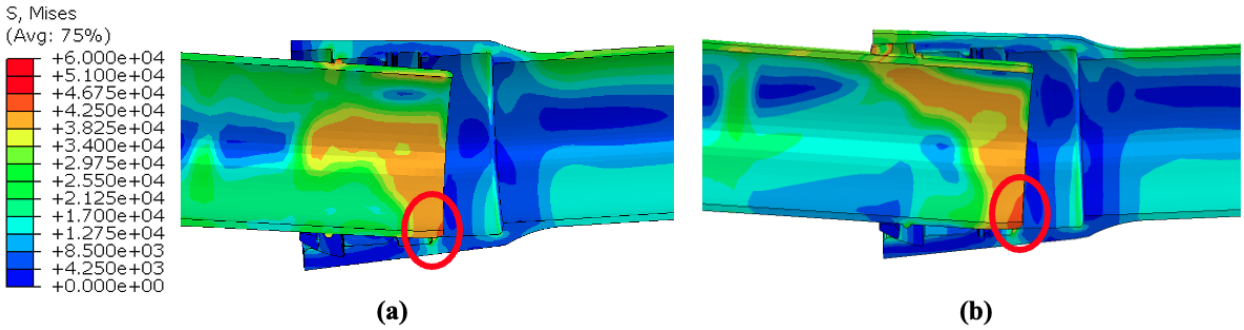


Fig. 5.26. Mises stress distribution of the specimens at 11-degree deflection of 8-inch ERDIP four-point bending test. (a) Specimen-12, (b) Specimen-9

severe localized cross-sectional distortion at the depth of insertion. Because the flexural rotation forced the downward-deflecting spigot into the rigid lower boundary of the bell cavity, compressive bearing forces were concentrated at the spigot's bottom invert. This highly localized crushing stress ultimately fractured the ductile iron wall, compromising hydraulic containment and precipitating the severe water leakage observed during testing.

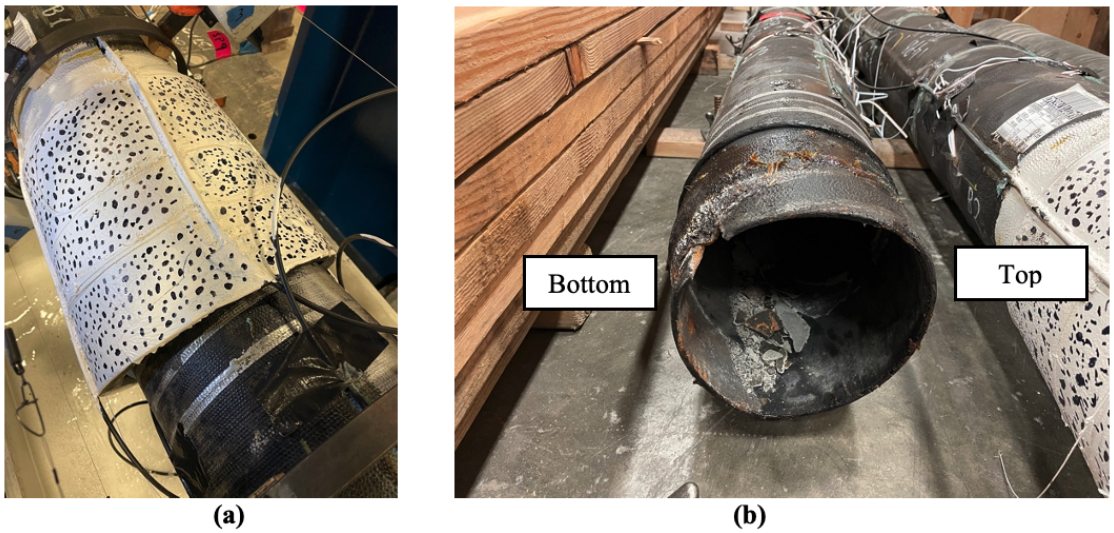


Fig. 5.27. Failure of Specimen-12 of 8-inch ERDIP four-point bending test. (a) Bell, (b) Spigot

The corresponding failure pattern for Specimen-9 is presented in Figure 5.28. Similar to Specimen-12, the bell sustained no visible cracking, with all permanent structural damage concentrated on the inserted spigot. However, the fracture in Specimen-9 was more severe. In addition to the localized structural punch-through at the bottom invert, a prominent

45-degree diagonal crack propagated circumferentially from the west springline, across the bottom invert, and extended upward toward the east springline.

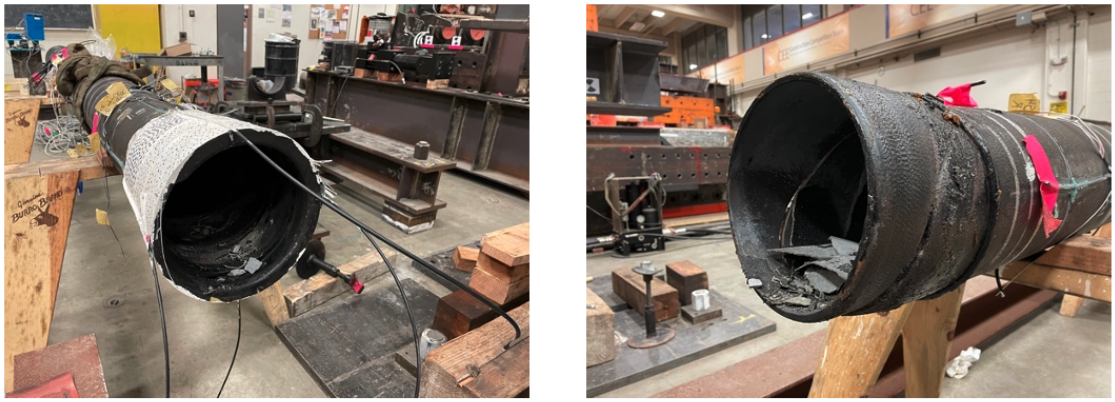


Fig. 5.28. Failure of Specimen-9 of 8-inch ERDIP four-point bending test. (a) Bell, (b) Spigot

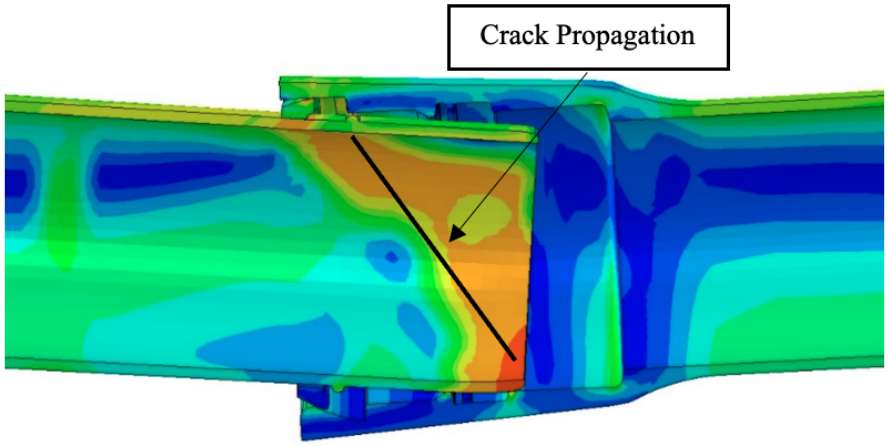


Fig. 5.29. Sketch of the failure mechanism of 8-inch ERDIP four-point bending test

This amplified damage mechanism is a direct consequence of the internal force transfer path generated during extreme joint rotation, as depicted schematically in Figure 5.29. Because the 12 o'clock position in Specimen-9 was occupied by a rigid metallic locking segment rather than a compressible rubber gasket, the top crown of the spigot established a hard bearing contact against the upper bell. This upper reaction point, paired with the lower bearing contact at the bell invert, formed a severe internal mechanical force couple. This rigid two-point contact subjected the constrained spigot to combined shear and bearing

stresses, ultimately driving the expansive 45-degree fracture that was absent in the softer Specimen-12 configuration.

Axial Strain

The longitudinal (axial) strain profiles captured by the discrete bi-axial rosettes for Specimen-12 and Specimen-9 are presented in Figures 5.30 and 5.31, respectively. As expected under bending flexure, both specimens exhibited a clear bending strain distribution: the extreme compressive fiber at the top crown (12 o'clock) demonstrated significant compressive strains, while the extreme tensile fiber at the bottom invert (6 o'clock) exhibited pronounced tensile strains. Theoretically, the primary springlines (3 and 9 o'clock) represent the neutral axis of the cross-section and should experience near-zero axial strain. However, because the gauge stations were intentionally offset by 20 degrees to accommodate the DSS routing, the "west" gauges were shifted downward into the tensile zone (toward 6 o'clock), and the "east" gauges were shifted upward into the compressive zone (toward 12 o'clock), predictably recording proportional tensile and compressive strains, respectively.

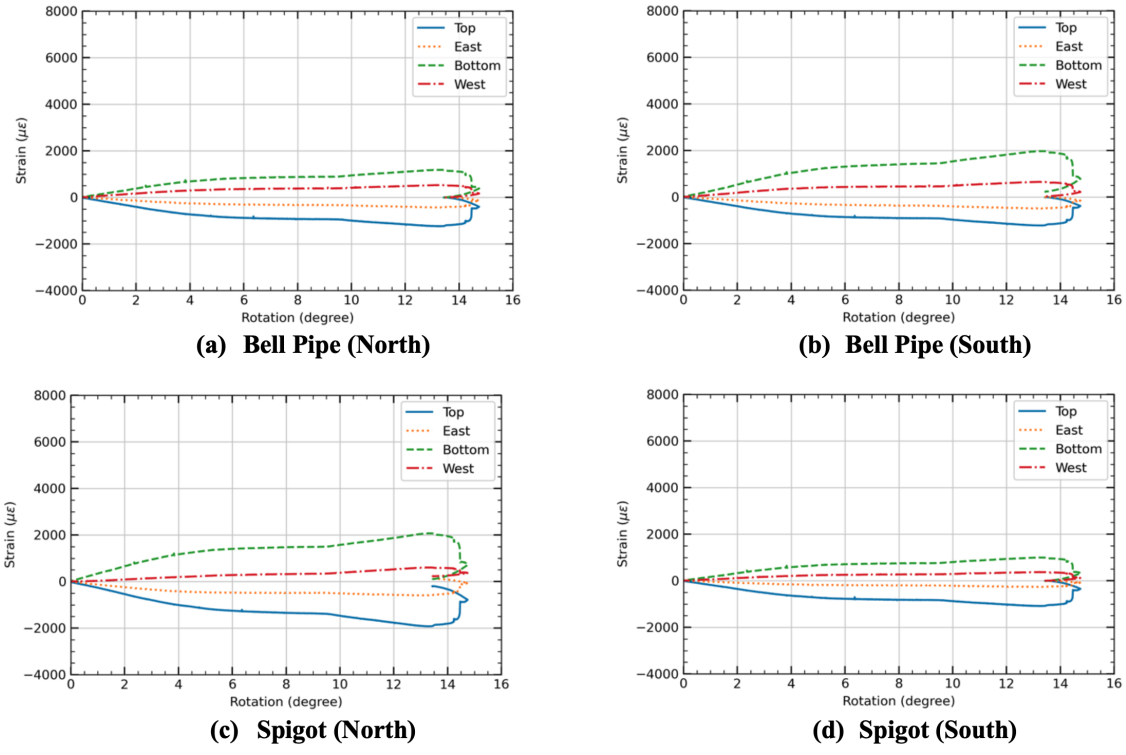


Fig. 5.30. Axial strain vs. rotation (defelction angle) of Specimen-12 of 8-inch ERDIP four-point bending test

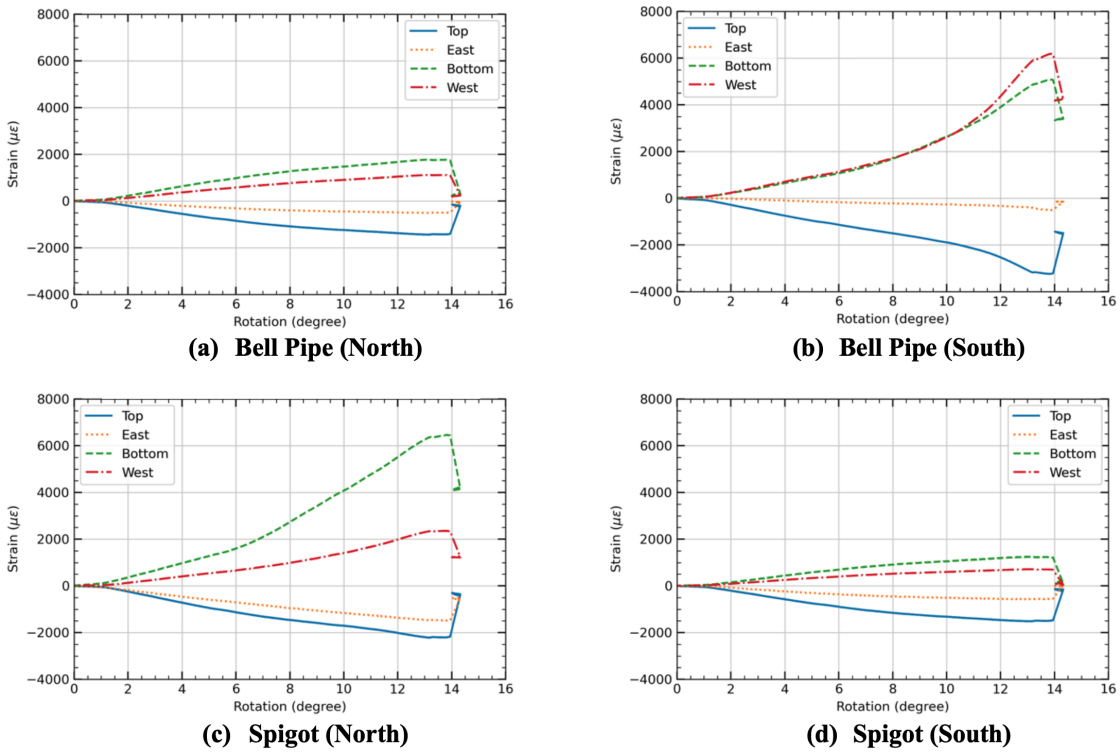
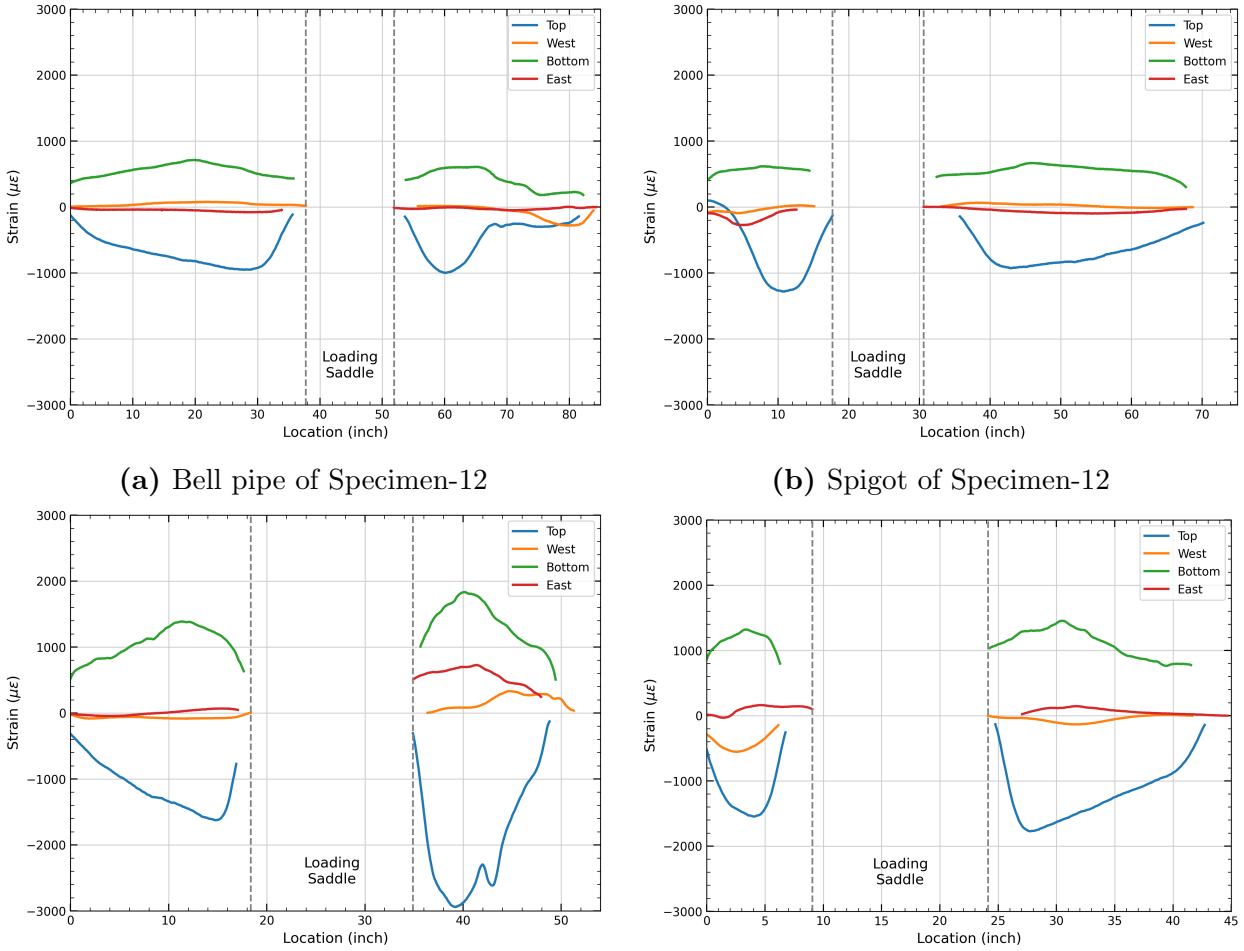


Fig. 5.31. Axial strain vs. rotation (defelction angle) of Specimen-9 of 8-inch ERDIP four-point bending test

While Specimen-12 exhibited relatively symmetric strain distributions along the longitudinal axis, Specimen-9 demonstrated localized strain amplifications immediately adjacent to the joint interface (i.e., the bell and the inserted spigot). This amplification supports the previously introduced hypothesis regarding initial seating imperfections. Rather than bearing evenly against the thickened internal bedding of the bell cavity (as depicted in the idealized schematic in Figure 5.29), the spigot of Specimen-9 likely slipped into the adjacent internal groove where the casing wall is thinner. This off-center bearing geometry locally elevated the longitudinal strains under severe flexural loading. Furthermore, the asymmetric configuration of the internal restraint in Specimen-9 (which features rigid locking segments on the east side but a compressible rubber retainer on the west side) created an uneven internal rotational stiffness. This asymmetry allowed the spigot to deform toward the softer rubber boundary, inducing a measurable out-of-plane lateral deflection that is resolved in the DSS data.

The continuous, high-resolution longitudinal strain profiles captured by the DSS network for Specimen-12, extracted at a global joint rotation of approximately 12.5 degrees, are presented in Figures 5.32a and 5.32b (plotted from north to south). These continuous profiles corroborate the discrete gauge data, capturing the global macro-bending mechanics of top-



(a) Bell pipe of Specimen-12

(b) Spigot of Specimen-12

(c) Bell pipe of Specimen-9

(d) Spigot of Specimen-9

Fig. 5.32. Axial strain distribution before failures (i.e., 12.5-degree rotation) of 8-inch ERDIP four-point bending tests

crown compression and bottom-invert tension. While the primary springline strains (3 and 9 o'clock) remained minimal globally, the strain distribution data revealed localized compressive strains on the west springline and tensile strains on the east springline immediately adjacent to the joint interface (located at the last 10-inches of Figure 5.32a). This suggests that even in the nominally symmetric Specimen-12 configuration, the complex internal wedging kinematics induce a minor degree of localized out-of-plane distortion.

The corresponding DSS longitudinal strain profiles for Specimen-9 are plotted in Figures 5.32c and 5.32d. While the global flexural mechanism mirrors Specimen-12, the strain magnitudes recorded near the joint interface in Specimen-9 are significantly more severe, explicitly corroborating the localized cross-sectional distortion caused by the spigot bearing directly against the thinner internal bell groove. Moreover, the DSS network successfully captured the out-of-plane kinematic shift induced by the asymmetric locking configuration. Near the bell interface, distinct tensile strains emerged on the east springline (3 o'clock) of both pipes, coupled with severe compressive strains on the west springline (9 o'clock) of the spigot. This strain profile suggests that the inserted spigot skewed laterally toward the unresisted west side, the location of the compressible rubber gasket, demonstrating how asymmetric restraint placement fundamentally alters the tri-axial load transfer path within the joint assembly.

Hoop Strain

Under severe flexural loading, cylindrical pipe cross-sections inherently tend to distort or ovalize. Generally, due to the Poisson effect, the induced circumferential (hoop) strains exhibit an inverse relationship to the primary longitudinal bending strains, though typically at lower magnitudes. However, within the complex boundary conditions of the joint assembly, these elastic responses are modified by localized internal bearing forces. The continuous DSS arrays provide a clear mapping of this cross-sectional "squatting" mechanism.

The circumferential strain profiles for Specimen-12 are presented in Figure 5.33. This data captures the sensor rings positioned at the bell end (F5), the mid-section of the bell cavity (F6), and directly over the internal locking segments (F7). Sensor F8 represents the circumferential ring on the spigot barrel immediately adjacent to the joint interface. The data from F5 and F8 reveals a distinct pattern of eccentric squatting just outside the joint constraints: the top crown (12 o'clock) exhibits circumferential expansion, while the bottom invert (6 o'clock) undergoes circumferential compression. Similar far-field ovalization patterns were recorded by the remaining sensors on the main pipe barrels [35].

Within the bell cavity itself, sensors F6 and F7 expose the complex internal force transfer. Sensor F6, located near the middle of the bell, recorded highly localized circumferential expansion at the bottom invert (6 o'clock). This is the exact location where the downward-deflecting spigot actively bears against the bell invert. Further back at sensor F7 (positioned over the locking segments), the localized squatting mechanism of the constrained joint is evident. The bell expands vertically at both the top crown and bottom invert (12 and 6 o'clock) while simultaneously contracting laterally at the springlines (3 and 9 o'clock). This

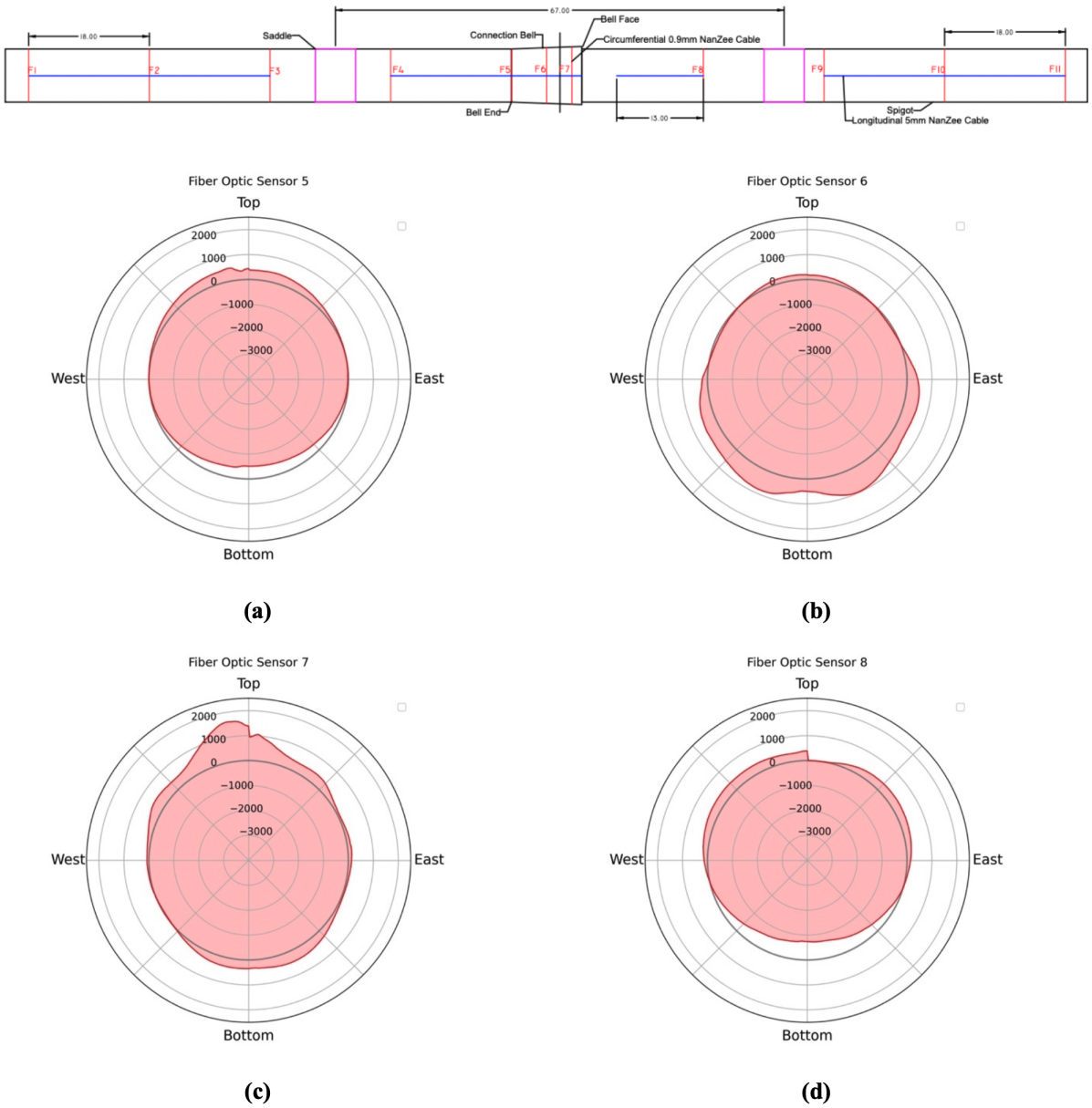


Fig. 5.33. Strain distribution in the circumferential direction of Specimen-12 under 12.5-degree rotation (defelction) condition of 8-inch ERDIP four-point bending test. (a) sensor on the bell end (b) sensor on the middle of the bell (c) sensor on 3.5-inch away from the bell face (d) sensor on the spigot about 18-inch away from the bell face

distortion is driven by the rigid internal force couple where the bottom of the spigot crushes against the bell invert, while the top of the spigot pivots upward to bear against the bell crown. A schematic detailing this internal mechanical interaction and the corresponding circumferential sensor locations are provided in Figure 5.34.

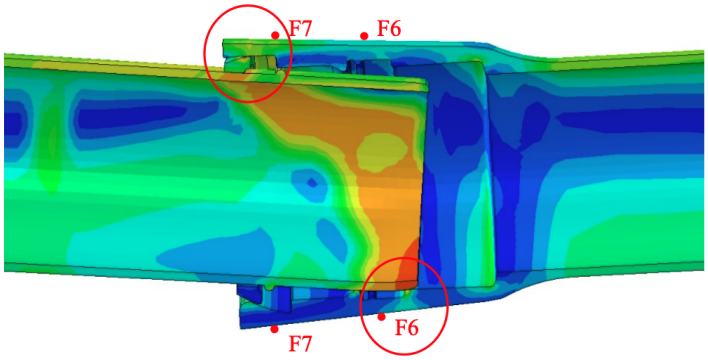


Fig. 5.34. Sketch of the mechanism of the bell and the corresponding locations of circumferential sensors.

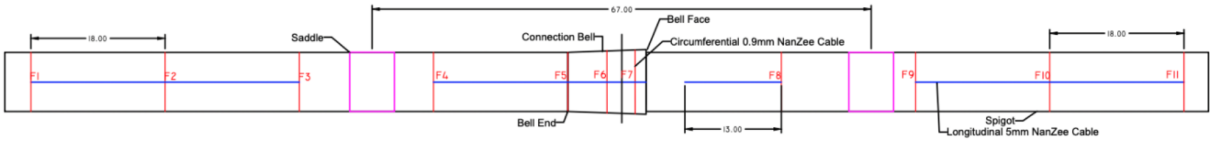
Figure 5.35 presents the corresponding circumferential strains for Specimen-9. While the global ovalization patterns remain similar to Specimen-12, the strain magnitudes are significantly amplified. As established previously, this amplification counld be attributed to the spigot bearing directly against the thinner internal groove wall rather than the thickened bedding surface.

The DSS rings on the Specimen-9 bell (Figure 5.35a–c) captured the asymmetric kinematics induced by the restraint configuration. Unlike Specimen-12, where the circumferential strain distribution remained largely symmetric across the vertical axis, the neutral axis of the strain profile in Specimen-9 is visibly skewed. The entire distortion pattern is rotated approximately 20 degrees off the vertical axis toward the west springline. This asymmetric expansion and lateral skewing indicates the out-of-plane lateral deflection caused by the presence of the unresisted rubber gasket at the 9 o'clock position.

Conclusion of 8-inch ERDIP four-point Bending Test

This experimental program evaluated the bending performance, continuous moment-rotation response, and ultimate limit states of nominal 8-inch ERDIP joints subjected to monotonic four-point bending. A primary objective was to characterize the influence of the internal restraint configuration by testing two varying circumferential orientations: Specimen-12 (insertion slot at the top crown, 12 o'clock) and Specimen-9 (insertion slot at the springline, 9 o'clock).

The macroscopic kinematic data revealed that both joint configurations possess massive, highly ductile rotational capacities. During the initial stages of loading, the spigots rotated



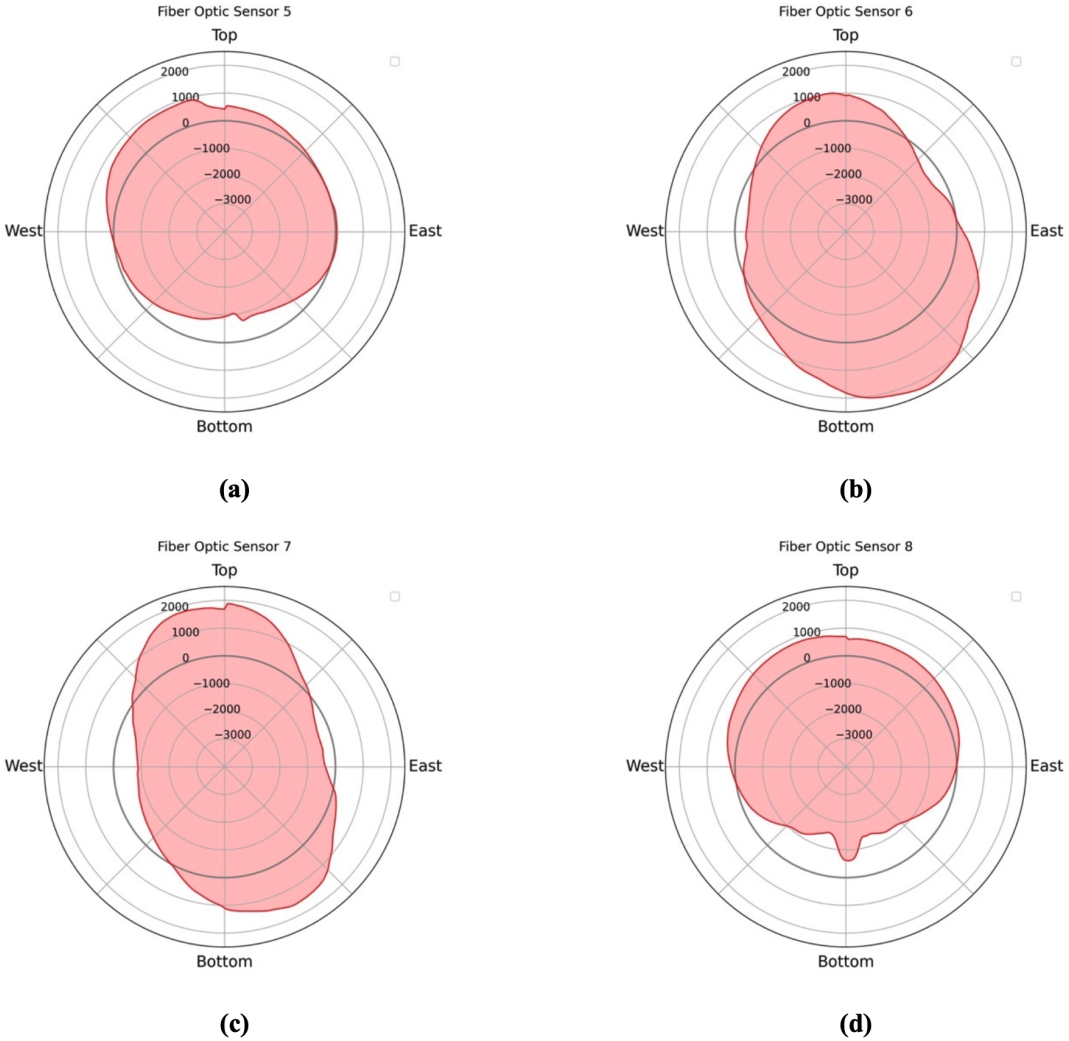


Fig. 5.35. Strain distribution in the circumferential direction of Specimen-9 under 12.5-degree rotation (defelction) condition of 8-inch ERDIP four-point bending test. (a) sensor on the bell end (b) sensor on the middle of the bell (c) sensor on 3.5-inch away from the bell face (d) sensor on the spigot about 18-inch away from the bell face

freely within the bell cavities, accommodating approximately 5.0 degrees of deflection for Specimen-12 and 4.0 degrees for Specimen-9 before establishing hard internal bearing contact—values that align perfectly with the manufacturer's baseline performance guidelines. Following engagement, both joints safely accommodated extreme flexural demands, reaching nearly identical structural limit states: structural fracturing initiated at 13.1 degrees for Specimen-12 and 13.2 degrees for Specimen-9.

While the ultimate kinematic deflection limits of the two specimens were nearly identical, their flexural stiffness and required ultimate moments varied significantly. The data explicitly demonstrates that the orientation of the internal locking segments governs the joint's moment resistance. Because Specimen-9 featured a rigid metallic locking segment at the 12 o'clock position, it generated a massive internal bearing force couple, resulting in a substantially stiffer joint requiring a higher applied moment. In contrast, the compressible rubber retainer located at the 12 o'clock position in Specimen-12 provided a softer boundary, reducing the required moment for a given deflection angle.

Ultimately, distributed high-resolution strain profile confirmed a consistent structural failure mechanism across both configurations. Regardless of the restraint orientation, ultimate failure was driven by intense localized plastic yielding at the spigot's bottom invert. As the spigot bore downward against the rigid bell cavity, the concentrated compressive bearing stress rapidly exceeded the ductile iron's plastic limit, precipitating the localized punch-through fractures. These findings demonstrate that while the specific placement of the restraint segments heavily dictates the internal stress distribution and global bending stiffness, the ultimate flexural capacity and failure mode of the joint are fundamentally governed by the overarching geometric interaction between the spigot and the bell.

5.3.3 36-inch ERDIP Bending Performance

Experimental Data Analysis

The 36-inch specimen was initially pressurized to a internal water pressure of approximately 75 psi. The testing protocol was executed in two primary phases: (1) self-weight deflection and (2) forced-actuation via the hydraulic actuator. In the first phase, temporary shoring was removed, allowing the unconstrained pipeline to deflect downward under its own self-weight until achieving static equilibrium. In the second phase, a monotonic vertical force was applied at the midpoint of the central spreader beam and transferred to the pipeline through two loading saddles spaced symmetrically at 144 inches from the joint centerline.

Figure 5.36a illustrates the continuous development of applied actuator force and internal water pressure throughout the loading history. Figure 5.36b presents the corresponding global moment-rotation response, with kinematic rotation calculated using two independent measurement arrays (vertical and horizontal string potentiometers). During the initial self-weight deflection phase, both measurement approaches identically recorded a vertical downward displacement of 2.12 inches, corresponding to a joint rotation of 1.35 degrees.

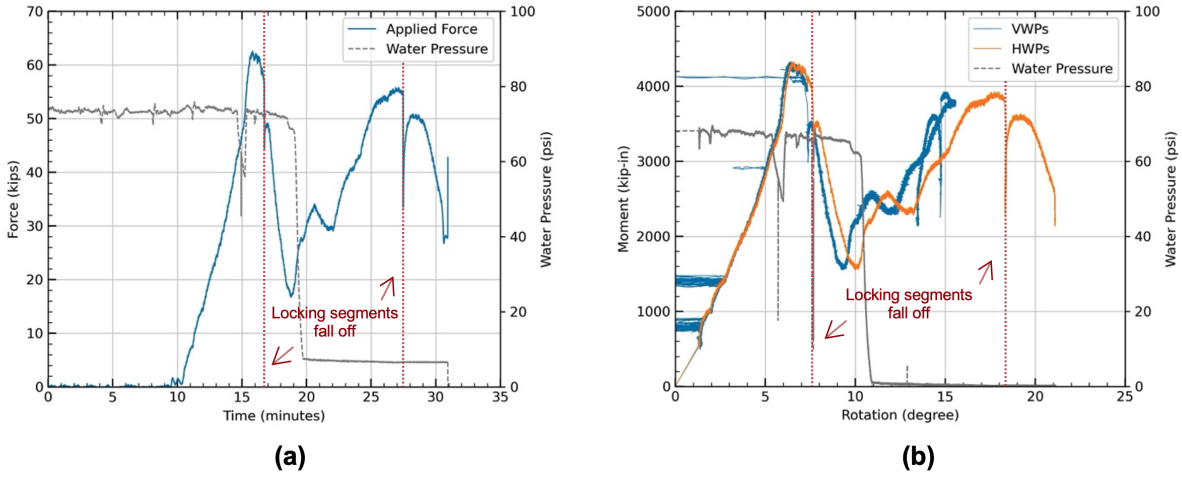


Fig. 5.36. ERDIP 36-inch four-point bending test data (a) Force, time, and water pressure (b) Moment, rotation, and water pressure

Following static equilibrium, the hydraulic actuator initiated monotonic vertical loading. Minor hydraulic weeping (approximately 3 to 5 gpm) was observed when the joint reached a rotation of between 5.1 and 5.3 degrees. However, upon further deflection, the internal elastomeric gasket kinematically reseated itself, successfully halting the leakage and restoring full hydraulic containment. The joint achieved its ultimate moment capacity at a rotation of 6.5 degrees, recording a peak applied load of 62.8 kips and a corresponding ultimate moment of 4,325 kip-in. Immediately following this peak resistance, the first set of internal locking segments was structurally compromised and physically dislodged from the bell cavity, precipitating a sudden drop in recorded force. Ultimate hydraulic failure—strictly defined as the total loss of internal pressure containment—occurred at a rotation of approximately 9.51 degrees (vertical measurement) and 10.25 degrees (horizontal measurement). Notably, this ultimate rotational capacity significantly exceeded the manufacturer's specified design limit of 7.0 degrees.

Following hydraulic failure, monotonic loading continued until the hydraulic actuator reached its absolute stroke limit. Post-peak behavior was characterized by internal load redistributions. Between the 21- and 23-minute marks (corresponding to extreme rotations of 12 to 13 degrees), a prominent acoustic emission (an audible "boom") was recorded, followed by a transient drop and subsequent recovery in actuator force. This mechanical signature indicates a sudden release of strain energy, suggesting that the remaining internal locking segments abruptly shifted and re-engaged against the bell casing to compensate for the previously dislodged components.

It is critical to note that following the ejection of the first locking segment set, a divergence emerged between the two independent rotational measurement methods. This discrepancy was mechanically induced by the dislodged iron segment falling and physically obstructing

the VWP positioned directly beneath the joint interface. Consequently, the kinematic data derived from the HWP is considered the accurate representation of global joint rotation beyond the initial structural failure point. A complete summary of the critical limit states is provided in Table 5.4.

Table 5.4. Summary of failure metrics for 36-inch ERDIP bending specimen

Max Moment (kip-in)	Rotation when fail – VWP (°)	Rotation when fail – HWP (°)	Max Force (kips)	Vert. Disp. when fail (inch)
4,325	9.51	10.25	62.80	12.53

Figure 5.37 presents the physical condition of the specimen following the conclusion of the experiment. While no macroscopic yielding or rupture of the primary ductile iron casing was visually evident, the internal restraint mechanism sustained progressive, severe damage. During the forced-actuation phase, prior to ultimate hydraulic failure, minor water leakage initiated and a pair of internal locking segments was structurally compromised and dislodged from the bell cavity. As monotonic deflection increased, an additional pair of locking segments was ejected. Ultimately, four of the twelve installed locking segments were completely detached, as mapped schematically in Figure 5.38. By the conclusion of the test, every locking segment located below the springline had been ejected, with the distinct exception of the single segment positioned precisely at the bottom invert of the bell (shown in Figures 5.37b and c).

The proposed mechanism driving this localized restraint failure stems from the complex relative kinematics between the spigot and bell casings during extreme flexure. As the joint was driven into severe rotation, the tensile region of the spigot (the portion below the neutral axis at the springline) underwent significant axial pullout relative to the bell face. This outward longitudinal translation forced the spigot's weld bead to bear heavily against the internal locking segments, inducing a severe outward radial thrust that locally expanded the bell casing, as illustrated in Figure 5.39. This radial dilation created an internal physical gap between the spigot and the bell below the springline (Figure 5.38b). Deprived of tight circumferential confinement, the internal locking segments in this tensile zone were subsequently either mechanically sheared from the cavity or hydrostatically ejected by the high-pressure water blow-by.

Conversely, the locking segment positioned at the extreme bottom invert remained securely engaged throughout the entire loading history. This survival is attributable to massive, localized compressive bearing forces. Because the joint was subjected to continuous downward vertical deflection, the bottom invert acted as the primary kinematic pivot point, subjecting the local locking segment to extreme compressive bearing stress between the downward-deflecting spigot and the upward-reacting bell casing. This massive normal force

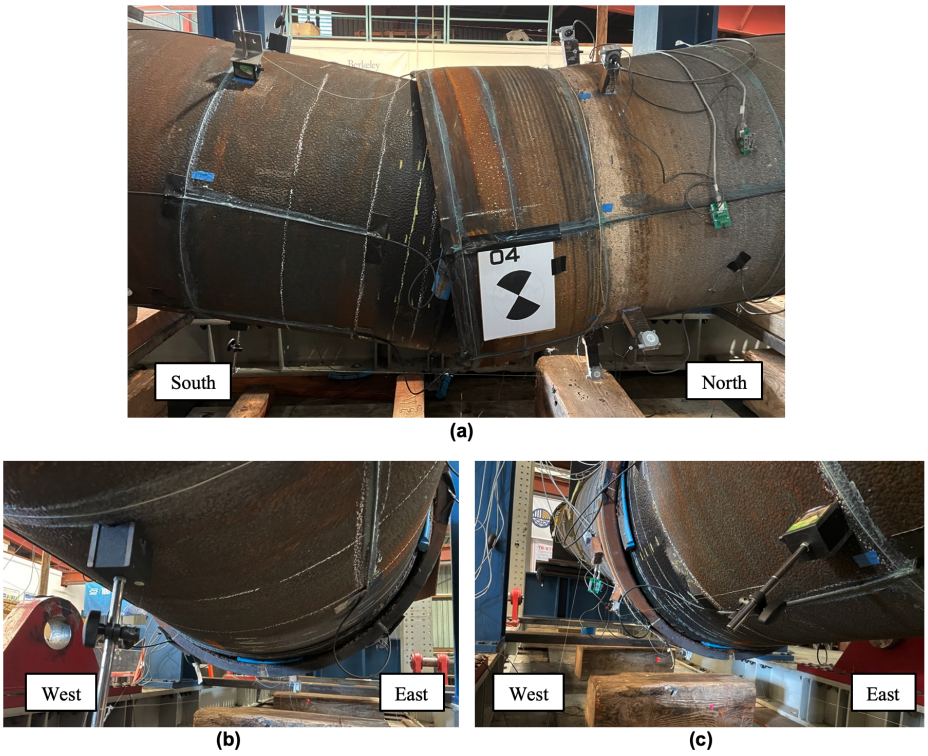


Fig. 5.37. Aftermath of ERDIP 36-inch four-point bending test specimen. (a) No obvious crack was found. (b)(c) Locking segments (blue) locations after the experiment

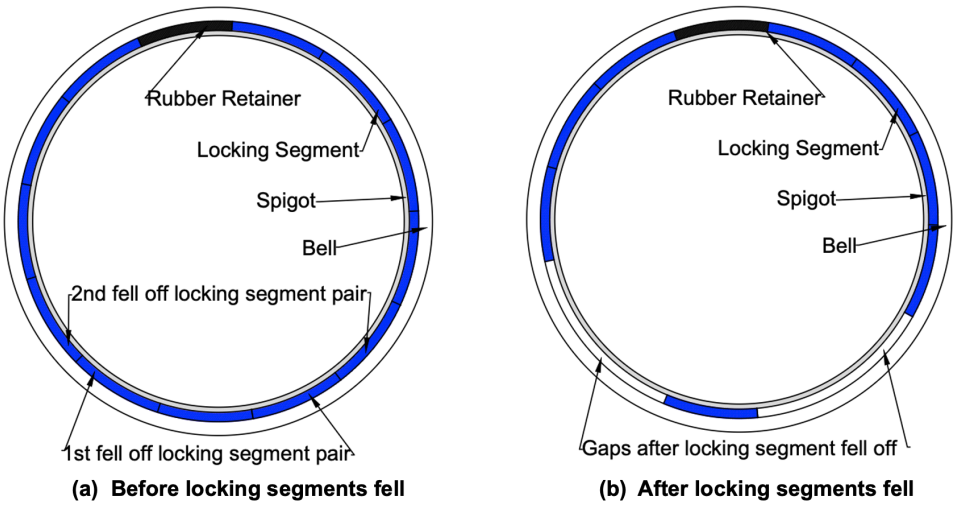


Fig. 5.38. Cross-sectional sketch of locking segments in 36-inch ERDIP bell

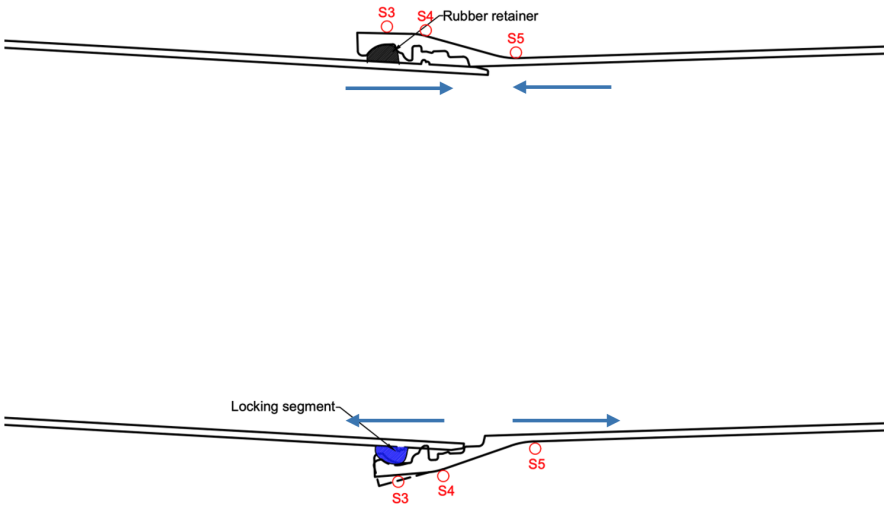


Fig. 5.39. Sketch of the 36-inch ERDIP bell bending deforming mechanism

generated overwhelming frictional resistance, effectively clamping the invert segment in place and preventing its ejection despite the surrounding structural dilation.

Axial Strain

The continuous axial strain profiles captured by the DSS arrays are presented in Figures 5.40 through 5.42. To analyze the progressive deformation mechanics, Figure 5.40 isolates the relationship between longitudinal strain and global joint rotation at four critical cross-sectional planes: (1) 1.5 feet south of the spigot face (S1), (2) 1.0 foot north of the spigot face (S2), (3) the midpoint of the bell casing (between S3 and S6), and (4) 1.5 feet north of the distal bell face (S7). Note that all global joint rotations referenced in this analysis were derived exclusively from the HWP kinematic array, as established in the preceding macroscopic analysis.

Prior to the structural compromise of the first locking segment set, the strain distributions at the far-field cross-sections (Figures 5.40a and d) strictly adhered to classical bending theory: pronounced compressive strains localized at the top crown, equivalent tensile strains developed at the bottom invert, and minimal strains were recorded along the springlines (the theoretical neutral axis). Conversely, the strain fields immediately adjacent to the joint interface (Figures 5.40b and c) were markedly more complex, and this complexity intensified rapidly following the ejection of the initial locking segments, indicating a fundamental shift in the internal force transfer mechanism.

Within the bell casing (Figure 5.40b), the pre-detachment strain profile generally resembled classical bending. However, as extreme rotation progressed toward the ejection of the second segment set, substantial tensile strains began developing at the theoretical springline. This critical observation confirms that the cross-sectional neutral axis shifted upward.

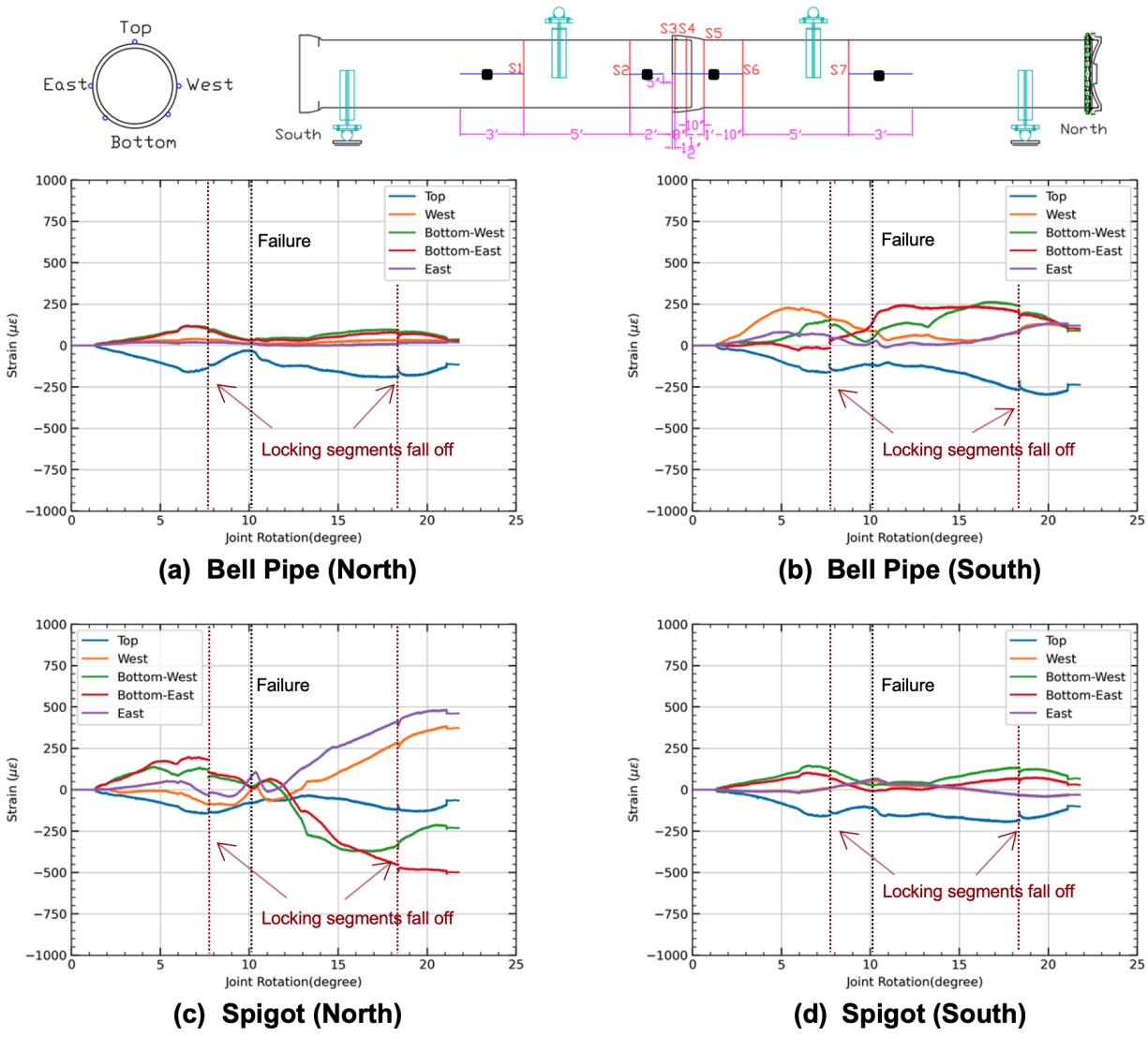


Fig. 5.40. Axial strain vs joint rotation of 36-inch ERDIP four-point bending test

Because the ejection of the lower locking segments destroyed the joint's tensile continuity below the springline, the remaining intact cross-section was forced to redistribute the internal tensile demands higher up the pipe wall to maintain equilibrium. Furthermore, as rotation continued, an irregular multi-axial strain state emerged: tension developed across the west, bottom-west, and east domains, while compression concentrated at the top and bottom-east domains. This distribution strongly suggests localized differential deformation, wherein inefficient force transfer between the rigid weld bead and the shifting locking segments created internal gaps, leading to the sequential blowout of the locking segments.

A corresponding mechanical shift was captured on the inserted spigot (Figure 5.40c). Following the initial segment detachment, unexpected compressive strains materialized at the bottom invert, an area typically dominated by tension. This anomaly suggests that under extreme rotation, the extreme tensile fiber of the downward-deflecting spigot established hard bearing contact directly against the internal bell invert. Because the internal bell cavity is characterized by a complex geometry of recessed seating grooves, this hard bearing contact likely subjected the spigot invert to intense, highly localized compressive crushing, temporarily overriding the bending tensile stresses [26].

Figure 5.41 maps the spatial longitudinal strain distribution along the unconfined bell pipe (the north assembly) at the ultimate failure state (10.25 degrees of rotation). In the far-field regions, the mechanics behave as expected: top sensors (e.g., S13) record compression, springline sensors (e.g., S14 and S17) remain neutral, and bottom sensors record tension. However, anomaly occurs within the first 10 inches of the bell face. Sensors located near the horizontal springlines recorded highly localized compressive strains. Mechanically, this indicates that as the spigot weld bead wedged against the lower locking segments, it forced them radially outward. This intense radial dilation introduces a secondary localized bending moment into the bell casing wall, creating extreme longitudinal compression on the exterior surface near the bell face (schematically detailed in Figure 5.39).

Conversely, sensors located directly below the springline (e.g., S15 and S16) recorded tensile demands at the bell face. This indicates that while the locking segments in this lower quadrant were actively being dislodged, they remained wedged tightly enough to transfer axial pullout forces into the bell casing before finally failing. Notably, none of these localized strain anomalies occurred at the top crown of the bell; because the 12 o'clock position was fitted with a compressible elastomeric gasket rather than a rigid iron segment, it lacked the mechanical stiffness to transfer these localized forces into the bell wall.

Finally, Figure 5.42 presents the longitudinal strain profile along the spigot (the south assembly) close to ultimate failure. While the extreme compressive fiber at the top crown (S8) yielded expected continuous compression, the remaining sensors (S9 through S12) highlighted the extreme localization of the joint's ductility. In the far-field region (0 to 40 inches from the distal support), axial strains were virtually zero. Moving toward the joint interface (110 to 120 inches), the strains rapidly amplified to match classical bending expectations (high tension at S10/S11, neutral at S9/S12). This spatial gradient proves that the ERDIP assembly effectively acts as a localized plastic hinge; the vast majority of the structural deformation is concentrated within the complex joint interface, leaving the main pipeline

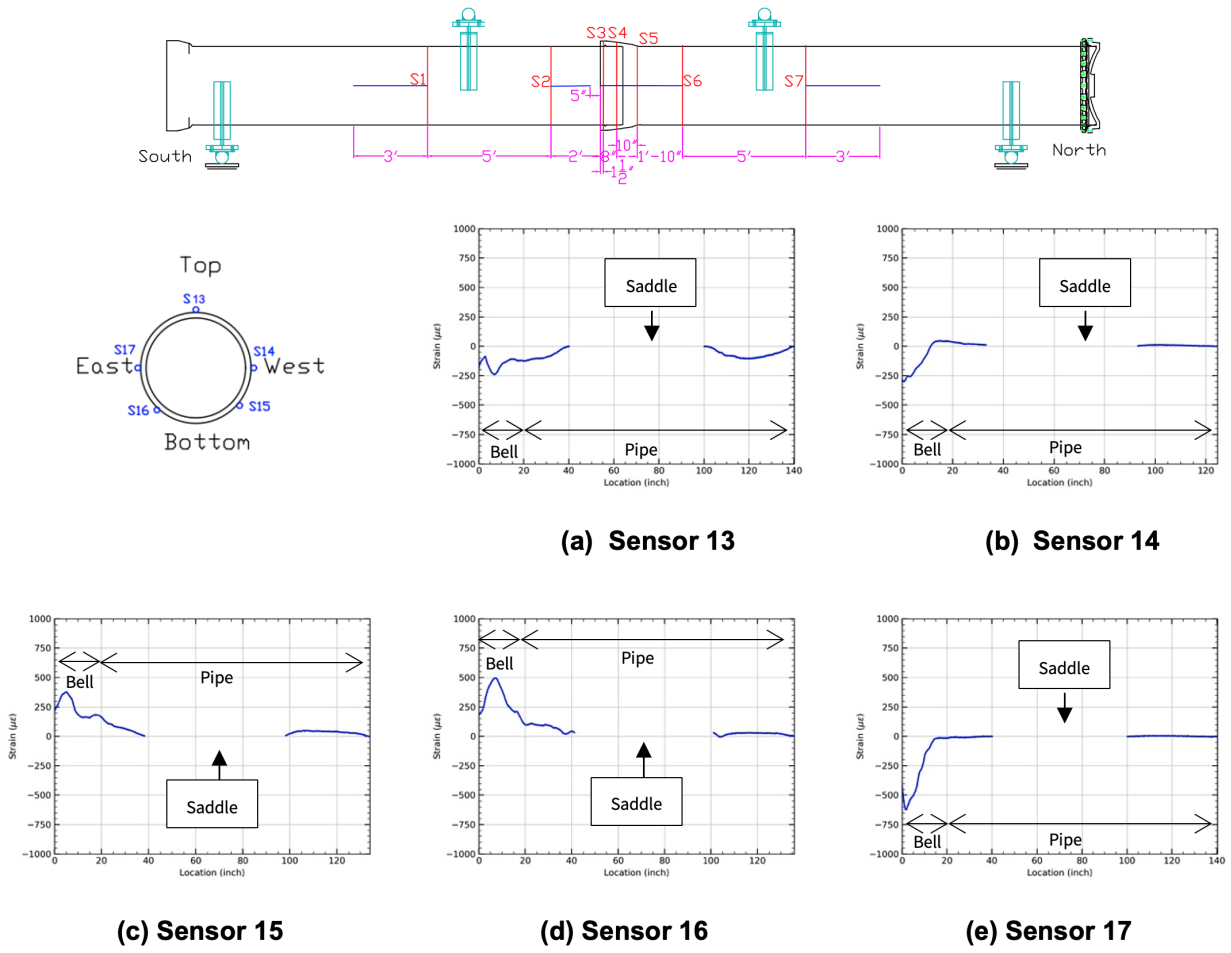


Fig. 5.41. Axial strain development of bell pipe (northside pipe) when fail (i.e., 10.25-degree HWP rotation)

barrels relatively unstressed even at catastrophic failure rotations.

Hoop Strain

The continuous circumferential (hoop) strain profiles captured by the DSS network are presented in Figure 5.43. This analysis isolates data from four critical circumferential rings: sensor S2, positioned on the unconfined spigot immediately adjacent to the joint interface; sensor S3, located directly over the internal locking segments on the bell casing; sensor S4, situated at the geometric midpoint of the bell cavity; and sensor S5, installed at the distal bell face.

The cross-sectional distortion of the spigot (Figure 5.43a) reveals a complex strain distribution. Compressive hoop strains localized at the top crown, as well as the bottom-west

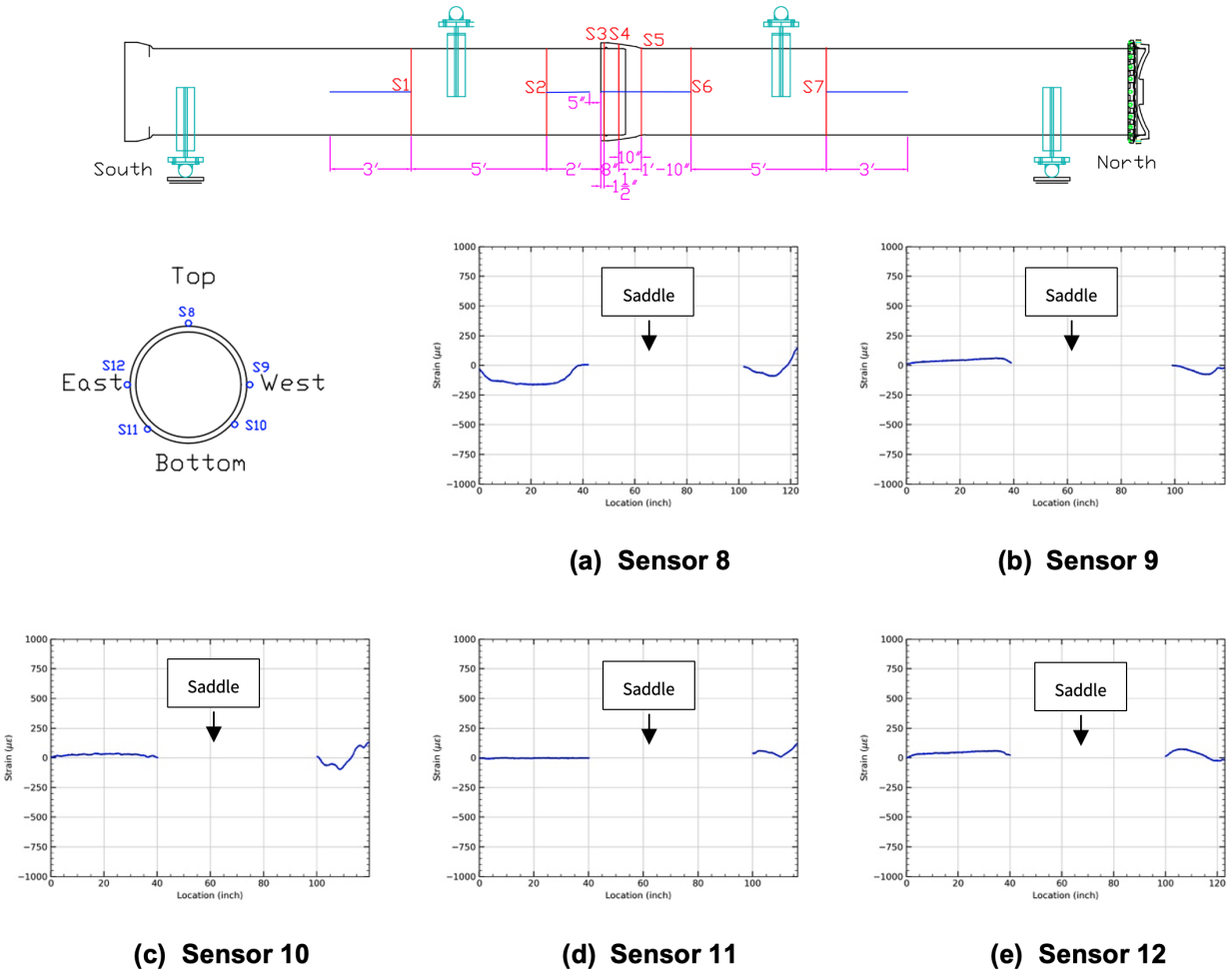


Fig. 5.42. Axial strain development of spigot (northside pipe) when fail (i.e., 10.25-degree HWP rotation)

and bottom-east quadrants, while the remaining regions exhibited radial expansion (tensile strain). The pronounced compression at the top crown is a direct consequence of hard internal bearing contact; as the joint rotated, the upward-pivoting spigot was driven directly into the rigid bell crown, inducing intense localized radial compression (schematically depicted in Figure 5.39). Conversely, the compressive strains at the lower-quadrant positions (bottom-west and bottom-east) correlate mechanically with the ejection of the locking segments in those specific zones. As these segments were forced radially outward and expelled, the spigot lost its tight circumferential confinement, allowing it to radially contract and further facilitate the structural release of the restraints.

Within the constrained bell cavity (sensors S3 and S4, Figures 5.43b and c), the hoop strain topologies are fundamentally dictated by the physical presence, or sudden absence,

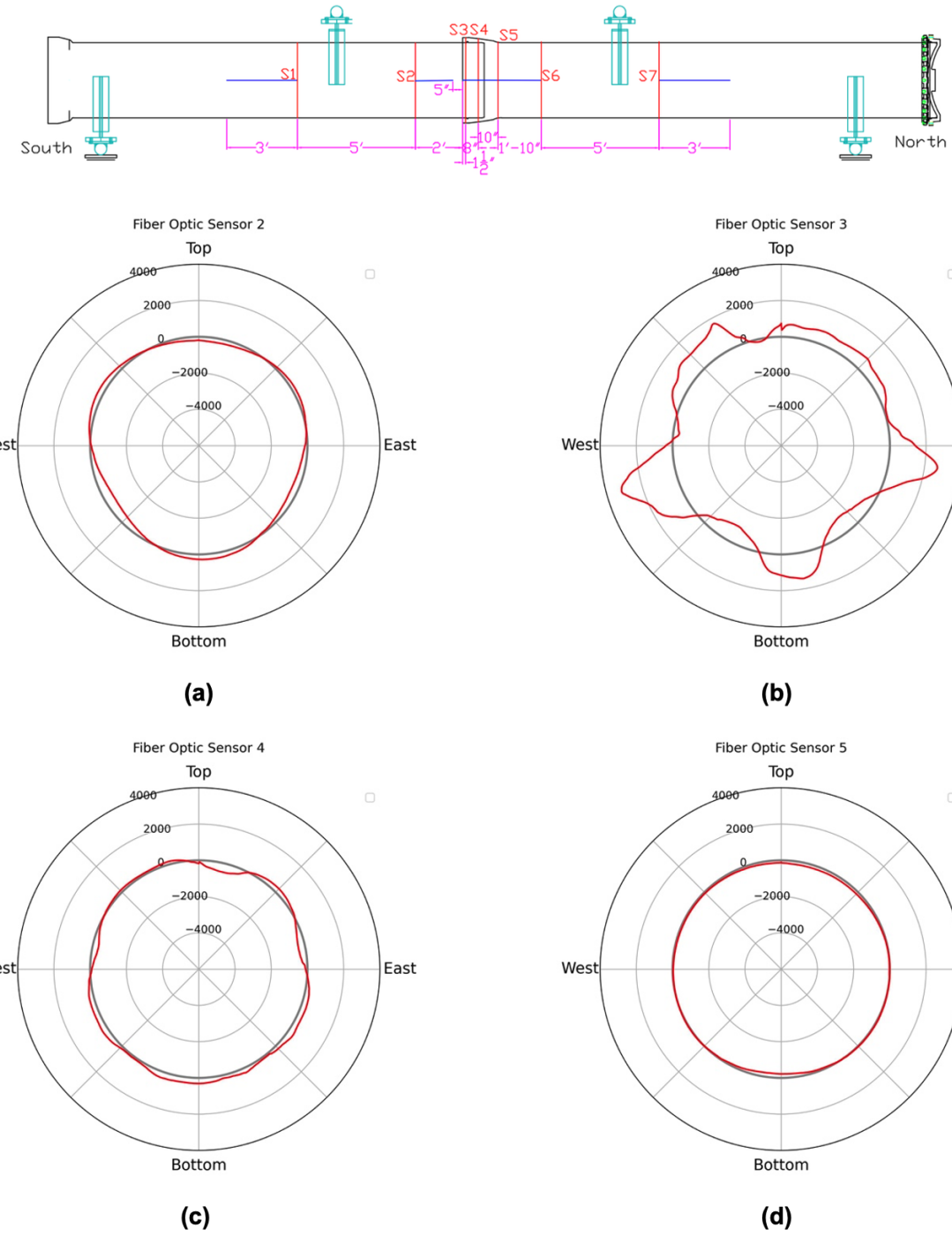


Fig. 5.43. Strain distribution in the circumferential direction when fail (i.e., 10.25-degree HWP rotation). (a) Sensor on the spigot (b) Sensor on the top of the inserts (c) Sensor on the centerline of the specimen (d) Sensor on the bell pipe

of the internal locking segments. At the top crown, where the cavity was fitted solely with a compressible rubber gasket, minimal hoop strains were recorded. In contrast, large compressive strains manifested at the bottom-west and bottom-east positions, the exact locations where the initial locking segments were ejected. The sudden absence of the rigid internal wedging restraints allowed the previously dilated bell casing to elastically rebound (contract) inward. Adjacent to these blowout zones, particularly slightly below the true springlines, the bell showed massive tensile strains. This captures the severe radial outward thrust exerted by the remaining, highly loaded locking segments as they fought to transfer the massive joint forces. Further up the springlines, strain magnitudes dropped significantly, reflecting the physical gaps that opened as the spigot shifted, abruptly terminating the local load transfer paths. While sensors S3 and S4 recorded functionally identical kinematic patterns, the magnitudes at S4 were marginally lower due to its physical offset from the immediate locking segment interface.

At the bell end (sensor S5, Figure 5.43d), the DSS ring recorded virtually zero circumferential strain. This rapid spatial attenuation indicates that the extreme cross-sectional distortion and complex bearing forces are localized within the active internal restraint mechanism, dissipating before reaching the outer longitudinal boundaries of the bell casing.

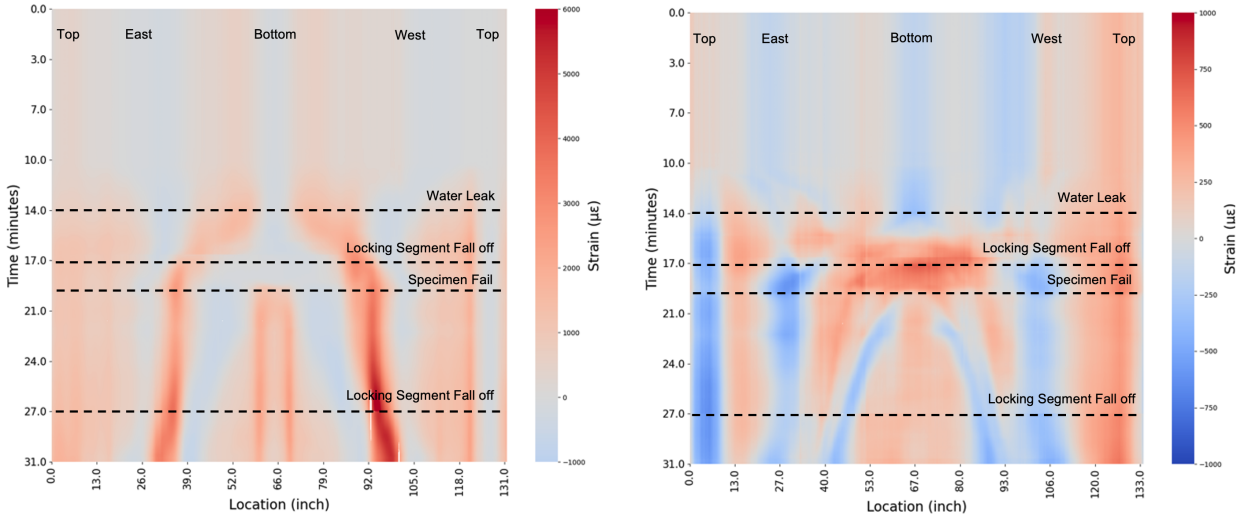


Fig. 5.44. Waterfall plot of strain development of sensors on the bell

Figure 5.44 presents the temporal evolution (waterfall plots) of the circumferential strains for sensors S3 and S4. This time-history data captures the highly dynamic, progressive failure mechanics of the internal restraint system, revealing multiple internal load redistributions throughout the testing protocol.

Although the specimen temporarily resealed itself and stopped leaking, the force transmission path changed following the failure of the first pair of locking segments. This marked

the beginning of a new load redistribution phase. Shortly afterward, the specimen lost its ability to maintain internal water pressure, indicating further disruption in load transfer. The altered load path remained relatively stable until the second pair of locking segments detached, prompting another significant redistribution of force.

Conclusion of 36-inch ERDIP four-point Bending Test

A full-scale four-point bending test was conducted on a nominal 36-inch ERDIP to evaluate its deflection capacity and ultimate failure mechanisms under extreme seismic loading conditions. The joint demonstrated massive rotational ductility, exceeding the manufacturer's specified design limit of 7.0 degrees to achieve an ultimate rotational capacity of approximately 10.25 degrees (as measured by the HWP kinematic array). The system sustained a maximum ultimate moment of 4,325 kip-in, with ultimate failure strictly defined by the total loss of internal hydraulic containment. Notably, the test was ultimately terminated upon reaching the absolute stroke limit of the hydraulic actuator, rather than due to catastrophic structural rupture of the pipeline barrel.

While the primary ductile iron casing did not experience global structural failure, the test captured the progressive limit state of the internal restraint mechanism. During the forced-actuation phase, minor hydraulic weeping (3 to 5 gpm) initiated between 5.1 and 5.3 degrees of rotation; however, the internal rubber gasket kinematically reseated itself to temporarily restore containment. Upon further severe deflection, the first pair of internal locking segments was physically ejected, triggering a sudden redistribution of internal forces and precipitating the ultimate drop in internal water pressure. As extreme flexure continued, a second pair of locking segments was dislodged, further altering the internal load transfer path.

High-resolution continuous strain profiles captured via the DSS network provided critical insights into these progressive failure mechanics. Far-field longitudinal strains generally adhered to classical bending theory, exhibiting expected top-crown compression and bottom-invert tension. However, localized anomalies emerged adjacent to the bell-spigot interface, confirming that the shifting locking segments fundamentally altered the load transfer mechanism. Furthermore, circumferential (hoop) strain data confirmed localized radial expansion of the bell casing in the specific regions where the locking segments remained actively wedged against the pipe wall. Ultimately, the complex interaction between the internal bell grooves, the spigot weld bead, and the progressively failing locking segments generated localized strain concentrations.

5.3.4 48-inch ERDIP Bending Performance

Experimental Data Analysis

The four-point bending testing procedure for the 48-inch specimen was executed in four primary stages: (i) self-weight deflection, (ii) internal pressurization to a baseline house

pressure of 75 psi, (iii) forced-actuation via the hydraulic actuator, and (iv) extreme internal pressurization to a target of 250 psi. In the first stage, temporary shoring was removed, allowing the unconstrained pipeline to deflect downward under its own self-weight until achieving static equilibrium. In the second stage, the internal water pressure was increased to 75 psi; this introduced a longitudinal tensile force that caused the specimen to lift slightly, partially reversing the initial deflection. In the third stage, a monotonic vertical load was applied at the midpoint of the central spreader beam and transmitted to the pipeline through two loading saddles spaced 144 inches apart (center-to-center). The final stage was conducted by maintaining the extreme deformation while driving the internal water pressure toward the 250 psi target.

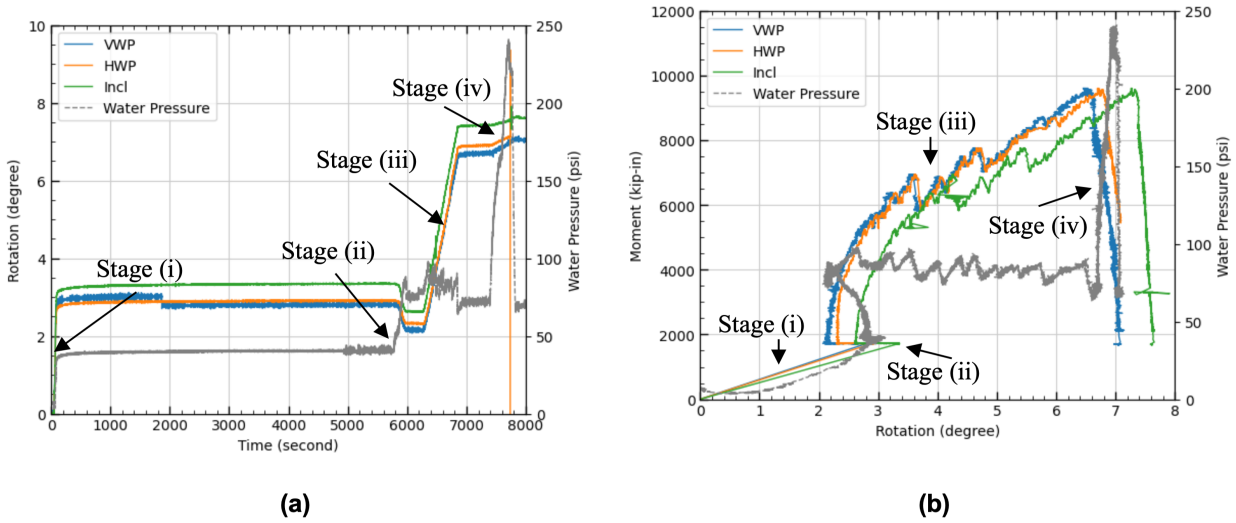


Fig. 5.45. Data of 48-inch ERDIP four-point bending test (a) Rotation, time, and water pressure (b) Moment, rotation, and water pressure

Figure 5.45a illustrates the continuous evolution of joint rotation and internal water pressure throughout the loading history, while Figure 5.45b presents the corresponding moment and water pressure plotted against global rotational deformation. The kinematics were calculated using three independent measurement arrays: inclinometers (incl), HWP through 4.6, and VWP with equation 4.5.

Following the initial self-weight deflection stage, the system reached static equilibrium with measured joint rotations of 3.3° (incl), 2.9° (HWP), and 2.8° (VWP). The internal water pressure was then elevated to the 75 psi baseline. The resulting longitudinal thrust force caused a partial rotational recovery of approximately 0.6° across all three measurement methods. Following this pressurization, the baseline rotations prior to actuator loading were recorded as 2.6° (incl), 2.3° (HWP), and 2.1° (VWP).

Subsequently, the hydraulic actuator applied monotonic vertical loading until the specimen reached peak extreme rotations of 7.27° (incl), 6.70° (HWP), and 6.45° (VWP). Notably,

no water leakage or structural failure of the restraint mechanism was observed during this purely flexural stage. At this peak deflection, the maximum applied load was 128 kips, corresponding to a peak bending moment of 9,600 kip-in.

In the critical final stage, the internal water pressure was aggressively increased. Upon reaching a maximum pressure of 240 psi, the severe biaxial loading caused the bottom-most internal locking segment to structurally detach from the bell cavity. Following this initial localized failure, the joint began to lose its ability to maintain hydraulic containment. Shortly thereafter, two adjacent locking segments were also physically dislodged, resulting in a rapid and total pressure drop, which dictated the termination of the test.

A complete summary of these critical limit states is provided in Table 5.5. It is important to note that the rotation values derived from the inclinometers (indicated by the green lines in Figure 5.45) are consistently larger than those derived from the HWP and VWP arrays. This discrepancy is likely attributable to the inclinometer's high sensitivity to initial micro-rotations, which can produce slightly larger relative errors when angles are near zero. Consequently, the kinematic data derived from the HWP and VWP arrays are considered the more reliable representations of the global joint rotation.

Table 5.5. Summary of failure metrics for 48-inch ERDIP bending specimen

Max Moment (kip-in)	**Max Force (kips)**	**HWP Rotation (°)**	**VWP Rotation (°)**	**Inclinometer Rotation (°)**
9,600	128	6.70	6.45	7.27

Figure 5.46 presents the physical condition of the specimen following the conclusion of the testing protocol. While no macroscopic yielding or global rupture of the primary ductile iron casing was visually evident, the internal restraint mechanism sustained critical localized damage. During the extreme internal pressurization stage, three of the fifteen internal locking segments were physically dislodged, ultimately precipitating a total loss of hydraulic containment. The specific circumferential locations of these ejected segments are mapped schematically in Figure 5.47.

The mechanism driving this ultimate failure is dependent on the unconstrained boundary conditions of the test setup. During the final pressurization stage, the massive internal water pressure acting against the physical end caps generated an immense hydrostatic thrust. This thrust induced a massive longitudinal tensile force, driving the spigot and bell casings apart. Because the experimental setup lacked longitudinal end restraints to absorb this thrust, the joint was subjected to a severe biaxial stress state, actively coupling extreme rotation with massive axial pullout demands.

Under this combined loading, severe localized outward radial dilation was observed at the joint interface. As the heavily rotated spigot underwent longitudinal pullout relative to the expanding bell casing, the spigot weld bead bore aggressively against the internal restraint

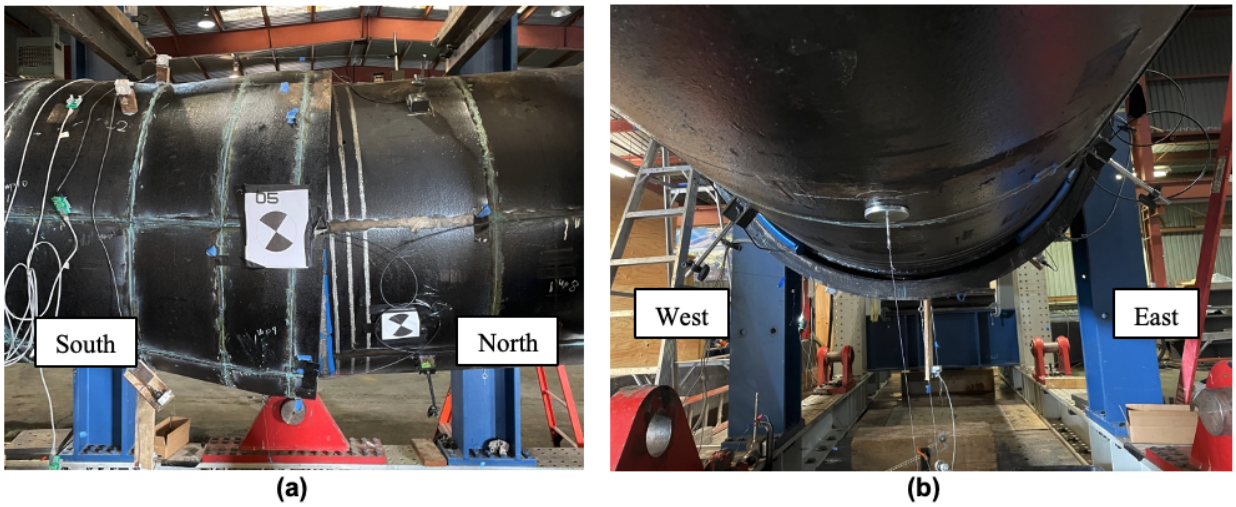


Fig. 5.46. Aftermath of the 48-inch ERDIP bending specimen. (a) No obvious crack was found. (b) Locking segments (blue) locations after the experiment

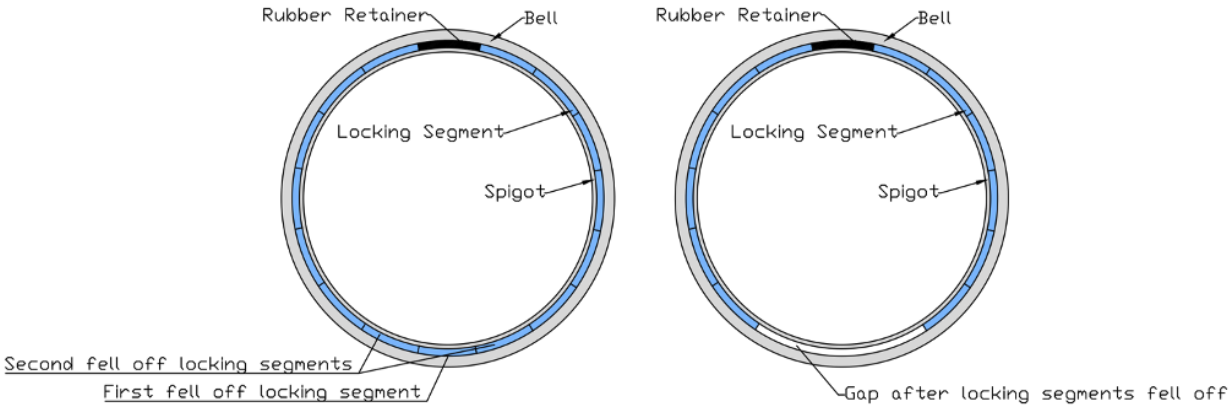


Fig. 5.47. Cross-sectional sketch of locking segments in bell

mechanism. This mechanical interaction ultimately sheared and ejected the locking segments situated below the springline, as indicated by the radial vectors in Figure 5.48.

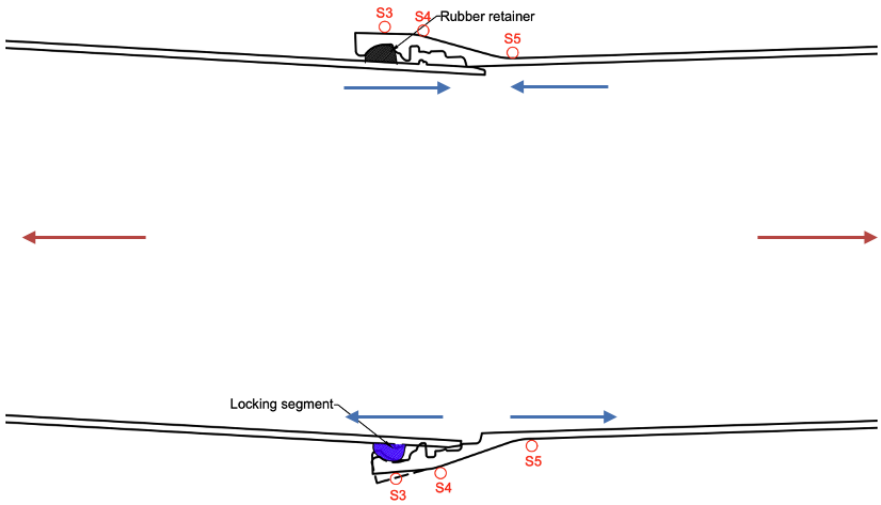


Fig. 5.48. Sketch of the bell deforming mechanism. Blue arrows indicate spigot–bell relative motion during bending; red arrows indicate axial tension induced by internal water pressure

Axial Strain

The continuous axial strain profiles captured by the DSS arrays are presented in Figures 5.49 and 5.50. To analyze the progressive deformation mechanics, Figure 5.49 isolates the relationship between longitudinal strain and global joint rotation at four specific cross-sectional planes: (1) 15 inches south of S1 (spigot), (2) 15 inches south of S2 (spigot), (3) the midpoint between S5 and S6 (bell casing), and (4) 15 inches north of S7 (bell casing). The kinematic joint rotations utilized in this analysis were derived exclusively from the VWP array, as established in equation 4.5.

Across all four designated planes, the extreme compressive fiber at the top crown consistently registered negative longitudinal strains, following classical flexural theory. However, Figures 5.49a, b, and d reveal that the remaining sensor locations across these cross-sections exhibited similar tensile strain magnitudes. Under theoretical pure bending, strains at the primary springlines (the nominal neutral axis) should remain near zero. This deviation indicates a fundamental shift in the internal force transfer mechanism. As the joint was driven into severe rotation, longitudinal pullout at the tensile invert compromised the local bearing contact between the spigot weld bead and the lower locking segments. This loss of structural continuity below the springline forced the neutral axis to shift upward, redistributing the tensile demands across the lower and lateral quadrants of the pipe wall.

In contrast, the cross-section located on the spigot immediately adjacent to the bell interface (Figure 5.49c) exhibited a strain profile much closer to classical bending expectations:

pronounced compression at the top crown, minimal strains near the nominal springline, and massive tensile strains at the bottom invert. This spatial gradient suggests that the intense, highly localized mechanical wedging between the spigot and the internal bell cavity enforced a stiff boundary condition, temporarily overriding the global upward shift of the neutral axis observed in the far-field regions.

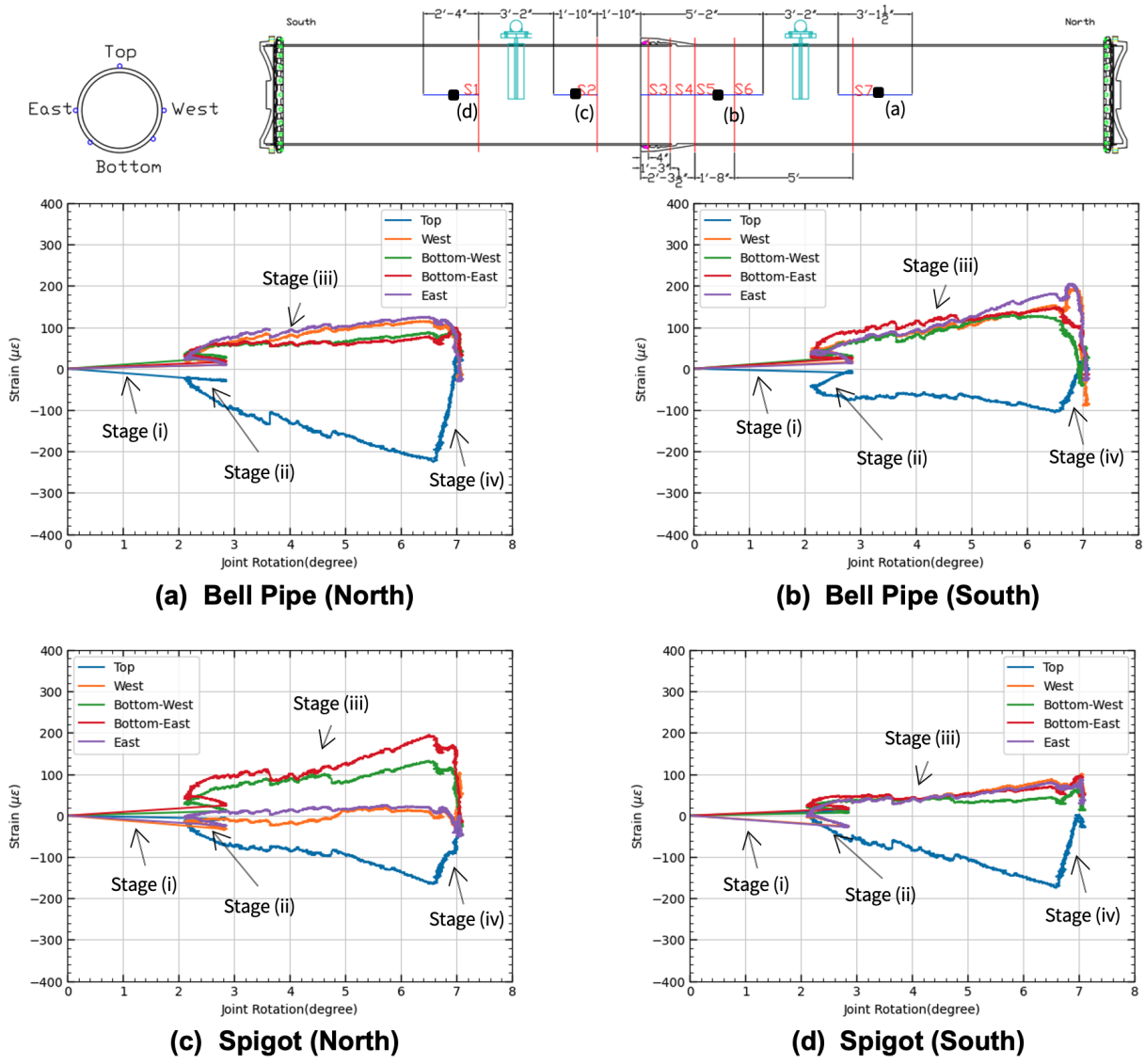


Fig. 5.49. Axial strain versus joint rotation based on the VWP measurement approach. The results are presented for four sequential test stages: (i) self-weight deflection, (ii) water pressurization to 75 psi, (iii) actuator loading, and (iv) water pressurization to 250 psi

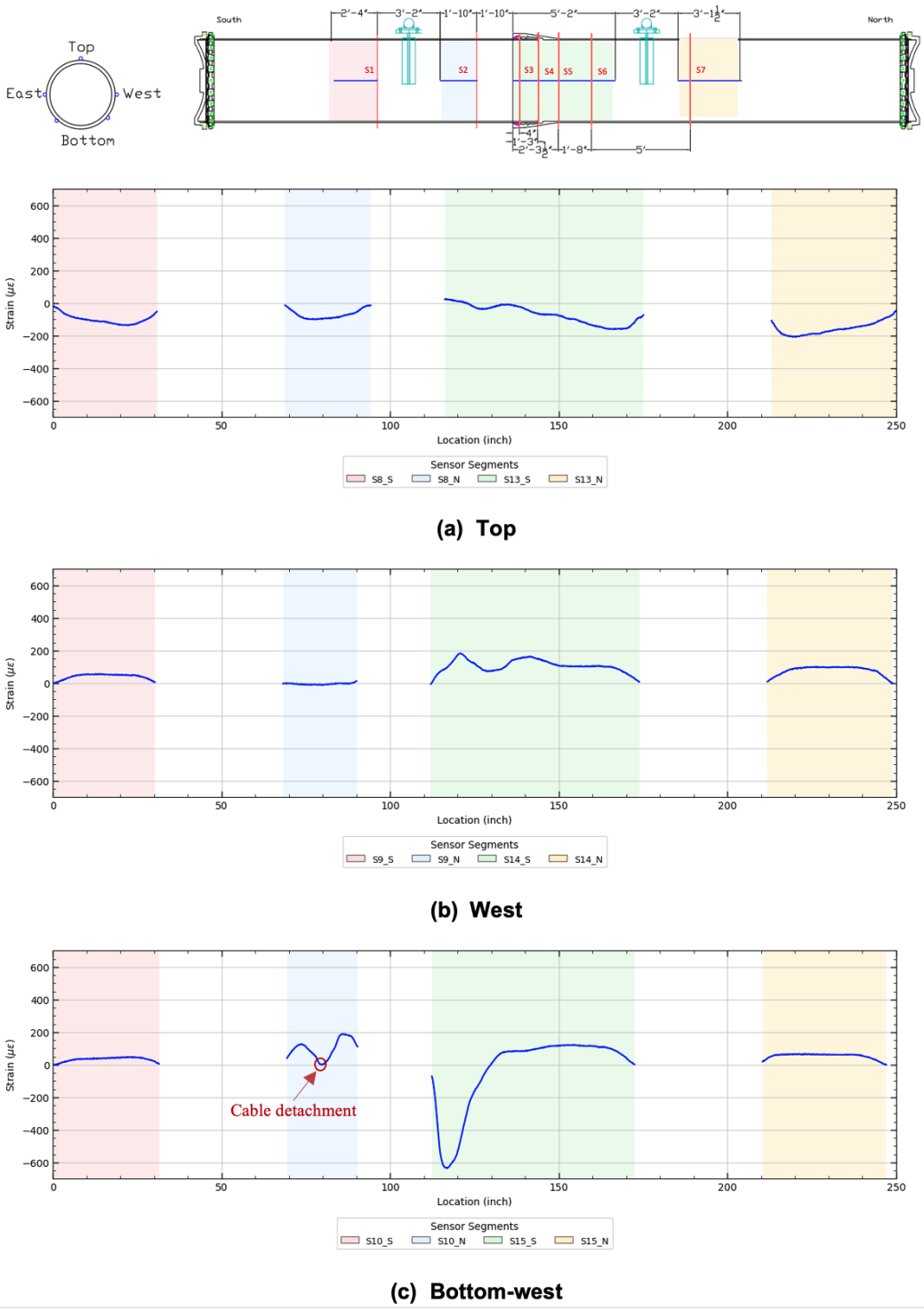
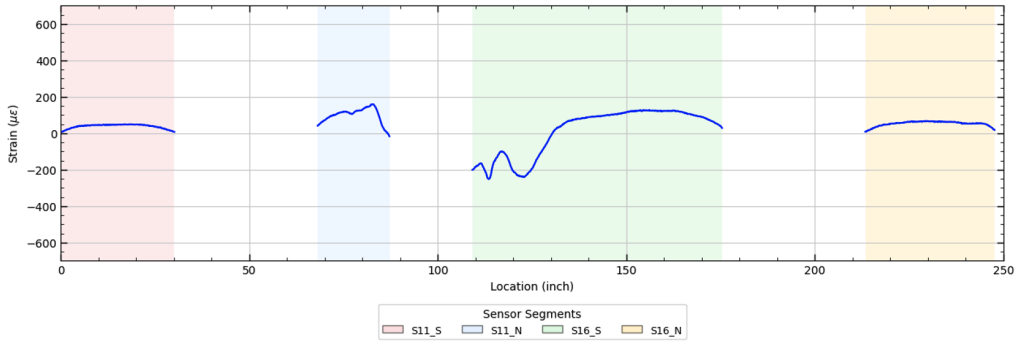
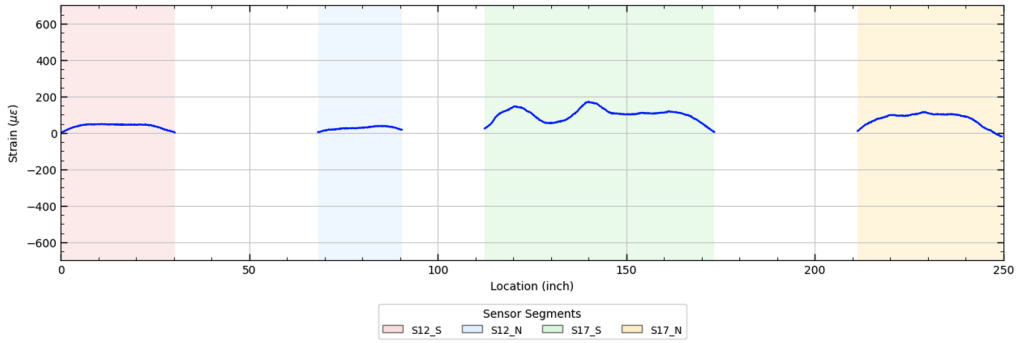


Fig. 5.50. Axial strain development of the pipe when close to failure (i.e., 6-degree VWP rotation). Note that the white spaces are the sensor gaps because of the joint or loading saddle. (a) Top (b) West (c) Bottom-west (d) Bottom-east (e) East. (a through c).



(d) Bottom-east



(e) East

Fig. 5.50. Axial strain development of the pipe when close to failure (i.e., 6-degree VWP rotation). (a) Top (b) West (c) Bottom-west (d) Bottom-east (e) East. Note that the white spaces are the sensor gaps because of the joint or loading saddle. (Continued: d and e)

Figure 5.50 maps the spatial longitudinal strain distribution along the pipeline immediately prior to the extreme high-pressure stage (the conclusion of Stage iii), corresponding to a joint rotation of approximately 6.0°. While sensors located above the horizontal centerline (Figure 5.50a) recorded expected compressive strains, tensile strains dominated the remainder of the pipeline—with one highly localized exception. Within the first 25 inches of the bell casing (the highlighted green zone), massive compressive strains manifested at the bottom-west and bottom-east positions.

Mechanically, this anomaly indicates that the downward-deflecting spigot was actively forcing the lower locking segments radially outward. This intense radial dilation introduced a secondary localized bending moment into the bell casing wall, creating longitudinal compression on the exterior surface near the bell face (schematically indicated by the blue radial vectors in Figure 5.48). This phenomenon was entirely absent at the top crown and springlines because, during positive flexure, the upper half of the inserted spigot pivoted inward (away from the bell wall), disengaging from the upper restraints and eliminating any outward

radial thrust.

Ultimately, the pervasive tensile strains recorded across the remaining non-top locations directly corroborate the mechanisms described above. As large bending drove the spigot and bell apart below the springline, the resulting physical gaps destroyed the localized bearing paths, forcing a global redistribution of the internal tensile demands.

Hoop Strain

The continuous circumferential (hoop) strain profiles captured by the DSS network are presented in Figure 5.51. This analysis isolates data from four critical circumferential rings: sensor S2, located on the spigot immediately adjacent to the joint interface; sensor S3, positioned directly over the internal locking segments on the bell casing; sensor S4, situated at the geometric midpoint of the bell cavity; and sensor S5, installed at the bell end. Comprehensive hoop strain data from the remaining sensor rings is cataloged in Chiu et al. (2025) [24].

The cross-sectional distortion recorded by sensor S2 on the spigot (Figure 5.51a) reveals a clear pattern of flexural ovalization. Compressive strains localized at the extreme top crown and bottom invert, driven by direct, hard bearing contact; as the joint rotated, the spigot was driven into the rigid crown and invert of the surrounding bell casing, inducing intense localized radial compression. Conversely, the pronounced tensile expansion at the springlines is characteristic of the Brazier effect. Under extreme bending moment demands, the cylindrical cross-section squats vertically, forcing the lateral springlines to bulge outward and generating the localized tensile strains recorded by DSS.

Within the constrained bell cavity at sensor S3 (Figure 5.51b), the strain topology is strictly governed by the physical presence and interaction of the internal restraints. At the extreme top crown, where only the compressible elastomeric gasket is present, minimal strain was recorded. However, significant tensile strains emerged across the upper quadrants, indicating that the upward-pivoting spigot forced the upper bell casing to dilate radially. Correspondingly massive tensile strains were recorded across the lower quadrants (below the centerline), confirming the intense localized outward radial thrust generated by the mechanical wedging of the lower locking segments against the bell wall.

This severe radial dilation attenuates rapidly along the longitudinal axis. Sensor S4 (Figure 5.51c), located at the bell cavity midpoint, captured a similar but weaker tensile pattern in the upper half of the cross-section, with virtually no radial expansion recorded at the bottom. Further downstream, sensor S5 (Figure 5.51d) at the distal bell face recorded negligible strain. This rapid spatial attenuation explicitly shows that the severe cross-sectional distortion and bearing stresses are localized within the immediate internal joint interface.

Figure 5.52 maps the temporal evolution (waterfall plots) of the circumferential strains for the bell-mounted sensors S3 and S4. This time-history data captures the dynamic internal mechanics of the joint, identifying two distinct internal load redistribution events throughout the testing protocol.

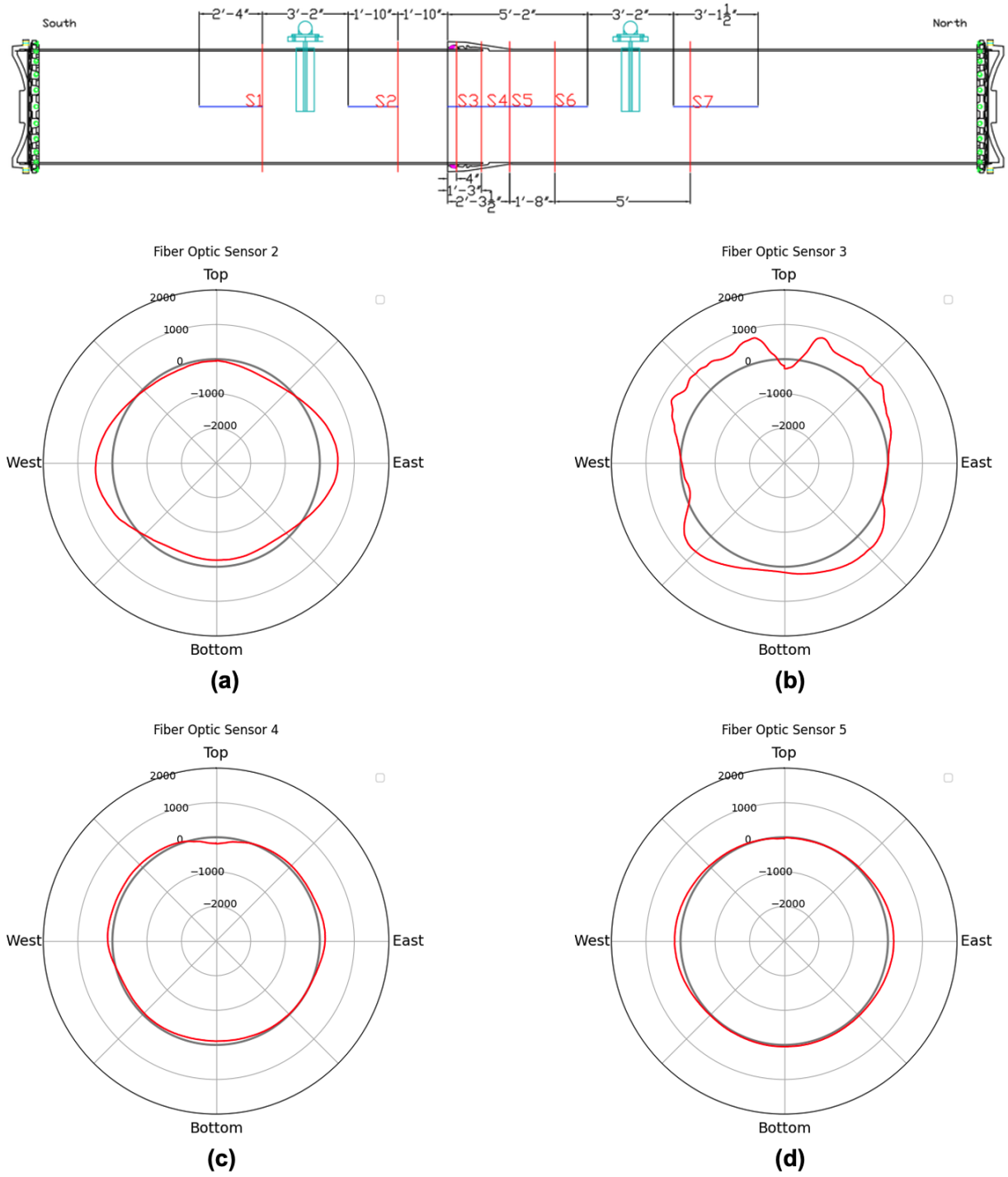


Fig. 5.51. Strain distribution in the circumferential direction when close to failure fail (i.e., 6-degree VWP rotation). (a) Sensor on the spigot (b) Sensor on the top of the inserts (c) Sensor on the center of the bell (d) Sensor on the edge of bell and pipe

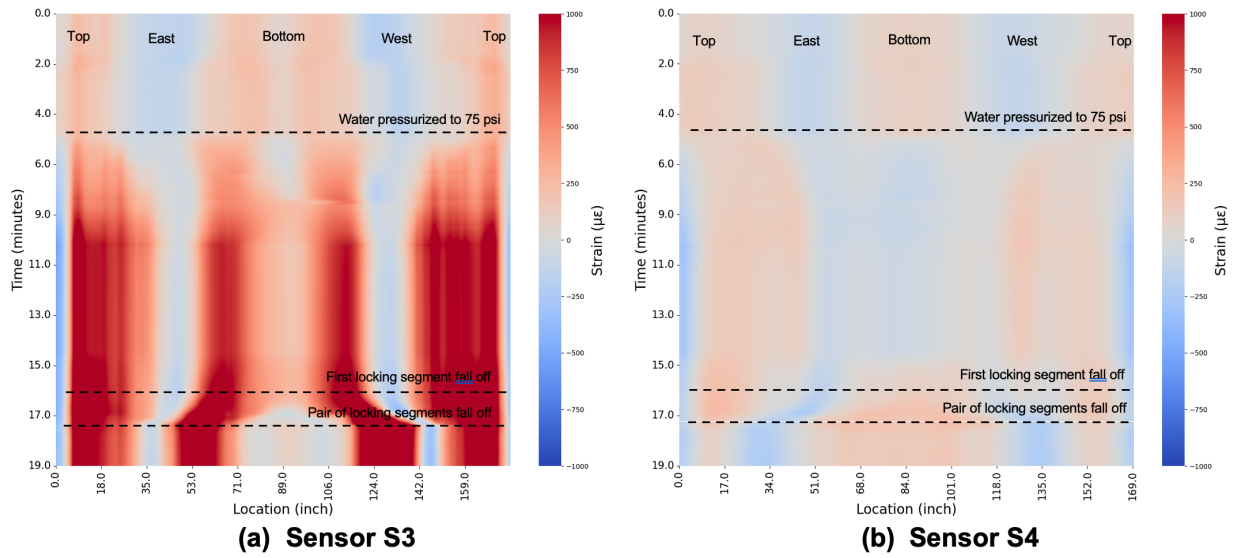


Fig. 5.52. Waterfall plot of strain development of sensors on the bell of 48-inch ERDIP four-point bending test

The first notable phase shift occurred following the initial 75 psi hydrostatic pressurization, as the newly introduced longitudinal tensile thrust altered the baseline internal bearing contact between the spigot and the restraints. The second event sequence occurred during the extreme final pressurization stage. The sequential structural ejection of the internal locking segments—first a singular segment, followed rapidly by two adjacent units—altered the local restraint boundaries. This progressive physical detachment triggered a sudden redistribution of strain across the bell casing, altering the ultimate load transfer path prior to total hydraulic failure.

Conclusion of 48-inch ERDIP four-point Bending Test

A full-scale four-point bending test was conducted on a nominal 48-inch ERDIP to evaluate its ultimate flexural ductility, spatial strain distribution, and internal force transfer mechanisms under combined bending and internal hydrostatic pressure. The experimental protocol progressed through four phases: (i) self-weight deflection, (ii) internal pressurization to a 75 psi baseline, (iii) forced-actuation via a hydraulic actuator, and (iv) extreme internal pressurization targeting 250 psi under locked severe flexure. The massive joint successfully exceeded its targeted design rotation of 5.5°, achieving an ultimate flexural capacity of 6.45° (VWP approach) under an applied peak moment of 9,600 kip-in (128 kips applied load). The test was ultimately terminated during the final extreme pressurization stage at 240 psi, when severe biaxial loading caused the sequential structural failure of the internal locking segments, precipitating a total loss of hydraulic containment.

The DSS network provided unprecedented insight into the complex internal bearing mechanics of the joint interface. Temporal strain evolution (waterfall plots) successfully identified two distinct internal load-redistribution phase shifts. The initial phase shift occurred following the 75 psi hydrostatic pressurization, as the introduced longitudinal thrust actively altered the baseline spigot-restraint bearing equilibrium. The second, critical phase shift occurred during the final extreme pressurization stage. The structural ejection of the first internal locking segment destroyed local boundary constraints, triggering a redistribution of strain. This progressive failure rapidly cascaded to the adjacent segments, resulting in their physical detachment and the ultimate catastrophic loss of hydraulic pressure.

Spatial strain analyses shows that the localized joint mechanics deviate from classical global flexural theory. Longitudinal strain data revealed that the internal force transfer path, dictated by the mechanical wedging between the spigot weld bead and the locking segments, forces the neutral axis to shift and introduces localized secondary bending moments into the casing wall. Furthermore, circumferential (hoop) strain data indicate cross-sectional distortion at the joint interface. The upper half of the bell casing expanded radially outward due to hard upward bearing contact from the pivoting spigot crown, while the lower half expanded as the spigot forced the lower locking segments radially outward against the bell wall. These findings also indicate that this interaction is highly localized to the immediate joint region and is not evident at locations farther from the bell.

5.3.5 Conclusion of ERDIP Bending Test

An extensive experimental testing program was conducted to evaluate the flexural performance, continuous moment-rotation response, and ultimate limit states of ERDIP joints. Full-scale monotonic four-point bending tests were executed across three distinct nominal diameters (8-inch, 36-inch, and 48-inch) to understand the joint kinematics and internal force transfer mechanisms under extreme seismic loading conditions. The summary of the tests are highlighted in Table 5.6.

Testing of the 8-inch specimens specifically isolated the mechanical influence of the internal restraint configuration by comparing Specimen-12 (insertion slot at the top crown) and Specimen-9 (insertion slot at the springline). The experimental data revealed that while the specific placement of the restraints dictates the internal stress distribution and global bending stiffness, it has a negligible impact on the ultimate flexural capacity.

Because Specimen-9 featured a rigid metallic locking segment at the 12 o'clock position, it generated a large internal bearing force couple, resulting in a stiffer joint requiring a higher ultimate moment. Conversely, the compressible rubber retainer located at the 12 o'clock position in Specimen-12 provided a softer boundary, reducing the required moment. Despite this difference in stiffness, both joints achieved identical structural limit states (failing at 13.1° and 13.2°, respectively). High-resolution strain profiling showed that ultimate failure for both 8-inch configurations was governed by the geometric interaction between the spigot and the bell; as the spigot bore downward against the rigid bell cavity, localized plastic

Table 5.6. Summary of experimental rotational capacities and failure mechanisms across ERDIP diameters

Nominal Diameter	Target Limit	Achieved Rotation	Max Moment (kip-in)	Primary Failure Mechanism
8-inch (Sp-12)	5.0°	13.1°	763.6	Spigot invert punch-through fracture
8-inch (Sp-9)	4.0°	13.2°	1,153.2	Spigot invert punch-through fracture
36-inch	7.0°	10.25°	4,325	Localized bell dilation & segment ejection
48-inch	5.5°	6.45°	9,600	Biaxial-induced sequential segment ejection

yielding and structural punch through fractures occurred at the spigot's bottom invert, regardless of locking segment orientation.

The large-diameter tests demonstrated that massive ERDIP joints possess rotational ductility that exceeds the manufacturer's baseline design limits. The 36-inch specimen achieved an ultimate rotational capacity of 10.25° (exceeding its 7.0° limit), while the 48-inch specimen achieved 6.45° (exceeding its 5.5° limit).

While both large-diameter specimens ultimately failed via the total loss of hydraulic containment, the 48-inch test highlighted the critical vulnerability of the internal restraint mechanism under severe biaxial loading. Unlike the 36-inch test (which progressed to hydraulic failure under pure flexure), the 48-inch joint was subjected to an extreme hydrostatic pressurization up to 240 psi while locked in severe flexure. This induced massive longitudinal thrust forces, prematurely altering the baseline spigot-restraint bearing equilibrium and forcing the neutral axis to shift. In both large-diameter pipes, the high-resolution strain profiles confirmed that the radial outward thrust generated by the spigot weld bead dilated the lower bell casing, leading to the sequential ejection of the locking segments.

Synthesizing the results across all three pipe diameters reveals a distinct, scale-dependent shift in the progressive failure mechanism:

- **Small-Diameter (8-inch) Mechanism:** Failure is dictated by the yielding of the pipe casing itself. The internal restraints survive the flexural wedging, forcing the downward-deflecting spigot invert to plastically yield and structurally fracture against the rigid bell cavity.
- **Large-Diameter (36-inch and 48-inch) Mechanism:** Failure is dictated by the ejection of the restraints. In large diameter pipes, the internal forces and radial thrusts generated by extreme flexure (and coupled high internal pressure) are immense. These

forces overcome the localized radial confinement of the bell casing, causing the bell to locally expand and mechanically eject the locking segments before the massive spigot barrel can structurally yield.

Despite these diverging failure mechanisms, continuous DSS spatial strain analyses confirmed one critical, universal behavior across all tested diameters. The structural damage, whether it manifests as spigot yielding (8-inch) or segment ejection (36-inch/48-inch), is localized entirely within the immediate joint interface. This mechanism effectively isolates the main pipeline barrels from structural distress, preserving the global integrity of the pipeline network even following the localized failure of the joint.

5.4 Biaxial Tension Performance

The ERDIP mechanism is specifically engineered to accommodate both longitudinal (axial) translation and flexural rotation. Historically, experimental evaluations of these jointed pipeline systems have predominantly isolated their pure flexural and rotational capacities. However, under actual seismic events or severe geotechnical ground deformations, pipeline joints are typically subjected to complex, multi-axial demands characterized by simultaneous longitudinal extension and bending. Consequently, this phase of the experimental program was designed with two primary objectives: (1) to evaluate the mechanical behavior, load transfer mechanisms, and ultimate limit states of the pipeline under combined bending and axial tensile forces, and (2) to characterize the influence of varying circumferential locking segment orientations on the joint's structural performance, expanding upon the findings from the pure four-point bending tests.

5.4.1 Experimental Setup and Instrumentation

A schematic of the complete setup is presented in Figure 5.53, with the fully assembled physical configuration shown in Figure 5.54. Custom-fabricated reaction collars (jackets) were engineered to securely grip the terminal ends of the pipeline assembly. The loading protocol utilized two high-capacity hydraulic actuators, each rated for 1,500 kips with a 24-inch stroke limit. A horizontal actuator was coupled to the spigot-end reaction collar to apply massive longitudinal tensile forces, while a vertical actuator was utilized to induce severe flexure. The vertical load was applied through a central steel spreader beam and symmetrically distributed to the bell and spigot casings via twin loading saddles.

Mirroring the experimental design of the pure four-point bending tests, two combined loading tests were conducted utilizing identical boundary conditions but varying the orientation of the internal locking segments, as detailed in Figure 5.18. In Specimen-9, the unresisted insertion slot (sealed solely by a compressible rubber gasket) was positioned at the west springline (9 o'clock), situating the three rigid iron locking segments at the top crown, east springline, and bottom invert. Conversely, in Specimen-12, the insertion slot

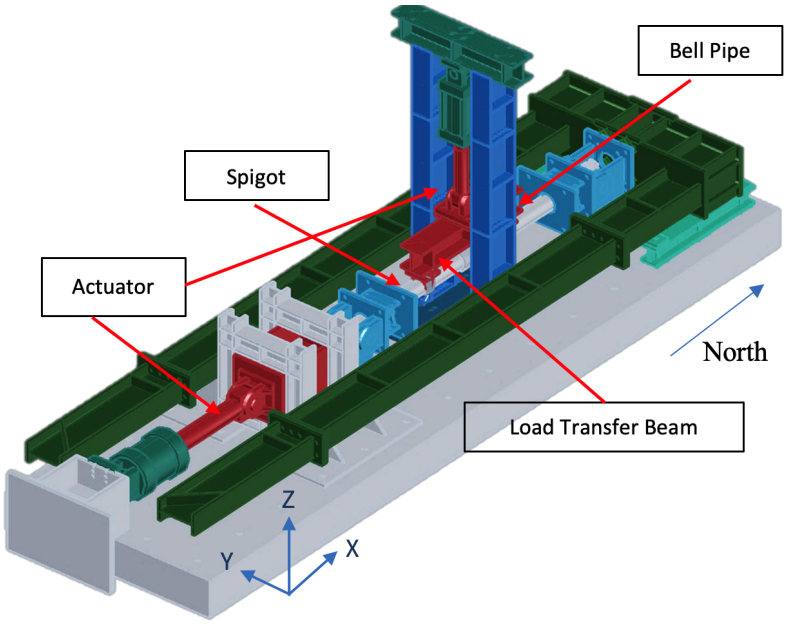


Fig. 5.53. Sketch of the experimental setup of 8-inch ERDIP bi-axial tension test

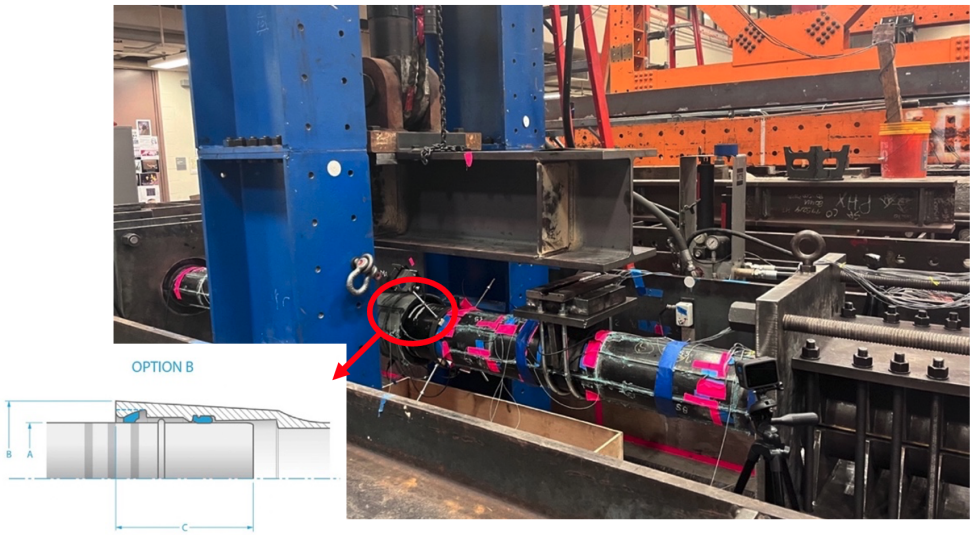


Fig. 5.54. Experimental setup of 8-inch ERDIP bi-axial tension test

was rotated to the top crown (12 o'clock), positioning the locking segments at the west, east, and bottom locations. The test log is listed in Table 5.7

Table 5.7. Summary of test schedule and specimen configurations for combined loading tests

Test No.	Specimen	Test Date	Locking Segments Orientation
1	Specimen-9	9/01/2022	9 o'clock
2	Specimen-12	9/28/2022	12 o'clock

The testing protocol was executed in four sequential phases: (i) Self-weight deflection, (ii) Forced-actuation, (iii) Internal pressurization, and (iv) Axial pullout. The structural boundary conditions were uniquely adapted for each phase. During the initial self-weight deflection phase, the end of the bell casing was constrained solely as a pinned connection (allowing z-axis rotation). Critically, the spigot end was configured as a sliding pin, permitting both z-axis rotation and unrestrained longitudinal (x-axis) translation. During this stage, the horizontal actuator was mechanically decoupled from the hydraulic system to ensure zero external axial force was applied. Temporary shoring was removed, allowing the assembly to deflect downward under its own weight until static equilibrium was achieved. Following equilibrium, the horizontal actuator was hydraulically locked to restrain the spigot from any further longitudinal translation.

Next, during the forced-actuation phase, the vertical actuator engaged the spreader beam to monotonically drive the joint downward until achieving a target global bending contraction of 8.0° (nominally 4.0° per pipe). The vertical force was transferred through the loading saddles, which were spaced symmetrically 33.5 inches from the joint's geometric center (defined as 3.25 inches offset from the bell face). Following bending lock-in, the assembly entered the internal pressurization phase, where the internal water pressure was elevated to a baseline of 50 psi.

In the final axial pullout phase, the horizontal actuator applied a monotonic tensile pull until severe structural damage and catastrophic water leakage occurred. Throughout this biaxial loading phase, the vertical actuator was stroke-locked in the upward direction to prevent the pipe from rebounding. This ensured that the minimum 8.0° rotational demand was strictly maintained, while still allowing the system to deflect further downward if localized structural yielding dictated.

The complete sequence of loading phases and corresponding boundary conditions is summarized in Table 5.8.

Four discrete cross-sectional strain planes were instrumented: two located on the bell casing and two on the inserted spigot barrel. Each plane consisted of four bi-directional strain gauge rosettes mounted orthogonally at the top crown (12 o'clock), west springline (3 o'clock), bottom invert (6 o'clock), and east springline (9 o'clock). Each rosette comprised

Table 5.8. Summary of testing phases, loading conditions, and structural boundary conditions

Test Procedure	Loading Condition	Boundary Condition
Self-weight deflection	Gravity force	Allow z-direction rotation on both ends and x-direction longitudinal movement on the spigot end.
Forced-actuation	Vertical actuator force	Allow z-direction rotation on both ends.
Water pressurization	Internal water pressure	Allow z-direction rotation on both ends. Restrain the bell from moving upward.
Axial pullout	Horizontal axial force	Allow z-direction rotation on both ends. Restrain the bell from moving upward.

two perpendicularly oriented gauges designed to capture highly localized longitudinal (axial) and circumferential (hoop) strains.

Global kinematics and relative joint deformations were monitored utilizing two independent arrays of wire potentiometers. To measure the relative joint opening, four potentiometers were mounted across the bell-spigot interface, positioned at 45-degree offsets from the primary orthogonal axes (i.e., at the octant points). An additional array of four potentiometers monitored global spatial displacement during the forced-actuation phase. These sensors were affixed to the bell and spigot casings at the bottom invert (to capture vertical deflection) and the east springline (to capture transverse horizontal translation). The complete spatial layout of these conventional instruments is detailed in Figure 5.55 [30].

The DSS network was deployed utilizing two distinct cable profiles manufactured by NanZee Sensing Technology Co.: a ruggedized 5.0 mm diameter armored cable designed to simulate field-deployment survivability, and a highly sensitive 0.9 mm diameter unarmored cable for intricate structural profiling. All DFOS cables were structurally bonded to the pipeline exterior utilizing 3M SCOTCH-WELD DP8010 structural epoxy. The specific sensor is illustrated in Figure 5.56.

The 5.0 mm armored cables (designated S9 through S25, visualized as blue lines) were routed strictly in the longitudinal direction to capture global flexural and axial strains. These arrays were bonded to both the bell and spigot casings at 45-degree circumferential increments. To capture complex cross-sectional distortions and highly localized radial dilations, the 0.9 mm cables (designated S1 through S9, visualized as red lines) were deployed in a continuous circumferential (hoop) configuration. Three primary circumferential rings were

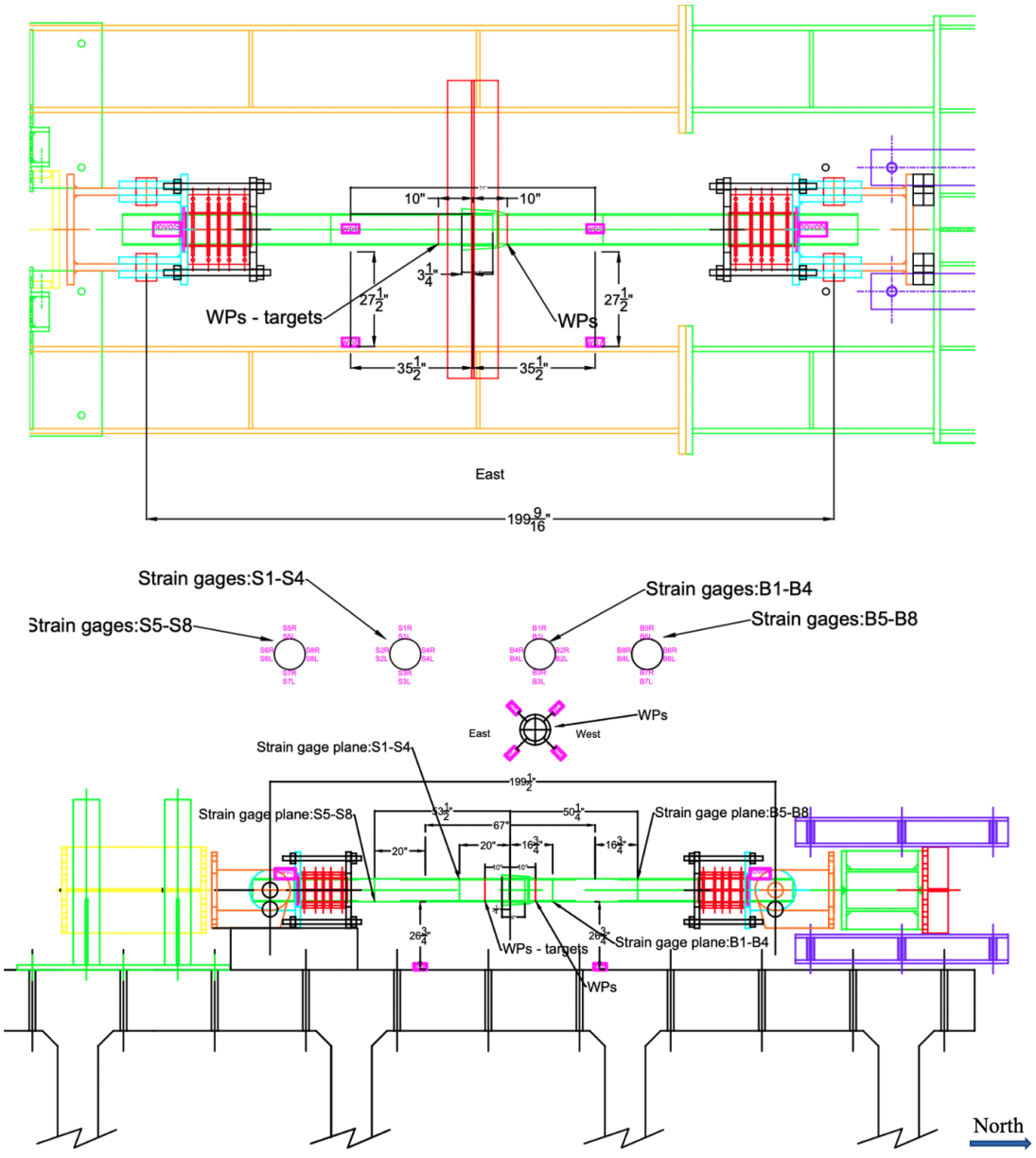


Fig. 5.55. Instrumentation plan of strain gauges and wired pots of the biaxial tension test

installed on the main barrels of both pipes at an approximate longitudinal spacing of 18 inches. Critically, to monitor the complex internal mechanics of the joint, three high-density circumferential rings were concentrated directly on the bell casing: one at the distal bell face, one at the geometric midpoint of the bell cavity, and one positioned precisely over the internal locking segments (approximately 3.5 inches from the bell face).

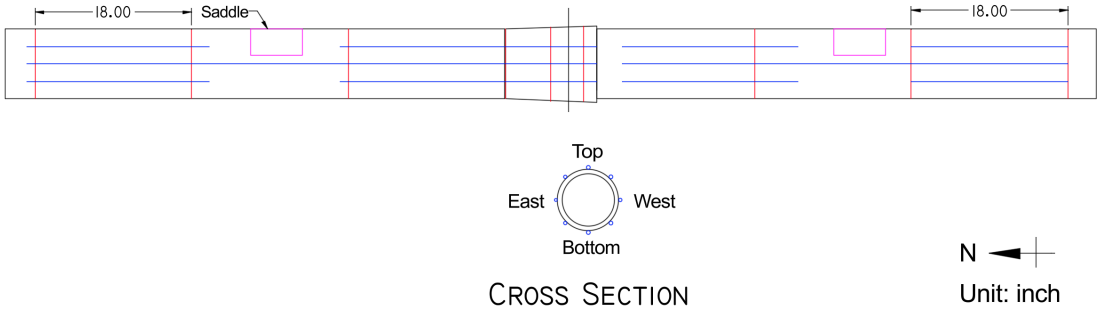


Fig. 5.56. Instrumentation plan of DSS of the biaxial tension test. Note that blue lines indicates longitudinal Nanzee 5mm fiber optic cables and red line is the Nanzee 0.9mm fiber optic cable installed in circumferential direction

5.4.2 Failure Mode

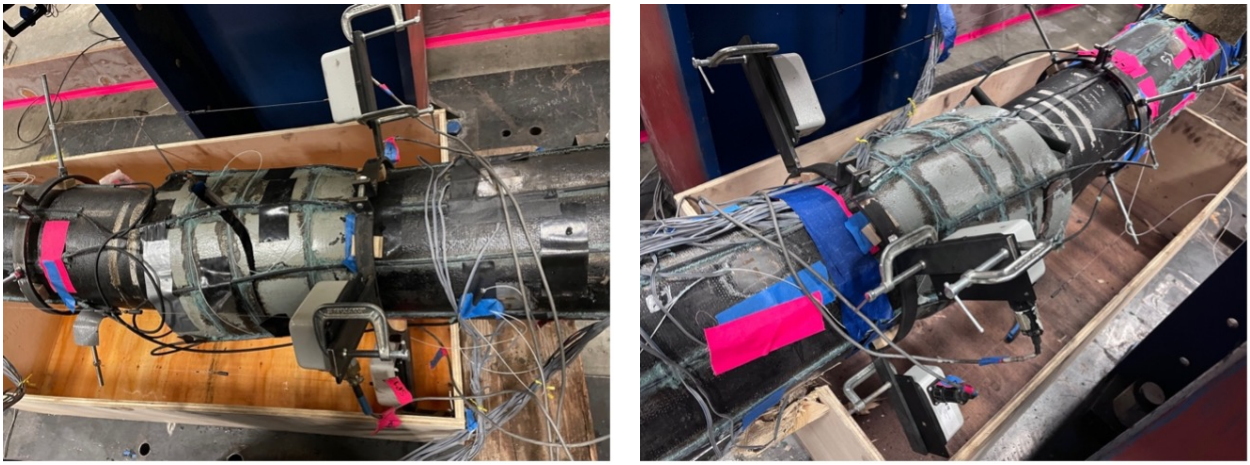
The experimental protocol was designed to push the joint to its ultimate limit state, strictly defined as catastrophic structural rupture or significant loss of internal hydraulic containment. Both tests were ultimately terminated due to severe structural fracturing of the bell in the immediate vicinity of the internal locking segments, as illustrated in Figure 5.57. Under severe biaxial loading, Specimen-9 reached ultimate hydraulic failure at an applied tensile load of 171 kips, corresponding to a longitudinal pullout displacement of 2.3 inches. Conversely, Specimen-12 failed at a significantly lower applied load of 145 kips and a pullout of 2.0 inches. This massive discrepancy explicitly demonstrates that the circumferential orientation of the internal restraint mechanism heavily dictates the ultimate seismic tensile capacity of the pipeline joint.

While the macroscopic fracture propagation paths diverged significantly between the two configurations, crack initiation occurred at identical geometric locations for both specimens. Fracturing invariably initiated at the transitional boundary between the rigid locking segment and the insertion slot. This confirms that the abrupt physical discontinuity at the insertion slot acts as a severe internal stress concentrator, creating the critical structural weak point of the bell.

For Specimen-9 (where the insertion slot was located at the 9 o'clock springline), the fracture initiated at the top-west boundary and propagated diagonally across the top crown toward the east springline, extending from the bell face deep into the main bell cavity

(Figure 5.57a). The diagonal trajectory of this rupture plane indicates that ultimate failure was driven by a complex principal stress state, coupling severe shear and longitudinal tensile stresses.

In contrast, Specimen-12 (where the insertion slot was located at the 12 o'clock crown) exhibited a primarily circumferential fracture plane. Initiating at the identical top-west discontinuity, the crack propagated downward toward the bottom-west quadrant (Figure 5.57b). This orthogonal fracture trajectory suggests that pure longitudinal tensile stress governed the ultimate failure of this restraint configuration.



(a) Specimen 9 **(b)** Specimen 12

Fig. 5.57. Failure of bell of bi-axial tension test

Figure 5.58 presents the global moment-rotation response for both joint configurations during the initial bending stages. During the self-weight deflection phase, Specimen-9 and Specimen-12 achieved static equilibrium at global rotations of 3.58° and 3.94°, respectively, driven by a baseline gravity moment of approximately 13.6 kip-in. Subsequently, the forced-actuation phase monotonically drove the joints to a targeted ultimate bending rotation of 8.36°. At this target deformation, Specimen-9 and Specimen-12 required applied bending moments of 1,033.5 kip-in and 871.4 kip-in, respectively.

As illustrated by the moment-rotation curves, Specimen-9 consistently exhibited a higher bending stiffness, requiring a larger applied moment to achieve equivalent rotations. This stiffness variation is directly governed by the circumferential orientation of the internal restraints. In Specimen-9, the upward-pivoting spigot crown must overcome hard bearing contact against a rigid locking segment situated at the top (12 o'clock). Conversely, Specimen-12 features a compressible rubber gasket at this critical 12 o'clock position. This softer boundary condition provides less internal restraint, resulting in a more compliant joint that accommodates larger deflections under equivalent moment demands. Consequently, as depicted in the mechanical schematic (Figure 5.59), the internal force couple generated in

Specimen-9 induces significantly higher concentrated stresses at the spigot invert compared to Specimen-12.

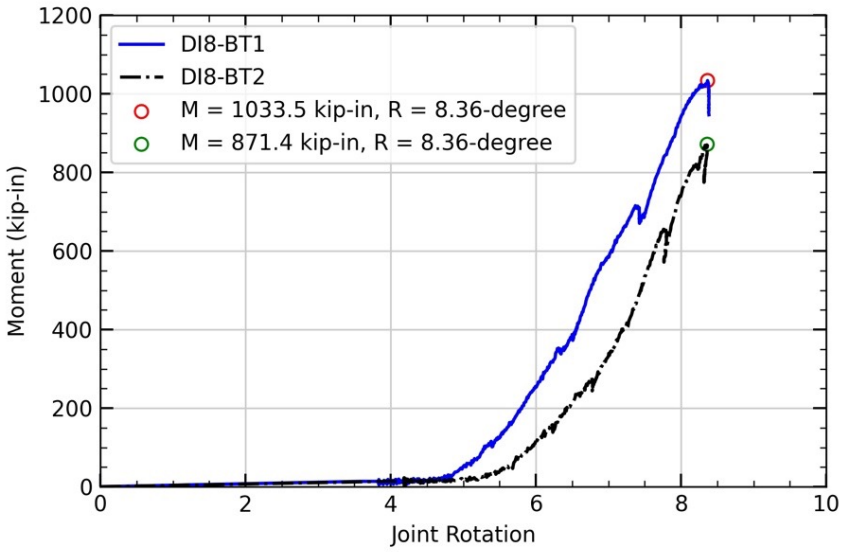


Fig. 5.58. Moment and rotation results of bi-axial tension test. Note that blue line indicates Specimen-9 while black line is from Specimen-12

Following the attainment of the 8.36° flexural target, the testing protocol transitioned to the axial pullout phase. The vertical actuator was stroke-locked to strictly enforce the minimum 8.36° joint rotation while the horizontal actuator applied a monotonic tensile pull until catastrophic structural failure occurred.

Figure 5.60 presents the global axial load versus relative joint opening (longitudinal pullout) curves for both specimens. Specimen-9 sustained a peak ultimate tensile capacity of 171 kips at an average joint opening of 2.3 inches. In contrast, Specimen-12 reached ultimate failure at only 145 kips with 2.0 inches of pullout. This substantial disparity in ultimate seismic capacity is explicitly linked to the interaction between the flexural and axial force transfer mechanisms.

Figure 5.61 illustrates the complex stress distribution and cross-sectional distortion of the bell casing during the pullout phase [30]. Under large axial tension, severe bearing and frictional forces developed between the spigot weld bead and the engaged locking segments. Because the joint was locked in severe downward bending, physical separation occurred below the springline, meaning the bottom-most locking segment (6 o'clock) experienced minimal mechanical engagement and transferred negligible axial force. However, because Specimen-9 featured an actively engaged locking segment at the highly compressed 12 o'clock position, where bending contact forces were highest, it benefited from substantially higher internal

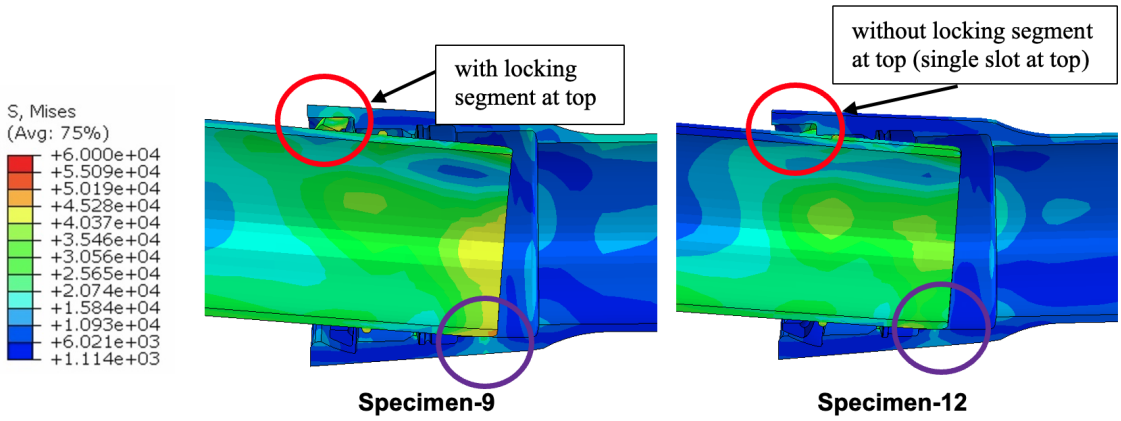


Fig. 5.59. Sketch of the bell after Push Down stage of bi-axial tension test

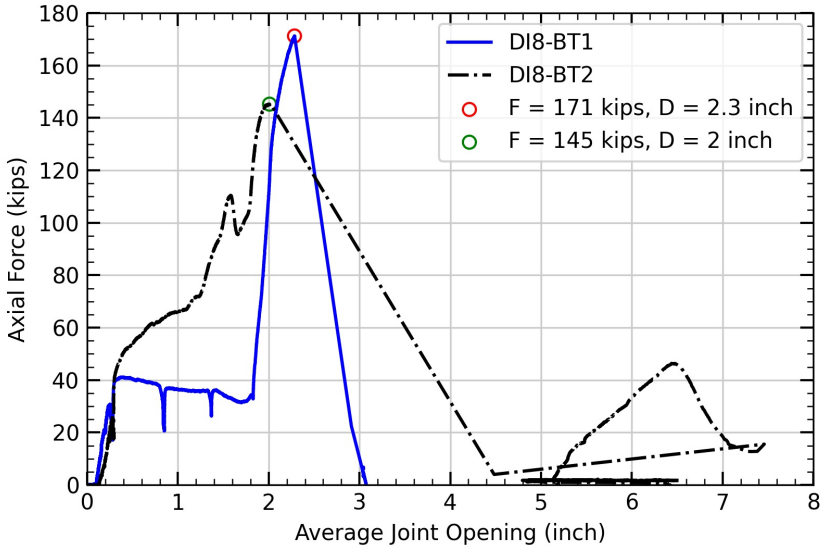


Fig. 5.60. Axial force and average joint opening of bi-axial tension test. Note that blue line indicates Specimen-9 while black line is from Specimen-12

bearing and frictional resistance against pullout. Furthermore, this discrete force transfer mechanism induced distinct cross-sectional distortion patterns; Specimen-12 exhibited a more symmetric bell ovalization due to the lack of rigid point-loading at the crown. Ultimately, these diverging internal stress distributions govern the structural limits summarized in Table 5.9.

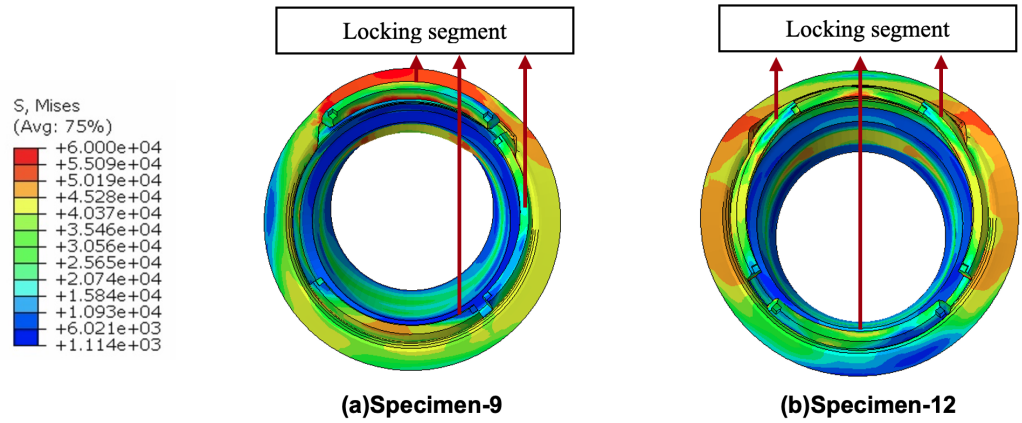


Fig. 5.61. Stress distribution of the cross-section of the bell under the Pull stage of bi-axial tension test

Table 5.9. Summary of ultimate limit states for 8-inch ERDIP combined loading tests

Specimen	Locking Segments Orientation	Max. Axial Load (kips)	Max. Ave. Joint Opening (in.)	Total Rotation (°)
Specimen-9	9 o'clock	171	2.0	8.36
Specimen-12	12 o'clock	145	2.3	8.36

5.4.3 Axial Strain

General

The continuous longitudinal (axial) strain time-histories captured by the bi-directional strain gauge rosettes are presented in Figures 5.62 and 5.63 for Specimen-9 and Specimen-12, respectively. During the initial self-weight deflection and forced-actuation phases, classical bending mechanics are evident: the top crown (12 o'clock) experiences global compression while the bottom invert (6 o'clock) is subjected to equivalent tension. However, the springline strains (3 and 9 o'clock) fundamentally diverge between the two configurations.

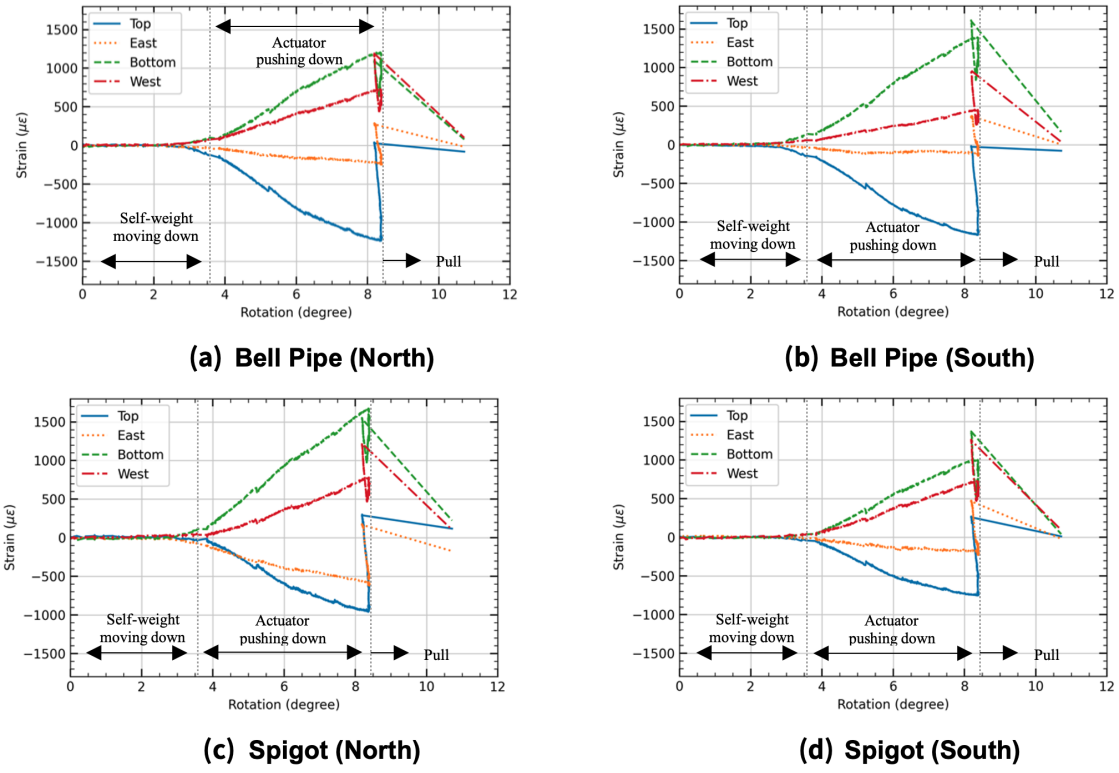


Fig. 5.62. Axial strain vs. rotation of Specimen-9 of bi-axial tension test

This divergence is driven by the asymmetric restraint configuration of Specimen-9. In this joint, locking segments were placed on the west side (9 o'clock) but not on the east side. Because the rigid locking segment provides a stiffer constraint than the rubber gasket, the pipe tends to move outward more on the rubber gasket side, introducing a secondary bending moment. Consequently, tensile strains developed at the west side (9 o'clock), and corresponding compressive strains developed at the east side (3 o'clock).

Conversely, since locking segments were placed at both the east and west sides of Specimen-12, this phenomenon is not observed. Theoretically, the axial strains at the east side (3 o'clock) and west side (9 o'clock) of Specimen-12 should remain close to zero under vertical bending; the minor non-zero strains recorded are attributed to slight installation offsets of the strain gauges. Ultimately, during the final axial pullout phase, tensile strains developed in both specimens' directions.

Bending Stage

Figures 5.64 and 5.65 map the spatial longitudinal strain distributions captured by the DSS arrays upon achieving the targeted ultimate bending contraction (i.e., 8.36° rotation, occurring at the end of the forced-actuation phase). The discrete strain gauge data are overlaid to

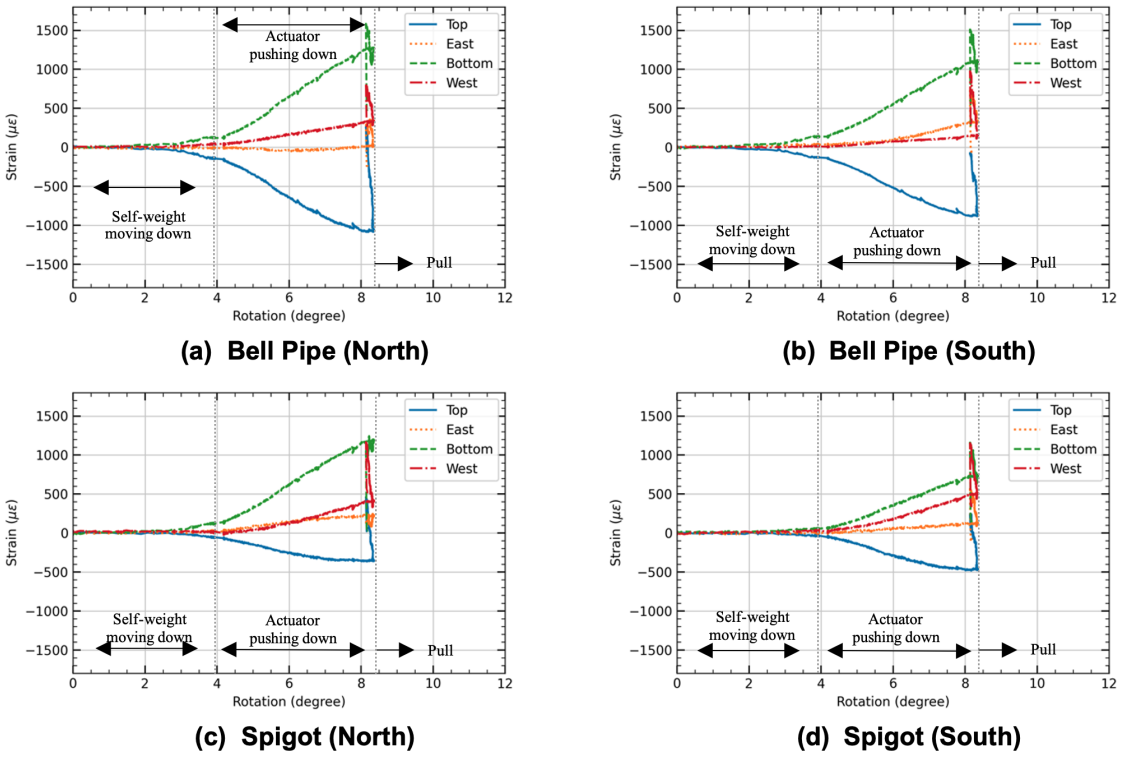


Fig. 5.63. Axial strain vs. rotation of Specimen-12 of bi-axial tension test

demonstrate compatibility between the two datasets. All continuous sensor distributions are plotted from north to south. Due to physical interference with the experimental setup, the fiber optic cables were not attached at the specific locations of the loading saddles, resulting in missing values in the middle sections of the plots.

Because the pipes were monotonically driven downward, the majority of the top crown (12 o'clock) was subjected to bending compression. However, a localized reduction in compressive strain magnitude is observed directly beneath the loading saddles. As the saddles transfer large vertical forces downward into the pipe, the material expands transversely via the Poisson effect, developing longitudinal tensile strains. Hence, the strains close to the saddles are a combination of global bending and localized Poisson effects.

At this stage, the specimen can be treated as experiencing near-pure bending forces. Hence, the axial strains at the west side (9 o'clock) remain small and close to zero. The slight differences between the strain gauge and fiber optic sensor results are due to spatial offsets between the instruments. Additional fiber optic sensor profiles are cataloged in Chiu et al. (2023) [30].

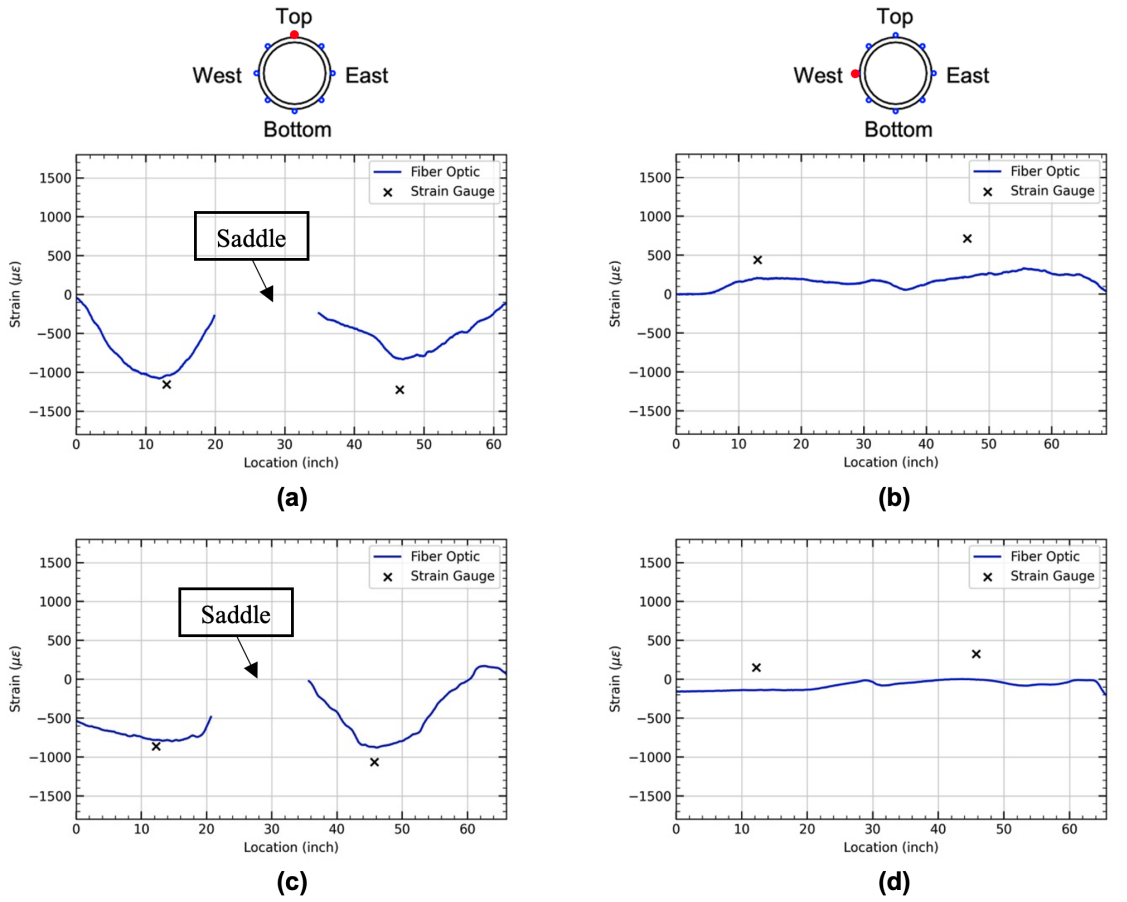


Fig. 5.64. Strain development of bell pipe in the longitudinal direction under 8.36-degree rotation. (a) Top side of Specimen-9, (b) West side of Specimen-9, (c) Top side of Specimen-12, (d) West side of Specimen-12

Pulling Stage

Figures 5.66 and 5.67 illustrate the complex strain distributions during the pullout phase under an applied longitudinal tensile force of 140 kips. A stark divergence in bell mechanics is evident between the two specimens.

Examining the west springline (9 o'clock), the majority of the sections are under tension due to the global axial force. However, a massive localized compressive zone shows immediately adjacent to the internal locking segment in Specimen-12. As the bell expanded, a secondary moment was introduced on the surface. Simultaneously, as the locking segments were dragged outward, this induced a significant compressive strain on the exterior surface near the segment (similar to the observations in direct tension test). Because no locking segment was placed at the west side (9 o'clock) of Specimen-9, the sensor array did not

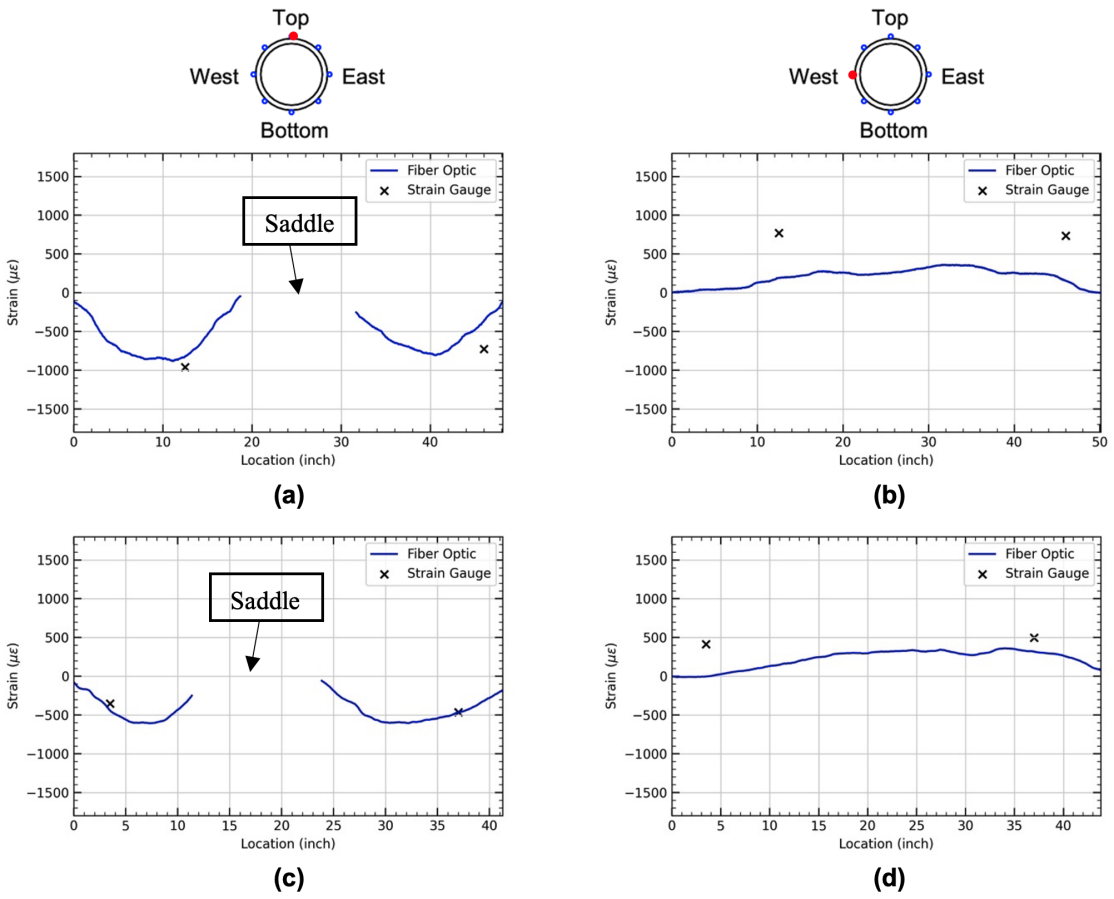


Fig. 5.65. Strain development of spigot in the longitudinal direction under 8.36-degree rotation. (a) Top side of Specimen-9, (b) West side of Specimen-9, (c) Top side of Specimen-12, (d) West side of Specimen-12

capture this severe localized wedging phenomenon.

Examining the top crown (12 o'clock) of Specimen-12, a larger tensile strain is observed close to the bell face. This likely occurs because as the locking segments on the lateral sides (3 and 9 o'clock) were pulled out, the localized thickness of the top bell section decreased, resulting in amplified tensile strains close to the bell section. Finally, the spigot strain profiles remain mechanically consistent between the two specimens. Since the specimens were rigidly locked at the desired deflection angle, the top sides were under baseline compression, and the bottom side under tension. During the pulling stage, although longitudinal tensile strains developed across all faces, the ultimate tensile strains at the heavily compressed top side remained the smallest, while the pre-tensioned bottom side experienced the largest additive strains. The axial strain results for the top and west sides of the two specimens are shown in Figures 5.66 and 5.67(c)-(d).

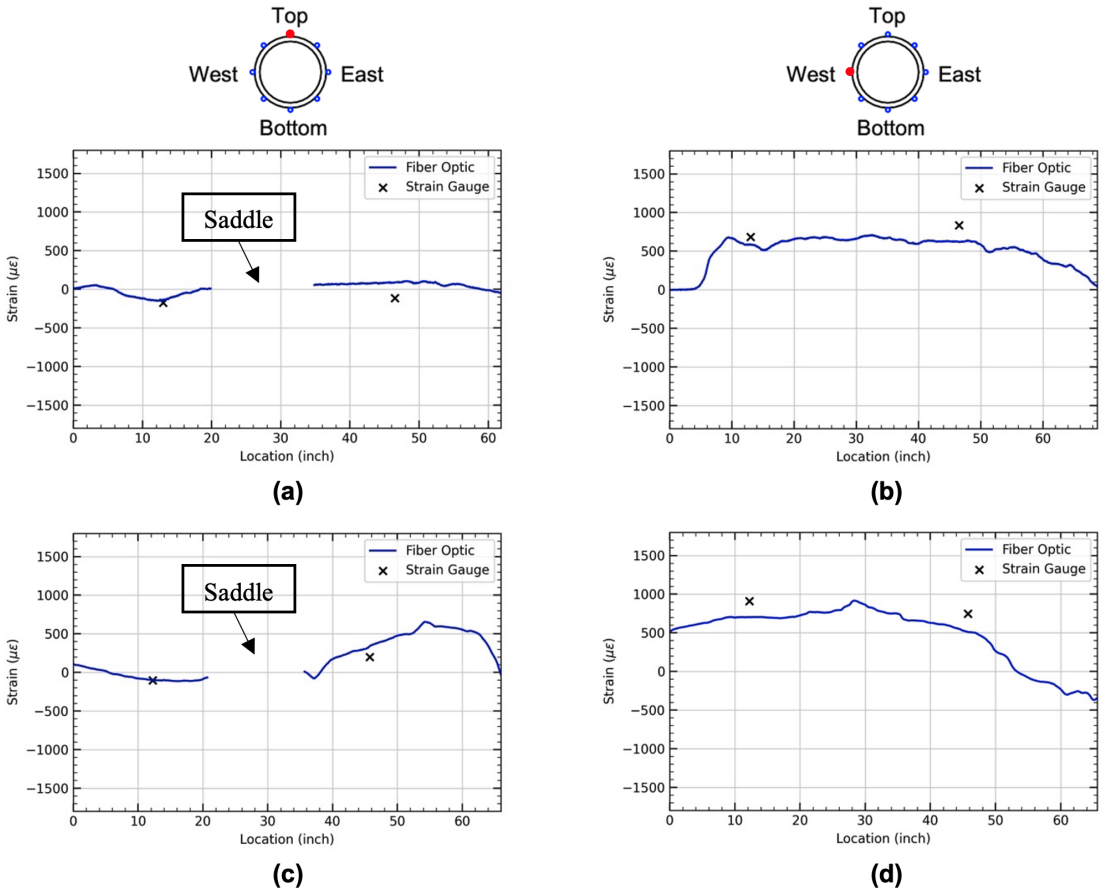


Fig. 5.66. Strain development of bell pipe in longitudinal direction under 140 kips axial force loading condition. (a) Top side of Specimen-9, (b) West side of Specimen-9, (c) Top side of Specimen-12, (d) West side of Specimen-12

5.4.4 Hoop Strain

General

Building upon the longitudinal strain mechanics discussed previously, the corresponding global circumferential (hoop) strain responses, plotted as a function of total joint rotation, are detailed in Figures 5.68 and 5.69 for Specimen-9 and Specimen-12, respectively. Captured via the bi-directional strain gauge rosettes, this data reveals that during the forced-actuation phase, the joint operates under near-pure flexural conditions. As established in the longitudinal strain analysis, the top crown (12 o'clock) undergoes severe longitudinal compression, while the bottom invert (6 o'clock) experiences longitudinal tension. Consequently, governed by the Poisson effect, the circumferential strains develop inversely: tensile hoop strains manifest at the top crown (indicating localized cross-sectional widening), and compressive hoop

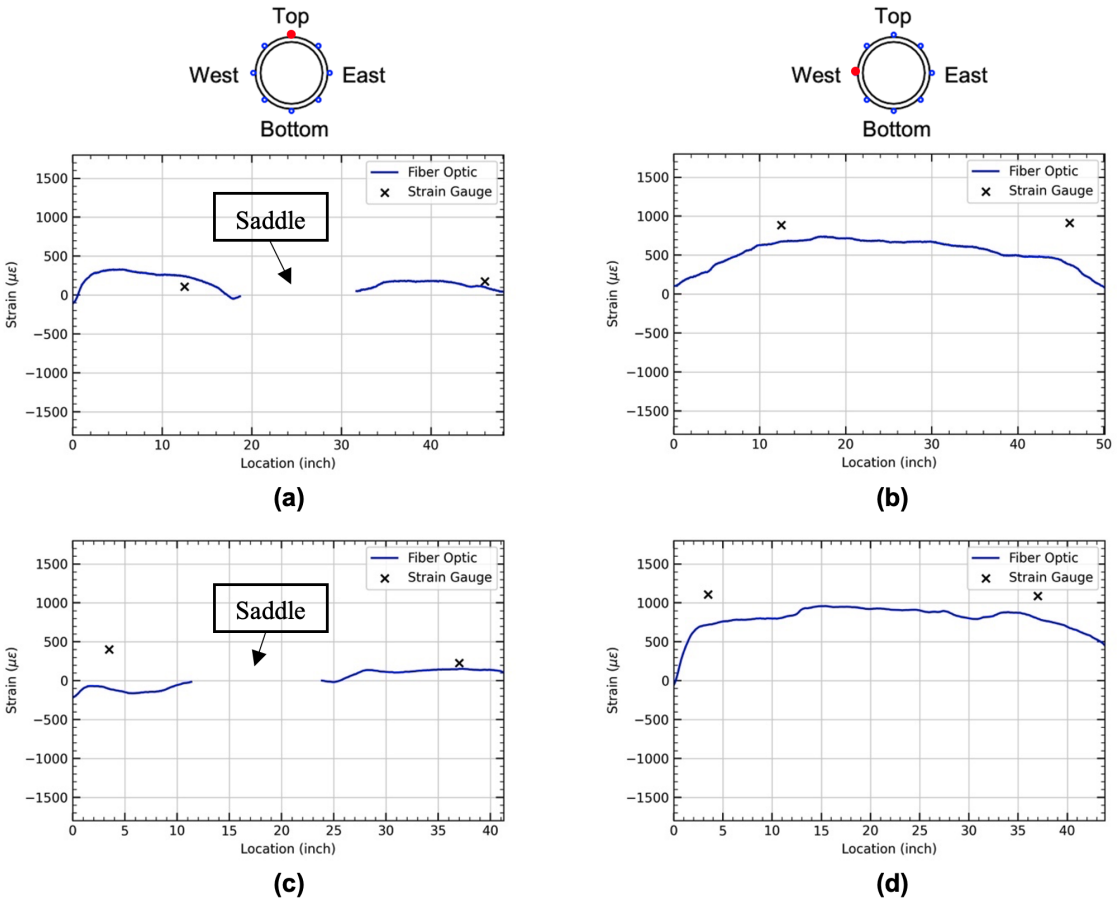


Fig. 5.67. Strain development of spigot in longitudinal direction under 140 kips axial force loading condition. (a) Top side of Specimen-9, (b) West side of Specimen-9, (c) Top side of Specimen-12, (d) West side of Specimen-12

strains develop at the bottom invert (indicating cross-sectional narrowing). The springline strains (3 and 9 o'clock) remain negligible and close to zero.

During the final axial pullout phase, the primary pipeline barrels exhibit a consistent cross-sectional distortion mechanism. However, the complex behavior of the bell casing diverges significantly based on the internal restraint orientation. As the rigid locking segments are forcibly dragged outward by the spigot, they exert a large radial outward thrust. To accommodate this internal wedging, the bell casing actively dilates in the specific regions housing the rigid segments, while simultaneously contracting in the unresisted zones corresponding to the compressible rubber insertion slot.

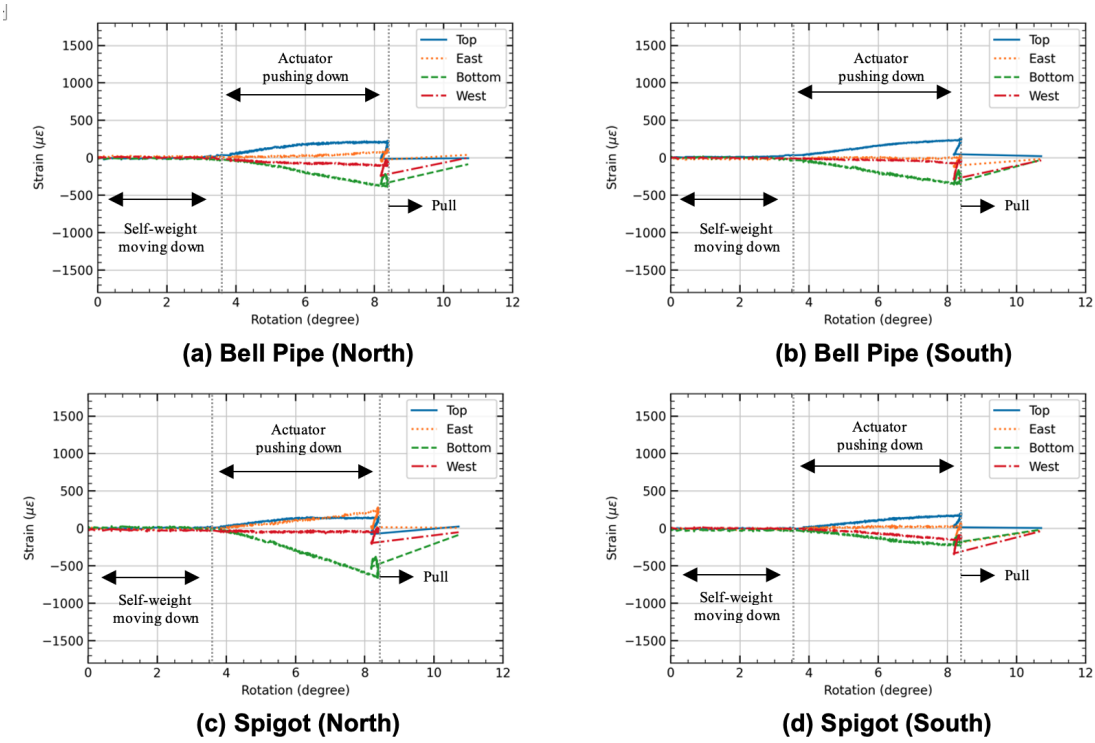


Fig. 5.68. Hoop strain vs. rotation of Specimen-9 of bi-axial tension test

Bending Stage

Figure 5.70 details the high-resolution continuous hoop strain profiles captured by the DSS arrays upon achieving the targeted ultimate bending contraction (8.36° rotation, marking the conclusion of the forced-actuation phase).

Throughout this bending stage, both specimens exhibit mechanically consistent strain topologies across the unconfined pipe barrels. As illustrated in Figures 5.70(a/d) and 5.71(a/d), distinct tensile hoop strains dominate the top crown (12 o'clock) while compressive strains govern the bottom invert (6 o'clock). This explicitly confirms bending ovalization (squatting) of the primary cylindrical cross-section under severe bending moments.

Conversely, complex internal bearing mechanics heavily affect the bell casing deformation. As depicted in Figures 5.70c and 5.71c, the extreme upward and downward pivoting of the inserted spigot creates large, localized point-bearing contact against the internal bell crown and invert. This hard contact forces the bell casing to dilate radially at the top and bottom (12 and 6 o'clock). Geometrically, this vertical expansion forces a corresponding radial contraction (measured as compressive hoop strains) across the lateral springlines (3 and 9 o'clock), a mechanism comprehensively mapped in the mechanical schematic provided in Figure 5.72 [30].

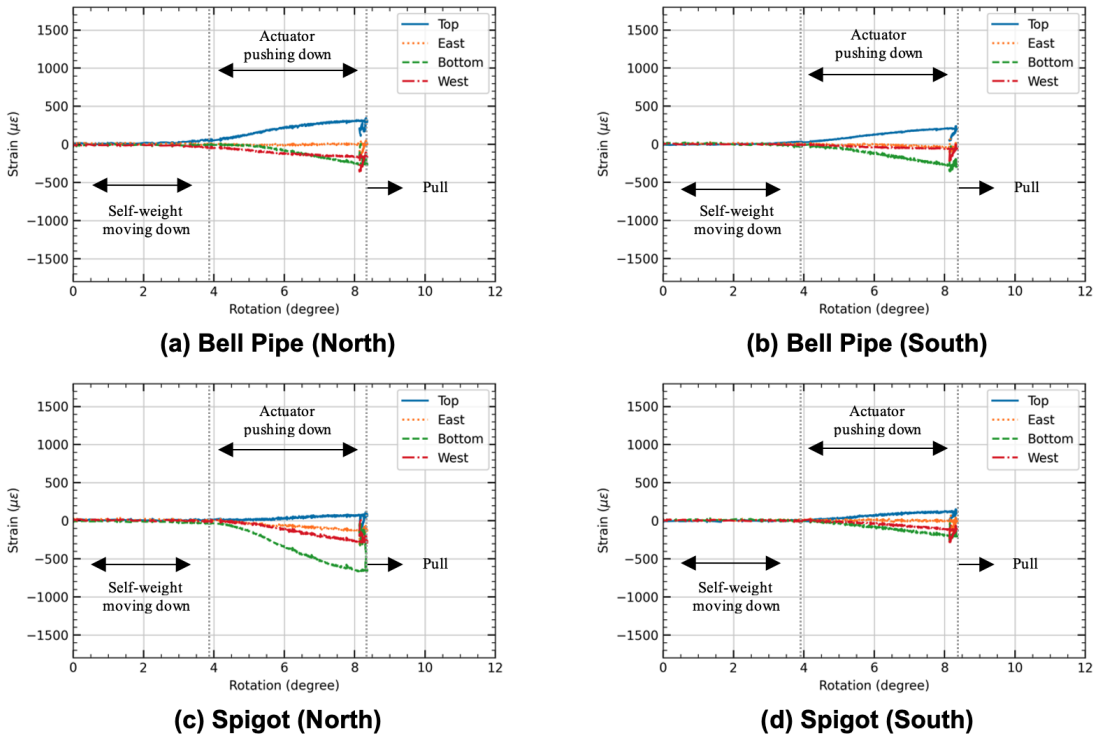


Fig. 5.69. Hoop strain vs. rotation of Specimen-12 of bi-axial tension test

Pulling Stage

Transitioning to the final axial pullout phase, Figures 5.73 and 5.74 map the continuous DSS hoop strain distributions under the extreme 140-kip longitudinal pullout force. Consistent with the bending stage, the unconfined pipeline barrels continued to experience circumferential tension at the top crown and compression at the bottom invert.

However, the intense mechanical wedging of the internal restraints induced different cross-sectional distortions in the bell casings. Under large longitudinal tension, the spigot weld bead bore against the internal locking segments, driving them radially outward. In Specimen-9, the rigid segments were located at the top, bottom, and east positions, while the rubber gasket occupied the west springline (9 o'clock). Consequently, the bell dilated radially across the vertical axis (12 and 6 o'clock) and contracted laterally across the horizontal axis (3 and 9 o'clock) to structurally accommodate the segment pullout. Conversely, Specimen-12 housed the compressible rubber gasket at the top crown (12 o'clock). This orientation forced the bell to contract vertically across the top and bottom quadrants while expanding laterally across the east and west springlines.

Ultimately, these intense, highly localized cross-sectional distortions precipitated structural rupture. While the macroscopic fracture trajectories varied, both specimens initiated failure at the identical geometric stress concentrator: the transitional boundary between the

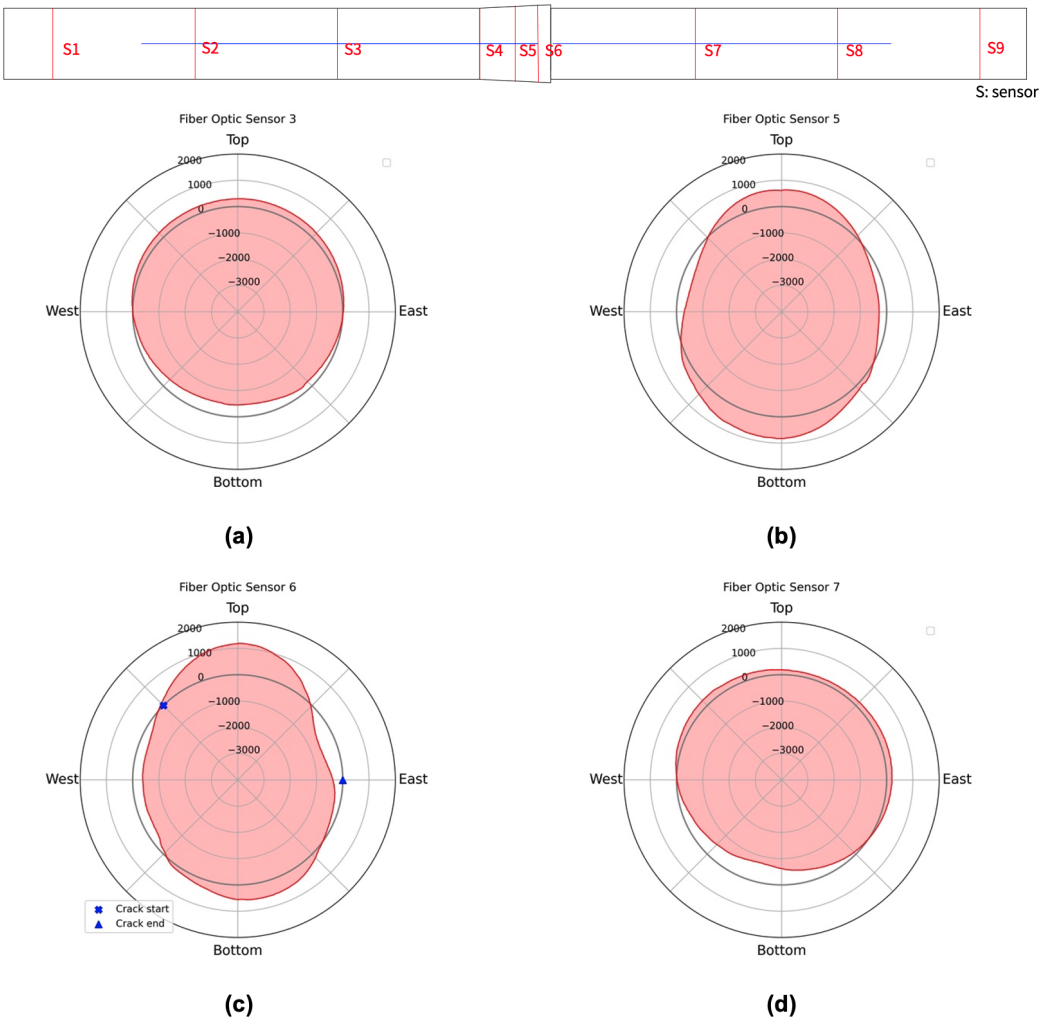


Fig. 5.70. Strain distribution in the circumferential direction of Specimen-9 under 8.3-degree rotation condition. (a) sensor on the bell pipe (b) sensor at the mid location of the bell (c) sensor on top of the locking segments on the bell (d) sensor on the spigot

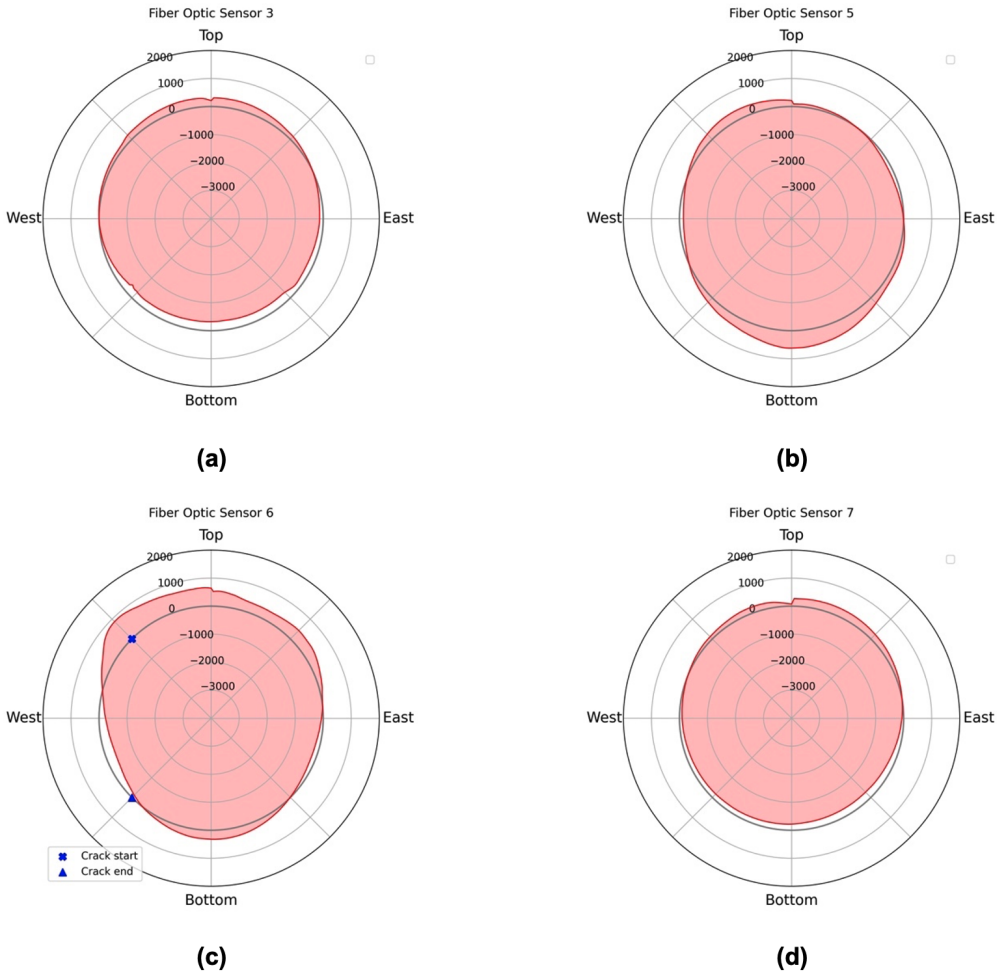


Fig. 5.71. Strain distribution in circumferential direction under Specimen-12 under 8.3-degree rotation condition. (a) sensor on the bell pipe (b) sensor at the mid location of the bell (c) sensor on top of the locking segments on the bell (d) sensor on the spigot

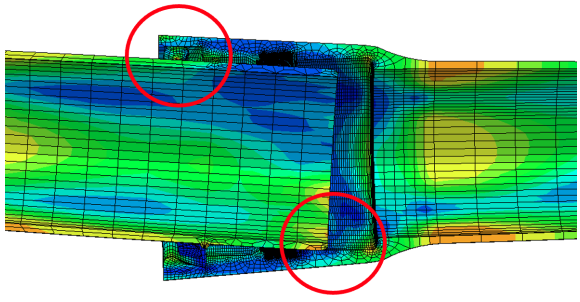


Fig. 5.72. Joint deformed mechanism in Push Down stage of bi-axial tension test

rigid locking segment and the insertion slot. In Specimen-9, fracturing initiated at the top-west boundary and propagated transversely across the top crown toward the east springline. In Specimen-12, a more localized rupture initiated at the identical top-west boundary but propagated downward toward the bottom-west invert. These critical initiation and termination nodes are explicitly mapped on the spatial profiles of Sensor 6 (positioned directly over the active locking segments) in Figures 5.73 and 5.74.

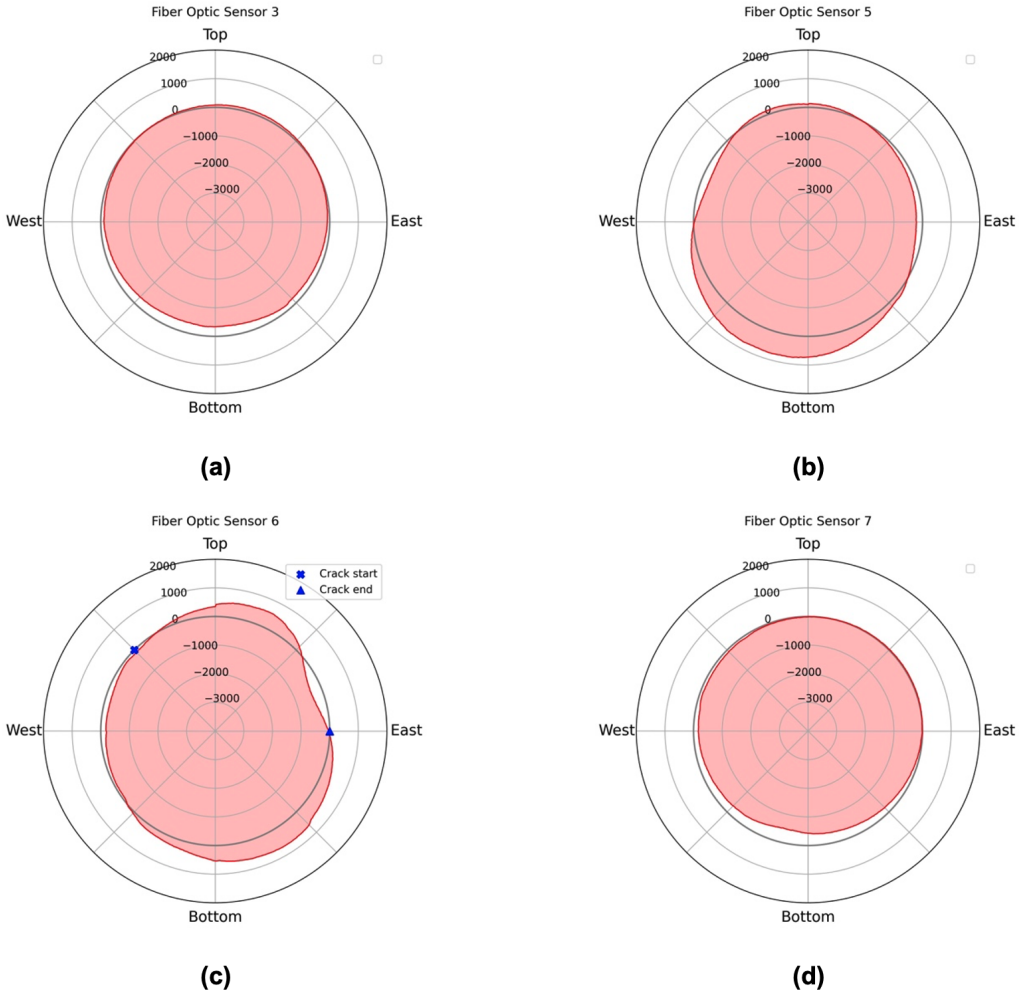


Fig. 5.73. Strain distribution in the circumferential direction of Specimen-9 under 140 kips loading condition. (a) sensor on the bell pipe (b) sensor at the mid location of the bell (c) sensor on top of the locking segments on the bell (d) sensor on the spigot

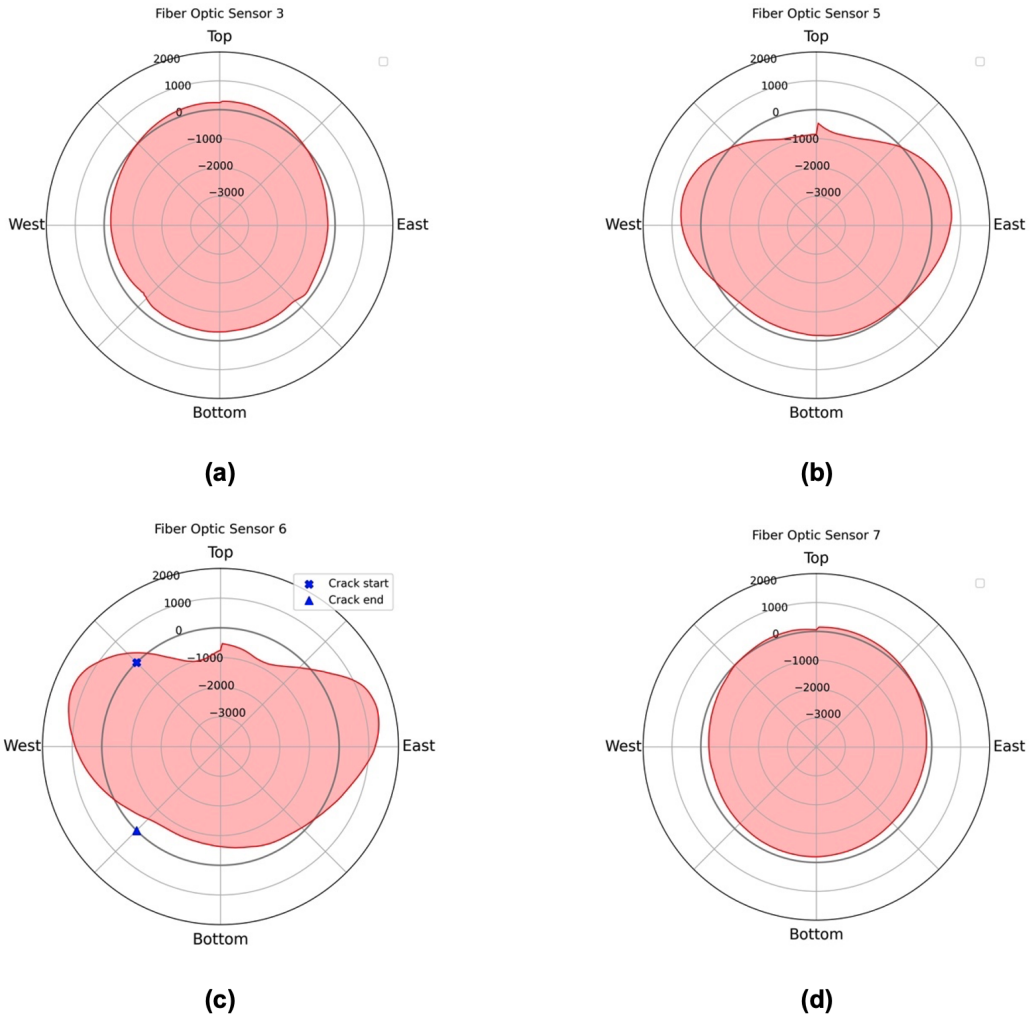


Fig. 5.74. Strain distribution in the circumferential direction of Specimen-12 under 140 kips loading condition. (a) sensor on the bell pipe (b) sensor at the mid location of the bell (c) sensor on top of the locking segments on the bell (d) sensor on the spigot

5.4.5 Conclusion of ERDIP Biaxial Tension Test

This phase of the experimental program evaluated the structural performance, internal load transfer mechanisms, and ultimate limit states of nominal 8-inch ERDIP joints subjected to severe biaxial loading (combined monotonic flexure and longitudinal tension). By testing two distinct internal restraint configurations, the data explicitly demonstrated that the circumferential orientation of the locking segments governs both the bending stiffness and the ultimate seismic tensile capacity of the joint.

Under identical kinematic boundary conditions, Specimen-9 (insertion slot at the 9 o'clock springline) sustained a substantially larger ultimate bending moment and achieved a peak axial pullout capacity of 171 kips. In contrast, Specimen-12 (insertion slot at the highly compressed 12 o'clock crown) provided a softer bending boundary but with a lower ultimate tensile capacity of 145 kips at a comparable joint opening.

Ultimately, both joints reached their absolute limit states via structural rupturing of the bell casing, leading to a total loss of hydraulic containment. In both configurations, fracture initiated at the same geometric location: the transitional boundary between the rigid locking segment and the compressible rubber insertion slot. This confirms that this structural discontinuity acts as a severe internal stress concentrator. However, the actively engaged locking segments induced diverging multi-axial stress states that dictated the final fracture propagation. In Specimen-9, the resulting crack propagated diagonally across the top crown, indicating a failure mechanism driven by complex, coupled shear and longitudinal tensile stresses. Conversely, Specimen-12 exhibited a predominantly circumferential fracture trajectory, demonstrating that its failure was governed almost entirely by pure longitudinal tensile stress.

5.5 Summary and Discussions of ERDIP Experiments

The comprehensive experimental program evaluated the kinematic ductility, internal load transfer mechanisms, and ultimate limit states of ERDIP joints under extreme seismic loading conditions. High-resolution continuous strain profiling, coupled with macroscopic force-displacement data, provided deep insights into the structural behavior of these systems. The findings are synthesized below, categorized by pipe diameter to highlight the distinct mechanical behaviors governed by geometric scaling.

5.5.1 Performance of 8-inch ERDIP Configurations

The structural response of the nominal 8-inch ERDIP assemblies was systematically evaluated under pure tension, four-point bending, and biaxial combined loading, as summarized in Table 5.10. The data explicitly demonstrate that while these joints possess massive ductile capacities, their ultimate performance is heavily dictated by internal geometric configurations—specifically, the restraint mechanism type and the circumferential orientation of the locking segments.

Table 5.10. Summary of experimental results across various testing configurations of 8-inch ERDIP tests

	Tension		**Four-point Bending**		**Bi-axial Tension**	
Parameter	**12 o'clock**	**Field Groove**	**9 o'clock**	**12 o'clock**	**9 o'clock**	**12 o'clock**
Extension	D = 2.46 in F = 174 kips	D = 0.51 in F = 190 kips	N/A	N/A	D = 2.30 in F = 171 kips	D = 2.00 in F = 145 kips
Deflection	N/A	N/A	R = 13.1° M = 1,153 kip-in	R = 13.2° M = 763 kip-in	R = 8.4° M = 1,042 kip-in	R = 8.4° M = 886 kip-in
Failure	Bell	Spigot	Spigot	Spigot	Bell	Bell

Under pure monotonic tension, a critical divergence in post-yield hydraulic resilience was observed between the factory-manufactured weld bead (Specimen-WB) and the field-installed snap ring (Specimen-FG). While both configurations successfully accommodated massive axial deformations, Specimen-WB exhibited a more robust and ductile failure. Extreme localized bearing forces ultimately fractured the bell casing; however, the internal elastomeric gasket successfully bridged the structural damage, maintaining water service for nearly three additional inches of forced pullout. Conversely, the unbonded snap ring in Specimen-FG permitted slight upward vertical shifting of the spigot, eliminating uniform concentric restraint and driving stress concentrations into the reduced wall thickness of the machined groove. This resulted in a sudden, catastrophic circumferential fracture of the main pipe barrel that entirely bypassed the sealing mechanism, offering zero post-peak hydraulic reserve.

Under bending and combined loading, the circumferential orientation of the internal locking segments fundamentally governed both the joint's bending stiffness and its ultimate seismic capacity. Specimen-9 (featuring the insertion slot at the 9 o'clock springline) consistently developed a large internal bearing force couple, resulting in a substantially stiffer joint requiring higher applied moments. This orientation maximized internal wedging resistance, yielding a peak axial pullout capacity of 171 kips under biaxial loading. In contrast, Specimen-12 (featuring the compressible insertion slot at the highly compressed 12 o'clock crown) provided a softer bending boundary, accommodating larger deflections under lower moment demands, but with a reduced ultimate tensile capacity of 145 kips.

Regardless of the loading protocol, the 8-inch specimens reached their ultimate limit states through structural rupturing of the ductile iron casing. In bending, this manifested as localized punch-through fractures at the spigot invert due to intense compressive bearing. Under biaxial tension, fracturing invariably initiated at the transitional boundary between the rigid locking segment and the compressible rubber insertion slot, confirming this discontinuity acts as a severe internal stress concentrator.

5.5.2 Bending Performance of Large-Diameter ERDIP

The full-scale four-point bending tests on the massive 36-inch and 48-inch ERDIP assemblies confirmed exceptional rotational ductility, with both systems significantly exceeding the manufacturer's specified design limits. The 36-inch joint achieved an ultimate rotation of 10.25° (design limit: 7.0°) under an ultimate moment of 4,325 kip-in, while the 48-inch joint achieved 6.45° (design limit: 5.5°) under a massive 9,600 kip-in moment and extreme 250 psi internal pressurization.

High-resolution longitudinal strain data captured the intense mechanical wedging between the spigot weld bead and the internal locking segments. As extreme kinematic deflection progressed, this wedging action introduced secondary bending moments into the casing wall, ultimately causing the internal locking segments to physically dislodge. This structural detachment fundamentally altered the internal load transfer path; consequently, it was this sudden loss of boundary constraint that forced the neutral axis to shift locally. Furthermore, prior to segment ejection, circumferential strains captured highly localized cross-sectional distortion: the upper half of the bell expanded radially due to upward bearing from the pivoting spigot crown, while the lower half expanded as the spigot forced the actively engaged locking segments radially outward.

Notably, the ultimate limit state for the large-diameter pipes was not defined by the structural rupture of the primary iron casing, but rather by this progressive failure of the internal restraint mechanism. In the 36-inch test, the progressive physical ejection of the internal locking segments triggered the sudden redistribution of internal forces, ultimately precipitating weeping and the loss of hydraulic containment. Similarly, the 48-inch joint failed when severe biaxial loading (flexure plus 240 psi hydrostatic thrust) caused the sequential structural detachment of the locking segments in a sudden water pressure drop.

5.5.3 Scaling Effects on Seismic Resilience

Synthesizing the results across all tested diameters reveals a fundamental shift in the ultimate failure hierarchy dictated by scale.

In the small-diameter (8-inch) assemblies, the internal locking segments and weld beads proved structurally stiffer and stronger than the localized regions of the primary pipe casing. Consequently, the ultimate limit state was consistently governed by the yielding and subsequent fracturing of the ductile iron itself—either via spigot punch-through in bending, groove rupture in the field-installed tension specimen, or bell fracture under tensile or biaxial loading.

Conversely, in the large-diameter (36-inch and 48-inch) assemblies, the primary casing is stronger. As global bending demands scaled up, the large internal bearing forces exceeded the wedging capacity of the segmented restraint system. This caused the locking segments to physically eject from their housing grooves before the heavy pipe wall could fracture.

This scaling effect shows distinct seismic performance paradigms. Small-diameter ERDIP failures are characterized by sudden, localized material ruptures (often driven by the stress

concentration at the insertion slot), though factory-welded beads demonstrate better post-rupture hydraulic bridging than field-grooved restraint. Large-diameter ERDIP failures are characterized by a progressive mechanical unzipping of the restraint system. While this segment-ejection prevents catastrophic snapping of the main pipeline barrel, it leads to unrecoverable losses of internal hydraulic pressure. Ultimately, these tests confirm that while macroscopic rotational capacities are highly ductile across all scales, the subtle geometric interactions at the joint interface govern the specific load transfer paths, failure modes, and post-earthquake hydraulic reliability of the infrastructure.

Chapter 6

Component-Level Mechanics of Alternative Ductile-Iron Joint Systems

6.1 High Deflection and High Pressure Restraint (HDSS) Pipe

This section provides a summary of the findings from a 4-point bending test conducted on a 48-inch US Pipe High Deflection and High Pressure Restraint (HDSS) Pipe.

6.1.1 Introduction of HDSS

The High Deflection and High Pressure Restraint (HDSS) ductile iron pipe manufactured by US Pipe is a highly engineered segmented system designed to provide robust axial restraint and multi-axial flexibility in critical water transmission networks. The joint architecture utilizes a specialized bell-and-spigot configuration (as shown in Figure 6.1) that relies on an internal mechanical locking system to safely accommodate ground deformation. To secure the connection and ensure watertight integrity, a structural rubber gasket is seated within the bell. Positive axial restraint is achieved via ductile iron locking segments, which are inserted through a singular access slot at the crown of the bell and fed into an internal circumferential cavity. Once fully seated, these segments mechanically engage a continuous retainer weldment located on the inserted spigot end. Finally, a rubber retainer is installed into the bell access slot between the locking segments, ensuring they remain securely positioned while allowing the joint to freely extend and engage the restraint under severe loading, as depicted in Figure 6.2.

At the 48-inch diameter scale, this specific HDSS configuration is engineered to sustain a nominal working pressure of 350 psi and provide a baseline rotational deflection capacity of 2.0 degrees. However, to systematically evaluate the resilience of this large-diameter infras-



Fig. 6.1. Photo of HDSS bell pipe and spigot

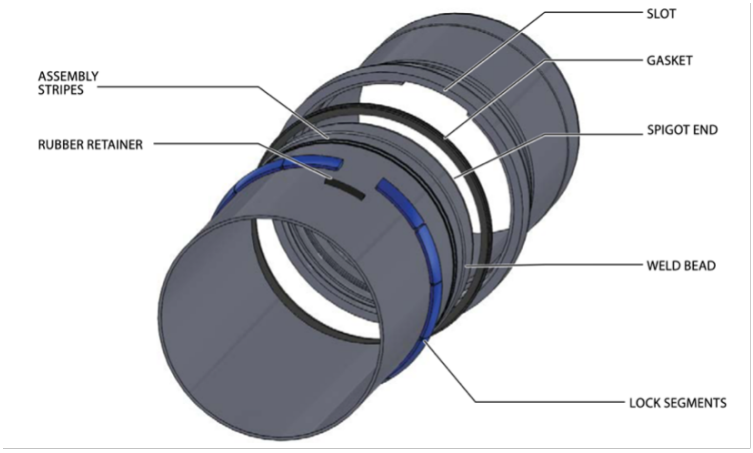


Fig. 6.2. Schematic of the joint of HDSS pipe [126]

tructure under extreme seismic or geomechanical loading, its ultimate structural limit states, which frequently exceed manufacturer operational thresholds, must be empirically quantified. The experimental evaluation comprised two sequential large-scale four-point bending tests performed on specimens outfitted with pre-installed endcaps. The initial test was designed to apply continuous bending forces until catastrophic structural or mechanical failure; however, the immense flexural resistance of the 48-inch assembly ultimately exceeded the maximum load capacity of the primary pushing actuator without inducing observable joint failure. Consequently, the loading apparatus was significantly upgraded for the second test, replacing the single actuator with twin high-capacity hydraulic cylinders to effectively reach the ultimate deflection capacity of the specimen. By analyzing the high-resolution strain and displacement data collected across both tests, this study characterizes the structural limits and underlying failure mechanisms of the large-diameter HDSS transmission pipe.

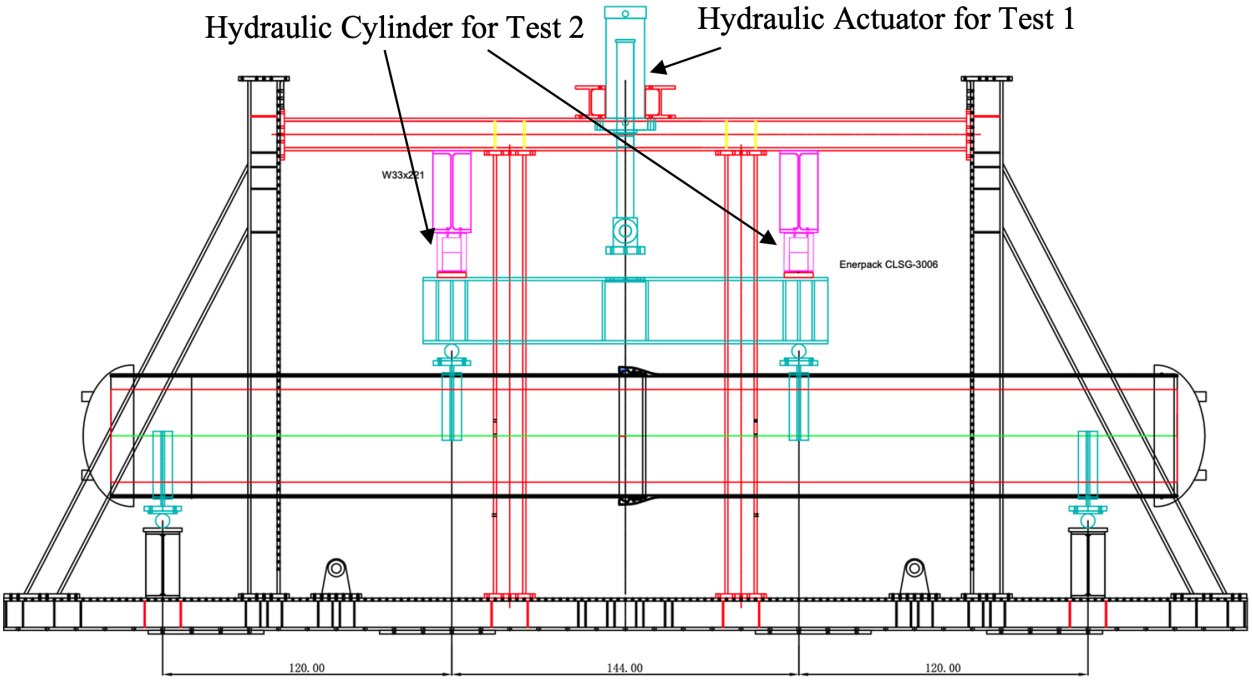


Fig. 6.3. Elevation view drawing of the HDSS four-point bending experimental setup

6.1.2 Experimental Setup and Instrumentation

The HDSS four-point bending experimental setup was designed as a self-reacting system. As presented in Figure 6.3 and Figure 6.4, it is comprised of two frames connected to each other by two wide-flange I-beams on top and two wide-flange I-beams on the bottom. In addition, the frames were bolted to four 2 inches steel plates at the base of the system.

The loading features were attached to a wide-flange I-beam that had 6 inches rollers spaced 12 feet from each other. Special saddles were designed and fabricated for the tests to achieve even force distribution on the pipe's surface. They were installed at the loading and reaction points of the pipe. The loading points correspond to the location of the rollers underneath the load spreader beam, which is 12 feet from each other on the top of the specimen. The reaction points were spaced 32 feet from each other on the bottom of the specimen. The centerline of the specimen was defined based on a fully retracted position of the joint. No water pressure was applied for both tests.

For the first test, a hydraulic actuator with an ultimate load capacity of 460 kips and 36 inches stroke capacity was utlized. The actuator connected to the mid-span of the wide-flange loading beam, which ensure the load to be applied at the center of the specimen. However, it was found in the first test that the capacity of the actuator used was not enough to fail the specimen For the second test, two hydraulic cylinders with a loading capacity of 660 kips and 5.91 inches storke capacity was used to replace the hydraulic actuator. The

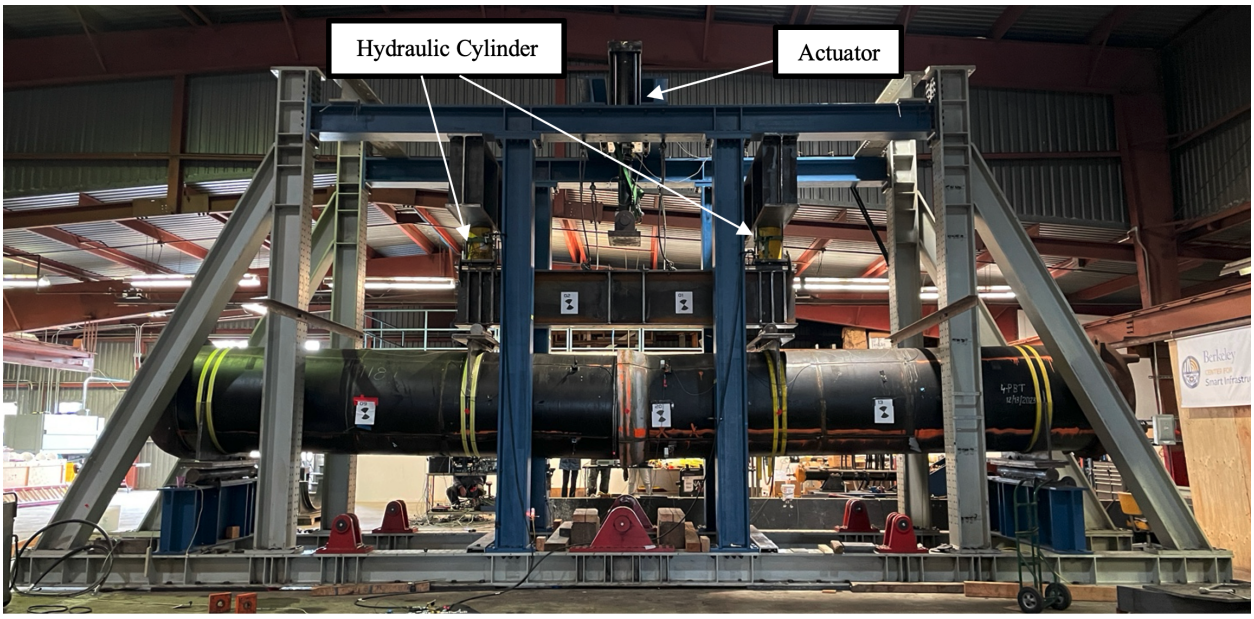


Fig. 6.4. Front view (north side on the left) of the HDSS four-point bending test setup. Note that the actuator was used for the first test while the hydraulic cylinders were used for the second test.

hydraulic actuator was disconnected during the second test.

The testing procedure consisted of two stages: (i) self-weight moving down and (ii) applied force pushing down. Initially, the temporary supports were removed to enable the pipes to move downward under their self-weight, inducing rotations in the specimen. Subsequently, the loading features pushed the pipeline further down to achieve greater rotation until reaching the capacity of the actuator or until a severe failure of the specimen was found. The summary of the tests is presented in Table 6.1.

Table 6.1. Summary of four-point bending test terminations

No.	Date	Note
1	12/13/2023	Terminated due to reaching loading actuator capacity
2	11/25/2024	Terminated due to severe pipe failure

The experimental setup was extensively instrumented to monitor applied forces and pipe segments displacements using a series of macro-scale instrumentations. Loading forces were continuously tracked utilizing the actuator's built-in load cell and piezometer-derived hydraulic pressures, while structural displacements across the cylinders, pipe segments, and

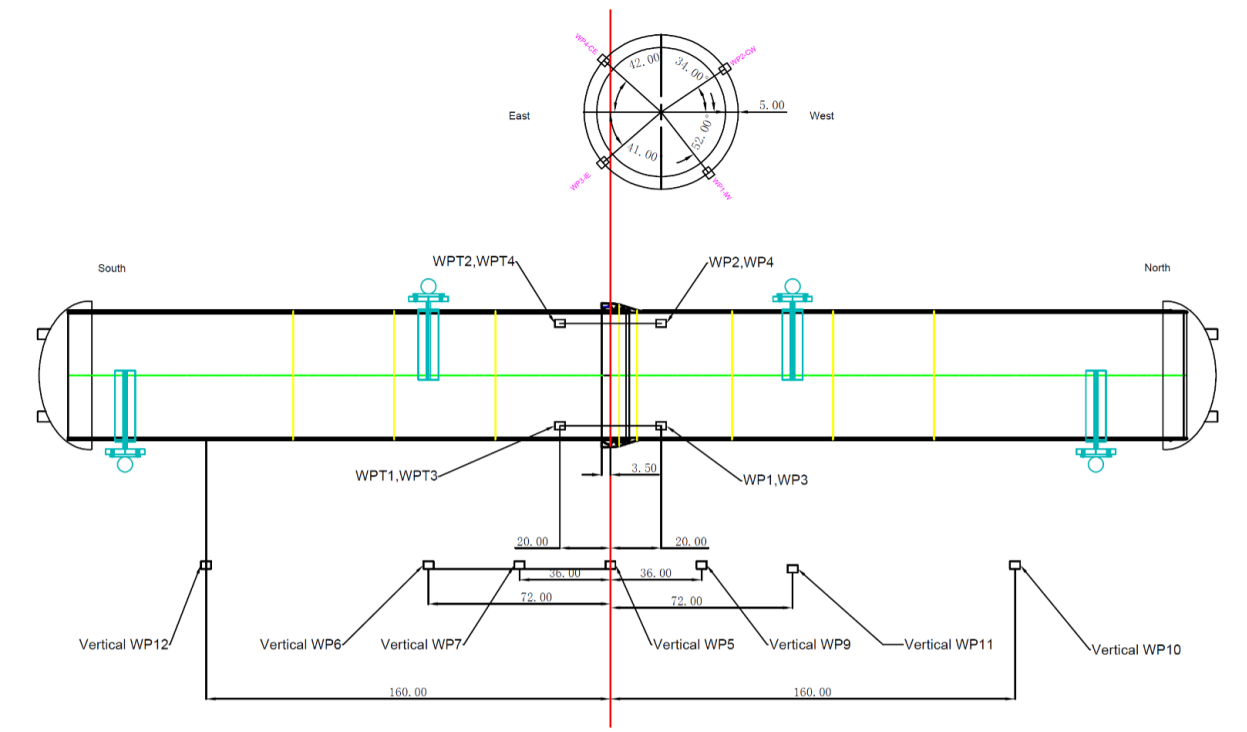


Fig. 6.5. HDSS four-point bending test position transducers setup

test frame were recorded using a network of position transducers. The macro-scale instrumentation is depicted in Figure 6.5. More details can be found in Chiu et al. (2025) [27].

To capture high-resolution structural mechanics (micro-scale strains), DSS cables were bonded to the specimens using Huntsman Araldite 2021-1 epoxy (Figure 6.6). To measure bending strains and mimic real-world field deployments, longitudinal sensors were installed along the length of both pipes at angular intervals of 0°, 45°, 135°, 215°, and 305°. Furthermore, circumferential sensors were installed at approximately 40-inch intervals along the pipe barrel. To capture the critical limit states of the joint, three highly targeted circumferential loops were applied directly to the bell assembly—specifically at the bell face, the specimen centerline, and directly over the internal locking segments.

6.1.3 Four-Point Bending Performance

Two testing stages were involved: (1) self-weight moving down, and (2) actuator pushing down. In the first stage, the temporary support were removed and the pipes were allowed to move downward due to their self-weight until reaching a static force equilibrium. Then, a monotonic force, perpendicular to the longitudinal axis of the pipeline, was applied to the load transfer beam then transferred to the pipes through the two loading saddles.

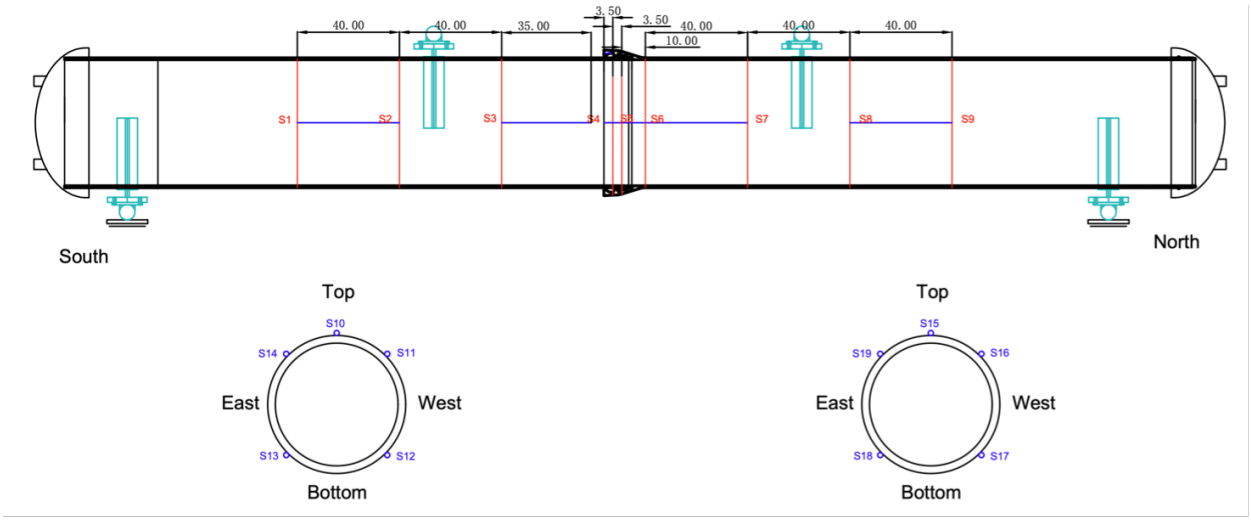


Fig. 6.6. HDSS four-point bending test DSS instrumentation plan

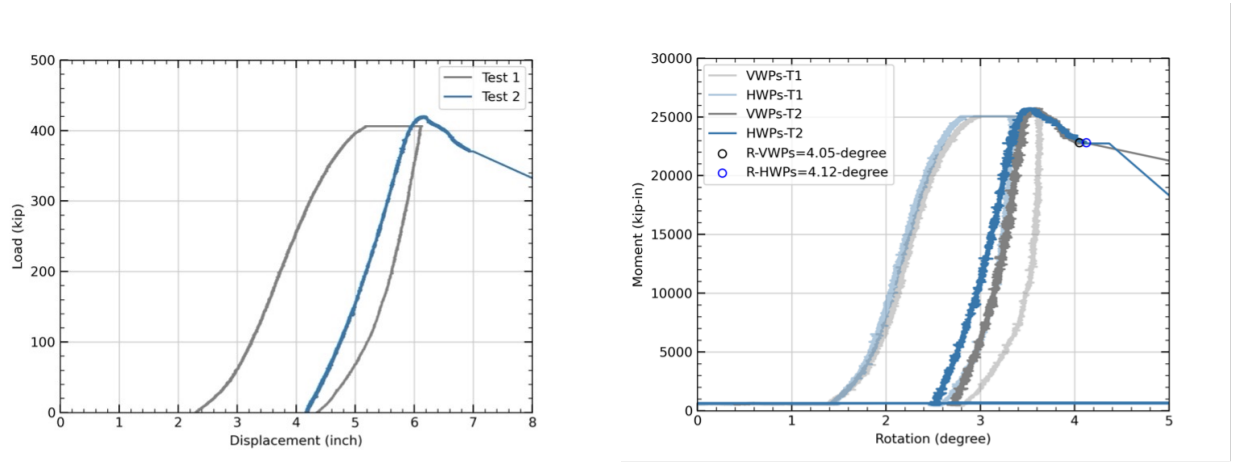
Failure Mode and Mechanism

The force versus deflection of the pipe at the joint (wp5) is presented in Figure 6.7a and the moment versus rotation result is shown in Figure 6.7b. The moments and rotations of the specimen were calculated using equation 4.6 (using wp3 and wp4) and equation 4.5 (using wp5 and wp11 for the bell pipe; wp5 and wp6 for the spigot). Looking at the grey lines (Test 1) in the figure, the joint moved 2.3 inches downward which corresponds to 1.4 degree rotation for both approaches during the first stage (self-weight moving down). Next, the actuator started to apply vertical forces. The test stoped because of reaching the actuator capacity which corresponds to 408.64 kips and 6.14 inches vertical joint displacement. That is about 3.63 degree rotation and 3.39 degree rotation from the two approaches, respectively. The corresponding moment is about 25,051 kip-in. It is noteworthy that the rotation has surpassed the manufacture's specification of 2 degree rotation before observing obvious pipe failure.

The first test was terminated due to reaching the loading actuator capacity without significant damage on the pipe. After the force was released, the specimen bounced back to approximately 2.5 and 2.7 degrees of deflection from the two approaches, which became the initial stage of the second test.

During the second test, the hydraulic cylinders pushed the specimen further down until severe damage on the pipe was found. A severe crack was found when the specimen reached 4.05 and 4.12 degrees deflection with approximately 25,740 kip-in moment, which corresponds to 6.94 inches vertical displacement at the center of the specimen with 420.13 kips force. The result is summarized in Table 6.2.

Figure 6.8 shows the aftermath of the failure of the joint. As can be seen from the figure, a piece of the steel close to the bottom of the bell face was ripped off due to the concentrated



(a) Force and Vertical Displacement **(b)** Moment and rotation

Fig. 6.7. Experimental results of HDSS four-point bending experiment. (a) Force and vertical displacement. (b) Moment and rotation.

Table 6.2. Summary of HDSS four-point bending test results

Moment (kip-in)	**Rotation – Approach 1** (degree)	**Rotation – Approach 2** (degree)	**Force** (kips)	**Vert. Disp.** (inch)
25,051	3.63	3.39	408.64	6.14
25,740	4.05	4.12	420.13	6.94

tensile forces on the bottom side of the bell. As the specimen beening pushed down, the bottom side of the spigot tended to move outward and therefore fully contacted with the locking segments. This results in large tensile stresses concentrated at these particular locations. The tensile crack was observed from 45-degree west of the bottom side to 45-degree east of the bottom side at the locations where the locking sementes were located, as illustrated in Figure 6.8a and 6.8b. A shearing crack was observed on the east side initiated at the end of the tensile crack on the east side. The shear crack propagated from the bell face to the bell pipe, as shown in 6.8b. The detailed failure mechanism is discussed in the following sections using DSS data.

Axial Strain

The axial strain results from the DSS data are shown in Figure 6.9 to Figure 6.11. Figure 6.9 shows the relationship between axial strain and joint rotation at four selected planes: (1) midpoints of S1 and S2 (spigot), (2) midpoints of S3 and S4 (spigot), (3) midpoints



Fig. 6.8. Joint failure of HDSS four-point bending test (a) West side (b) East side.

of S6 and S7 (bell pipe), and (4) midpoints of S7 and S8 (bell pipe), as measured by the longitudinal fiber optic sensors. The rotation used in this section is computed based on the second approach (HWPs) mentioned in the previous section. Both pipes exhibited the highest compressive strain at the top side, followed by sensors located on the top-west and top-east sides. This aligns with bending theorem expectations, where the top side undergoes the most compression and the bottom side experiences the greatest tensile strain. As the locations approach the bending central line, the strain decreases toward zero. Conversely, sensors placed on the bottom-west and bottom-east sides all experience tensile strain. The strain-versus-rotation patterns demonstrate similarities across the four selected planes, indicating eccentric squashing along the pipes.

Looking closer to Figure 6.9b, which indicates the strain development of the selected strain planes on the bell pipe closer to the bell face, one could observe that the compressive strain measured on the top side of the bell pipe become smaller than the ones measured from the top-west and top-east locations when the deflection reached above 3.6 degrees. This might be because of the bell failure mechanism. The ductil iron locking segments were placed all around the bell except the top side. A rubber gasket, which is compressible was placed on the top side of the bell to positioned the locking segments. As a result, the top side was expanding less than the other locations located above the springline when the bell was reaching it's ultimate capacity. The compressive strain developed because of the Poisson's effect was less on the top side. A more clear illustration of the bell mechanism will be discussed in the following section using the hoop strain result.

Figure 6.10 shows the axial strain results along the bell pipe (northside pipe) when the pipe reached about 4.0 degree rotation during the second test, which is right before the structural failure occurs. As mentioned previously, for the sensors placed above the horizontal central line of the specimen (i.e., S15, S16, S19), most of the sections on the

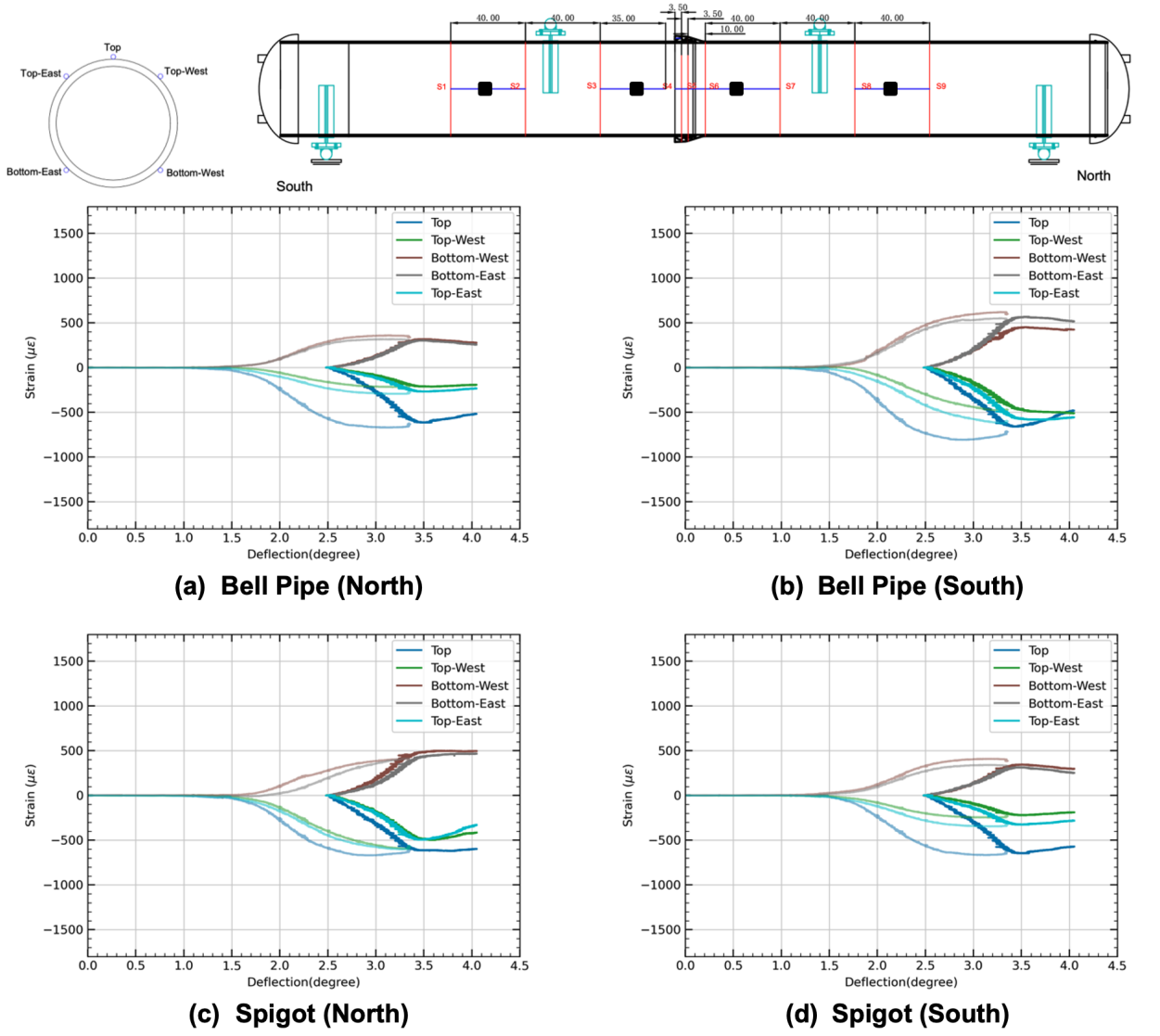


Fig. 6.9. Axial strain vs joint rotation of HDSS four-point bending test. Note that the lighter colors indicate the results from test 1 and the more vibrant colors indicate the results from test 2.

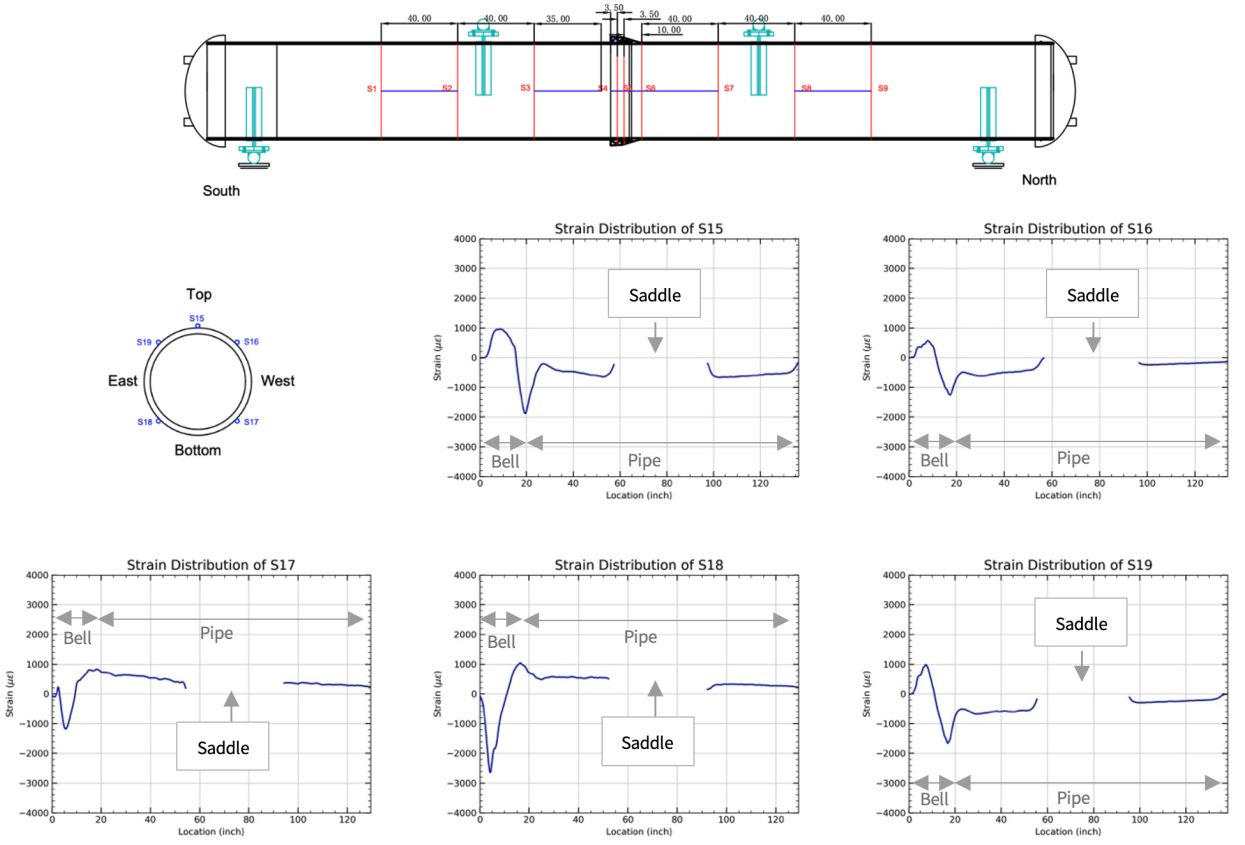


Fig. 6.10. Axial strain development of bell pipe (northside pipe) of HDSS four-point bending test under 4.0-degree deflection condition (before failure).

pipe are experiencing compressive forces; while the other sensors (i.e., S17, S18) are mainly experiencing tensile forces. However, different strain distribution patterns are found on the bell section. For the sensors above the horizontal center line, tensile strains are found on the section close to the bell face (location between 0-15 inches), followed by significant compressive strains observed at the location between the bell and the pipe (i.e., bell end, location between 15-25 inches). This phenomena likely arises from, when the pipe was being bent, the top of the spigot was moving inward and the locking segments were bearing against the crown of the bell, which introduced a moment and resulted in a compressive force at the bell end. At the same time, the locking segements were located in the grove and were restrained by the stopper close to the bell face, which introduced a tensile force at the locations close to the bell face.

On the other hand, for the sensors located beneath the horizontal center line, significant compressive strains are observed at the location close to the bell face (i.e., location between 0-10 inches). This indicates that the locking segments located on the bottom of the bell

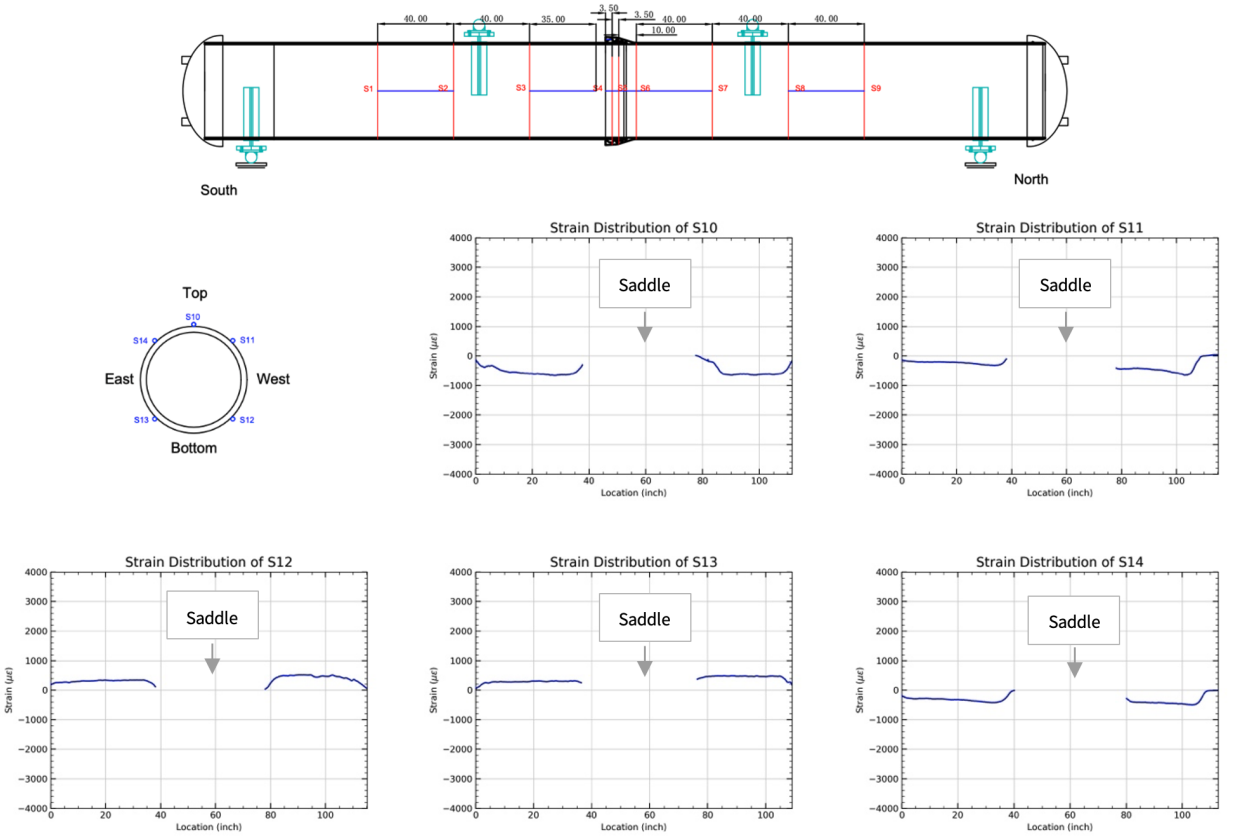


Fig. 6.11. Axial strain development of spigot (southside pipe) of HDSS four-point bending test under 4.0-degree deflection condition (before failure).

tended to move out. In order to move outward, the locking segments expanded the bell, which in turn introduced a moment. This resulted in a significant compressive force on the surface close to the bell face.

Figure 6.11 shows the results of the axial strain of the spigot (southside pipe) at the same loading condition. The strain distribution patterns are similar along the pipe where S10, S11, and S14 are under compression while S12 and S13 are under tension. However, for S11 and S14, located at 45 degrees apart from the top, smaller compressive strains are observed near the bell (above 110 inches). This observation is attributed to the locking segments in these regions being restrained by the stopper near the bell face, introducing tensile forces that transfer to the spigot. Consequently, smaller compressive strains are observed at locations on the spigot close to the bell. This phenomenon is less evident at the top of the spigot, where a rubber retainer is installed instead of a locking segment, allowing for more deflection but transferring fewer forces.

Hoop Strain

The hoop strain results measured by DSS are presented in Figure 6.12 which shows the results from the second test under 4.0 degree deflection consition, right before the failure point. The figures include the results obtained from sensor S3, which was placed on the spigot close to the bell, sensor S4 located on the centerline, sensor S5 positioned on the middle of the bell, and sensor S6 on the bell end.

The results from the sensors located on the pipes (i.e., sensor S3 and S6) indicate that the top and bottom sides (12 o'clock and 6 o'clock) of the bell are in compression, while the west and east sides (3 o'clock and 9 o'clock) are expanding. These strain distributions suggest that both of the pipes underwent eccentric squatting during bending. Similar strain patterns can be observed on the other circumferential sensors located on both of the pipes (i.e., S1-S2, and S7-S9). This might be because, while the specimen being bent, the bottom side of the pipe experienced the largest restrained force, which is in the axial direction, between the locking segments and the stopper located close to the bell face. This resulted in a large compressive strain on the bottom side in the hoop direction because of the Poisson's effect. Looking into the top side of the spigot, since the top of the spigot was contacting the crown of the bell, the top of the spigot was compressing. Hence, the compressive hoop strain is observed on the top side of the spigot. The absence of expansion on the top side of the bell pipe is due to the presence of a rubber retainer, which could accommodate more deformation comparing to the locking segments made of ductile iron. The phenomenom is illustrated in Figure 6.13.

Sensor S5, placed on the middle of the bell, exhibits a strain distribution similar to that observed on both pipes (i.e., expanding on the sides and shrinking on the top and bottom sides). However, the tensile hoop strain is observed toward the top side of the pipe cross-section. This can be attributed to the locking segments moving upward. A rubber retainer is positioned on the top side of the bell instead of a locking segment which is made of ductile iron. The locking segements possess superior stiffness comparing to rubber retainer.

For the sensor located on the centerline (sensor S4), close to where the locking segments were positioned, undergoes a similar strain pattern as sensor S5 except the bottom side is expanding instead of shrinking. This is because the bottom of the spigot was bearing agains the invert of the bell. Hence, a localized expansion is observed around this particular locations. The mechanism is illustrated in Figure 6.13. As the pipe being pushed down, the locking sements tended to move out and move toward the top side and therefore squeezed the rubber part. This mechanism is illustrated in Figure 6.14. Because of the locking segment moving upward, the bell was expanding more on the upper section.

6.1.4 Conclusion of HDSS Experiment

Two 4-point bending test were carried out on a 48-inch US Pipe HDSS ductile iron pipe. The first experiment stopped due to reaching the capacity of the actuator. By replacing the actuator with two hydraulic cylinders, severe pipe failure could be observed in the second

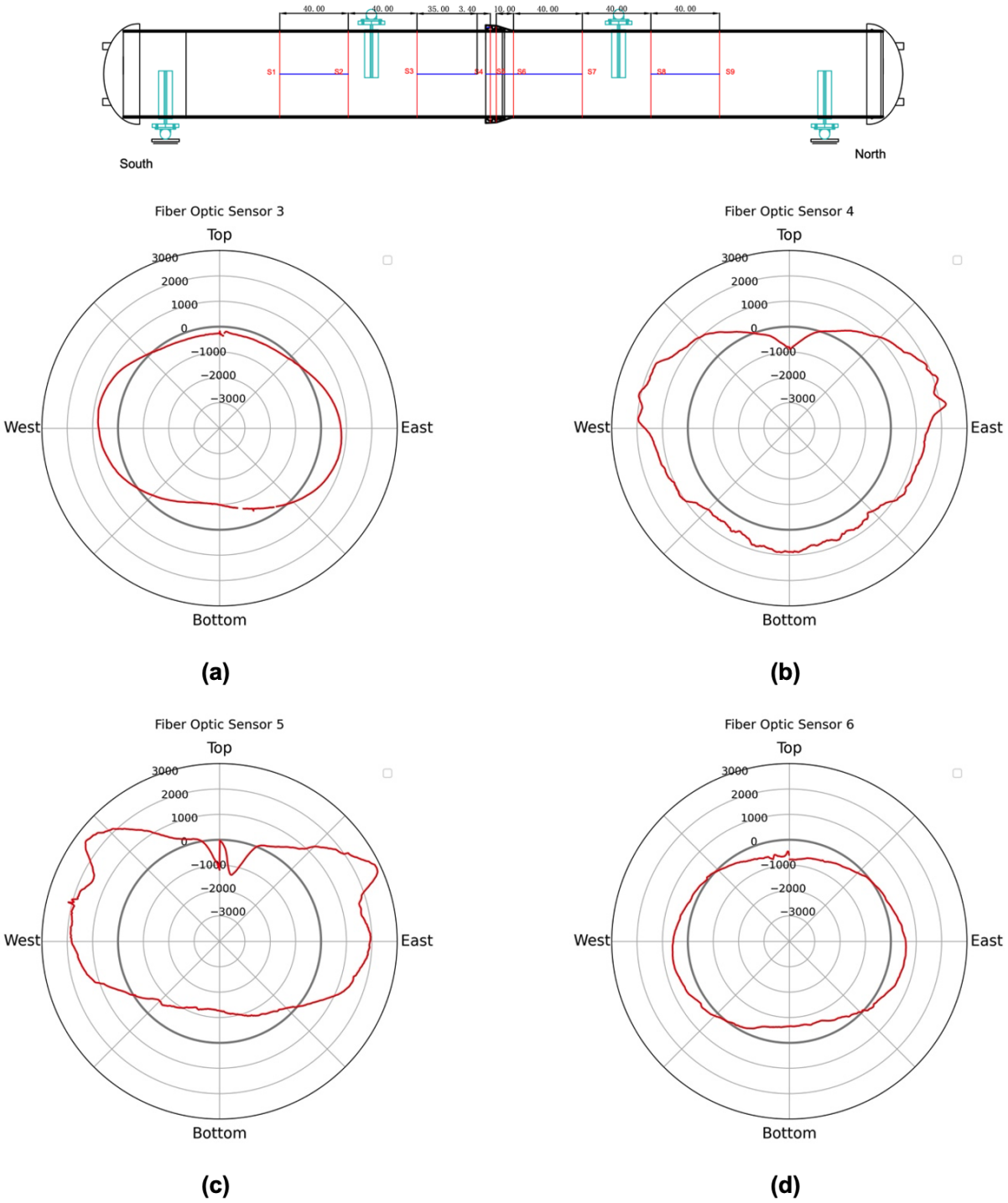


Fig. 6.12. Strain distribution in the circumferential direction under 4.0-degree deflection condition of HDSS four-point bending test. (a) sensor on the spigot (b) sensor on the top of the inserts (c) sensor on the centerline of the specimen (d) sensor on the bell pipe.

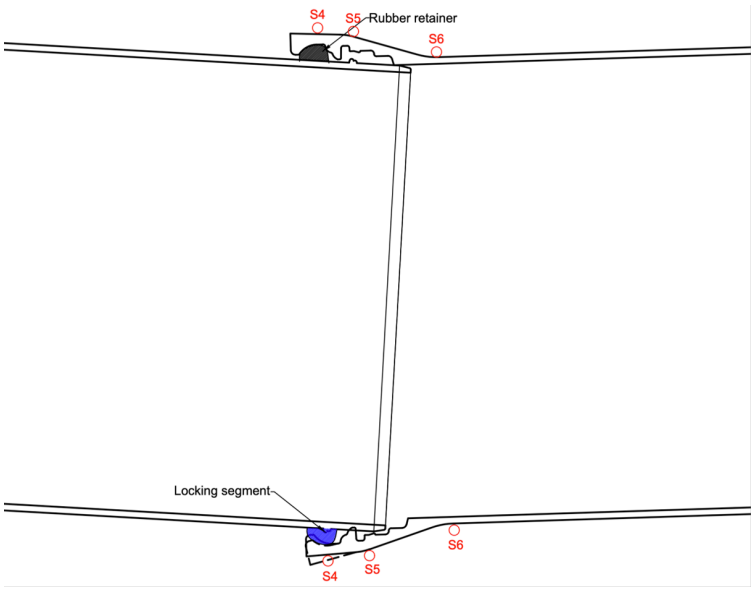


Fig. 6.13. Sketch of the bell deforming mechanism of HDSS four-point bending test.

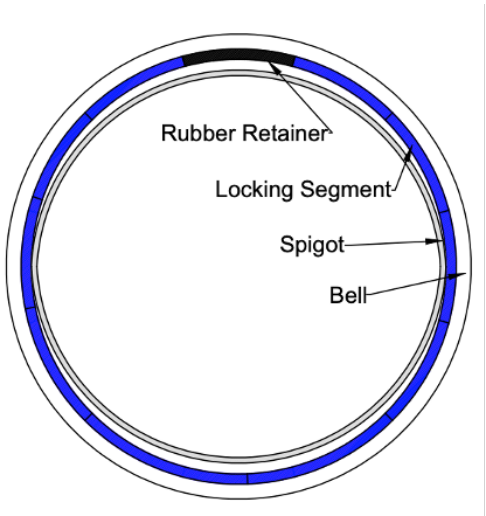


Fig. 6.14. Sketch of the locking segment moving mechanism of HDSS pipe. As the spigot squatt, the locking segments tend to separate and move upward.

experiment. The pipe surpassed the manufacturer's deflection capacity (i.e., 2.0 degrees) as it rotated up to approximately 4.0 degrees (HWPs approach) before encountering any failure. The maximum moment observed during the test reached approximately 25,740 kip-in.

The strain data collected from DSS offered insights into the behavior of the pipe during the 4-point bending tests. The analysis revealed compression along the top and bottom sides of the pipe, with expansion observed on the east and west sides. At the bell section, expansion occurred around its perimeter except on the top side. This expansion is attributed to the outward movement of the locking segments within the bell. The absence of expansion on the top side is due to the presence of a rubber retainer, which could accommodate more deformation comparing to the locking segments made of ductile iron. Furthermore, vertical displacement measurements obtained from the vertical wire pots suggest slight bending of the spigot near the bell, while the bell pipe maintained its rigidity.

Regarding the failure mechanism, the DSS data shows that large strain concentrations were found at the bell especially close to where the locking segements located (i.e., about 3.5 inches away from the bell face), which corresponds to the failure location found in the second experiment. A more detailed pipe failure mechanism will be examined with finite element analysis planned to be developed in the near future.

6.2 Hazard Resistant Ductile Iron Pipe (HRDIP)

This section provides a summary of the findings from a 4-point bending test conducted on a 24-inch Kubota NS-type ductile iron pipe.

6.2.1 Introduction of HRDIP

The Hazard Resistant Ductile Iron Pipe (HRDIP) [66] is manufactured by Kubota Corp., designed to withstand severe seismic events and maintain full water service even in the aftermath of large-scale ground failure. This high degree of resilience is achieved primarily through the use of Kubota's proprietary NS-type joint. The NS-type joint is a specialized restrained connection that features an internal locking ring mechanism combined with an elongated bell design. This configuration allows the spigot to slide axially within the bell, absorbing tectonic strains without compromising the watertight elastomeric seal. Specifically, the joint is built to accommodate up to 2.4 inches of expansion and 10.2 inches of contraction. Once the maximum expansion limit is reached, the locking ring fully engages to prevent pull-out, effectively transferring the axial load to adjacent pipe segments and allowing the pipeline to distribute strain/ stress to the pipeline system. Additionally, the joint's geometry permits an angular deflection of up to 7 degrees, which is critical for adjusting to lateral or vertical ground movement during a seismic event.

The pipe sections are joined using this specialized bell-and-spigot mechanism, which relies on a precise sequence of internal components. During assembly, the tapered spigot is inserted into the widened bell of the adjacent pipe. A specialized rubber gasket is positioned

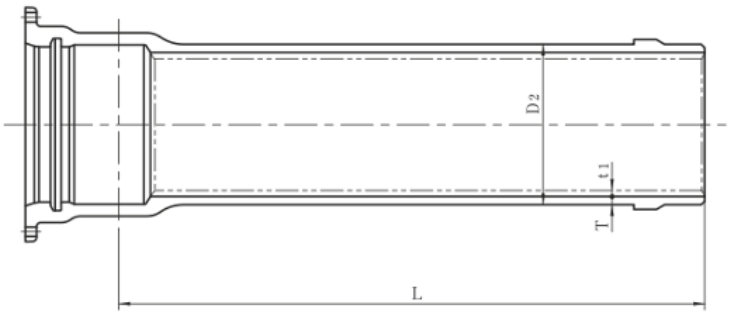
within the annular space between the spigot and the bell. To create the primary seal, a mechanical gland is driven into the joint using high-strength T-head bolts. As these bolts are tightened, the gland applies uniform axial pressure against the rubber gasket, compressing it to completely prevent water leakage. To protect this seal during extreme loading or seismic movement, a polyamide resin backup ring is incorporated into the assembly. This ring acts as a critical buffer between the locking mechanism and the rubber gasket, preventing excessive localized stress from damaging the elastomer. Finally, longitudinal restraint is provided by the split-ring locking mechanism, which is compressed and seated directly into the internal socket groove of the bell (typically installed with the split positioned at the top crown). A schematic of the individual bell components is provided in Figure 6.15, and the fully assembled joint configuration is illustrated in Figure 6.16.

While the high-performance capabilities of this HRDIP have been widely recognized, rigorous experimental validation remains critical. Previous large-scale component testing has successfully evaluated the mechanical limits of smaller-diameter variants of this pipe—most notably 6-inch (150-mm), 12-inch (300-mm), and 16-inch (400-mm) specimens—under direct tension, fault rupture simulations, and four-point bending [93, 94, 92]. However, as infrastructure projects increasingly demand higher-capacity transmission lines, understanding the scaled mechanical response of larger diameters is essential. Therefore, the experimental program detailed herein specifically for the 24-inch (600-mm) diameter variant. By building upon the foundational data from previous smaller-diameter studies, this research aims to determine the ultimate deflection capacity and localized strain behaviors of the large-diameter NS-type joint assembly under severe bending moments.

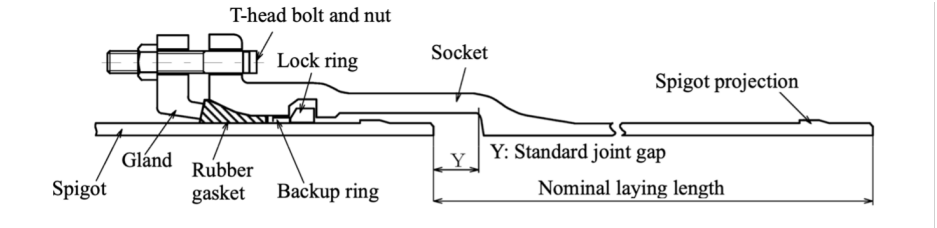
6.2.2 Experimental Setup and Instrumentation

The four-point bending testing setup utilized hydraulic actuators and various support components to apply and transfer forces to the pipe specimens. Figure 6.17 and Figure 6.18 illustrate the setup. A 346-kip pulling and 462-kip pushing capacity with 36 inches total stroke hydraulic actuator was utilized in the experiment. The actuator was positioned at the center of the specimens, which was defined as 3.5 inches away from the bell face. A steel spreader beam was placed beneath the actuator to facilitate load transfer. The force was initially applied to the beam and then transferred to two saddles on the pipes, located 72 inches from the center. The roller supports were situated 180 inches away from the center on both ends of the specimens.

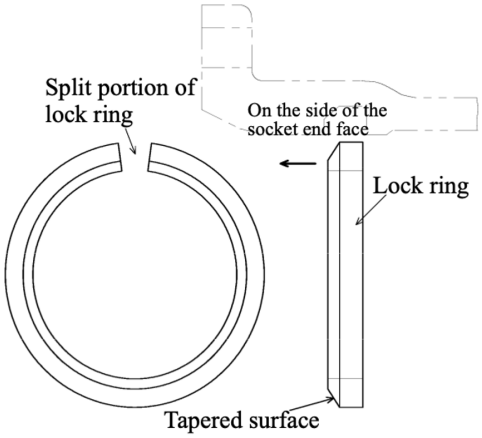
The testing procedure includes three stages: water pressurization, self-weight moving down, and actuator pushing down. In the first stage, the pipes were pressurized with water up to a pressure of 70 psi. This pressurization simulated the internal pressure conditions that the pipeline would experience during their regular operation. In the second stage, the temporary supports initially in place were removed. This allowed the pipes to move downward under the influence of their self-weight. As the pipeline moved downward, small rotations were introduced into the specimens. Finally, the hydraulic actuator was employed in the third stage to push the pipeline further downward, inducing larger rotations in the



(a) Cross section of the straight pipe [66]



(b) Cross section of the bell [65]



(c) Locking ring [65]

Fig. 6.15. Schematic of the bell of Kubota NS-type ductile iron pipe.

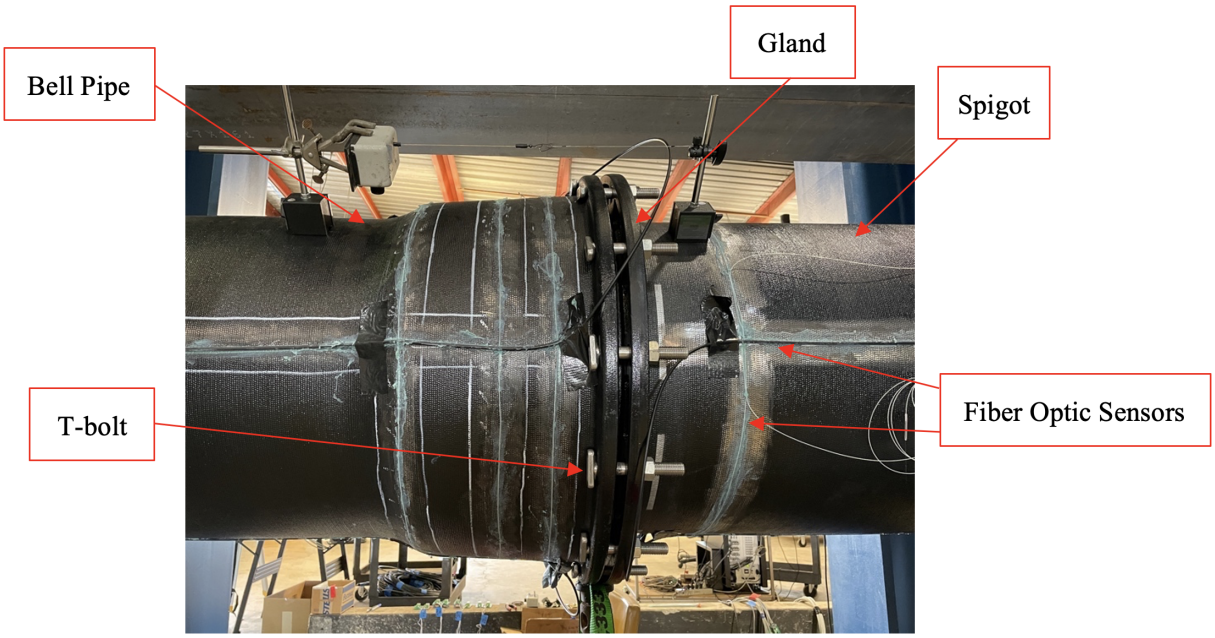


Fig. 6.16. HRDIP bell setup

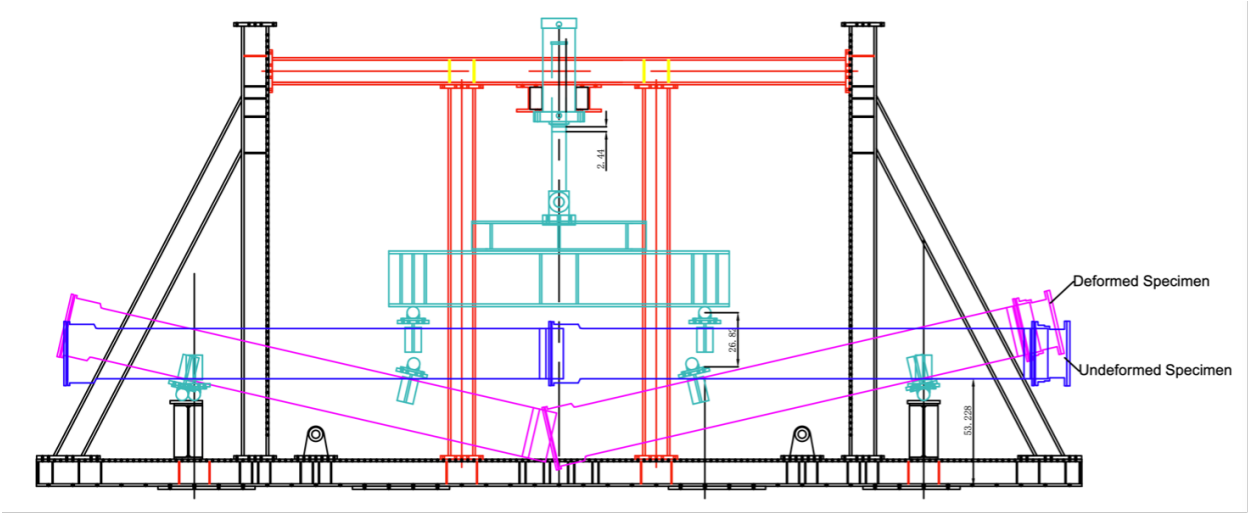


Fig. 6.17. HRDIP four-point bending experimental setup design



Fig. 6.18. HRDIP setup overview

specimen. The actuator applied a controlled force to the pipeline, progressively increasing the rotation until severe pipe damage and water leakage were observed. This stage aimed to test the ultimate deflection capacity of the pipe and assess its performance under severe bending forces.

The DSS layout was specifically designed to capture a comprehensive strain profile. To measure bending strains and mimic field deployments, longitudinal sensors were installed along the length of both pipes at 90-degree intervals. Furthermore, to evaluate complex localized deformation mechanisms, circumferential sensors were installed at approximately 40-inch intervals along the pipe barrel, with three additional loops applied directly to the bell assembly (at the bell face, middle of the bell, and specimen centerline).

To complement the continuous fiber optic data, the setup was extensively instrumented with conventional discrete sensors. A total of 32 conventional strain gauges, oriented to measure both axial and circumferential strains, were installed across four structural planes on the bell and spigot. To prevent interference with the DSS layout, these gauge sets were strategically offset by approximately 9 degrees from the pipe quarter points. Finally, macroscopic pipe segments behavior were monitored using eleven wire potentiometers: four dedicated to tracking localized joint opening dynamics, and seven positioned beneath the specimen to measure global vertical pipe displacements. The complete layout for all instrumentation are detailed in Figure 6.19 and Figure 6.20. More instrumentation details can be found in Chiu et al. (2023) [25].

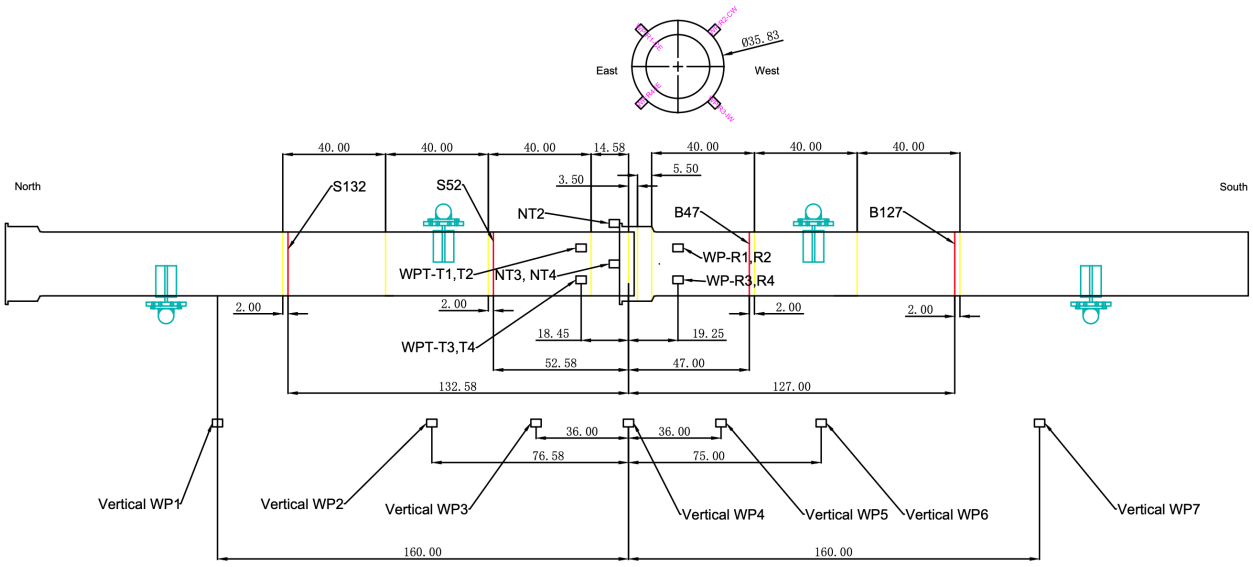


Fig. 6.19. HRDIP four-point bending experiment strain gauge, wire pots, and position transducer instrumentation plan

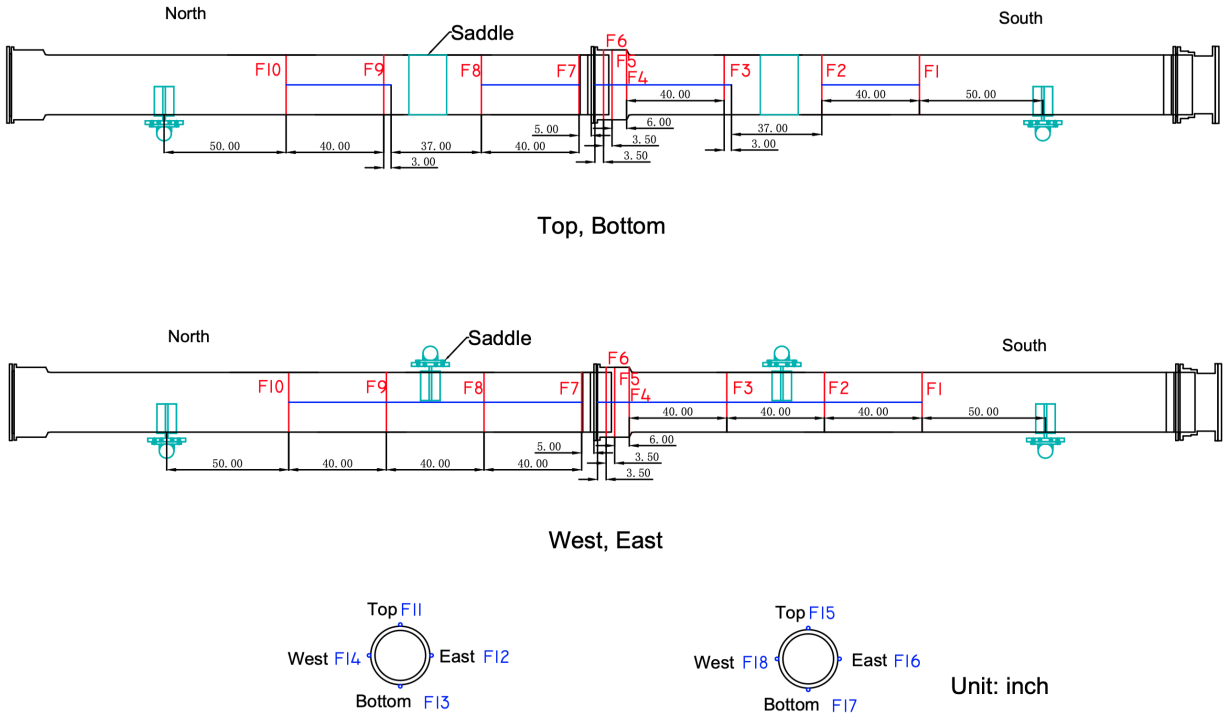


Fig. 6.20. HRDIP four-point bending experiment DFOS instrumentation plan

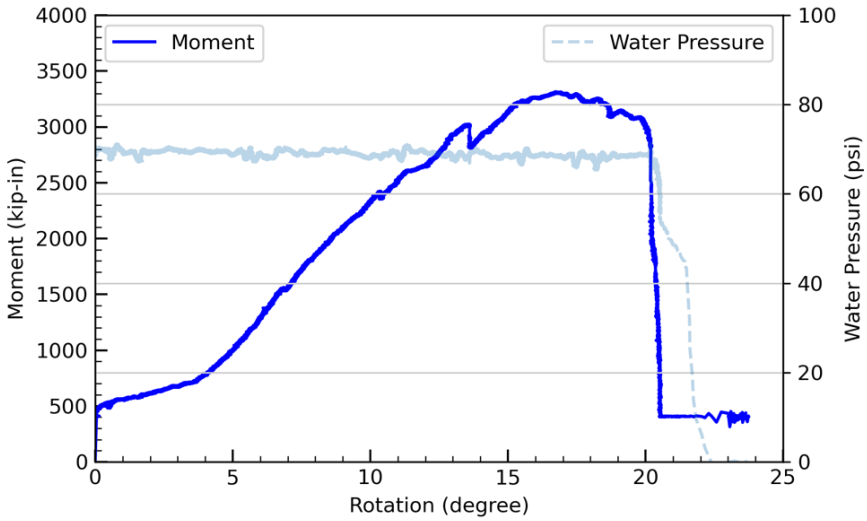


Fig. 6.21. Moment, rotation, and water pressure of HRDIP four-point bending experiment

6.2.3 Four-Point Bending Performance

During the experimental testing, the pipes were filled with water and pressurized to a level of 70 psi. A monotonic force, perpendicular to the longitudinal axis of the pipeline, was applied at the center point of the load transfer beam. This force was then transferred to the pipes through the two loading saddles. Using Equation 4.5 (where Δv_1 and Δv_2 were computed using WP1 and WP7; d_1 and d_2 are the distance between the end support and the wire pot, which is 360 inches), the moments and rotations of the specimen were calculated. The results are visualized in Figure 6.21. The maximum observed rotation reached approximately 20 degrees, nearly three times the manufacturer's specified deflection capacity of 7 degrees, with a maximum moment of 3,313 kip-in. In addition, no water leakage was detected in the specimens until the pipe joint reached a rotation of approximately 20 degrees.

Failur Mode and Mechanism

Figure 6.22 shows the figure of the specimen with large deformation and failure. Notably, a large crack was observed on the spigot while the specimen reached about 20-degree rotation, followed by significant water leakage. On the other hand, no apparent failure was observed on the bell section of the specimen. In addition, Figure 6.23 illustrates a portion of the gland that experienced failure on the top side, where the bolts were bent. This failure occurred due to the interaction between the gland and the spigot during the downward pushing of the pipe. As the gland exerted pressure against the spigot, a large shearing force was generated, leading to the cutting of the gland material. Consequently, this introduced significant deformation



Fig. 6.22. Large deformation and failure of HRDIP

to the surrounding bolts, resulting in their bending.

The cracks observed on the spigot of the specimen originated from the edge of the spigot projection, located approximately 2-1/4 inches from the spigot end, as shown in Figure 6.24. During the pushing-down process, the top side of the spigot exhibited a tendency to move inward towards the bell, while the bottom side tended to move away from the bell. Consequently, the bottom side of the spigot projection made full contact with the locking ring, resulting in a brittle tensile failure at the bottom side of the edge of the spigot projection. This specific location experienced a high stress concentration due to the contact forces and interactions between the spigot and the locking ring.

The initial crack at the edge of the bottom of the spigot projection then proceeded to propagate through the sides towards the top side. Shear forces primarily drove this propagation. The combination of the stress concentration at the edge of the spigot projection and the shear forces resulted in the formation and progression of the observed cracks, ultimately leading to the failure of the spigot and the subsequent water leakage.

Axial Strain

The axial strain results measured by the conventional strain gauges attached to the specimen are shown in Figure 6.25. Generally, the top side of the pipe (12 o'clock position) experiences compression. In comparison, the bottom side (6 o'clock position) undergoes tension. Theoretically, the axial strains at the east side (9 o'clock) and west side (3 o'clock) would



Fig. 6.23. Falure of the gland and bolt of HRDIP

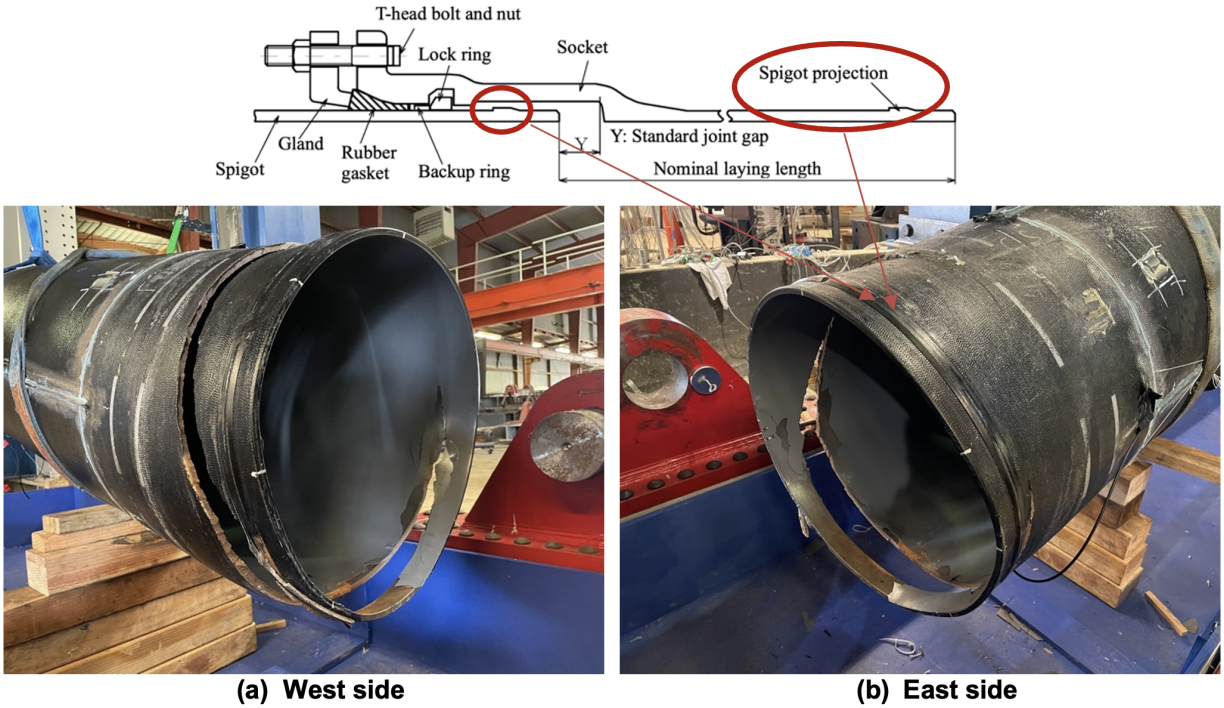


Fig. 6.24. Spigot failure of HRDIP test

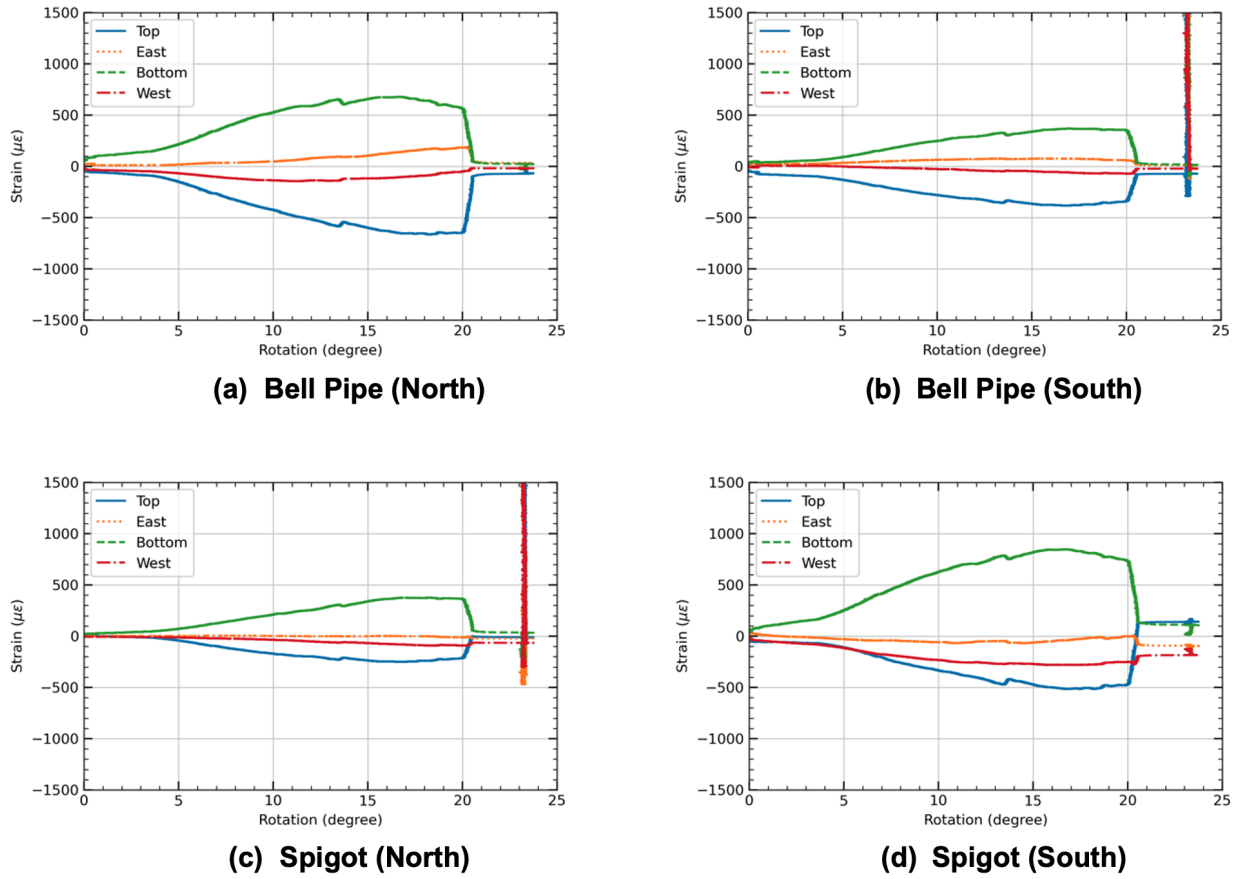


Fig. 6.25. Axial strain and joint rotation of HRDIP four-point bending experiment

be close to zero. However, due to installation constraints, the strain gauges were attached with a 9-degree (i.e., 2 inches) offset from the quarter points. As a result, the strain gauges labeled "east" were positioned 9 degrees towards the bottom side (6 o'clock), causing them to measure tension. Conversely, the strain gauges labeled "west" were located 9 degrees towards the top side (12 o'clock), leading to compression measurements.

The axial strain results measured by DSS are shown in Figure 6.26 and Figure 6.27. The strain gauge data are also plotted to show the two data sets are compatible with each other. The plots show the strain distribution when the total rotation reached about 19 degrees. All the strain distributions of the sensors are plotted from the north to the south. Consistent with the observations made from the strain gauge data, the plots illustrate that the top side of the pipe (12 o'clock) was subjected to compression, while the bottom side (6 o'clock) experienced tension. Additionally, the strains measured at the sides of the pipe (i.e., 3 o'clock and 9 o'clock) were generally minimal. This observation aligns with the pipe's theoretical expectation under bending forces.

Figure 6.26 shows the axial strain results of the bell pipe. Compressive strains were ob-

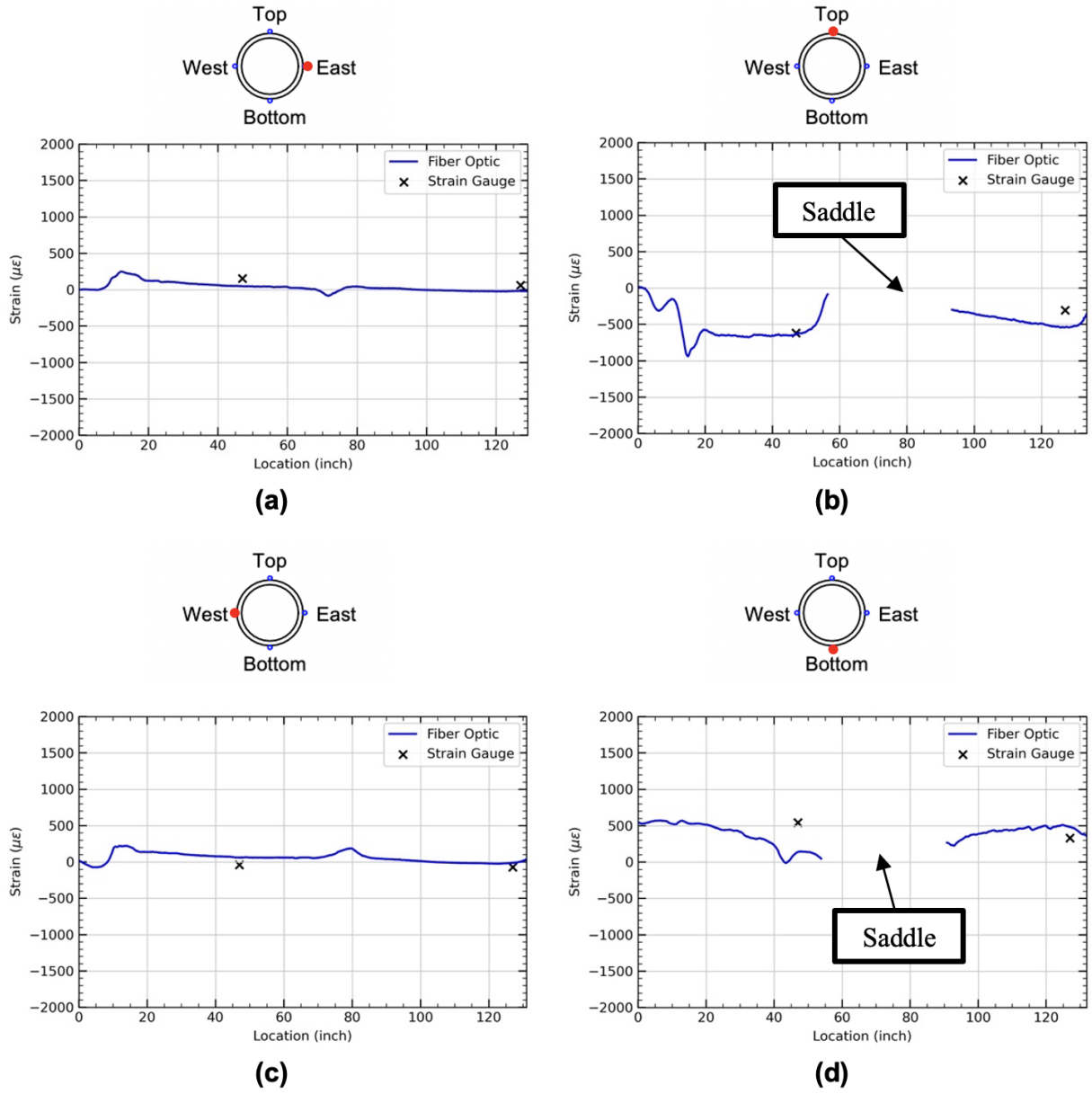


Fig. 6.26. Axial strain development of bell pipe under 19-degree rotation condition of HRDIP four-point bending test. (a) East side, (b) Top side, (c) West side, (d) Bottom side

served on both the west and east sides (3 o'clock and 9 o'clock positions) of the bell section (i.e., about 0 to 10 inches location), as depicted in Figure 6.26a and Figure 6.26c. This compressive strain pattern can be attributed to the expansion of the bell caused by the locking ring. As the bell expands, a moment is introduced on its surface, leading to compressive strains on the bell's outer surface. On the top side, as shown in Figure 6.26b, relatively small compressive strains were observed on the bell section. This might be because the split of the locking ring was located on the top side. While the pipe is being pushed downward, the locking ring might deformed or moved upward in order to tolerate the movement, which might result in tensile stress at the bell section.

Following the bell section (i.e, about 10 to 20 inches location), large tensile strains can be observed on the west and east side of the bell pipe, as shown in Figure 6.26a and Figure 6.26c, and large compressive strains on the top side of the bell pipe, as shown in Figure 6.26b. These locations correspond to the transition location from the bell to the pipeline. This phenomenon can be attributed to the geometry and wall thickness changes at this transition region. The altered geometry and wall thickness can lead to localized stress concentrations, resulting in the observed strain patterns.

Examining Figure 6.26a and Figure 6.26c in the axial strain results, noticeable strain fluctuations were observed at the loading saddle locations, which are situated at approximately 70-80 inches locations. These fluctuations were raised due to the concentrated forces acting within these regions during the bending tests. As a result, the pipe experiences larger deformation in these specific areas, leading to larger strains.

Figure 6.27 presents the axial strain results of the spigot under conditions where the rotation reaches approximately 19 degrees, which is close to the failure stage. The observed strain patterns align with the bending theorem, with compressive strains on the top side (12 o'clock) and tensile strains on the bottom side (6 o'clock) of the spigot. Additionally, minimal strains are recorded on the west and east sides (3 o'clock and 9 o'clock), as expected.

However, it is noteworthy that relatively smaller tensile strains were observed at the bottom side of the spigot near the bell, specifically in the 100-120 inches location shown in Figure 6.27d. This phenomenon might be attributed to the yielding or cracking at the bottom side of the spigot prior to failure (when the specimen reached approximately 20 degrees of rotation). The existence of these potential yielding/ cracking areas affected the proper transfer of stress at these particular locations, resulting in smaller tensile strains being measured.

Furthermore, a significant deformation was observed on the spigot near the bell. This deformation and the Poisson's ratio effect may contribute to the small tensile strains measured in this region. The axial deformation and associated stress concentration near the bell might lead to a reduction in tensile strains. The presence of yielding/ cracking areas and the Poisson's effect are potential factors influencing the observed strain behavior in the spigot near the bell.

Lastly, a fluctuation of the strains near the loading saddle, approximately 50-60 inches locations, was observed on the west and east sides of the spigot, as shown in Figure 6.27a and Figure 6.27c. These strain fluctuations can be attributed to the concentrated forces

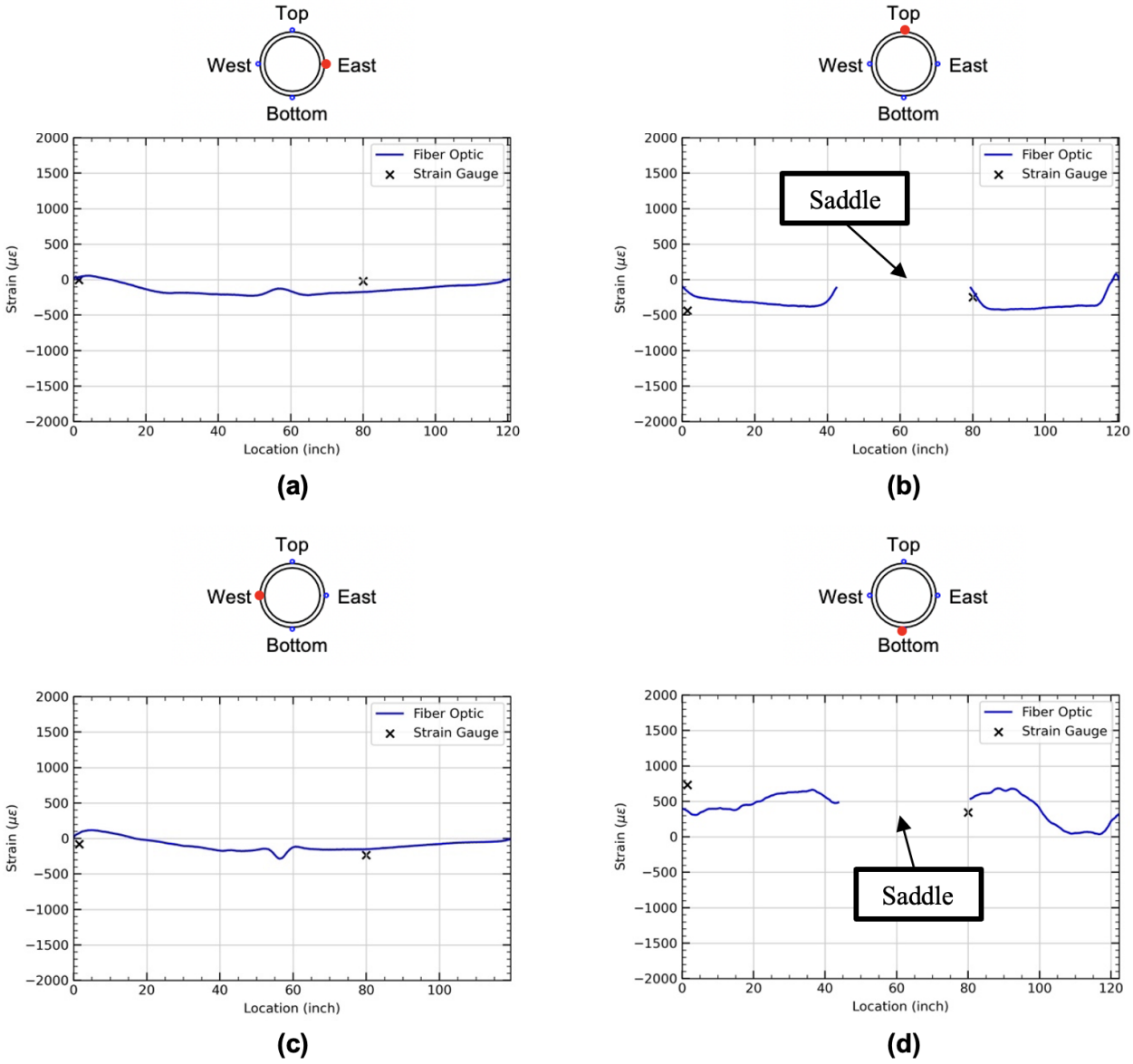


Fig. 6.27. Axial strain development of spigot under 19-degree rotation condition of HRDIP four-point bending test. (a) East side, (b) Top side, (c) West side, (d) Bottom side

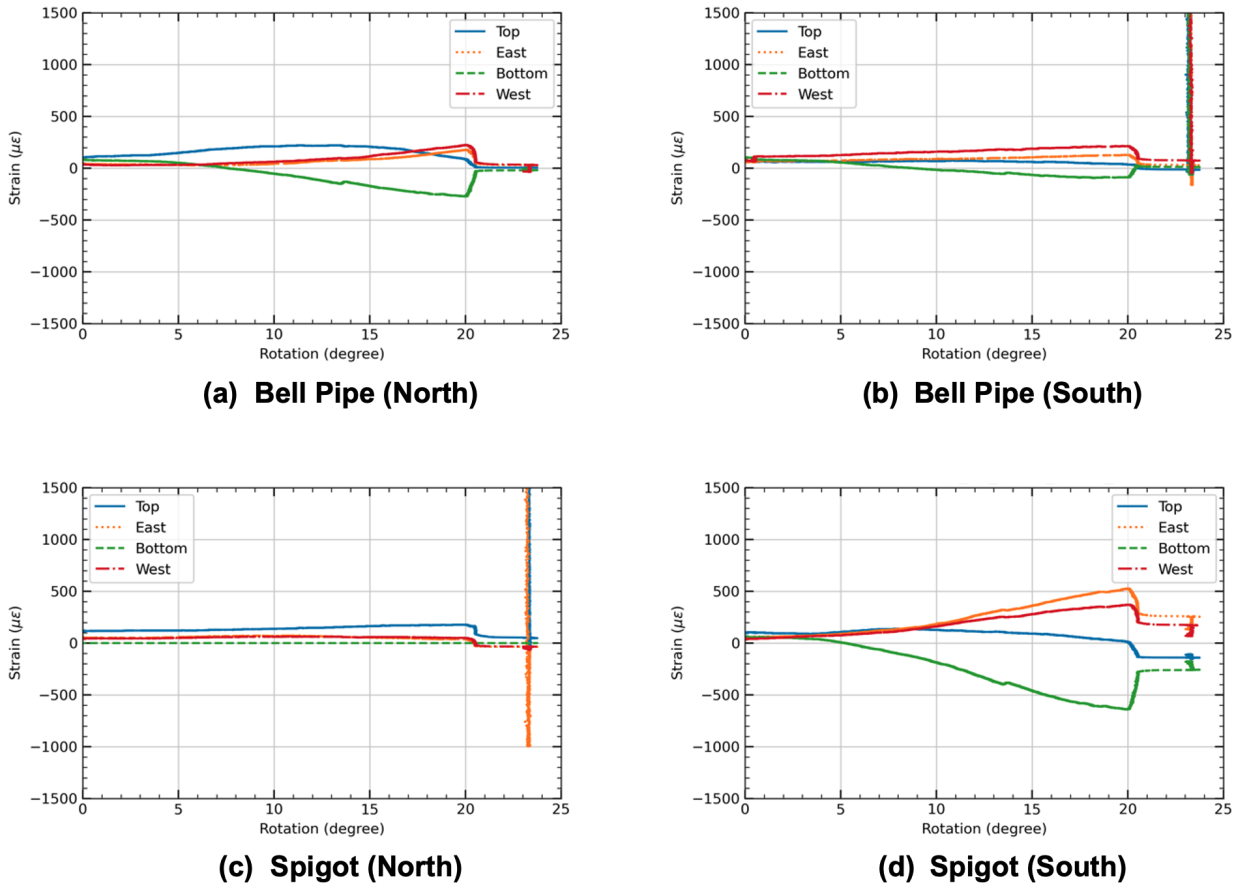


Fig. 6.28. Hoop strain and joint rotation of HRDIP four-point bending experiment

applied at these locations. The concentrated force application created a localized stress concentration, resulting in large deformation of the pipe in that region. As a consequence, larger strain values were recorded.

Hoop Strain

Figure 6.28 displays the relationships between the hoop strains, measured by strain gauges, and the rotation of the pipe specimen. Initially, when the specimen rotation is small (less than 3 degrees), the strains in the circumferential direction are primarily opposite in direction to those in the longitudinal direction, but with a smaller magnitude. This behavior can be attributed to the Poisson's effect, which refers to the lateral expansion or contraction of a material due to axial deformation.

However, as the rotation increases beyond this small range, the strain results exhibit a different pattern. The bell pipe and the spigot demonstrate expansion at the east and west sides, while experiencing shrinkage at the top and bottom sides. This distinctive strain

pattern indicates that the pipe undergoes a squatting deformation. A clear mechanism of the pipe deformation is provided in the following section using the DSS data.

In Figure 6.29, the hoop strain results measured by DSS are presented. The figures include the results obtained from sensor F4, which was placed on the bell end, sensor F5 located in the middle of the bell, sensor F6 positioned on the centerline, and sensor F7 on the spigot, which is the circumferential sensor closest to the bell.

The results from sensor F4 indicate that the top and bottom sides (12 o'clock and 6 o'clock) of the bell were experiencing compression, while the west and east sides (3 o'clock and 9 o'clock) were expanding. These strain distributions suggest that the bell pipes undergo eccentric squatting during bending. Similar strain patterns can be observed on the other circumferential sensors located on the bell pipes (i.e., F1-F3).

For sensors F5 and F6, the results indicate that the bottom side of the bell was expanding. This expansion is attributed to the contact between the bottom of the spigot and the invert of the bell during bending. This contact causes the bottom side of the bell to expand.

Sensor F7, placed on the spigot, exhibits a strain distribution where the top and bottom sides (12 o'clock and 6 o'clock) are shrinking, while the east and west sides (3 o'clock and 9 o'clock) are expanding. This behavior is attributed to the bottom side of the spigot bearing against the invert of the bell, leading to compression on the bottom side. Furthermore, as the spigot is bent, the top side contacts the crown of the bell, resulting in a concentrated compressive strain on the top of the spigot. Similar strain patterns can be observed from other sensors placed on the spigot (i.e., F8-F10), with the magnitude of the strain decreasing as the distance from the sensor to the bell increases.

6.2.4 Conclusion of HRDIP Experiment

The four-point bending evaluation of the 24-inch Kubota NS-type ductile iron pipe demonstrated substantial rotational capacity, reaching a maximum applied moment of 3,313 kip-in. The joint accommodated an ultimate rotation of approximately 20 degrees—significantly exceeding the manufacturer's specified deflection limits—while maintaining a watertight seal with no leakage detected prior to failure. The ultimate failure sequence initiated as a localized tensile crack at the bottom of the spigot projection, which subsequently propagated upward along the springlines due to shear forces, resulting in the complete structural failure of the spigot.

High-resolution data acquired from the integrated distributed strain sensors (DSS) and discrete strain gauges revealed complex, localized deformation mechanics throughout the loading protocol. The cross-sectional strain profiles indicated pronounced longitudinal compression at the top and bottom of the pipe barrel, coupled with outward expansion along the springlines. Furthermore, the sensors captured concentrated expansive strains at the bottom of the bell section, directly quantifying the severe localized bearing interaction between the bell and the inserted spigot during extreme rotation.

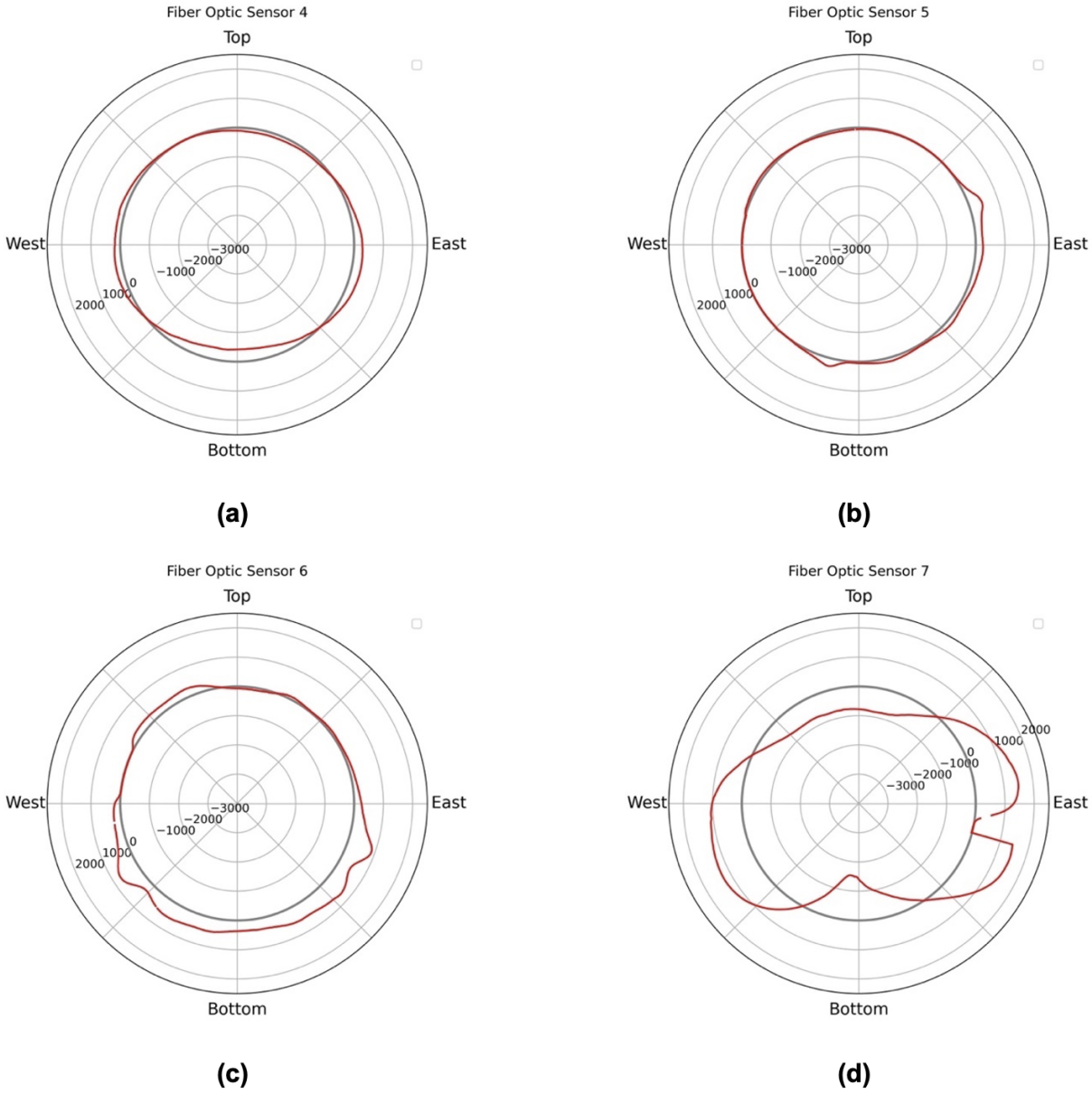


Fig. 6.29. Strain distribution in the circumferential direction under 19-degree rotation condition of HRDIP four-point bending test. (a) sensor on the bell end (b) sensor on the center of the bell (c) sensor on the centerline of the specimen (d) sensor on the spigot

Chapter 7

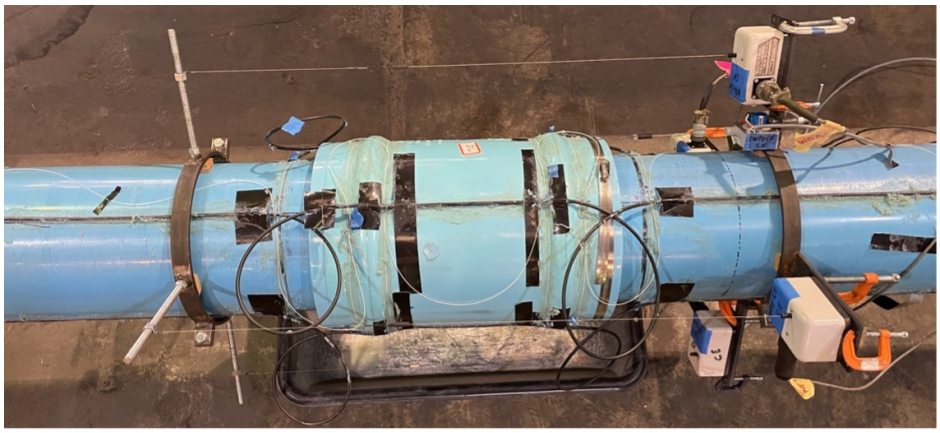
Component-Level Mechanics of Joints for iPVC Pipes

7.1 Introduction of iPVC Pipe

The 8-inch AWWA C900 DR14 integrally formed Polyvinyl Chloride (iPVC) pipe is the focus of a comprehensive experimental testing program aimed at evaluating its structural performance and joint behavior under different loading conditions. Owing to its corrosion resistance and ability to sustain large deformations, iPVC piping systems are increasingly considered for improving the seismic resilience of underground water distribution networks. Understanding their reliability and failure mechanisms under axial and bending demands is therefore essential for assessing their performance during ground deformation events.

To systematically investigate joint behavior and failure mechanics, three distinct types of fittings and restraint systems were evaluated: plastic fittings with toothed rubber gaskets, EBAA 1900 restraints, and RCT restraints (Figure 7.1). In these setups, the pipe is typically inserted into a bell or restraint through a rubber gasket that provides a watertight seal while the restraint mechanism restricts relative movement between the pipe segments.

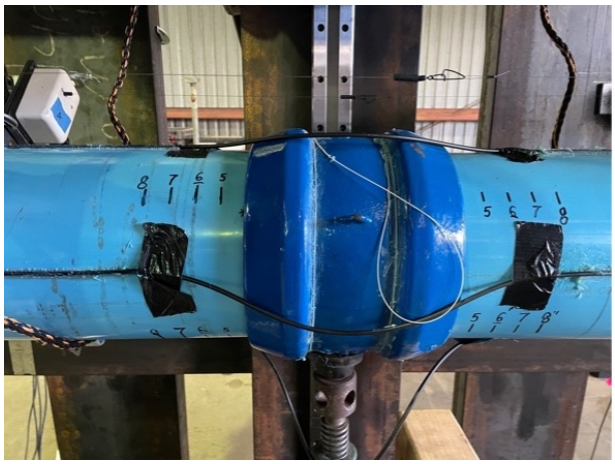
The plastic fittings rely on internal rubber gaskets designed with multiple teeth that engage the pipe surface to prevent leakage and resist axial separation. Two specific gasket designs were evaluated: TurnerLok (Figure 7.2a) and ReiberLok (Figure 7.2b). The ReiberLok gasket features a larger number of smaller teeth, while the TurnerLok design uses fewer, larger teeth. The EBAA 1900 and RCT restraints, conversely, are both constructed from ductile iron and rely on fundamentally different mechanical locking strategies. The EBAA 1900 restraint is an external system utilizing four connecting rods to prevent pipe separation. Two bolts apply clamping forces to serrated rings, generating normal pressure and relying on friction between the pipe surface and the rings to resist pullout. In contrast, the RCT restraint acts as an internal, one-way locking system using directionally oriented teeth; it allows the pipe to slide into the restraint but prevents withdrawal. Because of these distinct configurations, the pipe preparation varied: the EBAA 1900 restraint was applied directly



(a) iPVC fitting



(b) EBAA 1900 Restraints



(c) RCT Restraints

Fig. 7.1. Experimental test setups for the jointed pipes equipped with different fittings and restraints

over an intact joint, retaining the pipe's standard bell section. However, for both the RCT restraints and the plastic fittings, the standard bell section was removed, and two identical plain-end pipe segments were connected using the respective fittings alongside internal rubber gaskets.

The experimental testing program was structured into three primary loading phases to isolate the performance of these specific mechanisms. The first phase involved pure axial tension tests specifically focused on evaluating the locking effectiveness of the TurnerLok and ReiberLok gaskets within the plastic fittings. Results demonstrated that the ReiberLok gasket provided superior resistance to pullout compared to the TurnerLok configuration. Consequently, the ReiberLok gasket was selected as the standard configuration for all subsequent testing phases involving plastic fittings. The second phase examined axial



(a) TurnerLok **(b)** ReiberLok

Fig. 7.2. Gaskets for the plastic fittings

compression behavior, assessing the contraction capacity and structural response of pipe specimens assembled solely with plastic fittings with ReiberLok gaskets. Finally, to evaluate deformation capacity and failure behavior under bending, the test program concluded with four-point bending tests. This final phase evaluated the comprehensive testing matrix, utilizing specimens equipped with RCT restraints, EBAA 1900 restraints, and plastic fittings with ReiberLok gaskets.

7.2 Tension Performance

7.2.1 Experimental Setup and Instrumentation

A specialized testing apparatus was designed and constructed to evaluate the tensile and compressive behavior of jointed iPVC pipe assemblies. The system was developed with sufficient flexibility to accommodate both loading conditions through minor modifications while maintaining the same overall structural framework. This section describes the configuration used for the axial tension tests.

The apparatus consisted of a self-reacting, closed-loop structural frame designed to resist the large forces generated during testing without relying on external reaction elements. The frame was constructed using two 16.5-ft-long W14×132 wide-flange beams serving as the longitudinal members and two 7-ft-long W10×112 wide-flange beams serving as the transverse members. To facilitate assembly and load transfer, three reinforced openings with stiffeners were fabricated into each transverse beam. The two outer openings were used to connect the longitudinal and transverse beams, forming a rigid closed-loop frame, as illustrated in Figure 7.3 and Figure 7.4. The central opening served as the primary attachment point for the pipe specimen on both the reaction and loading sides.

Tensile loading was applied using a hollow hydraulic cylinder with an ultimate capacity of 132 kips and a stroke length about 6 inch. A hollow actuator was selected to allow the central loading rod to pass directly through the cylinder and be secured using a washer plate

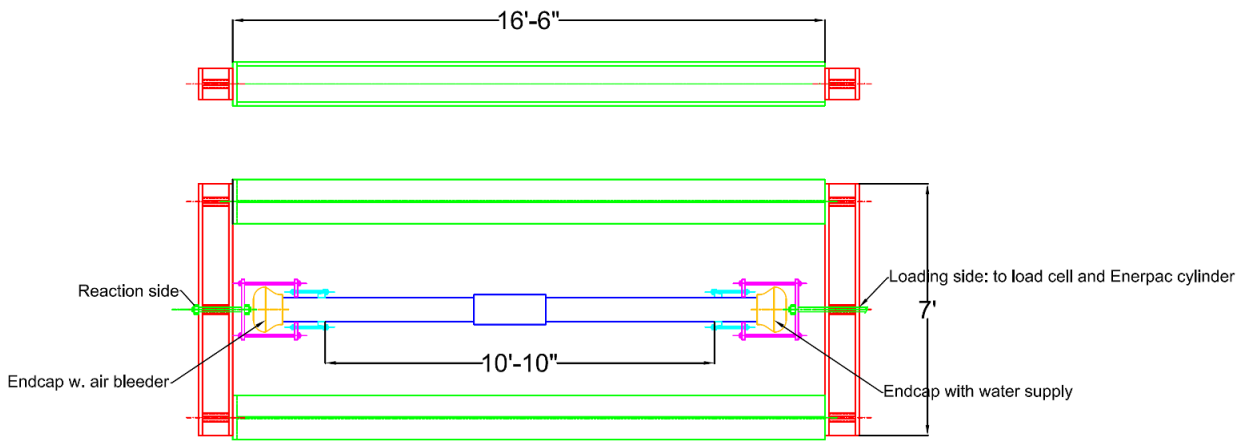


Fig. 7.3. Schematic drawing of the iPVC tension test experimental setup

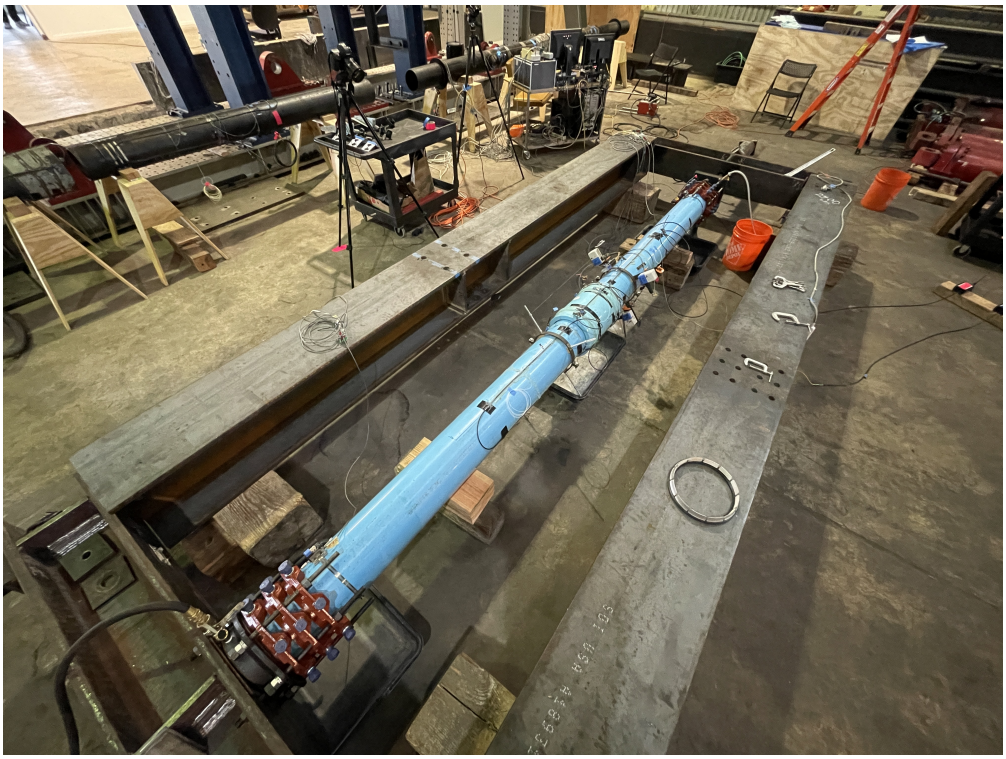


Fig. 7.4. Complete assembled iPVC tension test setup

and nut assembly. To accurately measure the applied load throughout testing, a load cell was installed between the hydraulic cylinder and the transverse reaction beam.

A specialized gripping system was developed to safely transfer tensile forces from the loading apparatus to the iPVC pipe specimen. At both ends of the specimen, three MegaLug restrainers (red assembly in both ends of the specimen in Figure 7.4) were attached to an endcap to provide a reliable mechanical connection. While the same restraining concept was used on both ends, the connection details differed slightly between the reaction and loading sides. On the reaction side, the MegaLug assembly was connected directly to the transverse beam using four 3/4-in.-diameter high-strength threaded rods. On the loading side, an additional 2-in.-thick steel transition plate was introduced to accommodate the hydraulic actuator. The four threaded rods from the MegaLug assembly were attached to this plate, which contained a central opening through which a 1-1/4-inch-diameter high-strength Williams rod was passed. This rod connected the transition plate to the hydraulic cylinder, enabling the tensile force to be transferred to the specimen.

To simulate operating conditions and monitor joint performance under pressure, the pipe specimen was internally pressurized during testing. An air-bleeder valve and pressure gauge were installed on the loading side of the specimen, while water was supplied through a hose connection located on the reaction side. The test specimen consisted of two identical segments of iPVC pipe joined at their center by a plastic sleeve fitting. Because the specimen configuration was symmetric about the joint, the centerline of the fitting was defined as the specimen centerline for all measurements and observations.

The tension testing program was conducted using two separate pipe assemblies to evaluate the axial performance of plastic fittings equipped with different restrained gasket systems. Specifically, two commercially available gasket designs, the TurnerLok and ReiberLok gaskets, were investigated. Both gasket types are intended to provide watertight sealing while resisting axial pullout through mechanical engagement with the pipe surface. By testing identical pipe assemblies with each gasket configuration, the influence of gasket design on joint tensile capacity and failure behavior could be directly assessed. The complete testing matrix for the tension phase is summarized in Table 7.1.

Table 7.1. Summary of iPVC tension test specimens

Specimen Name	Gasket	Date
Specimen-R	ReiberLok	10/17/2023
Specimen-T	TurnerLok	10/20/2023

The experimental setup and the specimen were extensively instrumented to capture the mechanical response during testing. The instrumentation consisted of a load cell, wire potentiometers (wire pots) measuring the relative displacement of the pipes across the joint, and an additional position transducer monitoring the displacement of the fitting sleeve on the loading side. Specifically, to measure the displacement across the joint, four wire pots were

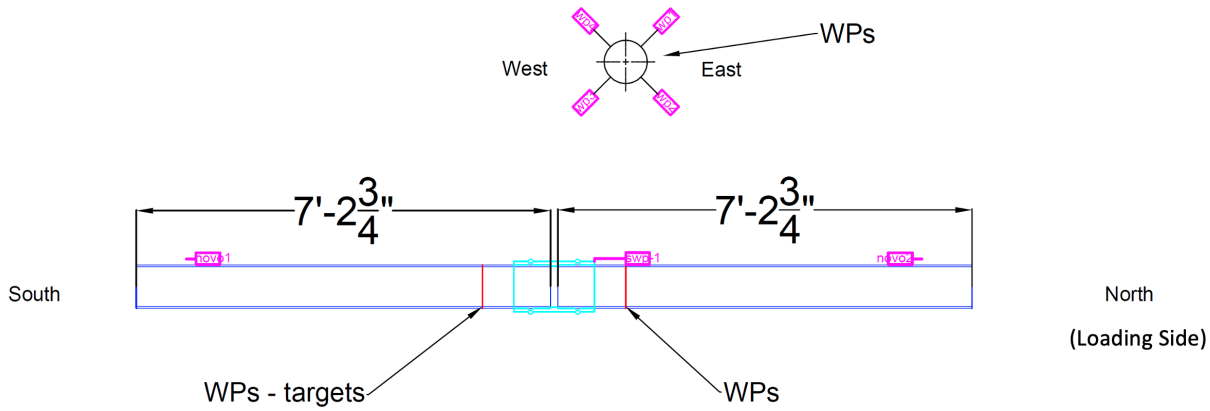


Fig. 7.5. Position transducers for displacement monitoring of the joint of the iPVC tension test

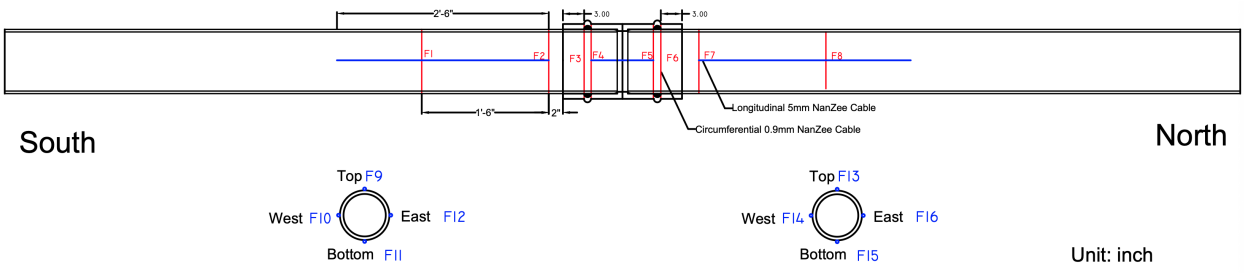


Fig. 7.6. Instrumentation plan of fiber optic sensors of the iPVC tension test specimens

distributed at 90-degree intervals around the circumference of the pipe. The main bodies of these sensors were affixed to the north (loading) side of the pipe, while their target wire attachments were anchored to the south (fixed) side, as shown in Figure 7.5.

To monitor the localized deformation mechanisms of the pipes during testing, DSS was deployed. The fiber optic cables were affixed to the pipe surfaces using 3M Scotch-Weld DP8010 structural epoxy. The overall layout and specific locations of the sensors are illustrated in Figure 7.6. The 5-mm cables (represented by blue lines in the schematics) were installed in the longitudinal direction. These longitudinal sensors, designated F9 through F16, were continuously attached along the lengths of both pipe segments at 90-degree intervals around the circumference. To capture cross-sectional expansion and contraction, the 0.9-mm cables (represented by red lines) were deployed to measure circumferential strains. These sensors, designated F1 through F8, were positioned strategically across the assembly. On the main bodies of both pipe segments, two circumferential sensors were installed with approximately 18 inches of longitudinal spacing. Additionally, to closely monitor the structural interaction at the joint, circumferential sensors were placed immediately on both sides

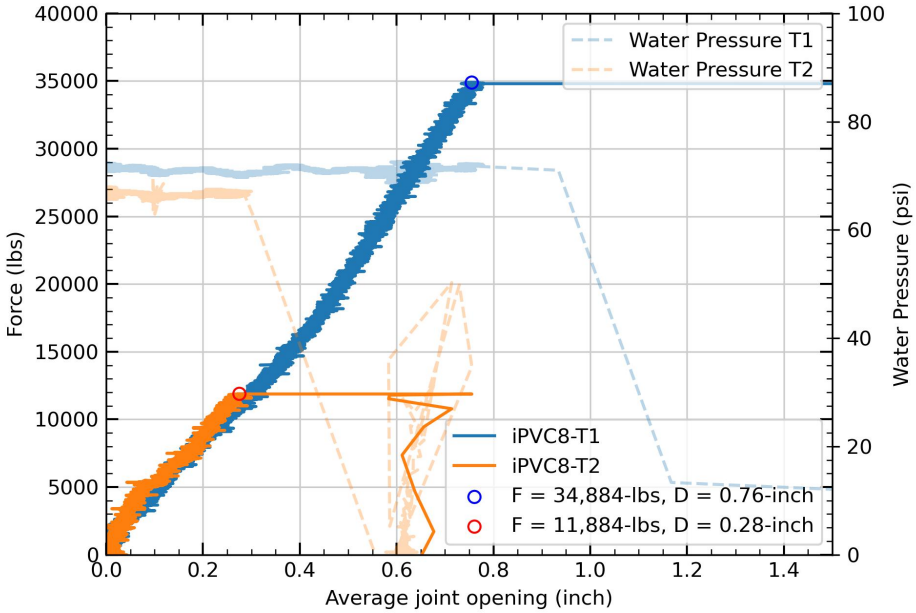


Fig. 7.7. Axial force, average joint opening, and water pressure results of the specimens. Note that iPVC8-T1 indicates Specimen-R while iPVC8-T2 is Specimen-T

of each locking gasket. Because the plastic fitting houses two independent gaskets to lock the respective pipe segments, a total of four circumferential sensors were wrapped around the fitting assembly.

7.2.2 Failure Mode

The pipe assemblies were filled with water and internally pressurized to approximately 70 psi prior to loading. A monotonic tensile force was then applied along the longitudinal axis of the pipeline. The average joint opening for each specimen was calculated as the mean of the reading from the four wire pots surrounding the joint. The relationship between the applied axial force and the average joint opening is presented in Figure 7.7. Specimen-R (equipped with the ReiberLok gasket) achieved a maximum axial capacity of 34,884 lbs at a corresponding joint displacement of 0.76 inches. In contrast, Specimen-T (equipped with the TurnerLok gasket) reached a maximum axial force of only 11,884 lbs at a displacement of 0.28 inches. For both specimens, ultimate failure was characterized by a sudden drop in internal water pressure occurring simultaneously with the peak axial force, indicating a critical loss of the joint's watertight seal.

The force-displacement trajectories prior to failure were highly consistent between the two specimens, indicating the uniformity of the initial experimental setups. However, Specimen-

T failed at a significantly earlier stage compared to Specimen-R. This discrepancy in ultimate capacity is primarily attributed to the fundamental differences in the gasket designs. It is hypothesized that the TurnerLok gasket, which utilizes fewer but larger teeth, introduced severe localized stress concentrations into the iPVC pipe wall, precipitating an earlier localized failure. Furthermore, as discussed in subsequent sections, the mechanical behavior of the jointed segments diverged as the loading increased, further contributing to the substantial difference in ultimate failure loads. A summary of the tension test results is provided in Table 7.2.

Table 7.2. Summary of iPVC tension test results

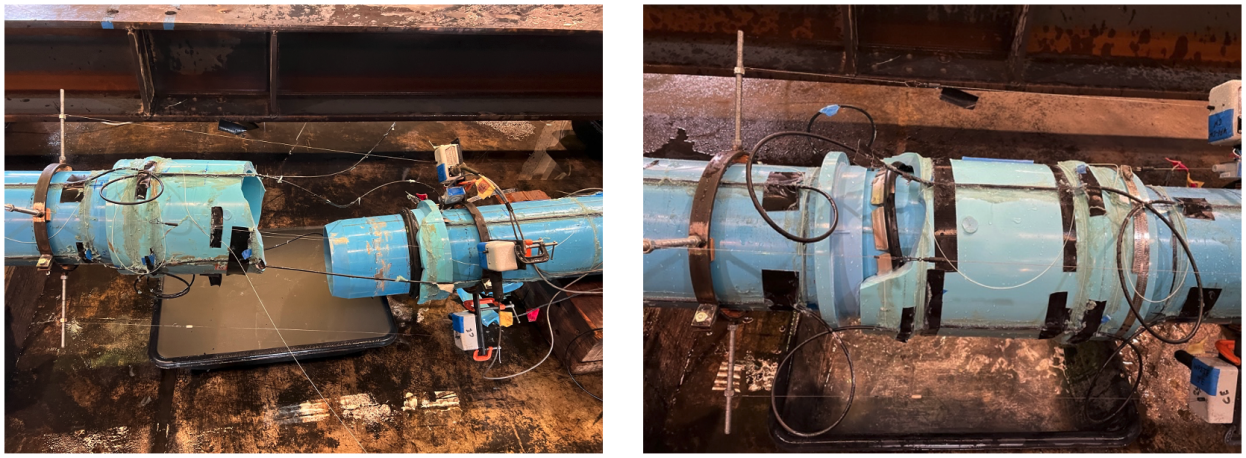
Specimen	Max. Axial Force (lbs)	Avg. Joint Opening (inch)	Gasket
Specimen-R	34,884	0.76	ReiberLok
Specimen-T	11,884	0.28	TurnerLok

For both test specimens, ultimate failure occurred within the joint segment adjacent to the locations where the metallic teeth engaged the pipe wall. This explicitly indicates that the failure mechanism was primarily driven by the mechanical interaction between the gasket teeth and the iPVC pipe material. The resulting physical failure modes for both specimens are illustrated in Figure 7.8. Although localized shear and tensile stresses at the gasket interfaces likely governed the ultimate capacity in both cases, the resulting macroscopic failure patterns differed significantly. In Specimen-R (equipped with the ReiberLok gasket), the failure propagated entirely around the circumference of the fitting. Conversely, in Specimen-T (equipped with the TurnerLok gasket), the failure was highly localized, occurring exclusively on the top side of the joint.

This divergence in failure patterns is attributed to the distinct geometric designs of the restraining gaskets. The ReiberLok gasket features numerous smaller teeth, which effectively distribute the applied axial load more evenly across a larger contact area. By engaging more teeth, the transfer force per tooth is minimized, thereby reducing localized stress concentrations around any individual point. In contrast, the TurnerLok gasket utilizes fewer, larger teeth, which concentrate greater stresses at their individual boundaries. This concentrated stress profile likely precipitated the premature, localized failure observed in Specimen-T.

Axial Strain

Figure 7.9 illustrates the relationship between the applied axial load and the longitudinal strain measured at the midpoints between circumferential sensors F1 and F2 (south pipe), and F7 and F8 (north pipe). While the data confirm that all pipe segments experienced the expected overall tensile stresses, spatial variations in strain magnitude were observed across different circumferential locations for both specimens.



(a) Specimen-R (ReiberLok gasket) (b) Specimen-T (TurnerLok gasket)

Fig. 7.8. Failure of Specimen-R and -T of iPVC tension test

For Specimen-R, the longitudinal strain profiles on the south pipe exhibited a slight variation between the top and bottom sensors, suggesting a minor upward bending of the pipe during axial loading. The strain development on the east and west sides remained symmetric and linear during the initial loading phase. However, as the applied load approached approximately 16,000 lbs, the rate of strain increase on these lateral sides noticeably decelerated. This divergence indicates a localized reduction in stress transfer, likely caused by cross-sectional elongation (ovalization) of the iPVC pipe. As the pipe deformed, the locking gasket lost partial engagement on the east and west sides, resulting in preferential force transfer through the top and bottom of the joint. This localized phenomenon is schematically illustrated in Figure 7.10.

In contrast, the north pipe of Specimen-R demonstrated a different and more complex strain distribution. Comparisons of the diametric sensors revealed simultaneous downward bending (evidenced by top versus bottom strains) and eastward bending (evidenced by west versus east strains). This complex multi-axis deformation pattern is likely attributable to initial relative movement or seating slip between the internal locking gasket and the pipe surface. As the components settled under the applied load, the gasket may have engaged the pipe along a slightly skewed, non-vertical plane. This asymmetric engagement would inherently induce secondary bending moments when subjected to the primary axial tension.

For Specimen-T (equipped with the TurnerLok gasket), the strain distribution on the south pipe revealed that while the longitudinal strain developments on the east and west sides were symmetric, their magnitudes were considerably smaller than those measured at the top and bottom. This discrepancy is largely attributed to the uneven installation and seating of the locking gasket. The data suggest that the gasket teeth on the top and bottom achieved superior initial engagement with the pipe wall, facilitating more effective stress transfer compared to the lateral sides. Mechanically, the TurnerLok gasket possesses lower flexural

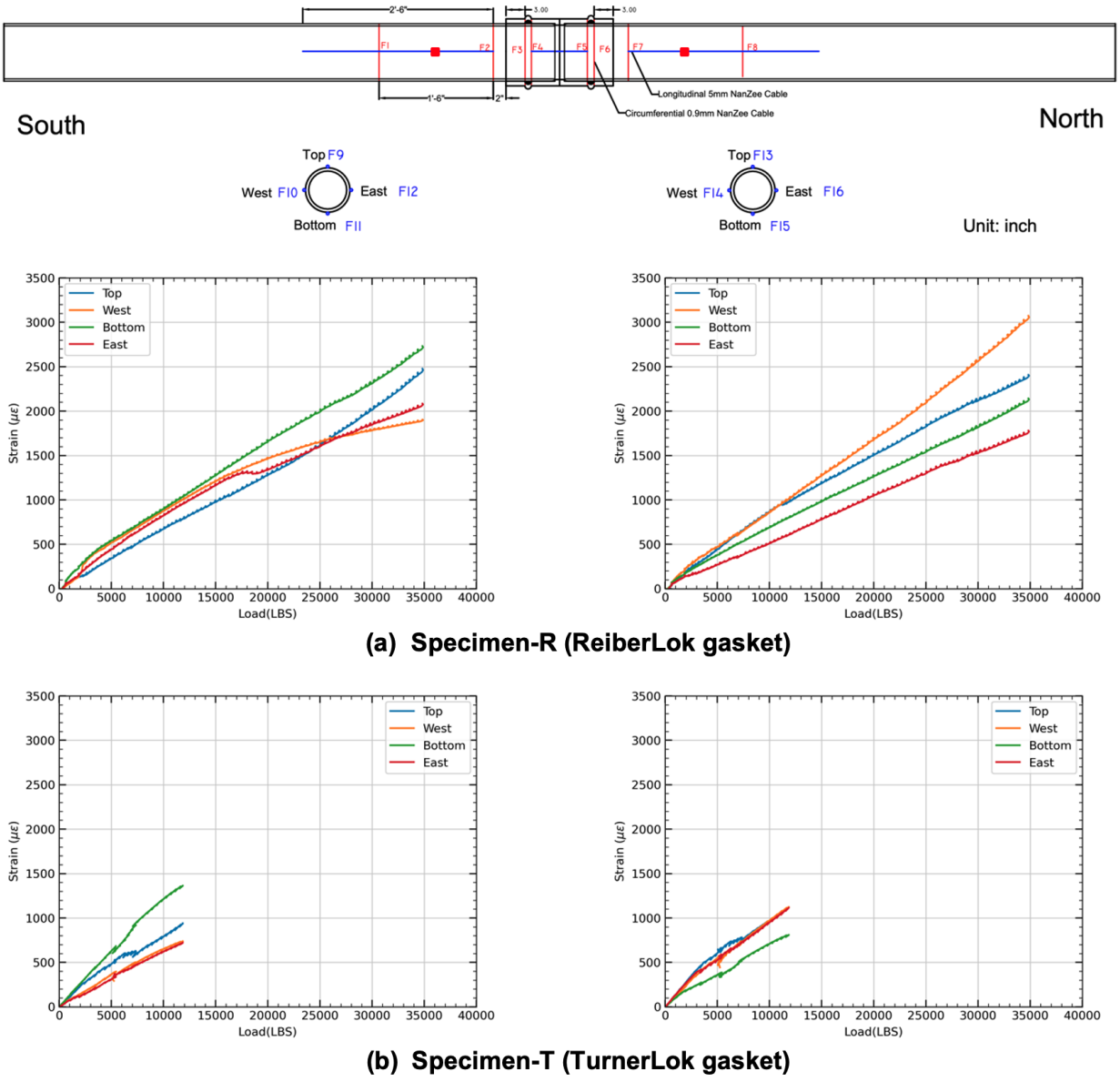


Fig. 7.9. Axial strain vs load of iPVC tension test. (Left) South pipe. (Right) North Pipe

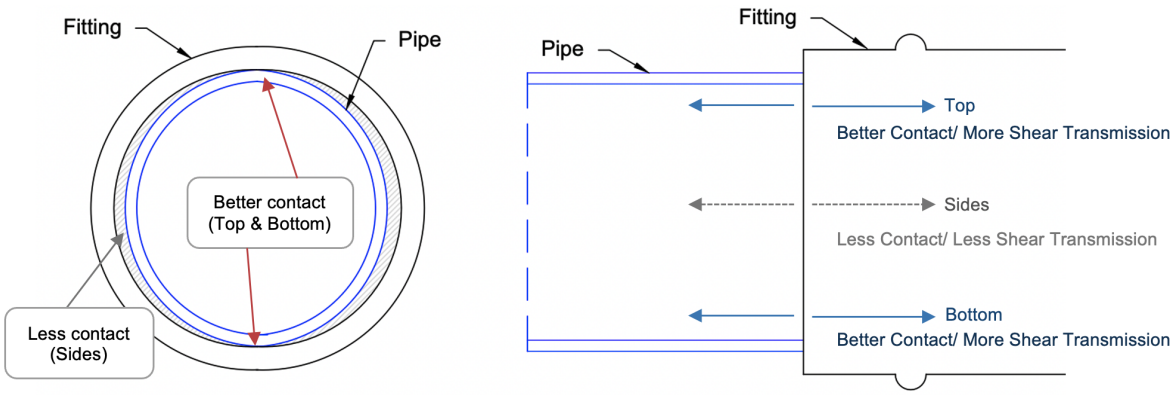


Fig. 7.10. Sketch of pipe-fitting deformation mechanism

stiffness than the ReiberLok gasket, making it highly susceptible to geometric distortion and challenging to maintain as a perfect circle during the assembly process. Consequently, this imperfect initial gasket-pipe interaction caused the tensile strains to develop asymmetrically across the pipe cross-section from the very onset of loading.

Conversely, on the north pipe of Specimen-T, the longitudinal strains developed relatively uniformly across most of the circumference, with a notable exception at the bottom sensor location. The strain magnitude measured at the bottom was significantly lower than at the other three monitored positions. Similar to the behavior observed on the south pipe, this localized reduction in strain is indicative of an imperfect seating of the locking gasket. Specifically, the data indicate that the bottom segment of the gasket teeth failed to fully engage with the iPVC pipe surface, thereby severely reducing the axial force transferred through the lower region of the joint.

For both test specimens, the location of the ultimate physical rupture directly correlated with the regions exhibiting the greatest spatial variation in strain, as captured by the distributed sensing measurements. In Specimen-R, structural failure occurred at the north pipe connection, where the data indicated significantly larger strain gradients, and consequently, more severe localized stress concentrations, compared to the relatively uniform load distribution on the south connection. Conversely, Specimen-T failed at the south pipe connection, which aligned with measurements revealing pronounced spatial strain variations driven by the severe diametric distortion of the more flexible TurnerLok gasket. In both scenarios, these asymmetric strain developments induced critical localized stress concentrations that ultimately precipitated the failure of the fittings.

Figure 7.11 illustrates the longitudinal strain distribution for Specimen-R at an applied axial load of 32,000 lbs, representing a state immediately prior to ultimate failure. The data is plotted spatially from the south pipe segment to the north pipe segment. The two distinct gaps visible in the plots correspond to the physical boundaries between the iPVC fitting and the inserted pipes, where the continuous attachment of the fiber optic cables was not feasible.

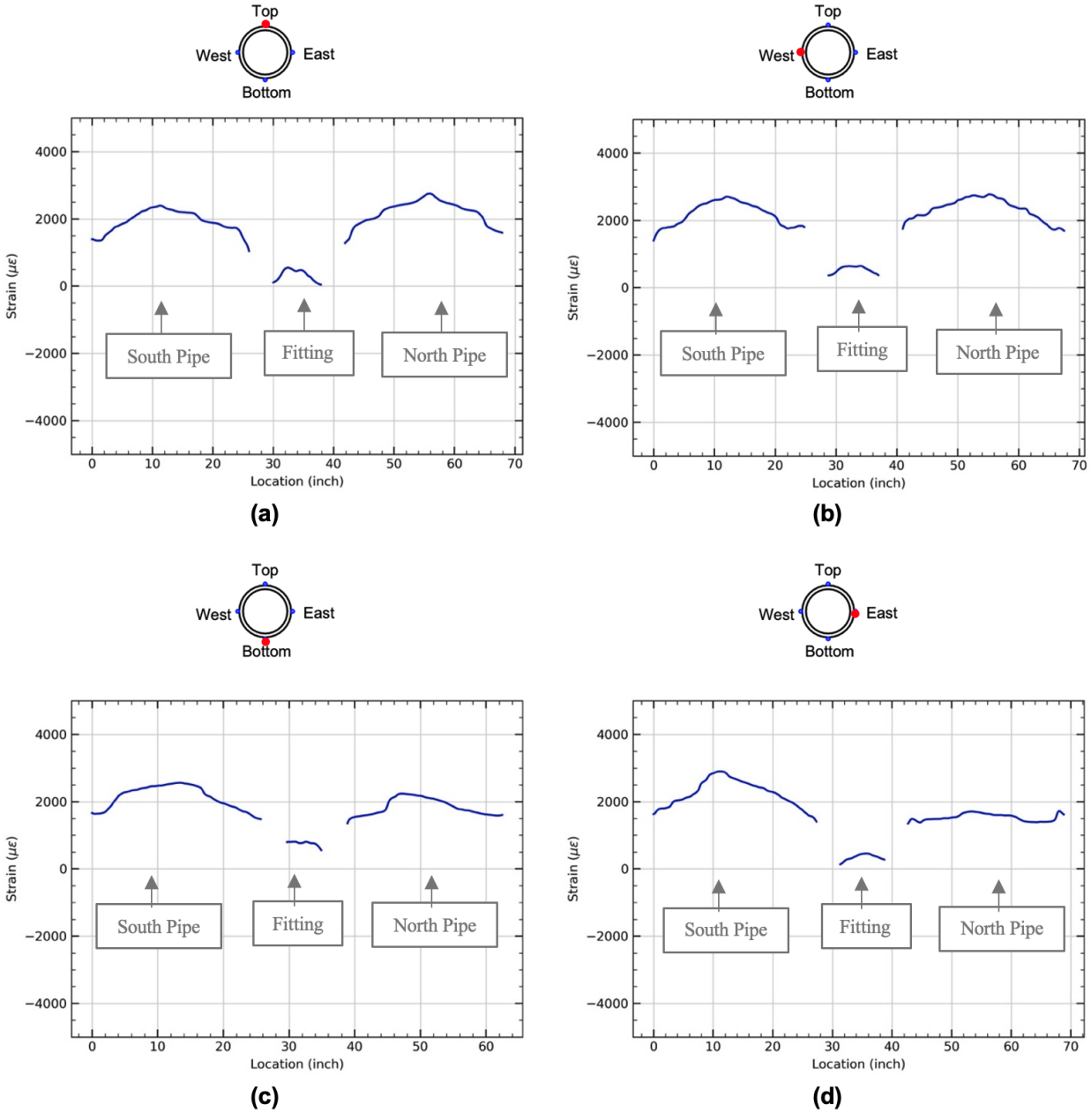


Fig. 7.11. Axial strain development along pipes of Specimen-R under 32,000-LBS axial loading condition. (a) Top, (b) West side, (c) Bottom, (d) East side

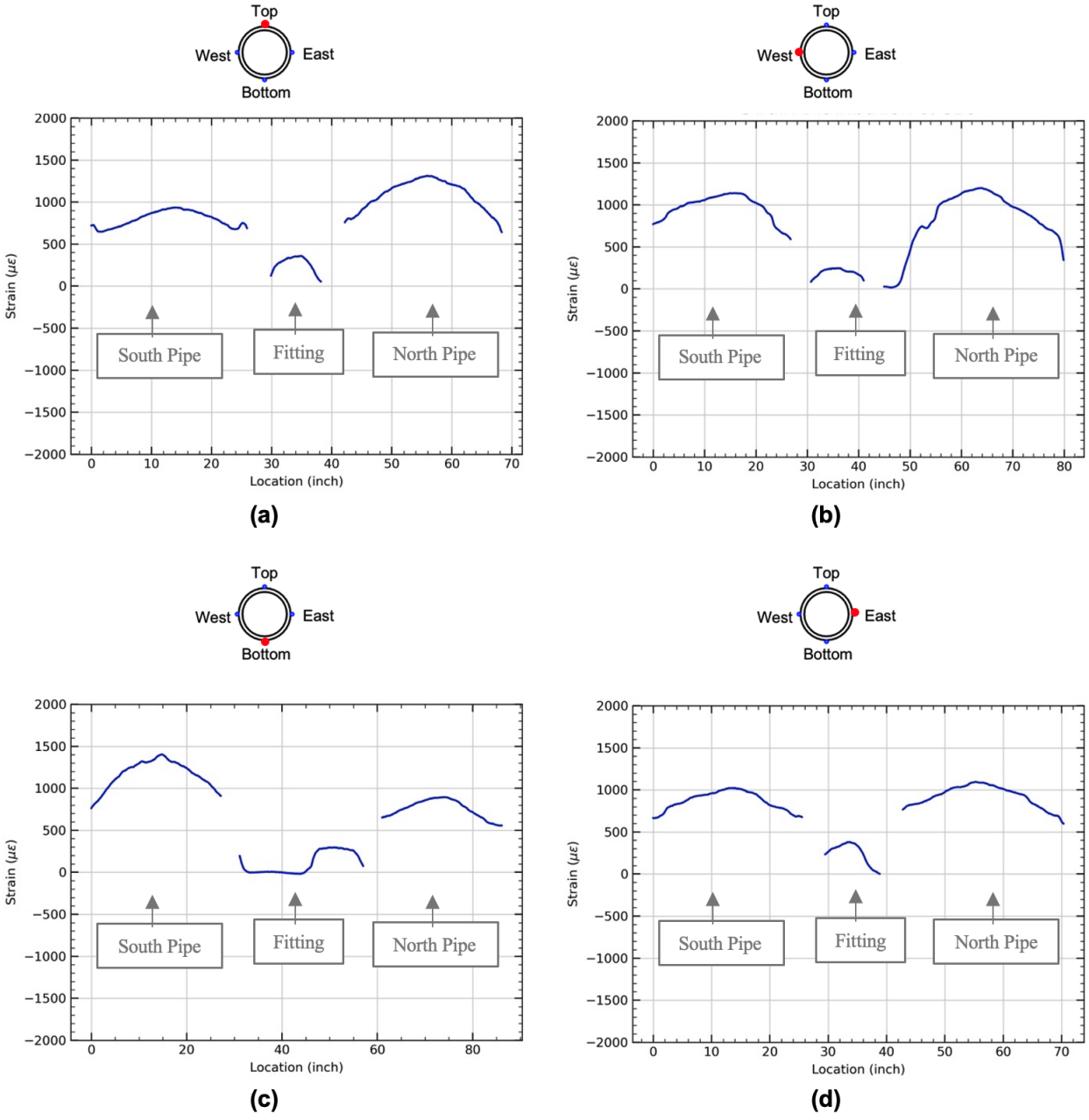


Fig. 7.12. Axial strain development along pipes of Specimen-T under 11,500-LBS axial loading condition. (a) Top, (b) West side, (c) Bottom, (d) East side

As expected under a global tensile regime, positive tensile strains were recorded across all continuously monitored locations. The longitudinal strain profiles developed symmetrically across both the south and north pipe segments. However, the magnitude of the strain measured along the central fitting was significantly lower than the strains measured on the adjacent pipe bodies. This discrepancy is directly attributable to the structural geometry of the components; the plastic fitting is manufactured with a substantially greater wall thickness than the standard C900 pipe. This increased cross-sectional area yields a higher localized axial stiffness, thereby resulting in proportionally smaller strains developing within the fitting under the same applied load.

Figure 7.12 presents the corresponding longitudinal strain measurements for Specimen-T under an applied axial load of 11,500 lbs, just prior to its premature failure. Consistent with the lower ultimate capacity of this specimen, the absolute magnitudes of the measured strains are correspondingly smaller than those recorded for Specimen-T. Despite this difference in overall magnitude, the fundamental pattern of the strain distribution remains consistent between the two tests. Specifically, Specimen-T also exhibited significantly larger tensile strains along the main pipe bodies compared to the central fitting, again confirming the influence of the fitting's greater wall thickness and localized stiffness on the overall deformation profile.

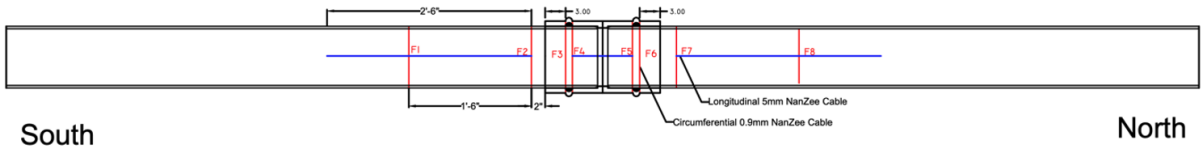
7.2.3 Hoop Strain

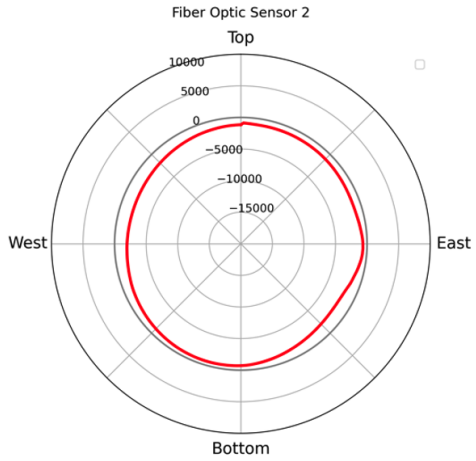
The circumferential (hoop) strain results measured for Specimen-R are plotted in Figure 7.13. This figure illustrates the data obtained from the sensors positioned directly on the fitting (F3 and F4) and the sensors located on the adjacent pipe segments nearest to the fitting (F2 and F7).

The readings from sensors F2 and F7 indicate compressive strains, demonstrating that the main pipe bodies contracted radially as they were subjected to axial pullout forces. This phenomenon is a direct consequence of the Poisson effect, where longitudinal tension induces corresponding circumferential compression.

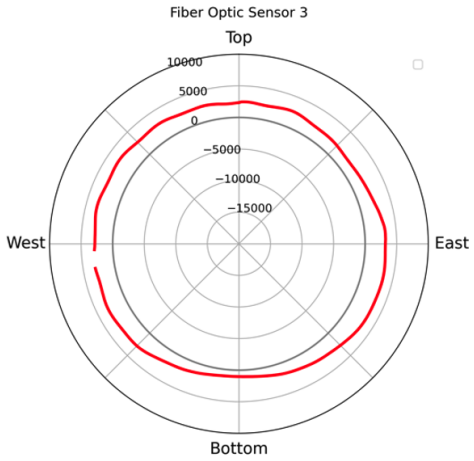
Within the fitting assembly, Sensor F3 was positioned outward (north) of the gasket, while Sensor F4 was located inward (south) of it. As the pipe was subjected to axial tension, the wedged profile of the gasket teeth pressed radially outward against the internal wall of the fitting. This mechanical interaction forced the outer sections of the fitting to expand, a deformation mechanism visualized in Figure 7.14. This radial expansion is clearly corroborated by the data from Sensor F3, which recorded uniform tensile strains around the entire circumference of the fitting. A nearly identical tensile pattern was recorded symmetrically at Sensor F6 [28].

Conversely, compressive hoop strains were observed on the inner (central) side of the fitting relative to the gasket, as indicated by the measurements from Sensor F4. As established in the preceding sections, the longitudinal strains in this thicker central section are relatively small, which correspondingly limits the magnitude of the Poisson-induced compressive hoop strains. Although symmetric behavior was anticipated at the corresponding inward location

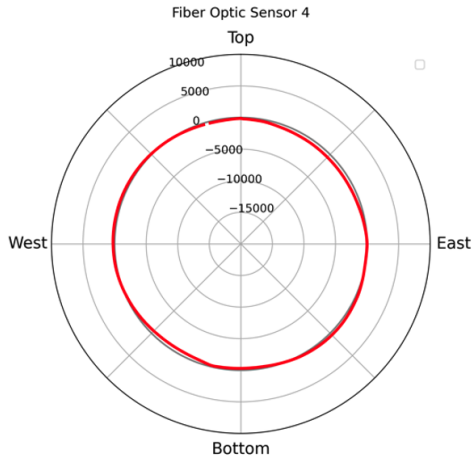




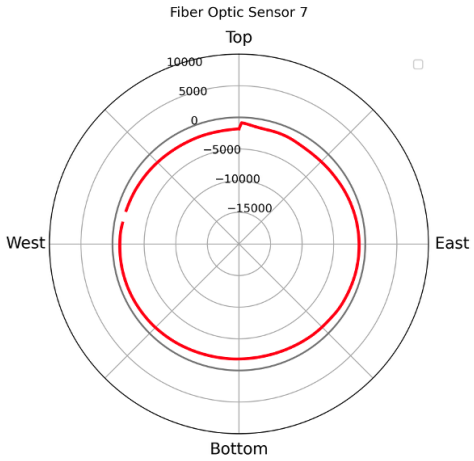
(a) Sensor F2



(b) Sensor F3



(c) Sensor F4



(d) Sensor F7

Fig. 7.13. Strain distribution in the circumferential direction of Specimen-R under 32,000-LBS loading condition

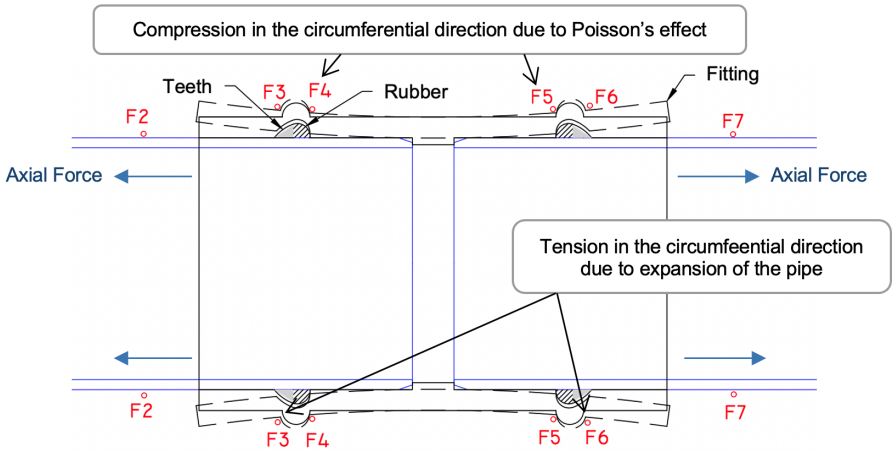


Fig. 7.14. Sketch of the fitting deformation under axial force

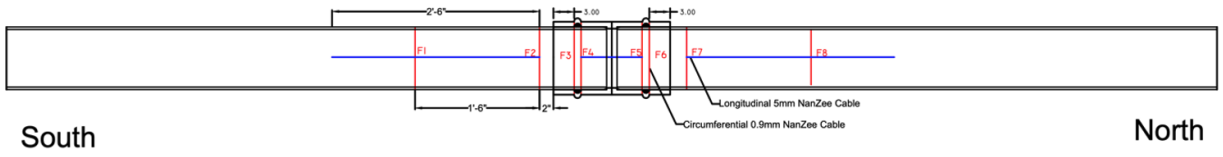
of Sensor F5, data from this channel is omitted from the present study due to sensor damage sustained during testing [28].

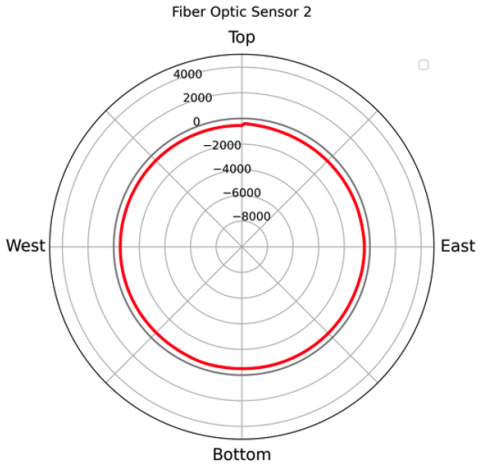
Figure 7.12 presents the corresponding hoop strain results for Specimen-T, utilizing an identical sensor layout to Specimen-R. Consistent with the primary observations from the first test, both the north and south pipe segments exhibited circumferential compression governed by the Poisson effect. Furthermore, circumferential tension was localized at the outer portions of the fitting (sensors F3 and F6), while compressive strains were concentrated in the middle section of the fitting (sensors F4 and F5). These results show that the fundamental kinematic deformation mechanism observed in Specimen-R is identical to that of Specimen-T.

7.2.4 Conclusion of iPVC Tension Test

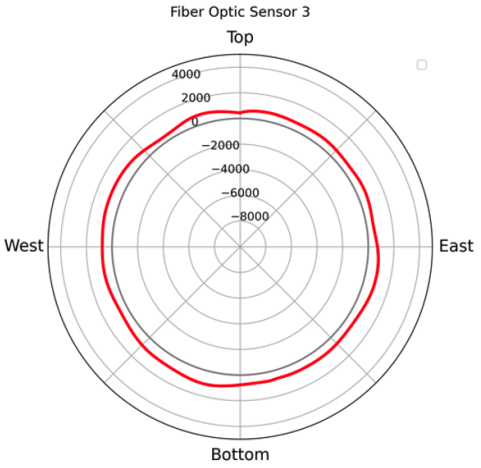
The testing program evaluated the structural performance and failure mechanisms of jointed assemblies utilizing two different internal rubber restraining gaskets (ReiberLok and TurnerLok) under monotonic tensile loading, terminating upon the onset of structural damage with sever water leakage.

While both specimens exhibited similar initial force-strain trajectories, their ultimate axial capacities diverged significantly. Specimen-R sustained a maximum tensile force of 34,884 lbs with a corresponding joint displacement of 0.76 inches. In contrast, Specimen-T reached a much lower ultimate capacity of 11,884 lbs at a displacement of 0.28 inches. Both tests culminated in a sudden drop in internal water pressure occurring simultaneously with the peak axial force. This disparity in performance is primarily attributed to the geometric design of the gasket teeth. The ReiberLok gasket's numerous smaller teeth effectively distributed the applied load over a broader contact area, mitigating local stress concentrations.

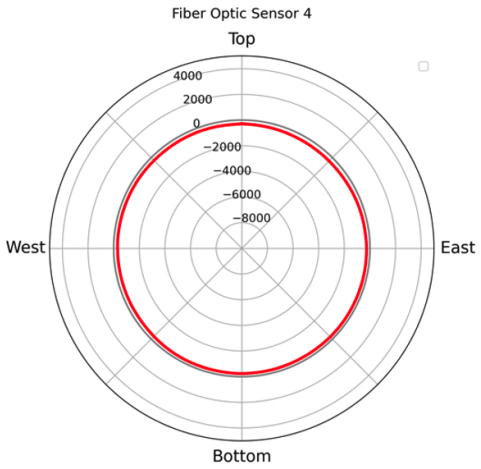




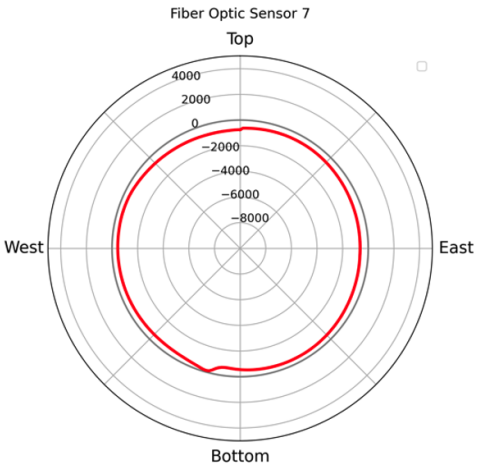
(a) Sensor F2



(b) Sensor F3



(c) Sensor F4



(d) Sensor F7

Fig. 7.15. Strain distribution in the circumferential direction of Specimen-T under 11,500-LBS loading condition

Conversely, the fewer, larger teeth of the TurnerLok gasket concentrated forces at individual tooth boundaries, precipitating premature, localized failure in the iPVC material.

DSS data showed the localized deformation mechanisms within the fitting assembly. The data revealed that the inner central section of the fitting underwent radial contraction, driven by the Poisson effect under longitudinal tension. Simultaneously, a radial expansion mechanism was captured at the outer extremities of the fitting, caused by the wedged teeth of the gaskets bearing forcefully outward against the internal wall during pipe pullout. Ultimately, the fittings experienced critical localized shear and tensile stresses at these specific gasket interfaces, dictating the ultimate physical failure locations.

Furthermore, the data demonstrated that the structural response was highly sensitive to the initial installation quality and engagement between the locking gaskets and the pipes. In Specimen-R, the south pipe exhibited reduced strain development on the lateral (east and west) sides after exceeding 16,000 lbs of applied load. This behavior indicates cross-sectional elongation (ovalization) of the pipe, which locally degraded the contact pressure on the lateral sides. On the north pipe of the same specimen, significant spatial variations in strain were observed from the onset of loading, suggesting that initial seating adjustments caused the gasket to engage along a skewed, non-vertical plane, thereby inducing continuous secondary bending moments.

Similar engagement-driven strain asymmetries compromised Specimen-T. In the south pipe, longitudinal strains on the top and bottom fibers were consistently higher than those on the lateral sides, highlighting uneven axial load transfer. The north pipe demonstrated generally aligned strain patterns with the critical exception of the bottom fiber, where anomalously low strains indicated poor localized tooth engagement. These installation imperfections are intrinsically linked to the mechanical properties of the TurnerLok gasket; its larger teeth and tendency to distort made it more difficult to maintain perfect circularity during assembly, inherently leading to suboptimal pipe-gasket engagement and contributing to its earlier failure.

7.3 Compression Performance

7.3.1 Experimental Setup and Instrumentation

The experimental setup for the compression tests utilized the same self-reacting, closed-loop structural frame and hydraulic loading system previously described for the tension phase. However, specific modifications were introduced to reverse the force direction and safely accommodate axial compression. On the loading side, the hydraulic cylinder and loading rod assembly were adjusted so that the locking nut was positioned with sufficient clearance from the transverse beam, allowing for unobstructed inward displacement toward the joint.

The specimen attachment mechanisms also required minor adjustments to safely handle compressive stresses. Most notably, the reaction-side endcap was placed in full, direct contact with the W10x112 transverse beam. This bearing configuration ensured that the compressive

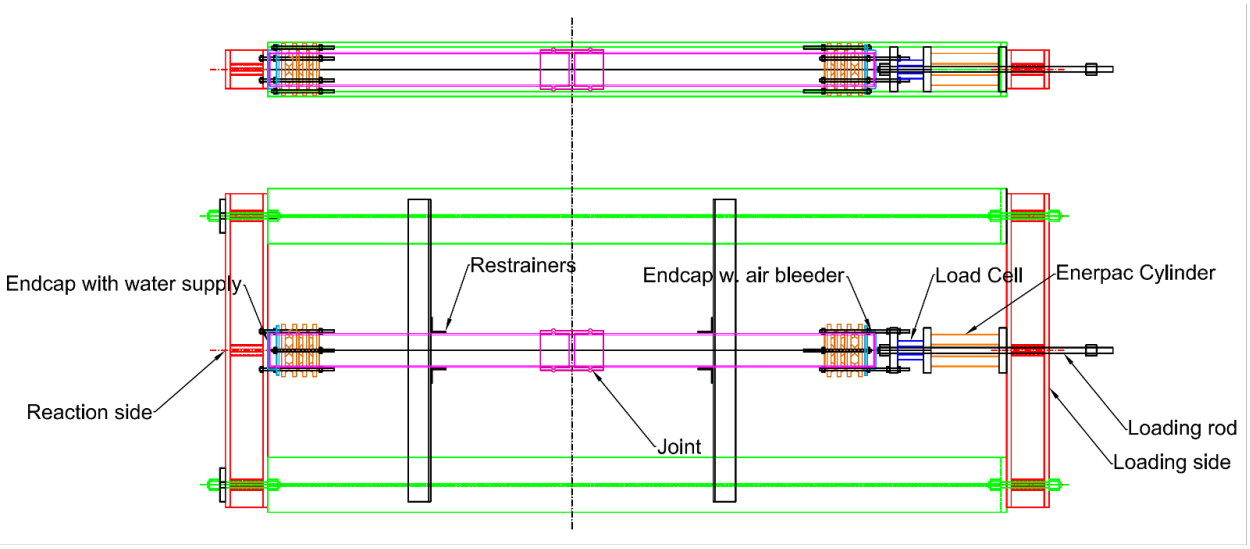


Fig. 7.16. Drawing of the iPVC compression test experimental setup

forces were transferred directly into the structural steel frame rather than relying on the threaded tension rods. Finally, because the pipe segments are highly susceptible to global buckling under compressive loads, two specialized restrainer frames were introduced into the syste. These anti-buckling frames were installed on the main pipe bodies on both sides of the centrally located sleeve joint to maintain strict axial alignment throughout the testing procedure. The setup plan and the setup assembly are shown in Figure 7.16 and Figure 7.17.

A single pipe assembly was evaluated during the compression testing phase, conducted on March 18, 2024. For this specimen, the plastic fitting was equipped with ReiberLok gaskets prior to assembly, and both iPVC pipe segments were fully inserted into the central sleeve joint to ensure maximum initial engagement. Prior to the application of the axial compressive load, the internal volume of the specimen was filled with water and pressurized to a standard house pressure of approximately 65 psi to monitor the watertight integrity of the joint throughout the test.

The instrumentation plan for the compression test was identical to that implemented during the tension testing phase (Figure 7.18 and Figure 7.19). To accurately capture the mechanical response and localized deformation mechanisms under compressive loading, the specimen was continuously monitored using the exact same configuration of external and internal sensors. This included a load cell to record the applied axial force, four wire potentiometers distributed circumferentially at 90-degree intervals to measure the relative displacement across the joint, and a position transducer to track the movement of the fitting sleeve on the loading side. Furthermore, the identical DSS layout was deployed, utilizing 5-mm cables for longitudinal strain measurement and 0.9-mm cables strategically wrapped around the pipes and plastic fitting to capture circumferential strains.

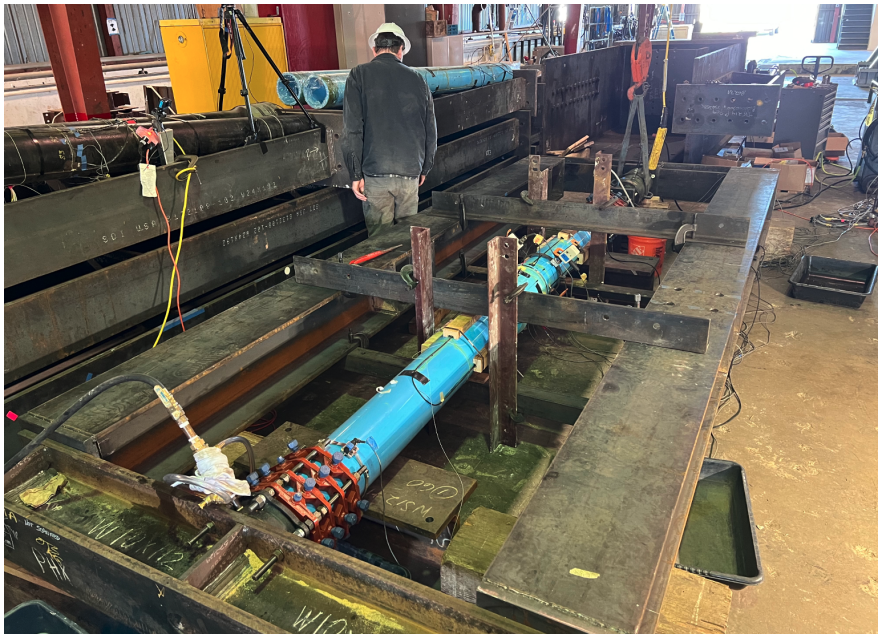


Fig. 7.17. Completely assembled iPVC compression test setup

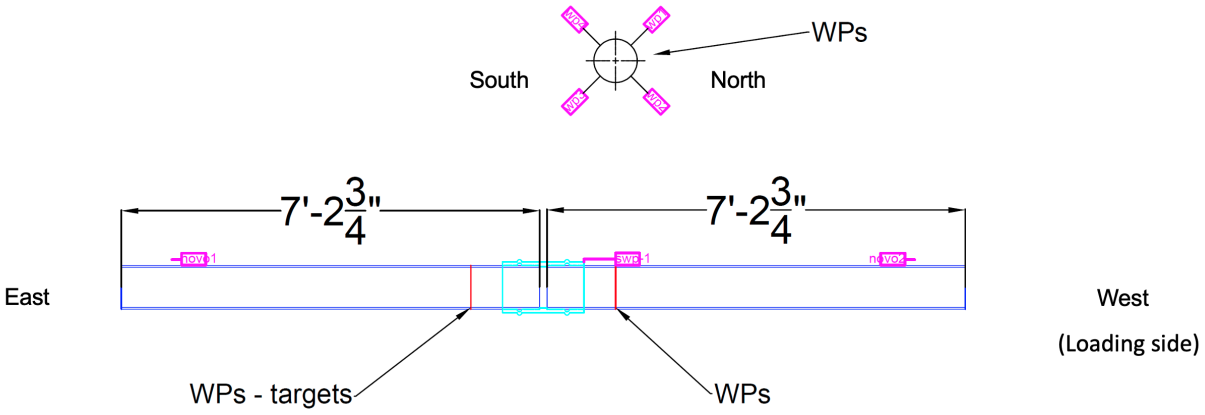


Fig. 7.18. Position transducers for displacement monitoring of the joint of the iPVC compression test

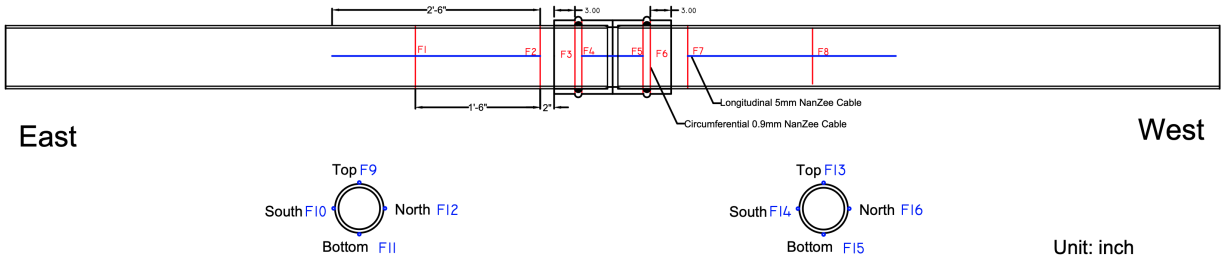


Fig. 7.19. Instrumentation plan of fiber optic sensors of the iPVC compression test specimens

7.3.2 Failure Mode

Prior to loading, the pipe assembly was filled with water and internally pressurized to approximately 65 psi. A monotonic compressive force was then applied along the longitudinal axis of the pipeline, pushing inward from the west (loading) side toward the central fitting. The resulting global load-displacement response is presented in Figure 7.20. The compressive displacement across the joint, denoted as the "average joint closing," was calculated by averaging the continuous readings from the four position transducers distributed across the connection. The specimen achieved a peak compressive resistance of 98.8 kips at a corresponding joint closing displacement of approximately 3.46 inches.

The experimental load-displacement curve exhibited a distinct multi-step pattern, characterized by significant behavioral shifts at approximately 20 kips, 62 kips, and the peak of 98.8 kips, followed by a post-peak force reduction to 60 kips. The initial yield step near 20 kips is attributed to the seating and kinematic readjustment of the internal rubber gaskets within the fitting. The second structural step, occurring at 62 kips, corresponds to the onset of localized buckling on the west (loading) pipe segment. Upon reaching the peak ultimate load of 98.8 kips, significant localized buckling fully developed on this west pipe. This severe geometric instability induced considerable rotation of the joint assembly. Consequently, this rotation introduced large secondary bending moments and concentrated compressive stresses around the fitting interface, leading to substantial structural deformation of the pipe wall. Following this peak, the axial force plateaued and eventually decreased as compressive deformation continued to grow without generating additional resistance.

Figure 7.21 visually corroborates these structural observations, highlighting the severe deformation localized at the interface between the plastic sleeve and the west pipe. Specifically, pronounced localized buckling was documented on the west pipe immediately adjacent to the edge of the fitting (Figure 7.21a). As the compressive force intensified, the buckling-induced rotation of the relatively rigid fitting imposed highly concentrated compressive bearing forces directly into the wall of the west pipe segment.

Remarkably, the watertight integrity of the joint was maintained throughout the entire active compressive loading phase, despite the severe structural distortion. Water leakage

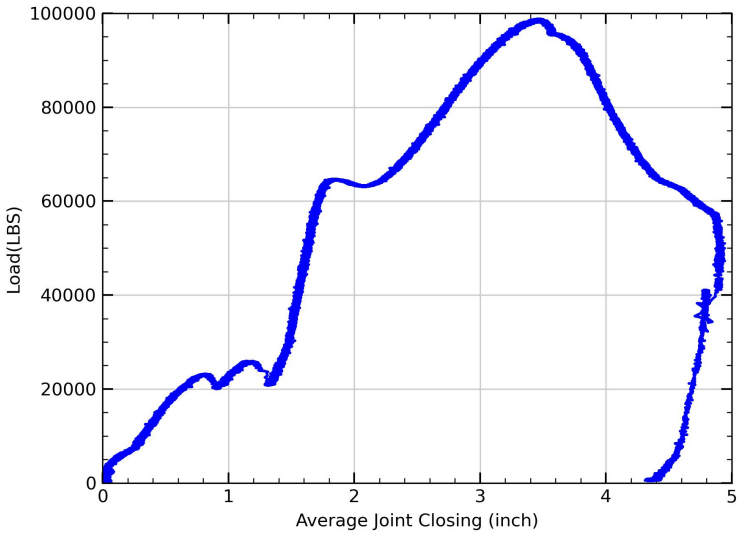


Fig. 7.20. Force versus average joint closing for the sleeve with Reiberlok gasket of iPVC compression test

was not detected until the specimen was actively unloaded from a maximum joint closing displacement of 4.9 inches. As illustrated in Figures 7.21b and 7.21c, ultimate physical failure occurred during this unloading phase, manifesting as a rupture adjacent to the fitting, directly coinciding with the zone that had experienced the most severe compressive stress concentration during the test

7.3.3 Axial Strain

The longitudinal strain data obtained from the DSS system are presented in Figure 7.22. This figure illustrates the relationship between the applied axial load and the longitudinal compressive strains measured at the midpoints between circumferential sensors F1 and F2 on the east (reaction) pipe, and F7 and F8 on the west (loading) pipe. While the data confirm that both pipe segments experienced the anticipated global compressive stresses, the onset of secondary bending moments and localized buckling became evident as the compressive force increased.

For the east pipe, an initial bending moment oriented toward the bottom fiber was detected at the onset of testing, likely induced by the self-weight of the assembly. As the active compressive force increased, an additional lateral bending moment developed toward the south side. Upon reaching an applied load of approximately 20,000 lbs, the strain measurements temporarily exhibited erratic fluctuations. This behavior indicates a kinematic shift and readjustment of the internal rubber gaskets as they sought a new equilibrium state, mo-

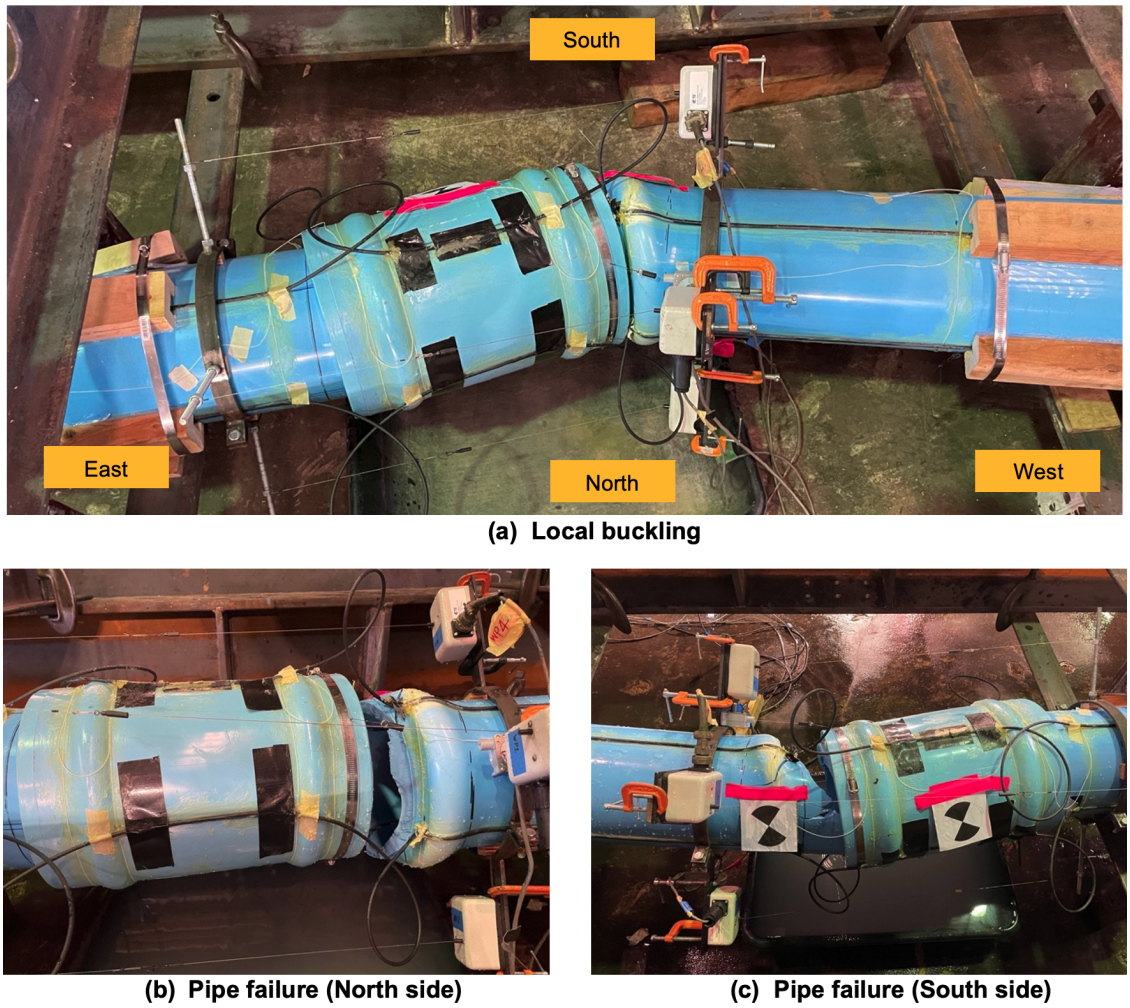


Fig. 7.21. Failure of the iPVC compression test specimen

mentarily altering the load transfer mechanism. Subsequently, at approximately 62,000 lbs, the onset of localized buckling at the interface between the central fitting and the west pipe triggered a sharp discontinuity in the strain data. This buckling-induced instability forced the global assembly downward and southward, imposing a complex secondary bending regime on the east pipe. Consequently, the east pipe experienced exacerbated compressive strains on its south and bottom sides, while the north and top sides exhibited correspondingly lower compressive strains.

Conversely, the west pipe exhibited no obvious initial bending at the start of the test. However, following the internal readjustment of the rubber gaskets near 20,000 lbs, a distinct secondary bending moment emerged, deflecting the pipe toward the top and north sides. As the applied force reached 62,000 lbs and localized buckling initiated, the stress distribu-

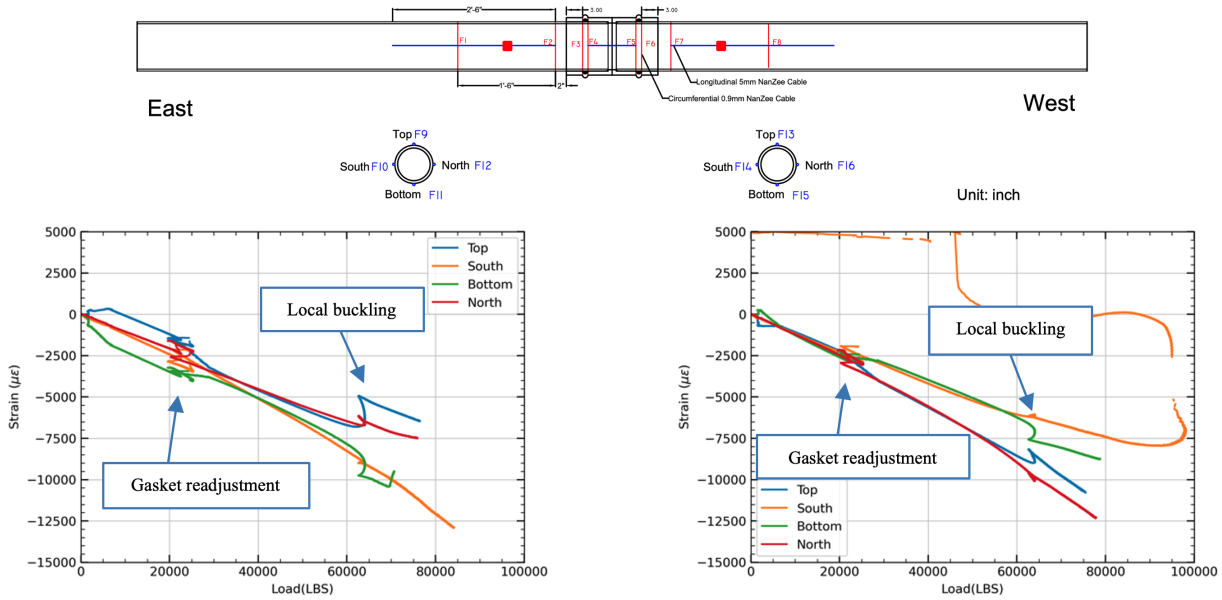


Fig. 7.22. Axial strain vs load of iPVC compression test. (Left) East pipe. (Right) West Pipe

tion shifted dramatically. This geometric instability induced significantly larger compressive stresses along the bottom fiber and reduced compressive stresses along the top fiber. Ultimately, this severe buckling phenomenon concentrated massive compressive deformations on the north and bottom sides of the west pipe. These highly localized zones of extreme structural distortion directly correlate with the physical locations where the pipe ruptured during the subsequent unloading phase.

Figure 7.23 illustrates the longitudinal strain distribution of the specimen under an applied compressive load of 70,000 lbs, representing a post-buckling state. Although ultimate physical failure of the specimen did not occur until the axial load reached 98,800 lbs, localized strain values at the 70,000 lbs threshold began to exceed the maximum measuring capacity of the DSS interrogator, preventing the acquisition of continuous data beyond this load level. The spatial data is plotted continuously from the east pipe segment to the west pipe segment, with the two distinct gaps corresponding to the physical boundaries between the internal pipes and the plastic fitting where continuous fiber optic cable attachment was not possible.

As expected under a global compressive regime, negative (compressive) strains were recorded across all continuously monitored locations. While the fundamental strain profiles on the west and east pipes exhibited general similarities, the magnitude of the compressive strain measured within the central fitting was significantly lower than the strains measured on the adjacent pipe bodies. Consistent with the tension test observations, this discrepancy is directly attributable to the geometric cross-section of the assembly; the thicker wall

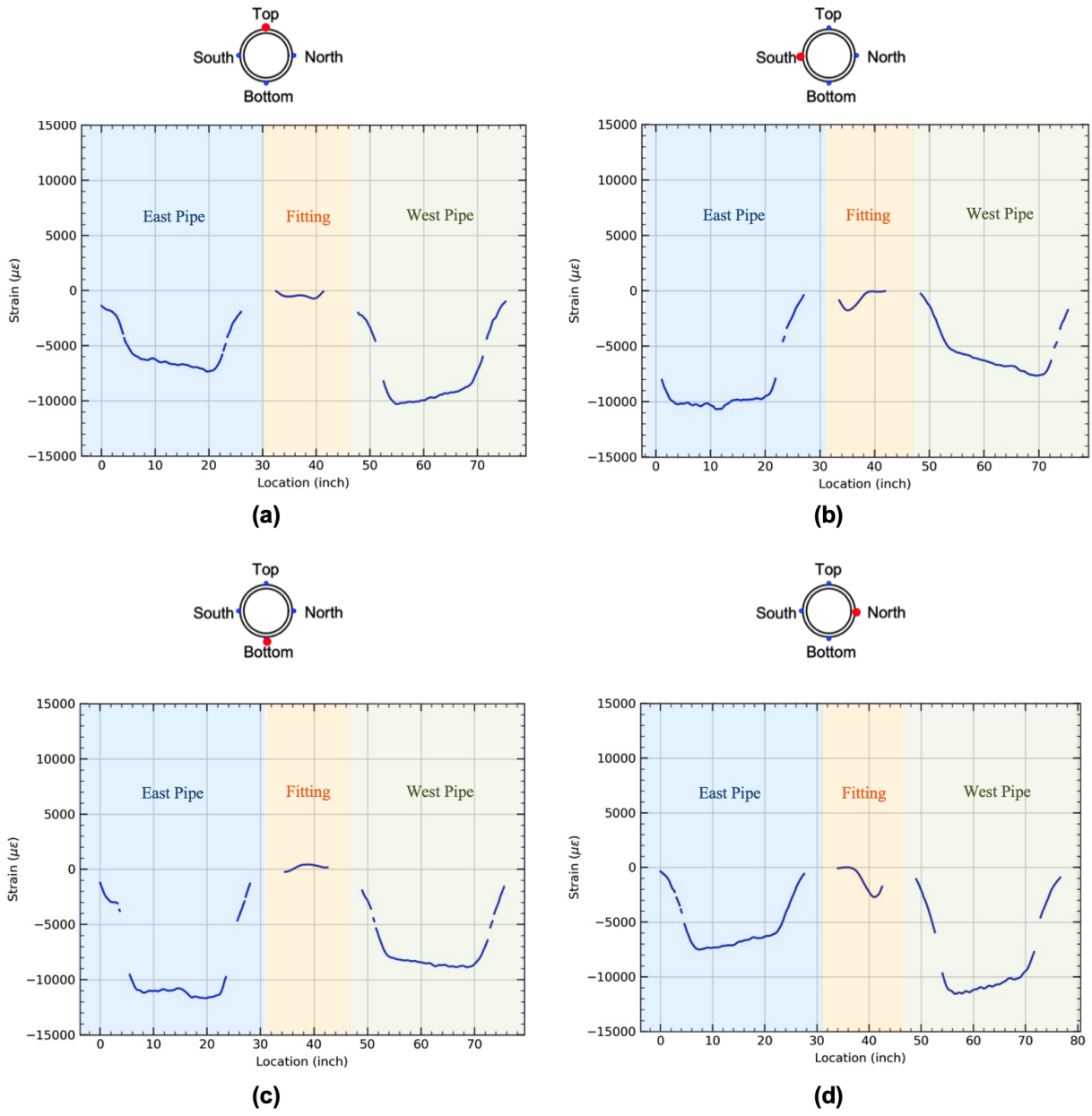


Fig. 7.23. Axial strain development of the iPVC compression specimen under 70,000-LBS axial loading condition. (a) Top, (b) South, (c) Bottom, (d) North

of the plastic fitting yields a substantially higher localized axial stiffness, thereby resisting deformation and limiting strain development relative to the standard pipe sections.

A closer examination of the pipe segments reveals a distinct asymmetry in absolute strain magnitudes between the east and west pipes. This spatial disparity is a direct structural consequence of the localized buckling that preferentially developed on the west pipe segment. As the global compressive force increased, this severe local buckling induced substantial secondary bending moments, fundamentally altering the uniform axial load transfer and producing the highly asymmetric strain profile captured in Figure 7.23.

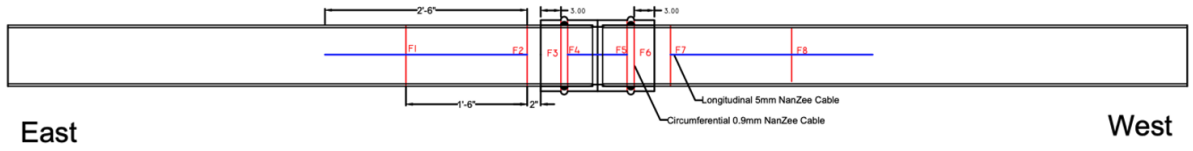
7.3.4 Hoop Strain

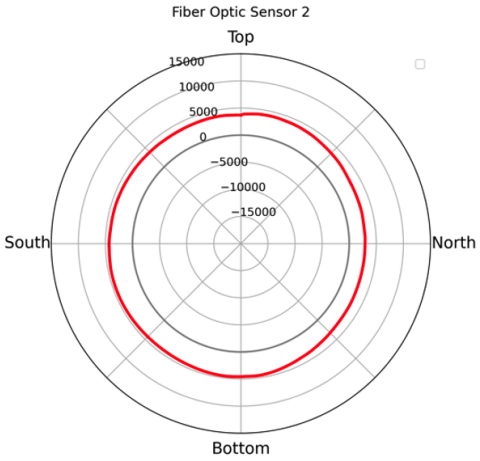
The circumferential (hoop) strain data obtained from the specimen are presented in Figure 7.24. To clearly illustrate the complex internal deformation mechanisms while maintaining focus on the most critical structural interactions, the plotted data and subsequent analysis center on a targeted subset of sensors: F3 and F4 positioned on the plastic fitting, alongside F2 and F7 located on the adjacent east and west pipe segments, respectively.

Data from sensors F2 and F7 show a general radial expansion of both main pipe bodies as they were subjected to global longitudinal compression. This fundamental volumetric response is driven by the Poisson effect, where longitudinal shortening induces corresponding circumferential tension (expansion). However, the strain profiles reveal eccentricities in this radial expansion, directly resulting from the localized buckling phenomena described in the previous section. Specifically, the east pipe (measured at F2) exhibited its maximum radial expansion along its south and bottom fibers, whereas the west pipe (measured at F7) expanded predominantly along its north and top fibers.

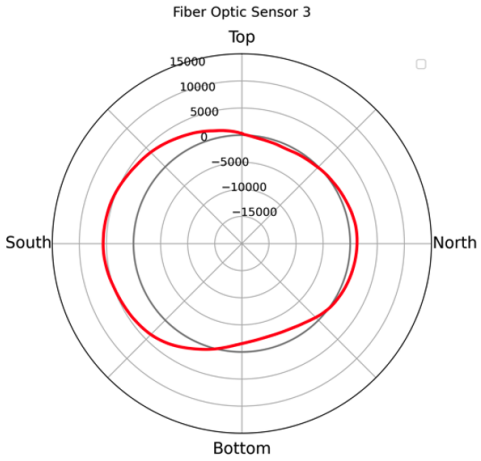
Moving to the structural interaction at the joint interface, Sensor F3 captured the hoop strains on the outer edge of the fitting. The data indicates a highly asymmetric radial expansion, with the south side of the fitting expanding substantially more than the remainder of the circumference. This localized, asymmetric expansion is a direct consequence of the severe geometric rotation of the entire fitting assembly induced by the buckling of the west pipe. As the fitting rotated off-axis, the misaligned east pipe bore heavily against the internal south face of the fitting. Consequently, the continued application of the axial compressive force wedged the pipe tightly against the inner wall, forcing the fitting to expand radially outward in this highly concentrated zone. This kinematic bearing mechanism is schematically illustrated in Figure 7.25.

Sensor F4, located on the inner central section of the fitting, recorded a mechanically compatible deformation pattern. The middle section of the fitting experienced a distinct transverse ovalization (or "squatting") effect, characterized by pronounced diametric expansion along the north-south axis. Once again, this spatial distortion is attributed to the buckling-induced rotation of the joint assembly, which forced the inwardly displaced pipe segments to push heavily outward against the lateral sidewalls of the plastic fitting.

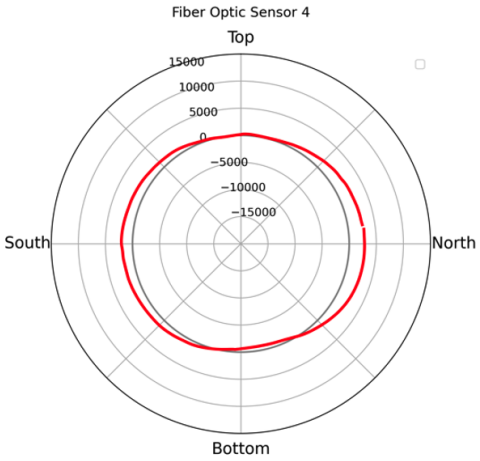




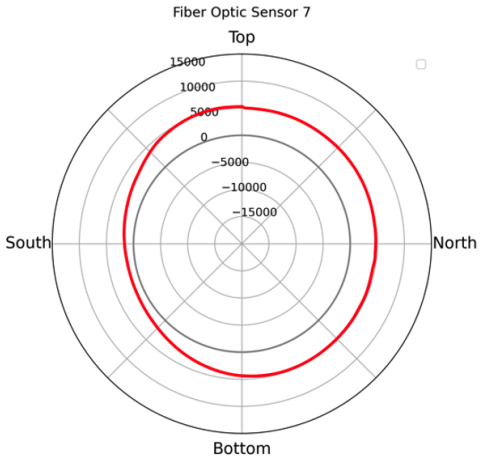
(a) Sensor F2



(b) Sensor F3



(c) Sensor F4



(d) Sensor F7

Fig. 7.24. Strain distribution in the circumferential direction of the Specimen under 32,000-LBS loading condition

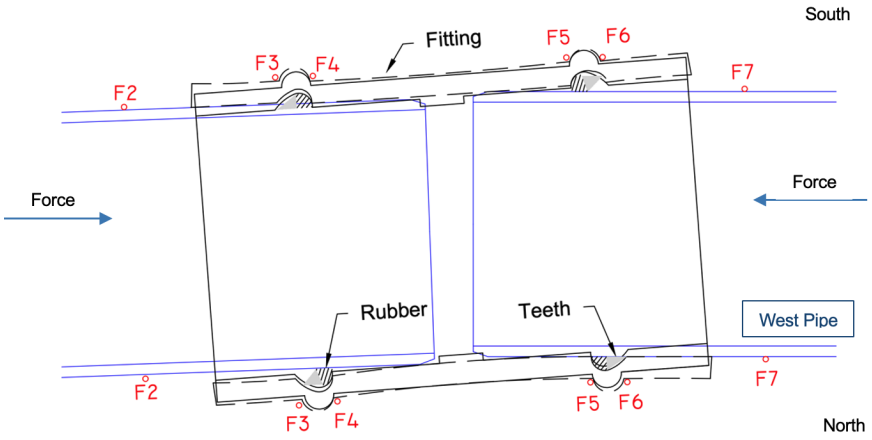


Fig. 7.25. Sketch of fitting deformed mechanism

7.3.5 Conclusion of iPVC Compression Test

The pure axial compression experiments evaluated the jointed iPVC pipe assembly (equipped with ReiberLok gaskets) under a monotonic compressive load. The specimen sustained a peak ultimate capacity of 98.8 kips at a joint closure of 3.46 inches, at which point severe localized buckling initiated on the west (loading) pipe segment. This geometric instability induced substantial rotation of the joint assembly and a subsequent drop in load capacity. Remarkably, the internal watertight seal (pressurized at 65 psi) was maintained throughout the entire active loading phase; leakage and ultimate physical rupture occurred exclusively during the subsequent unloading phase, with the failure localized at the interface between the plastic sleeve and the buckled west pipe.

DSS data confirmed that this localized buckling fundamentally governed the internal strain distribution and failure mode. While standard longitudinal compression and Poisson-induced radial expansion were observed globally, the buckling-induced rotation introduced severe spatial asymmetries. Specifically, the east pipe expanded predominantly on its south and bottom fibers, while the west pipe expanded primarily on its north and top fibers. This severe misalignment forced the pipes to bear unevenly against the internal walls of the plastic fitting. Consequently, the outer edges of the fitting experienced highly localized outward expansion, while its mid-section underwent transverse ovalization (or "squatting"). These concentrated structural distortions dictated the joint's ultimate rupture upon unloading.

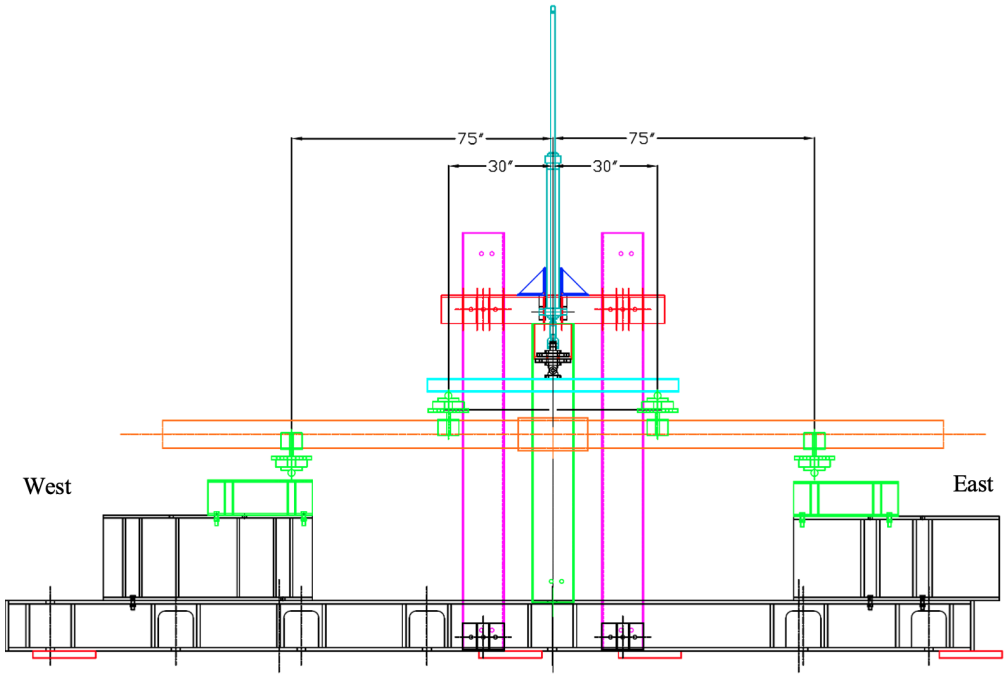


Fig. 7.26. Schematic drawing of the iPVC four-point bending experimental setup

7.4 Four-Point Bending Performance

7.4.1 Experimental Setup and Instrumentation

The four-point bending experimental setup was designed as a self-reacting structural frame capable of applying large bending deformations to the iPVC pipe specimens while maintaining stable and controlled loading conditions. The global load was applied using a hydraulic actuator with capacities of 20 kips in tension and 25 kips in compression and a total stroke length of 40 inches. To ensure that loading remained strictly vertical throughout the test, the actuator was guided by a linear bearing system that minimized unintended lateral movement.

The actuator force was transferred to the specimen through a steel spreader I-beam. Load was introduced at the midpoint of the spreader beam through a specialized clevis connection that allowed rotational movement of the beam. This articulation ensured that the actuator force was distributed evenly to two loading saddles positioned above the pipe specimen. The loading saddles were symmetrically located 60 inches apart, corresponding to 30 inches on either side of the specimen centerline. The design of the setup is shown in Figure 7.26 and the experimental setup is demonstrated in Figure 7.27.

The specimen was supported by two reaction saddles located beneath the pipe and spaced 150 inches apart, corresponding to 75 inches on either side of the centerline. To minimize localized stress concentrations and prevent premature damage to the iPVC pipe wall, all loading and reaction saddles were mounted on roller supports. These rollers allowed the



Fig. 7.27. Experimental setup of iPVC four-point bending test (Specimen-EBAA as example)

saddles to rotate and translate freely in the horizontal direction as the specimen deformed, thereby reducing secondary restraint forces and promoting a more uniform bending response. Additional safety features were incorporated into the setup to secure the hardware and maintain system stability in the event of unexpectedly large displacements during testing.

Prior to testing, each specimen was filled with water and internally pressurized to 70 psi to simulate operational conditions. The hydraulic actuator was aligned with the center of the specimen, although the exact location of the specimen center varied depending on the joint configuration being tested. For Specimen-EBAA, the centerline was defined as a point located 4.5 inches from the bell face. For Specimen-RCT, the centerline corresponded to the midpoint of the RCT restraint, while for Specimen-RL it was defined as the geometric center of the plastic fitting. The complete testing matrix and loading history for the four-point bending phase are summarized in Table 7.3.

All specimens were instrumented to monitor global deformations, local joint behavior, applied loads, and internal pressure throughout the testing program, as illustrated in Figure 7.28 to Figure 7.30. A total of eight string potentiometers (wire pots) were installed on each specimen to measure pipe displacements and joint movements. Four wire pots were positioned around the joint region at approximately 45° intervals to quantify joint opening and relative movement between the connected pipe segments. The remaining four wire pots were installed near the ends of the specimen to monitor global pipe displacements during testing. These instruments were mounted on both the north and bottom sides of the pipe.

Table 7.3. Summary of iPVC four-point bending test log

Test No.	Specimen	Test Date	Restraint
1	Specimen-EBAA	10/14/2022	EBAA 1900
2	Specimen-RCT	11/10/2022	RCT
3	Specimen-RL	03/27/2024	Plastic Fitting with ReiberLok

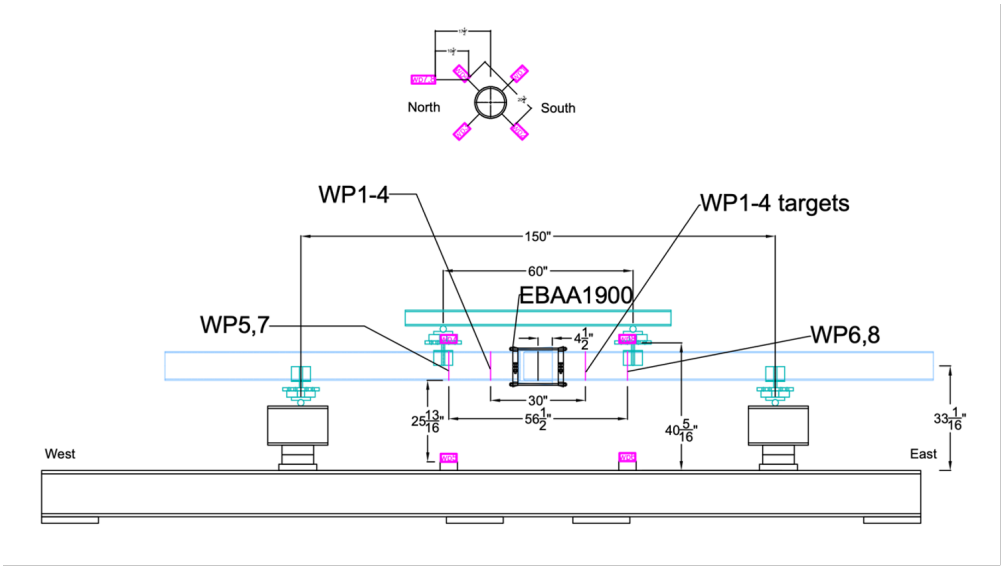


Fig. 7.28. Position transducers for displacement monitoring of Specimen-EBAA

The sensors located on the north side were configured to measure horizontal displacements, while those mounted on the bottom side measured vertical displacements.

In addition to displacement measurements, each test was monitored using a load cell integrated within the hydraulic actuator to record the applied force and a pressure gauge to track the internal water pressure maintained throughout testing. This instrumentation provided continuous measurements of the global load response and the pressurization conditions of the specimen.

Specimen-RL, which utilized the plastic fitting assembly, was instrumented more extensively to capture the local behavior of the sleeve joint. Additional position transducers were installed to measure the vertical displacements of the east and west ends of the sleeve, the relative displacement between the sleeve and pipe, and the rotation of the joint. Several displacement transducers were also arranged in a triangulated configuration on both sides of the fitting to quantify in-plane and out-of-plane movements of the sleeve assembly.

In addition to the conventional instrumentation, DSS was incorporated into the experimental program to provide high-resolution strain measurements and to better understand

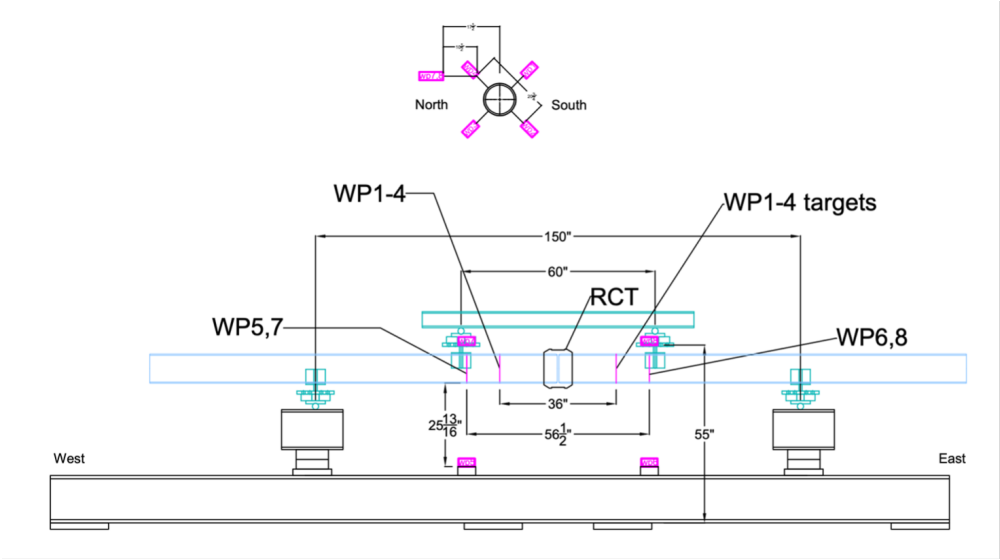


Fig. 7.29. Position transducers for displacement monitoring of Specimen-RCT

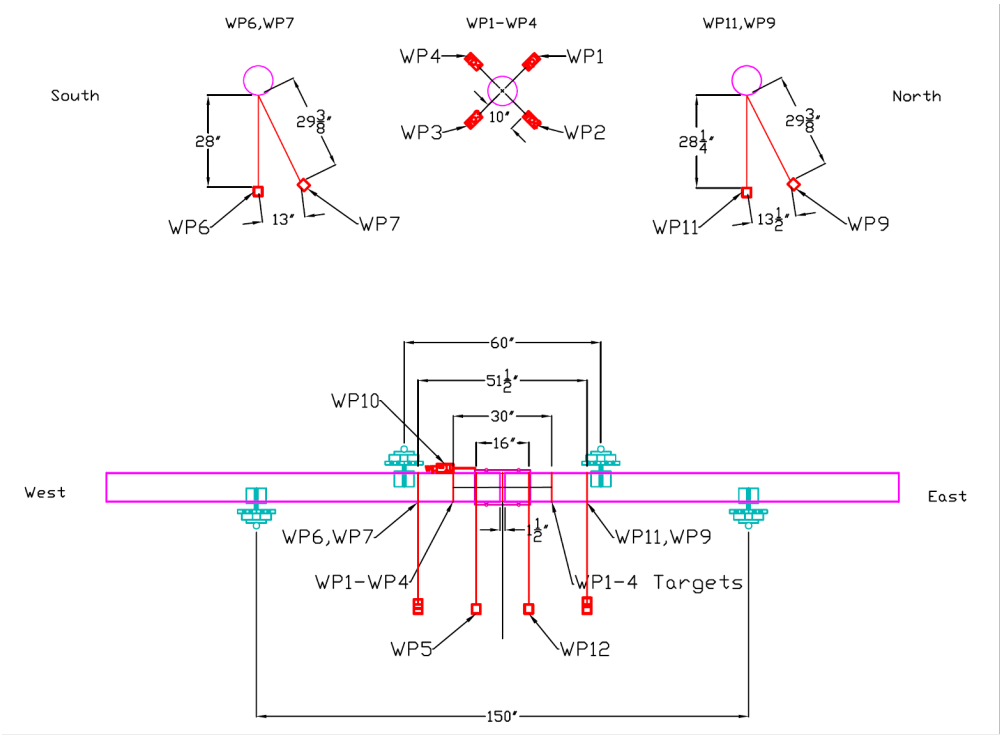


Fig. 7.30. Position transducers for displacement monitoring of specimen-RL

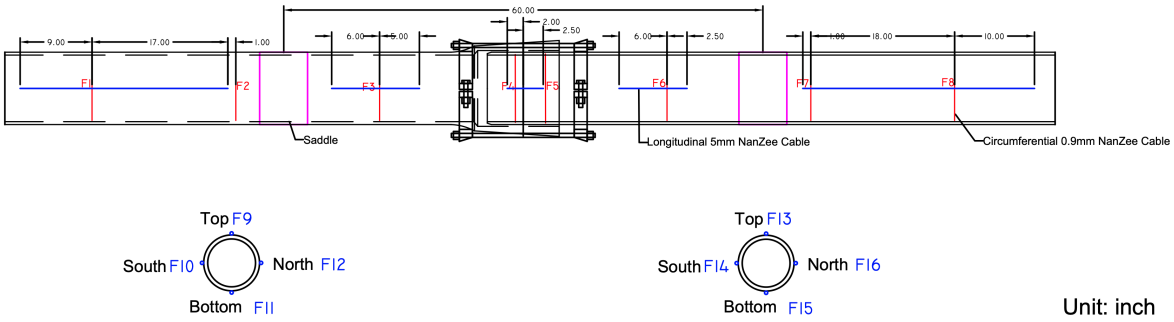


Fig. 7.31. DSS plan for Specimen-EBAA

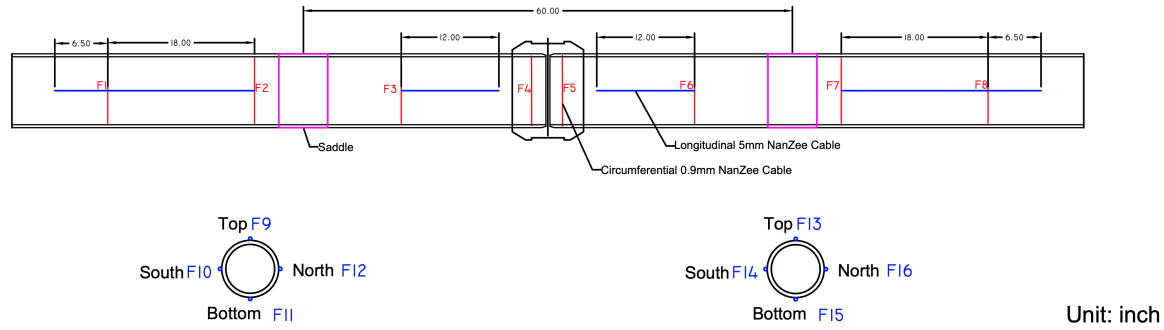


Fig. 7.32. DSS plan for Specimen-RCT

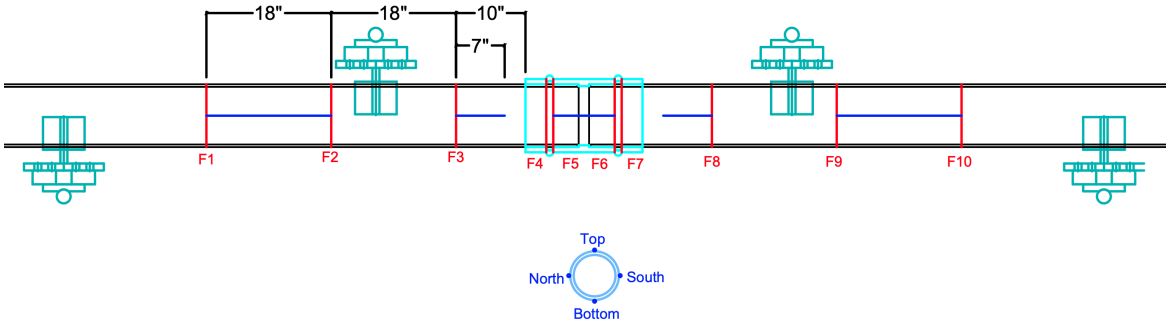


Fig. 7.33. DSS plan for specimen-RL

the deformation mechanisms of the pipe and joint assemblies. To bond these cables to the external pipe surfaces, two different industrial structural adhesives were employed depending on the testing phase: 3M SCOTCH-WELD DP8010 epoxy was utilized for Specimens-EBAA and Specimen-RCT, whereas Huntsman Araldite 2021-1 epoxy was selected for the Reiber-Lok specimen.

For longitudinal strain measurements, 5-mm cables (designated as blue lines in the layouts) were bonded continuously along both pipes to mimic standard field applications on construction sites. These sensors were positioned at 90-degree intervals around the pipe circumferences. In terms of nomenclature, these longitudinal arrays were numbered F9–F16 for Specimens-EBAA and -RCT, and designated as Top (T), North (N), South (S), and Bottom (B) for the ReiberLok specimen.

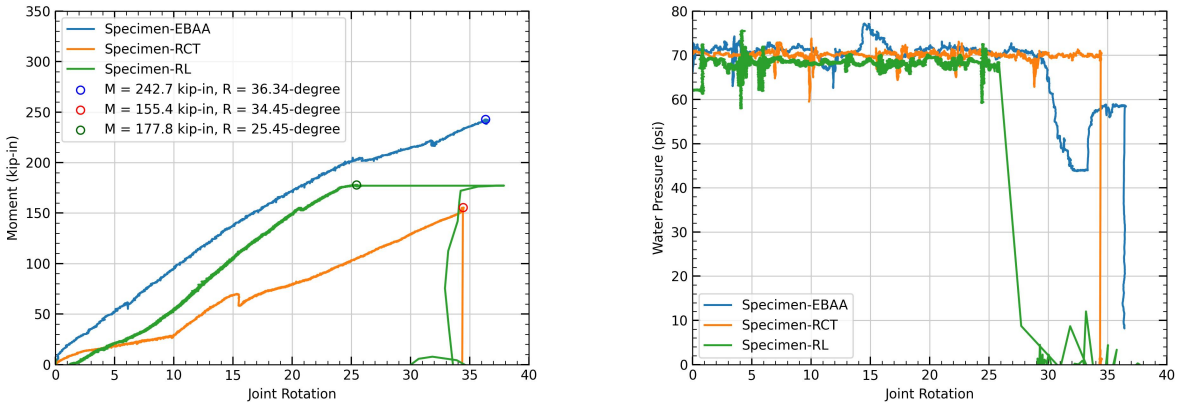
To measure localized circumferential (hoop) strains, thinner 0.9-mm cables (designated as red lines) were wrapped around the assemblies. Across all tests, three circumferential sensors were installed on the main pipe bodies with approximately 18-inch spacing. The instrumentation directly at the joint varied to accommodate the different restraint mechanisms. For Specimen-EBAA, two hoop strain sensors were attached at the bell section, while Specimen-RCT featured two sensors on the RCT restraint (collectively numbered F1–F9). For the ReiberLok specimen, four highly localized circumferential sensors were deployed directly on the plastic fitting, specifically, two sensors were placed flanking each of the two internal locking gaskets to capture pipe-gasket interactions (numbered F1–F10). The specific local names and corresponding locations for all DSS arrays are summarized in Figure 7.31 to Figure 7.33.

7.4.2 Failure Mode

Prior to testing, all pipe assemblies were filled with water and internally pressurized to approximately 70 psi. A monotonic vertical load, applied perpendicular to the longitudinal axis of the pipeline, was introduced at the center of the spreader beam and subsequently distributed to the specimen through the two loading saddles. To facilitate a direct comparison among the different joint configurations, the global bending moments and corresponding joint rotations were calculated using the vertical wire pots (VWP) approaches described in Equation 4.5.

The resulting moment–rotation relationships are presented in Figure 7.34a. The EBAA-restrained specimen exhibited the greatest deformation capacity, reaching a maximum joint rotation of 36.34° while sustaining a peak bending moment of 242.7 kip-in. The RCT-restrained specimen achieved a comparable rotation capacity of 34.45°, although at a substantially lower peak moment of 155.4 kip-in. The specimen utilizing the ReiberLok plastic fitting (Specimen-RL) reached a maximum rotation of 25.45° and a corresponding peak moment of 177.8 kip-in.

Significant differences in the rotational stiffness of the three joint systems were observed. For a given joint rotation, Specimen-EBAA consistently developed a greater bending moment than Specimen-RCT, indicating a stiffer overall response. This behavior might suggest



(a) Joint rotation and moment

(b) Joint rotation versus water pressure

Fig. 7.34. Moment, rotation, and water pressure of the tests

that the geometry and longitudinal extent of the restraint mechanism play a critical role in governing the flexural response of the assembly. The EBAA 1900 restraint spans a greater length than the RCT restraint, which likely mobilizes a larger resisting zone and consequently requires a greater applied moment to achieve the same level of rotation. In contrast, the lower stiffness observed in Specimen-RCT may be associated with its shorter engagement length and potential localized pipe movement or slip within the restraint, reducing the effectiveness of force transfer. The response of Specimen-RL fell between those of the two externally restrained systems; because its internal ReiberLok plastic fitting also spans a considerable length, greater than that of the RCT restraint, it developed higher moments than Specimen-RCT, though it remained less stiff than Specimen-EBAA at equivalent rotations.

The relationship between internal water pressure and joint rotation is presented in Figure 7.34b. Differences in pressure-retention performance were observed among the three joint configurations. Specimen-EBAA maintained its structural integrity throughout the test; however, minor and continuous leakage initiated at approximately 28° of rotation. Despite this leakage, no catastrophic failure or sudden loss of internal pressure occurred. In contrast, Specimen-RCT maintained full internal pressure throughout nearly the entire loading history and only experienced a rapid pressure loss following catastrophic pipe failure at its maximum rotation of 34.45°. Specimen-RL exhibited the lowest deformation capacity with respect to watertight performance. The assembly maintained the target internal pressure until reaching its peak capacity, at which point a sudden and complete loss of pressure occurred simultaneously with joint failure at a rotation of 25.45°. The results are shown in Table 7.4.

These results demonstrate that while the EBAA restraint provided the greatest flexural stiffness and rotational capacity, the RCT restraint exhibited superior pressure-retention per-

Table 7.4. Summary of four-Point bending test results

Specimen	Restraint Type	Peak Moment (kip-in)	Max Rotation (degrees)
Specimen-EBAA	EBAA 1900	242.7	36.34
Specimen-RCT	RCT	155.4	34.45
Specimen-RL	Plastic Fitting	177.8	25.45

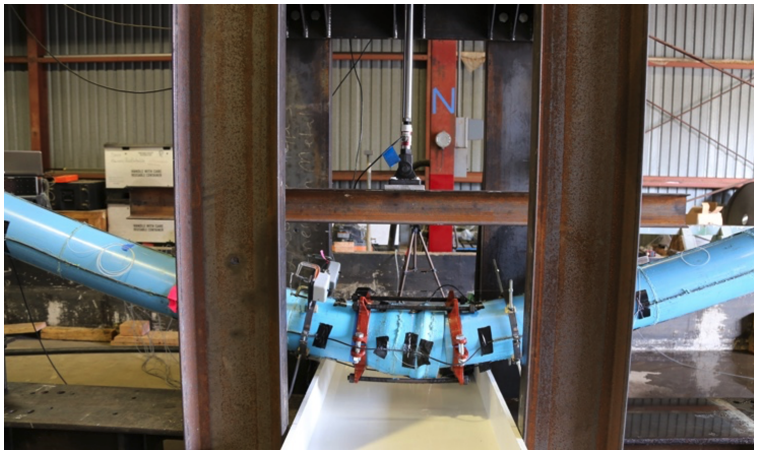


Fig. 7.35. Large deformation of Specimen-EBAA. Note that no structural failure was found

formance up to the point of structural failure. The ReiberLok fitting developed an intermediate flexural response but experienced an earlier loss of load-carrying and pressure-retention capacity compared with the externally restrained systems.

Visual inspections of the joint assemblies during and after the bending tests revealed distinct deformation kinematics and failure modes governed entirely by the specific restraint mechanisms. For Specimen-EBAA, no catastrophic structural rupture occurred (Figure 7.35). The EBAA 1900 utilizes an external locking ring configuration, which permitted a degree of relative kinematic movement between the pipe segments within the bell section. Under severe flexural bending, the geometric distortion forced the top crown of the spigot inward toward the back of the bell, while simultaneously forcing the bottom invert of the spigot to pull outward. This localized pull-out at the bottom fiber structurally compromised the gasket seal, directly causing the continuous, minor water leakage observed after reaching approximately 28 degrees of joint rotation.

Conversely, Specimen-RCT utilized an internal locking mechanism that rigidly prevented the spigot from pulling out of the connection section (Figure 7.36). Consequently, the watertight seal was strictly maintained throughout the loading phase. However, because the



(a) Large deformation of Specimen-RCT with structural failure and severe water leak



(b) Failure of Specimen-RCT around the joint

Fig. 7.36. Large deformation and failure of Specimen-RCT

rigid RCT restraint is longitudinally shorter than the EBAA system, the severe bending deformations generated highly concentrated compressive stresses at the structural boundary between the restraint and the main pipe body. This localized stress concentration ultimately precipitated the catastrophic, brittle rupture of the pipe material at the peak load.

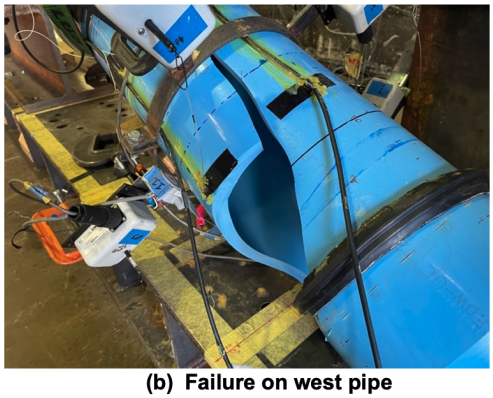
Specimen-RL, utilizing the internal ReiberLok plastic fitting, exhibited a complex, combined failure mode involving both the plastic fitting and the inserted west pipe. As detailed in Figure 7.37a, the ultimate failure originated in the immediate vicinity of the internal ReiberLok gasket. The gasket's integrated metallic gripping teeth, while essential for preventing axial joint separation, acted as severe geometric discontinuities that induced high localized stress concentrations under extreme flexural loading. These stress concentrations served as the initiation points for the subsequent structural fractures. The fracture sequence in Specimen-RL propagated through two distinct mechanisms. As illustrated in 7.37c, the failure of the plastic fitting initiated at the top crown, the zone subjected to maximum compressive flexural forces, and subsequently propagated downward along the lateral sides, driven by induced shear forces. Simultaneously, the west pipe failed at the bottom invert, the zone subjected to maximum tensile flexural stresses. The initial crack on the pipe wall manifested directly adjacent to the gasket interface, where the gripping teeth induced the critical stress concentrations, and propagated upward toward the top of the pipe as a distinct shear fracture (Figure 7.37b).

7.4.3 Axial Strain

The longitudinal (axial) strain results captured by DSS provide critical insight into the deformation mechanisms of the joints during flexural loading. While the maximum joint rotations for the assemblies reached up to 36 degrees, localized strains began to exceed the measurement capacity of the DSS interrogator after approximately 18 degrees of rotation



(a) Overall failure



(b) Failure on west pipe



(c) Failure on fitting

Fig. 7.37. Large deformation of Specimen-RL and failure mode

(corresponds to 12,000+ microstrain), resulting in signal loss for certain sensors. Despite this limitation at extreme deformations, the data captured during the primary loading phases captures the structural behavior of the pipes.

To compare the representative structural behavior across the different joint configurations, specific measurement locations along the longitudinal sensors were isolated for analysis: the midpoints between circumferential sensors F1 and F2 (west pipe) and F7 and F8 (east pipe) for all three specimens. These data extraction points are visually denoted by the red dots in the corresponding experimental sketches in Figure 7.38 to Figure 7.40. These specific locations were selected because they are situated sufficiently far from the central joint, ensuring that the measured strains reflect the fundamental global bending behavior of the pipe rather than being distorted by the complex, highly localized interactions at the

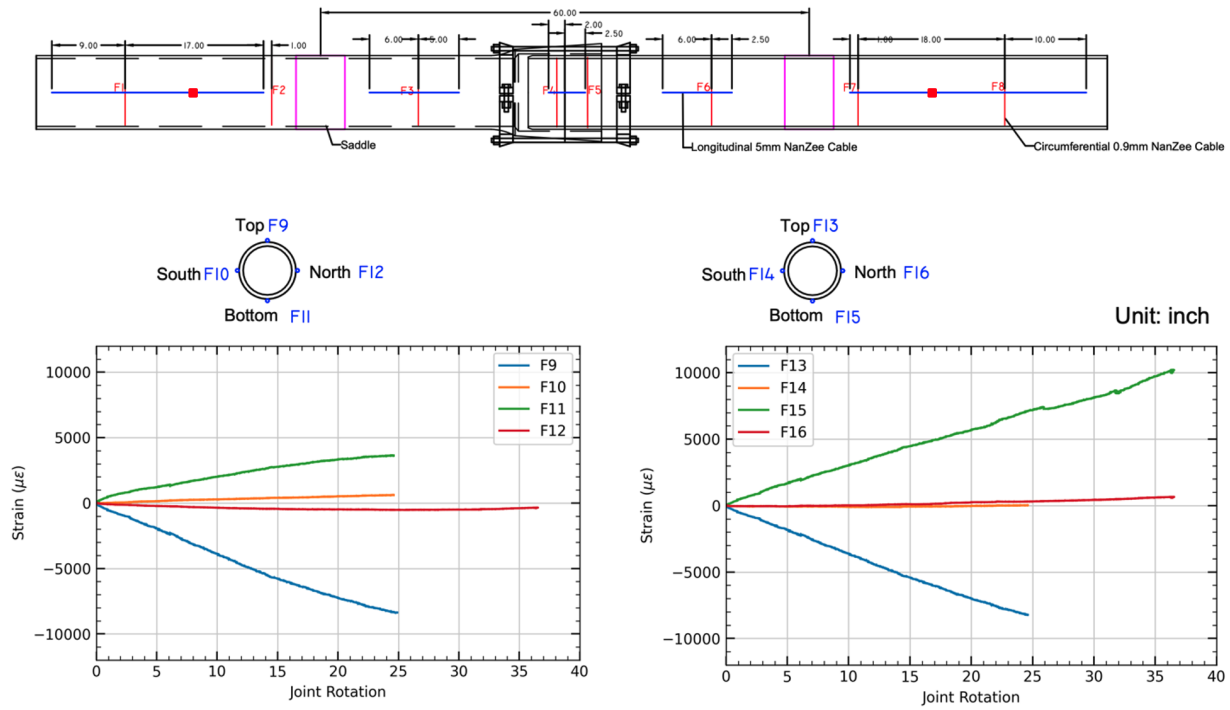


Fig. 7.38. Axial strain and joint rotation of Specimen-EBAA. West pipe on the left and East pipe on the right

pipe-restraint interface. At these critical cross-sections across all three specimens, the fundamental strain development followed classical beam bending theory. As the joints were rotated, the top fibers of the pipes were subjected to high compression, the bottom fibers were subjected to high tension, and the lateral sides (north and south) experienced minimal stresses, remaining close to the neutral axis.

Specimen-EBAA generally exhibited the largest global strain magnitudes distributed across the main pipe bodies, with tensile strains reaching approximately 10,000 microstrain and compressive strains reaching near -8,000 microstrain before sensor signal loss. The EBAA 1900's external locking mechanism allowed the spigot and bell to kinematically bear against one another, distributing large flexural deformations across the pipe length without inducing fatal localized stresses.

Conversely, the ductile iron RCT restraint utilized in Specimen-RCT possessed significantly higher structural stiffness. As a result, the measured global strains at these extraction locations were notably lower—peaking at only about 5,000 microstrain in both tension and compression, despite reaching a similar maximum joint rotation of roughly 35 degrees. This rigidity restricted global pipe deformation but created highly localized strain concentrations at the boundary between the rigid restraint and the relatively flexible iPVC pipe, directly causing the brittle rupture at the connection interface.

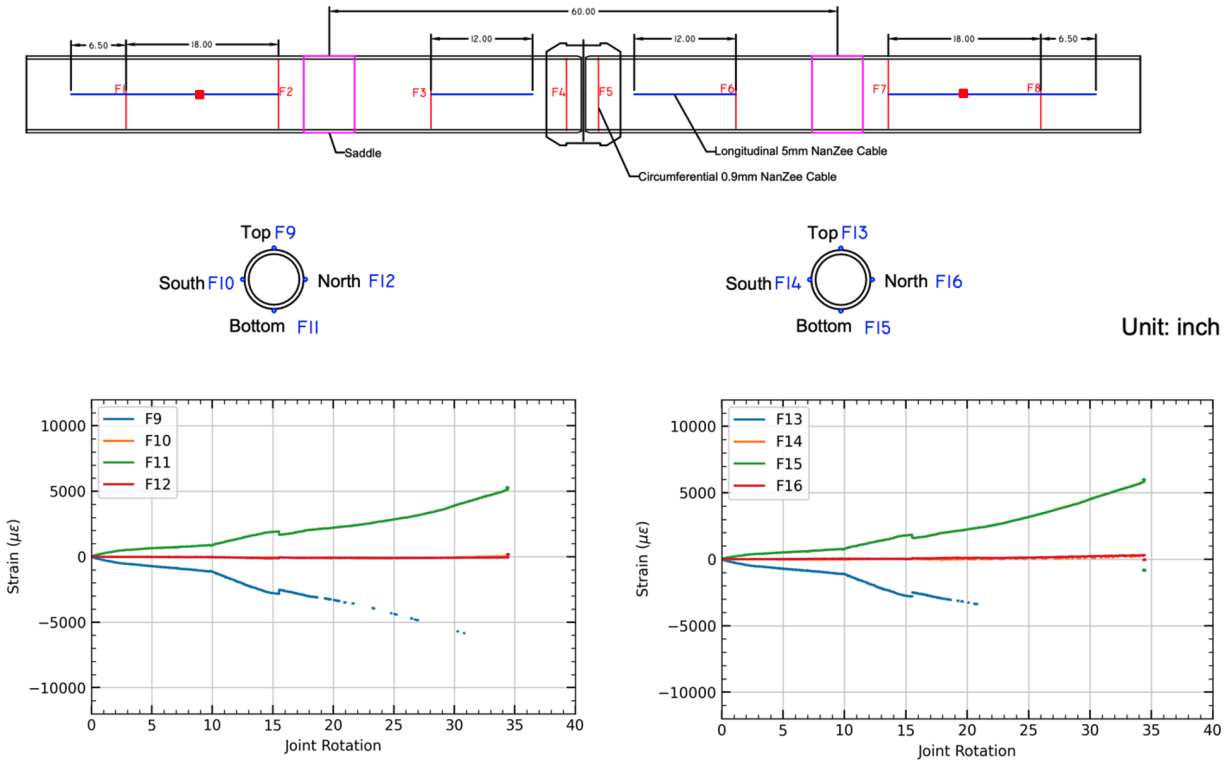


Fig. 7.39. Axial strain and joint rotation of Specimen-RCT. West pipe on the left and East pipe on the right

The strain profile of Specimen-RL reflected its intermediate stiffness and unique internal mechanics. It exhibited large top-fiber compressive strains (exceeding -8,000 microstrain) but comparatively moderate bottom-fiber tensile strains (roughly 4,000 microstrain). This asymmetry occurs may be because the pipe spigot bears directly against the top crown of the fitting, efficiently transferring compression. At the bottom invert, the joint relies on the ReiberLok gasket's metallic teeth to transfer tension. However, severe cross-sectional distortion under extreme bending could compromise this gripping mechanism. As the teeth lost their radial bite on the pipe wall, tensile force transfer could be limited.

The continuous spatial distribution of longitudinal (axial) strains provides a high-resolution map of how bending stresses developed along the length of the specimens. Figure 7.41 presents these spatial profiles. In all subfigures, the data is plotted horizontally from the west pipe on the left, across the central joint mechanism, to the east pipe on the right. Gaps in the continuous data traces along the main pipe bodies correspond to the loading saddles, where the DSS cables could not be attached. Across all three specimens, the main pipe bodies exhibited a fundamental adherence to classic beam bending theory: the top fiber (12 o'clock) underwent uniform compression, the bottom fiber (6 o'clock) experienced uniform tension, and the side fibers (3 and 9 o'clock) registered near-zero strains. However, the

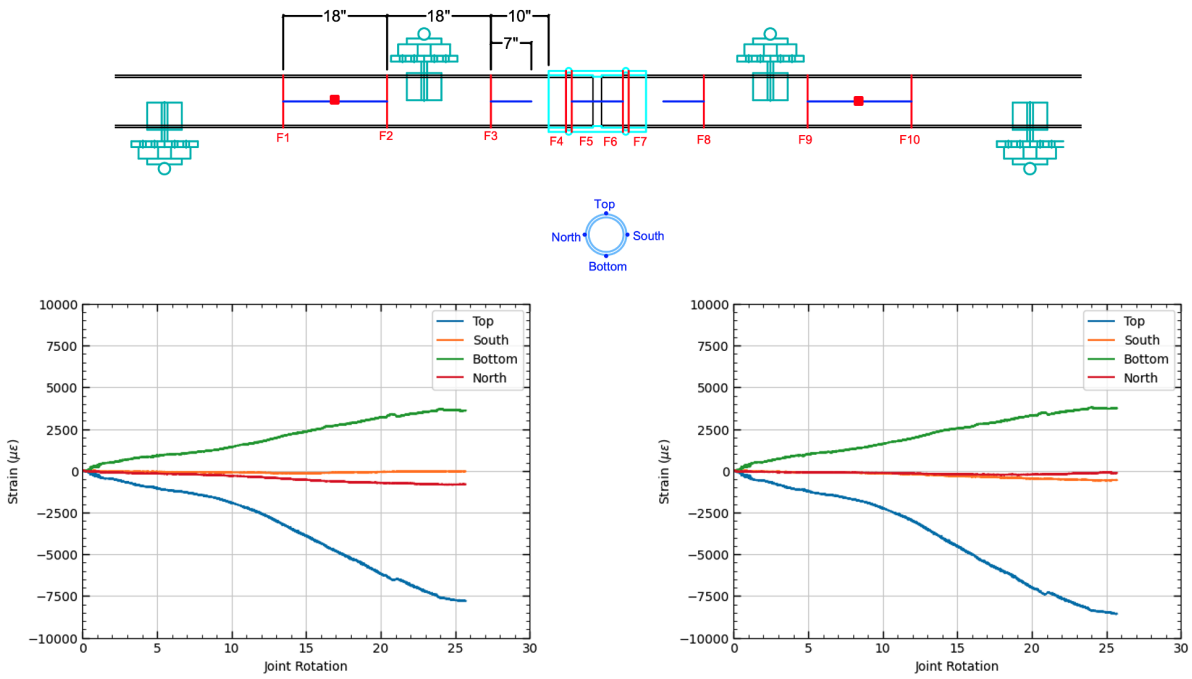
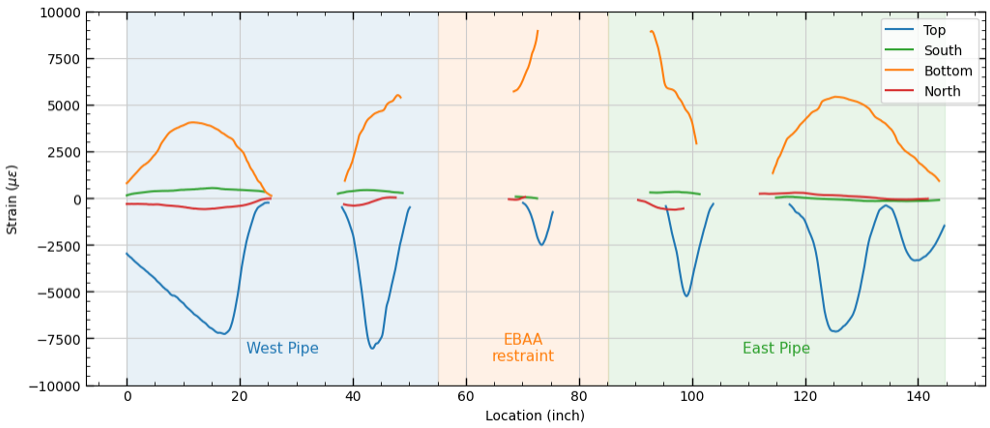


Fig. 7.40. Axial strain and joint rotation of Specimen-RL. West pipe on the left and East pipe on the right

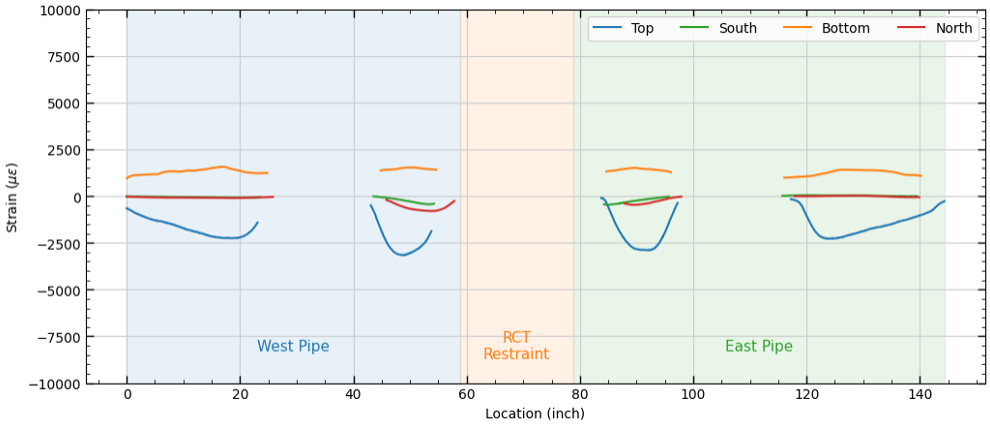
distinct mechanical properties of each joint system introduced localized deviations from this theoretical baseline.

For Specimen-EBAA (Figure 7.41a), additional data gaps near the center correspond to the external rings of the EBAA 1900 restraint. While the main pipes followed the classic bending profile, critical deviations emerged directly adjacent to the bell section. In this zone, the top fiber exhibited a noticeable reduction in compressive strain, while the bottom fiber experienced an exacerbation of tensile strain. This localized asymmetry supports the kinematic observation described previously: as the joint underwent severe bending, the spigot segment attempted to pull out from the bottom invert of the bell. Because the external EBAA restraint aggressively restricted this longitudinal movement, significant tensile stresses accumulated at this constrained boundary near the bell section.

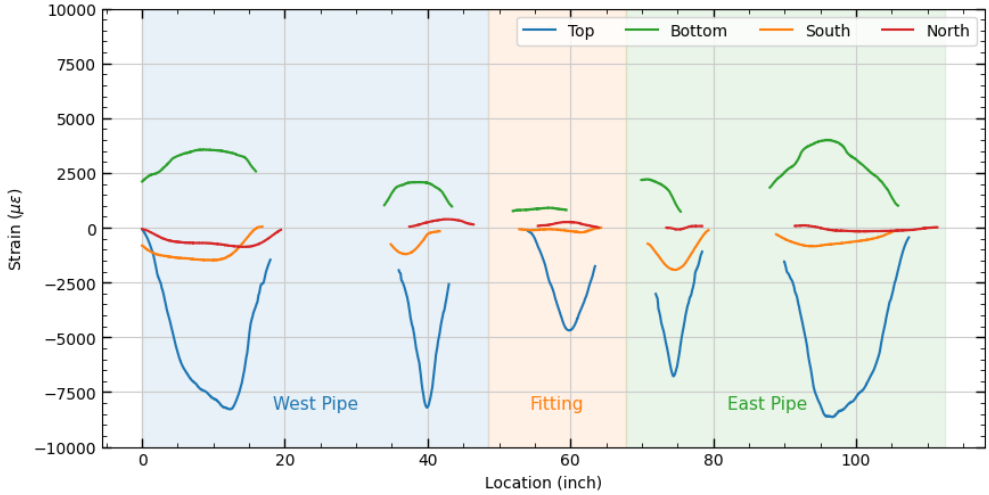
For Specimen-RCT (Figure 7.41b), the spatial strain distribution contrasts heavily with the other specimens in terms of magnitude. Due to the extreme structural rigidity of the internal ductile iron RCT restraint, global pipe deformation was severely restricted. (Note that the large data gap in the center of this plot exists because longitudinal DSS cables were not routed through or across the internal RCT restraint itself). Consequently, the measured longitudinal strains along the main bodies of both the west and east pipes remained remarkably low (generally below 2,500 microstrain), despite the assembly undergoing massive global rotation. This distinct, muted strain signature shows that the rigid RCT joint prevents



(a) Specimen-EBAA



(b) Specimen-RCT



(c) Specimen-RL

Fig. 7.41. Axial strain development under 18-degree rotation condition across all specimens

the smooth distribution of flexural forces, instead forcing critical stresses to concentrate abruptly at the narrow geometric boundary between the restraint and the pipe, leading to its brittle failure.

For Specimen-RL (Figure 7.41c), the magnitude of the measured strains transitioned abruptly at the interfaces with the central ReiberLok plastic fitting. Because the wall thickness of the plastic fitting is greater than that of the standard iPVC pipes, its localized bending stiffness is higher, resulting in correspondingly smaller strain developments within the fitting itself. Furthermore, a distinct asymmetry in strain magnitude between the top and bottom fibers was observed. Generally, the compressive strains along the top crown were of a larger absolute magnitude than the corresponding tensile strains along the bottom invert. This structural phenomenon is attributed to the internal kinematics of the pipe-fitting rotation: the top surface of the inserted spigot bore heavily into direct contact with the internal crown of the fitting, facilitating efficient compressive force transfer. Conversely, at the bottom invert, the bending rotation caused the pipe to pull slightly away from the internal wall, partially disengaging the tensile force transfer mechanism. Finally, while the side fibers generally registered the expected minimal strains, localized compressive strains were observed on the first 18 inches of the west pipe's north fiber and continuously along the east pipe's south fiber. These minor anomalies are not structural artifacts but rather the result of slight installation tolerances, where the 5-mm optical cables were bonded slightly above the true neutral springline.

7.4.4 Hoop Strain

The circumferential (hoop) strain data shown in Figure 7.42, Figure 7.44, and Figure 7.46, provides localized insights into the cross-sectional deformation mechanisms (i.e., pipe squashing and joint kinematics) occurring throughout the bending process. Across the main pipe bodies of all three specimens, a consistent fundamental deformation pattern emerged. Measurements taken at cross-sections away from the central joint (specifically F3 and F6 for Specimen-EBAA and Specimen-RCT, and F3 and F8 for Specimen-RL) demonstrated that the top crown of the pipe expanded while the bottom invert compressed, with minimal strains occurring along the springlines. This eccentric squashing behavior is a direct consequence of Poisson's effect: as the top fiber undergoes extreme longitudinal compression, it expands circumferentially, and conversely, as the bottom fiber undergoes extreme longitudinal tension, it contracts circumferentially. For all specimens, the magnitude of these hoop strains predictably decreased as the distance from the central bending point increased [34].

However, the localized hoop strains measured directly at the joint interfaces (specifically F4 and F5 for all specimens) varied, governed entirely by the specific restraint mechanics. For Specimen-EBAA, the sensors positioned directly on the bell section captured complex internal bearing mechanics. The external EBAA 1900 restraint allowed relative movement within the joint. As the assembly was forced into a curve, the inserted spigot pivoted inside the bell. The sensor on the west side of the bell center (F4) recorded larger expansion at the bottom invert, indicating the spigot was bearing down heavily against the bottom

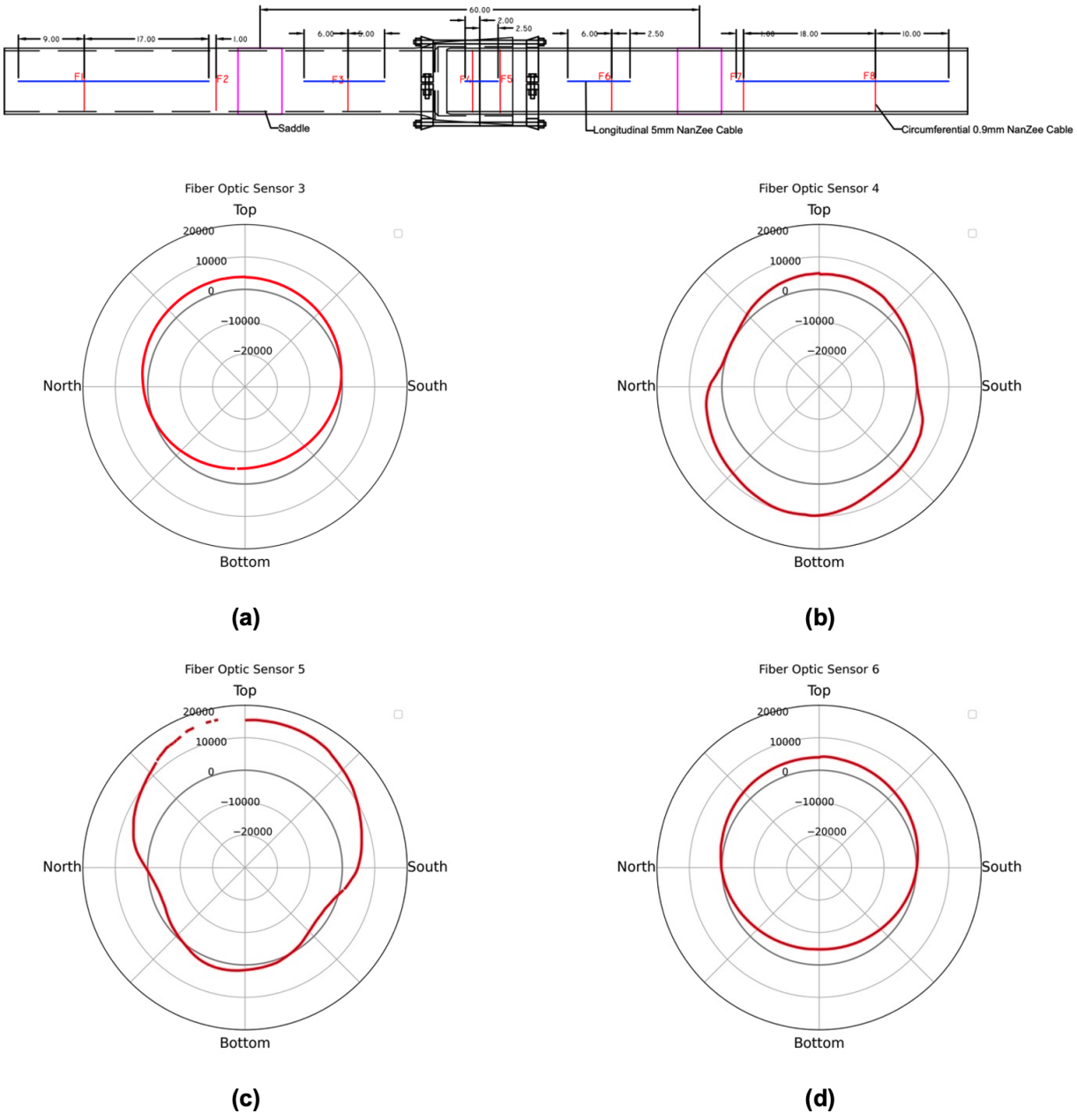


Fig. 7.42. Strain distribution in the circumferential direction of Specimen-EBAA under 18-degree rotation condition. (a) Sensor F3 (b) Sensor F4 (c) Sensor F5 (d) Sensor F6

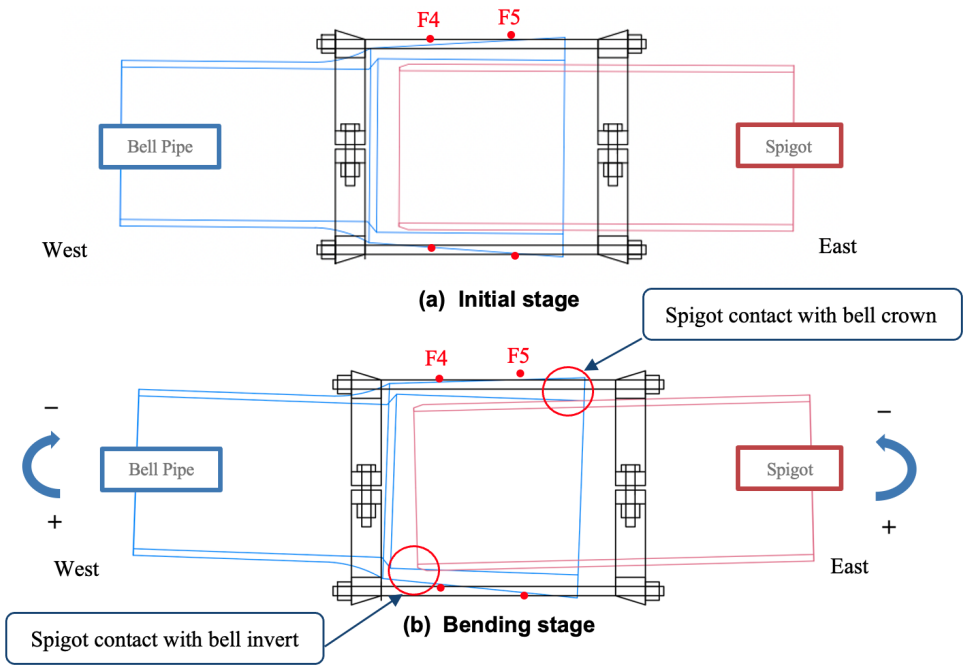


Fig. 7.43. Sketch of EBAA 1900 restraint deformation mechanism

inside surface of the bell. Conversely, the sensor on the east side (F5) recorded expansion at the top crown, indicating the spigot was prying upward against the inside top of the bell face. The mechanism is shown in Figure 7.43. This kinematic rotation allowed the joint to accommodate massive rotation without inducing fatal point loads. Furthermore, comparing the global hoop strains, Specimen-EBAA developed larger overall cross-sectional deformations across the main pipes than Specimen-RCT, reflecting the flexibility of this bearing mechanism.

In contrast, the sensors positioned directly on the RCT restraint itself (F4 and F5) in Specimen-RCT recorded hoop strains that were essentially zero throughout the test. Because the RCT restraint is fabricated from ductile iron, its circumferential stiffness vastly exceeds that of the iPVC pipe. Consequently, while the adjacent plastic pipe was squashing and deforming significantly, the restraint remained perfectly rigid. This mismatch in cross-sectional stiffness prevented the pipe from naturally ovalizing inside the restraint. Instead, massive shear forces and severe stress concentrations were generated precisely at the structural boundary where the deforming pipe met the unyielding rigid iron lip, as shown in Figure 7.45. This localized stress concentration, directly visible as the boundary point in the hoop strain plots, precipitated the sudden, brittle rupture of the pipe wall.

Finally, the hoop strains recorded directly on the ReiberLok plastic fitting in Specimen-RL revealed highly localized internal interactions. To fully capture these complex joint kinematics, sensors were strategically placed at two distinct functional zones on the fitting:

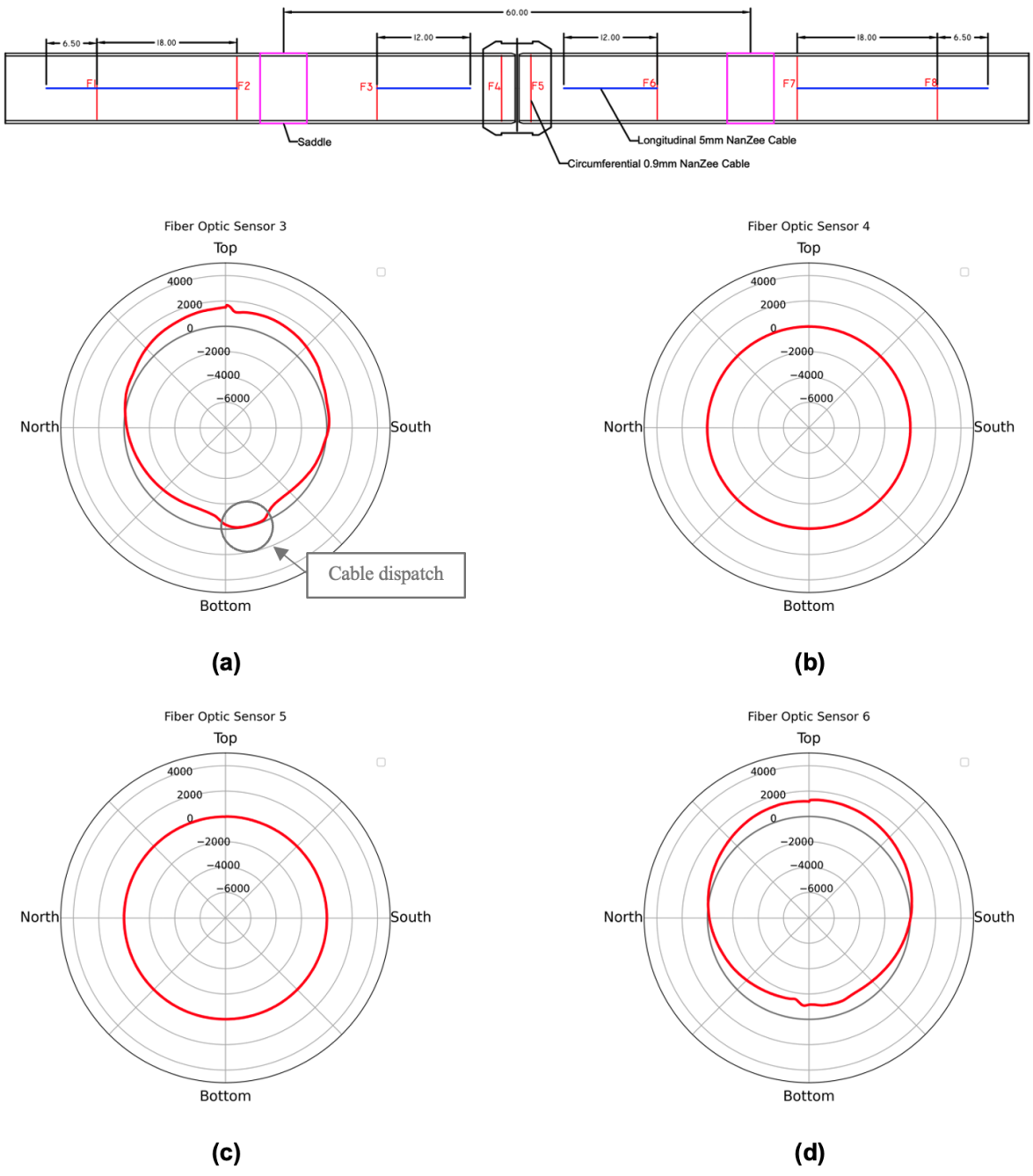


Fig. 7.44. Strain distribution in the circumferential direction of Specimen-RCT under 18-degree rotation condition. (a) Sensor F3 (b) Sensor F4 (c) Sensor F5 (d) Sensor F6

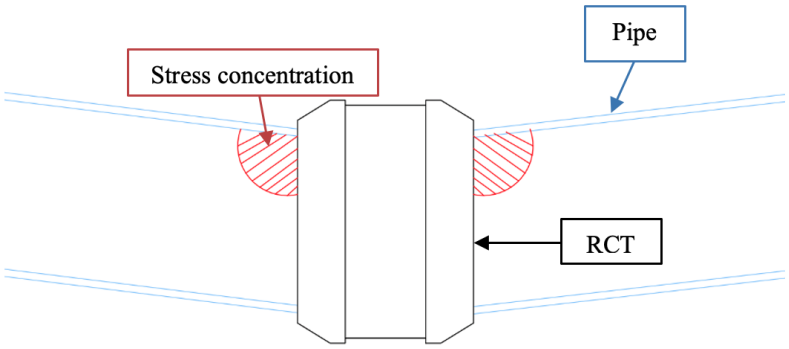


Fig. 7.45. Sketch of stress concentration at the boundary of pipe and RCT restraint of Specimen-RCT

F4 was located near the outer edge to specifically monitor the structural impact of the gripping gasket, while F5 was positioned at the middle section to measure the direct bearing forces of the inserted pipe. Unlike the completely rigid RCT restraint, the plastic fitting deformed under load. These targeted sensors captured tensile hoop strains at the bottom invert, driven by two simultaneous internal mechanisms. First, at the outer edge (measured by F4), as severe bending generated high longitudinal tension along the bottom fiber, the inserted spigot attempted to pull out. This forced the metallic gripping teeth of the gasket to dig in and pull outward radially, violently expanding the plastic fitting. Second, in the middle section (measured by F5), as the inserted spigot rotated during bending, its bottom surface bore heavily against the internal invert of the central fitting. The mechanism is illustrated in Figure 7.47.

7.4.5 Conclusion of iPVC Four-Point Bending Test

This section details the experimental investigation of 8-inch AWWA C900 DR14 iPVC pipe assemblies subjected to four-point bending loadings. The objectives were to evaluate the flexural capacity, deformation kinematics, and failure mechanisms of three distinct joint configurations: two utilizing external restraints (EBAA 1900 and RCT) and one utilizing an internal plastic fitting (ReiberLok). The assemblies were loaded until severe structural damage or catastrophic loss of internal water pressure occurred.

The joint restraint mechanism fundamentally dictated the structural capacity and failure mode of the pipeline. Specimen-EBAA, utilizing a flexible external locking ring, demonstrated the highest rotational capacity, reaching the physical limits of the testing setup (over 36 degrees of rotation) without catastrophic pipe rupture, though minor continuous leakage initiated at 28 degrees due to spigot pull-out. Specimen-RCT, constrained by a rigid, ductile iron internal locking mechanism, exhibited a lower rotational capacity and suffered a sudden, brittle pipe rupture at the restraint boundary at 34.45 degrees. Specimen-RL, utilizing the

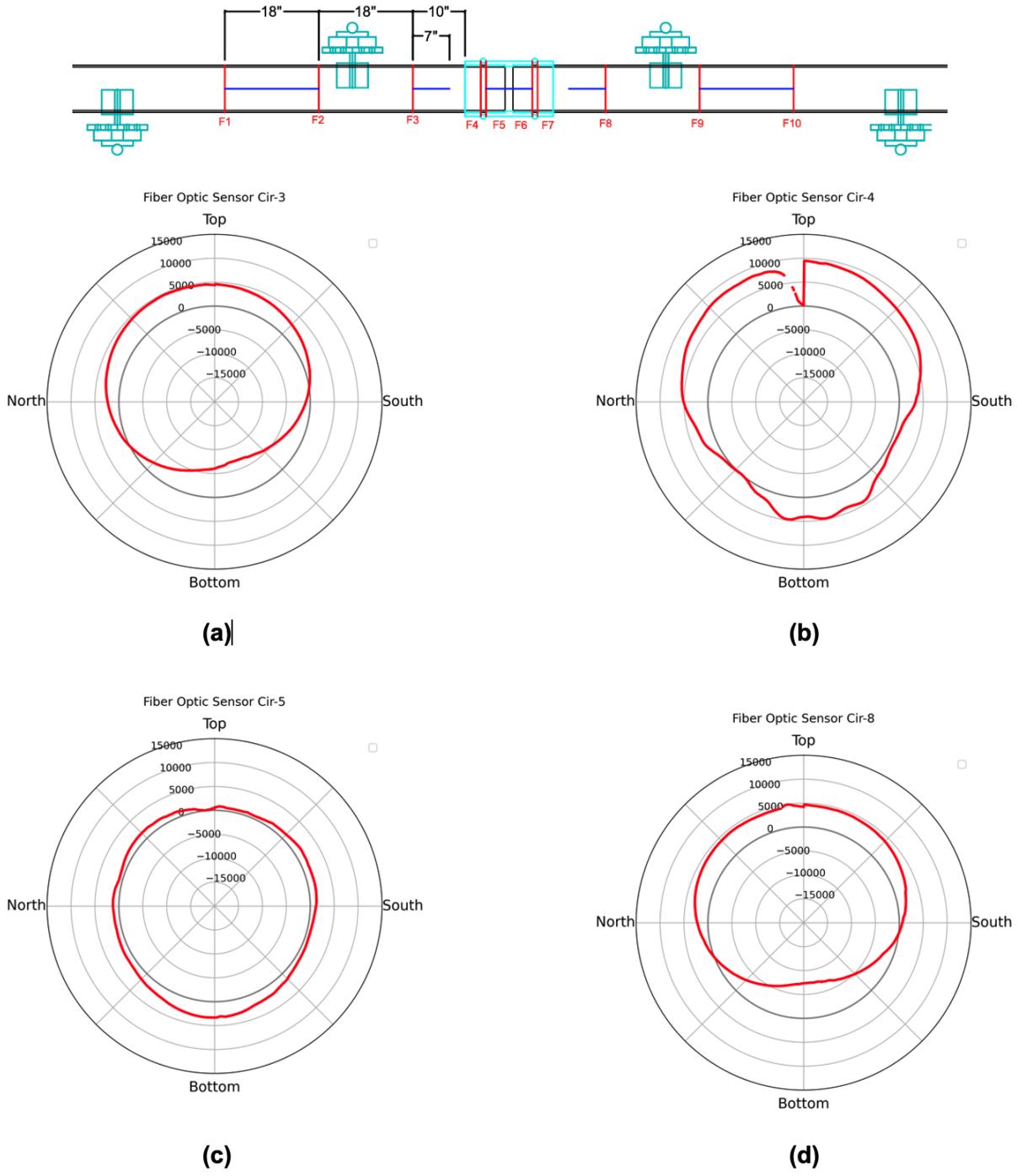


Fig. 7.46. Strain distribution in the circumferential direction of Specimen-RL under 18-degree rotation condition. (a) Sensor F3 (b) Sensor F4 (c) Sensor F5 (d) Sensor F8

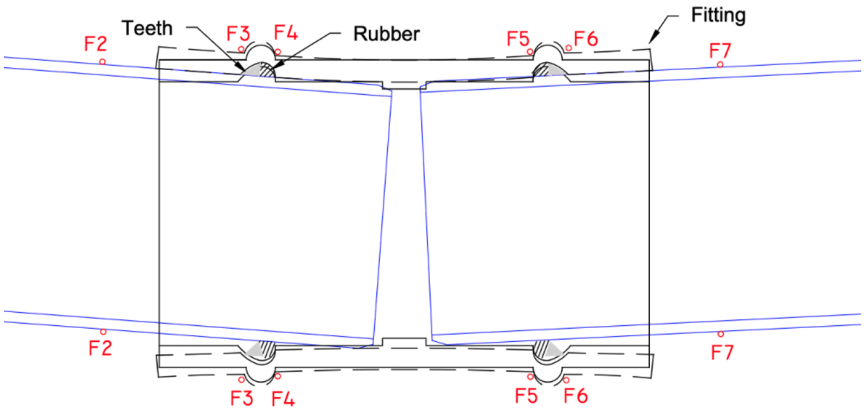


Fig. 7.47. Sketch of fitting deformed mechanism of Specimen-RL

internal ReiberLok plastic fitting, failed earliest at approximately 25.45 degrees of rotation, characterized by a complex combined fracture of the top crown of the plastic fitting under compression and the bottom invert of the inserted pipe under tension.

Furthermore, the longitudinal extent of the restraint directly influenced the overall bending stiffness of the assembly. Specimen-EBAA, with its longer external tie-rod configuration, generated the highest bending moments for a given rotation. The structural response of Specimen-RL fell intermediate to the two externally restrained systems, developing higher moments than Specimen-RCT prior to failure, while the shorter, rigid RCT restraint produced the lowest global moments.

High-resolution strain profile suggested that while the global pipe segments adhered to classical beam bending theory, exhibiting compression on top, tension on the bottom, and eccentric cross-sectional squashing due to Poisson's effect, the localized mechanics at the joints varied significantly. In Specimen-EBAA, the spigot bore against and pivoted within the bell, allowing large, smoothly distributed deformations. Conversely, in Specimen-RCT, the rigidity of the restraint prevented cross-sectional ovalization, forcing stress concentrations directly onto the plastic pipe wall. The internal kinematics of Specimen-RL revealed that the ReiberLok gasket's metallic gripping teeth acted as stress risers; as the joint underwent extreme bending, the teeth bite into the pipe invert to resist tensile pull-out, while simultaneously forcing the outer edges of the plastic fitting outward, ultimately initiating the structural fractures observed in both the pipe and the fitting.

7.5 Summary and Discussion of iPVC Experiments

The comprehensive testing program, encompassing monotonic tension, axial compression, and four-point bending, demonstrated that the structural performance of iPVC pipeline assemblies is governed primarily by the design and stiffness characteristics of the joint restraint

system. Although all specimens utilized the same pipe material, substantial differences were observed in load capacity, deformation compatibility, pressure-retention behavior, and failure mechanisms. The results indicate that restraint systems must not only provide sufficient resistance against pullout forces but also accommodate the large deformations and cross-sectional distortions that develop during extreme loading events.

The tension tests demonstrated that gasket geometry plays a critical role in the axial capacity of restrained plastic fittings. The ReiberLok gasket achieved nearly three times the tensile resistance of the TurnerLok gasket, indicating that the larger number of smaller teeth more effectively distributed forces around the pipe circumference. In contrast, the TurnerLok gasket transferred load through fewer contact points, producing localized stress concentrations that accelerated material damage. Furthermore, strain profile revealed that small installation imperfections and uneven gasket seating significantly influenced load transfer; incomplete engagement of restraint teeth produced localized strain concentrations and secondary bending effects that reduced the effective capacity of the joint. Regarding pressure retention, both systems maintained their watertight seals throughout the loading progression, with the sudden drop in internal water pressure occurring simultaneously with the peak axial force and ultimate physical failure of the joints.

The compression tests further demonstrated the sensitivity of the system to geometric instability. Although the pipe assembly sustained massive axial loads approaching 100 kips, global buckling altered the alignment of the pipe segments and produced nonuniform contact within the fitting. These changes induced localized ovalization and outward expansion of the sleeve, ultimately controlling the failure process. The pressure-retention behavior under compression was highly resilient; the internal watertight seal was maintained throughout the entire active loading and buckling phase. Leakage and ultimate physical rupture occurred exclusively during the subsequent unloading phase, with the failure localized at the highly distorted interface between the plastic sleeve and the buckled pipe segment.

The bending tests highlighted the critical importance of deformation compatibility between the restraint system and the relatively flexible iPVC pipe under combined loading. The EBAA 1900 restraint exhibited the highest rotational capacity, exceeding 36°. Its external tie-rod configuration allowed relative movement between pipe segments, smoothly distributing deformations over a larger region of the assembly. However, this flexibility came at the cost of earlier pressure loss; as the spigot pulled out from the bell during bending, minor, continuous water leakage initiated at approximately 28° of rotation. In contrast, the highly rigid RCT restraint generated a stiffer structural response, restricting natural cross-sectional ovalization. This stiffness concentrated deformation entirely near the restraint boundaries, ultimately leading to a sudden, brittle pipe-wall fracture at 34.45° and an immediate, catastrophic loss of water pressure. The internal ReiberLok fitting displayed an intermediate structural response. As joint rotation increased, the metallic teeth bit into the pipe wall to resist pullout, acting as a wedge that forced the outer edges of the fitting to expand outward. This initiated a complex structural fracture and simultaneous pressure loss at a earlier rotation of approximately 25.45°.

Overall, the results indicate that successful restraint design requires a delicate balance

between pullout strength, flexibility, and watertightness. Systems that effectively distribute forces while accommodating large deformations exhibited greater rotational capacity, though they may be susceptible to early, non-catastrophic leakage. Conversely, highly rigid restraint mechanisms maintained their seals longer but concentrated stresses that promoted sudden, localized, and catastrophic failure.

Chapter 8

Comparative Mechanics and Seismic Design Implications

8.1 Overview of the Component-Level Experimental Program

The component-level experimental program discussed in Chapter 5 to Chapter 7 encompassed restrained ductile iron and iPVC pipeline systems with diameters ranging from 8 to 48 in. The experiments included monotonic tension, axial compression, four-point bending, and combined tension–bending tests. Together, these loading configurations were used to characterize axial displacement, joint rotation, restraint engagement, load and moment transfer, hydraulic integrity, and ultimate failure.

Beyond establishing global force, moment, displacement, and rotation capacities, the experiments were designed to resolve the internal mechanics governing the observed response. Previous component-level studies have primarily reported overall joint capacity, leakage limits, and final failure modes. By integrating distributed strain sensing with conventional force, displacement, rotation, and pressure measurements, the present program captured localized mechanisms that have not previously been documented in comparable spatial detail. These include the development of bearing and wedging forces between restraint components, strain redistribution following restraint engagement, cross-sectional distortion of bells and fittings, shifts in local bending response after locking-segment displacement, and the progression from structural damage to hydraulic failure.

Table 8.1 summarizes the principal configurations and findings from the individual experimental programs presented in the preceding chapters.

The experiments demonstrate that the tested systems possessed substantial axial or rotational deformation capacity, frequently exceeding their nominal design limits. However, the observed response varied considerably with restraint geometry, loading path, pipe diameter, and relative component stiffness. The following sections synthesize these results through four cross-cutting themes: restraint-controlled load transfer, the distinction between structural

Table 8.1. Summary of the component-level experimental programs and principal findings.

Pipeline system	Configuration	Loading	Principal finding
8-in. ERDIP	Factory weld-bead and field-groove restraints	Monotonic tension	Both configurations developed large tensile resistance, but the factory weld-bead specimen failed through bell fracture while retaining substantial post-fracture hydraulic capacity. The field-groove specimen failed through circumferential spigot rupture with immediate loss of hydraulic containment.
8-in. ERDIP	Locking-segment insertion slot positioned at the springline or crown	Four-point bending	Both configurations achieved rotations of approximately 13°. Insertion-slot orientation strongly influenced joint stiffness and moment demand, while ultimate failure occurred through localized fracture of the spigot.
8-in. ERDIP	Locking-segment insertion slot positioned at the springline or crown	Combined tension and bending	Both configurations reached approximately 8.4° of rotation while sustaining substantial axial force. Failure localized at the transition between the locking segments and the compressible insertion slot.
36-in. ERDIP	Segmented internal locking restraint	Four-point bending	The joint reached 10.25° of rotation and a maximum moment of approximately 4,325 kip-in. Progressive displacement and ejection of the locking segments governed the ultimate loss of hydraulic integrity.
48-in. ERDIP	Segmented internal locking restraint	Four-point bending	The joint reached 6.45° of rotation and approximately 9,600 kip-in while pressurized to about 250 psi. Failure was governed by sequential detachment of the internal locking segments rather than fracture of the primary pipe casing.
48-in. HDSS	Segmented locking restraint	Four-point bending	The joint exceeded its specified 2° deflection capacity and reached approximately 4° of rotation and 25,740 kip-in. Distributed strain measurements identified severe strain localization and fracture within the bell near the locking-segment region.
24-in. HRDIP	Kubota NS-type continuous locking configuration	Four-point bending	The joint sustained approximately 20° of rotation and 3,313 kip-in without leakage before tensile cracking initiated at the spigot projection and propagated through the spigot.
iPVC	TurnerLok and ReiberLok toothed-gasket fittings	Monotonic tension	The ReiberLok fitting developed nearly three times the tensile resistance of the TurnerLok fitting. Tooth geometry and engagement controlled circumferential load distribution, localized strain, and ultimate joint capacity.
iPVC	ReiberLok restraint	Axial compression	The assembly sustained loads approaching 100 kips. Global buckling produced nonuniform fitting contact and ovalization; hydraulic integrity was maintained during loading, while leakage and rupture developed during unloading.
iPVC	EBAA 1900, RCT, and ReiberLok restraints	Four-point bending	The EBAA system provided the greatest rotational capacity but developed earlier leakage. The rigid RCT restraint maintained hydraulic integrity to a larger rotation but produced sudden pipe-wall fracture, while the ReiberLok fitting exhibited intermediate flexibility and a combined pipe–fitting failure.

and hydraulic performance, the effects of scale and material stiffness, and the localization of damage near the joint interface.

8.2 Influence of Restraint Geometry on Load Transfer Mechanisms

The experimental program demonstrated that the structural performance of restrained pipeline joints, either ductile iron or iPVC, is governed by the geometry and configuration of the restraint system. Although all tested joints were designed to prevent axial separation while maintaining hydraulic continuity, relatively small differences in restraint details produced substantial variations in stiffness, load-transfer mechanisms, deformation patterns, and ultimate failure modes. Across all pipe systems examined, restraint geometry consistently dictated how forces were transmitted through the bell-spigot interface and where critical stress concentrations ultimately developed.

The monotonic tension tests on the 8-inch ERDIP specimens provided the clearest example of this behavior. Despite exhibiting comparable ultimate tensile capacities, the factory-manufactured weld-bead configuration and the field-installed groove restraint developed fundamentally different internal load paths. The weld bead maintained a more concentric force-transfer mechanism between the spigot and bell, concentrating bearing stresses within the bell casing and ultimately producing a localized bell fracture. Conversely, the field-installed snap ring altered the internal force distribution and redirected stresses into the reduced wall thickness at the machined groove. This resulted in rupture of the pipe barrel rather than the bell. These findings demonstrate that similar global capacities do not necessarily correspond to similar structural performance or failure mechanisms.

This profound sensitivity to restraint geometry was equally apparent in the iPVC tension tests. Although testing the identical plastic pipe material, the ReiberLok gasket's numerous smaller teeth effectively distributed pullout forces over a broader contact area, achieving a tensile capacity nearly three times higher (34.8 kips) than the TurnerLok gasket (11.8 kips). The fewer, larger teeth of the TurnerLok gasket concentrated forces at individual boundaries, driving premature localized plastic failure.

A similar influence of restraint geometry was observed during the bending and biaxial loading tests. For the 8-inch ERDIP joints, changing the circumferential orientation of the insertion slot from the 12 o'clock position to the 9 o'clock position altered the stiffness of the joint and the magnitude of the internal bearing force couple. The large-diameter ERDIP and HDSS bending tests further highlighted the importance of restraint mechanics. In these systems, the interaction between the spigot weld bead and the locking segments generated large radial forces that progressively expanded the bell section during extreme rotation.

In the iPVC flexural applications, the choice of external versus internal restraint geometry completely dictated the system response. The external EBAA 1900 tie-rod system provided a highly flexible kinematic response, allowing the spigot to pivot smoothly within the bell

and distribute deformation. Conversely, the internal ductile iron RCT restraint was rigid; this extreme stiffness mismatch prevented natural cross-sectional ovalization, forcing massive, unyielding stress concentrations directly onto the plastic pipe wall. Collectively, these observations demonstrate that restraint geometry exerts a greater influence on structural performance than global pipe strength across both metallic and plastic systems.

8.3 Structural Capacity versus Hydraulic Resilience

One of the important findings of the experimental program is the distinction between structural capacity and hydraulic resilience. While these concepts are often treated as equivalent in pipeline performance assessments, the experimental results demonstrated that structural failure and loss of hydraulic functionality do not necessarily occur simultaneously.

The tension tests on the 8-inch ERDIP specimens clearly illustrate this distinction. In the factory-manufactured weld-bead specimen, severe structural damage developed in the bell casing under extreme axial loading. However, the elastomeric gasket remained engaged and continued to maintain a watertight seal, allowing hydraulic service to be preserved for nearly three additional inches of pullout following the initiation of structural failure. In contrast, the field-installed groove restraint experienced a circumferential rupture of the spigot groove that immediately severed the pipe barrel and bypassed the sealing mechanism. Consequently, hydraulic containment was lost instantaneously upon fracture despite a comparable global tensile capacity.

A similar distinction was observed in the large-diameter ERDIP and HDSS tests. In these systems, the ultimate failure state was governed by the progressive displacement and ejection of the discrete locking segments rather than the fracture of the primary ductile iron casing. Although the thick pipe walls remained largely intact, the loss of restraint engagement severely altered the internal force-transfer mechanism, which ultimately resulted in the loss of hydraulic containment. Conversely, the 24-inch Kubota NS joint, utilizing a massive, continuous locking mechanism, maintained a perfect watertight seal throughout substantial rotational deformation and exhibited no leakage prior to its ultimate structural fracture.

The iPVC testing program also demonstrates the trade-off between flexibility and hydraulic containment. During bending, the highly flexible EBAA restraint accommodated massive structural rotation (exceeding 36 degrees) without catastrophic structural failure, but permitted minor, continuous leakage starting at 28 degrees as the spigot pulled away from the gasket. Conversely, the rigid RCT restraint maintained perfect hydraulic containment up until 34.45 degrees, where it suffered a sudden, brittle fracture, resulting in an immediate and total loss of pressure.

These observations suggest that structural damage alone is not necessarily an appropriate indicator of system performance during extreme loading events. Some joint configurations exhibited significant reserve hydraulic capacity after the onset of structural damage, whereas others experienced immediate loss of serviceability upon fracture. Therefore, evaluation of

seismic pipeline performance should consider both structural integrity and hydraulic functionality.

8.4 Effect of Scale and Material Stiffness on Failure

Comparison of the experimental results across multiple pipe diameters revealed that scale influences the governing failure hierarchy. However, this transition is heavily governed by the specific design architecture of the restraint's locking mechanism and the relative stiffness between the pipe and the restraint.

In small-diameter systems, such as the 8-inch ERDIP, ultimate failure was consistently governed by the yielding and fracture of the ductile iron pipe casing itself. Under various loading conditions, failure occurred through localized punch-through fracture of the spigot invert, groove rupture, or bell fracture. In these cases, the restraint mechanisms remained fully engaged while the pipe material reached its structural limit, indicating that the restraint design was stronger than the surrounding pipe wall.

As pipe diameter increases into the large-diameter range, the governing failure mechanism diverges based on the design of the locking mechanism. For large-diameter pipes utilizing massive, integral locking mechanisms, such as the 24-inch Kubota NS joint, the pipe wall remains the weak link. A fundamentally different behavior emerged in large-diameter systems utilizing discrete, segmented locking mechanisms, such as the large-diameter ERDIP and HDSS systems. The substantially greater wall thickness and section stiffness of these large pipes vastly increased their resistance to structural yielding, forcing the discrete locking segments to transfer extreme forces through concentrated contact points. Failure (or water leak) was therefore controlled by the ejection of the segmented restraint rather than the rupture of the thick pipe barrel.

While diameter scale governs ductile iron systems, the iPVC experiments demonstrated that relative material stiffness exerts a similar controlling influence on the failure hierarchy. In the iPVC systems fitted with rigid RCT restraints, the extreme stiffness of the unyielding iron restraint overpowered the flexible plastic pipe, forcing the pipe wall to serve as the weak link and fail first. Conversely, when restrained by the ReiberLok plastic fitting, the intermediate stiffness led to a combined failure of both the pipe and the fitting. Consequently, understanding the specific design and relative stiffness of the locking mechanism is critical for predicting seismic performance.

8.5 Localization of Damage and Joint Ductility

Despite the wide range of pipe diameters, materials, restraint configurations, and loading conditions examined in this study, a consistent observation emerged regarding the localization of structural damage. In all experimental programs, the most severe strains, deformations, and fractures remained concentrated within the immediate vicinity of the joint interface.

Strain profile consistently identified large strain concentrations near locking segments, insertion slots, weld beads, groove transitions, and spigot-bell bearing interfaces. In the ERDIP specimens, extreme strains developed adjacent to the locking segments and insertion slot boundaries. In the HDSS tests, strain concentrations were observed near the locking-segment region within the bell section. Similarly, the Kubota NS joint exhibited localized deformation and fracture within the spigot projection region. In contrast, the adjacent pipe barrels generally remained elastic and exhibited comparatively small strain demands throughout the tests.

This highly localized behavior was perfectly mirrored in the iPVC specimens. Strain profile data confirmed that the main iPVC pipe bodies adhered to classical beam bending theory with relatively low strain demands, while extreme, anomalous strains were captured exactly at the internal ReiberLok gasket teeth (which acted as severe stress risers, gouging the pipe invert) or at the unyielding boundary of the RCT restraint.

This localization of damage demonstrates that restrained joints function as highly ductile deformation zones within the segmented pipeline system. Rather than distributing damage along the length of the pipe barrel, the joints concentrate rotation, displacement, and stress demands within a relatively short region surrounding the connection. Such behavior effectively protects the integrity of the main pipeline segments and limits the spatial extent of structural damage, acting as sacrificial mechanical fuses.

8.6 Implications for Seismic Pipeline Design

The findings from this experimental program have several implications for the seismic design and assessment of restrained pipeline systems. Most notably, all tested systems exhibited rotational capacities that substantially exceeded the manufacturer-specified deflection limits. The 8-inch ERDIP specimens achieved rotations exceeding 13 degrees, the 24-inch Kubota joint reached approximately 20 degrees, the large-diameter ERDIP and HDSS systems surpassed their prescribed design limits, and the 8-inch iPVC flexural specimens achieved massive rotations between 25 and 36 degrees prior to failure. These results indicate that modern restrained pipeline joints possess significant reserve deformation capacity beyond conventional design assumptions.

At the same time, the experiments demonstrated that ultimate performance is governed primarily by local restraint mechanics rather than global pipe strength. Small geometric details, including locking-segment orientation, insertion-slot location, weld-bead configuration, and gasket teeth geometry, were found to significantly influence stiffness, force-transfer mechanisms, failure progression, and hydraulic performance. These findings suggest that simplified design approaches based solely on pipe material properties or nominal rotational capacities may not adequately capture the true behavior of restrained joints under extreme loading.

The distinction between structural failure and hydraulic failure further highlights the need for performance-based evaluation criteria. Traditional strength-based design approaches

often define failure as the onset of structural damage; however, the experimental results show that substantial hydraulic functionality may remain after structural damage occurs. Conversely, some configurations experience immediate loss of containment despite retaining considerable structural capacity elsewhere within the system. Therefore, future design methodologies should incorporate both structural and serviceability performance objectives.

Overall, the results demonstrate that both ductile iron and iPVC restrained pipeline systems possess substantial inherent seismic resilience. However, this resilience is governed by highly localized interactions between restraint components, pipe geometry, and internal force-transfer mechanisms. Future seismic design frameworks should therefore place greater emphasis on joint-level mechanics, deformation compatibility, and post-damage functionality to more accurately represent the behavior of modern restrained pipeline infrastructure subjected to extreme ground deformation.

Chapter 9

System-Level Performance of Hazard Resilient Pipes under Large Ground Deformation

9.1 Introduction

Severe ground deformations associated with earthquakes represent a major hazard to buried lifeline infrastructure, particularly water distribution networks. The vulnerability of these systems to permanent ground deformation (PGD) has been repeatedly demonstrated during major seismic events. Unlike transient seismic-wave effects, PGD can impose concentrated axial, bending, and rotational demands where pipelines cross active faults, liquefaction-induced lateral spreads, landslides, or zones of differential settlement [84]. Field observations have repeatedly demonstrated the vulnerability of buried pipelines to these demands. The 1971 San Fernando earthquake produced extensive pipeline damage associated with surface faulting [83], while the 1994 Northridge earthquake caused widespread disruption through strong shaking and localized ground deformation [53]. Large fault offsets and soil displacements during the 1999 Izmit earthquake [122] and the Canterbury earthquake sequence [85] similarly damaged water-distribution systems and interrupted essential services. More recent reconnaissance and experimental studies continue to demonstrate that buried pipelines remain highly vulnerable where seismic ground movements exceed their deformation capacity [145, 132].

Pipeline response to PGD depends on the magnitude and orientation of ground movement, the mechanical behavior of the surrounding soil, and the structural properties and connection details of the pipeline. Continuous pipelines generally accommodate ground movement through axial strain, bending, ovalization, and localized yielding of the pipe barrel. Segmented pipelines respond differently because deformation can also be accommodated through axial slip, rotation, and restraint engagement at discrete joints. When appropriately designed, these joints can distribute deformation among several pipe segments and reduce

strain concentration in the barrels. Their performance, however, depends on available joint travel, rotational capacity, spacing, initial insertion, locking behavior, and interaction with the surrounding soil.

Analytical and numerical models provide essential tools for evaluating these coupled processes, but their reliability depends on experimental validation. Component-level testing can establish the axial, rotational, and leakage capacities of individual joints, yet it cannot reproduce the progressive activation of multiple joints in a buried assembly. Full-scale soil–pipeline experiments are therefore needed to determine how ground movement is transferred through the soil, pipe barrels, enlarged bells, and restrained connections before ultimate failure occurs.

This study investigates the system-level response of an 8-in. earthquake-resistant ductile iron pipeline (ERDIP) subjected to simulated fault rupture in a large-scale split-basin experiment. The pipeline assembly contains multiple restrained axial-slip joints and is monitored using conventional instrumentation together with distributed fiber optic sensing (DFOS). A complementary finite-element model is used to evaluate the evolving soil–pipeline interaction and reproduce the measured response throughout successive stages of fault displacement.

The objective is to characterize how a segmented ERDIP system accommodates PGD through progressive joint activation, axial force transfer, pipe bending, and localized soil resistance. Continuous distributed strain measurements are used to separate longitudinal response into axial and bending components and to identify mechanisms that are difficult to resolve using discrete strain gauges alone. Particular attention is given to frictional load transfer along the pipe barrels, passive resistance mobilized by enlarged joint bells, the transition associated with engagement of joint restraints, and the mechanism governing ultimate loss of serviceability. By integrating full-scale testing, DFOS measurements, and numerical simulation, the study provides a physically detailed basis for evaluating and designing segmented pipelines subjected to extreme ground deformation.

9.2 Literature Review

9.2.1 Pipeline Response to Permanent Ground Deformation

Early analytical work on fault-crossing pipelines focused primarily on continuous systems. Newmark and Hall represented the pipe using a tensioned-cable formulation in which axial deformation governed the response [79]. Kennedy et al. extended this approach by incorporating lateral soil resistance and the development of pipeline curvature near the ground-rupture zone [60]. Wang and Yeh subsequently introduced pipe bending stiffness and more refined representations of the deformed pipeline geometry [129]. These formulations established the fundamental dependence of pipeline response on fault offset, crossing angle, pipe stiffness, axial restraint, and soil resistance.

Later numerical studies incorporated nonlinear pipe behavior, large deformation, contact, and more detailed soil–pipeline interaction [137]. These models reproduced important

features of continuous-pipeline response, including tensile strain concentration, compressive wrinkling, ovalization, and changes in soil resistance as ground displacement increased. However, segmented pipelines cannot be represented solely through the constitutive response of the pipe barrel. Joint opening, closure, axial slip, rotation, and restraint engagement introduce discrete kinematic mechanisms that govern how deformation is distributed among connected pipe segments [75, 21].

Segmented systems can accommodate substantial PGD when joint deformation is mobilized before damaging barrel strains develop. Numerical studies have shown that axial-slip and rotational capacity can reduce strain concentration and redistribute displacement among multiple segments [75]. A joint with insufficient travel may reach its restraint limit prematurely, after which additional displacement is transferred into axial force and bending of the adjacent pipe barrels. Pipeline performance therefore depends on both component capacity and the sequence in which joints are activated.

9.2.2 Soil–Pipeline Interaction in Segmented Systems

The surrounding soil controls how permanent ground deformation is transferred to a buried pipeline. Relative soil–pipe movement mobilizes axial interface resistance along the pipe surface and transverse resistance against the pipe barrel, with the magnitude of these reactions depending on burial depth, soil density and condition, movement direction, and pipe geometry [102, 43]. In segmented ductile iron pipelines, enlarged joint bells introduce geometric discontinuities that can mobilize concentrated passive soil resistance and alter axial load transfer relative to a uniform cylindrical pipe [5].

For multi-joint systems, soil resistance interacts with joint slip, rotation, and restraint engagement to govern how imposed deformation is distributed along the pipeline. Previous full-scale tests and numerical studies indicate that ground movement may be shared among several connections rather than being accommodated entirely by the joint nearest the fault [93, 4, 21]. The resulting sequence of joint activation depends on factors such as joint position relative to the fault, available axial travel, pipeline geometry, and local soil restraint.

Analytical studies have also shown that conventional bearing-capacity formulations may not fully represent soil resistance under some modes of vertical pipeline movement [90]. Three-dimensional simulations of segmented ductile iron pipelines indicate that the response can shift between uplift- and bearing-controlled mechanisms depending on the position of the fault relative to the nearest joint [21]. Together with the localized resistance generated by enlarged bells, these findings demonstrate the importance of representing the actual segmented geometry and joint locations rather than idealizing the pipeline as a uniform beam or cable.

9.2.3 Full-Scale Split-Basin Testing

Much of the previous full-scale split-basin research on buried pipelines subjected to fault rupture was conducted at the Cornell Geotechnical Lifelines Large-Scale Testing Facility. The

Cornell apparatus was developed to reproduce abrupt ground deformation under controlled conditions while maintaining realistic burial, internal pressure, and soil–pipeline interaction. In a typical test, a pressurized pipeline was buried in compacted soil spanning stationary and hydraulically actuated portions of the basin. Relative movement between the two sections imposed ground displacement across a prescribed fault orientation, generating combined axial, bending, and soil-resistance demands representative of earthquake-induced permanent ground deformation. In 2022, the Cornell soil–pipeline fault-rupture apparatus was transferred to the University of California, Berkeley and incorporated into the Center for Smart Infrastructure at the Richmond Field Station. The apparatus was reassembled and reconfigured to support continued full-scale investigation of buried infrastructure under large ground deformation. The experiment presented in this chapter was conducted using this relocated facility

Foundational Cornell experiments examined the response of continuous, heat-fused HDPE pipelines subjected to large strike-slip fault movements [137]. These tests demonstrated the substantial tensile deformation capacity of HDPE while identifying pipe ovalization and loss of flow area as potentially important limit states. The resulting measurements also provided benchmark data for evaluating numerical models of large-deformation soil–pipeline interaction.

The split-basin methodology was subsequently extended to segmented thermoplastic pipelines. Tests of the Bionax SR PVCO system showed that axial slip and pipe-barrel deformation could be mobilized before rupture developed near an external joint restraint [120]. A later Bionax program evaluated an extended-bell configuration designed to provide additional joint displacement and reduce restraint-induced stress concentrations [133]. Testing of a restrained PPI iPVC pipeline further demonstrated how imposed ground movement is accommodated through a combination of joint opening, pipe-barrel strain, and bending before localized rupture [100].

Several earthquake-resistant ductile iron systems were also evaluated, including the Kubota ERDIP, AMERICAN Earthquake Joint, U.S. Pipe TR-XTREME, and McWane Seismic Flex Coupling systems [98, 97, 117, 99]. Although their joint configurations differed, these tests consistently showed that system response depends on the progressive distribution of axial displacement and rotation among multiple connections. As fault movement increased, available joint travel was mobilized sequentially, followed by restraint engagement and increased transfer of load into the adjacent bells, spigots, and pipe barrels. Leakage or localized fracture generally occurred only after a substantial portion of the cumulative deformation capacity had been exhausted.

The Geotechnical Lifelines research team also applied the split-basin approach to alternative deformation mechanisms and rehabilitated pipelines. The JFE steel pipeline accommodated compression and bending through controlled deformation of engineered SPF wave features without loss of pressure [134]. The Aqua-Pipe program examined a lined ductile iron pipeline and characterized the transfer of fault-induced deformation among the liner, host pipe, and existing host-pipe joints [88]. These programs demonstrate that the split-basin methodology can evaluate not only conventional continuous and segmented pipelines

but also specialized deformation-control and rehabilitation systems.

Table 9.1 summarizes the Cornell full-scale split-basin tests most relevant to the present study. Collectively, these experiments demonstrated that system performance depends on how deformation is distributed among joints or engineered features and is influenced by joint configuration, spacing, initial insertion, fault-crossing geometry, and soil restraint. However, prior programs generally relied on discrete strain gauges, displacement transducers, load cells, and pressure measurements, which characterized global capacity and selected local responses but did not resolve the continuous strain field between instrumented locations. The present study builds on this foundation by using DFOS to characterize the spatial evolution of axial strain, bending, joint activation, and load transfer throughout an 8-in. multi-joint ERDIP assembly.

Table 9.1. Representative Cornell full-scale split-basin pipeline tests.

System	Joint or deformation system	Key finding
HDPE [137]	Heat-fused continuous pipeline	Demonstrated high deformation capacity; ovalization and loss of flow area emerged as important limit states.
Bionax SR PVCO [120]	Bell-and-spigot joints with external restraint collars	Rupture occurred adjacent to a restraint after joint slip and pipe-barrel deformation were mobilized.
Bionax extended-bell PVCO [133]	Extended-bell restrained joints	Evaluated a redesigned joint intended to increase axial slip and reduce restraint-induced stress concentration.
PPI iPVC [100]	Bell-and-spigot joints with wedge-action restraints	Accommodated fault movement through joint opening, pipe strain, and bending before rupture adjacent to a restraint.
Kubota ERDIP [98]	Axial-slip bell-and-spigot joints with locking rings	Distributed axial pullout and rotation among multiple joints before fracture following restraint engagement.
AMERICAN Earthquake Joint [97]	Deep-socket restrained joints with split snap rings	Distributed extension and rotation among the joints before localized bell fracture and pressure loss.
U.S. Pipe TR-XTREME [117]	Restrained bell joints with locking segments	Distributed pullout and rotation among the joints before localized bell fracture and pressure loss.
McWane Seismic Flex Coupling [99]	Multi-joint couplings connecting TR Flex bell-and-spigot ends	Sequentially mobilized coupling components before spigot pullout and pressure loss near the extension limit.
JFE SPF Wave Feature [134]	Welded steel wave features	Accommodated substantial compression through controlled deformation of the wave features without leakage.
Aqua-Pipe [88]	CIPP liner spanning host-pipe joints	Maintained pressure and liner integrity through the available fault movement while deformation concentrated at host-pipe joints.

9.2.4 Distributed Fiber Optic Sensing for Buried Infrastructure

DFOS, specifically distributed strain sensing (DSS), provides continuous strain measurements along the length of an optical fiber, allowing spatial variations to be resolved at intervals substantially smaller than the spacing normally achievable with conventional gauges. DFOS has been applied to structural and geotechnical systems for detecting localized strain, deformation zones, cracking, and soil movement [47, 111, 114, 81]. Its distributed nature is particularly valuable for buried pipelines, where the location of maximum curvature or axial strain may evolve as soil resistance and joint restraints are progressively mobilized. Despite this potential, applying DSS to a full-scale segmented pipeline introduces several challenges. The optical fiber must remain bonded to the pipe under large deformation and accurately transfer strain without debonding or local damage. Measurements must also be interpreted across geometric discontinuities such as bells, spigots, and joint restraints.

Previous split-basin programs established the global response and ultimate capacity of several pipeline technologies, but they generally did not provide a continuous strain profile over the entire multi-joint assembly. Consequently, important aspects of progressive load transfer—including the spatial development of frictional resistance, the anchoring effect of enlarged bells, and redistribution following restraint engagement—remain incompletely resolved.

9.2.5 Research Gap and Contributions

Prior research has established three important foundations. Analytical and numerical models describe the response of continuous and segmented pipelines to PGD; component-level tests define joint displacement, rotation, and leakage capacities; and full-scale split-basin experiments demonstrate the integrated survivability of buried pipeline systems. However, a gap remains between establishing macroscopic system capacity and resolving the localized mechanics that govern progressive load transfer and ultimate failure.

Most previous full-scale ERDIP tests have focused on 6-in. pipelines and have relied primarily on discrete instrumentation. These programs successfully measured selected joint movements, end forces, bending moments, and local strains, but could not continuously track the strain field along each pipe barrel and through the regions adjacent to enlarged bells. As a result, the relative contributions of distributed pipe–soil friction, localized passive resistance, joint opening, barrel bending, and restraint engagement have not been fully quantified throughout the complete fault-rupture sequence.

The present study addresses these limitations through a full-scale split-basin test of an 8-in. multi-joint ERDIP assembly instrumented with DSS and conventional sensors. Its principal contributions are:

- Characterization of the system-level response and progressive joint activation of an 8-in. multi-joint ERDIP assembly subjected to full-scale buried fault rupture;

- Use of continuous DSS measurements to separate axial and bending strains and quantify frictional load transfer, passive resistance at enlarged joint bells, and the mechanisms governing serviceability and failure; and
- Validation of a finite-element model against synchronized strain, displacement, force, and pressure measurements throughout the staged fault-rupture response.

By connecting continuous strain observations with joint kinematics and numerical simulation, this study moves beyond demonstrating whether an ERDIP assembly survives a prescribed fault offset. It explains how deformation is transferred, redistributed, and ultimately concentrated within the buried multi-joint system. The resulting findings provide a more physically representative basis for evaluating segmented-pipeline resilience and improving numerical models and seismic design procedures.

9.3 Experimental Design

9.3.1 Split Basin Experimental Setup

The experimental setup and layout are shown in Figure 9.1. A self-reacting subfloor (gray) served as the platform on which the split-basin box (green) was anchored and allowed to slide, and it also functioned as the reaction frame to accommodate actuator loads. The actuators were mounted on a specially designed load-spread reaction beam system (dark blue) comprising four short columns anchored to the subfloor, with a load-spread beam bolted atop the columns. The actuators (pink) were then connected to this beam. The system employed three hydraulic actuators, each with a 400-kip push capacity and a 20-inch stroke, arranged parallel to the fault trace. Testing was conducted under displacement control at a rate of 1-inch (25-mm) per minute.

Five ERDIPs (light blue) were assembled in the split-basin box using a pipe-centric configuration, in which the pipe section, rather than a bell joint, crossed the fault. To restrain the pipeline, two specially designed jackets (red) were used to fix the end pipes to the box end walls. Consequently, no relative movement was expected between the end pipes and the box. Pipes and joints were labeled from west to east, from the fixed box toward the moving box, with joints numbered 1 through 4. Pipe W denotes the pipe fixed to the moving-box end wall; Pipe MW is the middle pipe within the moving box; Pipe M is the pipe that crosses the fault trace; Pipe ME is the middle pipe within the fixed box; and Pipe E is the pipe fixed to the fixed-box end wall.

To establish the initial experimental boundary conditions, Joints 2 and 3 were installed at the fully collapsed (fully inserted) position in accordance with manufacturer guidelines [128] to maximize localized rotational capacity, while boundary Joints 1 and 4 were initialized at the nominal midpoint extension. At all four connections, the single slot housing the locking restraints was oriented aligned with the crown (0°). The pipeline specimen was assembled on 1 ft (0.3 m) of compacted Class-1 soil bedding and overlain by 3 ft (1.0 m)

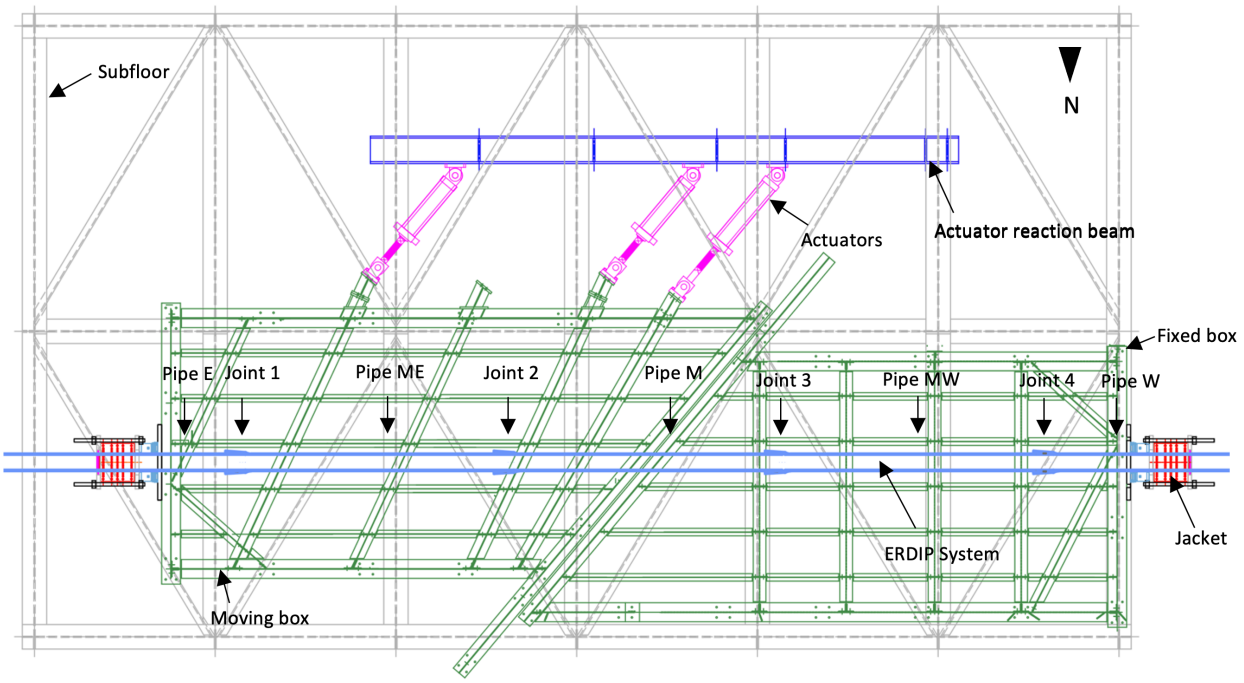
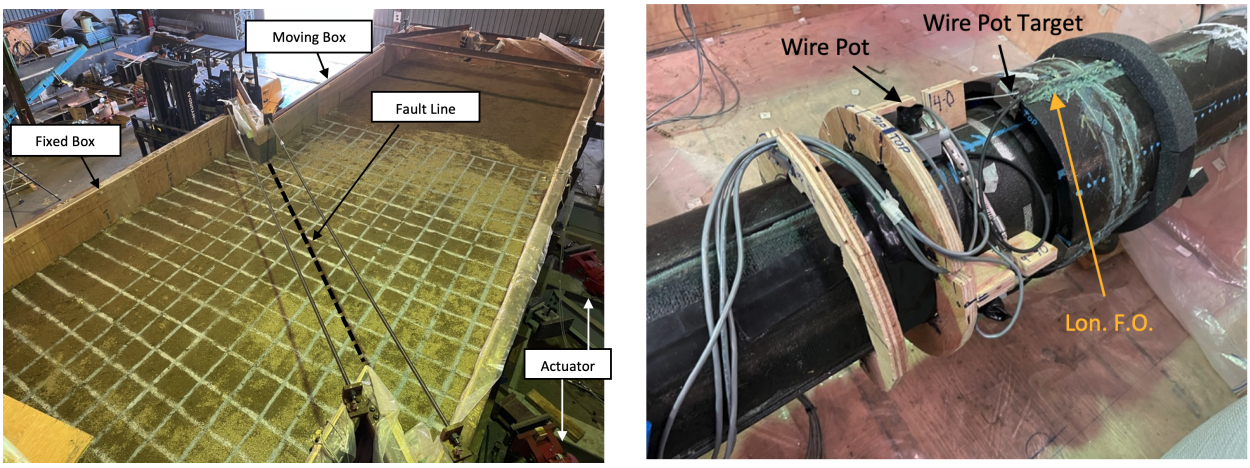


Fig. 9.1. Plan view of the split-basin experimental setup configured for a 50-degree strike-slip fault simulation. The apparatus utilizes three hydraulic actuators to drive the moving box relative to the fixed box. The testing array comprises five ERDIP segments, with the central two joints initially set to a fully inserted state and the outer two joints positioned at mid-extension. Local component labels for all pipe segments and joint assemblies is indicated.

of compacted Class-1 backfill cover. Prior to shearing, the internal network was pressurized to approximately 75 psi (517 kPa). Hydraulic actuators subsequently displaced the moving basin under quasi-static displacement control until ultimate structural failure and complete loss of water pressure occurred. The final embedment and testing configuration is illustrated in Figure 9.2a.

9.3.2 Instrumentation Layout and Data Acquisition Plan

To capture both the macroscopic boundary conditions and high-resolution localized structural mechanics of the pipeline under ground deformation, a comprehensive monitoring plan was deployed, integrating discrete position transducers and continuous DFOS. Discrete joint kinematics were resolved using four position transducers (herein referred to as wire potentiometers, or wire pots) installed at quarter points around the circumference of each connection to measure relative axial opening and localized rotation. Referenced directly to the adjacent bell face, a total of 16 wire potentiometers were deployed across the four



(a) **(b)**

Fig. 9.2. Experiment and instrumentation setups. (a) Plan view of the split-basin testing apparatus configured with a 5-foot (1.5-meter) total soil profile. The ERDIP system is positioned on a 1-foot (0.3-meter) compacted soil bedding and overlain by 3 feet (1.0 meter) of soil backfill. (b) Installation of position transducer and DSS at joints (Joint 4 for example).

connections, as illustrated in Figure 9.3. To protect the instruments during backfilling and compaction, and to prevent the surrounding soil from interfering with the mechanical extensions, a dedicated steel housing assembly was constructed over each joint. Circumferential wood supports were attached to the spigot end to act as spacers, accommodating the outer-diameter differential between the bell and the pipe barrel. Each wire potentiometer was mounted directly to the wood support, with its extendable wire connected to a small hooked target tab bonded to the bell face. A protective steel shield was then wrapped around the complete circumference and clamped tightly to the pipe. Example installations are shown in Figure 9.2b, depicting the assembly with the steel shield temporarily unwrapped to display the internal sensor configuration.

Complementing the discrete joint sensors, DFOS, specifically DSS, was selected to resolve spatially continuous strain fields along the pipe barrels. Because the FO cable itself functions as a continuous sensor, measurements can be acquired over long distances at thousands of discrete points using a single multiplexed line. Compared to conventional discrete gauges, DSS offer distinct advantages for buried geotechnical applications, including minimal size and weight, absolute immunity to electromagnetic interference, and exceptional resistance to corrosion and moisture.

For the DSS datqa acquisition system, a rayleigh-based optical frequency domain reflectometry (OFDR) analyzer, the Luna ODiSI 6100 series [71], was utilized. Operating at an ultra-dense spatial sampling interval of 0.65 mm, the instrument is capable of interrogating sensor lengths up to 100 m per channel with a measurement error rating at ± 1 $\mu\varepsilon$. Fibers

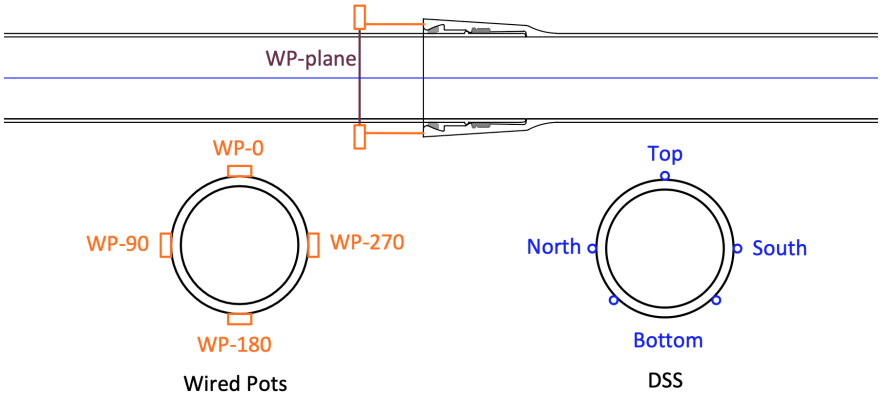


Fig. 9.3. Instrumentation plan for the split-basin fault rupture test. The wire potentiometers (WPs, marked in orange) are deployed to monitor localized joint rotations. Each monitoring array comprises four sensors mounted at 90-degree intervals around the spigot circumference with their target anchors secured directly to the adjacent bell face. Longitudinal fibers (marked in blue) are oriented along the crown (0°), springlines (90°, 270°), and oblique axes (135°, 215°) to capture primary flexural and axial strain gradients.

were bonded directly to the pipe specimens along both the axial direction (as shown in Figure 9.2b, enabling the continuous tracking of strain transfer mechanisms.

5-mm tight-buffer, steel-reinforced cable (NanZee 5 mm) [144] was selected for longitudinal runs to replicate standard field monitoring practices, as their robust, steel-reinforced construction protects the core fiber against shear forces during trench compaction. Five continuous longitudinal lines were bonded along the pipeline to capture axial strain profiles at the crown (0°), both springlines (90° and 270°), and at angles ±45° from the invert (180°), as shown in Figure 9.3.

9.3.3 Soil Property

The soil used for backfill is a well-graded coarse granular material, classified as Class I backfill in accordance with ASTM D2321-20. Its grain size distribution shows a mean grain size (D_{50}) of 3.2 mm and an effective grain size (D_{10}) of 1.4 mm, with a coefficient of uniformity (C_u) of 2.6 and coefficient of curvature (C_c) of 1.2, indicating good gradation and free-draining behavior. This material was selected for this experiment to simulate typical trench backfill around a buried pipeline, providing realistic conditions for evaluating soil-pipe interaction and backfill performance.

The soil was compacted during the backfill process. It was placed in 200 mm (0.7 ft) lifts and compacted to 150 mm (0.5 ft) layers. Compaction was performed manually for the layers below, at, and 150 mm (0.5 ft) above the pipe crown; a plate compactor was used for the remaining layers above. Nuclear gauge and sand cone tests were performed at multiple

locations within each layer (0.3, 0.45, 0.9, 1.2, and 1.5 m [1, 1.5, 3, 4, and 5 ft] elevations) to measure in-place density and moisture. Laboratory compaction testing established a maximum dry density of 2098 kg/m^3 (131 pcf) and an optimum moisture content of 11%. Field measurements showed moisture contents ranging from 4.4% to 5.4% and dry densities between 1778 and 1810 kg/m^3 (111–113 pcf) for the majority of layers, corresponding to 85–86% of the laboratory maximum. The intermediate layer at a 0.45 m (1.5 ft) depth, however, demonstrated enhanced compaction conditions, with a moisture content of 6.8% and a dry density of 1858 kg/m^3 (116 pcf) (about 88% of maximum). This might be attributable to the manual compaction near the pipe versus machine compaction above. Overall, the backfilled split basin box exhibited relatively uniform soil properties across most testing depths.

9.4 Definitions and Analytical Calculation Approaches

To characterize the structural response of the segmented pipeline under simulated fault rupture, macroscopic localized deformations and internal force distributions were derived from the discrete and continuous sensor networks. The analytical formulations governing joint kinematics, bending moments, and segmental lateral displacements are detailed below.

9.4.1 Joint Kinematics and Rotations

Localized joint kinematics were quantified using arrays of four wire potentiometers mounted at 90-degree intervals around the spigot circumference, measuring relative displacement to targets anchored on the adjacent bell face. The analytical derivation assumes that (i) the diametral center-to-center distances between opposing sensors do not deform macroscopically during loading, and (ii) the adjacent pipe segments undergo symmetric, small-angle rotations relative to the joint plane.

Let $wp0$, $wp90$, $wp180$, and $wp270$ denote the measured axial extensions at the crown (0°), north springline (90°), invert (180°), and south springline (270°) targets, respectively. The orthogonal rotational components are decoupled into in-plane rotation ($\theta_{\text{in-plane}}$), defined within the primary horizontal plane of bending, and out-of-plane rotation ($\theta_{\text{out-of-plane}}$), defined within the vertical axial plane:

$$\theta_{\text{in-plane}} = 2\tan^{-1}\left[\frac{wp90 - wp270}{2d_{\text{horizontal}}}\right] \tag{9.1}$$

$$\theta_{\text{out-of-plane}} = 2\tan^{-1}\left[\frac{wp0 - wp180}{2d_{\text{vertical}}}\right] \tag{9.2}$$

where $d_{\text{horizontal}}$ and d_{vertical} represent the exact center-to-center gauge distances between the opposing north-south and top-bottom wire potentiometers, respectively.

9.4.2 Bending Moment Approximation

Internal bending moments along the continuous pipe barrels were approximated from measured axial strains assuming linear-elastic, Bernoulli-Euler beam behavior. The longitudinal curvature κ at any given cross-section is directly proportional to the differential strain measured across the fibers of the bending plane. The internal bending moment M is expressed as:

$$M = EI\kappa = EI\left(\frac{\varepsilon_1 - \varepsilon_2}{d}\right) \tag{9.3}$$

where E is the material Young's modulus, I is the cross-sectional moment of inertia, and ε_1 and ε_2 are the longitudinal strains measured on opposing sides of the primary bending plane (corresponding to the north and south springlines in the split-basin setup). The parameter d defines the diametral distance between the sensor gauge lines, taken here as the nominal pipe outside diameter. For this analysis, the nominal pipeline properties correspond to a Young's modulus $E = 23,500,000$ psi (162 GPa), a cross-sectional moment of inertia $I = 96.735$ in^4 ($4,026$ cm^4), an outer diameter $OD = 9.0625$ in (230.2 mm), and an inner diameter $ID = 8.3125$ in (211.1 mm).

9.4.3 Segmental Lateral Displacement

To derive the global lateral deflection profile of the pipeline, cross-sectional curvatures (κ) obtained from the DSS arrays are integrated along the length of the specimen. However, because segmented pipelines accommodate severe ground deformation primarily through localized rotations and pullout at the connections, integrating continuously across the entire multi-segment pipeline would violate the kinematic boundary conditions. The discrete joints act as structural discontinuities where step-changes in slope and displacement occur.

Consequently, lateral displacement is calculated using a segment-by-segment piecewise integration strategy. For any individual continuous pipe segment i, the lateral deflection $y_i(x)$ along its local longitudinal axis x is derived by integrating the discrete curvature field $\kappa_i(x)$ twice:

$$y_i(x) = y_{i,0} + \theta_{i,0}x + \int_0^x \left(\int_0^\xi \kappa_i(\eta)\, d\eta\right) d\xi \tag{9.4}$$

where $y_{i,0}$ and $\theta_{i,0}$ represent the initial lateral displacement and initial slope at the upstream boundary ($x = 0$) of segment i. Establishing a zero-displacement boundary condition at the far end of the fixed basin, these integration constants are updated sequentially at each segment boundary by incorporating the discrete joint translations and rotations ($\theta_{\text{in-plane}}$) quantified by the joint monitoring arrays. This piecewise approach ensures that internal barrel flexure is accurately decoupled from localized joint kinematics.

9.5 Numerical Model

Previous studies on buried pipelines subjected to ground deformation have generally adopted either simplified beam-spring formulations or more detailed continuum FE models. Early analytical and numerical approaches [79, 60, 129, 90] idealized the pipeline as a continuous structural member interacting with the surrounding ground through nonlinear soil springs, providing an efficient and physically transparent basis for engineering assessment of fault-crossing pipelines . Although these Beam-on-Winkler-type models remain widely used, their representation of the soil as independent axial, lateral, and vertical springs limits their ability to capture localized joint kinematics, bell-induced anchoring, and coupled load-transfer mechanisms that may develop in segmented pipelines under large ground deformation. Continuum FE models, by contrast, can explicitly represent soil deformation, pipe–soil contact, and three-dimensional boundary effects, and have been applied to investigate buried pipeline response under fault rupture and related ground movement scenarios [137, 43, 21]. However, the high computational cost and the need for detailed calibration of soil behavior and contact interactions limit the practicality of these models for repeated assessments and large-scale pipeline system analyses.

For segmented water pipelines, the system response is further complicated by nonlinear joint engagement, axial slip, rotation, and localized passive resistance mobilized at enlarged bell geometries. Previous studies have shown that joint behavior and local geometric discontinuities can influence the deformation capacity and load-transfer mechanisms of jointed or hybrid-segmented pipelines [102, 5, 21]. Argyrou et al. [4] following the coupled beam–spring formulation of [86], developed a two-dimensional model with compression-only transverse gap elements and Coulomb-coupled longitudinal friction. The bell-spigot joints were represented by nonlinear axial, shear, and rotational springs calibrated from large-scale component tests, while the enlarged bell was modeled using an additional nonlinear spring derived from pull-out tests and adjusted for burial depth. The model reproduced the sequence of joint slip and showed good agreement with measured axial-force distributions for a 6-in. ductile iron pipeline up to approximately 380 mm of fault displacement. The present study extends this approach by using distributed fiber-optic strain measurements to compare continuous axial-force and bending-moment profiles along the entire pipeline rather than at discrete instrumented sections. The comparison is resolved across the three observed response stages and continues to 470 mm of fault displacement, covering the post-engagement, pre-fracture regime in which the reduced-order models begin to underpredict joint rotation. In addition, the joint axial and rotational properties are obtained from previous component tests that explicitly account for the influence of the initial bell–spigot position. This framework provides a computationally efficient means of examining how distributed barrel friction and localized bell anchoring contribute to the staged system-level response of the buried segmented pipeline.

To examine the influence of selected soil–pipe interaction mechanisms, the experimental response was compared with two reduced-order numerical models. Simulation 1 provides a simplified reference model in which axial and lateral soil resistances are represented by

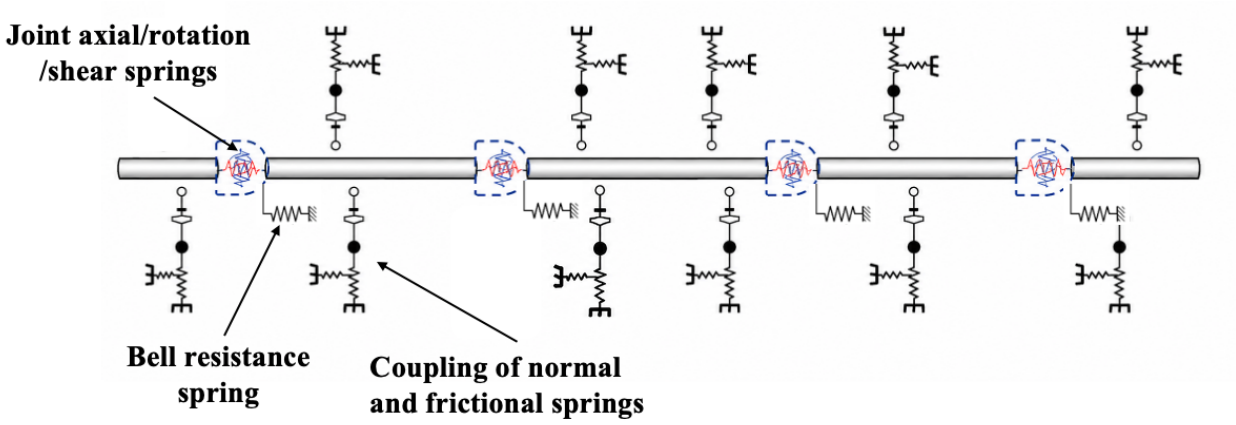


Fig. 9.4. Schematic representation of the buried jointed pipeline system.

independent springs and the localized resistance associated with the enlarged bells is omitted. Simulation 2 incorporates axial–lateral frictional coupling along the pipe barrels and distributes additional passive resistance over the bell regions. The two models are compared with the experimental measurements to assess how these mechanisms affect the staged response and spatial load redistribution, while also identifying limitations shared by both formulations.

A schematic of Simulation 2 is presented in Figure 9.4. The pipe barrels were discretized using structural pipe elements to represent axial load transfer and flexural deformation, while each bell–spigot joint was idealized as a discrete nonlinear connector with axial, rotational, and transverse components. The connector relationships were derived from previous component-level tests of the same ERDIP system [36, 144] and assigned according to the midpoint and collapsed joint positions used in the experiment. The surrounding backfill was represented by distributed nonlinear soil springs along the pipe barrels. In Simulation 2, axial resistance was coupled to the mobilized lateral soil reaction, and additional distributed springs were assigned over the enlarged bell regions to represent localized passive resistance. The geometric, material, and soil parameters used in the analyses are summarized in Table 9.2 and were selected to represent the split-basin test configuration.

9.6 Results

9.6.1 Ultimate Limit State and Fracture Mechanics

During the experiment, the pipes were first filled with water and pressurized to 517 kPa (75 psi). Three actuators were then controlled to push the moving box at a speed of 25 mm (1 in.) per minute. The test was terminated at a total actuator force of 943 kN (212 kips) and

Table 9.2. Calibrated soil and structural parameters used in the numerical simulations

Parameter	**Value**
Pipe outer diameter, ID	8.6 in. (218.4 mm)
Pipe wall thickness, t	0.3 in. (7.6 mm)
Pipe barrel length, l	12 ft. (3.66 m)
Bell joint length, l_0	10.5 in. (266.7 mm)
Pipe elastic modulus, E	23,500 ksi (162 GPa)
Pipe Poisson's ratio, ν	0.29
Pipe buried depth, H	3 ft. (0.91 m)
Soil density, γ	0.0663 lb/in^3 (18.0 kN/m^3)
Soil internal friction angle, α	40°
Pipe-soil interface friction angle, δ	32°
Coefficient of soil pressure at rest, K_0	0.36
Maximum lateral soil resistance, P_u	385.44 lb/in. (67.5 kN/m)

483 mm (19 in.) of fault displacement when a loud "boom" sound was heard, coincident with a sudden, sharp drop in the internal water pressure. Post-excavation observations showed larger rotations at Joint 2 and Joint 3, while Joint 1 and Joint 4 remained relatively straight. After the joints were uncovered, a severe crack was identified at Joint 4; the other three joints showed no significant damage. As documented in Figure 9.5, the crack initiated roughly 45° south of the joint crown, aligning with the edge of the single slot, which is a wall-thickness transition region on the bell used to house the locking segments (Figure 9.5a). In this installation, a rubber retainer occupied the single slot rather than a ductile-iron locking segment. The combination of the wall-thickness change and the stiffness mismatch between the rubber retainer and a typical locking segment likely produced a stress concentration at the slot edge.

As demonstrated in previous 200 mm (8 in.) ERDIP characterization studies [33, 31, 143], when tensile forces dominate the overall loading conditions, structural failure typically localizes at the pipe bell. The failure mode observed in this experiment closely resembles the behavior seen in the prior biaxial tension tests [31], as the bell was subjected to a combination of bending and axial tensile forces. Because of this combined loading, the resulting crack (Figure 9.5b) exhibits a combination of sudden tensile failure at initiation and shear-dominated growth, propagating through the bell at an angle of approximately 45°.

The premature failure of Joint 4 relative to central Joints 2 and 3 can be attributed to localized geometric constraints and stage-dependent rotational compliance. Specifically, the distance from the Joint 4 bell face to the rigid end wall of the fixed basin is approximately 762 mm (30 in.), corresponding to only 2.5 times the nominal bell diameter. This close proximity restricts the surrounding soil volume available to accommodate displacement, thereby limiting the joint's capacity to freely rotate and dissipate accumulating moments. Furthermore, a

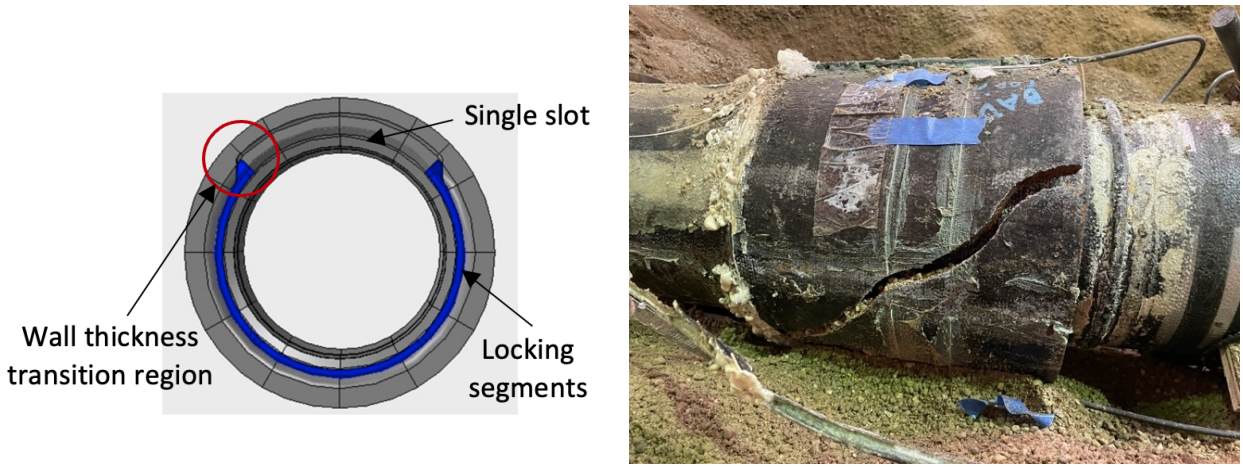


Fig. 9.5. Aftermath of pipe specimens where joint structural failure happened at Joint 4. (a) Crack started at the wall thickness transition region, single slot and locking segment boundary. (b) Crack initiated from bell face and propagated throughout the bell casing.

distinct difference in kinematic staging governs the central versus peripheral connections; as detailed in the subsequent section, central Joints 2 and 3 mobilized significant rotation prior to full axial engagement (Stage 1), whereas boundary Joints 1 and 4 experienced primarily axial pullout with minimal rotation until engagement occurred (Stage 2). Because rotational compliance is severely restricted once the locking mechanisms fully engage, the bending moment transferred to Joint 4 could not be effectively dissipated through rigid-body rotation, creating a localized stress concentration that precipitated ultimate failure. This boundary constraint was less pronounced at Joint 1 because the spigot end was anchored to the moving basin wall rather than the bell assembly, a geometric configuration that inherently provided greater kinematic freedom to accommodate transferred moments.

9.6.2 Progressive Joint Kinematics and Sequential Mobilization

Localized joint kinematics, specifically in-plane and out-of-plane rotations, were derived from the wire potentiometer arrays installed around the circumference of each connection. Figure 9.6 illustrates the evolution of joint rotation as a function of progressive fault displacement alongside the FEM predictions, revealing three distinct stages governing the system-level response: Stage 1 spans fault displacements from 0 to 191 mm (0 to 7.5 in.); Stage 2 captures the transition from 191 to 318 mm (7.5 to 12.5 in.); and Stage 3 encompasses displacements from 318 to 483 mm (12.5 to 19.0 in.).

During Stage 1, because the shear plane directly intersects the central pipe segment (Pipe M), the experimental measurements showed that the kinematic demand initially localized at Joints 2 and 3 adjacent to the fault-crossing segment. The simulations reproduce this

initial localization qualitatively. These connections mobilized progressive rotation with minimal axial restraint, while Joints 1 and 4 exhibited a negligible response. As the system deformed, Joint 3 achieved full axial engagement, defined as the spigot weld bead bearing directly against the internal locking segments, at approximately 165 mm (6.5 in.) of fault displacement, followed closely by Joint 2 engaging at roughly 191 mm (7.5 in.).

Entering Stage 2, the fully engaged weld beads at Joints 2 and 3 initiated large axial force transfer to the adjacent pipe barrels (Pipes ME and MW). Joints 2 and 3 continued to rotate to accommodate the accumulating offset, but the boundary locking forced the kinematic demand to propagate outward, initiating modest rotations and pullout at Joints 1 and 4.

At approximately 318 mm (12.5 in.) of fault displacement, the spigot weld beads at Joints 1 and 4 fully engaged their respective locking segments, transitioning the pipeline into Stage 3. In this final stage, the entire multi-segment system participated in sharing the ground deformation demand. The test ultimately terminated at 483 mm (19.0 in.) of global fault displacement when Joint 4 experienced catastrophic fracture. The measured joint-engagement sequence was used to divide the response to initial central localization, outward load propagation upon locking, and ultimate full-system participation. The simulations qualitatively reproduce the progression from central-joint mobilization to outward demand transfer and full-system engagement, although they do not capture the late-stage divergence of the central-joint rotations.

Under strike-slip fault rupture, the in-plane rotational component is theoretically expected to dominate the kinematic response, an assumption corroborated by the FEM results, which predicted negligible out-of-plane movement (dashed lines in Figure 9.6b). However, measurable out-of-plane rotations were recorded from the physical specimen. A primary driver of this multi-axial behavior is the non-uniform soil stiffness surrounding the pipe barrels; spatial variations in compacted density, particularly near the springlines and above the crown, create preferential deformation paths, causing the joint to rotate toward the zone of lower lateral confinement, a physical asymmetry not captured by the idealized uniform soil boundaries of the numerical model.

Examining the central connections, both Joints 2 and 3 accumulated in-plane rotation steadily up to approximately 343 mm (13.5 in.) of fault displacement. Beyond this threshold, their experimental behaviors diverged: Joint 3 continued to accumulate in-plane rotation, reaching a maximum of 8.49°, whereas the in-plane rotation at Joint 2 plateaued and subsequently decreased slightly with a peak value of 5.41°. While the FEM successfully tracks the general kinematic trend, it underpredicts the ultimate in-plane rotational magnitudes during Stages 2 and 3 (Figure 9.6a), plateauing at roughly 4° for both central joints. This underprediction is attributed to the simplified joint representation adopted in the reduced-order model. In the experiment, joint pullout and rotation occurred simultaneously, and the effective rotational resistance of the bell-and-spigot joint likely evolved as the relative position between the bell, spigot, gasket, and locking segments changed. As the joint extended, local contact and bearing conditions within the joint were altered, allowing rotation to develop more readily under a comparable bending demand. In contrast, the numerical model repre-

sents joint extension and rotation using independent axial and rotational spring components. This decoupled formulation does not capture the softening of rotational stiffness associated with progressive joint opening and contact redistribution. Consequently, the model provides excessive rotational restraint at large fault displacements and underestimates the measured joint rotations. Out-of-plane physical responses similarly diverged, with Joint 2 exhibiting a progressive increase in out-of-plane rotation throughout the test, while Joint 3 displayed a gradual decrease.

Peripheral Joints 1 and 4 similarly mobilized bi-directional rotations, though at significantly reduced magnitudes. Prior to the end of Stage 1, rotational components at Joint 4 remained minimal. Rotational demand only transferred to Joint 4 following the axial engagement of the central joints. Even after mobilization, the peak in-plane rotation at Joint 4 was restricted to 1.28°, indicating that local demand at the boundary was accommodated predominantly via axial slip rather than bending rotation. A comparable condition governed Joint 1, which maintained a negligible in-plane rotation throughout the entire test sequence (peaking at just 0.15°) alongside a minor out-of-plane component. These boundary observations show that transferred ground displacements at the peripheral joints were carried almost exclusively through axial force and translation, mobilizing a fraction of the rotational demand absorbed by the interior connections. A comprehensive summary of the peak rotational values is compiled in Table 9.3.

Table 9.3. Maximum joint rotations and sign conventions. In-plane: + bends toward the north side, − toward the south. Out-of-plane: + bends upward, − downward.

Rotation Type	Joint 1	Joint 2	Joint 3	Joint 4
In-plane rotation	−0.15°	−5.41°	+8.49°	+1.28°
Out-of-plane rotation	+0.93°	−1.78°	+1.42°	−0.52°

9.6.3 Evolution of Internal Flexure and Global Deflection

Building upon the preceding kinematic analysis, the integrated system-level behavior of the pipeline specimen throughout the testing sequence is driven by the evolution of internal bending moments. Quantitatively, internal bending moment distributions are derived directly from distributed axial strain measurements using Equation 9.3 and are mapped across progressive fault offsets alongside FEM predictions in Figure 9.7. To conceptualize these empirical force distributions, the corresponding physical deformation modes of the multi-segment assembly are summarized schematically in Figure 9.8, with macroscopic deflections exaggerated for illustrative clarity.

Figure 9.8a illustrates the initial structural response of the central segment (Pipe M) immediately following fault rupture initiation. Because the shear plane directly intersects Pipe M, kinematic demand initially localizes at central Joints 2 and 3. Localized joint

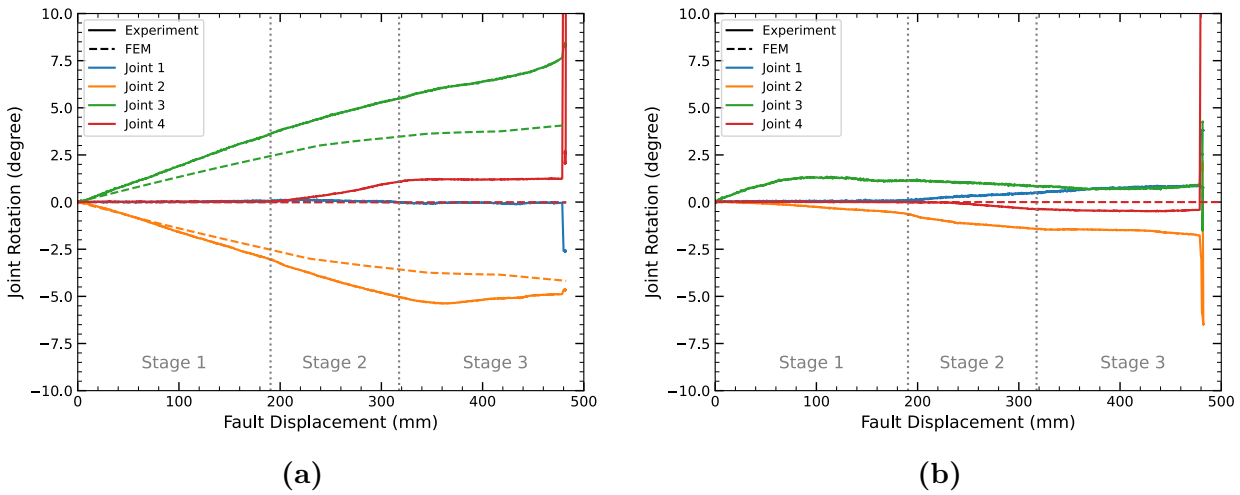


Fig. 9.6. Joint rotation and fault displacement. (a) In-plane joint rotation and fault displacement. (b) Out-of-plane joint rotation and fault displacement.

rotations mobilize at these fault-crossing interfaces, recorded by the wire potentiometer arrays as bending toward the south at Joint 2 and toward the north at Joint 3. Unlike baseline characterization tests conducted in unburied atmospheric conditions [36], where pipe segments displaced freely with minimal lateral restraint, the surrounding compacted backfill provides passive lateral support that anchors the pipeline, forcing continuous internal curvature to develop along the barrel walls. Consequently, reverse curvatures form at the boundaries of Pipe M during this initial phase, deflecting southward within the moving basin and northward within the fixed basin.

Quantitatively, the empirical moment distributions mapped by the solid green curves in Figure 9.7 confirm this localized response during Stage 1. It should be noted that while both numerical simulations slightly overpredict the peak moment magnitudes within Pipe M beginning in this initial stage, they accurately capture the fundamental spatial trends. Because Pipe M directly accommodates the primary shear plane deformation, internal bending moments along its length accumulate continuously from the onset of fault slip, developing a highly consistent antisymmetric bending pattern in both the experimental data and the corresponding FEM predictions. Concurrently, internal moments initiate localized growth along the peripheral pipes (Pipes ME and MW) during this phase. As central Joints 2 and 3 rotate, bending demand is transferred across the interfaces to overcome localized passive soil resistance, establishing an initial S-shaped reverse curvature profile along the outer segments as conceptualized in Figure 9.8b. Throughout this stage, the central connections pull out axially with minimal structural restraint until Joint 3 achieves full axial engagement, defined as the spigot weld bead bearing directly against the internal locking segments.

Entering Stage 2 (represented by the blue curves in Figure 9.7), the fully engaged weld beads at central Joints 2 and 3 initiate a pronounced transfer of axial force outward into Pipes

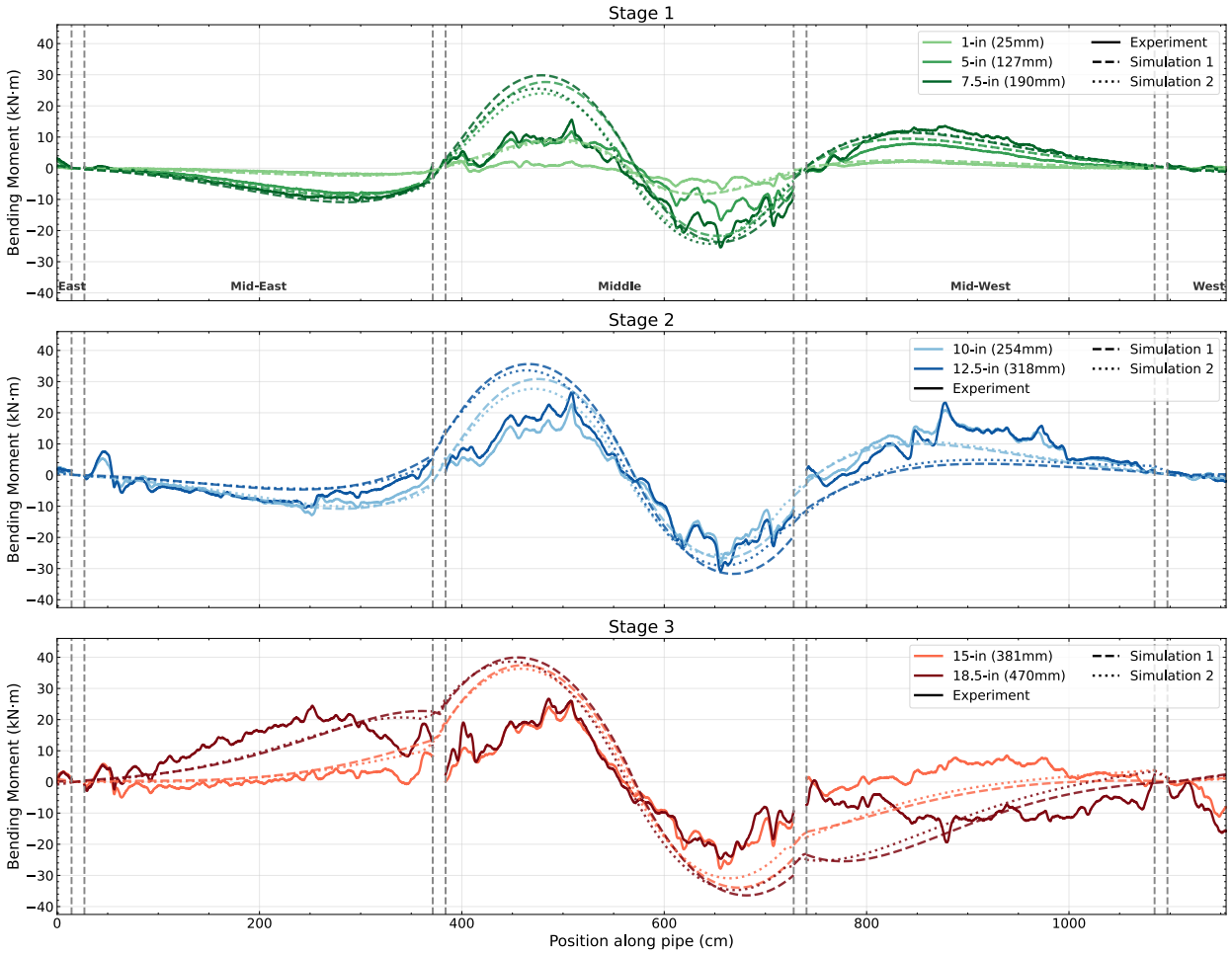
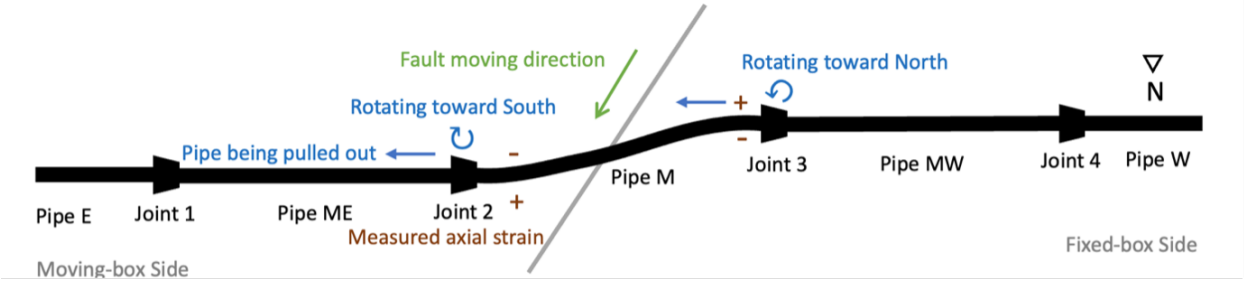


Fig. 9.7. Moment distribution on the specimen at multiple fault displacement conditions. Simulation 1 utilizes a conventional framework that omits friction-displacement coupling at the soil-pipe interface and localized joint anchoring, whereas Simulation 2 explicitly incorporates these complex interaction mechanics.

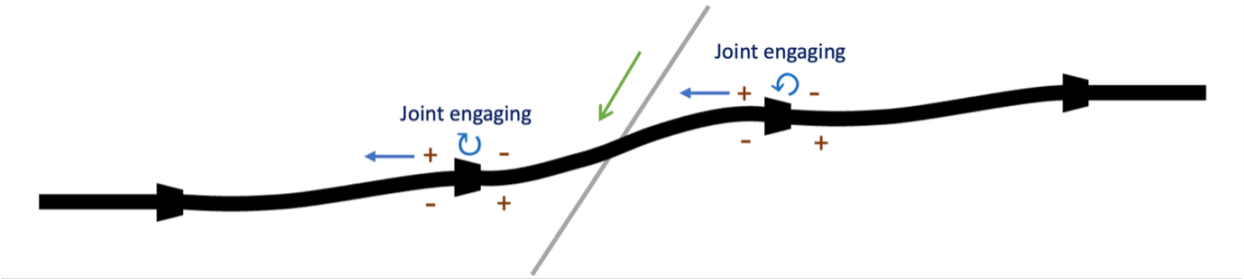
ME and MW. While internal bending moments along central Pipe M continue to intensify steadily due to accumulating global shear demand, the rate of moment accumulation along peripheral Pipes ME and MW exhibits a distinct plateau. Due to passive soil restraint resisting rigid-body translation, the internal moments induced along Pipe ME maintain an opposite sign relative to the moving-basin side of Pipe M, with a correspondingly reversed profile along Pipe MW relative to the fixed-basin side of Pipe M. As fault displacement progresses toward 318 mm (12.5 in.), boundary Joints 1 and 4 mobilize unconstrained axial pullout to accommodate the global fault offset, mitigating localized rotational and flexural demand on the outer pipes. Consequently, while the overall pipeline assembly maintains its previously established alternating moment profile at amplified magnitudes (Figure 9.8c), internal bending moments along Pipes ME and MW experience minimal growth throughout Stage 2. Both simulations reproduce the continued moment growth in Pipe M and the relative plateau along the adjacent segments. While simulation 2 predicts lower peak moments and is closer to the experimental measurements than Simulation 1.

At approximately 318 mm (12.5 in.) of fault displacement, the spigot weld beads at peripheral Joints 1 and 4 fully engage their respective locking segments, terminating the phase of unconstrained boundary slip and transitioning the system into Stage 3. With all four connections mechanically engaged, global tensile forces begin to dominate the system-level mechanics. Concurrently, the quantitative experimental moment distributions captured by the solid red curves in Figure 9.7 show a fundamental mechanical realignment. The longitudinal tensile forces override localized passive soil resistance, altering the internal curvature fields and forcing the internal bending moments along peripheral Pipes ME and MW to undergo a distinct reversal, flipping signs to match the primary flexural direction of the central pipe specimen. As illustrated schematically in Figure 9.8d, the global deformation pattern realigns to merge into a unified macro-profile that closely mirrors behavior observed in pure-bending characterization tests. Because massive tensile forces accumulate across the fully engaged system during this stage, the pipeline naturally tends to "straighten out". This straightening effect causes the individual pipe barrels to align more directly, which recovers a small portion of the earlier joint rotations and shifts the assembly slightly toward the yielding soil zone. Ultimately, these high tensile forces overpower the local soil resistance, forcing the separate pipe segments to bend together as a single continuous curve.

Both simulations successfully capture this fundamental structural realignment during Stage 3 (Figure 9.7 red curves). The numerical models correctly predict the moment reversal driven by the global straightening under axial tension. However, the peak bending moments across the assembly are consistently overpredicted by both frameworks. This overprediction is likely caused by underestimated joint rotation in the decoupled discrete springs. When numerical joint rotation is overly restrained and lacks physical "softening," a disproportionate share of the imposed global deformation is artificially transferred into the flexure of the pipe barrels. Two simulations produce similar peak responses, indicating that the added soil-interaction mechanisms have limited influence on the predicted peak value once all joints are engaged. The main distinction between the models at this stage lies instead in the spatial redistribution of axial force across the joint and adjacent barrel regions.



(a) Initial stage: Bending strains begin to develop on the fault-crossing pipe as Joints 2 and 3 undergo initial pullout and opposite rotations.

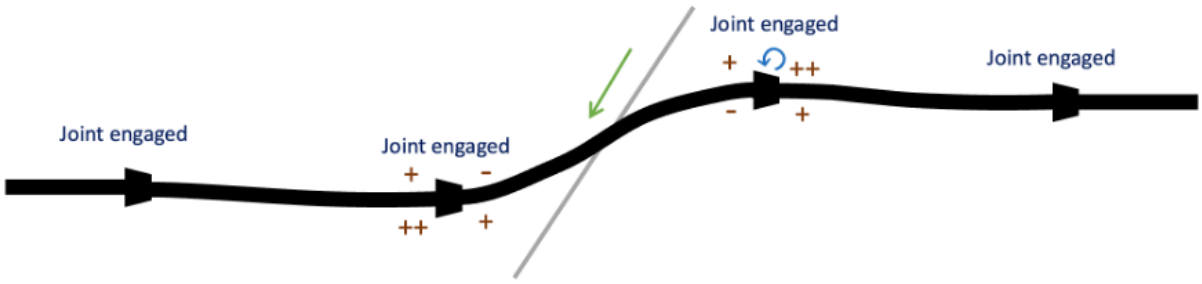


(b) Stage 1: As Joints 2 and 3 engaging, flexural deformation develops along Pipe M and propagates outward to segments ME and MW. Due to passive soil anchoring effects, the pipeline develops reverse curvature, characterized by opposing bending directions on the east and west sides of the engaging joints.

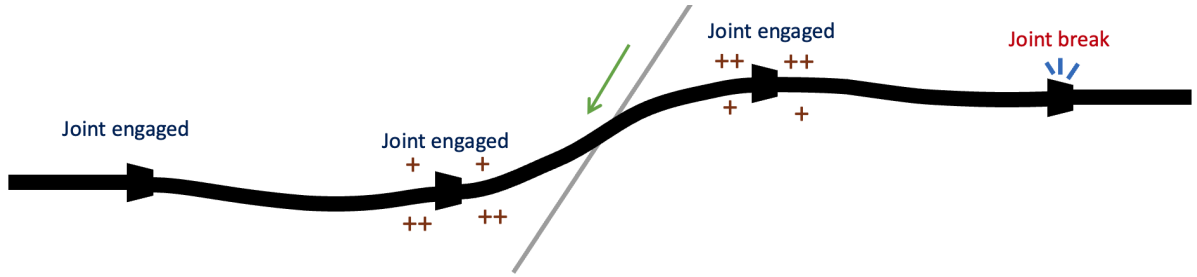


(c) Stage 2: Joints 2 and 3 engaged while Joints 1 and 4 experience pullout with minimal rotation. Curvatures east and west of Joints 2 and 3 maintain opposite directions.

Fig. 9.8. Progressive schematic of pipeline kinematics and moment-induced deformations under fault rupture. (Continued on next page.)



(d) Stage 3: All four joints engaged. Axial tension dominates as further rotation localizes exclusively at Joint 3, generating global tensile strains across Pipes ME and MW. Central dual curvatures coalesce into a single unified profile (++ indicates greater tensile strain).



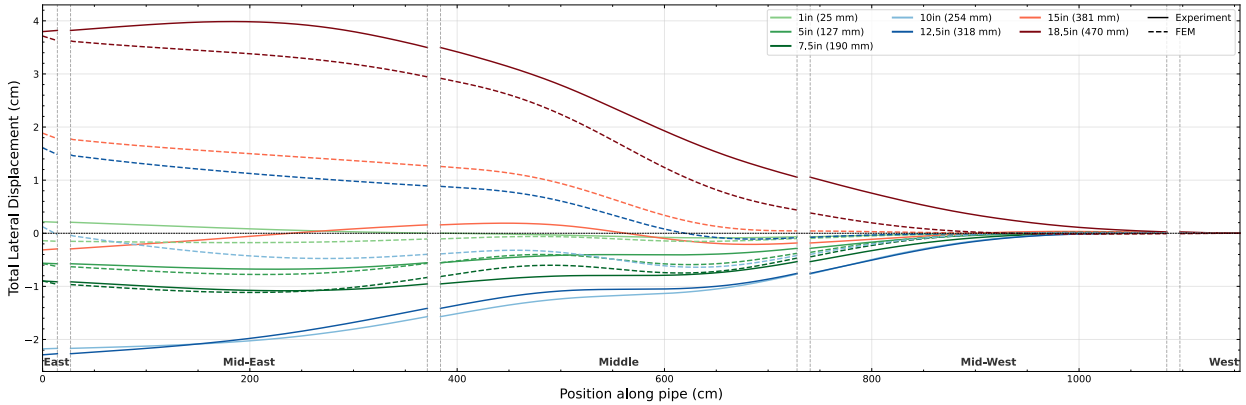
(e) Ultimate failure state: Continued fault displacement leads to the eventual failure of Joint 4.

Fig. 9.8. Progressive schematic of pipeline kinematics and moment-induced deformations under fault rupture. Note: Deformations are exaggerated for illustrative purposes.

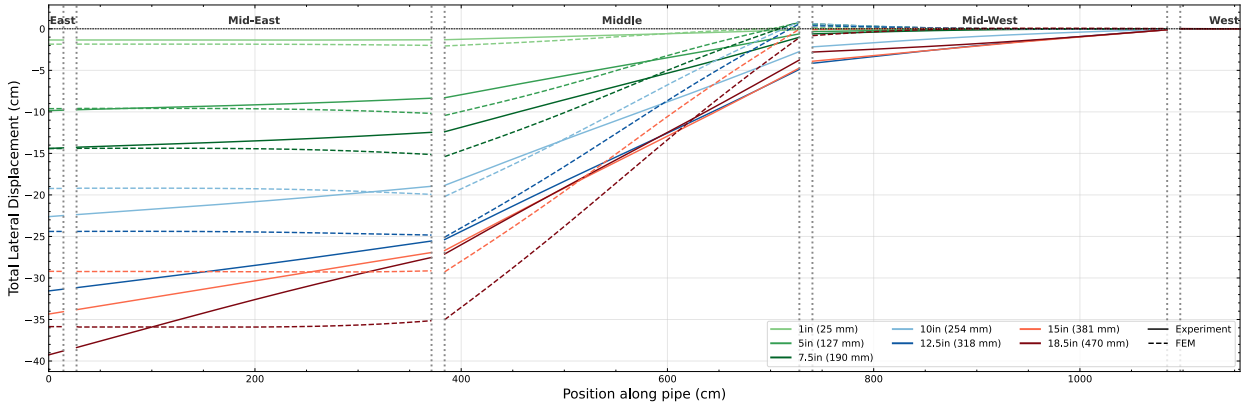
Under sustained fault displacement beyond the Stage 3 realignment, internal bending moments and multi-axial stresses intensify across all four connections. The continuous accumulation of extreme global tensile and bending demand ultimately exhausts the local structural capacity of the system, culminating in the complete fracture of Joint 4 at a final global fault displacement of 483 mm (19.0 in.), as represented in Figure 9.8e.

Because internal bending moments are directly proportional to longitudinal curvature ($\kappa = M/EI$), the macroscopic lateral deflection of the pipeline assembly can be reconstructed via spatial double integration of the distributed DSS profiles. To isolate the individual mechanical contributions governing global system compliance, integration was executed in two comparative phases: isolating pure pipe flexure versus reconstructing total joint-assisted kinematics.

Figure 9.9a first illustrates the pure segmental lateral displacement profiles calculated by double-integrating localized barrel curvatures (Equation 9.4) while strictly zeroing out discrete joint translations and rotations. This isolated view demonstrates that internal flexural deflections within the rigid ductile iron barrels remain highly constrained throughout the rupture sequence in the experimental setup, peaking at approximately ±1.5 in. (±38 mm). When plotted alongside the corresponding FEM results for both numerical frameworks



(a) Lateral displacement on the specimen at multiple fault displacement condition (not considering joint rotation-induced lateral movement).



(b) Lateral displacement on the specimen at multiple fault displacement condition (considering joint rotation-induced lateral movement)

Fig. 9.9. Lateral displacement along pipe.

(dashed lines), a nuanced, stage-dependent correlation emerges. During the initial fault displacements (Stage 1), both simulations accurately capture the magnitude of pure barrel bending, indicating that the initial soil-spring formulations effectively represent early-stage soil-pipe confinement. As the fault offset progresses into intermediate deformations (Stage 2), a slight divergence occurs. This transient discrepancy is likely attributable to the complex, non-linear mobilization of soil bearing capacity and localized gap formation in the physical basin, which standard elasto-plastic soil springs inherently oversimplify. However, at the ultimate fault displacement stage, the empirical and numerical profiles converge. This final alignment suggests that after the surrounding soil fully yields, the ultimate flexural demands on the pipe barrel are governed primarily by global geometric boundary constraints rather than transient soil stiffness, an end-state equilibrium that the FEM successfully captures.

To capture the true physical trajectory of the integrated assembly, Figure 9.9b presents

the total reconstructed lateral displacement profile derived using the updated piecewise integration strategy defined in Equation 9.4. Applying a fully restrained boundary condition at the West Tip anchor, integration constants were updated sequentially at each connection by superimposing the discrete joint translations and in-plane rotations quantified by the localized wire potentiometer arrays. In this total kinematic view, the predictions from both numerical models closely track the experimental data during initial fault offsets, successfully simulating the rigid-body translation of the pipe segments. However, as the system undergoes severe deformation, the numerical frameworks visibly under-predict the maximum lateral sweep at the eastern boundary. This discrepancy arises primarily because the localized joint rotations predicted by the decoupled FEM springs are smaller than those physically mobilized in the experiment. As the physical joints experience localized yielding, they achieve a coupled rotational compliance that neither Simulation 1 nor Simulation 2 can currently replicate. Consequently, when these underestimated rotational contributions are incorporated into the total kinematic profile, the numerical models project a reduced total lateral displacement.

Comparing the isolated barrel flexure against the total reconstructed profile conclusively demonstrates the primary seismic survival mechanism of the ERDIP system: macroscopic compliance is governed by discrete joint kinematics rather than structural barrel deformation. Mobilizing concentrated joint rotations allows the system to sweep through macro-deflections exceeding 15.5 in. (390 mm) at the eastern boundary. Consequently, the specialized seismic joints act as kinematic hinges that shield the individual pipe barrels, absorbing over 90% of the global displacement demand and preventing the ductile iron segments from exceeding their ultimate flexural capacities. This fundamental decoupling, underscored by the specific localized discrepancies observed in the FEM joint rotation projections across both simulations, demonstrates how segmented pipelines transform localized shear planes into distributed, highly survivable structural responses, while also highlighting the critical need to further calibrate discrete numerical joint models using high-resolution empirical data.

9.6.4 Axial Load Transfer and Frictional Soil Coupling

The staged flexural evolution documented in the preceding section is fundamentally governed by lateral soil restraint and localized bell anchoring. However, while this concentrated bearing resistance dictates the early flexural response, ongoing fault displacement simultaneously mobilizes interface shear along the longitudinal axis of the continuous pipe barrels. As global deformation escalates, the structural demand along the segmented assembly transitions from lateral bending to axial tension, driven by the continuous accumulation of this longitudinal soil friction. To quantify this progressive load transfer, axial force distributions along the continuous pipe barrels were derived directly from the DSS arrays. Figure 9.10 contextualizes these distributions across the entire multi-segment system alongside numerical predictions.

Because the central segment (Pipe M) directly accommodates the primary shear plane deformation, its translation forces the adjacent connections (Joints 2 and 3) to bear heavily against these localized passive soil blocks. The combination of distributed barrel confinement

and bell-induced anchoring prevents the peripheral barrels (Pipes ME and MW) from rigid-body translation. Instead, the localized fixity at the joints acts as a physical fulcrum, forcing internal bending moments to develop along the continuous segments. This coupled resistance mechanism explains the empirical observations documented during the early loading stages, where internal curvatures along Pipes ME and MW develop reverse signs relative to their central interfaces.

Capturing this interplay between distributed and localized soil restraint is critical for the advanced numerical modeling of segmented infrastructure. Standard modeling approaches often assume uniform soil-pipe interaction parameters along the entire pipeline length, ignoring the discrete anchoring of the connections. However, the empirical behaviors observed in this experiment indicate that accurate numerical replication requires explicitly decoupling the barrel and joint geometry. In discrete spring frameworks, this necessitates maintaining standard distributed interactions along the barrel while implementing localized, amplified lateral load-displacement ($p - y$) and axial ($t - z$) boundary elements at the joint nodes to accurately represent the increased passive bearing capacity.

Ultimately, the localized soil anchoring induced by the enlarged joint bells governs the initial flexural propagation and stage transitions of the ERDIP system. While this concentrated bearing resistance at the joint faces dictates the early flexural response, ongoing fault displacement progressively mobilizes interface shear along the continuous pipe barrels. As global deformation escalates, the structural demand along the segmented pipeline assembly is heavily dictated by this accumulating longitudinal soil friction operating concurrently with the localized bell anchoring. To quantify this continuous load transfer, axial force distributions along the continuous pipe barrels were derived directly from the DSS arrays. Figure 9.10 contextualizes these distributions across the entire multi-segment system alongside numerical predictions.

In accordance with fundamental soil-structure interaction frameworks, the rate of longitudinal force accumulation per unit length (f) mobilized along a buried pipe barrel is directly defined by the spatial gradient of the axial force profile ($P(x)$), expressed mathematically as $f = dP/dx$. This localized load gradient reflects the intensity of interface shearing resistance acting around the pipe circumference. To isolate uniform barrel load transfer from localized boundary disturbances induced by the enlarged joint bells, linear regression fits were applied separately to the left and right halves of the central pipe segment, as denoted by the dashed lines and shaded regions in Figure 9.11. The results are summarized in Table 9.4.

Table 9.4. Friction estimates at each fault displacement

Parameter	**Fault Displacement: in. (cm)**						
	1.0 (2.53)	5.0 (12.72)	7.5 (19.06)	10.0 (25.39)	12.5 (31.74)	15.0 (38.09)	18.5 (46.97)
f_{left} (kN/m)	10.85	59.06	78.34	94.97	111.75	153.09	209.50
f_{right} (kN/m)	41.43	101.31	107.59	107.50	110.98	173.77	306.93

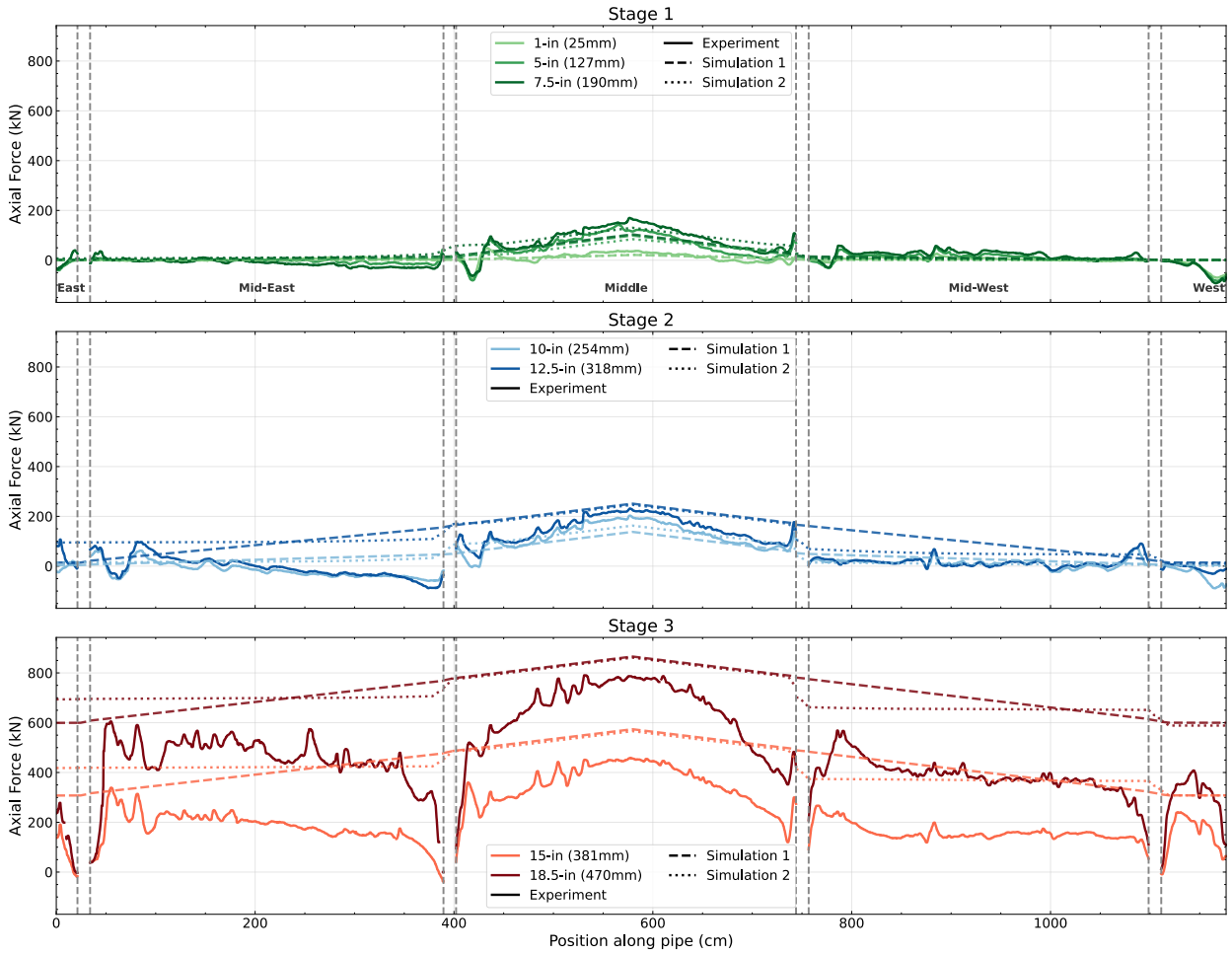


Fig. 9.10. Axial force distribution at multiple fault displacement condition.

Evaluating the empirical load gradients reveals a stage-dependent mechanical evolution governing the rate of longitudinal force accumulation. Following initial fault slip at 25 mm (1.0 in.) of offset, the localized shearing slopes display distinct asymmetry, measuring $f_{\text{left}} = 10.85$ kN/m and $f_{\text{right}} = 41.43$ kN/m. As displacement advances through the primary rotational phases (Stages 1 and 2), the rate of load transfer progressively mobilizes. By 318 mm (12.5 in.) of fault displacement, the friction rates on both sides of the central pipe effectively equalize, stabilizing at $f_{\text{left}} = 111.75$ kN/m and $f_{\text{right}} = 110.98$ kN/m.

Surpassing the 318 mm (12.5 in.) displacement threshold triggers a dramatic escalation in the rate of force accumulation. Corresponding directly with the full mechanical locking of peripheral Joints 1 and 4 (Stage 3), unconstrained boundary slip terminates, causing global tensile forces to escalate rapidly across the specimen. At 381 mm (15.0 in.) of fault displacement, the measured load gradients steepen significantly to $f_{\text{left}} = 153.09$ kN/m and

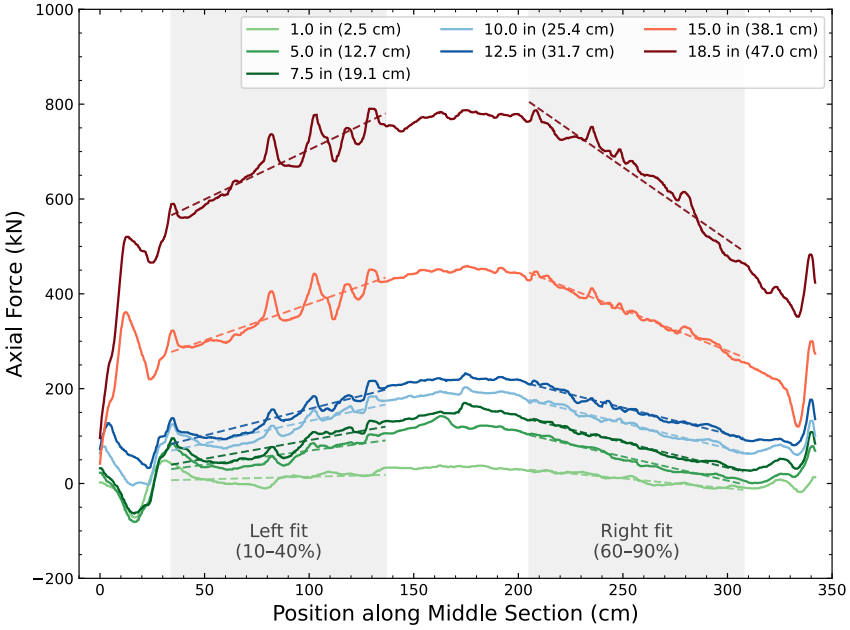


Fig. 9.11. Evolution of axial force along the middle pipe section (Pipe M) under progressive fault displacements. The shaded regions indicate the analytical domains-corresponding to 10–40% and 60–90% of the pipe length-where linear regression (dashed lines) was applied to the force profiles. The slopes of these regressions (dF/dx) represent the interfacial soil friction per unit length.

$f_{\text{right}} = 173.77$ kN/m. Ultimately, immediately prior to ultimate limit state fracture at 470 mm (18.5 in.) of fault offset, extreme global tension drives the peak axial force on Pipe M to approach 800 kN (180 kips). This large demand steepens the localized rate of force accumulation to the peaks of $f_{\text{left}} = 209.50$ kN/m and $f_{\text{right}} = 306.93$ kN/m.

This escalation in the longitudinal load gradient is primarily driven by the progressive development of passive earth pressure along the continuous pipe barrels. As the global fault displacement increases, the rigid pipeline is forced to translate laterally into the dense surrounding backfill. This lateral movement mobilizes a massive passive soil resistance against the pipe wall, increasing the radial confinement and contact pressure. As evidenced by the empirical measurements in Table 9.4, the magnitude of this passive confinement scales directly with the severity of the fault offset, causing the operational soil friction to surge correspondingly.

To accurately capture this displacement-dependent increase in soil friction, standard constant-yield soil springs are insufficient. Instead, this phenomenon is explicitly considered in the enhanced numerical framework (Simulation 2) through the implementation of a special soil-spring model designed to capture the escalation of frictional resistance as a function of fault displacement. As demonstrated in the axial force profiles in Figure 9.10, this specialized

spring formulation is capable of replicating the escalation of the longitudinal load gradient across the progressive loading stages, while showing the transition from a localized response near the fault-crossing region to broader system-level axial load transfer.

Before the joint engagement (Stage 1 to Stage 2), the numerical axial forces are generally lower than the experimental peak response (Figure 9.12c). This underprediction is consistent with the low-resistance pullout stage assigned to the joint axial springs, which allows early deformation to be accommodated by joint slip with limited axial force mobilization. In the physical experiment, additional early-stage resistance may have been provided by joint seating, gasket contact, bell-spigot bearing, and boundary effects, which are not explicitly resolved in the reduced-order formulation. Nevertheless, by capturing the localized bell anchoring, Simulation 2 predicts higher axial forces than Simulation 1 during Stage 2, thereby providing closer agreement with the experimental measurements.

With increasing fault displacement, both simulations show that axial force progressively propagates from the central fault-crossing region toward the adjacent pipe segments. This response is consistent with the experimental observation that deformation demand evolves from a localized central-joint response toward a more global, system-level engagement. After the joints engage (Stage 3), the predicted peak axial forces become conservative relative to the experimental measurements, and the maximum values obtained from Simulations 1 and 2 become comparable. This suggests that once the restrained joints lock out and the response is governed primarily by global tensile load transfer, the influence of localized bell anchoring and axial-lateral soil coupling on the peak axial force becomes secondary relative to the dominant contribution of joint engagement.

Although the two simulations predict similar peak axial forces during Stage 3, their spatial distributions differ. Simulation 2 more closely reproduces the localized changes in axial force across the joint regions and the relatively uniform force levels along portions of the adjacent pipe barrels. Simulation 1 instead produces a smoother outward decay. These comparisons indicate that the additional interaction mechanisms in Simulation 2 primarily affect the spatial redistribution of axial force rather than the Stage 3 peak value.

9.6.5 Evaluation of Peak Demands and Numerical Fidelity

To further evaluate the influence of localized soil-pipe interaction mechanisms on the system-level response, the experimental peak measurements were compared with the predictions from the two numerical models (Figure 9.12). Figures 9.12a and 9.12b compare the peak joint extension and peak joint rotation obtained from the experiment and the two simulations. Both simulations capture the overall increase in joint extension with fault displacement. Simulation 1 provides closer agreement during the early stage, whereas Simulation 2 tends to predict a slightly larger joint opening once the central joints begin to engage. However, as fault movement progresses into severe displacements, both numerical models significantly overpredict the ultimate joint extension. In contrast, both simulations severely underpredict the peak joint rotation. The experimental rotation continues to increase with fault displacement, whereas the numerical predictions plateau at approximately 4°. In the numerical

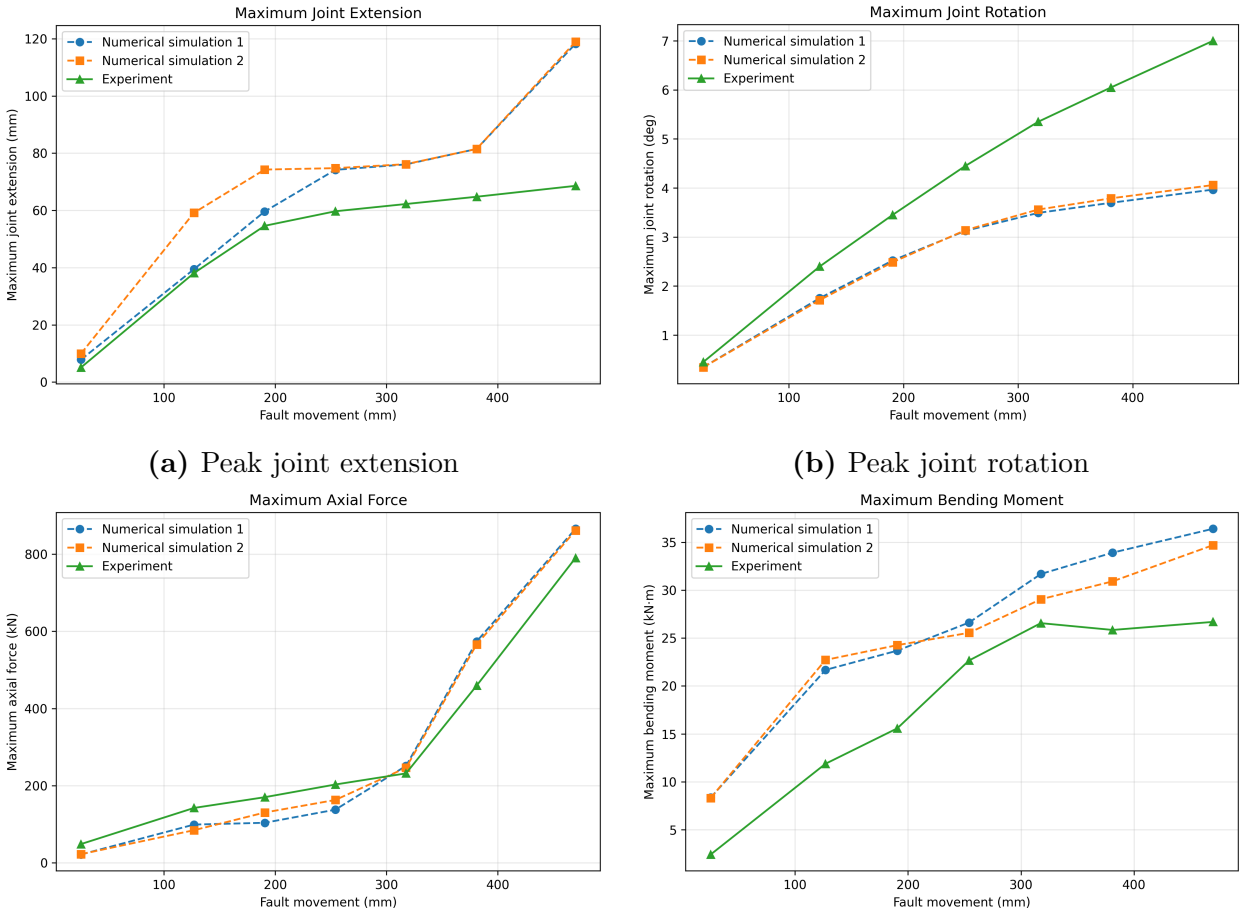
models, joint extension and rotation are represented by independent axial and rotational spring components. In the physical restrained bell-spigot joint, however, these deformation modes are highly coupled. As the spigot pulls out relative to the bell and undergoes severe rotation, the contact state between the bell and spigot changes, inducing localized yielding that reduces the effective rotational stiffness of the joint. Therefore, under a comparable kinematic demand, the experimental joint can rotate more readily once substantial joint opening has occurred. This extension-dependent rotational softening is not captured in the decoupled spring formulation; consequently, the simulations preserve excessive rotational restraint at large fault displacements and compensate for the global fault sweep by artificially overpredicting axial joint extension.

Evaluating the peak axial forces (Figure 9.12c), the numerical predictions are generally lower than the experimental response before full joint engagement (Stages 1 and 2). This underprediction is consistent with the low-resistance pullout stage assigned to the joint axial springs, which allows early deformation to be accommodated by joint slip with limited axial force mobilization. In the physical experiment, additional early-stage resistance is likely provided by joint seating, gasket contact, and bell-spigot bearing, which are not explicitly resolved in the reduced-order formulation. Nevertheless, by incorporating localized bell anchoring, Simulation 2 predicts higher axial forces than Simulation 1 during Stage 2, thereby providing closer agreement with the experimental measurements. After the joints fully engage (Stage 3), the response is governed primarily by global tensile load transfer. In this ultimate stage, the predicted peak axial forces from both models surge and become conservative relative to the experimental measurements, indicating that the influence of localized bell anchoring on the peak axial demand becomes secondary once the joints physically lock out.

The artificial kinematic restraint observed in the joint rotation directly impacts the peak bending moment projections (Figure 9.12d). Because the numerical joints resist physical rotation, the global displacement demand is forced into the flexure of the adjacent pipe barrels, resulting in consistent overpredictions of the maximum bending moment relative to the experiment. However, the localized interaction mechanics in Simulation 2 yield more accurate intermediate predictions. While Simulation 2 predicts a slightly higher moment initially, it crosses below Simulation 1 during Stage 2. By simulating the localized fixity of the bell anchors, Simulation 2 creates numerical pivot points within the soil that help distribute the lateral curvature more evenly across the assembly, thereby reducing the peak bending concentration compared to the unanchored Simulation 1 and aligning closer to empirical reality.

9.7 Conclusion

This study investigated the system-level response of a pressurized 8-in. (200-mm) earthquake-resistant ductile iron pipe (ERDIP) assembly subjected to strike-slip fault displacement using a large-scale split-basin experiment. The test specimen consisted of five full-scale pipe seg-



(a) Peak joint extension

(b) Peak joint rotation

(c) Maximum internal axial force

(d) Maximum internal bending moment

Fig. 9.12. Comparison of peak kinematic and structural responses between the large-scale experiment and FEM predictions across progressive fault displacements.

ments and four single-restrained bell-spigot joints embedded in compacted trench backfill. Distributed fiber optic sensing (DFOS) and discrete joint measurements were utilized to capture continuous pipe strain profiles, joint kinematics, and progressive deformation mechanisms throughout the test. Reduced-order numerical models were established to reproduce the primary experimental observations. The main findings are summarized as follows:

1. The split-basin experiment demonstrated that the response of the segmented ERDIP system was governed by joint kinematics rather than uniform deformation along the pipeline, with the joints accommodating over 90% of the total applied fault displacement. This high displacement capacity was achieved through a staged activation process. During the early stages of fault rupture, axial pullout and rotational demands localized primarily at the two central joints adjacent to the fault-crossing pipe segment.

Joint 3 reached mechanical engagement at approximately 165 mm (6.5 in.) of fault displacement, followed by Joint 2 at approximately 191 mm (7.5 in.). Once these central joints engaged, the unaccommodated kinematic demands were smoothly transferred outward to the boundary connections (Joints 1 and 4), which subsequently absorbed the remaining fault displacement until their eventual engagement at approximately 318 mm (12.5 in.).

2. Corresponding to the staged kinematic activation, experimental DFOS measurements and numerical simulations revealed a distinct, three-stage transition in the load-transfer mechanism. Initially, bending and rotational demands were highly localized near the fault-crossing pipe segment. Following the engagement of the central joints, axial forces transferred outward, though peripheral bending moments temporarily plateaued as the boundary joints freely accommodated displacement. Finally, once all four joints mechanically engaged, the system transitioned into a unified, full-pipeline response. Massive global tensile forces overrode localized soil resistance, triggering a fundamental structural realignment that reversed the sign of peripheral bending moments and forced the segmented assembly to bend as a single, continuous macro-curve.

3. The system's staged flexural response was governed by the combined effects of localized joint anchoring, distributed barrel confinement, and friction–displacement coupling. As fault displacement increased, the enlarged joint bells mobilized concentrated passive soil resistance that acted as localized fulcrums, while distributed lateral confinement along the pipe barrels restrained rigid-body translation, forcing adjacent pipe segments into reverse bending. Concurrently, friction–displacement coupling along the pipe barrels intensified with increasing fault offset as higher passive earth pressures enhanced radial confinement, increasing the longitudinal load transfer rate from approximately 111 kN/m (7.6 kips/ft) at the onset of Stage 3 to over 306 kN/m (21.0 kips/ft) immediately prior to ultimate failure.

4. Ultimate system failure localized at the peripheral Joint 4 bell due to coupled bending and axial tension, resulting in a 45° shear-dominated crack. This premature failure underscores the critical influence of localized boundary constraints. Joint 4's proximity to the rigid basin wall severely restricted the surrounding soil volume and its rotational capacity. Unlike the central joints, boundary joints primarily experienced axial pullout prior to engagement; once mechanically locked, they lacked the rotational compliance needed to dissipate transferred bending moments. This kinematic restriction induced severe stress concentrations that precipitated structural failure.

5. The numerical comparison showed that the influence of the additional soil-pipe interaction mechanisms was stage and response dependent. Simulation 2 provided its clearest improvement during Stage 2 and in the spatial redistribution of axial force across the joint and adjacent barrel regions, whereas the two simulations produced similar peak axial forces after full joint engagement. Both models underpredicted joint rotation and

overpredicted joint opening and pipe-barrel bending at large displacements. This finding suggests that future seismic modeling of segmented restrained pipelines should consider coupled axial-rotational joint behavior to better capture the large-displacement response while maintaining the computational efficiency of reduced-order analysis.

Ultimately, the primary contribution of this research lies in providing a high-fidelity, system-level empirical dataset that bridges the gap between isolated component testing and full-scale field behavior under extreme seismic hazards. By elucidating the complex interplay of staged joint kinematics, localized soil–pipe interaction, and load redistribution, this study offers insights for refining seismic design paradigms. These findings underscore the necessity of transitioning toward kinematically coupled numerical frameworks, which will help mitigate artificial design conservatism and support the development of more resilient, economically viable buried infrastructure.

Chapter 10

Conclusions and Future Works

10.1 Conclusions

The reliability and resilience of urban water infrastructure depend on two complementary engineering imperatives: mitigating the gradual deterioration of aging, largely unmonitored legacy networks, and ensuring the survivability of newly installed pipelines subjected to extreme geohazards. Recognizing that these challenges demand distinct methodologies, this dissertation presents a dual-perspective framework, coupling data-driven asset management for legacy systems with experimental and numerical investigations of new pipeline behavior under severe loading. Collectively, this research advances pipeline engineering beyond conventional, heuristic-based decision-making, driving a shift toward proactive life-cycle management and highly resilient pipeline design. The principal findings and contributions of this work are synthesized in the following sections.

Driving Factors in Pipeline Degradation

Long-term deterioration of buried water distribution pipelines is governed by the cumulative interaction of material properties, operational conditions, environmental stressors, and historical failure events, rather than chronological age alone. By applying a survival analysis framework to approximately 150 years of installation records and multi-decade failure histories, the study quantified deterioration trajectories across a heterogeneous water distribution network and established previous failure history as the dominant predictor of future performance. These findings confirm that pipeline deterioration is inherently cumulative and path-dependent, with each failure fundamentally altering the subsequent probability of future deterioration.

Beyond identifying failure history as the principal driver of future performance, the analysis revealed how intrinsic material behavior and physical characteristics influence degradation before the onset of failure. Brittle legacy materials exhibited strong sensitivity to environmental loading, while small-diameter pipelines were shown to be particularly vulnerable because of their reduced flexural rigidity and increased susceptibility to ground-induced

bending. The interaction between environmental loading, corrosion, and structural geometry further accelerates deterioration by progressively reducing structural capacity. At the network scale, the analysis also identified a survivorship effect among older infrastructure, whereby the remaining assets represent progressively more resilient populations following decades of deterioration and replacement. Collectively, these findings demonstrate that deterioration mechanisms evolve through the coupled effects of material aging, environmental exposure, and accumulated structural damage rather than through uniform time-dependent degradation.

The broader implication of this work is that predictive deterioration models can benefit from moving beyond strictly age-based representations. By explicitly accounting for evolving physical conditions and failure histories, survival analysis offers a statistical framework capable of accommodating the heterogeneous deterioration of different pipe materials. Ultimately, integrating these physically meaningful indicators with survival-based methodologies can help improve the accuracy of life-cycle predictions and support more risk-informed rehabilitation planning.

Transitioning from Heuristics to Operationally Aligned Predictive Analytics

Prioritizing the rehabilitation of buried water distribution infrastructure can be meaningfully improved by deploying data-driven method within an operationally realistic decision-making framework. By adopting a discrete three-year prediction horizon and evaluating performance using Top-(K) prioritization thresholds aligned with typical capital improvement program budgets, the proposed framework shifts failure prediction from a purely academic exercise toward a practical asset management tool. Rather than producing abstract failure probabilities, the framework generates rehabilitation priorities that directly support infrastructure investment decisions. The results demonstrate that ensemble learning methods outperform conventional heuristic-based approaches. This advantage becomes particularly pronounced as intervention scopes expand to investigate a larger portion of the water network, such as assessing the top 20% of assets, illustrating the value of integrating multiple infrastructure characteristics to identify hidden risks before deterioration becomes evident through a repeated break history.

Beyond predictive performance, this study provides insights into both the capabilities and limitations of data-driven infrastructure management. The models consistently identified a recognizable high-risk asset profile while also demonstrating the ability to capture a portion of first-time failures that would likely be overlooked by traditional experience-based prioritization methods. At the same time, the analysis highlighted the challenges associated with predicting failures for assets entering an accelerated deterioration period, particularly for material cohorts like asbestos cement pipes that exhibit rapidly evolving and non-stationary failure behaviors. On the other hand, spatial analysis revealed that actual pipe failures frequently occurred in close physical proximity to the pipes predicted to fail. This suggests that

model predictions could be strategic anchors for neighborhood-scale rehabilitation planning, where geographically coordinated replacement programs could inherently capturing nearby assets that remain difficult to predict individually.

The findings also reinforce that the long-term effectiveness of predictive asset management is fundamentally constrained by the quality and completeness of available infrastructure data. Current prediction models rely primarily on indirect indicators of deterioration, limiting their ability to fully characterize evolving pipe condition. Continued advances in condition assessment technologies, such as continuous monitoring, could offer a pathway toward richer datasets capable of supporting more physically representative predictive models. Collectively, data-driven method should be viewed not as a replacement for engineering judgment, but as a decision-support framework that complements engineering expertise, targeted condition assessment, and strategic infrastructure planning, ultimately enabling more proactive, resilient, and cost-effective management of aging water distribution systems.

Hazard-Resilient Joint Mechanics and Hydraulic Resilience

The comprehensive physical testing program fundamentally demonstrates that the seismic resilience of segmented pipelines is not governed by global material strength, but rather by the localized, kinematic behavior of the restrained joints. Across both ductile iron and iPVC systems, these connections act as highly ductile mechanical fuses, absorbing massive rotational and axial demands, localizing extreme strains, and effectively protecting the integrity of the primary pipe barrel during ground deformation. Modern hazard-resilient joints possess extraordinary reserve deformation capacity, consistently accommodating rotations and displacements well beyond manufacturer specifications.

However, the realization of this resilient behavior is profoundly sensitive to internal joint architecture, with distinct failure mechanisms governing metallic and plastic systems. In ductile iron pipelines, geometric variations, such as factory weld beads versus field, machined grooves, dictate internal load-transfer paths and alter the ultimate failure mode. This metallic failure hierarchy also scales diametrically; small-diameter systems typically yield at the pipe wall, whereas large-diameter assemblies concentrate failure at the restraint boundary through locking-segment ejection. In contrast, the structural response of iPVC systems is governed by internal gasket architecture and relative material stiffness of external restraints. The distribution of gripping teeth controls the internal load transfer, while extreme stiffness mismatches between rigid external restraints and flexible plastic pipes force premature, localized failure at the restraint boundary.

In addition, the distinction between structural failure and hydraulic failure needs to be defined carefully. While elastomeric seals can sometimes maintain watertight containment during severe plastic deformation, the inverse is also frequently observed: hydraulic failure can occur in the form of joint leakage long before any structural yielding takes place. Conversely, brittle structural fractures cause an immediate and total loss of both. Ultimately, these findings highlight the limitations of traditional design methodologies that assume structural and functional failures are coincident. To accurately predict and enhance infrastructure

survivability under extreme geohazards, future seismic design frameworks could decouple these limit states, evaluating structural integrity and hydraulic containment as independent design criteria.

Segmented Pipeline Response Under Fault-Induced Soil-Structure Interaction

The seismic response of restrained earthquake-resistant ductile iron pipe (ERDIP) systems subjected to strike-slip fault displacement is governed by staged joint kinematics and the progressive redistribution of deformation throughout the pipeline. Rather than deforming uniformly, the segmented pipeline accommodated the majority of fault movement through sequential activation of the restrained joints, beginning with the joints adjacent to the fault and subsequently transferring deformation outward following mechanical engagement. This staged response produced a corresponding transition from localized bending near the fault to a global structural response in which the entire pipeline acted as a continuous macro-curve. Ultimately, these complex kinematic interactions govern the overall capacity of the assembly, emphasizing the critical importance of evaluating restrained pipeline systems from a holistic, system-level perspective rather than relying solely on isolated component capacities.

The experimental measurements further revealed that soil-pipe interaction plays a fundamental role in load redistribution throughout fault rupture. Localized passive resistance mobilized around the enlarged joint bells provided anchoring points that controlled the evolution of system deformation, while distributed confinement along the pipe barrels progressively increased longitudinal load transfer as fault displacement accumulated. The combined effects of bell anchoring, barrel confinement, and friction-displacement coupling dictated the transition between successive stages of structural response and ultimately controlled the distribution of axial forces and bending moments along the pipeline.

Comparison between the large-scale experimental observations and reduced-order numerical simulations demonstrated that simplified system-level models are capable of reproducing the primary deformation mechanisms when key soil-pipe interaction effects are incorporated. Introducing distributed bell anchoring resistance together with axial-lateral frictional coupling improved the prediction of axial force redistribution and localized load transfer across restrained joints. Nevertheless, discrepancies in joint rotation and extension at large fault displacements indicate that representing axial and rotational joint behavior with independent spring elements limits the ability to capture the fully coupled response observed experimentally. Overall, this benchmark dataset bridges the gap between component-scale testing and full-scale buried pipeline behavior. By providing a better understanding of the complex kinematics of segmented pipeline systems, this work establishes the empirical foundation necessary for developing accurate numerical models and advancing seismic design.

10.2 Recommendations for Future Works

Building upon the findings presented throughout this dissertation, several opportunities exist to further improve the understanding, prediction, and design of resilient buried water distribution infrastructure.

1. **Enhancing Data-Driven Asset Management through Advanced Condition Monitoring**

   The predictive capability of machine learning models is fundamentally constrained by the quality and completeness of available asset information. Most utility databases primarily contain indirect indicators of deterioration, such as historical failures and environmental attributes, rather than direct measurements of structural condition. Future research should investigate the integration of advanced condition assessment technologies, such as distributed fiber optic sensing, into predictive frameworks. Transitioning from proxy variables toward direct measurements of pipe condition would enable more physically representative prediction models while supporting more informed rehabilitation planning.

2. **Further Strengthening Predictive Reliability and Stability**

   Future research could further strengthen the evaluation of data-driven pipeline failure models by drawing upon the Predictability, Computability, and Stability (PCS) framework for veridical data science [141]. Building on the predictive evaluation conducted in this dissertation, future studies could more systematically examine whether model performance, identified deterioration factors, and asset-priority rankings remain consistent under reasonable variations in data preparation and modeling choices. These variations may include alternative missing-data treatments, feature definitions, observation periods, training and testing windows, planning horizons, algorithms, and hyperparameter settings. Evaluating the stability of Recall@k performance and membership within the highest-priority asset groups would help distinguish persistent infrastructure-risk patterns from results that are sensitive to particular analytical decisions. Such analyses would further enhance the transparency, reproducibility, and reliability of data-driven decision support for utility asset management.

3. **Incorporating Temporal Deterioration into Data-Driven Frameworks**

   The current data-driven framework primarily relies on static asset attributes and historical failure records. However, deterioration is inherently dynamic, with certain material cohorts exhibiting accelerated degradation over time. Future work should investigate incorporating time-dependent variables, such as evolving failure rates, condition assessment histories, repair frequencies, pressure transients, and temporal environmental changes, into predictive models. Explicitly accounting for temporal deterioration may improve the prediction of rapidly evolving failure mechanisms that are difficult to capture using static datasets alone.

4. **Spatially Optimized Rehabilitation and Monitoring Strategies**

   The spatial analysis performed in this study demonstrated that many unpredicted failures cluster around the highest-priority pipeline segments identified by the data-driven framework. Rather than interpreting model predictions solely as individual asset rankings, future research should investigate clustering algorithms that identify high-risk rehabilitation zones. Such spatially optimized prioritization strategies could improve failure coverage by supporting neighborhood-scale replacement programs while simultaneously identifying strategic locations for permanent monitoring systems capable of tracking infrastructure deterioration over time.

5. **Standardized Evaluation of Restrained Joint Components**

   The component-level experiments demonstrated that relatively small differences in restraint geometry can fundamentally alter load-transfer mechanisms, stiffness, deformation capacity, and ultimate failure modes. Future research could expand experimental investigations to include a broader range of restrained joint systems from different manufacturers while developing standardized testing methodologies capable of consistently evaluating structural performance, hydraulic integrity, and post-damage functionality. Such standardized experimental benchmarks would facilitate objective comparison between competing restraint technologies and provide the high-quality calibration data needed for future analytical and numerical model development.

6. **Advanced Numerical Modeling of Restrained Joint Mechanics**

   The large-scale fault-crossing experiments demonstrated that the global response of segmented pipelines is governed primarily by restrained joint mechanics rather than pipe barrel behavior. Although the reduced-order models successfully reproduced the overall system response, simplified spring formulations were unable to fully capture the coupled axial–rotational behavior observed experimentally. Future studies should investigate more sophisticated joint representations, such as multi-degree-of-freedom bushing elements or constitutive models that explicitly couple extension, rotation, contact mechanics, and restraint engagement. Improved joint formulations would significantly enhance the predictive capability of system-level seismic simulations while maintaining practical computational efficiency.

7. **Large-Scale Parametric Investigation of Buried Segmented Pipeline Systems**

   The numerical models developed in this dissertation were calibrated against the dimensions of the experimental split-basin facility. While this calibration provides confidence in the simulated response, boundary constraints inevitably influence the measured behavior. Future research should extend these calibrated models to substantially longer pipeline systems through comprehensive parametric studies investigating pipe length,

joint spacing, burial conditions, fault geometry, and soil properties. Such investigations would provide a more representative understanding of full-scale field performance under permanent ground deformation.

Bibliography

[1] Stefanos A Andreou, David H Marks, and Robert M Clark. "A new methodology for modelling break failure patterns in deteriorating water distribution systems: Applications". In: *Advances in Water Resources* 10.1 (1987), pp. 11–20.

[2] Dayu Apoji et al. "Resolving Left Truncation Issues and Enabling Pipe-Specific Likelihood of Failure Models". In: *Pipelines 2024*. 2024, pp. 379–390.

[3] Krista Araica et al. "Design and Installation of Distributed Fiber Optic Sensing Technology to Monitor HDPE Pipelines at an Earthquake Fault Crossing". In: *Pipelines 2024*. 2024, pp. 561–571.

[4] Christina Argyrou et al. "Ductile iron pipeline response to earthquake-induced ground rupture". In: *Earthquake Spectra* 36.2 (2020), pp. 832–855.

[5] Gersena Banushi and Brad P Wham. "Deformation capacity of buried hybrid-segmented pipelines under longitudinal permanent ground deformation". In: *Canadian Geotechnical Journal* 58.8 (2021), pp. 1095–1117.

[6] Steven L Barfuss. "Water main break rates in the USA and Canada: A comprehensive study". In: (2023).

[7] Neal Andrew Barton et al. "Improving pipe failure predictions: Factors affecting pipe failure in drinking water networks". In: *Water research* 164 (2019), p. 114926.

[8] Neal Andrew Barton et al. "Predicting the risk of pipe failure using gradient boosted decision trees and weighted risk analysis". In: *NPJ Clean Water* 5.1 (2022), p. 22.

[9] Ramiz Beig Zali et al. "Semisupervised clustering approach for pipe failure prediction with imbalanced data set". In: *Journal of Water Resources Planning and Management* 150.2 (2024), p. 04023078.

[10] Xavier Bellagamba et al. "Development and validation of fragility functions for buried pipelines based on Canterbury earthquake sequence data". In: *Earthquake spectra* 35.3 (2019), pp. 1061–1086.

[11] Luigi Berardi et al. "Development of pipe deterioration models for water distribution systems using EPR". In: *Journal of Hydroinformatics* 10.2 (2008), pp. 113–126.

[12] Nicholas W Berty et al. "Seismic Performance Classification of Hazard Resilient iPVC Pipeline Systems". In: *Pipelines 2022*. 2022, pp. 232–241.

[13] Nicholas W. Berty et al. *Performance Assessment of iPVC Pipe and Couplings for Large Ground Movement*. Tech. rep. Prepared for the East Bay Municipal Utility District and Denver Water. Boulder, CO: Center for Infrastructure, Energy, and Space Testing, University of Colorado Boulder, Mar. 2022. URL: https://www.colorado.edu/center/ciest/sites/default/files/attached-files/performance_assessment_of_ipvc_pipe_and_couplings_v1.1.pdf (visited on 07/21/2026).

[14] Leo Breiman. "Random forests". In: *Machine learning* 45.1 (2001), pp. 5–32.

[15] Leo Breiman et al. *Classification and regression trees*. Chapman and Hall/CRC, 2017.

[16] Christopher F Brown et al. "Alphaearth foundations: An embedding field model for accurate and efficient global mapping from sparse label data". In: *arXiv preprint arXiv:2507.22291* (2025).

[17] California Department of Transportation. *California Road System: Functional Classification Database*. https://gis.data.ca.gov/datasets/caltrans::california-road-system-functional-classification. Accessed January 2024. 2024.

[18] California Department of Water Resources. *Groundwater Level Monitoring Data*. https://data.ca.gov/dataset/groundwater-levels. Accessed January 2024. 2024.

[19] California State Water Resources Control Board. *GeoTracker Database*. https://geotracker.waterboards.ca.gov/. Accessed January 2024. 2024.

[20] Gloria M Castro et al. "Corrosion Processes in Metals Buried in Sediments: Effects of Fines Content, Mineralogy, and Degree of Saturation". In: *Journal of Geotechnical and Geoenvironmental Engineering* 151.11 (2025), p. 04025134.

[21] Qingshu Chen and Pengpeng Ni. "Three-dimensional modeling of joint kinematic of ductile iron pipelines subjected to normal faulting". In: *Tunnelling and Underground Space Technology* 132 (2023), p. 104863.

[22] Tianqi Chen and Carlos Guestrin. "Xgboost: A scalable tree boosting system". In: *Proceedings of the 22nd acm sigkdd international conference on knowledge discovery and data mining*. 2016, pp. 785–794.

[23] Walter W Chen et al. "Seismic response of natural gas and water pipelines in the Ji-Ji earthquake". In: *Soil Dynamics and Earthquake Engineering* 22.9-12 (2002), pp. 1209–1214.

[24] Shih-Hung Chiu and Kenichi Soga. "Four-Point Bending Testing of 48-in. (1200-mm) Diameter Earthquake Resistant Ductile Iron Pipe (ERDIP)". In: *University of California, Berkeley* (2025).

[25] Shih-Hung Chiu, Shakhzod Takhirov, and Kenichi Soga. "Four-Point Bending Testing of 24-in.(600-mm) Diameter NS-type Ductile Iron Pipe". In: *Center for Smart Infrastructure, University of California, Berkeley. Report* 5 (2023).

[26] Shih-Hung Chiu, Shakhzod Takhirov, and Kenichi Soga. "Four-Point Bending Testing of 36-in.(900-mm) Diameter Earthquake Resistant Ductile Iron Pipe (ERDIP)". In: *University of California, Berkeley* (2025).

[27] Shih-Hung Chiu, Shakhzod Takhirov, and Kenichi Soga. "Four-Point Bending Testing of 48-in.(1200-mm) Diameter High Deflection and High Pressure Restraint (HDSS) Pipe". In: *University of California, Berkeley* (2025).

[28] Shih-Hung Chiu, Shakhzod Takhirov, and Kenichi Soga. *Tension Testing of 8-in. (200-mm) Diameter AWWA C900 DR14 iPVC Pipe*. Report. Center for Smart Infrastructure, University of California, Berkeley, 2024. DOI: 10.25350/B5C88R. URL: https://doi.org/10.25350/B5C88R.

[29] Shih-Hung Chiu, Shakhzod Takhirov, and Kenichi Soga. "Tension Testing of 8-in. (200-mm) Diameter TR-XTREMETMDuctile Iron pipe with HDSS Quiklok". In: *University of California, Berkeley* (2025).

[30] Shih-Hung Chiu et al. *Biaxial Tension Testing of 8-in. (200-mm) Diameter TR-XTREME Ductile Iron Pipe*. Tech. rep. University of California, Berkeley, Sept. 2023. DOI: 10.25350/B54S3V. URL: https://doi.org/10.25350/B54S3V.

[31] Shih-Hung Chiu et al. *Biaxial Tension Testing of 8-inch (200-mm) Diameter TR-XTREME Ductile Iron Pipe*. Report. Center for Smart Infrastructure, University of California, Berkeley, 2023. DOI: 10.25350/B54S3V. URL: https://doi.org/10.25350/B54S3V.

[32] Shih-Hung Chiu et al. "Direct Tension Testing of 8-in.(200-mm) Diameter TR-XTREMETM Ductile Iron Pipe". In: *University of California, Berkeley* (2023).

[33] Shih-Hung Chiu et al. *Direct Tension Testing of 8-inch (200-mm) Diameter TR-XTREME Ductile Iron Pipe*. Report. Center for Smart Infrastructure, University of California, Berkeley, 2023. DOI: 10.25350/B58G64. URL: https://doi.org/10.25350/B58G64.

[34] Shih-Hung Chiu et al. *Four-Point Bending Testing of 8-in. (200-mm) Diameter AWWA C900 DR14 iPVC Pipe with ReiberLok*. Report. Center for Smart Infrastructure, University of California, Berkeley, 2024. DOI: 10.25350/B5MS36. URL: https://doi.org/10.25350/B5MS36.

[35] Shih-Hung Chiu et al. *Four-point Bending Testing of 8-in. (200-mm) Diameter TR-XTREME Ductile Iron Pipe*. Report. Center for Smart Infrastructure, University of California, Berkeley, 2023.

[36] Shih-Hung Chiu et al. "Performance Evaluation of Earthquake Resistant Ductile Iron Pipe Joints Using Combined Experimental and Numerical Method". In: *Pipelines 2024*. 2024, pp. 261–271.

[37] Symeon Christodoulou and Alexandra Deligianni. "A neurofuzzy decision framework for the management of water distribution networks". In: *Water resources management* 24.1 (2010), pp. 139–156.

[38] David R Cox. "Regression models and life-tables". In: *Journal of the Royal Statistical Society: Series B (Methodological)* 34.2 (1972), pp. 187–202.

[39] Noel Cressie. *Statistics for spatial data*. John Wiley & Sons, 2015.

[40] Shamsuddin Daulat et al. "Evaluating the generalizability and transferability of water distribution deterioration models". In: *Reliability Engineering & System Safety* 241 (2024), p. 109611.

[41] Thikra Dawood et al. "Water pipe failure prediction and risk models: state-of-the-art review". In: *Canadian Journal of Civil Engineering* 47.10 (2020), pp. 1117–1127.

[42] East Bay Municipal Utility District. *Design Drawing*. Drafting Guidelines Sample Drawings. Accessed: 2026-07-21. URL: https://www5.ebmud.com/specsinternet/projects/01%20Drafting%20Guidelines/PipeHelp/SampleDwgs/DesignDrawing.pdf.

[43] Mohammad Hossein Erami et al. "Pipe–soil interaction for segmented buried pipelines subjected to dip faults". In: *Earthquake Engineering & Structural Dynamics* 44.3 (2015), pp. 403–417.

[44] Xudong Fan et al. "Machine learning based water pipe failure prediction: The effects of engineering, geology, climate and socio-economic factors". In: *Reliability Engineering & System Safety* 219 (2022), p. 108185.

[45] Juliana Ghani et al. "Factors Influencing Corrosion of Underground Metal Pipes in Clay Soil". In: *Journal of Advanced Research in Applied Sciences and Engineering Technology* 65.1 (2026), pp. 27–36. DOI: 10.37934/araset.65.1.2736. URL: https://doi.org/10.37934/araset.65.1.2736.

[46] Mónica Marcela Giraldo-González and Juan Pablo Rodríguez. "Comparison of statistical and machine learning models for pipe failure modeling in water distribution networks". In: *Water* 12.4 (2020), p. 1153.

[47] Branko Glisic and Yao Yao. "Fiber optic method for health assessment of pipelines subjected to earthquake-induced ground movement". In: *Structural Health Monitoring* 11.6 (2012), pp. 696–711.

[48] Qunfang Hu et al. "Predicting water pipe failures with graph neural networks: Integrating coupled road and pipeline features". In: *Water* 17.9 (2025), p. 1307.

[49] Y Hu and D W Hubble. "Factors contributing to the failure of asbestos cement water mains". en. In: *Canadian Journal of Civil Engineering* 34.5 (May 2007), pp. 608–621. ISSN: 0315-1468, 1208-6029. DOI: 10.1139/l06-162.

[50] Leandro Iannacone and Paolo Gardoni. "Physics-based repair rate curves for segmented pipelines subject to seismic excitations". In: *Sustainable and Resilient Infrastructure* 8.1 (2023), pp. 121–141.

[51] Cory R. Ihnotic, Jessica L. Ramos, and Brad P. Wham. *Seismic Evaluation of Hazard-Resistant Pipelines: PVC, PVCO, and iPVC Pipe with Coupling: Axial Testing Report*. Tech. rep. Prepared for the East Bay Municipal Utility District. Boulder, CO: Center for Infrastructure, Energy, and Space Testing, University of Colorado Boulder, Dec. 2019. URL: https://www.colorado.edu/center/ciest/sites/default/files/attached-files/2019_ebmud-ciest_rct_pipe_tests_final_report.pdf (visited on 07/21/2026).

[52] Carlos Jara-Arriagada and Ivan Stoianov. "Pipe breaks and estimating the impact of pressure control in water supply networks". en. In: 210 (2021), p. 107525. ISSN: 09518320. DOI: 10.1016/j.ress.2021.107525.

[53] Sang-Soo Jeon and Thomas D O'Rourke. "Northridge earthquake effects on pipelines and residential buildings". In: *Bulletin of the Seismological Society of America* 95.1 (2005), pp. 294–318.

[54] Hong Jin Jun, Jim K Park, and Cheol Ho Bae. "Economic valuation of aging water main improvements". In: *Journal of Pipeline Systems Engineering and Practice* 11.1 (2020), p. 04019053.

[55] Moera Gutu Jiru, Mesay Alemu Tolcha, and Dessalegn A Yeshanew. "Investigation of soil physicochemical effects on the corrosion of buried iron pipes". In: *Journal of Basic & Applied Sciences* 17 (2021), pp. 95–106.

[56] Golam Kabir et al. "Predicting water main failures: A Bayesian model updating approach". In: *Knowledge-Based Systems* 110 (2016), pp. 144–156.

[57] Edward L Kaplan and Paul Meier. "Nonparametric estimation from incomplete observations". In: *Journal of the American statistical association* 53.282 (1958), pp. 457–481.

[58] Michael G Katona. "Influence of soil models on structural performance of buried culverts". In: *International Journal of Geomechanics* 17.1 (2017), p. 04016031.

[59] Brent D Keil et al. "Experimental investigation of steel lap welded pipe joint performance under severe axial loading conditions in seismic or geohazard areas". In: *Pipelines 2020*. American Society of Civil Engineers Reston, VA, 2020, pp. 249–258.

[60] Robert P Kennedy, Robert A Williamson, and Andrew M Chow. "Fault movement effects on buried oil pipeline". In: *Transportation Engineering Journal of ASCE* 103.5 (1977), pp. 617–633.

[61] AJ Kettler and IC Goulter. "An analysis of pipe breakage in urban water distribution networks". In: *Canadian journal of civil engineering* 12.2 (1985), pp. 286–293.

[62] Melica Khashei, Rebecca Dziedzic, and Ehsan Roshani. "Comparative Review of Water Main Failure Prediction Models: Physical and Data-Driven Approaches". EN. In: *Journal of Water Resources Planning and Management* 151 (Nov. 2025), p. 03125003. DOI: 10.1061/JWRMD5.WRENG-6866.

[63] Yehuda Kleiner and Balvant Rajani. "Comprehensive review of structural deterioration of water mains: statistical models". In: *Urban water* 3.3 (2001), pp. 131–150.

[64] Yehuda Kleiner and Balvant Rajani. "Comprehensive review of structural deterioration of water mains: statistical models". In: *Urban Water*. Ground Water in the Environment 3.3 (2001), pp. 131–150. ISSN: 1462-0758. DOI: 10.1016/S1462-0758(01)00033-4.

[65] Kubota Co. *Assembling Procedure of 20"-40" NS Joint*. [Brochure]. 2014. URL: https://www.kubota.com/products/ironpipe/tech_info/pdf/Assembling_manual/NS-Type_Joint.pdf.

[66] Kubota Co. *Dimension Handbook*. [Brochure]. 2020. URL: https://www.kubota.com/products/ironpipe/tech_info/pdf/Dimension_handbook/NS-Type_DimensionHandbook.pdf.

[67] Avishek Kumar et al. "Using machine learning to assess the risk of and prevent water main breaks". In: *Proceedings of the 24th ACM SIGKDD International Conference on Knowledge Discovery & Data Mining*. 2018, pp. 472–480.

[68] Jerald F Lawless. *Statistical models and methods for lifetime data*. John Wiley & Sons, 2011.

[69] Weinan Li, Ram K Mazumder, and Yue Li. "Time-dependent reliability analysis of buried water distribution network: Combined finite-element and probabilistic approach". In: *ASCE-ASME Journal of Risk and Uncertainty in Engineering Systems, Part A: Civil Engineering* 7.4 (2021), p. 04021064.

[70] Laura L Lopez, Jakobus E van Zyl, and Brendon Harkness. "Analysis and modeling of pressure pipe failures in Auckland, New Zealand". In: *Journal of Water Resources Planning and Management* 150.4 (2024), p. 04024007.

[71] Luna Inc. *ODiSI 6000 Series Optical Distributed Sensor Interrogators [Data Sheet]*. Accessed: 2026-05-11. Luna Inc. 2022. URL: %5Curl%7Bhttps://lunainc.com/sites/default/files/assets/files/data-sheet/Luna%20ODiSI%206000%20Data%20Sheet.pdf%7D.

[72] JM Makar. "A preliminary analysis of failures in grey cast iron water pipes". In: *Engineering failure analysis* 7.1 (2000), pp. 43–53.

[73] Á Martínez-Codina et al. "Pressure as a predictor of occurrence of pipe breaks in water distribution networks". In: *Urban Water Journal* 13.7 (2016), pp. 676–686.

[74] Ram K Mazumder et al. "Asset management decision support model for water distribution systems: impact of water pipe failure on road and water networks". In: *Journal of Water Resources Planning and Management* 147.5 (2021), p. 04021022.

[75] Vasileios E Melissianos et al. "Numerical evaluation of the effectiveness of flexible joints in buried pipelines subjected to strike-slip fault rupture". In: *Soil Dynamics and Earthquake Engineering* 90 (2016), pp. 395–410.

[76] Homayoun Motiee and Mohsen Sattari. "Pipe Failure Prediction in Water Distribution Networks Using Interpretable Machine Learning under Imbalanced and Recurrent Failure Conditions". In: *Water Resources Management* 40.5 (2026), p. 202.

[77] Kabwe Mulenga et al. "Time-dependent reliability assessment of corroded metal structures based on Physics of Failure (PoF): With a case study of cast iron pipe". In: *Engineering Failure Analysis* 141 (2022), p. 106710.

[78] Engineering National Academies of Sciences, Medicine, et al. "Electrochemical Test Methods to Evaluate the Corrosion Potential of Earthen Materials". In: (2021).

[79] Nathan Mortimore Newmark. "Pipeline design to resist large fault displacement". In: *Proceedings of US national conference on earthquake engineering*. 1975, pp. 416–425.

[80] Hung Nguyen et al. "Joint maintenance planning of deteriorating co-located road and water infrastructures with interdependencies". In: *Reliability Engineering & System Safety* 226 (2022), p. 108678.

[81] P Ni, ID Moore, and WA Take. "Distributed fibre optic sensing of strains on buried full-scale PVC pipelines crossing a normal fault". In: *Géotechnique* 68.1 (2018), pp. 1–17.

[82] Michael Nishiyama and Yves Filion. "Review of statistical water main break prediction models". In: *Canadian Journal of Civil Engineering* 40.10 (2013), pp. 972–979.

[83] TD O'Rourke, Masanori Hamada, et al. "Large ground deformations and their effects on lifeline facilities: 1971 San Fernando earthquake". In: *Case studies liquefaction and lifeline performance during past earthquakes: United states case studies*. 1992, pp. 1–85.

[84] Thomas D O'ROURKE. "Geohazards and large, geographically distributed systems". In: *Géotechnique* 60.7 (2010), pp. 505–543.

[85] Thomas D O'Rourke et al. "Earthquake response of underground pipeline networks in Christchurch, NZ". In: *Earthquake Spectra* 30.1 (2014), pp. 183–204.

[86] Thomas D. O'Rourke, Jong-Keun Jung, and Christos Argyrou. "Underground pipeline response to earthquake-induced ground deformation". In: *Soil Dynamics and Earthquake Engineering* 91 (2016), pp. 272–283.

[87] Thomas D. O'Rourke, John Strait, and Connor Atkins. *Performance Evaluation of iPVC Fitting with Turner Lock Gasket*. Tech. rep. Prepared for PPI Pipe. Ithaca, NY: School of Civil and Environmental Engineering, Cornell University, Aug. 2022. URL: https://cpb-us-w2.wpmucdn.com/sites.coecis.cornell.edu/dist/a/38/files/2022/09/001-27August22-iPVC-Fitting-Report.pdf (visited on 07/21/2026).

[88] Thomas D. O'Rourke et al. *Performance Evaluation of Aqua-Pipe under Earthquake-Induced Ground Deformation*. Tech. rep. Project sponsor: Sanexen. School of Civil and Environmental Engineering, Cornell University, 2021.

[89] Frank W O'Callaghan and NZ Iplex Pipelines. "Pipeline performance experiences during seismic events in New Zealand, 1987 to 2015". In: *Water New Zealand Annual Conference*. 2015.

[90] Thomas D O'Rourke, Jai K Jung, and Christina Argyrou. "Underground pipeline response to earthquake-induced ground deformation". In: *Soil Dynamics and Earthquake Engineering* 91 (2016), pp. 272–283.

[91] Keita Oda, Shozo Kishi, and Masakatsu Miyajima. "The pipeline design method against large fault displacement". In: *Pressure Vessels and Piping Conference*. Vol. 57034. American Society of Mechanical Engineers. 2015, V008T08A017.

[92] Keita Oda et al. "Verification of design method of pipeline crossing fault with earthquake resistant ductile Iron pipe using large-scale split-box test". In: *The 10th JWWA/ WRF/ CTWWA water system seismic conference, Tainan, Taiwan*. 2017.

[93] C Pariya-Ekkasut et al. "Direct Tension and Split Basin Testing of 6-in.(150-mm)-Diameter Kubota Earthquake Resistant Ductile Iron Pipe". In: *School of Civil and Environmental Engineering, Cornell University* (2016).

[94] C Pariya-Ekkasut et al. "Four-Point Bending Testing of 6-in.(150-mm), 12-in.(300-mm), and 16-in.(400-mm)-Diameter Kubota Earthquake Resistant Ductile Iron Pipes". In: *School of Civil and Environmental Engineering, Cornell University, Hollister Hall, Ithca, NY* 14853 (2017).

[95] Chalermpat Pariya-Ekkasut et al. *Four-Point Bending and Direct Tension Testing of Twelve-Inch TR-XTREME Pipe Joint*. Tech. rep. Prepared for US Pipe, LLC. Ithaca, NY: School of Civil and Environmental Engineering, Cornell University, Sept. 2015. URL: https://lifelines.cee.cornell.edu/projects/ (visited on 07/21/2026).

[96] Chalermpat Pariya-Ekkasut et al. *Hazard Resilience Evaluation of US Pipe Ductile Iron TR-XTREME Joints: 4–16 in. (100–400 mm) Diameter Pipe*. Tech. rep. Prepared for US Pipe, LLC. Ithaca, NY: School of Civil and Environmental Engineering, Cornell University, Jan. 2016. URL: https://lifelines.cee.cornell.edu/projects/ (visited on 07/21/2026).

[97] Chanachai Pariya-Ekkasut et al. *American Earthquake Joint System for Resistance to Earthquake-Induced Ground Deformation*. Tech. rep. Project sponsor: American Cast Iron Pipe Company. School of Civil and Environmental Engineering, Cornell University, Jan. 2017.

[98] Chanachai Pariya-Ekkasut et al. *Direct Tension and Split Basin Testing of 6-in. (150-mm)-Diameter Kubota Earthquake Resistant Ductile Iron Pipe*. Tech. rep. Project sponsor: Kubota Corporation. School of Civil and Environmental Engineering, Cornell University, Feb. 2016.

[99] Chanachai Pariya-Ekkasut et al. *Evaluation of McWane Seismic Flex Coupling for Resistance to Earthquake-Induced Ground Deformation*. Tech. rep. Addendum issued August 2018; project sponsor: McWane Ductile. School of Civil and Environmental Engineering, Cornell University, Apr. 2018.

[100] D. Price et al. *Performance Evaluation of iPVC Pipe under Earthquake-Induced Ground Deformation*. Tech. rep. Project sponsor: Pyungwha Pipe Industry Co., Ltd. School of Civil and Environmental Engineering, Cornell University, Dec. 2018.

[101] B Rajani, C Zhan, and S Kuraoka. "Pipe soil interaction analysis of jointed water mains". In: *Canadian Geotechnical Journal* 33.3 (1996), pp. 393–404. ISSN: 0008-3674. DOI: 10.1139/t96-061.

[102] B Rajani, C Zhan, and SJCGJ Kuraoka. "Pipe soil interaction analysis of jointed water mains". In: *Canadian Geotechnical Journal* 33.3 (1996), pp. 393–404.

[103] Balvant Rajani and Jon Makar. "A methodology to estimate remaining service life of grey cast iron water mains". In: *Canadian Journal of Civil Engineering* 27.6 (2000), pp. 1259–1272.

[104] Jessica L Ramos et al. "Biaxial Loading of Jointed Thermoplastic Pipelines for Experimental Seismic Assessment". In: *Pipelines 2024*. 2024, pp. 585–594.

[105] Jessica L. Ramos et al. *Axial Capacity of C900 PVC Pipe with Reinforced Gasketed Joints*. Final Report. Prepared for Denver Water. Boulder, CO: Center for Infrastructure, Energy, and Space Testing, University of Colorado Boulder, Aug. 2020. URL: https://www.colorado.edu/center/ciest/media/9 (visited on 07/21/2026).

[106] Gema Sakti Raspati et al. "A risk-based approach in rehabilitation of water distribution networks". In: *International Journal of Environmental Research and Public Health* 19.3 (2022), p. 1594.

[107] Md Shahin Reza et al. "Enhanced seismic performance of non-standard bolted flange joints for petrochemical piping systems". In: *Journal of Loss Prevention in the Process Industries* 30 (2014), pp. 124–136.

[108] Andreas Scheidegger, Joao P Leitao, and Lisa Scholten. "Statistical failure models for water distribution pipes–A review from a unified perspective". In: *Water research* 83 (2015), pp. 237–247.

[109] Andreas Scheidegger, João P. Leitão, and Lisa Scholten. "Statistical failure models for water distribution pipes – A review from a unified perspective". In: *Water Research* 83 (Oct. 2015), pp. 237–247. ISSN: 0043-1354. DOI: 10.1016/j.watres.2015.06.027.

[110] Ibrahim Abdelfadeel Shaban, Abdelrahman EE Eltoukhy, and Tarek Zayed. "Systematic and scientometric analyses of predictors for modelling water pipes deterioration". In: *Automation in Construction* 149 (2023), p. 104710.

[111] Bryan Simpson, Neil A Hoult, and Ian D Moore. "Distributed sensing of circumferential strain using fiber optics during full-scale buried pipe experiments". In: *Journal of Pipeline Systems Engineering and Practice* 6.4 (2015), p. 04015002.

[112] Brett Snider and Edward A McBean. "Improving time to failure predictions for water distribution systems using extreme gradient boosting algorithm:(049)". In: *Wdsa/ccwi joint conference proceedings*. Vol. 1. 2018.

[113] Brett Snider and Edward A McBean. "Improving urban water security through pipe-break prediction models: Machine learning or survival analysis". In: *Journal of Environmental Engineering* 146.3 (2020), p. 04019129.

[114] Kenichi Soga and Linqing Luo. "Distributed fiber optics sensors for civil engineering infrastructure sensing". In: *Journal of Structural Integrity and Maintenance* 3.1 (2018), pp. 1–21.

[115] Alison M St. Clair and Sunil Sinha. "State-of-the-technology review on water pipe condition, deterioration and failure rate prediction models!" In: *Urban Water Journal* 9.2 (2012), pp. 85–112.

[116] Harry E. Stewart et al. *Hazard Resilience Testing of US Pipe Ductile Iron TR-XTREME Pipe Joints*. Tech. rep. Prepared for US Pipe, LLC. Ithaca, NY: School of Civil and Environmental Engineering, Cornell University, Feb. 2015. URL: https://lifelines.cee.cornell.edu/projects/ (visited on 07/21/2026).

[117] Harry E. Stewart et al. *Hazard Resilience Testing of US Pipe Ductile Iron TR-XTREME Pipe Joints*. Tech. rep. Project sponsor: US Pipe, LLC. School of Civil and Environmental Engineering, Cornell University, 2015.

[118] Harry E. Stewart et al. *Task 1: Material Testing of Bionax Pipe and Joints*. Tech. rep. Prepared for IPEX Management, Inc. Ithaca, NY: School of Civil and Environmental Engineering, Cornell University, Oct. 2013. URL: https://lifelines.cee.cornell.edu/files/2017/04/131021-PVC0-Task-1-Report-1h0um4t.pdf (visited on 07/21/2026).

[119] Harry E. Stewart et al. *Task 2: Four-Point Bending of Bionax Pipe and Pipe Joints*. Tech. rep. Prepared for IPEX Management, Inc. Ithaca, NY: School of Civil and Environmental Engineering, Cornell University, Dec. 2013. URL: https://lifelines.cee.cornell.edu/files/2017/04/131213-PVC0-Task-2-Report-2h3bwzr.pdf (visited on 07/21/2026).

[120] Harry E. Stewart et al. *Task 3: Large-Scale Testing of Fault Rupture Effects on Bionax Pipe and Pipe Joints*. Tech. rep. Project sponsor: IPEX Management, Inc. School of Civil and Environmental Engineering, Cornell University, Oct. 2013.

[121] Zheng Su, Ying Wu, and Jingkun Wang. "Dynamic Behavior of Buried PE Pipelines under Stochastic Track Loads: A Vehicle–Road–Pipe Coupled Modeling Approach". In: *Journal of Pipeline Systems Engineering and Practice* 17.2 (2026), p. 04026007.

[122] Alex K Tang. *Izmit (Kocaeli), Turkey, earthquake of August 17, 1999 including Duzce earthquake of November 12, 1999: lifeline performance*. Vol. 17. ASCE Publications, 2000.

[123] Selcuk Toprak et al. "Impact of Seismic Geohazards on water supply systems and pipeline performance: Insights from the 2023 Kahramanmaras Earthquakes". In: *Engineering Geology* 340 (2024), p. 107681.

[124] U.S. Department of Agriculture, Natural Resources Conservation Service. *Soil Survey Geographic (SSURGO) Database*. https://www.nrcs.usda.gov/resources/data-and-reports/ssurgo. Accessed January 2024. 2024.

[125] U.S. Geological Survey. *Quaternary Fault and Fold Database of the United States*. https://www.usgs.gov/programs/earthquake-hazards/faults. Accessed January 2024. 2024.

[126] U.S. Pipe. *HDSS High Deflection, High Pressure Restraint Pipe [Brochure]*. 2023. URL: https://www.uspipe.com/wp-content/uploads/USP_02_HDSS_Submittal_Digital.pdf.

[127] U.S. Pipe. *TR XTREME Brochure*. Accessed: 2026-05-13. 2020. URL: https://www.uspipe.com/wp-content/uploads/2020/12/USP_TR_XTREME_Brochure_03-03-2020-for-web.pdf.

[128] U.S. Pipe. *TR XTREME Seismic Joint Pipe [Brochure]*. Accessed: 2026-05-11. U.S. Pipe. 2024. URL: %5Curl%7Bhttps://www.uspipe.com/wp-content/uploads/USP_04_TRXTREME_SubmittalBook_2024_digital.pdf%7D.

[129] Leon Ru-Liang Wang and Yaw-Hue1 Yeh. "A refined seismic analysis and design of buried pipeline for fault movement". In: *Earthquake engineering & structural dynamics* 13.1 (1985), pp. 75–96.

[130] Muhammad Wasim et al. "Factors influencing corrosion of metal pipes in soils". In: *Environmental Chemistry Letters* 16.3 (2018), pp. 861–879.

[131] Waloddi Weibull. "A statistical distribution function of wide applicability". In: *Journal of applied mechanics* (1951).

[132] BP Wham et al. "Water supply damage caused by the 2016 Kumamoto Earthquake". In: *Lowland Technology International* 19.3 (2017), pp. 165–174.

[133] Brad P. Wham et al. *Large-Scale Testing of Bionax SR PVCO Pipe with Extended Bell Joints*. Tech. rep. Project sponsor: IPEX Management, Inc. School of Civil and Environmental Engineering, Cornell University, Dec. 2017.

[134] Brad P. Wham et al. *Large-Scale Testing of JFE Steel Pipe Crossing Faults: Testing of SPF Wave Feature to Resist Fault Rupture*. Tech. rep. Project sponsor: JFE Engineering Corporation. School of Civil and Environmental Engineering, Cornell University, Dec. 2016.

[135] Brad Parker Wham and Thomas Denis O'Rourke. "Jointed pipeline response to large ground deformation". In: *Journal of Pipeline Systems Engineering and Practice* 7.1 (2016), p. 04015009.

[136] Daniel Winkler et al. "Pipe failure modelling for water distribution networks using boosted decision trees". In: *Structure and Infrastructure Engineering* 14.10 (2018), pp. 1402–1411.

[137] Xiaojian Xie et al. "Numerical modeling of buried HDPE pipelines subjected to strike-slip faulting". In: *Journal of Earthquake Engineering* 15.8 (2011), pp. 1273–1296.

[138] Hao Xu and Sunil K Sinha. "Modeling pipe break data using survival analysis with machine learning imputation methods". In: *Journal of Performance of Constructed Facilities* 35.5 (2021), p. 04021071.

[139] Hao Xu and Sunil K. Sinha. "Modeling Pipe Break Data Using Survival Analysis with Machine Learning Imputation Methods". EN. In: *Journal of Performance of Constructed Facilities* 35.5 (Oct. 2021), p. 04021071. ISSN: 1943-5509. DOI: 10.1061/(ASCE)CF.1943-5509.0001649.

[140] Shridhar Yamijala, Seth D Guikema, and Kelly Brumbelow. "Statistical models for the analysis of water distribution system pipe break data". In: *Reliability Engineering & System Safety* 94.2 (2009), pp. 282–293.

[141] Bin Yu and Karl Kumbier. "Veridical Data Science". In: *Proceedings of the National Academy of Sciences* 117.8 (2020), pp. 3920–3929. DOI: 10.1073/pnas.1901326117.

[142] Janez Zavašnik, Andreja Šestan, and Srečo Škapin. "Degradation of asbestos–Reinforced water supply cement pipes after a long-term operation". In: *Chemosphere* 287 (2022), p. 131977.

[143] Qinglai Zhang et al. "Mechanical behaviour of a ground deformation-resistant segmented ductile iron pipeline under biaxial tension force". In: *Available at SSRN 6583525* ().

[144] Qinglai Zhang et al. "The role of locking segments on an earthquake-resistant segmented ductile iron water pipeline joint behavior under tension and bending". In: *Tunnelling and Underground Space Technology* 158 (2025), p. 106378.

[145] Bin Zhao and Fabio Taucer. "Performance of infrastructure during the May 12, 2008 Wenchuan earthquake in China". In: *Journal of Earthquake Engineering* 14.4 (2010), pp. 578–600.